# MODERN FLUID DYNAMICS

## Second Edition

Clement Kleinstreuer

CRC Press
Taylor & Francis Group

# Modern Fluid Dynamics
Second Edition

Taylor & Francis
Taylor & Francis Group
http://taylorandfrancis.com

# Modern Fluid Dynamics
## Second Edition

By
Clement Kleinstreuer


CRC Press
Taylor & Francis Group
Boca Raton London New York

CRC Press is an imprint of the
Taylor & Francis Group, an **informa** business

CRC Press
Taylor & Francis Group
6000 Broken Sound Parkway NW, Suite 300
Boca Raton, FL 33487-2742



Printed on acid-free paper

International Standard Book Number-13: 978-1-138-19810-4 (Hardback)

*To my family,*

*Christin, Joshua, Nicole, and Andrew*

Taylor & Francis
Taylor & Francis Group
http://taylorandfrancis.com

# *Contents*

# *Preface*

The second edition of *Modern Fluid Dynamics* (the first edition was published by Springer) has been thoroughly revised and updated based on multi-year feedback from graduate students as well as suggestions from colleagues. Specifically, the previous three book parts have been reduced to a new, two-part, streamlined and reorganized version with a now even stronger emphasis on the fundamentals, illustrative examples, and computer applications. As it is a text for first-year graduate students and advanced seniors, the sections on compressible flow and compartmental modeling have been deleted to provide extra space for more appropriate topics, such as scale analysis, non-Newtonian fluid flow, surface coating, convection heat transfer, fluid-particle dynamics, microfluidics, and microfluidics, and computational fluid dynamics applications. Thus, the first part of the new edition, that is, Chapters 1 through 3, is now easier to read, leading with the sample problem solutions and associated discussions to an enhanced understanding of the principles of fluid dynamics. With the new knowledge base gained and skill level acquired from studying Part A in conjunction with Appendix I, modern fluid dynamics applications are discussed in Chapters 4 through 8 of the new Part B. After basic introductions to real-world topics, such as mixture flows, lubrication systems, surface coating, microfluidics, and fluid–structure interactions, representative sample applications are discussed. Part B concludes with Chapter 9 on mathematical modeling and computer simulation with examples, while Chapter 10 deals with the development and execution of *course projects*. Specifically, guidelines are provided for project report writing, followed by lists of tutorial and numerical projects, both categories being illustrated with insightful project reports. The necessary background material in engineering math is reviewed in Appendix I, that is, tensor analysis, integration/differentiation, special integrals, ordinary differential equations, and all conservation laws. Appendix I now also contains OpenFOAM commands, some of which have been used in course-project solutions given in Chapters 9 and 10. Appendix II contains conversion factors and fluid properties as well as the Moody chart and drag coefficients for spheres and cylinders. While traditionally, fluid mechanics books present the material in progressive order, that is, employing an *inductive* approach from the simple to the more difficult, the present text adopts more of a *deductive* approach. Indeed, understanding the derivation of the basic equations and then formulating the system-specific equations with suitable boundary conditions are two key steps for proper problem solutions. *Understanding of the fundamentals and independent application skills are the main learning objectives.* For students to gain confidence and independence, an instructor may want to be less of a "sage on the stage" and more of a "guide on the side." Specifically, engaging students in "white-board performances," that is, interesting problem solutions, tutorial presentations of specific topics of Part B, and selected journal articles is highly recommended. Requiring an in-depth course project and its associated report (see Chapter 10) may be a crowning assignment or may even replace the final exam. *The need for the proposed text evolved primarily out of industrial demands and post-graduate expectations.*

Clearly, industry and government recognized that undergraduate fluid mechanics education had to change measurably due to the availability of powerful software that runs on workstations and because of the shift toward more complicated and interdisciplinary tasks that tomorrow's engineers are facing (see NAS "The Engineers of 2020" at http://national-academics.org). Also, an increasing number of engineering firms recruit only MS- and PhD-holders, wondering whether BS-degree engineers are able to follow technical directions, let alone build mathematical models and consequently analyze and improve/

design devices related to fluid dynamics. In the academic environment, a fine knowledge base and solid skill levels in modern fluid dynamics are important for success in more advanced thermal sciences courses, in emerging departmental programs, and for new thesis/dissertation requirements responding to future educational needs. Building on introductory courses in thermodynamics, fluid mechanics, heat transfer, and solid mechanics as prerequisites as well as on a junior-level math background, a differential approach is most insightful to teach the fundamentals in fluid mechanics and convection heat transfer. Pedagogical elements include a 50:50 physics-mathematics approach when introducing new material, illustrating concepts, showing flow visualizations, and solving problems. The problem solution format strictly follows the sequence System Sketch, Assumptions, and Method—**before** starting the solution phase, which consists of symbolic math model development (see Appendix I), numerical solution, graphs, and comments on "physical insight." After some illustrative examples, most solved text examples have the same level of difficulty as suggested assignments and/or exam problems. The ultimate goals are that the more serious student will be able to solve basic fluid dynamics problems *independently*, provide *physical insight*, and suggest, via a course project, system *design improvements*. All figures appearing in this book will be hosted on the CRC Press website: www.crcpress.com/9781138198104. In addition, an updated and expanded solutions manual, previously authored by post-doc Dr. Jie Li and now redeveloped by Curtis Promislow and Sriram Chari, will be available later on for instructors adopting the textbook.

The new edition could not have been completed without the superb assistance provided by Curtis Promislow in terms of text and equation typing, finalizing figures and tables, and manuscript formatting. Also, the fine project contributions from Dr. Zelin (Luke) Xu and Sriram Chari, as well as the professional help from editor Jonathan Plant and his team, are gratefully acknowledged.

For technical correspondence, please contact the author via e-mail (ck@ncsu.edu).

**Clement Kleinstreuer**
*North Carolina State University*
*Raleigh, NC*

# *Author*

**Clement Kleinstreuer** is a professor in the mechanical and aerospace engineering and biomedical engineering departments at North Carolina State University in Raleigh, NC. He received his Dipl. Ing degree at the Technical University, Munich; his MS at Stanford University; and his PhD at Vanderbilt University. He also serves as an adjunct professor in the Department of Surgery at the University of North Carolina School of Medicine in Chapel Hill, NC. He has also served as an assistant professor at Rensselaer Polytechnic Institute (Troy, NY) and as an adjunct professor at the University of Canterbury in Christchurch, New Zealand.

Taylor & Francis
Taylor & Francis Group
http://taylorandfrancis.com

# Part A

# Fluid Dynamics Fundamentals with Applications

Part A consists of the first three chapters which discuss the essentials in fluid dynamics, highlighted with some introductory applications. Specifically, Chapters 1 and 2 revisit the basic concepts learned in undergraduate fluid mechanics with some extensions, in preparation for Part B. Chapter 3 then focuses on internal versus external laminar flows as well as turbulent boundary layer and tubular flows.

Taylor & Francis
Taylor & Francis Group
http://taylorandfrancis.com

# 1

# *Review of Basic Concepts*

"Fluid dynamics" implies momentum transfer, that is, fluid flow and associated forces described by vector equations, as well as convective heat transfer and species-mass transfer described by scalar transport equations. Specifically, this chapter reiterates some basic definitions and continuum mechanics concepts, with an emphasis on how to describe standard fluid flow phenomena. Most of the material of Part A is also covered in undergraduate fluid mechanics and heat transfer texts. After refreshing his/her knowledge base, the student should solve the assigned Homework Problems *independently* (see Section 1.5) in conjunction with Appendix I. Please see Table 1.1 for acquiring good study habits. While a good grade is a primary objective, a thorough understanding of the subject matter and mastery in solving engineering problems should be the main focus. Once that is achieved, a good grade comes as a natural reward.

It should be noted that the material of Part A is an extension of the introductory chapters of the author's *Biofluid Dynamics* text (CRC Press, 2006; with permission).

## 1.1 The Continuum Mechanics Hypothesis

Fundamental to the description of all transport phenomena are the conservation laws, concerning mass, momentum, and energy, as well as their applications to continua. For example, Newton's second law of motion holds for both molecular dynamics, that is, interacting molecules, and for continua, such as air, water, plasma, and oils. *Thus, fluid flow fields are assumed to be continua as long as the local material properties can be defined as averages computed over material elements/volumes sufficiently large when compared with microscopic length scales of the fluid, but small relative to the macroscopic structure*. Variations in fluid flow quantities can be described with differential equations. The *continuum mechanics method* is an effective tool to physically explain and mathematically describe various transport phenomena without detailed knowledge of their internal nano/micro structures. Specifically, fluids are treated as continuous media characterized by certain field quantities associated with the internal structure, such as density, viscosity, temperature, and velocity. In summary, continuum mechanics deals with three aspects:

- *Kinetics*: That is, fluid element motion regardless of the cause
- *Dynamics*: That is, the origin and impact of forces and fluxes generating fluid motion and waste heat; for example, the stress tensor, heat flux vector, and entropy
- *Balance principles:* That is, the mass, momentum, and energy conservation laws

Also, all flow properties are in *local thermodynamic equilibrium*, implying that the macroscopic quantities of the flow field can adjust swiftly to their surroundings. This local

**TABLE 1.1**

Suggestions for Students Interested in Understanding Fluid Dynamics and Acquiring a Sufficient Skill Level

*1. Review Topics*

*Eng. Sciences* (Prerequisites)

- Problem solution FORMAT: System sketch, assumptions, method; solution, properties, results; graphing with comments
- Differential force, energy and mass balances (i.e., free-body diagram, control volume analysis, etc.)
- Symbolic math analyses, where # of unknowns ≙ # of equations

Math Background (see Appendix I)

- Algebra, tensor calculus, and Taylor series expansion
- Calculus and functional analysis
- Graphing of profiles and correlations
- Surface and volume integrals
- Differential equations subject to inlet/boundary conditions

*2. Preparation*

- Study book chapters, lecture notes, and problem assignments
- Learn from solved book examples, lecture demos, and review problem solutions (*work independently*!)
- Practice graphing of results and drawing of velocity or temperature profiles and streamlines
- Ask questions (in-class, after class, office, email)
- Perform "special assignments" in-class, such as White-board Performance, lead in small-group work, etc.
- Solve old test problems with your group
- Solve test-caliber questions and problems: well-paced and INDEPENDENTLY

*3. Participation*

- Enrich your knowledge base and sharpen your communication skills via presentations
- Understand some fluid mechanics topics in more depth from exploring flow visualizations as well as doing tutorial or computer project work and report writing

adjustment to varying conditions is rapidly achieved if the fluid has very small characteristic length and time scales of molecular collisions when compared with the macroscopic flow variations. However, as the channel (or tube) size, typically indicated by the hydraulic diameter $D_h$, is reduced to the *micro- or even the nano-scale*, the surface-area-to-volume ratio becomes larger, because $A/V \sim D_h^{-1}$. Thus, as discussed in Chapter 7, wall-surface effects may become important; for example, wall-roughness and surface forces as well as discontinuities in gas velocity and temperature relative to the wall have to be dealt with. Furthermore, when flow microconduits are short, as in microscale cooling devices and microelectromechanical systems (MEMS), nonlinear entrance effects dominate, while for long microconduits, viscous heating (for liquids) or compressibility (for gases) may become a factor. In such cases, the validity of the continuum mechanics assumption may have to be re-examined (see Chapter 7).

As implied, any flow field can be described at either the molecular/microscopic or the macroscopic level. The *microscopic* or molecular models consider the position, velocity, and state of every molecule of a single fluid or multiple "fluids" at all times. Averaging discrete-particle information (i.e., position, velocity, and state) over a local fluid volume yields macroscopic quantities, for example, the velocity field $\vec{\mathbf{v}}(\vec{\mathbf{x}}, t)$, at any location in the flow. The advantages of the molecular approach include general applicability, that is, no need for submodels (e.g., for the stress tensor, heat flux, turbulence, wall conditions, etc.), and an absence of numerical instabilities (e.g., due to steep flow field gradients). However, considering myriads of molecules, atoms, and nanoparticles requires enormous computer resources, and hence, only simple channel or stratified flows with a finite number of interacting molecules (assumed to be solid spheres) can be presently analyzed. For example,

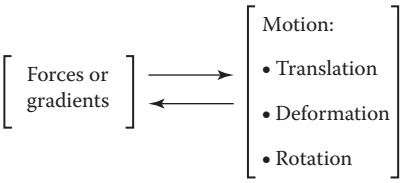


(a) Cause-and-effect dynamics

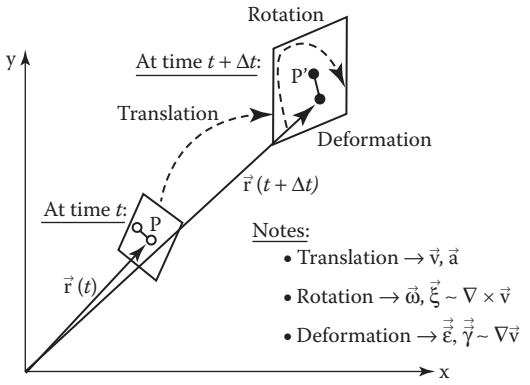


(b) Kinematics of a 2-D fluid element (Lagrangian frame)

**FIGURE 1.1**
Dynamics and kinematics of fluid flow in 2-D.

in a 1-mm cube there are about 34 billion water molecules (about a million air molecules at STP), which makes molecular dynamics simulation prohibitive, but on the other hand, intuitively validates the continuum assumption (see Kleinstreuer, 2006).

Here, the overall goal is to find and analyze on the *macro-scale* the interactions between *fluid forces*, for example, pressure, gravity/buoyancy, drag/friction, inertia, and so on, and *fluid motion*, that is, the velocity vector field and pressure distribution from which everything else can be directly obtained or derived (see Figure 1.1a,b). In turn, scalar transport equations, that is, convection mass and heat transfer, can be solved based on the velocity field to obtain critical magnitudes and gradients (or fluxes) of species concentrations and temperatures.

*In summary, unbalanced surface/body forces and gradients cause motion in the form of fluid translation, rotation, and/or deformation, while temperature or concentration gradients cause mainly heat or species-mass transfer.* Note that flow visualization videos plus web-based university sources provide fascinating videos of complex fluid flow, temperature, and species concentration fields (see Section 1.5.1 assignments).

## 1.2 Definitions, Fluid Properties, and Constitutive Equations

### 1.2.1 Definitions

Elemental to mass/momentum/energy transport phenomena is the description of fluid flow, that is, the equation of motion, which is also called the *momentum transfer equation*, in conjunction with the continuity equation, which is a statement of fluid-mass conservation.

For non-isothermal problems, the heat transfer equation, describing energy conservation, is also necessary. The momentum equation is an application of Newton's second law, $\sum \vec{\mathbf{F}}_{\text{ext.}} = m\vec{\mathbf{a}}$, which Newton postulated for the motion of a particle. For most engineering applications, the equation of motion is nonlinear but independent of the mass and heat transfer equations; that is, fluid properties are not measurably affected by changes in solute concentration and temperature. Hence, the major emphasis in Chapter 1 is on the description, solution, and understanding of the physics of fluid flow. Here is a review of a few definitions:

- A *fluid* is an assemblage of gas or liquid molecules that deforms continuously; that is, it *flows* under the application of a shear stress. Note, solids do not behave like that; but what about borderline cases, that is, the behavior of materials such as jelly, grain, sand, and so on?
- Key fluid properties are *density* $\rho$, *dynamic viscosity* $\mu$, *species diffusivity D*, *heat capacities* $c_p$ *and* $c_v$, *and thermal conductivity k.* In general, all six are temperature and species concentration dependent. Most important is the viscosity (see also kinematic viscosity $\nu \equiv \mu/\rho$), representing frictional (or drag) effects. Certain fluids, such as polymeric liquids, blood, foodstuffs, latex paints, and so on, are also shear-rate dependent, and are hence called *non-Newtonian fluids* (see Section 4.2).
- *Flows* can be categorized into:

| **Internal flows** | **External flows** |
|---|---|
| • Oil, air, water, or steam in pipes and inside devices<br>• Blood in arteries/veins or air in lungs<br>• Water in rivers or canals | • Air past vehicles, buildings, and planes<br>• Water past pillars, submarines, and so on<br>• Polymer coating on solid surfaces |

- *Driving* forces for fluid flow include gravity, pressure drops or gradients, temperature differences or gradients, surface tension, electromagnetic forces, and so on.
- Any fluid flow is described by its *velocity* and *pressure* fields, which are the key unknowns in the momentum equation. The velocity vector of a fluid element can be written in terms of its three scalar components:

$$\vec{v} = u\hat{i} + v\hat{j} + \omega\hat{k} \qquad < \text{rectangular coordinates} > \tag{1.1a}$$

or

$$\vec{\mathbf{v}} = v_r\hat{e}_r + v_\theta\hat{e}_\theta + v_z\hat{e}_z \quad < \text{cylindrical coordinates} > \tag{1.1b}$$

$$\vec{\mathbf{v}} = v_r\hat{e}_r + v_\theta\hat{e}_\theta + v_\phi\hat{e}_\phi \quad < \text{spherical coordinates} > \tag{1.1c}$$

Its total time derivative is the fluid-element acceleration:

$$\frac{d\vec{\mathbf{v}}}{dt} \cong \frac{D\vec{\mathbf{v}}}{Dt} = \vec{\mathbf{a}}_{\text{total}} = \vec{\mathbf{a}}_{\text{local}} + \vec{\mathbf{a}}_{\text{convective}} \tag{1.2}$$

where $D/Dt = \partial/\partial t + (\vec{v}\cdot\nabla)$ in Equation 1.2 is also known as the *Stokes*, *material*, or *substantial time derivative*, following the fluid element in motion (see Appendix AI.2.1).

- *Streamlines* for the visualization of flow fields are lines to which the local velocity vectors are tangential. For example, for steady two-dimensional (2-D) flow:

$$\frac{dy}{dx} = \frac{v}{u} \tag{1.3}$$

  where the 2-D velocity components $\vec{\mathbf{v}} = (u, v, 0)$ have to be given to obtain, after integration, the streamline equation $y(x)$.
- Forces acting on a fluid element can be split into *normal* and *tangential forces* leading to pressure and normal/shear stresses. Clearly, on any surface element:

$$p \text{ or } \tau_{\text{normal}} = \frac{F_{\text{normal}}}{A_{\text{surface}}} \tag{1.4}$$

while

$$\tau_{\text{shear}} = \frac{F_{\text{tangential}}}{A_{\text{surface}}} \tag{1.5}$$

As Stokes postulated, the stress can be viewed as a linear derivative; that is, $\vec{\vec{\tau}} \sim \nabla\vec{\mathbf{v}}$ (see Appendix AI.1.2), where relative motion of viscous fluid elements (or layers) generate a shear stress, $\tau_{\text{shear}}$. In contrast, the total pressure sums up the mechanical (or thermodynamic) pressure, which is experienced when moving with the fluid (and therefore labeled *static pressure* and measured with a piezometer or Pitot tube, as shown in Figure 2.8). The dynamic pressure is due to the fluid motion (i.e., $\rho v^2/2$), and the hydrostatic pressure is due to gravity (i.e., $\rho gz$):

$$\begin{aligned} p_{\text{total}} &= p_{\text{static}} + p_{\text{dynamic}} + p_{\text{hydrostatic}} \\ &= p_{\text{static}} + \frac{\rho}{2}v^2 + \rho gz = \not{c} \end{aligned} \tag{1.6a,b}$$

where

$$p_{\text{static}} + p_{\text{dynamic}} = p_{\text{stagnation}} \tag{1.7}$$

Recall for a stagnant fluid body (i.e., a reservoir), where h is the depth coordinate:

$$p_{\text{hydrostatic}} = p_0 + \rho gh \tag{1.8}$$

Clearly, the hydrostatic pressure due to the fluid weight appears in the momentum equation as a body force per unit volume, that is, $\rho\vec{g}$ .

- *Dimensionless groups*, that is, ratios of forces, fluxes, or process or system parameters, indicate the importance of specific transport phenomena. For example, the Reynolds number is defined as

$$\text{Re}_L \equiv \frac{F_{\text{inertia}}}{F_{\text{viscous}}} := vL/\nu \tag{1.9}$$

where:

| | |
|---|---|
| $v$ | is an average system velocity |
| L | is a representative system "length" scale (e.g., the tube diameter $D$) |
| $\nu \equiv \mu/\rho$ | is the kinematic viscosity of the fluid |

Other dimensionless groups with applications in engineering include the Womersley number and the Strouhal number (both dealing with oscillatory/transient flows), the Euler number (pressure difference), the Weber number (surface tension), the Stokes number (particle dynamics), the Schmidt number (diffusive mass transfer), the Sherwood number (convective mass transfer), and the Nusselt number (the ratio of heat conduction to heat convection). The most common source, or derivation, of these numbers is the nondimensionalization of partial differential equations describing the transport phenomena at hand, or more directly using *scale analysis* (see Section 1.4).

### 1.2.2 Thermodynamic Properties

*Thermodynamic properties*, such as mass and volume (extensive properties) or velocity, pressure, and temperature (intensive properties), characterize a given system. In addition, there are *transport (or material) properties*, such as viscosity, diffusivity, and thermal conductivity, which are all temperature dependent and may greatly influence, or even largely determine, a fluid flow field. Just consider tubular flow of air versus honey (at different temperatures) for the same pressure drop. Any extensive, that is, mass-dependent, property divided by unit mass is called a *specific property*, such as the specific volume $v = V/m$ (where its inverse is the fluid density) or the specific energy $e = E/m$. An *equation of state* is a correlation of independent intensive properties, where for a simple compressible system, just two describe the state of such a system. A famous example is the ideal-gas relation, $pV = mRT$, where $m = \rho V$, and $R$ is the gas constant.

### 1.2.3 Constitutive Equations

When considering the conservation laws derived in Chapter 2 for fluid flow as well as heat and species-mass transfer, it is apparent that additional relationships must be found to solve for the field variables $\vec{\mathbf{v}}$, $p$, and $T$ as well as $\vec{\mathbf{q}}$ and $\vec{\vec{\tau}}$. This is necessary for reasons of (1) mathematical closure; that is, a number of unknowns require the same number of equations, and (2) physical evidence; that is, additional material properties other than the density $\rho$ are important in the description of system/material/fluid behavior. These additional relations, or *constitutive equations*, are fluxes that relate via "material properties" to gradients of the principal unknowns. Specifically, for basic *linear* proportionalities, we recall

- Hooke's law, that is, the stress–strain relation in tensor (or index) notation is

$$\boldsymbol{\sigma}_{ij} = D_{ijkl}\boldsymbol{\varepsilon}_{kl} \tag{1.10}$$

  where $D_{ijkl}$ is the Lagrangian elasticity tensor.
- Fourier's law, that is, the heat conduction flux in vector notation is

$$\vec{\mathbf{q}} = -k\nabla T \tag{1.11}$$

  where $k$ is the thermal conductivity.

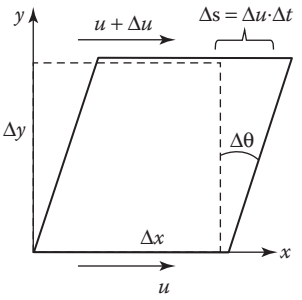


**FIGURE 1.2**
Illustration of the shear stress derivation for simple Couette flow where $\tau_{yx} = \tau_{wall}$ = constant because $u(y)$ is linear.

- The diffusion flux of species $c$ is

$$\vec{j}_c = -\mathcal{D}_{AB}\nabla c \tag{1.12}$$

  where $\mathcal{D}_{AB}$ is the species-mass diffusion coefficient.
- Stokes' postulate, that is, the fluid shear stress tensor for incompressible fluid flow:

$$\vec{\vec{\tau}} = \mu(\nabla\vec{\mathbf{v}} + \nabla\vec{\mathbf{v}}^T) \tag{1.13}$$

  where μ is the dynamic viscosity.

Of special importance are the stresses and associated viscosity**.** Clearly, to move fluid elements relative to each other, a driving force (e.g., a net pressure force a simply a pulling force) is necessary, to which a shear force $F_{tangential} = \tau_{Shear} A_{interface}$ reacts (see Figure 1.2). As postulated by Stokes, the shear stress is proportional to $\nabla\vec{\mathbf{v}}$ and the dynamic viscosity, which is temperature dependent for Newtonian fluids (e.g., air, water, and oil) or shear-rate dependent for non-Newtonian fluids. Specifically, for incompressible fluid flow, Equation 1.13 holds, so that for simple shear flow (see Figure 1.2),

$$\tau_{yx} = \mu\, du/dy \tag{1.14}$$

1. Tangential force $F_{pull} = -F_{drag}$:

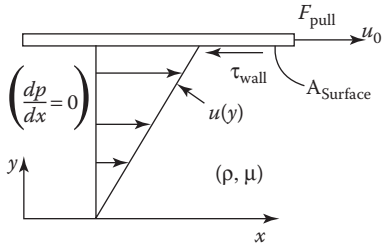


*We observe:* $\tau_{wall} = \dfrac{F_{drag}}{A_{surface}}$ where $F_{drag} = F_{pull}$

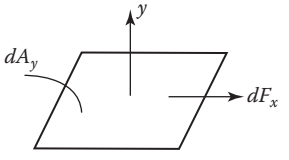


In general, anywhere in the fluid: $\tau_{yx} = \dfrac{dF_x}{dA_y}$

2. Resistance to fluid element deformation:

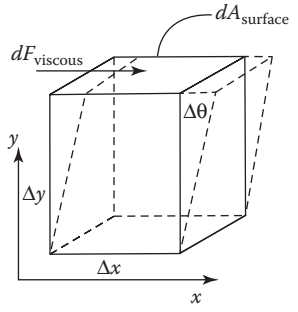


- *Physics*:

$$\tau_{ij} = \lim_{\delta A_j \to 0} \frac{\delta F_i}{\delta A_j} \triangleq \frac{\text{surface force}}{\text{unit area}}$$

$$\tau = \frac{dF_v}{dA_s} \sim \frac{\Delta\theta}{\Delta t}$$

- *Geometry*:

$$\tan\Delta\theta \approx \Delta\theta = \frac{\Delta s}{\Delta y} = \frac{\Delta u \cdot \Delta t}{\Delta y}$$

- Combining both:

$$\tau \sim \frac{\Delta u}{\Delta y}$$

where in the limit with the proportionality factor, μ for unidirectional flow:

$$\tau_{yx} = \mu \frac{du}{dy}$$

### 1.2.4 Stress Tensors and Stress Vectors

While the illustration of a one-dimensional (1-D) shear stress provides some physical insight (see Figure 1.2), a three-dimensional (3-D) viscous flow field actually features nine stress components. Generally, in the equation of motion (see Section 2.3), *total stress tensor* $\vec{\vec{T}}$ is an unknown. That constitutes a closure problem; that is, $\vec{\vec{T}}$ has to be related to the principal variable $\vec{\mathbf{v}}$ or its derivatives. In expanded form,

$$\vec{\vec{T}} = -p\vec{\vec{I}} + \vec{\vec{\tau}} \tag{1.15}$$

where:

$p$ is the *thermodynamic pressure* (or the hydrostatic pressure for $\nabla\vec{v} = 0$)

$\vec{\vec{I}}$ is the necessary unit tensor for homogeneity

$\vec{\vec{\tau}}$ is the stress tensor, consisting of six shear stresses and three normal stresses

For any coordinate system, the stress vector $\vec{\tau}$ relates to the *symmetric* second-order tensor $\vec{\vec{T}}$ as

$$\vec{\vec{\tau}} = \hat{n} \times \vec{\vec{T}} = \vec{\vec{T}} \times \hat{n} \tag{1.16}$$

where $\hat{n}$ is the normal (unit) vector. Without tensor symmetry, that is, $T_{ij} \neq T_{ji}$, an infinitesimal fluid element ($\Delta\forall \to 0$) would spin as $|\vec{\omega} \to \infty|$. It is more insightful to write Equation 1.15 in tensor notation, so that the total stress tensor reads:

$$T_{ij} = -p\delta_{ij} + \tau_{ij} \tag{1.17}$$

where:

$-p\delta_{ij}$ is interpreted as the isotropic part (e.g., fluid statics and inviscid flow)

$\tau_{ij}$ is the deviatoric part, for which a constitutive equation has to be found. Physically, $\tau_{ij} \hat{=} \tau_{(i=\text{surface-normal})(j=\text{stress-direction})}$ represents a force field per unit area as a result of the resistance to the rate of deformation of fluid elements, that is, internal friction (Figure 1.2). This fact leads for fluids to the postulate related to solid mechanics, that is,

$$\tau_{ij} = fct(\varepsilon_{ij}) \tag{1.18}$$

where $\varepsilon_{ij} = \frac{1}{2}\left(v_{i,j} + v_{j,i}\right)$ is the rate-of-deformation tensor.

The relation between $\tau_{ij}$ and $\varepsilon_{ij}$ (plus vorticity tensor $\zeta_{ij}$) can be more formally derived, starting with a fluid element displacement from point P (with $\vec{\mathbf{v}}$ at $t$) to point P′ $(\vec{\mathbf{v}} + d\vec{\mathbf{v}} \text{ at } t + dt)$ a distance $ds$ apart (see Figure 1.1b). Expanding the total derivative in Cartesian coordinates,

$$d\vec{\mathbf{v}} = \begin{bmatrix} \frac{\partial u}{\partial x} & \frac{\partial u}{\partial y} & \frac{\partial u}{\partial z} \\ \frac{\partial v}{\partial x} & \frac{\partial v}{\partial y} & \frac{\partial v}{\partial z} \\ \frac{\partial w}{\partial x} & \frac{\partial w}{\partial y} & \frac{\partial w}{\partial z} \end{bmatrix} d\vec{\mathbf{s}}_{\mathrm{i}} = \nabla\vec{\mathbf{v}} d\vec{\mathbf{s}} \tag{1.19}$$

The spatial changes (or deformations) the fluid element is experiencing can be expressed as the rate-of-deformation tensor, that is,

$$\frac{d\vec{\mathbf{v}}}{d\vec{s}} = \nabla\vec{\mathbf{v}} := \frac{\partial \mathrm{v}_i}{\partial x_j} \tag{1.20}$$

Equation 1.20 can be decomposed into the strain-rate tensor $\varepsilon_{ij}$ <symmetrical part> and the vorticity (or rotation tensor) $\zeta_{ij}$:

$$\frac{\partial v_i}{\partial x_j} = \varepsilon_{ij} + \zeta_{ij} \tag{1.21}$$

It can be readily shown that

- $\zeta_{yx} = -\zeta_{xy} = \omega_z$, $\zeta_{xz} = -\zeta_{zx} = \omega_y$, and $\zeta_{zy} = -\zeta_{yz} = \omega_x$, where $\omega_z = \frac{1}{2}\left(\frac{\partial v}{\partial x} - \frac{\partial u}{\partial y}\right)$, and so on;

  thus, the tensor $\zeta_{ij}$, collapses to $2\vec{\omega} = \nabla \times \vec{\mathbf{v}} = \vec{\zeta}$, *the vorticity vector*
- $\varepsilon_{ii} := \dot{\gamma}_{ii} \equiv \partial v_i / \partial x_i$ indicates volume change (dilation)
- $\varepsilon_{ij} := \frac{1}{2}\dot{\gamma}_{ij}, i \neq j$, represents element distortion

- The shear-rate tensor $\dot{\gamma}_{ij} = \dfrac{\partial v_i}{\partial x_j} + \dfrac{\partial v_j}{\partial x_i}$ and hence the 1/2 in $\varepsilon_{ij} = \dfrac{1}{2}\dot{\gamma}_{ij}$ is mathematically necessary to match Equation 1.21.

As mentioned, Stokes suggested that $\vec{\vec{\tau}}$ is a *linear* function of $\vec{\vec{\varepsilon}}$, which is not the case for non-Newtonian fluids, rarefied gases, and some fluid flows in microscale devices, for example, bioMEMS. Specifically, for Newtonian fluids, that is, air, water, and most oils,

$$\vec{\vec{\tau}} = \lambda(\nabla \cdot \vec{v})\vec{\vec{I}} + 2\mu\vec{\vec{\varepsilon}} \tag{1.22}$$

where the viscosity coefficients $\lambda$ and $\mu$ depend only on the thermodynamic state of the fluid. For incompressible flow, $\nabla \cdot \vec{\mathbf{v}} = 0$ (see Section 2.2.2), and the total stress tensor reduces to

$$T_{ij} = -p\delta_{ij} + 2\mu\varepsilon_{ij} \tag{1.23}$$

where

$$2\mu\varepsilon_{ij} \equiv \tau_{ij} = \mu\left(\frac{\partial v_i}{\partial x_j} + \frac{\partial v_j}{\partial x_i}\right) := \mu\dot{\gamma}_{ij} \tag{1.24}$$

Here, $\dot{\gamma}_{ij} \equiv 2\varepsilon_{ij}$ is called the *shear-rate tensor* (see Appendix AI.5.5 for all stress and shear-rate components in rectangular, cylindrical, and spherical coordinates).

Of great importance are the wall shear stress vector ($\vec{\tau}_{\text{wall}} \equiv WSS$) as a result of frictional (or viscous) effects and the *no-slip condition* for macro-scale systems, that is, at any solid surface:

$$\vec{\mathbf{v}}_{\text{fluid}} = \vec{\mathbf{v}}_{\text{wall}} \tag{1.25}$$

Typically, $\vec{\mathbf{v}}_{\text{wall}} = 0$; that is, the wall is stationary and impermeable. The experimentally verified no-slip condition for macro-flow generates velocity gradients normal to the wall at all axial flow speeds. As illustrated in Figure 1.2, the WSS-elements are:

$$\tau_{\text{wall}} \equiv WSS \sim \begin{cases} \partial u / \partial n & \text{(due to the no-slip condition)} \\ \mu & \text{(due to viscous fluid effects)} \\ F_{\text{tang}} / A & \text{(tangential force per unit surface area)} \end{cases}$$

Very high or low WSS values have been related to device malfunctions and arterial diseases (Kleinstreuer, 2006). Integration of $\vec{\tau}_{\text{wall}}$ over the entire surface of a submerged body or inside a conduit yields the frictional drag:

$$F_{\text{viscous}} = \int_A \tau_{\text{wall}}\, dA \tag{1.26}$$

Viscous drag (frictional effect) plus form drag (pressure effect) make up the total drag:

$$F_{\text{drag}} = \int_A (\tau_w + p)\, dA \tag{1.27}$$

For most cases, it would require elaborate computational fluid dynamics (CFD) analysis to evaluate the WSS and pressure distributions on a submerged body surface and then to integrate (see Section 3.2.3).

### 1.2.5 Flux Vectors

Expanding on Section 1.2.3, *flux* implies the transport of a quantity per unit area and time. For example, in heat transfer, energy moves, for example, heat conducts, by molecular interaction from a point of high temperature to one at lower temperature in a fluid or solid. A simple steady 1-D experiment of a homogeneous plate (of area $A$ and thickness $L$) with one side at $T_1$ and the other one at $T_2$ (where $T_1 > T_2$) would show that the heat flow rate $Q \sim A(T_1 - T_2)/L$. Thus, with $Q/A$ being the conductive heat flux in the $x$-direction, $q_x$ (in kilojoules per second per meter squared), and recognizing that in the limit $\Delta T/L$ is the temperature gradient in the $x$-direction, we have $q_x \sim dT/dx$ or

$$q_x = -k dT/dx \tag{1.28}$$

where $k$ is the thermal conductivity, which may vary with temperature (see Appendix II) and direction; that is, $k_x \neq k_y \neq k_z$. In general, $k_{\text{metal}} > k_{\text{liquid}} > k_{\text{gas}}$, largely due to differences in intermolecular spacing for the three states. In 3-D, the *law of heat conduction* after Fourier reads:

$$\vec{q} = -k \nabla T \tag{1.29}$$

Clearly, the negative sign ensures that in light of the negative temperature gradient, the heat flows in the positive direction, that is, of decreasing temperature (see second law of thermodynamics).

It should be recalled that $k/(\rho c_p)$ is the *thermal diffusivity* $\alpha$, which has the same dimensions ($L^2/T$) as the kinematic viscosity (or momentum diffusivity) and the (binary) mass diffusivity $D_{AB}$. The ratio of $v/\alpha = \text{Pr}$ is the *Prandtl number*. So, it is not surprising that for ordinary diffusion, that is, one species A (a dye) in a solvent B (say, water), a somewhat similar transfer process takes place, driven by the concentration gradient of species $c$:

$$\vec{\mathbf{j}}_c = -\mathcal{D}_{AB} \nabla c \tag{1.30}$$

where:

$\vec{\mathbf{j}}_c$ (in kilograms per second per meter squared) is the mass flux vector of species $c$

$\mathcal{D}_{AB}$ is the binary diffusion coefficient; that is, for dilute suspensions of nanoparticles (see Chapter 8) $\mathcal{D}_{AB} = \mathcal{D}$ can be evaluated from the Stokes–Einstein equation as

$$\mathcal{D} = \frac{\kappa_B T}{3\pi\mu d_p} \tag{1.31}$$

where:

$\kappa_B$ is the Boltzmann constant
$T$ is the temperature in Kelvin
$d_p$ is the particle/molecule diameter, typically $d_p < 100$ nm

## 1.3 Derivation and Modeling Approaches

A sound understanding of the physics of fluid flow with mass and heat transfer, as well as statics/dynamics and stress–strain theory, and a mastery of basic solution techniques are important prerequisites for studying, applying, and improving engineering systems. As always, the objective is to learn to develop mathematical models; here, to establish approximate representations of actual transport phenomena in terms of differential or integral equations. *The* (analytical or numerical) *solutions to the describing equations should produce testable predictions and allow the analysis of system variations, leading to a deeper understanding and possibly to new or improved engineering procedures or devices.* Fortunately, most systems are governed by continuum mechanics laws (see Section 1.1). Notable exceptions are certain micro- and nano-scale processes, which require modifications of the classical boundary conditions (see Chapter 7) or even molecular models solved via statistical mechanics or molecular dynamics simulations.

Clearly, transport phenomena, that is, mass, momentum, and heat transfer, form a subset of *mechanics*, which is part of *classical* (or Newtonian) *physics* (see Figure 1.3). Physics is the mother of all hard-core sciences, engineering, and technology. The hope is that one day, advancements toward a "universal theory" will unify classical with modern physics, resulting in a fundamental equation from which all visible/detectable phenomena can be derived and described.

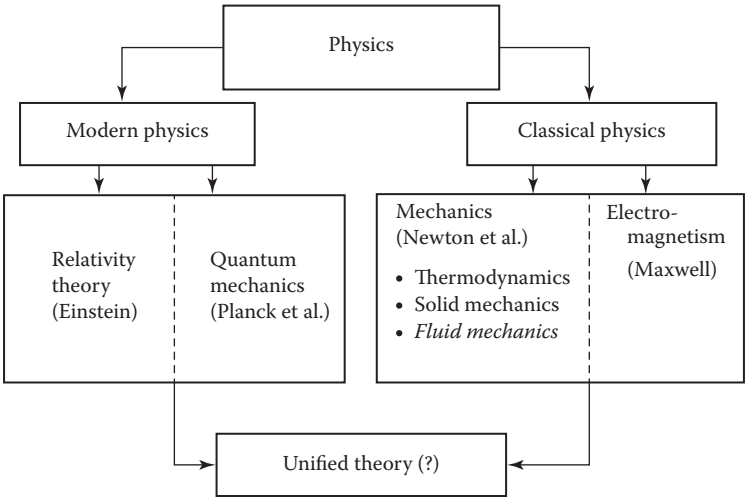


**FIGURE 1.3**
Subsets of physics and the quest for a unifying theory.

### 1.3.1 Approaches to Problem Solving

Traditionally, the answer to a given problem is obtained by copying from available sources suitable equations, needed correlations (or submodels), and boundary conditions with their appropriate solution procedures. This is called *matching*, and it may result in a good first-step learning experience. However, it should be augmented later on by more *independent work*; for example, deriving governing equations, obtaining data sets, plotting and visualizing results, improving basic submodels, finding new, interdisciplinary applications, exploring new concepts, interpreting observations in a more generalized form, or even pushing the envelope of existing solution techniques or theories. In any case, the triple pedagogical goals of advanced *knowledge*, *skills*, *and design* can be achieved only via independent practice, hard work, and creative thinking. To reach these lofty goals, a deductive or "top-down" approach is adopted, that is, from the fundamental to the specific, whereby the general transport phenomena are recognized and mathematically described, and then special cases are derived and solved—after the acquisition of necessary fluid property values and input data sets.

As a first task, exact *flow problem identification* is very important and sometimes the most difficult, especially in industrial settings. After obtaining some basic information and reliable data, it helps to think and speculate about the physics of the fluid flow, asking:

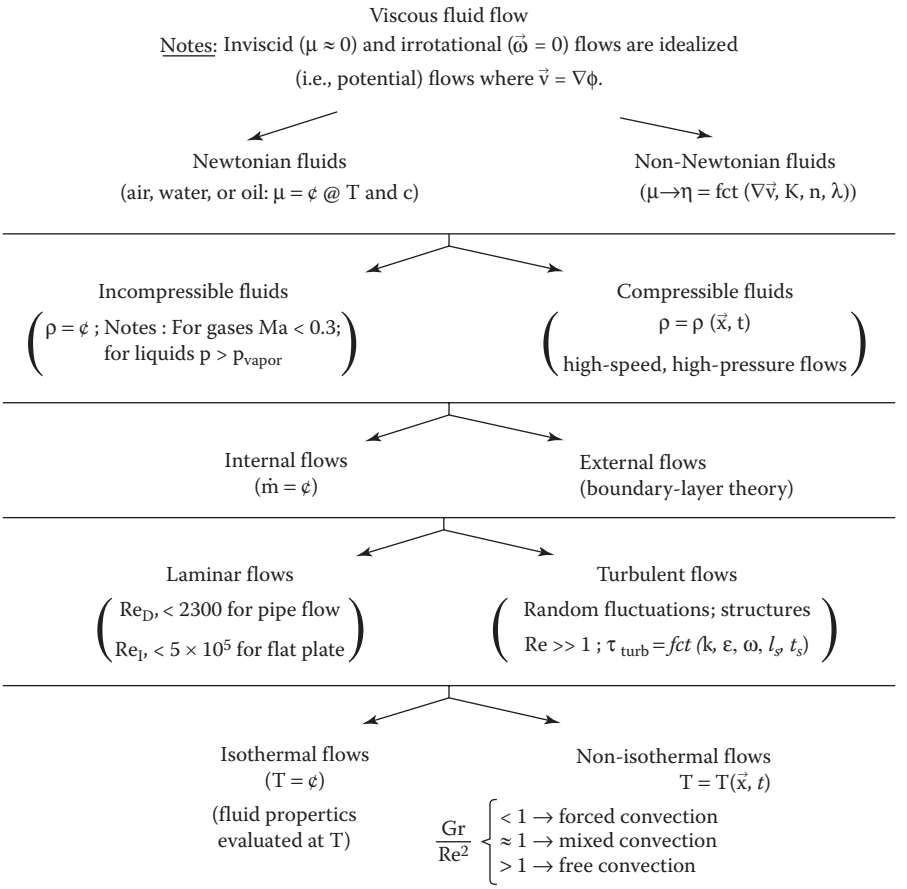


**FIGURE 1.4**
Special cases of viscous fluid flows.

1. What category does the given flow system fall into, and how does it respond to normal as well as extreme changes in operating conditions? Figure 1.4 may be useful for the categorization of real fluids and types of flows.
2. What variables and system parameters play an important role in the observed transport phenomena, that is, linear or angular momentum transfer, fluid-mass or species-mass transfer, and heat transfer?
3. What are the key dimensionless groups, and what are their expected ranges (see Section 1.4)?

Answers to these questions assist in grouping the flow problem at hand. For example, with the exception of "superfluids," all others are viscous, some more (e.g., syrup) and some less (e.g., rarefied gases). However, with the advent of *Prandtl's boundary-layer concept* (Sections 3.2.1 and 3.3.1), the flow field, say, around an airfoil has been traditionally divided into a very thin (growing) viscous layer and beyond that an unperturbed *inviscid region*. This paradigm helped to better understand actual fluid mechanics phenomena and to simplify velocity and pressure as well as drag and lift calculations. Specifically, at sufficiently high approach velocities, a fluid layer adjacent to a submerged body experiences steep gradients due to the "no-slip" condition and hence constitutes a *viscous flow region*, while outside the boundary layer, frictional effects are negligible. Clearly, with the prevalence of powerful CFD software and engineering workstations, such a fluid flow classification is becoming more and more superfluous (see discussion in Section 3.2).

While, in addition to air and water, almost all oils are *Newtonian*, some synthetic motor-oils are shear-rate dependent, and that holds as well for a variety of new (fluidic) products. This implies that modern engineers have to cope with the analysis and computer modeling of *non-Newtonian fluids* (see Section 4.2). For example, latex paint is shear-thinning; that is, when painting a vertical door, rapid brush strokes induce high shear rates ($\dot{\gamma} \sim dw/dz$), and the paint viscosity/resistance is very low. When brushing stops, locally thicker paint layers (due to gravity) try to descend slowly; however, at low shear rates, the paint viscosity is very high, and hence, "tear-drop" formation is avoided, and a near-perfect coating can dry on the door.

All natural phenomena change with time and hence are *unsteady* (i.e., *transient*), while in industry, it is mostly desirable that processes are steady, except during production line start-up, failure, or shutdown. For example, turbines, compressors, and heat exchangers operate continuously for long periods of time and hence are labeled *steady-flow devices*; in contrast, pacemakers, control systems, and drink-dispensers work in a time-dependent fashion. In some cases, such as a heart valve, devices change their orientation periodically, and the associated flows oscillate about a mean value. In contrast, it should be noted that the term *uniform* implies "no change with system *location*," as in uniform (i.e., constant over a cross-section) velocity or uniform particle distribution, both of which could still vary with time.

Mathematical flow field descriptions become complicated when *laminar flow* turns unstable due to high speed and/or geometric irregularities ranging from surface roughness to complex conduits. The deterministic laminar flow turns *transitional* on its way to becoming *fully turbulent*, that is, chaotic, transient 3-D with random velocity fluctuations, which help in mixing but also induce high apparent stresses. As an example of "flow transition," picture a group (on bikes or skis) going faster and faster down a mountain, while the terrain gets rougher. The initially quite ordered group of riders/skiers may change swiftly into an unbalanced, chaotic group. So far, no *universal model for turbulence*, let alone for the transitional regime from laminar to turbulent, has been found. Thus, major efforts focus on direct

numerical simulation (DNS) of turbulent flows, which are characterized by relatively high Reynolds numbers and chaotic, transient 3-D flow pattern (see Sections 3.2 and 3.3).

### 1.3.2 Derivation Techniques

There are basically four ways of obtaining specific transport equations reflecting the conservation laws. The points of departure for each of the four methods are either given (e.g., Boltzmann equation or Newton's second law) or derived based on differential mass, momentum, and energy balances for a representative elemental volume (REV).

1. *Lattice-Boltzmann method and molecular dynamics approach:* Fluid properties and transport equations can be obtained from kinetic theory and the Boltzmann equation, respectively, employing statistical means. Alternatively, for molecular dynamics simulations, $\sum \vec{\mathbf{F}} = m\vec{\mathbf{a}}$ is solved for each fluid molecule or bundle of particles using direct numerical integration.
2. *Integral approach:* Starting with the Reynolds Transport Theorem (RTT) for a fixed open control volume (Euler), specific transport equations in integral form can be obtained (see Section 2.1).
3. *Differential approach:* Starting with 1-D balances over an REV and then expanding them to 3-D, the mass, momentum, and energy transfer equations in differential form can be formulated. Alternatively, the RTT is transformed via the divergence theorem, where in the limit, the field equations in differential form are obtained (see Sections 2.2 through 2.4).
4. *Phenomenological approach*: Starting with balance equations for an open system, that is, a control volume, transport phenomena in complex flows are derived largely based on empirical correlations and dimensional analysis considerations. A very practical example is the description of transport phenomena with compartment models. These "compartments" are either well mixed, that is, transient lumped-parameter models without any spatial resolution, or transient with a 1-D resolution in the axial direction (see Kleinstreuer, 2006).

### 1.3.3 Basic Flow Assumptions and their Mathematical Statements

Once a given fluid dynamics problem has been categorized (Figure 1.4), some justifiable assumptions have to be considered to simplify the general transfer equations, as exemplified here:

| Flow Assumption | Consequence (Eulerian Description of Section 1.3.4) |
|---|---|
| Time dependence | $\frac{\partial}{\partial t} = 0$ , that is, steady-state; $\vec{\mathbf{v}} = \vec{\mathbf{v}}(t)$, that is, transient flow |
| Dimensionality | Required number of space coordinates $\vec{\mathbf{x}} = (x, y, z)$ |
| Directionality | Required number of velocity components $\vec{\mathbf{v}} = (u, v, w)$ |
| Unidirectional flow | Special case when all but one velocity component are zero |

| | |
|---|---|
| Development phase | $\frac{\partial v}{\partial s} = 0$ , that is, fully-developed flow, where $s$ is the axial coordinate |
| Symmetry | $\begin{cases} \frac{\partial}{\partial n} = 0 : \text{midplane} (n \text{ is the normal coordinate}) \\ \frac{\partial}{\partial \theta} = 0 : \text{axisymmetry} \end{cases}$ |

### 1.3.4 Closed versus Open Systems and Associated Flow Descriptions

After a flow problem has been well posed and categorized in terms of the viscous-flow grouping (see Figure 1.3) in conjunction with a set of proper assumptions, a suitable solution technique has to be selected. That decision, however, requires first a brief review of possible flow field descriptions in terms of the *Lagrangian versus Eulerian framework* within the continuum mechanics assumption (Section 1.1). Specifically, two basic flow field descriptions are of interest, that is, the Lagrangian viewpoint and the Eulerian (or control-volume) approach (see Figure 1.5, where C. ∀. ≙ control volume and C.S. ≙ control surface).

For the *Lagrangian description*, consider Particle A moving on a path-line with respect to a fixed Cartesian coordinate system. Initially, the position of A is at $\vec{\mathbf{r}}_\mathbf{o} = \vec{\mathbf{r}}_\mathbf{o}(\vec{\mathbf{x}}_\mathrm{o}, t_\mathrm{o})$ and a moment later at $\vec{\mathbf{r}}_\mathbf{A} = \vec{\mathbf{r}}_\mathbf{A}(\vec{\mathbf{r}}_\mathbf{o}, t_o + \Delta t)$ , as depicted in Figure 1.6, where $\vec{\mathbf{r}}_\mathbf{A} = \vec{\mathbf{r}}_\mathbf{o} + \Delta\vec{\mathbf{r}}$ . Considering all distinct points and following their motion for $t > t_0$, solid particle (or fluid element) motion can be described with the position vector:

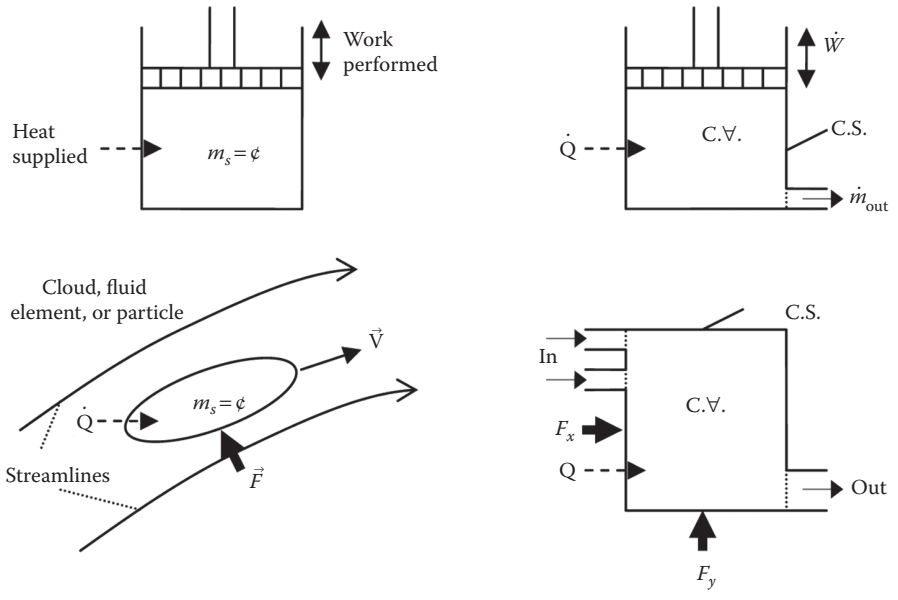


(a) Closed systems (Lagrange)

(b) Open systems (Euler)

**FIGURE 1.5**
Closed versus open systems.

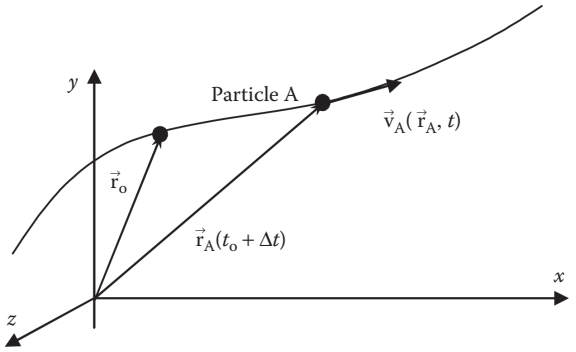


**FIGURE 1.6**
Incremental fluid particle motion.

$$\vec{\mathbf{r}} = \vec{\mathbf{r}}(\vec{\mathbf{r}}_\mathbf{o}, t) \tag{1.32}$$

where in the limit we obtain the fluid velocity and acceleration as

$$\frac{d\vec{\mathbf{r}}}{dt} = \vec{\mathbf{v}} := d\vec{\mathbf{x}}/dt \tag{1.33}$$

and

$$\frac{d^2\vec{\mathbf{r}}}{dt^2} = \frac{d\vec{\mathbf{v}}}{dt} = \vec{\mathbf{a}} \tag{1.34}$$

To illuminate the Lagrangian versus Eulerian flow description, the common scenario of "river flow" is considered. In the Eulerian fixed coordinate frame, river is approximated as steady 1-D axial flow; that is, for a stationary observer,

$$v(x) = v_0 + \Delta v\left(1 - e^{-ax}\right)$$

It implies that at $x = 0$, the water moves at $v_0$, and then accelerates, so that very far downstream, $v(x \to \infty) = v_0 + \Delta v$. Now, derive an expression for $v = v(v_0, t)$ in the Lagrangian frame. As shown, $\vec{\mathbf{v}} = d\vec{\mathbf{r}}/dt$, which reads in the present 1-D case:

$$\frac{dx}{dt} = v(x) = v_0 + \Delta v\left(1 - e^{-ax}\right)$$

Separation of variables and integration yields

$$\int_0^x \frac{dx}{(v_0 + \Delta v) - \Delta v e^{-ax}} = \int_0^t dt$$

so that

$$x + \frac{1}{a}\ln\left[1 + \frac{\Delta v}{v_0}\left(1 - e^{-ax}\right)\right] = (v_0 + \Delta v)t$$

Now, replacing the two $x$-terms with expressions from the $v(x)$-equation, that is, $x = -\frac{1}{a}\ln\left(1-\frac{v-v_0}{\Delta v}\right)$ and $e^{-ax} = 1-\frac{v-v_0}{\Delta v}$, we can write the Lagrangian velocity as

$$v(t) = \frac{v_0(v_0+\Delta v)}{v_0+\Delta v\exp[-a(v_0+\Delta v)t]}$$

Graph 1:

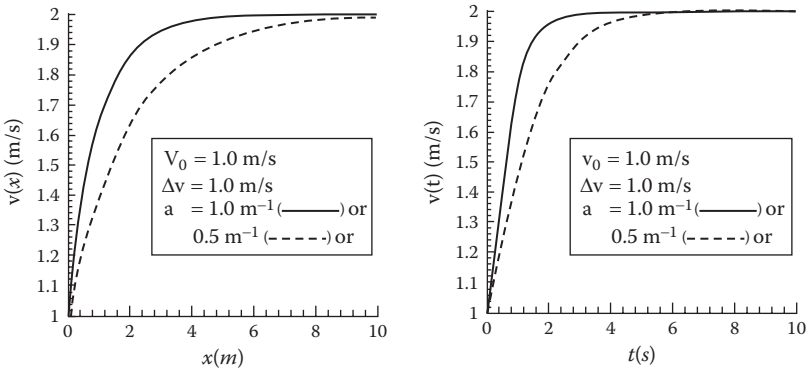


*Comments:*

- Clearly, the $v(x)$-dependence in the Eulerian frame has been replaced by $v(t)$; that is, even during "steady" (Eulerian) processes, time evolves in the Lagrangian frame.
- Although the graphs look quite similar because of the rather simple $v(x)$-function considered, subtle differences are transparent when comparing the velocity gradients (i.e., $dv/dx$ and $dv/dt$) rather than just the magnitudes $v(x)$ and $v(t)$.
- The mathematical river flow description is much more intuitive and simpler in the *Eulerian frame of reference*, which is preferred by engineers.

### 1.3.5 Material (or Stokes) Derivative

The material-point concept can be extended to *a material volume with constant identifiable mass*, forming a "closed system" that moves and deforms with the flow, but no mass crosses the material volume surface, because it is closed (see Figure 1.5a). Again, the system is tracked through space, and as time passes, it is of interest to know what the changes in system mass, momentum, and energy are. This can be expressed in terms of the system's extensive property $N_s$, which is either mass $m$, momentum $m\vec{\mathbf{v}}$, or total energy E. Thus, the key question is: "How can we express the fate of $N_s$?" or in mathematical shorthand, what is the material time derivative "$DN_s/Dt$"? Clearly, $D/Dt \equiv \partial/\partial t + \vec{v}\cdot\nabla$ follows the closed system and records the total time-rate-of-change of whatever is being tracked (see Section 2.2).

Expanding on previous remarks, a brief illustration of the various *time derivatives*, that is, $\partial/\partial t$ (local), $d/dt$ (total of a material point or solid particle), and $D/Dt$ (total of a fluid element), is in order. Their differences can be illustrated using acceleration (see also Appendix AI.2.1):

- $a_{x,\text{local}} = \dfrac{\partial u}{\partial t}$, where $u$ is the fluid element velocity in the $x$-direction.

- $\vec{\mathbf{a}}_{\text{particle}} = \dfrac{d\vec{\mathbf{v}}}{dt}$ is employed in solid particle dynamics. However,
- $\vec{\mathbf{a}}_{\substack{\text{fluid}\\\text{element}}} = \dfrac{\mathrm{D}\vec{\mathbf{v}}}{\mathrm{D}t} = \underbrace{\dfrac{\partial \vec{\mathbf{v}}}{\partial t}}_{\vec{\mathbf{a}}_{\text{local}}} + \underbrace{(\vec{\mathbf{v}}\cdot\nabla)\vec{\mathbf{v}}}_{\vec{\mathbf{a}}_{\text{convective}}}$ is the total fluid-element acceleration.

*Clearly*, the material (or Stokes) derivative, $\dfrac{D}{Dt} = \partial/\partial t + (\vec{\mathbf{v}}\cdot\nabla)$, operating on the velocity vector is a powerful operator, describing the "total time-rate-of-change" (i.e., acceleration) of a fluid flow field. For illustration purposes, an arbitrary velocity field, $\vec{\mathbf{v}} = \vec{\mathbf{v}}(x, y, z; t)$, is considered, and its total differential is formed.

*Recall:* The total differential of any continuous and differentiable function, such as $\vec{\mathbf{v}} = \vec{\mathbf{v}}(x, y, z; t)$, can be expressed in terms of its infinitesimal contributions in terms of changes of the independent variables:

$$d\vec{\mathbf{v}} = \frac{\partial \vec{\mathbf{v}}}{\partial x}dx + \frac{\partial \vec{\mathbf{v}}}{\partial y}dy + \frac{\partial \vec{\mathbf{v}}}{\partial z}dz + \frac{\partial \vec{\mathbf{v}}}{\partial t}dt$$

Now, the derivation steps are:

- Divide through by $dt$ and recognize that $dx/dt = u$, $dy/dt = v$, and $dz/dt = w$ are the local velocity components:

$$\frac{d\vec{\mathbf{v}}}{dt} = \frac{\partial \vec{\mathbf{v}}}{\partial x}u + \frac{\partial \vec{\mathbf{v}}}{\partial y}v + \frac{\partial \vec{\mathbf{v}}}{\partial z}w + \frac{\partial \vec{\mathbf{v}}}{\partial t}$$

- Substitute the "particle dynamics" differential with the "fluid element" differential to obtain

$$\frac{d\vec{\mathbf{v}}}{dt} \hat{=} \frac{D\vec{\mathbf{v}}}{Dt} = \frac{\partial \vec{\mathbf{v}}}{\partial t} + u\frac{\partial \vec{\mathbf{v}}}{\partial x} + v\frac{\partial \vec{\mathbf{v}}}{\partial y} + w\frac{\partial \vec{\mathbf{v}}}{\partial z} \equiv \frac{\partial \vec{\mathbf{v}}}{\partial t} + (\vec{\mathbf{v}}\cdot\nabla)\vec{\mathbf{v}} = \vec{\mathbf{a}}_{\text{local}} + \vec{\mathbf{a}}_{\text{conv.}}$$

As discussed (see Figure 1.5), in the *Eulerian frame*, an "open system" is considered where mass, momentum, and energy may readily cross boundaries, that is, being convected across the control volume surface, and local fluid flow changes may occur within the control volume over time. The fixed or moving control volume may be a large system/device with inlet and outlet ports, it may be small finite volumes generated by a computational mesh, or it may be in the limit a "point" in the flow field. In general, the Eulerian observer, fixed to an inertial reference frame, records temporal and spatial changes of the flow field at all "points," or in the case of a control volume, transient mass, momentum, and/or energy changes inside and fluxes across its control surfaces.

In contrast, the *Lagrangian observer* stays with each (closed) fluid element or material volume and records its basic changes while moving through space. Section 2.1 employs both viewpoints to describe mass, momentum, and energy transfer in integral form, known as the RTT. *Thus, the RTT simply links the conservation laws from the Lagrangian to the Eulerian frame.* In turn, a surface-to-volume integral transformation then yields the conservation laws in differential form in the Eulerian framework, also known as the *control-volume approach.*

## 1.4 Scale Analysis and Dimensionless Groups

Scale analysis is a simple algebraic procedure whereby ratios of forces (or fluxes) are formed, based on selected terms of problem-specific equations and physical insight. Without going through elaborate schemes (e.g., Buckingham's pi-theorem) or solving complex equations, scale analysis can provide directly dimensionless groups as well as their functional dependence on dependent variables. The derivations of the Reynolds number and the Strouhal number may serve as illustrative examples. The necessary physical insight is that both are (naturally) dimensionless ratios of selected forces appearing in the equation of fluid-element acceleration.

Even more insightful and powerful applications of scale analysis will be presented throughout the text. For example, in Section 2.4 of Chapter 2, it is shown that for fully developed pipe flow, the Nusselt number Nu = (convection)/(conduction) is constant; in contrast, in Example 2.9 of natural convection along a vertical (heated) wall, it is demonstrated that the thermal boundary-layer thickness $\delta(x) \sim x^{1/4}$, while the average air-velocity $u_{avg} \sim x^{1/2}$. So, while scaling cannot provide numerical values (or exact functions), it can provide the type of functional dependence for dimensionless groups, dependent variables, system parameters, and so on.

### 1.4.1 Examples of Scaling

Known from Newton's Second Law, the total fluid-particle acceleration is caused by several *net* forces per unit mass:

$$\vec{\mathbf{a}}_{\text{total}} \equiv \underbrace{\frac{\partial \vec{\mathbf{v}}}{\partial t}}_{\substack{\text{transient}\\ \text{term}}} + \underbrace{(\vec{\mathbf{v}}\cdot\nabla)\vec{\mathbf{v}}}_{\substack{\text{inertia}\\ \text{term}}} = \underbrace{-\frac{1}{\rho}\nabla p}_{\substack{\text{pressure}\\ \text{force}}} + \underbrace{\nu\nabla^2\vec{\mathbf{v}}}_{\substack{\text{viscous}\\ \text{force}}} + \underbrace{\vec{\mathbf{g}}}_{\text{gravity}}$$

$$\vec{a}_{\text{total}} \equiv \frac{\partial \vec{v}}{\partial t} + (\vec{\mathbf{v}}\cdot\nabla)\vec{\mathbf{v}} = \sum \frac{\vec{F}_{\text{net}}}{m} = -\frac{1}{\rho}\nabla p + v\nabla^2\vec{\mathbf{v}} + \vec{\mathbf{g}} \tag{1.35}$$

Now, by definition:

$$\text{Re} = \frac{\text{inertial force}}{\text{viscous force}} := \frac{(\vec{\mathbf{v}}\cdot\nabla)\vec{\mathbf{v}}}{\nu\nabla^2\vec{\mathbf{v}}} \tag{1.36a}$$

Employing the scales $\vec{\mathbf{v}} \sim \mathrm{v}$ and $\nabla = \left(\frac{\partial}{\partial x}, \frac{\partial}{\partial y}, \frac{\partial}{\partial z}\right) \sim \frac{1}{L}$, where $v$ may be an average velocity and $L$ a system-characteristic dimension (e.g., the pipe diameter or plate length), we obtain

$$\text{Re} = \frac{\left(v \cdot \frac{1}{L}\right)v}{\nu \mathrm{L}^{-2} v} = \frac{v\mathrm{L}}{\nu} \tag{1.36b}$$

#### *1.4.1.1 A Note on the Reynolds Number*

The Reynolds number is considered to be "always important." Actually, this is not always the case. For example, for Poiseuille flow Re = 0, the inertia term $(\vec{\mathbf{v}}\cdot\nabla)\vec{\mathbf{v}}$ is identical to zero, while the fluid flow is in dynamic equilibrium between the driving force (i.e., pressure gradient) and resistance (i.e., shear stress). Thus, on a case-by-case basis, some dimensionless groups may need reinterpretation. For steady pipe flow, we could rewrite the Re#-definition as the ratio of flow momentum to wall resistance:

$$\mathrm{Re}_D = \frac{4\dot{m}}{\pi\mu D} \tag{1.37}$$

Another example is the Strouhal number, defined as

$$\mathrm{Str} = \frac{\text{local acceleration}}{\text{convective acceleration}} \equiv \frac{\text{transient term}}{\text{inertia term}} = \frac{\partial\vec{\mathbf{v}}/\partial t}{(\vec{\mathbf{v}}\cdot\nabla)\vec{\mathbf{v}}} \tag{1.38a}$$

We can write with system time scale T (e.g., cardiac cycle: T = 1 s)

$$\frac{\nu/T}{\nu L^{-1}\nu} = \frac{L}{\nu T} = \mathrm{Str} \tag{1.38b}$$

Clearly, when $T \gg 1$, $\mathrm{Str} \to 0$, and hence the process, or transport phenomenon, is quasi-steady.

### 1.4.2 Non-Dimensionalization of Equations

An alternative approach to generate dimensionless groups is the formal *non-dimensionalization of the governing equations* describing the system dynamics. Taking the transient laminar boundary-layer equation (see Section 2.3.2) as an example,

$$\rho\left(\frac{\partial u}{\partial t} + u\frac{\partial u}{\partial x} + v\frac{\partial u}{\partial y}\right) = -\frac{\partial p}{\partial x} + \mu\frac{\partial^2 u}{\partial y^2} \tag{1.39}$$

We non-dimensionalize each variable with suitable, constant reference quantities. Specifically, approach velocity $U_0$, plate length $\ell$, system time $T$, and atmospheric pressure $p_0$ are such quantities. Then, the dimensionless variables are

$$\hat{u} = u/U_0, \hat{v} = v/U_0;\ \hat{x} = x/\ell;\ \hat{y} = y/\ell;\ \hat{p} = p/p_0, \text{and}\ \hat{t} = t/T.$$

*Note:* In Section 3.2.1, $\hat{y}$ is defined as $\hat{y} = y/\delta(x)$, where $\delta(x)$ is the varying boundary-layer thickness. Being in the plate's normal direction, $\delta(x)$ is a physically better length-scale than the plate length $\ell$.

Inserting all variables, that is, $u = \hat{u}U_0, t = \hat{t}T$, and so on, into the governing Equation 1.39 yields

$$\frac{\rho U_0}{T}\frac{\partial\hat{u}}{\partial\hat{t}} + \left[\frac{\rho U_0^2}{\ell}\right]\left(\hat{u}\frac{\partial\hat{u}}{\partial\hat{x}} + \hat{v}\frac{\partial\hat{u}}{\partial\hat{y}}\right) = \left[\frac{p_0}{\ell}\right]\frac{\partial\hat{p}}{\partial\hat{x}} + \left[\frac{\mu U_0}{\ell^2}\right]\frac{\partial^2\hat{u}}{\partial y^2} \tag{1.40a}$$

Dividing the entire equation by, say, $\left[\frac{\rho U_0^2}{\ell}\right]$ generates

$$\underbrace{\left[\frac{\ell}{Tu_0}\right]}_{\text{Strouhal \#}}\frac{\partial \hat{u}}{\partial \hat{t}}+\hat{u}\frac{\partial \hat{u}}{\partial \hat{x}}+\hat{v}\frac{\partial \hat{u}}{\partial \hat{y}}=-\underbrace{\left[\frac{p_0}{\rho U_0^2}\right]}_{\text{Euler \#}}\frac{\partial \hat{p}}{\partial \hat{x}}+\underbrace{\left[\frac{\mu}{\rho U_0 \ell}\right]}_{\substack{\text{inverse}\\ \text{Reynolds \#}}}\frac{\partial^2 \hat{u}}{\partial \hat{y}^2} \tag{1.40b}$$

*Comments:*

Clearly, three goals have been achieved:

- The governing equation is now dimensionless.
- The variables vary only between 0 and 1.
- The overall fluid flow behavior can be assessed by the magnitudes of three groups, that is, Str, Eu, and Re numbers.

## 1.5 Homework Assignments

Solutions to homework problems done individually or in, say, three-person groups should help to further illustrate fluid dynamics concepts, and in conjunction with Appendix I, sharpen the readers' math skills. Note, there is no substantial correlation between good homework assignment (HA) results and fine test performances, only vice versa. Table 1.1 summarizes three suggestions for students to achieve a good grade in fluid dynamics—for that matter, in any engineering subject. The key word is "independence"; that is, equipped with an equation sheet (see Appendix I), the student should be able (1) to satisfactorily answer all concept questions and (2) to solve correctly all basic fluid dynamics problems.

The questions in Section 1.5.1 emerged directly out of the Chapter 1 text, while the problems of Section 1.5.2 were taken from lecture notes in modified form when using White (2006), Cimbala and Cengel (2008), and Incropera et al. (2007). Additional examples, concept questions, and problems may be found in any undergraduate fluid mechanics and heat transfer text, or on the Web (see websites of MIT, Stanford, Cornell, University of Michigan (UM), and so on).

### 1.5.1 Physical Insight

*Whenever possible, answers to* **Physical Insight** *questions should feature a sample illustration (or system sketch), a brief description/explanation and some math in terms of definitions or derivations.*

1.1. Test and discuss the hypothesis that doing an excellent job with the three preliminaries, that is, *Sketch*, *Assumptions*, and *Method*, may provide up to 60% of the correct problem solution.

1.2. What would a "Unified Theory" accomplish (see Figure 1.3), and what type of practical applications do you expect for Modern Fluid Dynamics?

1.3. Recalling the continuum mechanics hypothesis (CMH) of Section 1.1 discuss if flowing seeds, grains, rocks, mud, powders, jelly, and so on, form continua.

1.4. With examples, compare fluid motion due to unbalanced versus balanced forces or gradients.

1.5. What are the advantages of the differential over the integral approach, and what could be the disadvantages?

1.6. Why are flows divided into *internal* and *external* flows in mechanical engineering? List other useful categorizations!

1.7. Streamlines: (a) derive Equation 1.3 and provide an example; (b) draw streamlines in a channel partially occluded by a block; (c) draw streamlines behind a sphere in uniform flow at low and high Reynolds numbers.

1.8. Considering Equation 1.4, how does $\tau_{normal}$ differ physically from $p$? Give an illustrative example.

1.9. Derive Equation 1.8 for a prismatic fluid element and show that in any static fluid container, $p = p(h)$ only.

1.10. What is the usefulness of dimensionless groups? Provide three applications.

1.11. Compare the math conditions for the continuum hypothesis and the thermodynamic equilibrium.

1.12. In Section 1.3, it is claimed that "flow problem identification" (FPI) is an important and challenging task. Provide FPIs for (a) loud noise in an industrial pipe network; (b) scatter-marks on a machined part (e.g., a cylinder shaped with a lathe); (c) a person's left arm turning cold and losing any feeling.

1.13. When, where and why are inviscid flow calculations still being carried out?

1.14. Provide two examples of where, even by engineers, the Lagrangian modeling approach is preferred over the Eulerian approach.

1.15. Derive the material derivative $D/Dt$ from a geometric viewpoint, and explain with an illustration $\vec{\mathbf{a}}_{local}$ vs. $\vec{\mathbf{a}}_{conv.}$.

1.16. Why was "enthalpy" $dh = du + d(pv)$ introduced in thermodynamics, and why is $h = h(T)$ only for an ideal gas?

1.17. In Equations 1.15 and 1.17 why exactly is the unit tensor necessary and what happens when $\nabla\vec{\mathbf{v}} = 0$?

1.18. Equation 1.24 is sometimes written with a "minus" sign; on what physical grounds?

1.19. Consider steady laminar unidirectional flow in a pipe of radius $R$ and length $L$ with maximum centerline velocity $u_{max}$, that is,

$$u(r) = u_{max}\left[1 - \left(\frac{r}{R}\right)^n\right]$$

a. What is $u_{max}$ dependent on?

b. Draw velocity profiles for $n = 0.5$, 1.0, and 2.0, and comment!

c. Develop an equation for $\tau_{wall}$, and compute the drag force exerted by the fluid onto the pipe wall. Why is $F_D$ independent of $R$?

1.20. Categorize the flow described by

$$\vec{v} = (u_0 + bx)i - byj$$

in terms of time dependence, compressibility, dimensionality, and fluid-element spin.

1.21. Explain the rationale for Equation 1.21, where mathematics merges into physics: (a) prove that $2\vec{\omega} = \nabla \times \vec{\mathbf{v}} \equiv \vec{\zeta}$; and (b) compare two circular flows, that is, $v_\theta = \omega r$ and $v_\theta = \dfrac{C}{r}(r \neq 0)$, compute the vorticity fields, and sketch them.

1.22. Having the strain-rate tensor already, why was the shear-rate tensor introduced, and how would you (in an alternative way to the book) derive the total stress tensor $T_{ij} = -p\delta_{ij} + \mu\dot{\gamma}_{ij}$ for incompressible flow of Newtonian fluids?

1.23. Heat flux and mass flux are standard flux vector examples. What makes them "vectors," and what is the (associated) momentum flux?

### 1.5.2 Engineering Problems

Before launching into an engineering-problem solution, three preliminary tasks should be carefully executed:

- A system *Sketch* with coordinates, expected velocity/temperature profiles, and given/unknown parameters in symbolic form.
- A detailed list of *Assumptions* concerning flow-field characteristics, system simplifications, submodels, and fluid properties.
- Solution *Method* in terms of concepts and approach, expressed as brief mathematical statements.

1.24. A car (with a door 1.2 m × 1 m wide) plunges into a lake 8 m deep to the top of the door. (a) Find the hydrostatic force on the door and the point-force location; (b) can a strong driver who generates 1 kN m torque (or moment) open the door under water?

1.25. An inverted cone ($D = 12$ cm, $d = 4$ cm, $L = 12$ cm) rotates at $\omega_0 = 200$ rad/s in a tight housing with all around clearance of $h = 1.2$ mm filled with oil, where $\mu_1(20°\text{C}) = 0.1$ N s/m$^2$ and $\mu_2(80°\text{C}) = 0.0078$ Pa s. Assuming linear velocity profiles, find the total power requirement $P_{\text{total}} = P_{\text{top}} + P_{\text{bottom}} + P_{\text{side}}$ (where $dP = \omega dT$ and $dT = rdF$) for the two viscosities, and comment.

1.26. Consider the velocity field described by $\vec{\mathbf{v}} = (0.5 + 0.8x)\hat{i} + (1.5 - 0.8y)\hat{j}$, where $\hat{i}$ and $\hat{j}$ are unit vectors in the $x$- and $y$-direction, respectively. (a) Classify the velocity flow field; (b) find the coordinates of the stagnation point; (c) calculate the material accelerations at point $x = 2$ m and $y = 3$ m; (d) draw some streamlines and fluid acceleration vectors in the domain, say, $-3 \leq x \leq 3$ m and $-1 \leq y \leq 6$ m.

1.27. Consider simple shear flow, such as the Couette profile $u(y) = u_0\, y/h$, where $h$ is the parallel-plate spacing. Calculate the vorticity component in the z-direction, that is, $\zeta_z$, and determine the direction of rotating fluid particles, if any.

1.28. Compute the temperature in a very thin silicon chip (which receives $q_{\text{chip}} = 10^4$ W/m$^2$ and where the allowable $T_{\max} = 85°\text{C}$) for the following system. The chip sits via an epoxy joint (thermal resistance $R_{E_j} \approx 10^{-4}$ m$^2$ K/W) on an aluminum block (8 mm high, $k = 240$ W/m K), and both sides (i.e., top of chip + bottom of block) are exposed to moving air $T_\infty = 25°\text{C}$, $h \approx 100$ W/m$^2$ K).

*Note:* This problem is adapted from Incropera et al. (2007).

*Recall:* The 1-D heat flux is $q_x = -k\,dT/dx$, and hence the heat flow rate for linear conduction

$$Q = qA = \frac{kA}{L}(T_1 - T_2)$$

where:

$L$ is the wall thickness
$A$ is the surface area
$T_{1,2}$ are the surface temperatures

Now, with the thermal resistance $R_{th} = L/kA$, $Q = \Delta T/R_{th}$, and for several resistances in series

$$Q = \frac{\Delta T}{\sum R_{th}}$$

where $\Delta T = T_{\infty,1} - T_{\infty,n}$ and $\sum R_{th} = \frac{1}{Ah_1} + \sum_1^n \left(\frac{L}{kA}\right)_i + \frac{1}{Ah_n}$

Taylor & Francis
Taylor & Francis Group
http://taylorandfrancis.com

# 2

# *Conservation Laws with Illustrative Examples*

Every other day, one may observe puzzling fluid mechanics phenomena. Such natural, but somewhat counter-intuitive, examples include:

1. Keeping the tailgate of a pick-up truck *up* reduces aerodynamic drag (why?) and hence saves gasoline; although, most drivers intentionally keep it *down* and even install "airflow" nets to retain cargo when accelerating.
2. Under otherwise identical conditions, it is easy to *blow* out a candle but nearly impossible to *suck* it out. Why?
3. Very high (horizontal) winds can *lift* pitched roofs *off* houses. How?
4. When a spoon is brought near a jet, for example, a faucet stream, it gets *sucked into* the stream. Try it out and explain!
5. Chunks of metal are *torn out* from ship propellers at high speeds after a long period of time in operation. Why?
6. The long hair of a girl driving a convertible is pushed *into her face* rather than *swept back*. How come?
7. A snowstorm leaves a cavity *in front* of a pole or tree and deposits snow *behind* the "vertical cylinder." Impossible?
8. Three-dimensional (3-D) effects in river bends create unusual (axial) velocity profiles right after the bend and subsequently, lateral material transport results in shifting riverbeds. Explain!
9. Certain non-Newtonian fluids when stirred in an open container *climb up* the rotating rod, rather than forming a depressed, parabolic free surface. Weird!
10. Airplanes flying through microbursts (or high up in the blue sky) may crash. What is happening during these two very different weather types?
11. Racecar (and motorcycle) tires are hardly threaded, but passenger car tires are. Why?
12. Consider a tsunami (Japanese for "great harbor wave") hitting either a very shallow shore or a deep sea near the shoreline. Describe cause-and-effect for these two scenarios.
13. Wildfires spread rapidly because they create their own local weather pattern. Describe the underlying convection system and how "back-fires" work.
14. A very small amount of carbon nanotubes added to a liquid measurably increases the apparent (or effective) thermal conductivity, k, of the dilute mixture (called a *nanofluid*) when compared with k (watts per meter per degree Kelvin) of the pure base fluid. Why?
15. Gas flow in *microchannels* may exhibit significantly higher flow rates than predicted by conventional theory. What's happening?

So, what are the underlying physical explanations and mathematical descriptions of these and much more complex phenomena of fluid flow, convection heat transfer, and fluid-particle dynamics? Questions (1) through (15) can be quickly answered by visualizing the unique fluid flow pattern via streamline drawings, assuming steady laminar flow, and applying basic definitions or Bernoulli's equation. Others require some extra background reading and sharp thinking. In any case, the answers rely on an equal dose of physics, that is, insight into the transport phenomena, as well as applied mathematics, that is, system modeling and simulation.

The *objectives* of the next sections (plus Chapter 3) are to provide mathematical modeling tools and application skills to solve basic fluid flow and convective heat transfer problems, leading to new physical insight and improved modeling skills. These goals are accomplished, first, in the form of derivations of the mass, momentum, and energy conservation laws with introductory examples. Then, simplified forms of the conservation equations are employed to solve standard fluid dynamics problems. *Derivation* of the modeling equations (Sections 2.2 through 2.4) is a very important task, because that process provides a deeper understanding of the physics. Specifically, derivation highlights the important transport phenomena, mathematically represented by each term of the final equations, and provides a sense of the underlying assumptions, that is, the limitations of a particular mathematical model. Of course, most people regard derivations as boring and mathematically quite taxing; however, it's time for them to become converts, for the two beneficial reasons stated. In addition, *scaling* and *dimensional analysis* are standard laboratory/computational tools for deriving dimensionless groups, estimating the impact of dominant transport phenomena, graphing results to evaluate engineering systems, and testing kinematic/dynamic similarities between a physical model and the actual prototype (see Section 1.4).

Outside the cutting-edge research environment, fluid dynamics problems are solved as special cases; that is, the conservation equations are greatly reduced based on justifiable assumption on a case-by-case basis. As a result, the featured problems of Sections 2.2 through 2.4 have analytic solutions, because they are basically one-dimensional (1-D). Nevertheless, the example problems are insightful demonstrations of the conservation principles with direct applications in engineering fluid mechanics.

As indicated in Chapter 1, for setting up and solving fluid mechanics problems, we follow a three-step approach (see Figure 2.1):

1. Classification of the fluid flow system
2. Mathematical description of the system
3. Solution of the modeling equations with result graphing plus comments

*Characterization of the fluid flow system via system sketch, assumptions, and method, that is, concepts/approach with postulates, may present half of the problem solution*. Because it is a direct guide for system modeling and obtaining the correct results (see Figure 2.1). As was mentioned, in this chapter the conservation equations for mass, momentum, and energy transfer are first derived in *integral* form, that is, in terms of the Reynolds Transport Theorem (RTT), linking the Lagrangian closed system with the Eulerian control volume (i.e., open system) as illustrated in Section 1.3.4. Then, via a straight integral transformation using the divergence theorem (Appendix AI.3.1), the fundamental transport equations in *differential* form are obtained. To provide additional physical insight, a microscale derivation approach is given as well, that is, balancing mass, momentum, and energy for a representative elemental volume $\Delta\forall$ (open system). Clearly, the preferred modeling equations are in

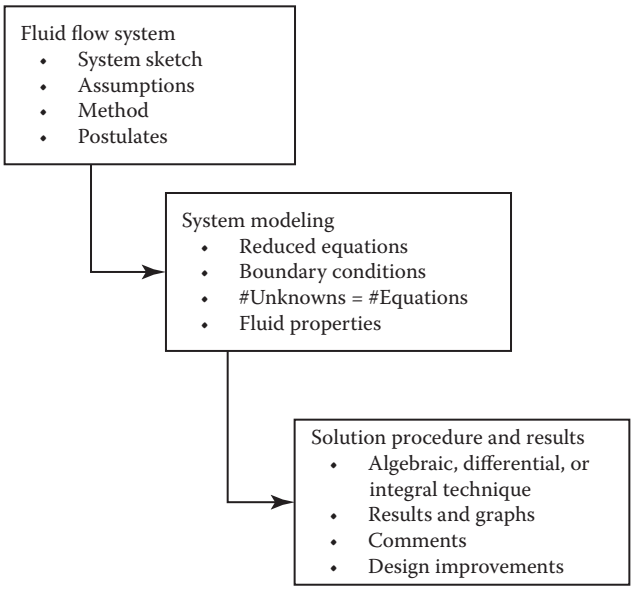


**FIGURE 2.1**
Sequential steps in problem solving.

differential form, providing more detailed information and physical insight. As mentioned throughout Chapter 1, both the *type of fluid* (e.g., Newtonian, non-Newtonian, or homogeneous mixture) and *flow-system characteristics* (e.g., dimensionality, time dependence, flow regime, etc.) must be determined/assumed *a priori* for any given system or problem.

## 2.1 The Reynolds Transport Theorem

Consider $\boldsymbol{B}$ to be an arbitrary extensive quantity of a *closed system* (or a moving material volume). Such a closed system may include an ideal piston-cylinder device with enclosed (constant) gas mass, a rigid tank without any fluid leaks, or an *identifiable fluid mass*—all subject to forces and energy transfer. In any case, $\boldsymbol{B}$ represents the system's mass, momentum, or energy (see Fluid Element in Figure 1.5).

*Task 1* is to express in the Lagrangian frame the fate of $\boldsymbol{B}$ in terms of the material derivative, $D\boldsymbol{B}/Dt$, that is, the total time-rate-of-change of $\boldsymbol{B}_{\text{system}}$ (see Appendix AI.2.1 discussing the operator $D/Dt$). Clearly, for

$$\boldsymbol{B} \equiv m_{\text{system}} = \not{c} \rightarrow \frac{Dm}{Dt} = 0 \tag{2.1a}$$

(conservation of mass)

$$\boldsymbol{B} \equiv (mv)_{\text{system}} \rightarrow m\frac{D\vec{v}}{Dt} = m\vec{a}_{\text{total}} = \sum \vec{F}_{\text{surface}} + \Sigma\vec{F}_{\text{body}} \tag{2.1b}$$

(conservation of momentum or Newton's second law)

$$\boldsymbol{B} \equiv E_{\text{system}} \rightarrow \frac{DE}{Dt} = \dot{Q} - \dot{W} \tag{2.1c}$$

(conservation of energy or first law of thermodynamics)

In *Task 2*, the conservation laws, in terms of $D\boldsymbol{B}/Dt$, are related to an *open system,* that is, in the Eulerian frame. Here, for a fixed control volume (*C.∀.*) with material streams flowing across the control surface (C.S.) and possibly accumulating inside (*C.∀.*)., we observe with specific quantity $\beta \equiv \boldsymbol{B}/m$

$$\left\{\begin{array}{l}\text{Total time-rate-of-change of system}\\ \text{property } \boldsymbol{B}\end{array}\right\} = \left\{\begin{array}{l}\text{Local time-rate-of-change of } \boldsymbol{B}/\forall = \rho\beta\\ \text{within the } C.\forall.\end{array}\right\}$$

$$+\left\{\begin{array}{l}\text{Net efflux of } (\rho\beta),\\ \text{i.e., net material}\\ \text{convection across}\\ \text{control surface C.S.}\end{array}\right\}$$

In mathematical shorthand:

$$\left.\frac{D\boldsymbol{B}}{Dt}\right|_{\text{closed system}} = \frac{\partial}{\partial t}\iiint_{C.\forall.}(\rho\beta)\,d\forall + \iint_{C.S.}(\rho\beta)\,\vec{\mathbf{v}}\cdot d\vec{\mathbf{A}} \tag{2.2a}$$

Clearly, the specific quantity $\beta$ can be expressed as

$$\beta \;\hat{=}\; \frac{\boldsymbol{B}}{m} := \begin{cases} 1 & \text{(mass per unit mass)} \\ \vec{\mathbf{v}} & \text{(momentum per unit mass)} \\ e & \text{(energy per unit mass)} \end{cases} \tag{2.2b through d}$$

Equation 2.2a can be more formally derived and generalized by employing the Leibniz theorem (see 1-D version in Appendix AI.3.2) to describe the total time derivative of a transient transport function $F(\vec{x},t)$. Starting in 1-D, we write the total time derivative of an integral of a function with respect to $x$ and $t$ for which the integral limits are also functions of time (see Figure 2.2).

Specifically, in 1-D,

$$\frac{d}{dt}\left(\int_{x=a(t)}^{x=b(t)} F(x,t)\,dx\right) = \int_{x=a(t)}^{x=b(t)} \frac{\partial F(x,t)}{\partial t}\,dx + F\big(b(t),t\big)\frac{db(t)}{dt} - F\big(a(t),t\big)\frac{da(t)}{dt} \tag{2.3a}$$

Then, with the Leibniz theorem applied to 3-D, the total time-derivative of $F$ can be expressed in compact form as

$$\frac{d}{dt}\int_{\forall(t)} F\big(\vec{x},t\big)\,d\forall = \underbrace{\int_{\forall(t)} \frac{\partial F(x,t)}{\partial t}\,d\forall}_{\text{Local time-rate-of-change}} + \underbrace{\int_{S(t)} F(x,t)\,\vec{v}_s.\hat{n}\;dS}_{\text{Net efflux}} \tag{2.3b}$$

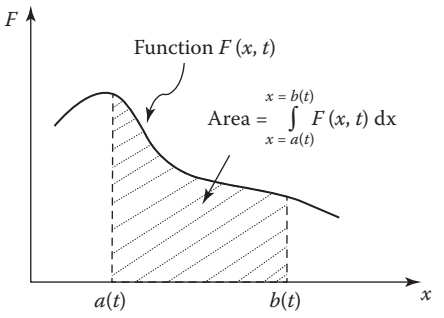


**FIGURE 2.2**
Transport function $F(x, t)$ and its integral.

Now, replacing the moving (deforming) volume $\forall(t)$ with surface S($t$) by control volume (C.$\forall$.) with control surface (C.S.) and, of course, $F\left(\vec{x},t\right) \cong \rho\beta$, where $\beta \triangleq \mathbf{B}_{\text{syst}}/m$, we have

$$\frac{d}{dt}\int_{\text{C.}\forall.} \rho\beta \, d\forall \equiv \quad \frac{D\mathbf{B}_{\text{syst}}}{Dt} \quad = \int_{\text{C.}\forall.} \frac{\partial(\rho\beta)}{\partial t} d\forall + \int_{\text{C.S.}} \rho\beta \, \vec{v}_{\text{rel}} . \, d\vec{A} \tag{2.4}$$

### 2.1.1 Extended Cases

It is implied in Equation 2.4 that for a *moving* control volume, the fluid velocity $\vec{v}$ is replaced by $\vec{v}_{\text{relative}} = \vec{v}_{\text{fluid}} - \vec{v}_{\text{C.}\forall.}$. The operator $\partial/\partial t$, acting on the first term on the RHS, has to be replaced by $d/dt$ when the control volume is *deformable*, that is, the C.S. moves with time, as in the case of a draining tank. For a *non-inertial* coordinate system (see Figure 2.3), for example, when tracking an accelerating rocket, $\Sigma\vec{\mathbf{F}}_{\text{external}}$ of Equation 2.1b is expressed as

$$m\vec{a}_{\text{abs}} = m\left(\frac{d\vec{v}}{dt} + \vec{\mathrm{a}}_{\text{rel}}\right) \tag{2.5a}$$

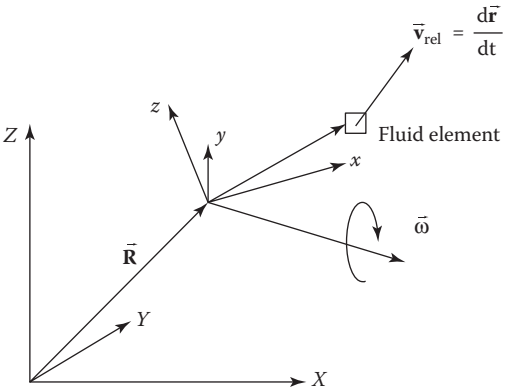


**FIGURE 2.3**
Inertial coordinate system and moving/rotating frame.

where $m\vec{\mathbf{a}}_{\text{rel}}$ accounts for non-inertial effects (e.g., arbitrary *C*.∀. acceleration):

$$\vec{\mathbf{a}}_{\text{rel}} = \frac{d^2\vec{\mathbf{R}}}{dt^2} \tag{2.5b}$$

In the case of *C*.∀. rotation,

$$\vec{\mathbf{a}}_{\text{rel}} = \frac{d\vec{\omega}}{dt} \times \vec{\mathbf{r}} \tag{2.5c}$$

Specifically, for a *rotating* material volume, the fluid angular momentum per unit volume $\beta \equiv \rho\left(\vec{\mathbf{r}} \times \vec{\mathbf{v}}\right)$ must be considered. The law of *conservation of angular momentum* states that the rate-of-change of angular momentum of a material volume is equal to the resultant moment on the volume (see any undergraduate fluids text for details).

### 2.1.2 Setting up the Reynolds Transport Theorem

There are a few sequential steps necessary for tailoring the general RTT toward a specific flow system description and solving the resulting integral equations:

1. Identify the extensive quantity $\boldsymbol{B}_{\text{system}}$, for example, the mass of the identifiable material, linear (or angular) momentum, or total energy. As a result, the specific property of the closed system $\beta = \boldsymbol{B}/m_{\text{system}}$ is known (see Equations 2.1 and 2.2).
2. Determine $D\boldsymbol{B}/Dt|_{\text{system}}$ for each conservation case, that is, mass, system momentum, or energy (see Equation 2.1).
3. Select a "smart" control volume and determine whether
   - The control volume is fixed, or moving at $\vec{\mathbf{v}}_{\text{C.V.}} = \text{¢}$, or accelerating at $a_{\text{rel}} = \text{¢}$, or accelerating and rotating (see "Extended Cases").
   - The flow problem is steady or transient; that is, it is $\frac{\partial}{\partial t} = 0$ or $\frac{\partial}{\partial t} \neq 0$ (note, $\frac{\partial}{\partial t}\iiint_{\text{C.V.}} (\rho\beta)d\forall \doteq 0$ when the rate-of-change of $(\rho\beta)$ inside the *C*.∀. is negligible).
   - A control surface moves; that is, we have a deformable *C*.∀. where $\frac{\partial}{\partial t} \to \frac{d}{dt}$.
   - The fluid properties are constant or variable.
   - The inflow/outflow velocity fields are constant, that is, uniform, or a function of inlet/exit space variables.
   - The resulting integral balance equations for mass and momentum (or energy) are decoupled or not.
4. Set up the momentum, that is, force balance, equation for each coordinate direction.
5. Solve the volume and/or surface integrals (use integration tables if necessary).
6. Follow the inflow/outflow sign convention (see Figure 2.4); that is, IN ≙ "–" and OUT ≙ "+."
7. Check the results for correctness; that is, apply common sense!

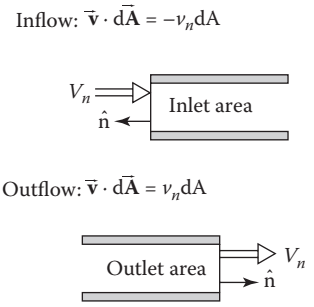


**FIGURE 2.4**
Sign convention for the "net efflux" RTT term. *Recall:* cos(180°) = –1 and cos(0°) = 1.

## 2.2 Fluid-Mass Conservation: The Continuity Equation

Conservation of mass is very intuitive and a standard occurrence in daily life. One can observe that a given mass of a fluid may change its thermodynamic state, that is, liquid or gaseous, but it can neither be destroyed nor created. This, like the other two conservation laws, can be expressed in *integral form* for a control volume of any size and shape, or it can be derived in *differential form.*

### 2.2.1 Fluid-Mass Conservation in Integral Form

To track within the Lagrangian frame an identifiable constant mass of fluid, we set (see Equation 2.2b)

$$\boldsymbol{B}_{\text{system}} \equiv m \text{ and hence } \beta \equiv 1 \tag{2.6a, b}$$

So, the conversation principle requires that for any closed system, $m = \text{¢}$, that is, $Dm/Dt = 0$, and hence, Equation 2.1a reads

$$0 = \frac{\partial}{\partial t}\iiint_{C.\forall.} \rho d\forall + \iint_{C.S.} \rho \vec{\mathbf{v}} \cdot d\vec{\mathbf{A}} \tag{2.7}$$

Thus, we just completed Steps (i) and (ii) of the "setting-up-the-RTT" procedure. Aspects of Step (iii) are best illustrated with a couple of examples.

**Example 2.1: Volumetric Flow Rate**

Consider a liquid-filled tank (depth $H$) with a horizontal slot outlet (height $2h$ and width $w$) where the locally varying outlet velocity can be expressed as (see Sketch 1)

$$u \approx \sqrt{2g(H - z)}$$

A constant fluid mass flow rate, $\dot{m}_{\text{in}}$, is added to maintain the liquid depth $H$. The $z$-coordinate indicates the location of the center of the outlet. Find $Q_{\text{outlet}}$ as a function of $H$ and $h$.

**Sketch 1**

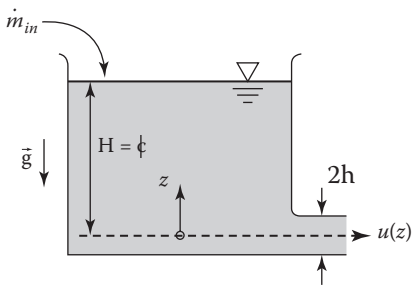


**Assumptions**

- Steady incompressible flow
- Outflow velocity $u(z) = \sqrt{2g(H-z)}$ based on Torricelli's law

**Method**

- Mass RTT
- Fixed, non-deforming *C.∀.*
- $\frac{\dot{m}_{in}}{\rho} = Q$, the volumetric flow rate

*Solution:* Derivation of the *u(z)*-equation is assigned in Section 2.5. Now, with $\frac{\partial}{\partial t}\iiint \rho d\forall = 0$ (steady-state because no system parameter changes with time) and $\rho = ¢$ (incompressible fluid), Equation 2.7 reduces to

$$0 = \iint_{C.S.} \vec{v} \cdot d\vec{A} \tag{E.2.1.1}$$

*Graph 1:*

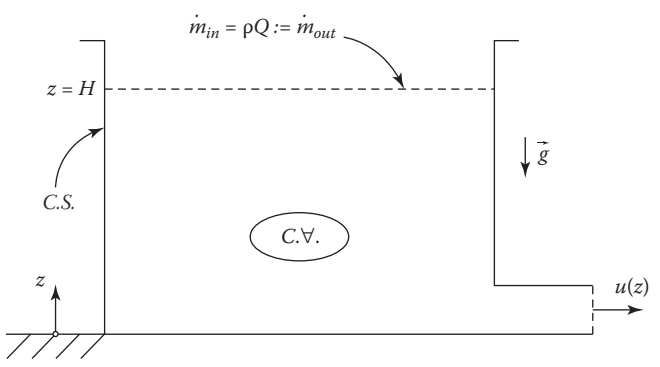


Fluid mass crosses the control surface at two locations (see Graph). Recalling that "inflow" is negative and "outflow" positive (see Figure 2.4), Equation E.2.1.1 reads:

$$-Q + \iint_{A_{slot}} \vec{v} \cdot d\vec{A} = 0 \quad \text{or}$$

$$Q = \int_A v_n dA \tag{E.2.1.2}$$

Here:

$Q \equiv Q_{\text{outlet}}$

$v_n = u(z) = \sqrt{2g(H-z)}$

$dA = w\, dz$

so that

$$Q_{\text{outlet}} = w\sqrt{2g}\int_{-h}^{h} \sqrt{H-z}\; dz$$

which yields (as $Q = Q_{in} = Q_{out}$)

$$Q_{\text{outlet}} = K\left[(H+h)^{3/2} - (H-h)^{3/2}\right] \tag{E.2.1.3}$$

where $K \equiv \frac{2}{3} w\sqrt{2g}$

For $h \ll H$, as is often the case, Equation E.2.1.3 can be simplified to

$$Q_{\text{outlet}} \approx 2wh\sqrt{2gH} \tag{E.2.1.4}$$

The following observations can be made from Example 2.1:

- Equation E.2.1.4 is known as *Torricelli's law.*
- We can deduce that for *incompressible* fluid flow through a conduit,

$$\iint_{\text{C.S.}} \vec{v} \cdot d\vec{A} = 0 \tag{2.8a}$$

or

$$-Q_{in} + \int_{A_{\text{outlet}}} \vec{v} \cdot d\vec{A} = 0 \tag{2.8b}$$

In general,

$$Q = \int_A \vec{v} \cdot d\vec{A} = \int_A v_n dA = \overline{v}A \tag{2.8c}$$

where $\overline{v} = Q / A$ is the area-averaged velocity.

- We also recall that the mass flow rate at any point in a conduit is

$$\dot{m} = \rho\overline{v}A = \rho Q = \text{constant} \tag{2.9}$$

which holds for any fluid and is a key "internal flow" condition, reflecting conservation of mass.

- Clearly, for a C.∀. with multiple inlets and outlets,

$$\Sigma Q_{in} = \Sigma Q_{out} \tag{2.10}$$

The next example considers a *deforming* (e.g., shrinking) control volume inside a tank due to a single outflow in terms of a variable velocity. Thus, Equation 2.7 has to be rewritten as

$$0 = \frac{d}{dt}\iiint_{\text{C.}\forall\text{.}} \rho d\forall + \iint_{\text{C.S.}} \rho\vec{\mathbf{v}} \cdot d\vec{\mathbf{A}} \tag{2.11a}$$

For incompressible fluid flow, we have

$$\left.\frac{d\forall}{dt}\right|_{\text{C.}\forall\text{.}} = -\iint_{\text{C.S.}} \vec{\mathbf{v}} \cdot d\vec{\mathbf{A}} \tag{2.11b}$$

**Example 2.2: Draining of a Tank**

Consider a relatively small tank of diameter D, initially filled to height $h_0$. The fluid drains through a long pipe of radius $r_0$ (as Poiseuille flow—see Example 2.7) according to

$$u(r) = 2\bar{u}\left[1 - \left(\frac{r}{r_0}\right)^2\right]$$

where:
the average velocity is $\bar{u} = \sqrt{2gh}$ (see Example 2.1)
$r_o$ is the outlet pipe radius
$r$ is its variable radius, $0 \le r \le r_0$

The fluid depth is $h_0$ at time $t = 0$. Find $h(t)$ for a limited observation time $\Delta t$.

*Note:* The tank is represented by a "deformable C.∀." because the fluid level decreases, and hence, we have a shrinking C.∀. with moving C.S.

| **Sketch 2** | **Assumptions and Method** | **Deforming Control Volume** |
|---|---|---|
| 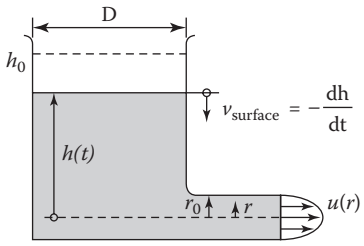  | • *Transient* laminar incompressible flow, that is, $\dot{m}_{in} = 0$ and $\dot{m}_{out} = fct.(t)$ for observation time $\Delta t$<br>• Stationary tank but deforming, that is, shrinking, liquid volume C.∀.<br>• *Method:* Reduced Mass RTT | 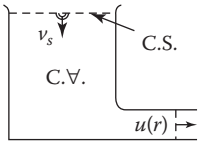  |

*Solution:* In light of the shrinking C.∀., Equation 2.11b can be rewritten with $\forall_{C.\forall.} = \frac{D^2\pi}{4}h(t)$ as

$$\left(\frac{D^2\pi}{4}\right)\frac{dh}{dt} = -\int_0^{r_0} u(r)\,dA \tag{E.2.2.1}$$

where $dA = 2\pi r dr$ is the variable ring element as part of the cross-sectional area of the outlet pipe. Thus,

$$\frac{dh}{dt} = -\frac{16\sqrt{2gh}}{D^2}\int_0^{r_0}\left[1 - \left(\frac{r}{r_0}\right)^2\right] r dr \tag{E.2.2.2a}$$

or

$$\frac{dh}{dt} = -4\sqrt{2g}\left(\frac{r_0}{D}\right)^2\sqrt{h} \tag{E.2.2.2b}$$

subject to $h(t = 0) = h_0$.
Separation of variables and integration yields

$$\sqrt{h_0} - \sqrt{h} = \sqrt{8g}\left(\frac{r_0}{D}\right)^2 t$$

or

$$\frac{h(t)}{h_0} = \left[1 - \sqrt{\frac{8g}{h_0}}\left(\frac{r_0}{D}\right)^2 t\right]^2 \tag{E.2.2.3}$$

*Graph 2:*

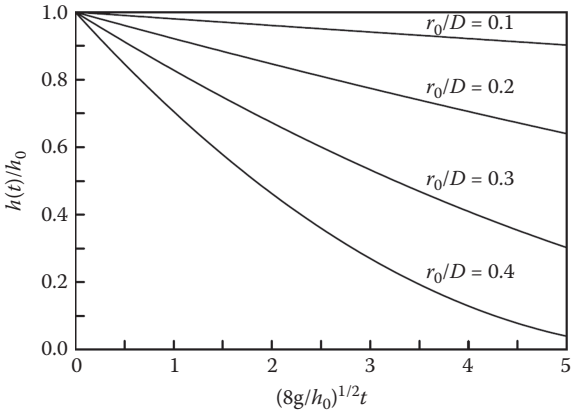


*Comments:*

- The standard assumption that $h$ = constant, that is, being a *reservoir*, is only approximately true when $r_0/D > 0.1$.
- A variable free-surface speed $dh/dt$, that is, accelerated tank-draining, occurs when $r_0/D > 0.2$.

### 2.2.2 Continuity in Differential Form

In general, the RTT is great for computing global (or integral) quantities, such as flow rates and mass fluxes or forces and energies, without knowledge of the detailed fluid flow field *inside* the open system (i.e., the control volume). However, if it is necessary to find point-by-point density variations as well as velocity and pressure distributions to analyze fluid flow patterns, the conservation laws in *differential* rather than integral form have to be solved.

The conservation equations can be readily derived from the RTT, that is, Equation 2.7, by considering an infinitesimally small control volume $d\forall$ and then expressing each term in the form of a volume integral. So, because Equation 2.7 contains a surface integral, it has to be transformed into a volume integral, employing Gauss's divergence theorem (Appendix AI.3.1):

$$\iint_S \vec{\mathbf{v}} \cdot dS \equiv \iiint_{\forall} \nabla \cdot \vec{\mathbf{v}} d\forall \tag{2.12}$$

where:

| | |
|---|---|
| $\vec{\mathbf{v}}$ | is a vector in surface $S$ |
| $\nabla$ | is the del operator (see Appendix AI.1.2) |
| $(\nabla \cdot \vec{\mathbf{v}})$ | is the divergence of the vector field |

Using Equation 2.12 to express the surface integral in Equation 2.7 as a volume integral, Equation 2.7 can be written as

$$\frac{\partial}{\partial t} \iiint \rho d\forall + \iiint \nabla \cdot (\rho \vec{\mathbf{v}})\, d\forall = 0 \tag{2.13a}$$

or, following Leibniz's rule (Appendix AI.3.2) and switching the operation for the first term, we have

$$\iiint \left[ \frac{\partial \rho}{\partial t} + \nabla \cdot (\rho \vec{\mathbf{v}}) \right] d\forall = 0 \tag{2.13b}$$

Clearly, either $d\forall = 0$ (not physical) or

$$\frac{\partial \rho}{\partial t} + \nabla \cdot (\rho \vec{\mathbf{v}}) = 0 \tag{2.14}$$

Equation 2.14 is known as the *continuity equation*, stating fluid-mass conservation on a differential basis. Note the special cases:

$$\text{For steady flow} \left( \frac{\partial}{\partial t} \equiv 0 \right): \quad \nabla \cdot (\rho \vec{\mathbf{v}}) = 0 \tag{2.15}$$

$$\text{For incompressible fluids} (\rho = \text{const.}): \quad \nabla \cdot \vec{v} = 0 \tag{2.16}$$

It should be noted that the widely applicable Equation 2.16 holds for transient velocity fields as well.

#### *2.2.2.1 Differential Mass Balance*

To gain more physical insight, Equation 2.14 is now derived for a differential control volume (see Figure 2.5), that is, a 3-D mass balance over an open system, say, a cube of volume $\Delta\forall = \Delta x \Delta y \Delta z$. The *global mass balance* then reads:

$$\Sigma \dot{m}_{\text{in}} - \Sigma \dot{m}_{\text{out}} = \left. \frac{\partial m}{\partial t} \right|_{\Delta\forall} \tag{2.17}$$

However, in 1-D on a *differential basis* (see Figure 2.3),

$$\left[ (\rho u)\big|_x - (\rho u)\big|_{x+\Delta x} \right] \Delta y \Delta z = \frac{\partial \rho}{\partial t} \Delta\forall \tag{2.18}$$

Now, with Taylor's truncated series expansion (see Appendix AI.2.3),

$$f\big|_{x+\Delta x} = f\big|_x + \frac{\partial f}{\partial x} \Delta x + \cdots\cdots$$

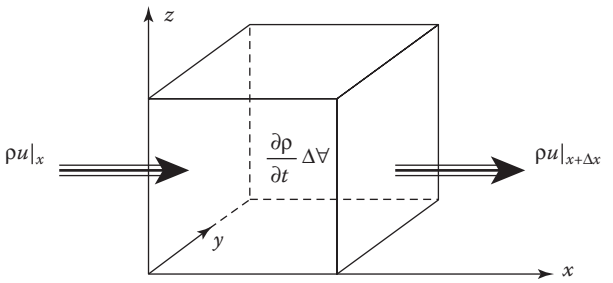


**FIGURE 2.5**
1-D fluid mass balance for a 3-D control volume.

we obtain

$$-\frac{\partial(\rho u)}{\partial x}\Delta x\Delta y\Delta z=\frac{\partial \rho}{\partial t}\Delta x\Delta y\Delta z$$

Adding the other two net fluxes ($\rho v$) and ($\rho w$) in the $y$- and $z$-directions, respectively, and dividing by the *arbitrary* volume, $\Delta\forall$, yields

$$-\frac{\partial(\rho u)}{\partial x}-\frac{\partial(\rho v)}{\partial y}-\frac{\partial(\rho w)}{\partial z}=\frac{\partial \rho}{\partial t} \tag{2.19}$$

In general,

$$\frac{\partial \rho}{\partial t}+\nabla\cdot(\rho\vec{\mathbf{v}})=0 \tag{2.20}$$

**Example 2.3: Use of the Continuity Equation**

*Note:* (A) "fully developed flow" and (B) "accelerating flow."

**Problem (A):** For steady laminar fully developed pipe flow of an incompressible fluid, known as *Poiseuille flow* (see Example 2.6), the axial velocity distribution is described by

$$v_z(r)=v_{\max}\left[1-\left(\frac{r}{r_0}\right)^2\right] \tag{E.2.3.1}$$

Show that, indeed, the radial (or normal) velocity $v_r=0$.

| **Sketch 3** | **Assumptions** |
|---|---|
| 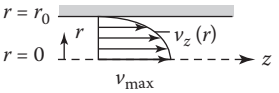 <br>Note: $v_{\max}=2v_{\text{average}}$ for Poiseuille flow | • Steady implies: $\frac{\partial}{\partial t}\equiv 0$<br>• Incompressible fluid: $\rho=$ ¢<br>• Axisymmetric pipe: $\frac{\partial}{\partial \theta}\equiv 0$<br>• Fully developed flow: $\frac{\partial}{\partial z}\equiv 0$, that is, no changes in axial direction |

*Method and Solution:* Based on the assumptions, Equation 2.20 is appropriate and reads for steady 3-D flow in cylindrical coordinates (see Appendix AI.5.1):

$$\frac{1}{r}\frac{\partial(rv_r)}{\partial r}+\frac{1}{r}\frac{\partial v_\theta}{\partial \theta}+\frac{\partial v_z}{\partial z}=0 \tag{E.2.3.2}$$

Clearly, the given velocity profile $v_z$ ($r$) (see Equation E.2.3.1) is not a function of $z$, that is, $\partial v_z/\partial z=0$, which implies with $\partial/\partial\theta=0$ (axisymmetry) that Equation E.2.3.2 reduces to

$$\frac{\partial(rv_r)}{\partial r}=0 \tag{E.2.3.3}$$

Partial integration yields

$$v_r=f(z)/r \tag{E.2.3.4}$$

where $0 \le r \le r_0$, *noting that r could be zero*. That fact and the boundary condition, $v_r$ $(r = r_0) = 0$, that is, no fluid penetrates the pipe wall, forces the physical solution $v_r = 0$. Indeed, if $v_r \neq 0$, such a radial velocity component would alter the axial velocity profile to $v_r = v_r$ $(r, z)$, which implies *developing* flow. That happens, for example, in the pipe's entrance region or due to a porous pipe wall through which fluid can escape or is being injected.

**Problem (B):** Consider 2-D steady laminar symmetric flow in a smooth converging channel, that is, of infinite extent in the $z$-direction, where axial velocity values were measured at five points (see Sketch 4). Estimate the fluid-element acceleration $a_x$ at point C as well as the normal velocity $v$ at point B′. All distances are 2 cm, and the centerline velocities are 5 m/s at A; 7 m/s at B; 10 m/s at C; and 12 m/s at D.

| **Sketch 4** | **Method** |
|---|---|
| 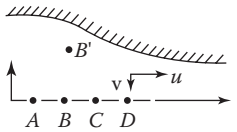 | • Approximate, via simple finite differencing, the reduced acceleration and continuity equations.<br>• Obtain numerical values. |

*Solution:*
From Appendix AI.5.2 (or see also Section 1.3), the axial acceleration can be written as

$$a_x = \frac{\partial u}{\partial t} + u\frac{\partial u}{\partial x} + v\frac{\partial u}{\partial y} + w\frac{\partial u}{\partial z} \tag{E.2.4.3}$$

Based on the stated assumptions $\left(\frac{\partial}{\partial t} = 0, \frac{\partial}{\partial y} = 0, w = 0\right)$:

$$a_x = u\frac{\partial u}{\partial x} \approx u\frac{\Delta u}{\Delta x} = u_c\frac{u_D - u_B}{x_D - x_B} = 10\frac{12-7}{0.04}$$

$$\therefore \quad \boxed{a_x\big|_C \approx 1250 \text{ m/s}^2}$$

to find $v|_B$, we employ the 2-D continuity equation in rectangular coordinates (see Appendix 5.2.1):

$$\frac{\partial u}{\partial x} + \frac{\partial v}{\partial y} = 0 \tag{E.2.4.4}$$

which can be approximated as

$$\frac{\Delta v}{\Delta y} = -\frac{\Delta u}{\Delta x}$$

Hence,

$$\Delta v = -\frac{10-5}{0.04}0.02 = -2.5 \text{ m/s}$$

Recall that $\Delta v = v|_{B'} - v|_B$ where $v_B = 0$ <symmetry> so that

$$\boxed{v|_{B'} = -2.5 \text{ m/s}}$$

*Comments:*

- This is an example of first-order finite differencing, where derivatives are approximated by finite differences of all variables.
- Discretization of the governing equations describing the conservation laws is the underlying principle of computational fluid dynamics (CFD) software (see Section 9.2).

## 2.3 Momentum Conservation Equations: Linear Momentum Transfer and Vorticity Transport

Focusing first on *linear momentum transfer*, the momentum conservation law is again derived in two ways, that is, via integral as well as differential approaches. Not surprisingly, Newton's second law of motion is the foundation of the momentum balance, better known as the *equation of motion*.

### 2.3.1 The Momentum Equation in Integral Form

Forces acting on an identifiable *fluid* element accelerate it as described by Newton's second law of motion, that is, $\left(m\vec{\mathbf{a}}\right)_{\text{fluid}} = \Sigma\vec{\mathbf{F}}_{\text{external}}$. Specifically, we set for the RTT (see Equation 2.1b)

$$B_{\text{system}} \equiv m\vec{\mathbf{v}} \text{ and hence } \beta \equiv \vec{\mathbf{v}} \tag{2.21a, b}$$

As previously indicated (see Section 2.1), with $m = ¢$, $m\dfrac{D\vec{\mathbf{v}}}{Dt} = \Sigma\vec{\mathbf{F}}_{\text{ext}}$, and hence, Equation 2.2a reads:

$$m\frac{D\vec{\mathbf{v}}}{Dt} = m\vec{\mathbf{a}}_{\text{total}} = \Sigma\vec{\mathbf{F}}_{\text{body}} + \Sigma\vec{\mathbf{F}}_{\text{surface}} = \frac{\partial}{\partial t}\int_{C.\forall.} \rho\vec{\mathbf{v}}d\forall + \int_{C.S.} \vec{\mathbf{v}}\rho\vec{\mathbf{v}}\cdot d\vec{\mathbf{A}} \qquad \text{(2.22a through c)}$$

As an aside, for control volumes *accelerating* without rotation relative to inertial coordinates, an additional force $\vec{\mathbf{F}}_{\text{inertia}} \sim \vec{\mathbf{a}}_{\text{relative}}$ appears, where $\vec{\mathbf{a}}_{\text{rel}}$ is the C.∀. acceleration relative to the fixed frame of reference X-Y-Z (see Figure 2.2a). Thus, with

$$\left(\vec{v}_{XYZ} = \vec{v}_{xyz} + \vec{v}_{\text{relative}}\right) \text{ or } \vec{a}_{XYZ} = \vec{a}_{\text{absolute}} = \frac{d\vec{v}}{dt} + \vec{a}_{\text{rel}}$$

we can state that the sum of all forces causes fluid-element acceleration, that is, $\sum\vec{F}_{\text{total}} = m\vec{a}_{\text{abs}} = m\left(\dfrac{D\vec{v}}{Dt} + \vec{a}_{\text{rel}}\right)$. So, for an *accelerating and deforming* control volume,

$$m\frac{D\vec{\mathbf{v}}}{Dt} = \Sigma\vec{\mathbf{F}}_B + \Sigma\vec{\mathbf{F}}_S - \int_{C.\forall.} \vec{a}_{\text{rel}}dm = \frac{d}{dt}\int_{C.\forall.} \rho\vec{\mathbf{v}}d\forall + \int_{C.S.} \vec{\mathbf{v}}\rho\vec{\mathbf{v}}_{\text{rel}}\cdot d\vec{A} \tag{2.23}$$

Returning to Equation 2.22, Example 2.4 illustrates its use by calculating the *total* drag on an arbitrary submerged body in steady laminar flow based on a measured velocity profile behind the body.

**Example 2.4: Force on a Submerged Body**

Find the total drag on a submerged elliptic rod of characteristic thickness $h$, taking into account the simple velocity profile downstream from the body, that is,

$$u(y) = \frac{u_\infty}{4}\left[1 + \frac{y}{h}\right]; 0 \le y \le 3h$$

| Sketch 5 | Assumptions and Method |
|---|---|
| 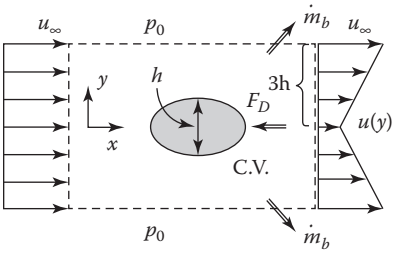  | • *Assumptions*: Steady state, 2-D, constant properties, fixed C.∀., infinite extent in the $z$-direction.<br>• *Method:* Set up and solve reduced integral mass and momentum balances (i.e., RTTs). |

*Solution:* a. Mass Conservation:

$$\dot{m}_{\text{in}} = \dot{m}_{\text{boundary}} + \dot{m}_{\text{out}} \tag{E.2.4.1}$$

$$0 = \int_{C.S.} \rho\vec{\mathbf{v}} \cdot dA = \rho u_\infty 2(3h) + \dot{m}_{\text{boundary}} + 2\rho\frac{u_\infty}{4}\int_0^{3h}\left(1 + \frac{y}{h}\right)dy \tag{E.2.4.2a}$$

$$\therefore \quad \dot{m}_{\text{boundary}} = 6\rho h u_\infty - \frac{15}{4}\rho h u_\infty = \frac{9}{4}\rho h u_\infty \tag{E.2.4.2b}$$

b. Momentum Conservation ($x$-momentum):

$$-F_D = \int_{C.S.} v_x \rho\vec{v} \cdot d\vec{A} := \left(\dot{m}v_x\big|_{\text{exit}} + \dot{m}v_x\big|_b\right) - \dot{m}v_x\big|_{\text{inlet}} \tag{E.2.4.3a}$$

$$-F_D = -u_\infty \rho u_\infty (6h) + u_\infty\left(\frac{9}{4}\rho h u_\infty\right) + 2\rho\int_0^{3h}[u(y)]^2 dy \tag{E.2.4.3b}$$

$$F_D = \frac{9}{8}\rho h u_\infty^2 \tag{E.2.4.3c}$$

*Comments:*

- The fluid flow field inside the C.∀., especially behind the submerged body, is very complex, although the measured outflow profile is very simple.
- The RTT treats the entire flow field as a "black box," and one elegantly obtains $F_D = F_{fixation}$ via the (linear) "velocity defect" measurement, $u = u(y)$.
- While the flow field is 2-D (with $z \to \infty$), after integration the result, $F_x = -F_D$, is obtained in 1-D.

### 2.3.2 Momentum Conservation in Differential Form

To obtain the equation of motion describing any *point* in a fluid flow field, all terms in the RTT have to be first converted to volume integrals, employing Gauss's divergence theorem (see Equation 2.12).

#### *2.3.2.1 The Equation of Motion*

The prevailing *body forces* in Equation 2.22 are problem specific and expressed in terms of volume integrals, that is,

$$\vec{\mathbf{F}}_B = \iiint_{C.\forall.} \rho \vec{\mathbf{f}}_B d\forall \tag{2.24a}$$

while *surface forces* appear as surface integrals, that is,

$$\vec{\mathbf{F}}_S = \iint_{C.S.} \vec{\vec{T}} \cdot d\vec{\mathbf{A}} \tag{2.24b}$$

where:

$\vec{\mathbf{f}}_B$ is a body force per unit mass (e.g., gravity or electrostatic force)

$\vec{\vec{T}}$ is the total stress tensor (i.e., pressure as well as normal and tangential stresses, as discussed in Section 1.2.4)

Now, for a stationary control volume, the linear momentum equation in integral form reads:

$$\int_{C.\forall.} \rho \vec{\mathbf{f}}_B d\forall + \int_{C.S.} \vec{\vec{T}} \cdot d\vec{\mathbf{A}} = \frac{\partial}{\partial t} \int_{C.\forall.} \rho \vec{\mathbf{v}} d\forall + \int_{C.S.} \vec{\mathbf{v}} \rho \vec{\mathbf{v}} \cdot d\vec{\mathbf{A}} \tag{2.25}$$

*Recall:* This is a vector equation for basically the three-component velocity field $\vec{\mathbf{v}}$. It contains $\vec{\vec{T}} \equiv -p\vec{\vec{I}} + \vec{\vec{\tau}}$, that is, the (nine-component) total stress tensor (see Section 1.2.4 and Appendix AI.5.5), as an additional unknown, because in most cases, $\vec{f}_B$ is simply weight per unit mass $(\vec{\mathbf{g}})$. Thus, to solve Equation 2.25, we have to know the *thermodynamic pressure p* and an expression for the *stress tensor* $\vec{\vec{\tau}}$. Recall that $\vec{\vec{I}}$ is the unit tensor, that is, only ones on the diagonal and zeros everywhere else in the $3 \times 3$ matrix; it elevates the product $p\vec{\vec{I}}$ to a "pseudo-tensor," because $p$ is just a scalar.

Now, converting all surface integrals into volume integrals (see Appendix AI.3.1) yields

$$\iiint_{C.\forall.} \left[ \frac{\partial(\rho \vec{\mathbf{v}})}{\partial t} + \nabla \cdot (\rho \vec{\mathbf{v}} \vec{\mathbf{v}}) + \nabla \cdot (p\vec{\vec{I}} - \vec{\vec{\tau}}) - \rho \vec{\mathbf{g}} \right] d\forall = 0$$

or

$$\frac{\partial(\rho \vec{\mathbf{v}})}{\partial t} + \nabla \cdot (\rho \vec{\mathbf{v}} \vec{\mathbf{v}}) = -\nabla p + \nabla \cdot \vec{\vec{\tau}} + \rho \vec{\mathbf{g}} \tag{2.26}$$

Equation 2.26 is *Cauchy's equation* of motion (or linear momentum equation) *for any fluid* and with gravity as the body force. To reduce its complexity and provide some physical meaning, let's consider *constant fluid properties* and express the unknown stress tensor, employing Stokes' hypothesis (see Section 1.2), in terms of the principal variable $\vec{\mathbf{v}}$. In vector notation:

$$\vec{\vec{\tau}} = \mu\left(\nabla\vec{\mathbf{v}} + \nabla\vec{\mathbf{v}}^{tr}\right) = \mu\vec{\vec{\dot{\gamma}}} \tag{2.27a}$$

and in index (or tensor notation):

$$\tau_{ij} = \mu\left(\frac{\partial v_i}{\partial x_j} + \frac{\partial v_j}{\partial x_i}\right) = \mu\dot{\gamma}_{ij} \tag{2.27b}$$

where $\dot{\gamma}$ is the shear rate.

*Recall:* Physically, $\tau_{ij}$ represents a force field per unit area (see Sections 1.2.3 and 1.2.4 and Example 2.6) as a result of the resistance to the rate of deformation of fluid elements, that is, internal friction. As mentioned in Section 1.2.4, this insight leads for Newtonian fluids, such as air, water, typical oils, and so on, to the postulate

$$\tau_{ij} = fct\left(\varepsilon_{ij}\right)$$

where $\varepsilon_{ij} = \frac{1}{2}(v_{i,j} + v_{j,i})$ is the rate-of-deformation tensor. Now, Stokes suggested that $\vec{\vec{\tau}}$ is a *linear function* of $\vec{\vec{\varepsilon}}$, which is not the case for non-Newtonian fluids (Section 4.2.2), rarefied gases, and some fluid flows in microscale devices, for example, microelectromechanical systems (MEMS) (see Section 7.2). Specifically, for Newtonian fluids:

$$\vec{\vec{\tau}} = \lambda\left(\nabla\cdot\vec{\mathbf{v}}\right)\vec{\vec{I}} + 2\mu\vec{\vec{\varepsilon}} \tag{2.28c}$$

where the viscosity coefficients $\lambda$ and $\mu$ depend only on the thermodynamic state of the fluid. For incompressible flow, $\nabla\cdot\vec{\mathbf{v}} = 0$ (see Equation 2.16), and the total stress tensor reduces to

$$\tau_{ij} = 2\mu\varepsilon_{ij} \tag{2.28d}$$

As mentioned,

$$\varepsilon_{ij} = \frac{1}{2}\left(\frac{\partial v_i}{\partial x_j} + \frac{\partial v_j}{\partial x_i}\right) = \frac{1}{2}\dot{\gamma}_{ij} \tag{2.29}$$

so that

$$\tau_{ij} = \mu\left(\nabla\vec{\mathbf{v}} + \nabla\vec{\mathbf{v}}^{tr}\right) = \mu\dot{\gamma}_{ij} \tag{2.30a, b}$$

In summary, Equation 2.30 in conjunction with Equation 2.26 provides closure when solving the Cauchy equation.

### *2.3.2.2 Force Balance Derivation*

A more physical approach for deriving the momentum equation starts with a force balance for a representative elementary volume (REV). Employing rectangular coordinates and *assuming constant fluid properties*, external surface and body forces accelerate an REV of mass $m$, so that we can write Newton's second law of motion per unit volume as (cf. Figure 2.6a)

$$\rho \frac{D\vec{v}}{Dt} = \Sigma \vec{f}_{\text{surface}} + \Sigma \vec{f}_{\text{body}} \tag{2.31}$$

Using the definition of the material (or Stokes) derivative (Appendix AI.2.1), from the Eulerian point of view (see Section 1.3), the REV is a control volume for which we record local and convective momentum changes due to *net* pressure, viscous, and gravitational forces. Again, starting with a 1-D force balance and applying the truncated Taylor series expansion, we obtain (see Figure 2.6b)

$$f_{\substack{\text{net} \\ \text{pressure}}} = f_p\big|_x - f_p\big|_{x+\Delta x} = -\frac{\partial f_p}{\partial x}\Delta x$$

and with

$$f_p \equiv \frac{p\Delta A}{\Delta V}, f_{\substack{\text{net} \\ \text{pressure}}} = -\frac{\partial p}{\partial x}\frac{\Delta y \Delta z}{\Delta x \Delta y \Delta z}\Delta x = -\frac{\partial p}{\partial x}$$

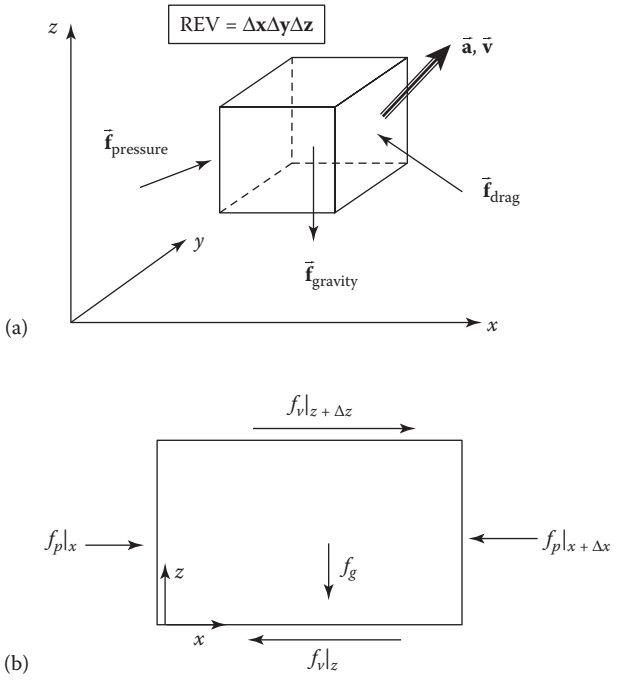


**FIGURE 2.6**
(a) Closed system, i.e., accelerating material volume (REV). (b) Control volume for 1-D force balances.

In 3-D:

$$\vec{f}_{\substack{\text{net}\\\text{pressure}}} = -\nabla p = -\left(\frac{\partial p}{\partial x}\vec{\mathbf{i}} + \frac{\partial p}{\partial y}\vec{\mathbf{j}} + \frac{\partial p}{\partial z}\vec{\mathbf{k}}\right)$$

Similarly, the net viscous force per unit volume in the *x*-direction reads (see Figure 2.6b):

$$f_{\substack{\text{net}\\\text{viscous}}} = f_v\big|_z - f_v\big|_{z+\Delta z} = -\frac{\partial f_v}{\partial z}\Delta z$$

and with

$$f_v \equiv \frac{\tau \Delta A}{\Delta V}, f_{\substack{\text{net}\\\text{viscous}}} = -\frac{\partial \tau}{\partial z}\frac{\Delta x \Delta z}{\Delta x \Delta y \Delta z}\Delta z = -\frac{\partial \tau}{\partial z}$$

In 3-D, the net frictional force can be expressed as

$$\vec{f}_{\substack{\text{net}\\\text{viscous}}} = \nabla \cdot \vec{\vec{\tau}} = \left(\frac{\partial \tau_{xx}}{\partial x} + \frac{\partial \tau_{yx}}{\partial y} + \frac{\partial \tau_{zx}}{\partial z}\right)\vec{\mathbf{i}} + \left(\frac{\partial \tau_{xy}}{\partial x} + \frac{\partial \tau_{yy}}{\partial y} + \frac{\partial \tau_{zy}}{\partial z}\right)\vec{\mathbf{j}} + \left(\frac{\partial \tau_{xz}}{\partial x} + \frac{\partial \tau_{yz}}{\partial y} + \frac{\partial \tau_{zz}}{\partial z}\right)\vec{\mathbf{k}}$$

As discussed, with Stokes' hypothesis for incompressible Newtonian fluids, we have again

$$\vec{\vec{\tau}} = \mu\left(\nabla \vec{\mathrm{v}} + \nabla \vec{\mathrm{v}}^{tr}\right) \tag{2.30}$$

With all the forces inserted into Equation 2.31, we obtain the Navier–Stokes (N-S) equation:

$$\rho\left[\frac{\partial \vec{\mathbf{v}}}{\partial t} + (\vec{\mathbf{v}} \cdot \nabla)\vec{\mathbf{v}}\right] = -\nabla p \; + \; \mu \nabla^2 \vec{\mathbf{v}} + \rho \vec{\mathbf{g}} \tag{2.32}$$

### 2.3.3 Special Cases of the Equation of Motion

Returning to Equation 2.26, which is generally known as Cauchy's *equation of motion*, we now introduce simplifications of increasing magnitude. Fluid properties, that is, density ρ and dynamic viscosity μ, are typically constant. However, occasionally ρ and μ are functions of temperature *T*, pressure *p* (for gases), and species concentration *c*. Clearly, the underlying assumptions for $\rho = \not{c}$, $\mu = \not{c}$, and $c \ll 1$ include:

- Only relatively small temperature variations occur.
- There is a low Mach number for gas flow, that is, $M \equiv v_{\text{fluid}} / a_{\text{sound}} < 0.3$.
- Pressure drops in gas flow are relatively small, and cavitation in liquid flow is avoided.
- Concentration variations of components in mixture flows are small.

Keeping these restrictions in mind, the first simplified form of the equation of motion is the Navier–Stokes (N-S) equation.

### *2.3.3.1 The Navier–Stokes Equation*

Dividing Equation 2.26 throughout by the constant density ρ, and recalling that $\mu/\rho = \nu$, the kinematic viscosity, we recover Equation 2.32, assuming Stokes' hypothesis (Equation 2.30):

$$\underbrace{\frac{\partial \vec{\mathbf{v}}}{\partial t} + (\vec{\mathbf{v}} \cdot \nabla)\vec{\mathbf{v}}}_{\frac{D\vec{\mathbf{v}}}{Dt} = \vec{\mathbf{a}}_{\text{total}}} = \underbrace{-\frac{1}{\rho}\nabla p}_{\vec{\mathbf{f}}_{\text{net pressure}}} + \underbrace{\nu \nabla^2 \vec{\mathbf{v}}}_{\vec{\mathbf{f}}_{\text{net viscous}}} + \underbrace{\vec{\mathbf{g}}}_{\vec{\mathbf{f}}_{\text{body}}} \tag{2.33}$$

Clearly, Equation 2.33 is Newton's particle dynamics equation applied to fluid elements. This equation and the continuity equation, $\nabla \cdot \vec{\mathbf{v}} = 0$, are called the *Navier–Stokes equations.*

For example, for *steady two-dimensional flow*, the N-S equations read in rectangular coordinates (see Appendix AI.5.2):

$$\text{(Continuity)} \qquad \frac{\partial u}{\partial x} + \frac{\partial v}{\partial y} = 0$$

$$(x\text{-momentum}) \qquad u\frac{\partial u}{\partial x} + v\frac{\partial u}{\partial y} = -\frac{1}{\rho}\frac{\partial p}{\partial x} + \nu\left(\frac{\partial^2 u}{\partial x^2} + \frac{\partial^2 u}{\partial y^2}\right) + g_x \tag{2.34a through c}$$

$$(y\text{-momentum}) \qquad u\frac{\partial v}{\partial x} + v\frac{\partial v}{\partial y} = -\frac{1}{\rho}\frac{\partial p}{\partial y} + \nu\left(\frac{\partial^2 v}{\partial x^2} + \frac{\partial^2 v}{\partial y^2}\right) + g_y$$

In general, for transient laminar incompressible 3-D flow, the set of four partial differential equations (PDEs), subject to appropriate boundary conditions, is now being routinely solved for the four unknowns, *u*, *v*, *w*, and *p*, using numerical software packages on workstations, high performance computer (HPC) clusters, and supercomputers (see Chapter 9). In a classroom environment, only reduced forms of Equations 2.34a through c can be solved, as illustrated in Chapters 3 through 8.

### *2.3.3.2 Prandtl's Boundary-Layer Equations*

Based on the no-slip condition, the fluid velocity is zero at a stationary wall of a submerged body. Now, consider relatively high-speed fluid flow past a (horizontal) solid surface, say, a flat plate. That uniform, high–Reynolds number stream suddenly has to reduce to zero at the wall, producing a growing thin shear region in the normal direction. This growing region of high-velocity gradients is called the *boundary layer* (*B-L*). For example, Figure 2.7 depicts such a (laminar) boundary layer of thickness $\delta(x)$, formed along a horizontal stationary flat plate (e.g., a giant razor-blade). It is approached by a uniform fluid stream of velocity $u_\infty$, that is, for laminar B-L flow within a Reynolds number range of $10^3 < \text{Re} < 5 \times 10^5$. It can be readily demonstrated that the $\nu\dfrac{\partial^2 u}{\partial x^2}$ -term (axial momentum diffusion) of Equation 2.34b is negligible (see Section 3.2.1) and that the *y*-momentum

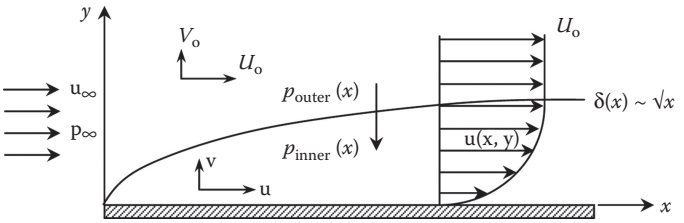


**FIGURE 2.7**
Laminar flat-plate boundary layer.

equation collapses to $-\frac{1}{\rho}\frac{\partial p}{\partial y} = 0$; that is, $p = p(x)$ only. As a result, Equations 2.34a through c reduce to (see Appendix A1.7.2):

$$\frac{\partial u}{\partial x} + \frac{\partial v}{\partial y} = 0 \tag{2.35a}$$

and

$$u\frac{\partial u}{\partial x} + v\frac{\partial u}{\partial y} = -\frac{1}{\rho}\frac{\partial p}{\partial x} + v\frac{\partial^2 u}{\partial y^2} \tag{2.35b}$$

inside the boundary layer $0 \le y \le \delta(x)$ and $0 \le x \le \ell$, where $\ell$ is the plate length.

#### *2.3.3.3 Stokes Equation*

When the viscous forces are dominant, the Reynolds number is very small (see Section 1.4). As a result, the term $(\vec{\mathbf{v}} \cdot \nabla)\vec{\mathbf{v}}$ in Equation 2.33 is negligible for *creeping* (*or Stokes*) *flow*. So, the *Stokes equation* describing slow flow is in the form

$$\rho\frac{\partial \vec{\mathbf{v}}}{\partial t} = -\nabla p + \mu\nabla^2\vec{\mathbf{v}} \tag{2.36}$$

Such $\mathrm{Re} < 1.0$ flows, that is, either $\mu \gg 1$ and/or $\ell \ll 1$, are encountered in food processing, porous-media flows, microscale flows, and some fluid-particle flows.

#### *2.3.3.4 Euler Equation*

For frictionless flows ($\mu \equiv 0$), Equation 2.33 reduces to

$$\rho\frac{D\vec{v}}{Dt} = -\nabla p + \rho\vec{g} \tag{2.37}$$

which is the *Euler equation*. Although ideal fluids, that is, inviscid flows, hardly exist, the second-order term vanishes. For example, flow outside a boundary layer is assumed to be frictionless, as indicated by the velocity profile in Figure 2.7. In fact, aerodynamics people employ Equation 2.37 to find the outer pressure field around airfoils (see $p_{outer}$ in Figure 2.7), which is imposed onto the thin-shear layer, that is, $p_{outer} = p_{inner}$, because $\partial p/\partial y = 0$. Then, the velocity field inside the boundary layer is obtained via a solution to Prandtl's equations (Equation 2.24a,b).

### *2.3.3.5 Bernoulli Equation*

Equation 2.37 applied to a representative streamline along coordinate $S$ yields in general (see Figure 2.8)

$$\frac{\partial v_s}{\partial t} + v_s \frac{\partial v_s}{\partial s} + \frac{1}{\rho}\frac{\partial p}{\partial s} + g \underbrace{\sin\theta}_{\partial z/\partial s} = 0 \tag{2.38a}$$

which leads to the *Bernoulli equation*. For example, assuming *steady incompressible inviscid flow*, multiplying Equation 2.38a through by $\partial s$ and integrating, yields

$$\frac{v^2}{2} + \frac{p}{\rho} + gz = C \tag{2.38b}$$

where:

- $v$ and $p$ are locally averaged quantities along a representative streamline
- the $z$-coordinate extends against the direction of gravity

Thus, for two points on a representative streamline, the total energy per unit mass is balanced; that is,

$$\frac{v_1^2}{2} + \frac{p_1}{\rho} + gz_1 = \frac{v_2^2}{2} + \frac{p_2}{\rho} + gz_2 \tag{2.39}$$

For example, for a given system where $v_2 = 0$ (e.g., Point 2 of a streamline is on the front of a submerged body) and $g\Delta z \approx 0$, we have

$$p_2 = p_1 + \frac{\rho v_1^2}{2} \tag{2.40}$$

where:

| | |
|---|---|
| $p_2$ | is the total or *stagnation point pressure* |
| $p_1$ | is the *thermodynamic* (or a *static) pressure* at Point 1 |
| $\rho v_1^2 / 2$ | is the *dynamic pressure* at Point 1 |

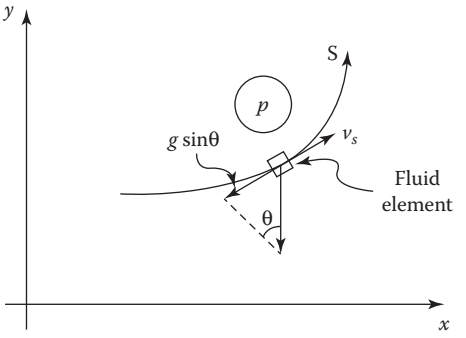


**FIGURE 2.8**
A fluid element along a representative streamline depicting steady laminar 2-D flow.

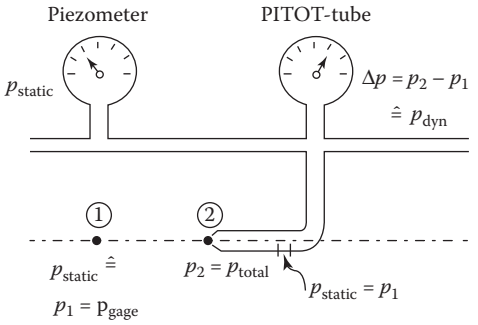


**FIGURE 2.9**
Different manometers to measure different pressures.

One application of Equation 2.40 is the Pitot-static tube, which measures $\Delta p = p_2 - p_1$, so that $v_1 = \sqrt{2(p_2 - p_1)/\rho}$ (see Figure 2.9).

*2.3.3.5.1 Notes on Bernoulli's Equation*

Although "steady inviscid flow along a streamline," as described by Bernoulli's equation, is a very idealized case of the momentum equation, some astonishing (approximate) results can be obtained with this simple flow model:

$$\frac{p}{\rho g} + \frac{v^2}{2g} + z = const. \tag{2.41}$$

To demonstrate the power and versatility of the Bernoulli equation, simple answers are given to the next four questions, related to complex transport phenomena:

A. *Why do airplanes fly? Well*, they need a lift force larger than the weights of plane + passengers + baggage.

**Sketch 6**

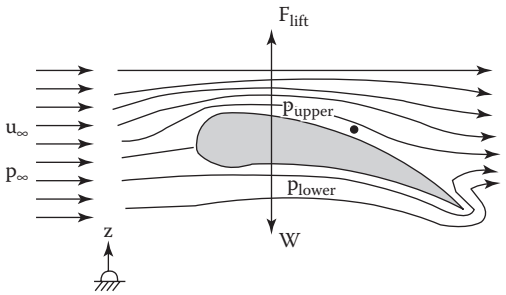


**Rationale:**

- Bernoulli states that with $z_\infty = z_{lower} \approx z_{upper}$

$$p_e + \frac{\rho}{2} v_e^2 = p_u + \frac{\rho}{2} v_u^2 = p_\infty + \frac{\rho}{2} v_\infty^2 \tag{2.42}$$

**Observations:**

- Above the wing (or airfoil), streamlines cluster, and the air-velocity is very high, so that with $z \approx$ constant , $p_{upper}$ is low according to Bernoulli.

- The opposite occurs below the wing, that is, $v_{\text{lower}} \downarrow\ p_{\text{lower}} \uparrow$.
- Hence, for an effective airfoil surface $A_{\text{surf}}$:

$$F_{\text{lift}} = \left(p_l - p_u\right) A_{\text{surface}} > W \tag{2.43}$$

B. *Why do roofs fly off houses during episodes of very high winds?* Actually, because the pressure field above the pitched roof is much lower than the atmospheric pressure in the attic.

**Sketch 7**

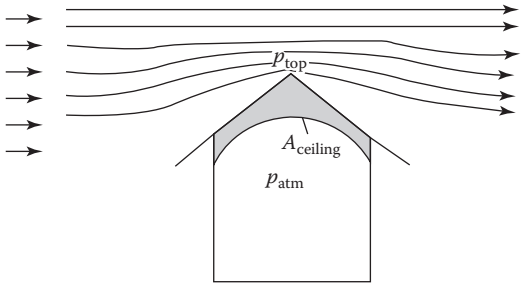


**Rationale**:

- Similar to the explanation for Question (A), the pressure field on the roof due to the locally very high wind velocity is very low, so that the pressure force inside the house, $p_{\text{atm}} A_{\text{ceiling}}$, blows the roof off the house.

C. *What is the wind force on a high-rise window?* It is assumed that the air is incompressible and approaches the window horizontally at a uniform and steady velocity (see Sketch 8).

**Sketch 8**

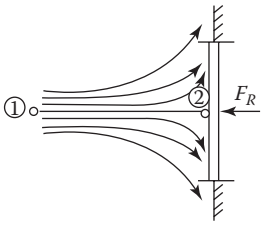


**Solution:** As stated,

$$\frac{v_1^2}{2g} + \frac{p_1}{\rho g} + z_1 = \frac{v_2^2}{2g} + \frac{p_2}{\rho g} + z_2 \tag{2.44}$$

With the given information, Equation 2.44 reduces to

$$p_2 = \frac{\rho}{2} v_1^2 \tag{2.45}$$

and hence,

$$F_R = \int pdA \approx p_2\ A_{\text{window}} \tag{2.46}$$

For example, with a 65 mph wind, $F_R \approx 1$ kN for a typical window.

D. *How can one describe the vertical motion of a disk suspended on a fluid jet?* Specifically, a horizontal disk of mass M can only move vertically when a water jet ($d_0$, $v_0$) strikes the disk from below. Obtain a differential equation for the disk height $h(t)$ above the jet exit plane when the disk is initially released at $H > h_0$, where $h_0$ is the equilibrium height. Find an expression for $h_0$, sketch $h(t)$, and explain.

**Sketch 9**

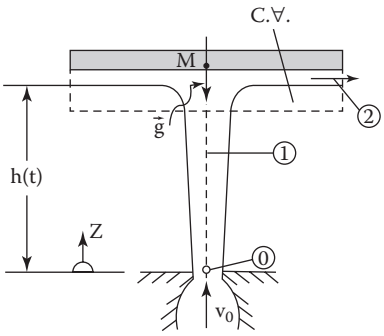


The assumptions are:

- Steady laminar frictionless flow represented by a streamline with points 0, 1, 2
- Near $z = 0$: $\rho = \text{¢}$, $v_0 = \text{¢}$, and $p_0 = p_1 = p_2$
- Moving, accelerating, C.∀., that is, $v_{\text{rel}} = v_{\text{fluid}} = v_{C.V}$ and $a_{C.V} = d^2h/dt^2$
- Averaged velocities, that is, $v_{C.V} = dh/dt$; $v_2 \approx 0$
- $M_{\text{disk}} \gg m_{\text{fluid}}\big|_{C.\forall}$ and $A_1 > A_0$

*Solution:*

- (Bernoulli) $\dfrac{p_0}{\rho} + \dfrac{v_0^2}{2} + gz_0 = \dfrac{p_1}{\rho} + \dfrac{v_1^2}{2} + gz_1$ can be reduced to

$$\frac{v_0^2}{2} = \frac{v_1^2}{2} + g\ h(t) \Rightarrow v_1 = \sqrt{v_0^2 - 2gh} \tag{2.47a, b}$$

- $\left(\text{Continuity}\right) v_0\ A_0 = v_1\ A_1 \Rightarrow A_1 = A_0\ \dfrac{v_0}{v_1}$ (2.48)

- (Momentum RTT)

$$F_s + F_B - \int_{C.\forall.} a_{C.\forall.}\, \rho d\forall = \frac{\partial}{\partial t} \int_{C.\forall.} v\rho d\forall + \int_{c.s.} v\rho \vec{v}_{\text{rel}} \cdot d\vec{A} \tag{2.49}$$

can be reduced to

$$-Mg - Ma = v_{\text{vel}}[-\rho(v_{\text{rel}} A_1)] + v_2 \dot{m}_2 \tag{2.50}$$

with $v_{\text{rel}} = v_1 - \dfrac{dh}{dt}$ and $a = \dfrac{d^2h}{dt^2}$, we have

$$M\left(g + \frac{d^2h}{dt^2}\right) = \rho\left(v_1 - \frac{dh}{dt}\right)^2 A_1 \tag{2.51}$$

Substituting $v_1$ and $A_1$ yields

$$\ddot{h} - \frac{\rho v_0 A_0}{M\sqrt{v_0^2 - 2gh}}\left(\sqrt{v_0^2 - 2gh} - \dot{h}\right)^2 + g = 0 \tag{2.52}$$

Now, at equilibrium height, $h = h_0$, $\dot{h} = \ddot{h} = 0$. Thus,

$$-\rho\sqrt{v_0^2 - 2gh_0}\ A_0 v_0 + Mg = 0 \tag{2.53a}$$

or

$$h_0 = \frac{v_0^2}{2g}\left[1 - \left(\frac{gM}{\rho v_0^2 A_0}\right)^2\right] := \frac{v_0^2}{2g}\left[1 - \left(\frac{Mg}{\dot{m} v_0}\right)^2\right] \tag{2.53b, c}$$

**Graph 3:**

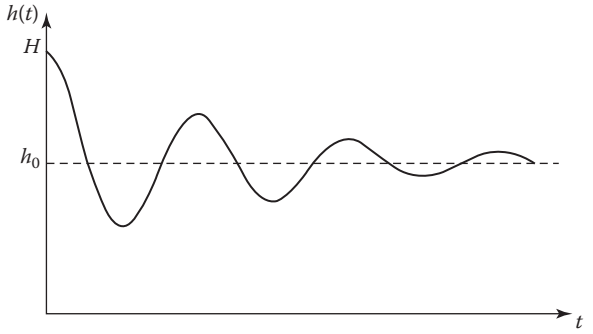


**Comments:**

1. Although frictionless flow was assumed, the ordinary differential equation (ODE) for $h(t)$ is nonlinear, which implies oscillations as well as a decrease in amplitude.
2. This problem solution couples Bernoulli's equation with mass and momentum conservation and shows the interactive nature of fluid mechanics.
3. The Bernoulli equation is even more powerful when extended to include frictional and form losses; for example, in pipe flow with entrance effects, changes in cross-sectional area, valves, and so on.

### 2.3.4 Basic Examples of Linear Momentum Transfer

To enhance the meaning of each term in the continuity equation as well as in the equation of motion (i.e., the N-S equation) and to provide a formalism to reduce the coupled equation for specific applications, three examples are discussed.

**Example 2.5: Shear Stress in Simple COUETTE Flow**

Consider Couette flow, that is, a viscous fluid between two parallel plates a small gap $h$ apart, where the upper plate moves with a constant velocity $u_0$ due to a tangential force, $F_{\text{pull}}$. Typically, also an axial pressure gradient is applied; that is, $\partial p / \partial x = -\Delta p / L = \not<$.

| Sketch 10 | Assumptions | Method |
|---|---|---|
| 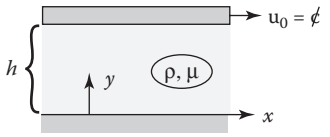 | • Steady laminar fully developed (unidirectional) flow<br>• Constant fluid properties<br>• Only the pulling force at the upper plate maintains the fluid motion | • Reduced N-S equations based on assumptions and boundary conditions<br>• Specifically, the pressure gradient is zero and $u = u(y)$ only |

*Solution:* Translating the problem statement plus assumptions into mathematical shorthand, we have:

- Movement of the upper plate due to a constant pulling force keeps the viscous fluid between the plates in motion from $u(y=h)=u_0$ to $u(y=0)=0$ via frictional effects, which propagate normal to the plate.
- *Steady flow* $\Rightarrow$ all time derivatives are zero, that is, $\dfrac{\partial}{\partial t} \equiv 0$.
- Laminar *unidirectional flow* $\Rightarrow$ only one velocity component is non-zero, that is, $\vec{v} = (u,0,0)$, where $u = u(y)$ only. This implies *parallel* or *fully developed flow*, where $\dfrac{\partial}{\partial x} \equiv 0$ and hence $v = 0$.

In summary, we can postulate that

$$u = u(y),\ v = w = 0$$

$$\frac{\partial u}{\partial x} = 0;\ \frac{\partial p}{\partial x} = 0; g_x = 0$$

Checking Equations 2.34a through c with these postulates, we realize the following:

- Continuity equation confirms $v = 0 \Rightarrow \dfrac{\partial u}{\partial x} = 0$; that is, fully developed flow.
- $x$-momentum yields

$$0 + 0 = 0 + v\left(0 + \frac{\partial^2 u}{\partial y^2}\right) + 0 \qquad \text{(E.2.5.1)}$$

and

$y$-momentum collapses to $\dfrac{\partial p}{\partial y} = \rho g_y <$ fluid statics $>$

Thus, Equation E.2.5.1 can be written as

$$\frac{d^2u}{dy^2} = 0 \tag{E.2.5.2}$$

subject to the "no-slip" conditions

$$u\left(y=0\right) = 0 \text{ and } u\left(y=h\right) = u_0 \tag{E.2.5.3a, b}$$

Double integration and inserting the boundary conditions (BCs) yields

$$u\left(y\right) = u_0 \frac{y}{h} \tag{E.2.5.4}$$

Of the stress tensor (Equation 2.27b), $\tau_{ij} = \mu\left(\frac{\partial u_i}{\partial x_j} + \frac{\partial u_j}{\partial x_i}\right)$, only $\tau_{yx}$ is non-zero, that is,

$$\tau_{xy} = \mu\left(\frac{\partial u}{\partial y} + \frac{\partial v}{\partial x}\right) \tag{E.2.5.5}$$

With $v \equiv 0$ and Equation E.2.5.5,

$$\tau_{xy} = \mu u_0 / h = \not{c}$$

Of the vorticity vector $= \vec{\zeta} = 2\vec{\omega} = \nabla \times \vec{v} = curl\,\vec{v}$ (Appendix AI.1), only $\omega_{yx}$ is non-zero, that is,

$$\omega_{yx} = \frac{\partial u}{\partial y} - \frac{\partial v}{\partial x} \coloneqq u_0 / h = \not{c} \tag{E.2.5.6a–c}$$

This implies that the fluid elements between the plates rotate with constant angular velocity $\omega_{yx}$ while translating with $u(y)$.

*Note:* The wall shear stress at the upper (moving) plate is also constant, that is,

$$\tau_w = \mu \frac{\partial u}{\partial y}\bigg|_{y=h} = \mu\left(\frac{u_0}{h}\right) \tag{E.2.5.7.a, b}$$

so that the pulling force equal to the drag is

$$F_{\text{drag}} = -\int \tau_w dA_{\text{plate}} = F_{\text{pull}} = \frac{\mu u_0}{h} A_{\text{surface}} = \text{constant} \tag{E.2.5.8a–d}$$

*Profile 1:*

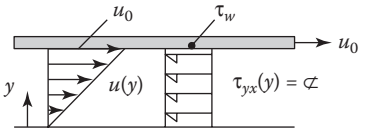


*Comments:*

- In the absence of a pressure gradient, only viscous effects set the fluid into (linear) motion.

- The necessary "pulling force" is inversely proportional to the gap height; that is, the thinner the fluid layer, the larger is the shear stress and hence $F_{pull}$.
- As a first-order approximation, the Couette flow model is applicable to planar lubrication.

**Example 2.6: Poiseuille Flow**

Consider steady laminar fully developed (unidirectional) flow of an incompressible fluid in a horizontal pipe of length $L$ and constant cross-sectional area (radius $r_0$), known as *Poiseuille flow*. Establish reduced forms of the N-S equations and solve for the axial velocity $u(r)$.

| Sketch 11 | Assumptions | Method and Postulates |
|---|---|---|
| 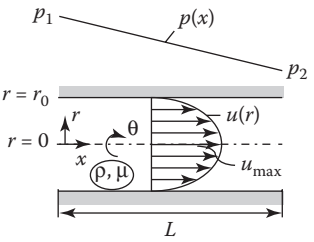 | As stated:<br>• $\partial/\partial t = 0$ (steady-state)<br>• $\vec{\mathbf{v}} \Rightarrow u$ (unidirectional)<br>• $\partial/\partial x = 0$ (fully developed)<br>• $\partial/\partial\theta = 0$ (axisymmetric) | Reduced N-S eqs. based on the assumptions and postulates.<br>*Postulates:*<br>$\vec{\mathbf{v}} = (u, 0, 0)$, where $u = u(r)$ only;<br>$-\nabla p \Rightarrow -\dfrac{\partial p}{\partial x} \hat{=} \dfrac{\Delta p}{L}$<br>$= \dfrac{p_1 - p_2}{L} = \text{¢}$ |

*Solution:*

- Check continuity: With $v = 0$, $\nabla \cdot \vec{\mathbf{v}} = 0$ can be reduced to $\dfrac{\partial u}{\partial x} = 0$, that is, fully developed flow.
- The equation of motion (Equation 2.33) reduces to

$$0 = -\nabla p + \mu \nabla^2 \vec{\mathbf{v}} \tag{E.2.6.1}$$

Expanded with the *postulates* and Appendix AI.5.3, we have

$$0 = \left(\frac{\Delta p}{L}\right) + \mu \frac{1}{r} \frac{d}{dr}\left(r \frac{du}{dr}\right) \tag{E.2.6.2}$$

subject to the boundary conditions: $u(r = r_0) = 0$ (no slip) and at $r = 0$, $du/dr = 0$ (axisymmetry).

*Note:* Using the centerline condition $u(r = 0) = u_{max}$ is physically/mathematically correct, but we do not know $u_{max}$.
So, double integration and invoking the two boundary conditions yields

$$u(r) = \frac{1}{4\mu}\left(\frac{\Delta p}{L}\right)\left(r_0^2 - r^2\right) = u_{max}\left[1 - \left(\frac{r}{r_0}\right)^2\right] \tag{E.2.6.3}$$

*Comments:*

- The solution (E.2.6.3) is the base case for steady laminar *internal* flows with numerous applications in terms of industrial pipe flows, such as pipe networks, heat exchangers, and fluid transport, as well as idealized tubular flows in biomedical, chemical, environmental, mechanical, and nuclear engineering.

- Equation E.2.6.3 not only provides the parabolic velocity profile $u(r)$ but can also be used to calculate the volumetric flow rate Q (Equation 2.5), wall shear stress $\tau_w$, and pressure drop $\Delta p$ (using Equation 2.8).
- Solved problems in Section 3.1 and sample applications in Part B further illustrate the use of the Poiseuille-flow solution (E.2.6.3).

While the previous examples fall into the category of "internal flows," the next one deals with "external" flow, that is, a gravity-driven thin film of constant thickness.

**Example 2.7: Thin-Film Flow**

Consider a liquid fed from a reservoir forming a thin film pulled down on an inclined plate by gravity. Obtain the velocity profile, flow rate, and wall shear force, assuming a constant film thickness in the test section $0 < x < \ell$.

**Sketch 12**

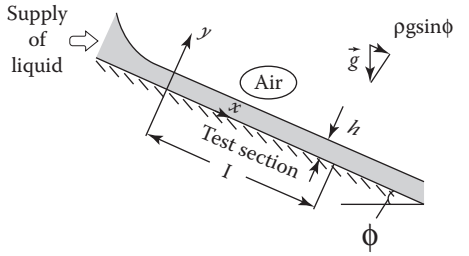


*Assumptions*

- Steady laminar fully developed flow
- Negligible air–liquid shear stress
- Constant $h$, $p$, $\rho$, and $\mu$
- Neglect end effects, that is, $h = \text{const.}$

*Method*

- Reduced N-S eqn. $\vec{\mathbf{v}} = (u, 0, 0)$; $u = u(y)$ only; $\nabla p = 0$
- Only gravity, $\rho g \sin\phi$, drives the film flow
- $\text{Re} \leq 20$ to avoid film-surface rippling

*Solution:*
An *inclined x–y coordinate system* is attached to the plate; that is, the $x$-momentum equation is of interest (note, the $y$- and $z$-momentum equations are both zero). Considering Sketch 12 and based on assumptions $\vec{\mathbf{v}} = (u, 0, 0)$, $\nabla p \approx 0$ (thin-film condition or no significant fluid-state pressure variations), and $\partial/\partial t = 0$ (steady-state), the N-S equations are reduced as follows. With $v = w = 0$, continuity $\nabla \cdot \vec{\mathbf{v}} = 0$ indicates that

$$\frac{\partial u}{\partial x} + 0 + 0 = 0 \tag{E.2.7.1}$$

which implies fully developed (or unidirectional) flow; thus, $u = u(y)$ only.
Consulting the equation sheet (Appendix AI.5.3) and invoking the postulates $u = u(y)$, $v = w = 0$, and $\partial p/\partial x = 0$, we have with the body force component $\rho g \sin\phi$

$$0 = \mu \frac{d^2 u}{dy^2} + \rho g \sin\phi \tag{E.2.7.2}$$

subject to $u(y = 0) = 0$ <no slip> and $\tau_{\text{interface}} = \mu \left.\dfrac{du}{dy}\right|_{y=h} \approx 0$, which implies that at $y = h \longrightarrow du/dy = 0$. Double integration of Equation E.2.7.2 in the form $u'' = K$ (see Appendix AI.4) yields after invoking the two BCs

$$u(y) = -\frac{\rho g h^2 \sin\phi}{2\mu}\left[\left(\frac{y}{h}\right)^2 - 2y/h\right] \tag{E.2.7.3a}$$

Clearly,

$$u(y=h) = u_{\max} = \frac{\rho g h^2}{2\mu}\sin\phi \tag{E.2.7.3b}$$

The average velocity is

$$u_{\text{av}} = \frac{1}{A}\int_A \vec{\mathbf{v}}\cdot d\vec{\mathbf{A}} := \frac{1}{h}\int_0^h u\, dy = \frac{\rho g h^2 \sin\phi}{3\mu} \tag{E.2.7.4a}$$

Hence,

$$u_{\text{av}} = \frac{2}{3}u_{\max} \tag{E.2.7.4b}$$

To determine the film thickness, we first compute the volumetric flow rate $Q$, which is usually known.

$$Q = \int \vec{\mathbf{v}}\cdot d\vec{\mathbf{A}} := b\int_0^h u\, dy \;:= u_{\text{av}}(hb) \tag{E.2.7.5a}$$

where $b$ is the plate width. Thus,

$$Q = \frac{pgb\sin\phi}{3\mu}h^3 \tag{E.2.7.5b}$$

from which

$$h = \left(\frac{3\mu Q}{\rho g b \sin\phi}\right)^{1/3} \tag{E.2.7.5c}$$

The shear force (or drag) exerted by the liquid film onto the plate is

$$F_s = \int_A \tau_{yx}\, dA = b\int_0^l \left(-\mu\left.\frac{du}{dy}\right|_{y=0}\right) dy \tag{E.2.7.6a}$$

Thus,

$$F_s = \rho g b h l \sin\phi \tag{E.2.7.6b}$$

which is the $x$-component of the weight of the whole liquid film along $0 \le x \le 1$.

*Graph 4:*

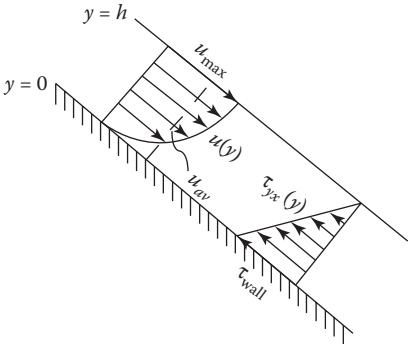


*Comments:*

- Numerical film values can be used to compute the film Reynolds number, $\mathrm{Re}_h = \frac{u_{av}\, h}{v}$, and check whether $\mathrm{Re}_h < \mathrm{R}_{ecritical} \approx 20$.
- Given $Q$ (or $\dot{m} = \rho Q$ ), the coating thickness can be estimated.

*Notes:* The case of wire coating, that is, falling film on a vertical cylinder, is assigned as a homework problem (see Section 2.5). Additional surface-coating (and film-drawing) systems are discussed in Chapter 6.

### 2.3.5 Vorticity Dynamics

The momentum equation (see Equation 2.26, or its simplified form Equation 2.33) describes the flow-field interactions of pressure, viscous, and body forces, leading to fluid-element acceleration. A complementary way of flow field description can be obtained in terms of *vorticity transport.*

#### *2.3.5.1 Vorticity Vector and Fluid Circulation*

Clearly, unbalanced shear stresses set fluid elements into rotation, that is, spinning around their own axes. This can be expressed with the vorticity vector (see Section 1.2.4 as well as Appendix AI.1.1 and AI.1.2):

$$\vec{\zeta} = 2\vec{\omega} = \nabla \times \vec{v} = curl\, \vec{v} \tag{2.55}$$

For example, the circumferential velocity $v_\theta$ of a hurricane can be depicted as a combination of "solid-body-rotation" $v_\theta = \omega r$ (the eye of a hurricane) and a "potential vortex" $v_\theta = K/r$ (the outer region), as shown in Figure 2.10.

In cylindrical coordinates with $\vec{v} = (0; v_\theta; 0)$, $\vec{\zeta}$ reduces to $\zeta_z = \frac{1}{r}\frac{\partial}{\partial r}(r v_\theta)$, which implies that the eye of the hurricane is rotational $\zeta_z = 2\omega$, while irrotational ($\zeta_z = 0$), that is, frictionless, in the outer region. Generalizing the observation, one can conclude that vorticity dynamics analysis allows a flow field to be separated into one with viscous and one with inviscid effects. A simple analogy is that rotational circular flow is like a rotating roundabout, while irrotational circular flow is analogous to a moving Ferris wheel.

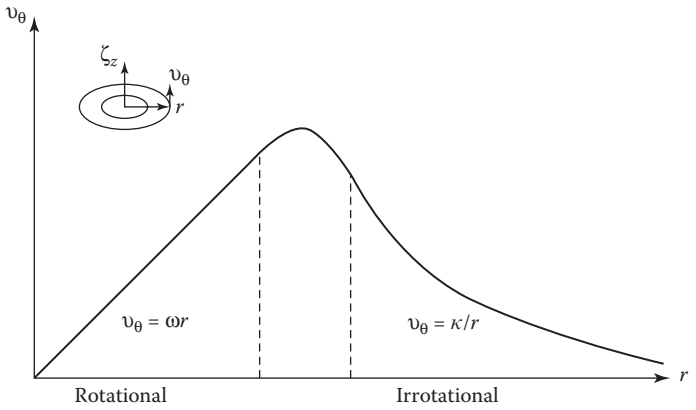


**FIGURE 2.10**
Vorticity regimes of a hurricane.

A quantity directly related to rotational flow is circulation:

$$\Gamma = \oint \vec{\mathbf{v}} \cdot d\vec{r} \tag{2.56}$$

which is the line (or contour) integral of the tangential velocity around a closed path. Employing Stokes' theorem, where the contour integral is transformed into a surface integral, we have

$$\Gamma = \oint \vec{\mathbf{v}} \cdot d\vec{r} = \iint_S \underbrace{\left(\nabla \times \vec{\mathbf{v}}\right)}_{\equiv \vec{\zeta}} \cdot \hat{n}\, dS \tag{2.57}$$

For example, for the previous 2-D flow field, described by $v_\theta = \omega r$ within $0 < r < r_0$, we have with $\zeta_z = 2\omega$ and $dS = 2\pi\, rdr$ an expression for the vortex strength:

$$\Gamma = 2\pi \int_0^r (2\omega)\, rdr = 2\pi\omega r^2 \tag{2.58a, b}$$

or

$$v_\theta = \frac{\Gamma}{2\pi r} \tag{2.59}$$

For $r \geq r_0$, $\Gamma \to \Gamma_0 = 2\pi\omega r_0^2$, resulting in

$$v_0 = \frac{\Gamma_0}{2\pi r_0} \tag{2.60}$$

Equation 2.60 is known as the *free vortex*.

### *2.3.5.2 Vorticity Transport Equation*

To transform the N-S equation, we employ the vector identities (see Appendix AI.1.3):

- $\left(\vec{\mathbf{v}} \cdot \nabla\right)\vec{\mathbf{v}} = \nabla\left(\frac{1}{2}\vec{\mathbf{v}} \cdot \vec{\mathbf{v}}\right) - \vec{\mathbf{v}} \times \vec{\zeta}$;

- $\nabla \times \nabla\left(\frac{1}{2}\vec{\mathbf{v}} \cdot \vec{\mathbf{v}}\right) = 0;$
- $\nabla \times \nabla\left(p + \phi\right) = 0$, where $\phi$ is a potential function with $\nabla\phi = f_b$ being a conservative body force; and
- $\nabla \cdot \vec{\zeta} = 0.$

Specifically, we take the curl ($\nabla\times$) of each term of the N-S equation, rewritten in the form

$$\frac{\partial \vec{\mathbf{v}}}{\partial t} + \underbrace{\nabla\left(\frac{1}{2}\vec{\mathbf{v}} \cdot \vec{\mathbf{v}}\right) - \vec{\mathbf{v}} \times \vec{\zeta}}_{(\vec{v}\cdot\nabla)\vec{v}} = \frac{1}{\rho}\nabla p + \nu\nabla^2\vec{\mathbf{v}} + \underbrace{\vec{f}_b}_{\nabla\phi} \tag{2.61}$$

This results in

$$\frac{\partial \vec{\zeta}}{\partial t} + \left(\vec{\mathbf{v}} \cdot \nabla\right)\vec{\zeta} \equiv \underbrace{\frac{D\vec{\zeta}}{Dt}}_{\substack{\text{Total time-rate-of-}\\ \text{change of fluid-}\\ \text{element vorticity}}} = \underbrace{\vec{\zeta} \cdot \nabla\vec{\mathbf{v}}}_{\substack{\text{Rate of}\\ \text{deforming}\\ \text{vortex lines}}} + \underbrace{\nu\nabla^2\vec{\zeta}}_{\substack{\text{Net rate of}\\ \text{viscous diffusion}\\ \text{of vorticity}}} \tag{2.62a, b}$$

Clearly, the vorticity is not only being convected $\left(\vec{\mathbf{v}} \cdot \nabla\vec{\zeta}\right)$ and diffused $\left(\nu\nabla^2\vec{\zeta}\right)$ but also generated by a vortex-stretching mechanism via $\vec{\zeta} \cdot \nabla\vec{\mathbf{v}}$.

*Note:* Equation 2.62 still has two vector unknowns; so, it is of interest to formulate a higher-order equation, say in 2-D, with only the stream function $\psi(x, y)$ as the dependent variable. Recalling that $u = \partial\psi\partial y$ and $v = -\partial\psi/\partial x$ to satisfy continuity and that $\vec{\zeta} \to \zeta_z = \frac{\partial v}{\partial x} - \frac{\partial u}{\partial y} = -\nabla^2\psi$, the reduced N-S equation now reads:

$$\frac{\partial \zeta}{\partial t} + u\frac{\partial \zeta}{\partial x} - v\frac{\partial \zeta}{\partial y} = \nu\nabla^4\zeta \tag{2.63}$$

Using $\zeta \equiv \zeta_z = -\nabla^2\psi$, we obtain

$$\frac{\partial}{\partial t}\left(\nabla^2\psi\right) + \frac{\partial \psi}{\partial y}\frac{\partial}{\partial x}\left(\nabla^2\psi\right) - \frac{\partial \psi}{\partial x}\frac{\partial}{\partial y}\left(\nabla^2\psi\right) = \nu\nabla^4\psi \tag{2.64}$$

Special forms of both the vorticity equation (Equation 2.63) and the stream function equation (Equation 2.64) were of importance in aerodynamics until the advent of commercial and open-source software plus associated platforms.

Next, the physical meaning of the terms of Equation 2.62 is discussed. The equation's left-hand side describes the local and convective changes in fluid-element vorticity with time, that is, total "temporal changes in element-spin rates." The two terms of the equation's right-hand side describe vorticity generation/destruction via vortex-line straining, $\vec{\zeta} \cdot \nabla\vec{\mathbf{v}}$, and vorticity diffusion due to fluid friction, $\nu\nabla^2\vec{\zeta}$, respectively.

#### *2.3.5.3 Vortex-Line Straining*

Vorticity generation/destruction occurs via vortex-line stretching or turning. Vortex lines are lines that are everywhere tangent to the vorticity vectors. In pipe flow, they are rings

throughout the flow field, while in boundary-layer flows, they are concentrated near the solid surface (and in the wake region) but vanish in the outer regions, which are assumed to be irrotational. Consider, for example, a wall in the $x$–$y$ plane with $z$ as the normal direction. The vorticity vector components are (see Appendix AI.1.1 and AI.1.2)

$$\zeta_x = \frac{\partial w}{\partial y} - \frac{\partial v}{\partial z} = -\left.\frac{\partial v}{\partial z}\right|_{z=0}; \zeta_y = \frac{\partial u}{\partial z} - \frac{\partial w}{\partial x} = \left.\frac{\partial u}{\partial z}\right|_{z=0}; \text{and } \zeta_z = \frac{\partial v}{\partial x} - \frac{\partial u}{\partial y} = 0$$

As $\zeta_z = 0$, the vorticity vector lies on the wall, that is, $\vec{\zeta} = \zeta_x \hat{i} + \zeta_y \hat{j} = -\left.\frac{\partial v}{\partial z}\right|_{z=0} \hat{i} + \left.\frac{\partial u}{\partial z}\right|_{z=0} \hat{j}$. Now, the wall vortex lines are

$$\left.\frac{dx}{dy}\right|_{\substack{\text{vortex}\\\text{lines}}} = \left.\frac{\zeta_x}{\zeta_y}\right|_{\text{wall}} = \frac{-\left.\frac{\partial v}{\partial z}\right|_{z=0}}{\left.\frac{\partial u}{\partial z}\right|_{z=0}}$$

In contrast, the wall streamlines are described by

$$\left.\frac{dy}{dx}\right|_{\substack{\text{stream-}\\\text{lines}}} = \frac{\left.\frac{\partial u}{\partial z}\right|_{z=0}}{\left.\frac{\partial v}{\partial z}\right|_{z=0}} = -\frac{1}{\left.\frac{dx}{dy}\right|_{\substack{\text{vortex}\\\text{lines}}}}$$

Clearly, wall vortex lines are orthogonal to wall streamlines, which also holds for 2-D and axisymmetric flows; that is, $\vec{\mathbf{v}}$ and $\vec{\zeta}$ are perpendicular.

Now, the flow field vorticity vector (see Equation 2.55) has a component along the vortex line, causing line stretching, while its orthogonal component causes vortex-line turning. Clearly, vortex-line extension and turning actions are absent in *planar flows*. Specifically, the vorticity vector being perpendicular to the velocity vector, $\vec{\zeta} = \nabla \times \vec{\mathbf{v}}$, the vortex lines are normal and uniform to the planar flow. Hence, the lines maintain a constant length and do not turn.

#### *2.3.5.4 Vorticity Diffusion*

Similarly to momentum diffusion, $\nu\nabla^2\vec{\mathbf{v}}$, viscous action can diffuse vorticity throughout a flow field. In fact, in planar flow with only one non-zero-velocity component $\zeta_z$ and the term $\vec{\zeta}\cdot\nabla\vec{\mathbf{v}}$ being always zero, Equation 2.62 reduces to

$$\frac{D\zeta_z}{Dt} = \nu\nabla^2\zeta_z \tag{2.65}$$

This equation is analogous to the scalar convection-diffusion equations discussed in Section 2.4.2. Considering steady laminar fully developed flows, such as Couette, Poiseuille-type, and thin-film flows (see Examples 2.5 through 2.6), the vorticity transport equation collapses to

$$0 = \nu\frac{\partial^2\zeta_z}{\partial y^2} \text{ or } \frac{d\zeta_z}{dy} = \text{constant} \tag{2.66a, b}$$

Equation 2.66b can be interpreted as *vorticity flux*, similar to a constant heat flux $q_x$ or species mass flux $j_x$.

#### *2.3.5.5 Helicity*

Helical flow is simply a translating vortex, that is, generating a corkscrew-like motion. Examples in nature include draining bath water, a dust-devil, flow in a meandering river, Dean's flow in a curved conduit, vortex shedding from a delta wing, and the Karman vortex street behind bluff bodies.

The helicity of a flow field of domain $D$ is defined as

$$H(t) = \iiint_D \vec{\mathbf{v}} \cdot \vec{\zeta} dV = \iiint_D h dV \tag{2.67a, b}$$

where the dot product $\vec{\mathbf{v}} \cdot \vec{\zeta}$ is the scalar quantity $h$. Thus, the *helicity density* reads

$$h = \vec{v} \cdot (\nabla \times \vec{\mathbf{v}}) \tag{2.68}$$

typically with units of meters per second squared, that is, the same as acceleration. Clearly, $h$ is zero whenever the velocity vector is orthogonal to the vorticity vector. This implies that *helicity can be viewed as a measure of the complexity of a given flow field.* An expression of the *helical structure of flow* in dimensionless form is the *helical flow index* (*HFI*) with the range $-1 \le HFI \le 1$, that is,

$$HFI(\vec{x}, t) \equiv \frac{\vec{\mathbf{v}} \cdot \vec{\zeta}}{|\vec{\mathbf{v}}||\vec{\zeta}|} \tag{2.69}$$

For example, flows in tubes with bends and changing cross sections as well as in bifurcations (see Chapter 9) exhibit varying HFI values. Nevertheless, helicity in certain (biomedical) flows may be advantageous by stabilizing the flow, by suppressing wall shear-stress distributions, and for reducing areas of flow stagnation.

**Example 2.8: Rotationality of a Steady 2-D Flow Field**

Given $\vec{\mathbf{v}} = \hat{i}x^2 + \hat{j}(-2xy - 1)$, check whether the flow field is rotational or not.

**Graph 5:**

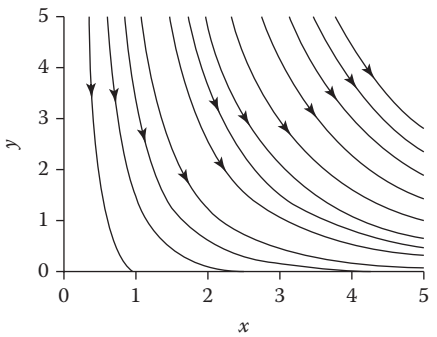


| **Assumptions** | **Method** |
|---|---|
| • Steady 2-D flow<br>• Incompressible fluid | Reduced vorticity vector $\vec{\zeta} = \nabla \times \vec{v}$ being either non-zero or zero |

*Solution:*

From Appendix AI.1.1:

$$\nabla \times \vec{\mathbf{v}} = \vec{\zeta} = \hat{i}\left(\frac{\partial w}{\partial y} - \frac{\partial v}{\partial z}\right) + \hat{j}\left(\frac{\partial u}{\partial z} - \frac{\partial w}{\partial x}\right) + \hat{k}\left(\frac{\partial v}{\partial x} - \frac{\partial u}{\partial y}\right) \tag{E.2.8.1}$$

It reduces to

$$\vec{\zeta} = \hat{k}\left(\frac{\partial v}{\partial x} - \frac{\partial u}{\partial y}\right) \hat{=} \zeta_z \tag{E.2.8.2}$$

With the given $\vec{\mathbf{v}} = [u, v]$, we obtain

$$\zeta_z = -2y = 2\omega_z \tag{E.2.8.3}$$

Thus, the flow field is rotational, and the fluid elements spin with an angular velocity of $\omega_z = -y$ while moving along the streamlines (see Graph 5).

As an aside, with $\nabla \cdot \vec{\mathbf{v}} = \frac{\partial u}{\partial x} + \frac{\partial v}{\partial y} = 2x - 2x = 0$, the fluid is, indeed, incompressible.

## 2.4 Scalar Transport Equations: Energy and Species-Mass Conservation

Although many natural and industrial fluid flow problems are non-isothermal, fluid mechanics education typically deals only with constant-temperature flows, leaving thermal flows for separate thermodynamics and convection heat transfer courses. Species-mass transfer is entirely left to chemical and biomedical engineers. Thus, we highlight the energy RTT plus the resulting heat transfer equation with an analogy to species-mass transfer to lay the groundwork for some interesting engineering applications in the remaining chapters.

### 2.4.1 Macro-Scale Energy Balance

The first law of thermodynamics states that energy forms can be converted but the total energy is constant, that is, conserved:

$$E_{\text{total}} = E_{\text{kinetic}} + E_{\text{potential}} + E_{\text{internal}} + \ldots = \text{constant} \tag{2.70a}$$

For *observation time* $\Delta t$, the macro-scale energy balance for *any* system can be written as (see Figure 2.11)

$$\underbrace{\Sigma E_{in} - \Sigma E_{out}}_{\substack{\text{Net energy transfer by heat,} \\ \text{work, and/or mass flow in/out}}} = \underbrace{\Delta E_{\text{system}} \coloneqq [\Delta kE + \Delta pE + \Delta U]_{\text{system}}}_{\substack{\text{Change of total energy inside the system} \\ \text{(e.g., kinetic, potential and internal energies)}}} \tag{2.70b}$$

where the internal energy $U$ is the sum of all microscopic energy forms, that is, mainly due to molecular vibration.

On a rate basis:

$$\Sigma \dot{E}_{in} - \Sigma \dot{E}_{out} = \left.\frac{dE}{dt}\right|_{\text{system}} \approx \left.\frac{\Delta E}{\Delta t}\right|_{\text{system}} \tag{2.71}$$

For example, for a *closed system* with heat transferred to the system and work done by the system (see Figure 2.11a),

$$\dot{Q} - \dot{W} = \frac{\Delta E}{\Delta t} \tag{2.72}$$

or during $\Delta t$, considering only an internal energy change from State 1 <initial> to State 2 <final>,

$$Q - W = \Delta U = U_2 - U_1 \tag{2.73}$$

Heat, $Q$, can be transferred via conduction, convection, and/or thermal radiation; work done by the closed system, such as a piston-cylinder device, is typically boundary work:

$$W = \int_1^2 F ds := \int_1^2 p d\forall \tag{2.74}$$

For an *open system*, energy forms flowing in and out of the system have to be accounted for. Thus, Equation 2.71 can be written for a fixed control volume with uniform streams entering and leaving (see Figure 2.9b):

$$\left.\frac{\Delta E}{\Delta t}\right|_{c.\forall.} = \Sigma[\dot{Q} + \dot{W}]_{in} - \Sigma[\dot{Q} + \dot{W}]_{out} + \Sigma\left[\dot{m}\left(h + \frac{v^2}{2} + gz\right)\right]_{in} - \Sigma\left[\dot{m}\left(h + \frac{v^2}{2} + gz\right)\right]_{out} \tag{2.75}$$

where:

$h \equiv \tilde{u} + p/\rho = c_p T$ is the enthalpy per unit mass, combining internal energy, $\tilde{u} = c_v T$, and flow work due to pressure $p$ moving specific volume $v$, that is, $pv$

$e_{kin} = v^2/2$ is the kinetic energy

$e_{potential} = gz$ is the potential energy per unit mass

As an aside, for steady, single-inlet/outlet, frictionless flows without heat transferred and work done, the Bernoulli equation appears as

$$\left[\frac{p}{\rho} + \frac{v^2}{2} + gz\right]_{in} = \left[\frac{p}{\rho} + \frac{v^2}{2} + gz\right]_{out}$$

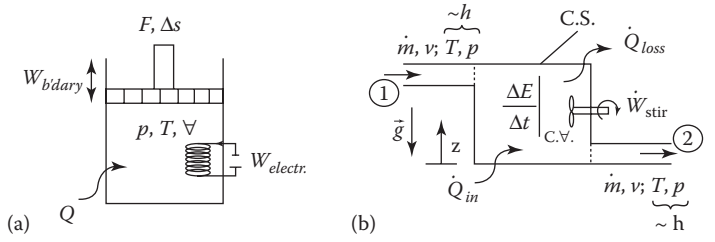


**FIGURE 2.11**
Energy transfer for closed and open systems. (a) Closed system. (b) Open system.

### 2.4.2 The Convection-Diffusion Equation for Heat Transfer

Expressing energy conservation in integral form, we select $\boldsymbol{B}_{system} \equiv E_{total}$ and hence $\beta = e_t$, so that the *energy RTT* reads (*Recall:* Equations 2.1 and 2.72)

$$\left.\frac{DE_t}{Dt}\right|_{\substack{\text{closed}\\ \text{system}}} \equiv \dot{Q} - \dot{W} = \frac{\partial}{\partial t}\int_{C.V.} \rho e_t dV + \int_{C.S.} \rho e_1 \vec{\mathbf{v}} \cdot d\vec{\mathbf{A}} \tag{2.76}$$

A simple form of energy conservation (see Equation 2.70), directly usable to solve convection heat transfer problems, starts with $e_{\text{total}} \equiv h = \tilde{u} + p/\rho$ (i.e., the enthalpy per unit mass) as the principal unknown. The change in total energy may be composed of net heat conduction, that is, based on Fourier's law, and net energy dissipation due to viscous stresses. Thus, after applying the divergence theorem (Appendix AI.3.1) again, we obtain

$$\frac{\partial}{\partial t}(\rho h) + \nabla \cdot (\rho \vec{\mathbf{v}} h) = -\nabla \cdot \vec{\mathbf{q}} + \mu\Phi \tag{2.77}$$

With $dh \equiv c_p dT$, or simplified to $h = c_p T$ when $c_p$ is constant, $\vec{\mathbf{q}} = -k\nabla T$ (after Fourier), and $\mu\Phi = \tau_{ji}\partial v_i/\partial x_j$, we obtain for thermal flow with constant fluid properties the *heat transfer equation*

$$\frac{\partial T}{\partial t} + (\vec{\mathbf{v}} \cdot \nabla)T = \alpha\nabla^2 T + \frac{\mu}{\rho c_p}\Phi \tag{2.78}$$

where $\alpha = k/\rho c_p$ is the thermal diffusivity.

In contracted form, with $S_T$ being possible heat sources and sinks, Equation 2.78 reads:

$$\frac{DT}{Dt} = \alpha\nabla^2 T + S_T \tag{2.79}$$

***Example 2.9: Thermal Pipe Flow ( $q_{wall} = ¢$ )***

Consider Poiseuille flow (see Example 2.6) where a uniform heat flux, $q_w$, is applied to the wall of a pipe with radius $r_0$.

(A) Set up the governing equations for the fluid temperature assuming thermally fully developed flow, that is,

$$\frac{T_w - T}{T_w - T_m} \equiv \Theta\left(\frac{r}{r_0}\right) \tag{E.2.9.1}$$

where:
$T_w(x)$ is the wall temperature
$T = T(r, x)$ is the fluid temperature
$T_m(x)$ is the temperature averaged over the cross-sectional area, that is,

$$T_m = \frac{1}{\bar{u}A}\int_A uT dA \tag{E.2.9.2}$$

Note that the *dimensionless temperature* $\Theta = \Theta(r)$ only, describing thermally ful ly developed flow. Solve a reduced form of the heat transfer equation (Equation 2.79) and develop an expression for the Nusselt number, defined as

$$Nu = \frac{\text{convection}}{\text{conduction}} = \frac{2r_0}{k}\frac{q_w}{T_w - T_m} := \frac{hD}{k} \qquad \text{(E.2.9.3a, b)}$$

where:

- $h$ is the convection heat transfer coefficient
- $k$ is the fluid conductivity
- $D$ is the pipe diameter

| Sketch 13 | Assumptions | Method |
|---|---|---|
| 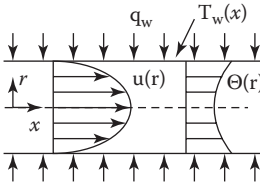  | As stated, that is,<br>• $u(r)$ as in Equation E.2.9.3<br>• $\partial T/\partial t = 0$ <steady-state><br>• $(\vec{v}\cdot\nabla)T \Rightarrow u\partial T/\partial x$<br>$\alpha\nabla T \Rightarrow \frac{\alpha}{r}\frac{\partial}{\partial r}\left(r\frac{\partial T}{\partial r}\right)$ | Reduced heat transfer equation (Equation 2.79) based on assumptions and postulates |

*Solution:*

A. With the result of Example 2.6 and the reduced heat transfer equation in cylindrical coordinates from Appendix I (see also list of assumptions), we have

$$\frac{u(r)}{\alpha}\frac{\partial T}{\partial x} = \frac{1}{r}\frac{\partial}{\partial r}\left(r\frac{\partial T}{\partial r}\right) \qquad \text{(E.2.9.4)}$$

B. Employing the dimensionless temperature profile $\Theta\left(\frac{r}{r_0}\right) \equiv \Theta(\hat{r})$ given as Equation E.2.9.1, we can rewrite Equation E.2.9.4 as

$$-2\frac{hD}{k}(1-\hat{r}^2) = \frac{d^2\Theta}{d\hat{r}^2} + \frac{1}{\hat{r}}\frac{d\Theta}{d\hat{r}} \qquad \text{(E.2.9.5)}$$

Specifically,

$$\text{For } q_w = ¢, \frac{\partial T}{\partial x} = \frac{dT_w}{dx} = \frac{dT_m}{dx} = \frac{2}{r_0}\frac{q_w}{\rho c_p \bar{u}} = ¢ \qquad \text{(E.2.9.6a–c)}$$

$$\text{As stated, } hD/k \equiv Nu_D := \frac{D}{k}\frac{q_w}{T_w - T_m} = ¢ \qquad \text{(E.2.9.7a, b)}$$

And with $dT/d\hat{r}$ being finite at $\hat{r} = 0$, we obtain

$$T - T_w = -(T_w - T_m)Nu_D\left(\frac{3}{8} - \frac{\hat{r}^2}{2} + \frac{\hat{r}^4}{8}\right)$$

Now, by definition:

$$T_w - T_m = \frac{2\pi}{\pi r_0{}^2\bar{u}}\int_0^{r_0}(T_w - T)u(r)r\,dr \qquad \text{(E.2.9.8)}$$

so that, when combining both equations and integrating, we have

$$1 = 4Nu_D \int_0^1 \left( \frac{3}{8} - \frac{\hat{r}^2}{2} + \frac{\hat{r}^4}{8} \right) (1 - \hat{r}^2) \hat{r} d\hat{r} \tag{E.2.9.8}$$

from which we finally obtain

$$Nu_D = \frac{48}{11} = 4.36 \tag{E.2.9.9}$$

*Comments:*

- It is interesting to note that for hydrodynamically and thermally fully developed flow in a tube, subject to a constant wall heat flux, the Nusselt number (or the heat transfer coefficient) is constant.
- The same holds for the isothermal wall condition; however, the Nu-value is lower (see Kleinstreuer, 1997 or Bejan, 2012).

As announced in Section 1.4, scale analysis can produce valuable results without solving the conservation laws. Specifically, dimensionless groups, which govern the system dynamics at hand, can be derived as well as the functional proportionalities. However, numerical equations relating such dimensionless groups require experimental measurements or computational analysis.

**Example 2.10: Scale Analysis of Natural Convection along a Vertical Wall**

Consider steady laminar free convection where, for example, air near a heated vertical wall rises against gravity. Within that thin thermal wall layer, the governing equations are (see Sketch 14)

$$\text{(air flow)} \quad \underbrace{u\frac{\partial u}{\partial x} + v\frac{\partial u}{\partial y}}_{\text{inertia}} = \underbrace{\nu\frac{\partial^2 u}{\partial y^2}}_{\text{friction}} + \underbrace{g\beta\left(T - T_\infty\right)}_{\text{buoyancy}} \tag{E.2.10.1}$$

where:

$\beta$ is the volumetric expansion coefficient ($\beta \approx -1/T$ for air)
$T_\infty$ is the ambient air temperature far away from the heated wall
$T$ is the actual air temperature within the thermal boundary layer

Thus, a second equation for $T$ is necessary:

$$\text{(air temperature)} \quad \underbrace{u\frac{\partial T}{\partial x} + v\frac{\partial T}{\partial y}}_{\text{heat convection}} = \underbrace{\alpha\frac{\partial^2 T}{\partial y^2}}_{\text{heat conduction}} \tag{E.2.10.2}$$

*Note:* Equations E.2.10.1 and E.2.10.2 are special cases of Equations 2.33 and 2.79, respectively. Now, perform the following (see Section 1.4):

(i) Non-dimensionalize Equation E.2.10.1, using $u \to \overline{u}$, $v \to \overline{v}$; $\partial x \to \ell$, $\partial y \to \delta$; and $\Delta T = T_w - T_\infty$ as scales, that is, reference parameters, where $l$ is the wall height, $\delta$ is the (variable) boundary-layer thickness, and $T_w$ is the (high) wall temperature.

(ii) Form proportionalities between different terms in these equations, representing forces and fluxes, to generate both dimensionless groups and functional dependencies for $(x)$ and $\overline{u}(x)$.

**System Sketch 14**

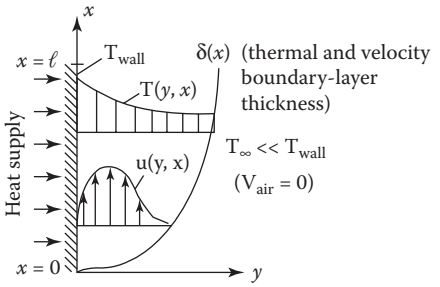


**Sketch for Scaling 15**

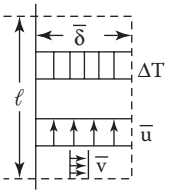


Solution:

(i) Replacing the variables $u$, $v$, $x$, $y$, and $T$ by $u = \hat{u}\,\bar{u}$, $v = \hat{v}\,\bar{v}$, $x = \hat{x}\,\ell$, $y = \hat{y}\,\delta$, and $T = \hat{T}\Delta T$ in Equations E.2.10.1 and E.2.10.2, we obtain

$$\left(\frac{\bar{u}^2}{\ell}\right)\bar{u}\frac{\partial \hat{u}}{\partial \hat{x}} + \left(\frac{\bar{u}\,\bar{v}}{\delta}\right)\hat{v}\frac{\partial \hat{u}}{\partial \hat{y}} = \left(\frac{\nu \bar{u}}{\delta^2}\right)\frac{\partial^2 \hat{u}}{\partial \hat{y}^2} + (g\beta\Delta T)$$

or, dividing through by $(\bar{u}^2 / \ell)$, we obtain

$$\bar{u}\frac{\partial \hat{u}}{\partial \hat{x}} + \underbrace{\left(\frac{\bar{v}}{u}\right)\left(\frac{\ell}{\delta}\right)}_{\substack{\varepsilon\cdot\varepsilon^{-1} \\ O(1)}}\frac{\partial \hat{u}}{\partial \hat{y}} = \underbrace{\frac{\nu}{\bar{u}l}}_{\mathrm{Re}^{-1}}\underbrace{\left(\frac{\ell}{\delta}\right)^2}_{\varepsilon^{-2}}\frac{\partial^2 \hat{u}}{\partial \hat{y}^2} + \underbrace{\frac{g\beta\Delta T}{\bar{u}^2}\ell}_{\substack{\sim Ri(Richardson\ number)}} \qquad \text{(E.2.10.3)}$$
$$O(1)$$

where by definition $\varepsilon < 1$, $\mathrm{Re}\ell \gg 1$, and the Richardson number

$$Ri = \frac{g\beta\Delta T\ell^3}{\nu^2\left(\frac{u\ell}{\nu}\right)^2} \equiv \frac{Gr}{\mathrm{Re}^2} \cong \frac{\text{Grashof\#}}{\text{Reynolds \# squared}} \qquad \text{(E.2.10.4)}$$

Clearly, we obtained a dimensionless PDE for buoyancy-driven flow plus a new dimensionless group, the Richardson number, which encapsulates buoyancy, inertia, and viscous forces.

(ii) Scale analysis of the first convection term in Equation E.2.10.2 balanced by the thermal diffusion term yields with $\delta T \longrightarrow \Delta T = T_w - T_\infty$

$$\bar{u}\frac{\Delta T}{\rho} \sim \alpha\frac{\Delta T}{\delta^2} \quad \text{or} \quad \bar{u} \sim \frac{\alpha\ell}{\delta^2} \qquad \text{(E.2.10.5a, b)}$$

Recall from Equation E.2.10.1 that very near the vertical wall, where the inertia effects are negligible (i.e., $u < 1$, $\partial u/\partial x < 1$, and $v \ll 1$), upward buoyancy forces are counteracted by viscous forces via

$$g\beta\Delta T \sim \nu\frac{\bar{u}}{\delta^2} \qquad \text{(E.2.10.6)}$$

Eliminating $\bar{u}$ in Equation E.2.10.6 with Equation E.2.10.5 yields

$$\nu\frac{\alpha\ell}{\delta^4} \sim g\beta\Delta T$$

or

$$\frac{\delta}{\ell} \sim \left( \frac{g\beta\Delta T}{\alpha\nu} \ell^3 \right)^{-\frac{1}{4}} = \mathrm{Ra}_\ell^{-1/4} \tag{E.2.10.7}$$

where:
Ra = GrPr is the Rayleigh number, a ratio of buoyancy to thermal/viscous forces
Pr = $\nu/\alpha$ is the Prandtl number, relating the fluid's kinematic viscosity and thermal diffusivity

Replacing the wall or plate height $\ell$ by $x$, we can deduce that the boundary-layer thickness (here $\delta = \delta_{th}$ for Pr = 1) varies as

$$\delta \sim x^{1/4} \tag{E.2.10.8a}$$

Combining Equation E.2.10.5 with Equation E.2.10.7 provides an expression for the vertical mean or reference velocity, that is,

$$\bar{u} \sim \sqrt{x} \quad \text{or} \quad u_{\text{ref}} = \sqrt{g\beta(T_w - T_\infty)\ell} \tag{E.2.10.8b, c}$$

### 2.4.3 The Species Convection-Diffusion Equation

Similarly to heat transfer (see Equation 2.79), species-mass transfer in a flow field is described by a scalar transport equation of the form

$$\frac{Dc}{Dt} \equiv \frac{\partial c}{\partial t} + \left(\vec{\mathbf{v}} \cdot \nabla\right) c = -\nabla \cdot \vec{j}_c \pm S_c = \boldsymbol{\mathcal{D}} \vec{\mathbf{v}}^2 c \pm S_c \tag{2.80a through c}$$

where:
$c$ (in mass per volume [e.g., kilograms per cubic meter]) is the species concentration, say, a dye in water, pollutants in the air, nanodrugs in blood, and so on
$\vec{\mathbf{v}}$ is the fluid flow velocity vector
$\vec{j}_c$ is the species mass flux $\left(\vec{j}_c = \boldsymbol{\mathcal{D}} \nabla c\right)$
$S_c$ are possible sinks and sources of $c$
$\boldsymbol{\mathcal{D}}$ with dimensions [length$^2$/time] is the diffusion coefficient (or diffusivity). It is typically expressed for binary systems with the Stokes–Einstein equation:

$$\boldsymbol{\mathcal{D}} = \frac{k_B T C_{\text{slip}}}{3\pi\mu d_p} \tag{2.81}$$

where:
the Boltzmann constant $k_B = 1.38 \times 10^{-23}$ J/K
the temperature $T$ is in $K$
$C_{slip} = \mathcal{O}(1)$
$d_p$ is the mean diameter of the dissolving molecules of chemicals, or of spreading nanoparticles less than 100 nm

To better understand Equation 2.80, it is instructive to analyze each of the terms:

- The term $\frac{\partial c}{\partial t}$ measures temporal concentration changes at a fixed point in a fluid; for example, the increase of toxins over time in a farmer's well.

- The term $(\vec{\mathbf{v}} \cdot \nabla)c$ describes the species convection (or advection); for example, spatial concentration changes of a chemical in a stream between discharge point and drinking-water intake.
- The term $-\nabla \cdot \vec{j} \equiv \nabla \cdot (\mathcal{D} \nabla c)$ represents the spatially net diffusion process of, say, a dye in water. Clearly, the diffusive flux, $\vec{j} = -\mathcal{D} \nabla c$, occurs from points of high $c$-values to areas of low $c$-values.
- The source term, $S_c$, represents creation (or destruction) of a quantity, say, via chemical reaction.

The Peclet number is a useful dimensionless constant, which compares the rates of species-mass transfer due to convection and diffusion. The Peclet number is defined as

$$Pe = \frac{\text{convective transport}}{\text{diffusive transport}} = \frac{(\vec{\mathbf{v}} \cdot \nabla)c}{\nabla \cdot \mathcal{D} \nabla c} \tag{2.82}$$

Scaling the Peclet number with $\vec{\mathbf{v}} \sim U$ and $\nabla \sim \frac{1}{L}$, it is found that

$$Pe = \frac{U \cdot \frac{1}{L} \cdot c}{\frac{1}{L} \mathcal{D} \frac{1}{L} c} = \frac{UL}{\mathcal{D}} \tag{2.83a, b}$$

Equation 2.81 can be reduced and depicted for transient convection and diffusion in the form (see Figure 2.12)

$$\frac{\partial c}{\partial t} + \nabla \cdot \vec{j}_{total} = S_c \tag{2.84a}$$

that is,

$$\frac{\partial c}{\partial t} + \nabla \cdot (-\mathcal{D} \nabla c + \vec{\mathbf{v}} c) = S_c \tag{2.84b}$$

Simplified forms of Equation 2.84 and problem solutions are discussed and applied in Bird et al. (2002) and Kleinstreuer (2006), among others.

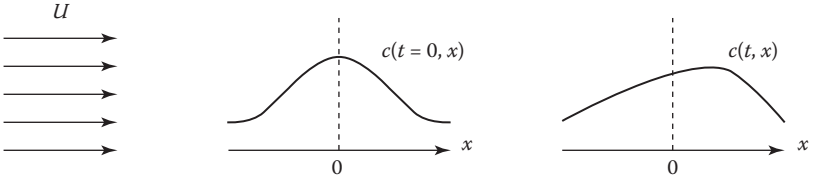


**FIGURE 2.12**
Transient 1-D species convection and diffusion.

## 2.5 Homework Assignments

Solutions to homework problems done individually, or initially in three-person groups, should help to further illustrate fluid dynamics concepts as well as approaches to problem solving, and in conjunction with Appendix I, sharpen the reader's math skills. Unfortunately, there is no substantial correlation between good homework-set results and fine test performances, only vice versa. Table 1.1 summarizes three suggestions for students to achieve a good grade in fluid dynamics—for that matter, in any engineering subject. Working independently, the student should be able (i) to satisfactorily answer all concept questions and (ii) to solve correctly all basic fluid dynamics problems.

The "Insight" questions (Section 2.5.1) emerged directly out of the Chapter 2 text, while some "Problems" (Section 2.5.2) were taken from lecture notes in modified form when using White (2006), Cimbala and Cengel (2008) and Incropera et al. (2007) for teaching undergraduate courses over the years. Additional examples, concept questions and problems may be found in any introductory fluid mechanics and heat transfer text, or on the Web (see websites of MIT, Stanford, Cornell, Penn State, University of Michigan, etc.).

### 2.5.1 Physical Insight

*Whenever possible, answers to* **Physical Insight** *questions should feature a sample illustration (or system sketch), a brief description/explanation, and some math in terms of definitions or derivations*

2.1 Provide quick answers (sketches, streamlines, math, and physics) to the following counter-intuitive fluid-flow scenarios:

(a) Keeping the tailgate of a pick-up truck *up* reduces aerodynamic drag (Why?) and hence saves gasoline, although most drivers intentionally keep it *down* and even install "airflow" nets to retain cargo when accelerating.

(b) Under otherwise identical conditions, it is easy to *blow* out a candle but nearly impossible to *suck* it out. Why?

(c) When a spoon is brought near a jet, for example, a faucet stream, it gets *sucked into* the stream. Try it out and explain!

(d) Chunks of metal are *torn out* from ship propellers at high speeds after a long period of time in operation. Why?

(e) The long hair of a girl driving a convertible is pushed *into her face* rather than *swept back.* How come?

(f) Consider a humming bird being quasi-stationary in your moving car. What happens to it if you suddenly brake?

2.2 Consider the del operator $\nabla$ (see Appendix AI.1.2):

(a) Explain $\nabla \cdot \vec{\mathbf{v}}$, $\nabla \vec{\mathbf{v}}$, and $\nabla \times \vec{\mathbf{v}}$, where $\vec{\mathbf{v}}$ is a velocity vector.

(b) Show that $\nabla \cdot \nabla = \nabla^2$, the Laplacian operator.

(c) What is the physical meaning of $(\vec{\mathbf{v}} \cdot \nabla)\vec{\mathbf{v}}$, and how can the result (Equation AI.1.15) be interpreted?

2.3 In light of Section AI.2.3, derive a finite-difference approximation for, say, $f'(x_i)$ of second-order accuracy.

2.4 The theorem of Green (or Gauss), known as the "divergence theorem" (see Equation AI.3.1 in Appendix I), transforms a surface integral of a vector function into a volume integral and vice versa. (a) Would the conversion also work for a scalar function? (b) Provide a graphical illustration with physical explanation of Equation AI.3.1.

2.5 Plot the error functions (AI.3.3) and (AI.3.4) and give two applications.

2.6 Classify the following ODEs and suggest best possible solution techniques:

(a) $y' = a(x) + b(x)y + c(x)y^2 + d(x)y^3$

(b) $y' = a(x)y^n + b(x)y$

(c) $f(xy' - y) = g(y')$

(d) $x^2y'' + xy' - (x^2 + n^2)y = f(x)$

2.7 In Section 2.1, under "Fundamental Assumptions", it is stated that a fluid is a continuum when $\Delta\forall_{\min} \leq 10^{-9}$ mm$^3$, that is, $L_{\min} \leq 1$ μm. What is the ratio of $\lambda_{\text{fluid}}/L_{\text{system}}$ for (a) air and (b) water when $\lambda_{\text{fluid}}$ is an appropriate molecular length scale and $L_{\text{system}} \approx L_{\min}$?

2.8 Discuss three ways of deriving the RTT. Can it be applied to quantities in all three tensor ranks, that is, scalar, vector, and tensor? Give one example each!

2.9 Of interest is the conservation of *angular momentum* in terms of the RTT, that is,

$$\frac{D}{Dt}\vec{\mathbf{H}}_{\text{system}} = \sum \vec{\mathbf{M}}$$

where:

$\vec{\mathbf{H}}_{\text{system}} = \vec{\mathbf{r}} \times m\vec{\mathbf{v}}$ is the angular momentum with m being the constant mass

$\sum \vec{\mathbf{M}}$ is the net moment applied to the system $\vec{r}$

is the moment radius (or arm)

Express $\sum \vec{\mathbf{M}}$ for any control volume, that is, stationary, moving, or deforming.

2.10 A horizontal fire-hose (nozzle diameter 6 cm) discharges typically 5 m$^3$/min of water ($\rho = 1000$ kg/m$^3$). Find the force (and direction) to hold the fire-hose in place. Comment!

2.11 Consider a jet-plane with the engine mounted at the rear end discharging $\dot{m}_{\text{gas}} = 18$ kg / s of exhaust gases at $v = 250$ m/s relative to the plane. To shorten landing, a deflector-vane (called a "thrust reverser") is lowered into the path of the exhaust stream, which deflects the gases and hence aids in braking. Analyze the effect of the vane angle, θ, on the braking force, that is, from a horizontal $\theta = 0°$ (no effect) to a 180° (full effect). Discuss the $F_{brake}$ (θ) plot!

2.12 A skydiver ($m_{\text{total}} = m_{\text{person}} + m_{\text{gear}}$) jumps out of a plane, and at terminal velocity $v_T$, he/she opens at $t = 0$ a parachute ($F_{\text{drag}} = kv^2$) and lands with a final velocity $v_F$. Show that $k = mg/v_F^2$ and derive an equation for $v(t)$. Note that $v = v(t, v_T, v_F, g)$, but not $m_{total}$; why? Plot $v(t)$ for typical parameter values and comment.

2.13 Consider a radial water turbine where water from a nozzle enters the impeller at its outer edge (diameter $D$) with velocity $v$ (and mass flow rate $\dot{m}$) under angle θ w.r.t. the radial direction. The water leaves with $v$ in the radial direction. What are the resulting shaft torque and turbine power output when the maintained angular velocity is $\omega_0$?

2.14 Provide a physical interpretation of Equation 2.22 and sketch an example with all four terms appearing.

2.15 Employing the REV approach of Section 2.2.2, derive the transient 3-D continuity equation in *cylindrical* coordinates. Is the $\nabla \cdot \vec{\mathbf{v}} = 0$ also valid for transient flows?

2.16 List the pros and cons of the integral approach, say, using the RTT or lumped-parameter method, versus the differential approach, that is, solving reduced forms of the continuity and Cauchy or N-S equations. Give two examples each of when to use which methodology.

2.17 Derive the Bernoulli equation in two distinct ways, relying on first principles. Interpret each term of the resulting equation in three ways.

2.18 Discuss with examples *boundary work* versus *flow work*, and explain why on a differential basis, we start with $\delta W$ rather than $dW$?

2.19 Elaborate on the origin/derivation and similarities between Equations 2.79 and 2.80.

### 2.5.2 Engineering Problems

Before launching into an engineering-problem solution, three preliminary tasks should be carefully executed:

1. A system Sketch with coordinates, expected velocity/temperature profiles, and given/unknown parameters in symbolic form.
2. A detailed list of Assumptions concerning flow field characteristics, system simplifications, submodels, and fluid properties.
3. Solution Method in terms of concepts and approach, expressed as brief mathematical statements.

2.20 Liquid flow velocity at a solid wall: (a) Empirical evidence shows that $\vec{\mathbf{v}}_{\text{fluid}} = \vec{\mathbf{v}}_{\text{wall}}$, for example, if the wall/surface is stationary and impermeable, $u = v = w = 0$; however, wall-velocity-slip may occur; but when and why? (b) From the viewpoint of two reference frames, that is, one fixed on the ground and the other fixed to the moving object (say, an airplane), what is $\vec{\mathbf{v}}_{\text{air}}$ in the two reference-frame cases, and what is $\vec{\mathbf{v}}_{\text{air}}$ far away from the plane in both reference frames?

2.21 Oil at 60°C ($\rho = 864$ kg/m$^3$; $\mu = 72.5 \times 10^{-3}$ kg/m · s) is pushed ($\Delta p_{\text{gauge}} = 1$ atm) between two horizontal parallel plates ($L = 1.5$ m, $W = 0.75$ m) a small distance $h$ apart. Plot the Reynolds number, $\text{Re}_h = \rho u_{\text{mean}} h/\mu$, as a function of spacing $h$ for 10 μm $\leq h \leq$ 1 mm, and comment.

2.22 A velocity field is given/measured as

$$\vec{\mathbf{v}} = (ax + b)i + (cx^2 - ay)j$$

where a, b, and c are constants. (a) Classify this flow field; (b) check whether the associated pressure field, $p = p(x, y)$, is a smooth function. *Hint:* Cross-differentiation of the pressure gradients should generate the same results for "function smoothness," that is,

$$\frac{\partial}{\partial x}\left(\frac{\partial p}{\partial y}\right)=\frac{\partial}{\partial y}\left(\frac{\partial p}{\partial x}\right)$$

2.23 Compare "gravity-film flow" for (i) two vertical parallel walls a distance $h$ apart and (ii) a vertical wall with smooth falling film of thickness $h$. Assume constant pressure and no end effects. Plot both velocity profiles and discuss the impact of $h$ on $Q$, the volumetric flow rate. Provide one sample application each.

2.24 Consider a vertical concentric shaft rotating and translating ($d$, $\omega_0$, $u_0$) inside a stationary cylinder (i.e., housing of inner diameter $D$) with a lubricant (or slurry) of properties $\rho$ and $\mu$. (a) What industrial operation can be modeled with this shaft/pipe annulus? (b) Set up the reduced N-S equations plus BCs based on suitable assumptions and postulates. (c) Can you solve for the velocity field and draw a representative velocity profile? (d) Estimate the amount of lubricant that must be constantly supplied.

2.25 Consider levitation of a sphere ($D$, $\rho_{sp}$) in an upward stream of air ($\rho$, $u$, $T$). (a) What is the necessary air-velocity $v(D)$ for different property ratios $\rho_{sp}/\mu_{air}$? (b) Does your analysis hold for droplets as well?

*Recall:* $\mathrm{Re}_D=\dfrac{\rho v D}{\mu}<1.0$ for creeping flow analysis.

Taylor & Francis
Taylor & Francis Group
http://taylorandfrancis.com

# 3

# *Incompressible Viscous Fluid Flow Applications*

The previous chapter featured several examples with detailed solutions to illustrate each topic introduced or just to review them for some readers. They included a few special cases of the conservation laws in both integral form (i.e., the simplified Reynolds Transport Theorem [RTT]) and in differential form, that is, the reduced Navier–Stokes (N-S) equations, being the continuity plus linear momentum equations. In this chapter, additional *physical insight* is provided via a few new applications, which also play a role in preparation for the theories/models in Part B dealing with modern fluid dynamics topics. Specifically, in Sections 3.1 through 3.3, three basic areas in fluid dynamics are discussed to better prepare students for the subsequent chapters as well as for follow-up courses in the thermal sciences and for industrial demands.

## 3.1 Internal Laminar Flows

Numerous industrial and some natural flows are *laminar*; that is, the flow fields do not exhibit any *random velocity/pressure/temperature fluctuations*. However, the Reynolds number can be quite high; for example, up to 2400 in pipe flow (based on the pipe diameter) and $5 \times 10^5$ in flat-plate boundary-layer flow (based on the plate length). For fluids moving inside or around non-uniform geometries, the flow fields can be very complex, exhibiting flow separation, recirculation zones, wakes, and vortices of different sizes. Highly viscous and many non-Newtonian fluid flows (e.g., polymeric liquids, foodstuff, etc.) are laminar, that is, characterized by relatively low Reynolds numbers. Generally, laminar (transient three-dimensional [3-D]) flows can now be readily solved with commercial (or open-source) software on engineering workstations. One-dimensional (1-D) and unidirectional flow fields have analytical solutions, while near-parallel flows have approximate solutions, all based on reduced forms of the N-S equations (see Section 2.3.3). Indeed, such solutions are most desirable for a better understanding of the physics of fluid flow, that is, "physical insight," as well as for benchmark computer model validations.

In *unidirectional* flows, the velocity vector has only one component; for example, in rectangular coordinates $\vec{v} = (u, 0, 0)$, where in general $\vec{v} \Rightarrow u(y, z, t)$ and hence, Stokes' equation (Equation 2.36) has to be solved. Unidirectional and 1-D flows are fully developed, typically with a constant pressure gradient and/or gravity as the driving force. Thus, the resulting 1-D momentum equation expresses a dynamic equilibrium at all times between an axial force and the frictional resistance; here, in terms of (Newtons per cubic meter):

$$\underbrace{\frac{\partial p}{\partial x} \text{ and/or } \rho g_x}_{\text{driving forces}} = \underbrace{\frac{\partial \tau_{xy}}{\partial y}}_{\text{resistance}} \tag{3.1}$$

In the next sections, applications of Equation 3.1 are discussed with illustrative examples for a variety of laminar unidirectional flows: steady as well as transient, quasi-unidirectional, and non-isothermal.

### 3.1.1 Steady Fully-Developed Flows

For steady 1-D incompressible flow, $u = u(y)$, or $v_z = v_z(r)$ in cylindrical coordinates, as already discovered when discussing Couette and Poiseuille flows in Examples 2.5 and 2.6. In terms of the reduced $x$-momentum of the N-S equations, where $u = u(y)$ only and $\partial p/\partial x =$ constant, we have (see Appendix AI.5.3)

$$0 = -\left(\frac{\partial p}{\partial x}\right) + \mu \frac{d^2u}{dy^2} + \rho g_x \tag{3.2a}$$

Rewriting Equation 3.2a with $-\frac{\partial p}{\partial x} \approx \frac{\Delta p}{l} = \left(p_{\text{in}} - p_{\text{out}}\right)/l$ yields

$$\frac{d^2u}{dy^2} = \frac{1}{\mu}\left[\left(\frac{\Delta p}{l}\right) - \rho g_x\right] = \text{¢} \tag{3.2b}$$

it is apparent that steady laminar 1-D parallel flows can be described by a second-order ordinary differential equation (ODE) (see Appendix AI.4):

$$u'' = K \tag{3.3}$$

subject to two boundary conditions, for example, "no slip" at the wall and symmetry.

In general, Table 3.1 summarizes for any fluid flow system, necessary *assumptions and their consequences.* To understand and appreciate the "differential approach" for solving modern fluid dynamics problems, solutions of Equation 3.3 are discussed in subsequent examples. Working out these solutions (Examples 3.1 through 3.4) *independently* should

- Strengthen engineering modeling and applied math skills
- Provide some interesting insight into the physics of fluid flow

For all practical purposes, the generic steps for *setting up differential analysis problems* in fluid mechanics and solving the resulting differential equation include the following:

1. Clever placement of the appropriate coordinate system into the system sketch is important; this also reveals the principal flow direction and hence, identifies the momentum component of interest.
2. The velocity vector $\vec{\mathbf{v}}$ and pressure gradient $\nabla p$ are the key unknowns; thus, based on the given flow system and with the help of Table 3.1, *postulates* for $\vec{\mathbf{v}}$ and $\nabla p$ have to be provided first. Specifically, determine which $\vec{\mathbf{v}}$-component and $\nabla p$-component is non-zero and what are their functional dependences. That can be determined via the stated assumptions, boundary conditions, and checking of the continuity equation (see Examples 2.5 through 2.7).
3. Once functional postulates are determined, the non-zero component of the N-S equations can be deduced and the resulting ODE integrated, subject to appropriate boundary conditions.

**TABLE 3.1**

Flow Assumptions and Their Impact

| Flow Assumption | Explanation | Examples |
|---|---|---|
| Time dependence | $\frac{\partial}{\partial t} = 0$ implies steady-state, but flow is transient when $\vec{\mathbf{v}} = \vec{\mathbf{v}}(t)$ | Transient flow examples: pulsatile flow; fluid-structure vibration; flow start-up/shutdown; and so on. |
| Dimensionality | Required number of space coordinates | 1-D: Couette flow; Poiseuille flow; thin-film flow<br>2-D: Boundary-layer flow; pipe-entrance flow<br>3-D: Everything real … |
| Directionality | Required number of velocity components: $\vec{v} = (u, v, w)$ or $\vec{v} = (v_z, v_r, v_\theta)$ | Usually same as "Dimensionality" with some exceptions: for example, for the rotating parallel disk (or viscous clutch) problem, $\vec{\mathbf{v}} = (0, v_\theta, 0)$, where $v_\theta = v_\theta(r, \theta)$ is unidirectional, but the system is 2-D |
| Development phase | $\frac{\partial v}{\partial s} = 0$: fully developed flow ($s \hat{\equiv}$ axial coordinate) | "Fully developed" … implies no velocity profile changes in that direction, say, *s* |
| Symmetry | $\frac{\partial}{\partial n} = 0$: mid-plane ($n \hat{\equiv}$ normal coordinate)<br>$\frac{\partial}{\partial \theta} = 0$: axisymmetry | Self-explanatory |

*Flow regime:* $\begin{cases} \text{Laminar} \rightarrow \text{Re}_{\max} < \text{Re}_{\text{critical}} \\ \text{Turbulent} \rightarrow \text{Re} > \text{Re}_{\text{critical}} \end{cases}$ where $\text{Re}_{\text{critical}} \approx \begin{cases} 2400 \text{ for pipe flow} \\ 5 \times 10^5 \text{ for flat plate B-L flow} \end{cases}$

For Part B homework assignments, test, and exams, it is suggested that the *Transport Equations* (see Appendix AI.5) are the only information source when setting up detailed math models for specific problem solutions.

*Notes:*

- Viscosity dependence:
- When $\mu = ¢$ or $\mu = \text{fct. (T)}$, use the N-S equation. When $\mu \rightarrow \eta = \eta$ (shear rate, etc.), use the Cauchy equation. Momentum decoupling from heat (or species-mass) transfer if the fluid properties are constant

Now, for the next four examples, the goals should be to learn how to

1. Set up a math model based on the three prelims, that is, Sketch, Assumptions and Method with *Postulates* for $\vec{v}$ and $\nabla p$
2. Integrate the resulting ODE with appropriate boundary conditions (BCs)
3. Graph the results, that is, profiles, functions, etc.
4. Comment, providing explanations of unique features, summarizing new physical insight and possible applications

**Example 3.1: Generalized Parallel Plate Flow**

Consider viscous fluid flow between parallel tilted plates a small constant distance $h$ apart, where the flow is fully developed for the test section $0 \le x \le l$ of interest. Here, the flow is generated due to the moving upper plate at $u_0 = ¢$, a constant pressure gradient, $dp/dx$, and a component of gravity (see also the special case in Example 2.5).

| Sketch 1 | Assumptions | Method and Postulates |
|---|---|---|
| 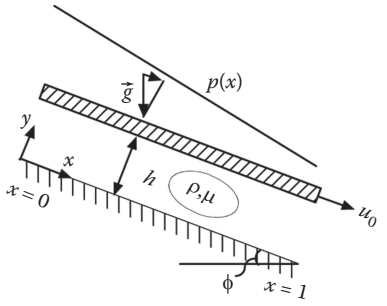  | • Steady laminar unidirectional flow<br>• Constant $h$, $\partial p/\partial x$, and fluid properties | • Reduced N–S equation where $\vec{\mathbf{v}} = (u,0,0)$ and $-\frac{\partial p}{\partial x} \approx \frac{\Delta p}{l} = ¢$<br>• $u = u(y)$ only |

*Solution:*

With the postulates

$v = w = 0$, $u = u(y)$ only, $-\frac{\partial p}{\partial x} \approx \frac{\Delta p}{l} = ¢$ and $f_{\text{body}} = \rho g \sin\phi$, continuity is fulfilled, and the $x$-momentum equation (see Appendix AI.5.3) reduces to

$$0 = \frac{1}{\rho}\left(\frac{\Delta p}{l}\right) + v\frac{d^2u}{dy^2} + g\ \sin\phi \tag{E.3.1.1a}$$

or

$$\frac{d^2u}{dy^2} = \frac{-1}{\mu}\left[\left(\frac{\Delta p}{l}\right) + \rho g\ \sin\phi\right] = ¢ \tag{E.3.1.1b}$$

subject to $u(y=0) = 0$ and $u(y=h) = u_0$. Again, we have to solve an ODE of the form $u'' = K$. Introducing a dimensionless pressure gradient

$$P \equiv -\frac{h^2}{2\mu u_0}\left[\left(\frac{\Delta p}{l}\right) + \rho g\ \sin\phi\right] \tag{E.3.1.2}$$

we can write the solution $u(y)$, known as Couette flow, in a more compact form, that is,

$$\frac{u(y)}{u_0} = \frac{y}{h} - P\left(\frac{y}{h}\right)\left(1 - \frac{y}{h}\right) \tag{E.3.1.3}$$

*Graph 1* ($\phi = 0$)*:*

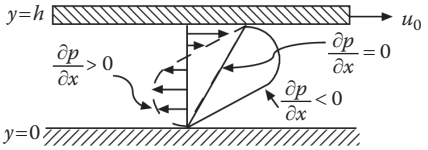

*Comments:*

- The pressure gradient, $P$ or $\partial p/\partial x$, greatly influences $u(y)$. Clearly, $\partial p/\partial x < 0$ implies a "favorable" and $\partial p/\partial x > 0$ an "adverse" pressure gradient.
- For $u_0 = 0$, we have flow between parallel plates, driven by a pressure force and gravity:

$$u(y) = +\frac{h^2}{2\mu}\left[\left(\frac{\Delta p}{l}\right) + \rho g \sin\phi\right]\left[\frac{y}{h} - \left(\frac{y}{h}\right)^2\right] \tag{E.3.1.4}$$

**Example 3.2: Steady Laminar Fully Developed Flow in a Pipe (see Example 2.6)**

| **Sketch 2** | **Assumptions** |
|---|---|
| 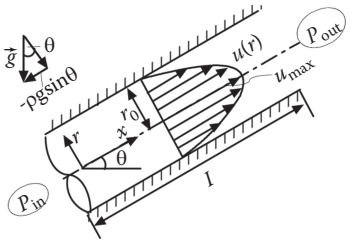 | • As stated<br>• Constant $-\partial p/\partial p \approx \nabla p / l$<br>*Note:* $\partial p/\partial x \approx (p_1 - p_2)/(x_1 - x_2)$ or<br>• $-\frac{\partial p}{\partial x} = \frac{p_{in} - p_{out}}{x_l - 0} = \frac{\Delta p}{l}$<br>• Constant fluid properties ρ and μ |



**Method**

Reduced N-S equations in cylindrical coordinates:

- $\partial/\partial t = 0$<steady-state>
- $\partial/\partial\theta = 0$<axisymmetric>
- $\partial/\partial x = 0$<fully developed>

*Postulates:* $\vec{v} = (u,\ 0,\ 0)$; $u = u(r)$ only; $\nabla p \to \dfrac{\partial p}{\partial x} = \not{c}$

*Boundary Conditions:* The obvious one is $u(r = r_0) = 0$, and the second one could be $u(r = 0) = u_{\max}$; however, $u_{\max}$ is unknown. Thus, we use symmetry on the centerline, that is,

$$\left.\frac{du}{dr}\right|_{r=0} = 0$$

Continuity: $\dfrac{\partial u}{\partial x} + 0 + 0 = 0 = \ \succ\ \dfrac{\partial u}{\partial x} = 0$ (i.e., fully developed flow confirmed)

*x-Momentum:*

$$0 = -\frac{\partial p}{\partial x} + \mu\left[\frac{1}{r}\frac{\partial}{\partial r}\left(r\frac{\partial u}{\partial r}\right)\right] - \rho g \sin\theta \tag{E.3.2.1}$$

With $u = u(r)$ only and $-\partial p/\partial x = \Delta p/l$, we write

$$\frac{1}{r}\left[\frac{d}{dr}\left(r\frac{du}{dr}\right)\right] = \frac{1}{\mu}\left[\left(\frac{-\Delta p}{l}\right) + \rho g \sin\theta\right] \equiv K = \not{c} \tag{E.3.2.2}$$

After separation of variables:

$$\int d\left(r\frac{du}{dr}\right) = K\int r dr + C_1 \tag{E.3.2.3a}$$

so that

$$\frac{du}{dr} = \frac{K}{2} + \frac{C_1}{r} \tag{E.3.2.3b}$$

A second integration yields

$$u = \frac{K}{4} r^2 + C_1 \ln r \; + \; C_2 \tag{E.3.2.3c}$$

From the first B.C.:

$$0 = \frac{K}{4} r_0^2 + C_1 \ln r_0 \; + \; C_2 \tag{E.3.2.4a}$$

while the second B.C. (see Equation E.3.4.2b) yields

$$0 = 0 + \frac{C_1}{r}$$

which forces $C_1$ to be zero. From Equation E.3.4.3a, we have

$$C_2 = -\frac{K}{4} r_0^2 \tag{E.3.2.4b}$$

so that with $K \equiv \frac{1}{\mu}\left(\frac{-\Delta p}{l} + \rho g \sin\theta\right)$, we obtain

$$u(r) \; = \; \frac{K r_0^2}{4}\left[1 - \left(\frac{r}{r_0}\right)^2\right] \tag{E.3.2.4}$$

For a horizontal pipe, $\theta = 0$, and hence,

$$u(r) = \frac{r_0^2}{4\mu}\left(\frac{\Delta p}{l}\right)\left[1 - \left(\frac{r}{r_0}\right)^2\right] = u_{\max}\left[1 - \left(\frac{r}{r_0}\right)^2\right] \tag{E.3.2.5a, b}$$

*Notes:*

- The average velocity, $u_{av} \equiv \bar{u} = \frac{1}{A}\int u(r) dA$ where $dA = 2\pi r dr$, is the cross-sectional ring, so that

$$\bar{u} = \frac{1}{2\mu}\left(\frac{\Delta p}{l}\right)\int_0^{r_0}\left[1 - \left(\frac{r}{r_0}\right)^2\right] r dr = \frac{r_0^2}{8\mu}\left(\frac{\Delta p}{l}\right) \tag{E.3.2.6a, b}$$

- The volumetric flow rate, $Q = u_{av} A$, where $A = \pi r_0^2$, can be used to calculate the necessary pressure drop to maintain the flow:

$$Q = \frac{\pi r_0^4}{8\mu}\left(\frac{\Delta p}{l}\right) \tag{E.3.2.7}$$

so that with a given $Q$-value (or Reynolds number)

$$\Delta p = \frac{8\,\mu\, Q}{\pi\, r_0^4} l \tag{E.3.2.8}$$

- The pressure drop $\Delta p = p_{in} - p_{out}$ is positive, while the pressure gradient

$$\frac{\partial p}{\partial x} < 0$$

- By inspection of Equation E.3.4.5, $u(r=0) = u_{max}$, where

$$u_{max} = \frac{r_0^2}{4\mu}\left(\frac{\Delta p}{l}\right) = \frac{1}{2}u_{av} \tag{E.3.2.9}$$

- The wall shear stress, that is, the frictional impact of viscous fluid flow on the inner pipe surface, is

$$\tau_{wall} \equiv \tau_{rx}\Big|_{r=r_0} = -\mu \frac{du}{dr}\Big|_{r=r_0} \tag{E.3.2.10a}$$

$$\tau_w = \frac{r_0}{2}\left(\frac{\Delta p}{l}\right) \tag{E.3.2.10b}$$

Thus, a second expression for the pressure drop (or gradient) is found:

$$\Delta p = \frac{2\tau_w}{r_0} l \tag{E.3.2.11}$$

*Comments:*

- The *Poiseuille flow* result (Equation E3.2.5) is fundamental in approximating and analyzing laminar flow of a Newtonian fluid in straight tubes, blood vessels, porous-media pores, microconduits, and so on.
- Equations E.3.2.7 and E3.2.11 will be also valuable in solving industrial pipe-flow problems in conjunction with the extended Bernoulli equation.
- Poiseuille-type flows appear also in other parallel-plate geometries, as illustrated with Example 3.1.

**Examples 3.3: Two Cases of Parallel Flow in Cylindrical Tubes**

**Case A:** Consider flow through an annulus with tube radius $R$ and inner concentric cylinder $aR$, where $a < 1$, creating a ring-like cross-sectional flow area.

| Sketch 3 | Assumptions | Method |
|---|---|---|
| 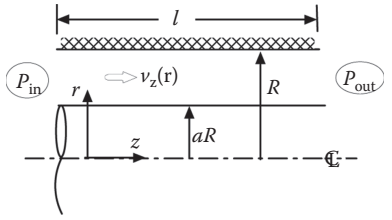 | • Steady laminar axisymmetric flow<br>• Constant $\partial p/\partial z$ and constant ρ and μ | Reduced N-S equations in cylindrical coordinates |

*Postulates:* $\vec{\mathbf{v}} = (0, 0, v_z)$; $\nabla p \Rightarrow \dfrac{\partial p}{\partial z} \approx -\dfrac{\Delta p}{l} = ¢$; $v_z = v_z(r)$ only $\partial/\partial t = 0$<steady-state>; $\partial/\partial \phi = 0$ <axisymmetric>

*Continuity Equation:* $0 + 0 + (\partial v_z/\partial z) = 0$, that is, fully developed flow

*Boundary Conditions:* $v_z(r = aR) = 0$ and $v_z(r = R) = 0$.

*Solution:*
Of interest is the $z$-momentum equation, that is, with the stated postulates (see Appendix AI.5):

$$0 = -\frac{\partial p}{\partial z} + \mu\left[\frac{1}{r}\frac{\partial}{\partial r}\left(r\frac{\partial v_z}{\partial r}\right)\right] \tag{E.3.3.1a}$$

Thus, with $P \equiv \frac{1}{\mu}\left(-\frac{\Delta p}{l}\right)$:

$$\frac{d}{dr}\left(r\frac{dv_z}{dr}\right) = P \cdot r \tag{E3.3.1b}$$

After double integration, we obtain

$$v_z(r) = \frac{P}{4}r^2 + C_1 \ln r \; + \; C_2 \tag{E.3.3.2}$$

Invoking the BCs yields two equations for $C_1$ and $C_2$ as

$$0 = \frac{P}{4}(aR)^2 + C_1 \ln(aR) + C_2$$

and

$$0 = \frac{P}{4}R^2 + C_1 \ln R + C_2$$

Inserting the $C$-expressions into Equation E.3.3.2 results in

$$v_z(r) = \frac{PR^2}{4}\left[1 - \left(\frac{r}{R}\right)^2 - \frac{1-a^2}{\ln(1/a)}\ln\left(\frac{R}{r}\right)\right] \tag{E.3.3.3}$$

The axial shear stress, counteracting the pressure-driven flow, is

$$\tau_{rz} = \mu\frac{dv_z}{dr} := \frac{\mu P}{2}R\left[\left(\frac{r}{R}\right) - \frac{1-a^2}{2\,\ln(1/a)}\left(\frac{R}{r}\right)\right] \tag{E.3.3.4a, b}$$

Comments and Additional Results:

- For Poiseuille flow, that is, no inner cylinder, the solution is (see Example 3.2)

$$v_z(r) = \frac{R^2}{4\mu}\left(\frac{\Delta p}{l}\right)\left[1 - \left(\frac{r}{R}\right)^2\right] \tag{E.3.3.5}$$

  *This solution is not recovered when letting $a \to 0$ because of the prevailing importance of the natural logarithm term near the inner wall.*
- The maximum annular velocity is not in the middle of the gap $aR \le r \le R$ but closer to the inner cylinder wall, where the velocity gradient is zero, and hence,

$$\tau_{rz}\big|_{r=bR} = 0$$

  This equation can be solved for $b$, so that $v_z(r = bR) = v_{\max}$

- The average velocity is $v_{av} = \int v_z(r)dA$, where $dA = 2\pi r dr$ $\langle$cross – sectional ring of thickness $dr\rangle$, so that

$$v_{av} = \frac{R^2}{8\mu}\left(\frac{\Delta p}{l}\right)\left[\frac{1-a^4}{1-a^2} - \frac{1-a^2}{\ln\left(\frac{1}{a}\right)}\right] \tag{E.3.3.6}$$

and hence,

$$Q = v_{av}\left[\pi R^2\left(1-a^2\right)\right] := \frac{\pi R^4}{8\mu}\left(\frac{\Delta p}{l}\right)\left[\left(1-a^4\right) - \frac{\left(1-a^2\right)^2}{\ln\left(\frac{1}{a}\right)}\right] \tag{E.3.3.7}$$

- The *net* force exerted by the fluid on the solid surfaces comes from two wall shear stress contributions:

$$F_s = \left(-\tau_{rz}\big|_{r=aR}\right)(2\pi aRl) + \left(\tau_{rz}\big|_{r=R}\right)(2\pi Rl) \tag{E.3.3.8a}$$

$$\therefore F_s = \pi R^2 \Delta p\left(1-a^2\right) \tag{E.3.3.8b}$$

**Case B**: Again, we have two concentric cylinders, but now with $\partial p/\partial z \equiv 0$ and the inner cylinder rotating at constant angular velocity $\omega_0$, while the outer cylinder rotates with a constant $\omega_1$. In the case that one of the cylinders is stationary, we are dealing with *cylindrical Couette flow.*

| Sketch 4 | Assumptions | Method |
|---|---|---|
| 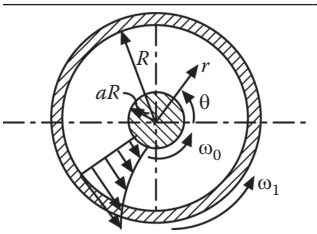 | • Steady laminar axisymmetric flow<br>• Long cylinders, that is, no end effects<br>• Small ω's to avoid Taylor vortices | • Reduced N-S equations in cylindrical coordinates<br>• *Postulates*: $\vec{\mathbf{v}} = (0, v_\theta, 0)$ and $\frac{\partial p}{\partial \theta} = \frac{\partial p}{\partial z} = 0$ |

*Solution:*

Clearly, $v_r = v_z = 0$ and $\frac{\partial}{\partial t} = \frac{\partial}{\partial \theta} = 0$. Also, $v_\theta = v_\theta(r)$ only (see Continuity and BCs); thus, we can reduce the θ-component of the N-S equation (Appendix AI.5) to

$$0 = 0 + \mu\left[\frac{\partial}{\partial r}\left(\frac{1}{r}\frac{\partial}{\partial r}(rv_\theta)\right)\right] \tag{E.3.3.9a}$$

subject to

$$v_\theta(r = aR) = \omega_0(aR) \quad \text{and} \quad v_\theta(r = R) = \omega_1 R\,. \tag{E.3.3.9b, c}$$

Again, as in simple Couette flow after start-up, the moving wall–induced frictional effect propagates radially, and the forced cylinder rotations balanced by the drag resistance generate an equilibrium velocity profile.

Double integration yields

$$v_\theta(r) = C_1 r + \frac{C_2}{r} \tag{E.3.3.10a}$$

where:

$$C_1 = \frac{\omega_1 R^2 - \omega_0 (aR)^2}{R^2 - (aR)^2} \tag{E.3.3.10b, c}$$

and

$$C_2 = \frac{a^2 R^4 (\omega_0 - \omega_1)}{R^2 - (aR)^2}$$

*Additional Results:*

- The *r*-momentum equation reduces to

$$-\frac{v_\theta^2}{r} = -\frac{1}{\rho}\frac{\partial p}{\partial r} \tag{E.3.3.11}$$

  Thus, with the solution for $v_0(r)$ known, Equation E.3.3.11 can be used to find $\partial p/\partial r$ and ultimately, the load-bearing capacity.
- Applying this solution as a first-order approximation to a journal bearing where the outer tube (or sleeve) is fixed, that is, $\omega_1 = 0$, we have in dimensionless form

$$\frac{v_\theta(r)}{\omega_0 R} = \frac{a^2}{1 - a^2}\left(\frac{R}{r} - \frac{r}{R}\right) \tag{E.3.3.12}$$

- The torque necessary to rotate the inner cylinder (or shaft) of length $l$ is

$$T = \int (aR) dF := (aR) \int_0^l \tau_{r\theta}\big|_{r=aR}\, dA \tag{E.3.3.13}$$

where:

$dA = \pi(aR) dz\mu$

$$\tau_{r\theta}\big|_{r=aR} = \mu\left[r\frac{d}{dr}\left(\frac{v_\theta}{r}\right)\right]_{r=aR}$$

Hence, with

$$\tau_{\text{surface}} \equiv \tau_{r\theta}\big|_{r=aR} = 2\mu\frac{\omega_o R^2}{R^2 - (aR)^2} \tag{E.3.3.14}$$

the torque needed is

$$T = \tau_{\text{surf}} A_{\text{surf}}(aR) := 4\pi\mu(aR)^2 l \frac{\omega_0}{1 - a^2} \tag{E.3.3.15}$$

*Graph 2:*

$$T/\left[4\pi\mu R^2 l\omega_0\right]$$

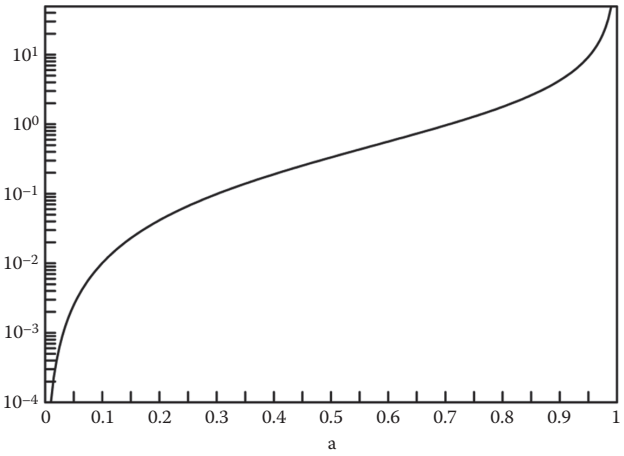


*Comments:*

- An electric motor may provide the necessary power, $P = T\omega_0$, which turns into thermal energy, which has to be removed to avoid overheating.
- Graph 2 depicts the nonlinear dependence of $T(a)$ for a given system. As the gap between rotor (or shaft) and stator widens, the wall stress increases (see Equation E.3.3.14) as well as the surface area *and hence, the necessary torque.*

**Example 3.4: The Cone-Plate Viscometer**

Determine the viscosity of a fluid in a basic cone-plate viscometer with given cone angle θ and radius $R$, applied torque $T$, and resulting constant angular velocity ω. Plot the result as $T = T(R, \mu)$ *Hint:* Assume a linear $v_0(z)$ and justify.

| **Sketch 5** | **Assumptions** | **Method** |
|---|---|---|
| 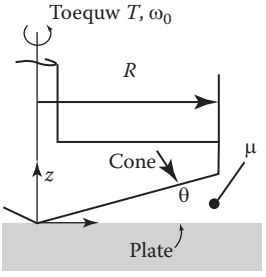  | • Steady circumferential unidirectional flow, that is, $v_r$ and $v_z$ are zero<br>• $\theta \ll 1$, that is, $v_\theta(z)$ is linear and $\cos(\theta) \approx 1$<br>• Constant $T$, $\omega_0$, $\mu$<br>• No end effects, that is, $\omega_0 < 1$ | • Differential approach $dT = rdF = r\tau_{wall}dA$<br>• Integrate over "wetted surface" $dA = 2\pi rds$<br>• Note that $ds = \dfrac{dr}{\cos\theta} \approx dr$ |

*Solution 1:*
Instead of solving the reduced N-S equations in cylindrical coordinates, we build on the assumption of a linear $v_0(z)$ as graphed and start with the differential expression for the torque, that is, $dT = rdF$.

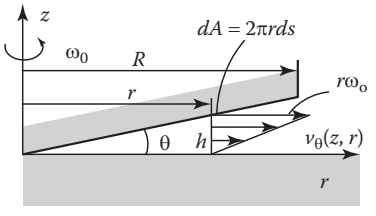

- From the graph, the linear circumferential velocity $v_\theta$ can be deduced as

$$v_\theta = (r\omega_o)\frac{z}{h} = \frac{r\omega_o}{r\tan\theta}z \qquad \text{(E.3.4.1)}$$

- Also, $dT = rdF$; $dF = \tau_w dA$; where

$$\tau_w = \mu \left.\frac{dv_\theta}{dz}\right|_{z=h} \qquad \text{(E.3.4.2a through c)}$$

$$\therefore dT = 2\pi\mu\frac{\omega_o}{\tan\theta}r^2 dr \qquad \text{(E.3.4.3)}$$

- Hence

$$T = K\int_0^R r^2 dr = \frac{K}{3}R^3 \qquad \text{(E.3.4.4)}$$

- Finally, with $K = 2\pi\omega_0/\tan\theta$, the test-fluid viscosity is

$$\mu = \frac{\frac{3}{2}T\tan\theta}{\pi\omega_0 R^3} \qquad \text{(E.3.4.5)}$$

| **Graph 2:** | **Comments:** |
|---|---|
| 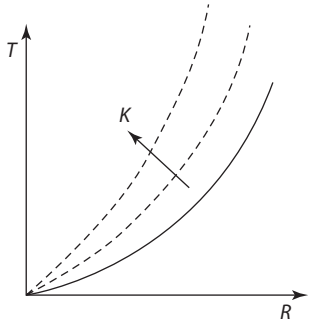  | • Because of the stated assumptions, $v_\theta = v_\theta(z)$ only and $T = T(R, \mu, \omega_0, \theta)$.<br>• As expected, the device size, in terms of $R$, has the strongest influence on $T$. |

*Note:* A more involved steady laminar flow problem, which has an analytic solution, is the Von Karman pump (see Homework Assignment Section 3.4), where a thin disk rotating in a reservoir (an infinite body of a quiescent viscous fluid) sucks the fluid in, swirls it, and distributes it radially.

### 3.1.2 Near-Parallel Flows

Steady laminar flows in conduits with *slightly non-parallel* walls have some practical importance. Examples include tapered tubes, cone-plate viscometers, slider bearings, converging/diverging slit flows, and so on. For such cases, the key assumption is that of "unidirectional" flow (as in Poiseuille or Couette flows), although there is a *small* second velocity component, which is first ignored. Then, the slight geometric changes, and hence more realistic flow fields, are incorporated by invoking the "no-slip" condition at the

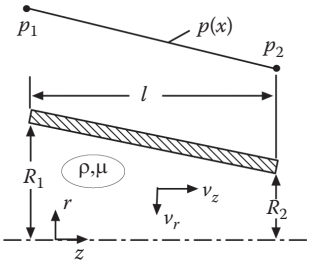


**FIGURE 3.1**
Slightly tapered tube.

converging or diverging wall. To illustrate the two-step procedure, let us consider a mildly tapered pipe where the radius changes *linearly* as (Figure 3.1)

$$R(z) = R_1 - \frac{\Delta R}{L} z \tag{3.4}$$

With the underlying assumption of Poiseuille flow, the $z$-momentum equation reduces to

$$0 = -\frac{\partial p}{\partial z} + \mu\left[\frac{1}{r}\frac{\partial}{\partial r}\left(r\frac{\partial v_z}{\partial r}\right)\right] \tag{3.5}$$

which implies that pressure $p(z)$ is linear and radial velocity $v_r = 0$ (see also continuity). As usual, the boundary condition at $r = 0$ is $dv_z/dr = 0$ because of symmetry, but the no-slip condition at the tube wall now reads:

$$v_z\left[r = R(z)\right] = 0 \tag{3.6}$$

Equation 3.6 introduces the unique tube geometry and approximately the two-dimensional (2-D) flow pattern. The solution is (see Example 3.2)

$$v_z = v_z\left(r,\ z\right) = v_{\max}\left[1 - \left(\frac{r}{R(z)}\right)^2\right] \tag{3.7}$$

Checking the continuity equation for axisymmetric flow

$$\frac{1}{r}\frac{\partial}{\partial r}(r\ v_r) + \frac{\partial v_z}{\partial z} = 0 \tag{3.8}$$

we see that $v_r \neq 0$ because $v_z = v_z(z, r)$. In fact, Equation 3.8 can be employed to find an expression for $v_r(r, z)$ considering that $v_r(r = 0) = 0$ or $v_r[r = R(z)] = 0$. Also of interest is a reasonable limit on $R(z)$ to keep $v_r \ll v_z$, that is, to justify the assumption of (initial) Poiseuille flow (see HA in Section 3.4). Additional examples of *nearly* unidirectional flows include lubrication and stretching flows, which are discussed in Chapters 5 and 6. The topics are further analyzed in Papanastasiou (1994), Kleinstreuer (1997), Middleman (1998), and Panton (2013), as well as in more specialized texts and review articles.

In the next section, temperature effects are included as part of basic momentum transfer to model fluid heating and cooling.

### 3.1.3 Forced Convection Heat Transfer

The incompressible viscous fluid flow applications discussed so far can be readily extended to *non-isothermal systems.* Indeed, most natural and industrial flow fields are subjected to heat fluxes; for example, in airflows due to unique weather pattern and in heat exchangers for residential, business, and industrial applications. Descriptions of such thermal flows require the solutions of special forms of both the momentum equation and the heat transfer equation (see Section 2.4). Figure 3.2 summarizes the interactions between fluid mechanics and heat transfer. Specifically, in Section 1.2.3, the heat flux vector, that is, Fourier's law, was introduced as

$$\vec{\mathbf{q}} = -k\,\nabla T \tag{3.9}$$

where $k$ is the (isotropic) thermal conductivity.

Then, in Section 2.4.2 focusing on *forced convection*, the heat transfer equation was derived:

$$\frac{\partial T}{\partial t} + (\vec{\mathbf{v}}\cdot\nabla)T = \alpha\,\nabla^2 T + \frac{\mu}{\rho c_p}\Phi \pm S_{\text{heat}} \tag{3.10}$$

where:

| | |
|---|---|
| $\alpha \equiv k/(\rho c_p)$ | is the thermal diffusivity |
| $\mu\Phi = \tau_{ij}\partial v_i/\partial v_j$ | is the viscous dissipation function |
| $S_{\text{heat}}$ | is an additional source or sink of energy, for example, due to chemical reaction |

In rectangular coordinates, we have (see also Appendix AI.5.6)

$$\begin{aligned}\Phi = 2&\left[\left(\frac{\partial u}{\partial x}\right)^2 + \left(\frac{\partial v}{\partial y}\right)^2 + \left(\frac{\partial w}{\partial z}\right)^2\right] \\ &+ \left[\left(\frac{\partial u}{\partial y} + \frac{\partial v}{\partial x}\right)^2 + \left(\frac{\partial v}{\partial z} + \frac{\partial w}{\partial y}\right)^2 + \left(\frac{\partial w}{\partial x} + \frac{\partial u}{\partial z}\right)^2\right] \\ &- \frac{2}{3}\left(\frac{\partial u}{\partial x} + \frac{\partial v}{\partial y} + \frac{\partial w}{\partial z}\right)^2\end{aligned} \tag{3.11}$$

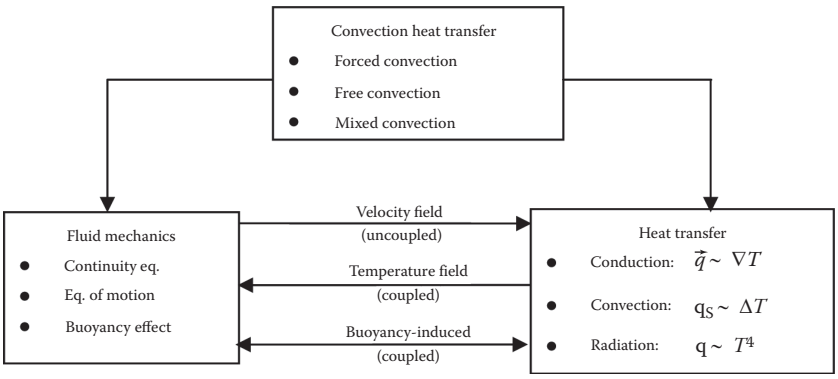


**FIGURE 3.2**
Convection heat transfer components.

where for most flows, the $(\partial u/\partial y)^2$ term in Equation 3.11 is most significant. Specifically, flow field regions with steep velocity gradients and fluids of high viscosity may generate measurable temperature increases. Equation 3.9 is used for Equation 3.10; that is, the net heat conduction term reads for constant fluid properties:

$$-\nabla \cdot \vec{\mathbf{q}} = k\, \nabla^2\, T \tag{3.12}$$

While in Equation 3.10, heat conduction, $\alpha\nabla^2 T$, is a diffusional transport phenomenon, heat transfer by convection, $(\vec{v}\cdot\nabla)T$, occurs typically much more rapidly. Nevertheless, it is the thermal diffusion process, $\alpha\nabla^2 T$, that is the essence of convection heat transfer. Specifically, as fluid elements of different temperatures are convected and brought into contact, heat is transferred from regions of high to low temperatures via conduction.

Now, with an eye on practical applications, we focus on the surface/wall heat flux, $q_s$, which moves from a hot surface of temperature $T_s$ into a moving stream with reference temperature $T_{\text{ref}}$. Simpler to use than Equation 3.9, $q_s$ can be based on the temperature difference $\Delta T = T_s - T_{\text{ref}}$, as attributed to Newton:

$$q_s = h\left(T_s - T_{\text{ref}}\right) \tag{3.13}$$

where:

- $h$ is the convective heat transfer coefficient
- $T_{\text{ref}}$ is either the $T_{\text{mean}}$, the cross-sectionally averaged fluid temperature, that is, $T_m(x)$, or $T_\infty$, as in thermal boundary-layer theory (Sections 3.2 and 3.3.1), or the fluid bulk temperature $T_b = (T_{\text{in}} + T_{\text{out}})/2$, with $T_\infty$ and $T_b$ being constant. As always, the heat flow rate is then

$$Q = A_s\, q_s \tag{3.14}$$

where $A_s$ is the surface area through which the heat flux $q_s$ transfers.

#### *3.1.3.1 Convection Heat Transfer Coefficient*

The heat transfer coefficient $h$ in Equation 3.13 encapsulates all possible system parameters, such as temperature difference, thermal boundary-layer thickness, Reynolds number, fluid Prandtl number, and wall geometry. Clearly, $h$ is not a property such as $k$, but it is a convenient artifact to calculate $q_s$ or $T_s$ and ultimately, $Q$, which also greatly depends on the heat transfer area $A_s$ (see Figure 3.3a). For example, for boundary-layer flow (Figure 3.3b), combining Equation 3.13 and the 1-D version of Equation 3.9, we have

$$h = \frac{q_S}{T_S - T_\infty} = \frac{-k}{T_S - T_\infty}\left.\frac{\partial T}{\partial y}\right|_{y=0} \tag{3.15a, b}$$

Typical $h$-values range from 20 to 300 for gases to 5000–50,000 W/(m$^2$ °C) for liquid metals. As expected, $h$-values are much larger for turbulent flow than for laminar flow due to the intense microscale mixing effect of near-wall turbulence (Figure 3.3b).

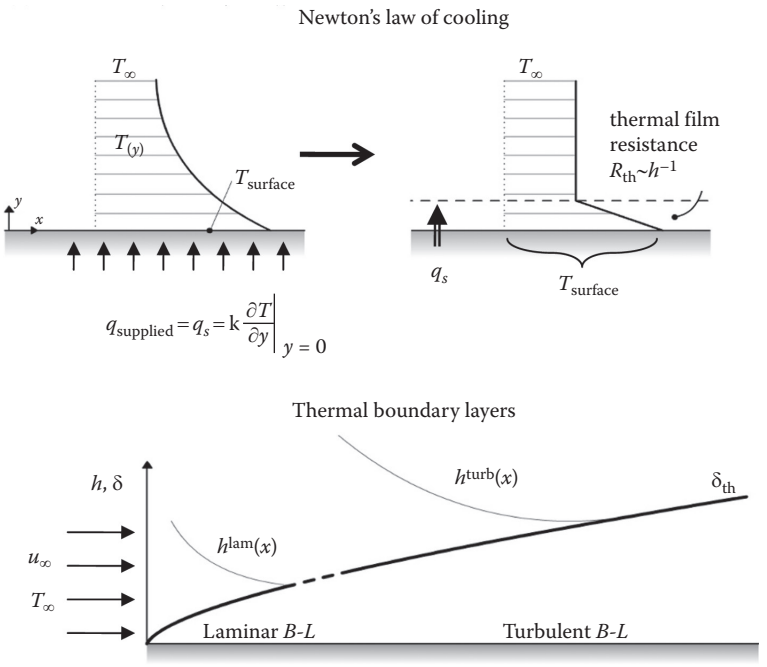


**FIGURE 3.3**
The convection heat transfer coefficient.

### *3.1.3.2 The Nusselt Number*

Equation 3.15a can be non-dimensionalized by inspection, using the axial coordinate $x$ as a length scale, that is,

$$\frac{h\,x}{k} \equiv Nu_x = \frac{q_s\,x}{k\left(T_s - T_\infty\right)} \tag{3.16a, b}$$

where $Nu_x$ is known as the *local Nusselt number*, being the ratio of convection over conduction. Similarly, the *average Nusselt number* based on system length $L$, where $L$ could be a plate length or a pipe diameter, is

$$\overline{Nu_L} = \frac{\bar{h}L}{k} \tag{3.17}$$

where

$$\bar{h} = \frac{1}{L}\int_0^L h(x)dx \tag{3.18}$$

For forced convection, neglecting buoyancy and viscous dissipation, we have the local Nusselt number dependence of the form

$$Nu_x = Nu_x\left(\frac{x}{L}; \mathrm{Re}, \mathrm{Pr}\right) \tag{3.19}$$

The functional dependence of the Nusselt number can be obtained via scale analysis (see Section 1.4 and HWA in Section 3.4).

In summary, the main objective is to find the temperature field $T = T(x,y,z;t)$ and then obtain $h$ (or $Nu_x$) to calculate the surface heat flux or surface temperature as well as the total heat transfer rate. The following solution steps are for constant-property fluids, that is, one-way coupled problems:

- Solve, subject to appropriate boundary conditions, a reduced form of Equation 3.10 after securing a computed (or measured) velocity profile (see Sections 3.1 through 3.3).
- Calculate the wall temperature gradient and obtain, via Equation 3.15, $h(x)$ and then $Nu(x)$.

### *3.1.3.3 The Reynolds-Colburn Analogy*

Note that, as an *alternative approach*, Reynolds and Colburn established an analogy between heat and momentum transfer. It is based on the similarity between dimensionless temperature and velocity profiles in boundary layers (see Section 3.4 for HWAs):

$$\frac{1}{2} C_f(x) = St_x \, \mathrm{Pr}^{2/3} \quad \text{for} \quad 0.6 < \mathrm{Pr} < 60 \tag{3.20}$$

By definition, the skin-friction coefficient and Stanton number are

$$C_f = \frac{2\tau_{\text{wall}}}{\rho \, u_\infty^2} \quad \text{and} \quad St_x = Nu_x/(\mathrm{Re}_x \, \mathrm{Pr}) = h(x)/(\rho c_p u_\infty) \tag{3.21a through c}$$

Clearly, once the wall shear stress of a thermal boundary-layer problem is known, $Nu(x)$ or $h(x)$ can be directly obtained. An illustrative example is given in Section 3.2.2.

**Example 3.5: Simple Couette Flow with Viscous Dissipation**

As an example of planar "lubrication" with significant heat generation due to oil-film friction, consider *simple thermal Couette flow* with adiabatic wall and constant temperature of the moving plate.

| Sketch 6 | Assumptions | Method |
|---|---|---|
| 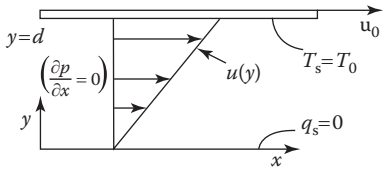 | • Steady laminar 1-D flow<br>• $\nabla p = 0$<br>• $u_0$ and $d$ are constant | • Reduced N-S and heat transfer equations.<br>• Constant thermal wall conditions. |

*Solution:*

Based on the *postulates* $\vec{\mathbf{v}} = [u(y),\ 0,\ 0]$ and $\nabla p \equiv 0$, the N-S equations reduce to

$$0 \ = \ 0 \qquad < \text{continunity} >$$

and

$$0 = \frac{d^2u}{dy^2} \qquad \text{< x-momentum >} \tag{E.3.5.1a}$$

subject to $u(y=0)=0$ and $u(y=d)=u_0$. Thus,

$$u(y) = u_0 \frac{y}{d} \tag{E.3.5.1b}$$

The heat transfer equation (Equation 3.10) with $\Phi = \left(\frac{\partial u}{\partial y}\right)^2$ from Equation 3.11 reduces to

$$k\frac{d^2T}{dy^2} = -\mu\left(\frac{u_0}{d}\right)^2 \tag{E.3.5.2}$$

subject to $\left.\frac{dT}{dy}\right|_{y=0} = 0$ and $T(y=d)=T_0$

Double integration yields

$$T(y) = T_0 + \frac{\mu\, u_0^2}{2k}\left[1-\left(\frac{y}{d}\right)^2\right] \tag{E.3.5.3}$$

At the plate surface with $q_s = q(y=d) = -k\left.\frac{\partial T}{\partial y}\right|_{y=d}$, we have

$$q_s = \mu\frac{u_0^2}{d} \tag{E.3.5.4}$$

*Graph 3:*

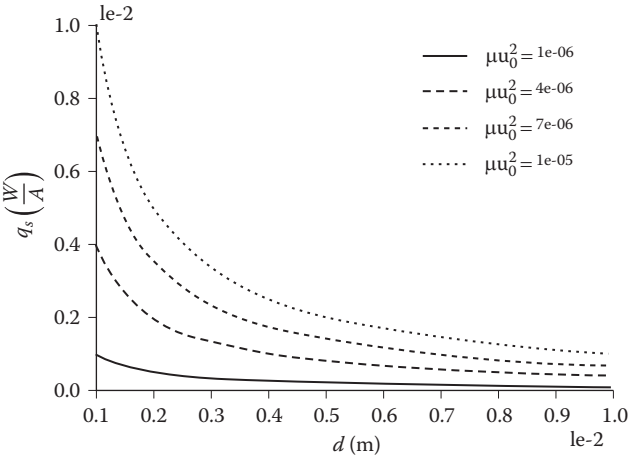


*Comments:*

- Clearly, as μ and $u_0$ increase and the spacing decreases, $q_s$ shoots up.
- For simple Couette flow, $du/dy$ evaluated at $y=d$ is equal to $u_0/d$, so that $q_s = u_0\tau_{wall}$ here, which is a simple example of the heat transfer and momentum transfer relation (see Reynolds-Colburn analogy).

- Of interest would be the evaluation of the mean fluid temperature, $T_m = \frac{1}{\dot{m}} \int_A \rho\, u\, T\, dA$ , to estimate $h$ from $q_s = h(T_0 - T_m)$.

**Example 3.6: Lubricated Shaft Rotation with Heat Generation**

Somewhat similarly to Example 3.3 (Case B), consider thermal cylindrical Couette flow where the rotating shaft ($R_i$, $\omega_i$) is adiabatic, and the stationary housing ($R_0$, $T_0$) is isothermal. In light of viscous dissipation, find $T(r)$ as well as $T_{max}$ at $r = R_i$ and $\hat{Q}_{\text{wall}}(r = R_0)$.

| Sketch 7 | Assumptions | Method |
|---|---|---|
| 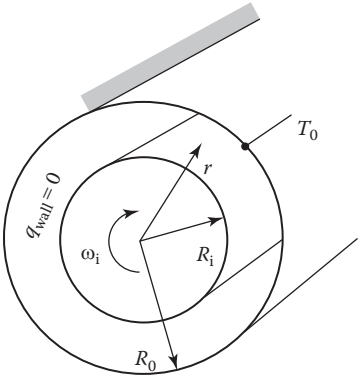  | • Steady laminar 1-D axisymmetrical flow<br>• No gravity or end effects<br>• Constant properties, that is, only one-way coupling | • Reduced $\theta$-momentum equation<br>• *Postulates:*<br>• $v_\theta = v_\theta(r)$ only and $\nabla p = 0$<br>• Constant thermal wall BCs |

*Solution:*

Based on the postulate and assumptions, the Continuity Equation is satisfied, and the θ-momentum equation in cylindrical coordinates reduces to (see Appendix AI.5.3)

$$\frac{d}{dr}\left(\frac{1}{r}\frac{d}{dr}(r\, v_\theta)\right) = 0 \qquad \text{(E.3.6.1a)}$$

subject to

$$v_\theta(r = R_i) = (\omega\, R)_i \quad \text{and} \quad v_\theta(r = R_0) = 0 \qquad \text{(E.3.6.1b, c)}$$

Double integration and invoking the BCs yields

$$v_\theta(r) = \frac{\omega_i R_i (R_0/R_i)^2}{\left(\frac{R_0}{R_i}\right)^2 - 1}\left[\frac{R_i}{r} - \frac{r}{R_i}\right] \qquad \text{(E.3.6.2)}$$

The heat transfer equation (see Appendix AI.5.4) reduces to

$$0 = \frac{k}{r}\frac{d}{dr}\left(r\frac{dT}{dr}\right) - \mu\, \Phi \qquad \text{(E.3.6.3a)}$$

where

$$\Phi = \left(\frac{dv_\theta}{dr} - \frac{v_\theta}{r}\right)^2 \qquad \text{(E.3.6.3b)}$$

As stated,

$$\left.\frac{dT}{dr}\right|_{r=R_i} = 0;\ T\left(r=R_0\right)=T_0 \qquad \text{(E.3.6.3c, d)}$$

With $v_\theta(r)$ given, Equation E.3.6.3b can be determined, and hence, Equation E.3.6.3a can be integrated subject to Equations E.3.6.3c and d. Thus,

$$T(r)=T_0+\frac{\mu}{4k}\left[\frac{2\omega_i R_i}{1-\left(\frac{R_i}{R_0}\right)^2}\right]^2\left[\left(\frac{R_i}{R_0}\right)^2-\left(\frac{R_i}{r}\right)^2+2\ln\left(\frac{R_0}{r}\right)\right] \qquad \text{(E.3.6.4)}$$

Now, either by inspection of Equation E.3.6.4 or by setting $dT/dr$ to zero, $T_{\max}$ occurs at $r=R_i$. In dimensionless form,

$$\frac{T_{\max}-T_0}{\frac{\mu}{4k}\left[\frac{2\omega_i R_i}{1-\left(\frac{R_i}{R_0}\right)^2}\right]^2}=\left[\left(\frac{R_i}{R_0}\right)^2-1+2\ln\left(\frac{R_0}{R_i}\right)\right] \qquad \text{(E.3.6.5)}$$

The wall heat transfer rate per unit length is

$$\hat{Q}_{\text{wall}}=\left(2\pi R_0\right)q\left(r=R_0\right) \qquad \text{(E.3.6.6a, b)}$$

$$\text{where}\ \ q(r=R_0)=-k\left.\frac{dT}{dr}\right|_{r=R_0}$$

Hence,

$$\hat{Q}_w=\frac{4\pi\mu(\omega R)_i^2}{1-\left(\frac{R_i}{R_0}\right)^2} \qquad \text{(E.3.6.6c)}$$

*Graphs 4:*

(a) Velocity profiles

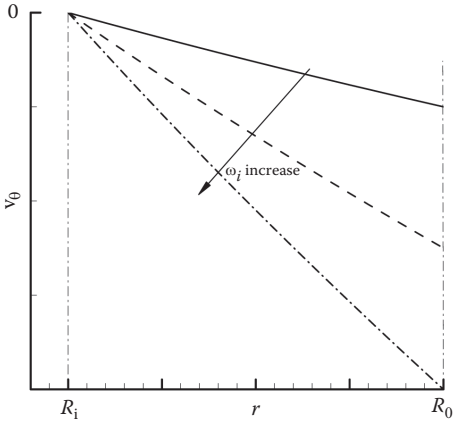

(b) Temperature profiles

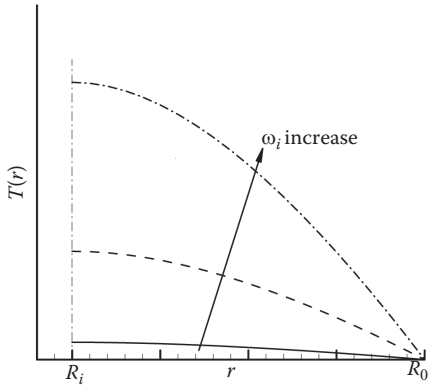


(c) Wall heat flow rate

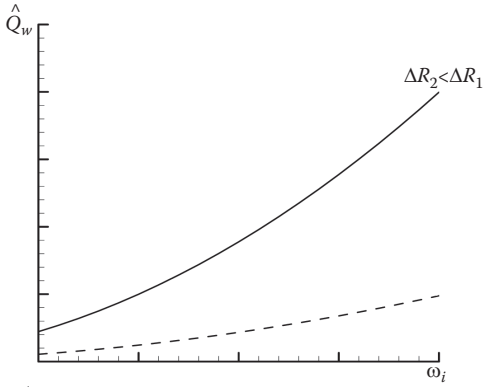


*Comments:*

- For small gaps, that is, $R_0 - R_i \ll 1$, the velocity profiles are almost linear, despite the hyperbolic term in Equation E.3.6.2. Clearly, with $\Delta R \ll 1$, $v_0(r)$ is "linearized."
- This is not the case for $T(r)$ due to the strong viscous heating effect (see Graph 4b).
- As expected, $\hat{Q}_w(\omega_i)$ decreases with a strong nonlinear influence of the gap size (see Graph 4c).

The next section returns to isothermal flow, but transient in nature, that is, $u = u(r, t)$. Of the three problem solutions discussed, Stokes' first problem is a very important one, because it paves the way to an understanding of Prandtl's boundary-layer theory.

### 3.1.4 Transient One-Dimensional Flows

Time-dependent viscous flows occur in nature (e.g., blood flow and respiratory airflow as well as tidal motion and wind pattern) as well as in industry (e.g., flow-induced vibration, internal flow start-up or shutdown, pressure waves, etc.). As such flow phenomena are

even more interesting than steady unidirectional flows, the necessary inclusion of time renders the mathematics involved a bit more complicated. In short, instead of ODEs, partial differential equations (PDEs) have to be solved. The reward is that more realistic fluid flow problems can be solved, and some of these basic transient flow solutions provide new physical insight into more complex flow phenomena.

Of the two start-up problems considered, the first one (after Stokes, 1845) is a suddenly accelerated plate above which a body of viscous fluid is set into motion due to frictional effects. The resulting expression for the thickness of that region of influence indicates the existence of a boundary layer, some 56 years later fully described by Ludwig Prandtl for a very different scenario. The second problem solution is a suddenly applied (constant) pressure gradient for tubular flow, which, after some time, establishes itself as Poiseuille flow.

### *3.1.4.1 Stokes' First Problem: Thin Shear-Layer Development*

Consider a horizontal plate (or wall) carrying a stagnant body of fluid (i.e., $u = 0$ when $t \le 0$ for all $y$; see Figure 3.2). Suddenly, the solid surface (at $y = 0$) attains a finite velocity, that is, $u = U_0$ when $t > 0$. Recalling that $v_{\text{wall}} = v_{\text{fluid}}$ (no-slip condition), this plate motion sets up, within a growing layer, parallel flow of the viscous fluid, that is, $u = u(y, t)$. The atmospheric pressure is constant everywhere.

Thus, with the postulates

$$\vec{v} = \left[ u\left(y,\ t\right),\ 0,\ 0 \right] \text{ and } \nabla p = 0 \tag{3.22a, b}$$

we can reduce the $x$-momentum equation to be

$$\frac{\partial u}{\partial t} = \nu \frac{\partial^2 u}{\partial y^2} \tag{3.23}$$

Equation 3.23 is known as the *transient one-dimensional diffusion equation* (cf. Equation 2.80). In the present case, it describes "momentum diffusion" normal to the axial parallel flow induced by the wall motion and transmitted by frictional forces.

As implied, the associated initial/boundary conditions are that $u(t \le 0, y) = 0$, but $u(t > 0; y = 0) = U_0$, while for $y \to \infty$, $u = 0$

Because the evolution of $u(y)$ with time shows similar profiles (see Figure 3.4), the independent variables $y$ and $t$ can be combined in conjunction with the fluid viscosity $v$ to a new *dimensionless* similarity variable:

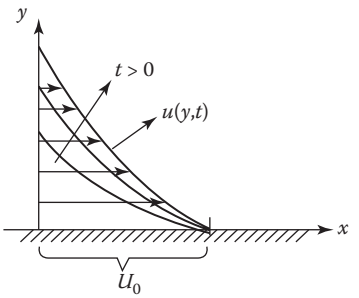


**FIGURE 3.4**
Changing velocity profiles with time inside thin shear layer.

$$\eta = \eta\left(y,\ t;\ \nu\right) \tag{3.24a}$$

Thus, we formally demand:

$$[\eta] \hat{=} y^a t^b \nu^c = [1] \tag{3.24b}$$

Via non-dimensionalization (pi-theorem) or by simple inspection with $a = 1$, we obtain

$$\eta = \frac{y}{t^{0.5}\nu^{0.5}} \hat{=} [1] \tag{3.24c}$$

For convenience, the dimensionless independent variable can be written as

$$\eta = \frac{y}{2\sqrt{\nu t}} \tag{3.24d}$$

It is apparent that

$$u\left(y,\ t\right) \sim f\left[\eta\left(y,\ t\right)\right] \tag{3.25a}$$

where $f(\eta)$ is a dimensionless dependent variable. To turn the proportionality into an equation, we use the plate speed $U_0$, so that

$$u\left(y,\ t\right) = U_0 f\left(\eta\right) \tag{3.25b}$$

Now, with Equations 3.24d and 3.25b, the governing PDE Equation 3.23 can be transformed into an ODE for $f(\eta)$ by applying the chain rule $\left(e.g.,\ \frac{\partial u}{\partial t} = U_0 \frac{df}{d\eta}\frac{\partial \eta}{\partial t} = \frac{-U_0 y}{4\sqrt{\nu t}\, t} f' = -\frac{U_0}{2t}\eta f', \text{etc.}\right)$, as outlined in Section 3.2.1:

$$f'' + 2\eta f' = 0 \tag{3.26}$$

subject to

$$f\left(\eta = 0\right) = 1 \text{ and } f\left(\eta \to \infty\right) \to 0 \tag{3.27a,b}$$

The solution is $f(\eta) = 1 - \text{erf}(\eta)$, where erf($\eta$) is the error function (Appendix AI.3.2), so that

$$\frac{u}{U_0} = 1 - \frac{2}{\sqrt{\pi}} \int_0^{\eta} \exp\left(-\eta^2\right) d\eta \tag{3.28}$$

When plotting Equation 3.28, it turns out that for $\eta = 2.0$, the moving-plate effect on the fluid body peters out, that is, $f\left(\eta = 2\right) \equiv \frac{u}{U_0} \approx 0.01$. This implies that the region of frictional influence, that is, $0 \le y \le \delta$, can be estimated from $y(\eta = 2) = \delta$ as

$$\delta \approx 4\sqrt{\nu t} \tag{3.29a}$$

Replacing $t$ in terms of the plate travel time, that is, $t = x/U_0$, Equation 3.16a can be rewritten as

$$\delta \approx 4\sqrt{\nu \frac{x}{U_0}} \tag{3.29b}$$

which can also be expressed as

$$\frac{\delta}{x} \approx \frac{4}{\sqrt{\mathrm{Re}_x}} \tag{3.30}$$

where:

$\mathrm{Re}_x = U_0 x/\nu$ is the local Reynolds number
$\delta$ is the steady-state extent of the shear layer in which $u = u(y)$

Outside the shear layer, that is, $y \geq \delta$, $u = 0$ in this case.

*Note:* The system parameter $\delta(x)$ is fundamental to laminar thin-shear-layer (TSL) or boundary-layer (B-L) theory (see Section 3.2).

Akin to Stokes' First Problem is his Second Problem, which is that of an oscillating flat plate (see White, 2006; Panton, 2013, among others). As mentioned, laminar flow generated by the start-up of a rotating disk in a reservoir of a viscous fluid is even more complicated. It is 3-D, because fluid exits the finite disk ($v_r$-component) radially due to of the centrifugal force; this vanishing fluid is constantly replaced by swirling, incoming fluid (i.e., the $v_\theta$ and $v_z$ components). Setting up these and other transient flow problems is part of the HWAs in Section 3.4.

### *3.1.4.2 Transient Pipe Flow*

An industrial application, that is, sudden start-up of fluid flow in a pipe, is given in Example 3.7. Another famous example of transient internal flow is pulsatile flow in a tube, for example, blood flow in a straight artery. It was first solved analytically in 1955 by Womersley, as discussed in Nichols and O'Rourke (1998), and is here given as Example 3.8.

**Example 3.7: Start-Up Flow in a Tube**

Consider a viscous fluid at rest in a horizontal tube when suddenly a constant pressure gradient, $\Delta p/L$, is applied. For example, a valve connecting a pipe to a reservoir is suddenly opened. Find an expression for the resulting $u(r,t)$ function.

| Sketch 8 | Assumptions | Method |
|---|---|---|
| 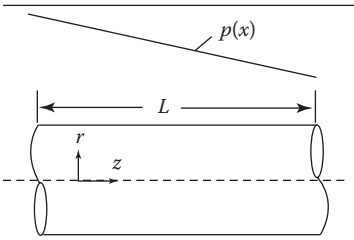 | • Pressure gradient at $-\frac{\partial p}{\partial x} \approx \frac{\Delta p}{L} = ¢$ for all times<br>• Transient laminar 1-D flow<br>• Constant fluid properties | • Reduced N–S equations<br>• Superposition of steady and transient flow contributions |

*Solution*:

It is postulated that the actual velocity $u(r,t)$ can be decomposed into a steady-state part and a transient part, that is,

$$u(r,t) = u(r)\big|_{SS} + u(r,\ t)\big|_{tr} \tag{E.3.7.1}$$

With $\vec{\mathbf{v}} = \left[u(r,t);\, 0;\, 0\right]$ and $-\nabla p \to \dfrac{\Delta p}{L} = \not{c}$, the governing momentum equation is (Appendix AI.5.3)

$$\frac{\partial u}{\partial t} = \frac{1}{\rho}\left(\frac{\Delta p}{L}\right) + \frac{\nu}{r}\frac{\partial}{\partial r}\left(r\frac{\partial u}{\partial r}\right) \tag{E.3.7.2}$$

subject to

$$u(r, t=\ 0) =\ 0;\, u(u\ =\ r_0, t) = 0,\ \text{and}\ \left.\frac{\partial u}{\partial r}\right|_{r=0} = 0 \quad \text{(E.3.7.3a through c)}$$

Clearly, the steady-state part, $u_{ss}$, is the Poiseuille-flow solution; that is,

$$u_{ss}(r) = u_{\max}\left[1 - \left(\frac{r}{r_0}\right)^2\right] \tag{E.3.7.4a}$$

where

$$u_{\max} = \frac{1}{4\mu}\left(\frac{\Delta p}{L}\right) \tag{E.3.7.4b}$$

Knowing $u_{ss}(r)$, the following dimensionless variables are employed:

$$\hat{u}\ =\ \frac{u_{tr}}{u_{\max}},\quad \hat{r}\ =\ \frac{r}{r_0},\quad \text{and}\quad \hat{t}\ =\ \frac{\nu t}{r_0} \tag{E.3.7.5a–c}$$

So, Equation E.3.7.2 can be transformed to the well-known "transient 1-D diffusion" form:

$$\frac{\partial \hat{u}}{\partial \hat{t}} = \frac{1}{\hat{r}}\frac{\partial}{\partial \hat{r}}\left(\hat{r}\ \frac{\partial \hat{u}}{\partial \hat{r}}\right) \tag{E.3.7.6}$$

subject to

$$\hat{u}\left(\hat{t} = 0\right) = 1 - \hat{r}^2;\quad \hat{u}\left(\hat{r} = 1\right)\ =\ 0,\quad \text{and}\quad \left.\frac{\partial \hat{u}}{\partial \hat{r}}\right|_{\hat{r}=0} = 0 \quad \text{(E.3.7.7a through c)}$$

The product solution consists of an $fct.(\hat{r})$, in terms of an infinite series, times a decaying exponential function in $\hat{t}$. Thus,

$$\hat{u}\ \sim \sum fct\left(\hat{r}\right) * e^{-\hat{t}} \tag{E.3.7.8}$$

*Graph 5:*

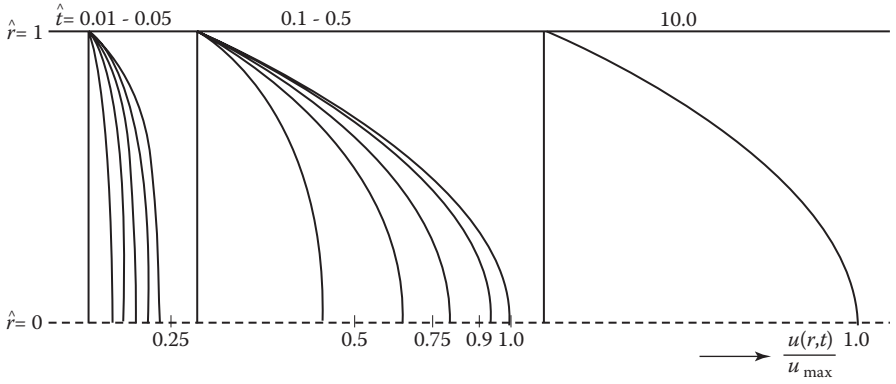


*Comments:*

- The final solution for the axial tubular velocity $u\left(\hat{r},\ \hat{t}\right)$ is graphed for $0 \le \hat{r} \le 1$ and $0 \le \hat{t} \le 10.0$. When at $\hat{t} \approx 10.0$, $u_{tr} \to 0$ and $u = u_{ss}$; that is, Poiseuille flow has been established.
- It is interesting to note that the suddenly elevated tube-inlet pressure starts the core-fluid off almost uniformly (for $0.01 \le \hat{t} < 0.05$), and then, after $\hat{t} = 0.2$, in conjunction with the no-slip condition, a parabolic velocity profile forms.

**Example 3.8: Pulsatile Blood Flow through an Artery**

| Sketch 9 | Assumptions | Method |
|---|---|---|
| 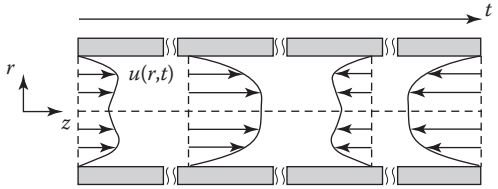  | • Laminar, fully developed flow with constant fluid properties<br>• Fixed tube walls with no slip<br>• Pressure gradient follows harmonic function | • Reduced N–S equations<br>• Prescribed pressure waveform<br>• Complex function postulated for $u(r,t)$ |

*Solution:*

The velocity profile for flow through a rigid tube driven by a pulsatile pressure gradient was first given by Womersley (Womersley, 1955) under the assumptions of fully developed, laminar flow with constant fluid properties. Based on these assumptions, the governing equation for the fluid motion is the time-dependent 1-D momentum equation, expressed here in cylindrical coordinates:

$$\frac{\partial u}{\partial t} = -\frac{\partial p}{\partial z} + \frac{\nu}{r}\frac{\partial}{\partial r}\left(r\frac{\partial u}{\partial r}\right) \tag{E3.8.1}$$

It is assumed that the pressure gradient can be modeled as a simple harmonic function, that is,

$$\frac{\partial p}{\partial z} = -\frac{\Delta p}{L} = A^* e^{i\omega t} = A^*\left[\cos(\omega t) + i\sin(\omega t)\right] \tag{E.3.8.2}$$

where:

$A^*$ is the complex conjugate of the amplitude of the harmonic function $A$
$\omega = 2\pi f$ is the angular frequency ($f$ is the frequency at which the pressure gradient oscillates)

Note that Euler's equation has been used in the last step to convert the complex exponential into a sum of sine and cosine terms. Substituting Equation E.3.8.2 into E.3.8.1 yields

$$\frac{\partial u}{\partial t} = \frac{1}{\rho}\left(A^* e^{i\omega t}\right) + \frac{\nu}{r}\frac{\partial}{\partial r}\left(r\frac{\partial u}{\partial r}\right) \tag{E.3.8.3}$$

Equation E.3.8.3 can be simplified by postulating $u = ae^{i\omega t}$, where $a = f(r)$ is some function that contains the radial dependence of the velocity profile. Substituting this assumed form for the velocity profile into Equation E.3.8.3 yields

$$\frac{\partial}{\partial t}\left(ae^{i\omega t}\right) = \frac{1}{\rho}\left(A^* e^{i\omega t}\right) + \frac{\nu}{r}\frac{\partial}{\partial r}\left(r\frac{\partial}{\partial r}\left(ae^{i\omega t}\right)\right) \tag{E.3.8.4}$$

where $f(r)$ is some function that is dependent on the radial position. This is based on the knowledge that the velocity profile will also be time dependent. Differentiating and algebraic simplification produces

$$\frac{1}{r}\frac{\partial}{\partial r}\left(r\frac{\partial a}{\partial r}\right) + \left(\frac{A^*}{\mu} - \frac{ia}{\nu}\right) = 0 \tag{E.3.8.5}$$

Expanding the first term on the left-hand side (LHS) reveals this expression to be a form of the Bessel differential equation (Nichols and O'Rourke, 2005). The solution, subject to the appropriate boundary conditions, is then

$$a = \frac{A^*}{i\rho}\left[1 - \frac{J_0\left(r\sqrt{1/\nu}\, i^{3/2}\right)}{J_0\left(r_0\sqrt{1/\nu}\, i^{3/2}\right)}\right] \tag{E.3.8.6}$$

where $J_0$ is the zeroth order Bessel function of the first kind (Nichols and O'Rourke, 2005). The Womersley number is defined as

$$\alpha = r_0\sqrt{\omega/\nu} \tag{E.3.8.7}$$

So, the solution for the velocity profile is

$$u = \frac{A^* r_0^2}{i\mu\alpha^2}\left[1 - \frac{J_0\left(\alpha i^{3/2}\frac{r}{r_0}\right)}{J_0\left(\alpha i^{3/2}\right)}\right]e^{i\omega t} \tag{E.3.8.8}$$

Now that the velocity profile is known, the volumetric flow rate can be determined by integrating over the cross section of the tube:

$$Q = \iint u dA = \frac{\pi r_0^2 A^*}{i\rho}\left[1 - \frac{2J_1\left(\alpha i^{3/2}\right)}{\alpha i^{3/2} J_0\left(\alpha i^{3/2}\right)}\right]e^{i\omega t} \tag{E.3.8.9}$$

*Graphs 6a through c:*

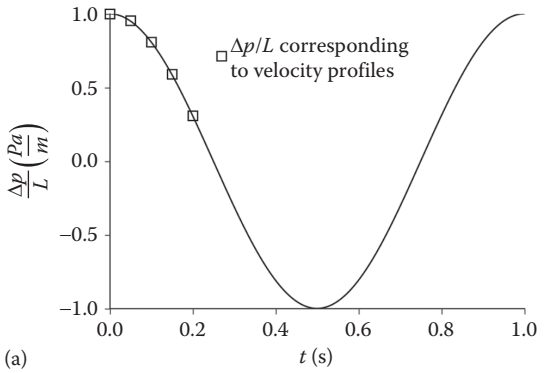


(a)

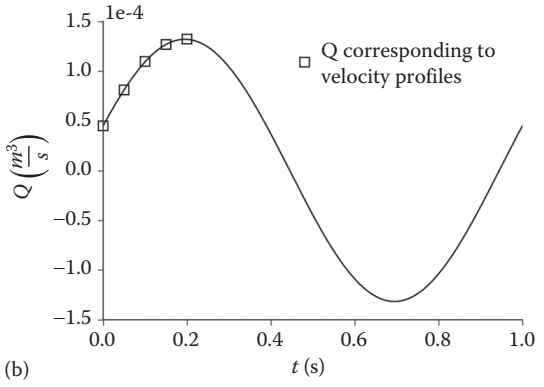


(b)

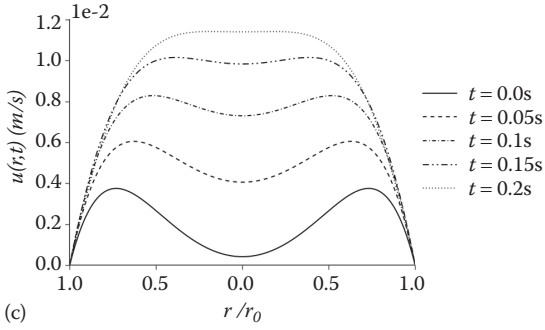


(c)

*Comments:*

- Although the assumed $p(t)$-profile does not represent an actual cardiac cycle, the resulting axial velocity distributions clearly show the well-known M-profile evolution with time.
- The transient flow rates lag somewhat behind the $p(t)$ -profile. Why?

## 3.2 External Laminar Flows

So far, with the exception of thin-film analyses, all flows have been internal—as is the case in numerous applications. Specifically, we learned that *internal fully developed* flows, such as Couette and Poiseuille, are uniformly dominated by viscous effects throughout the entire flow domain. However, *entrance flows* in tubes, pipes, slits, and so on feature highly viscous effects *confined* to rapidly growing "wall layers" in the entrance region with a reducing uniform core in the center zone. Such entrance flows are two-dimensional (2-D); that is, they are *developing flows*. In any case, for internal flow, a basic condition is that $\dot{m}$ = constant, which cannot be generally applied to external flow fields.

*External, high–Reynolds number* flows past plates or over submerged bodies develop thin shear layers, featuring steep velocity gradients. Clearly, the effect of no-slip wall velocity triggers an expanding *boundary layer* (Figure 3.4). As demonstrated via the solution to Stokes' First Problem in Section 3.1.4, the boundary-layer thickness relates to the fluid's kinematic viscosity and the axial coordinate as (see Equation 3.29)

$$\delta \sim \sqrt{\nu} \text{ and } \delta \sim x^{1/2} \tag{3.31a, b}$$

From Equation 3.30, Prandtl's hypothesis of 1904 can be deduced; that is, for high Reynolds numbers resulting in thin shear layers;

$$\delta \sim \sqrt{\frac{\nu L}{u_\infty}} \text{ and } \delta/L \sim \mathrm{Re}_L^{-1/2} \tag{3.32a, b}$$

On physical grounds, as the oncoming (free-stream) fluid particles are reaching the submerged body surface, say, a flat plate (see Figure 3.5), they stick to the solid surface (see "no-slip condition"). That affects the neighboring fluid layers, and hence, the frictional effect propagates outwards, that is, normal to the solid surface, until at distance $\delta(x)$ the presence of the flat plate is no longer registered. Thus, for high–Reynolds number flows, a thin shear layer $\delta(x)$ forms. Using Equation 3.32a and scaling the continuity equation yields

$$\frac{\delta}{L} \sim \frac{v}{u} \tag{3.33a}$$

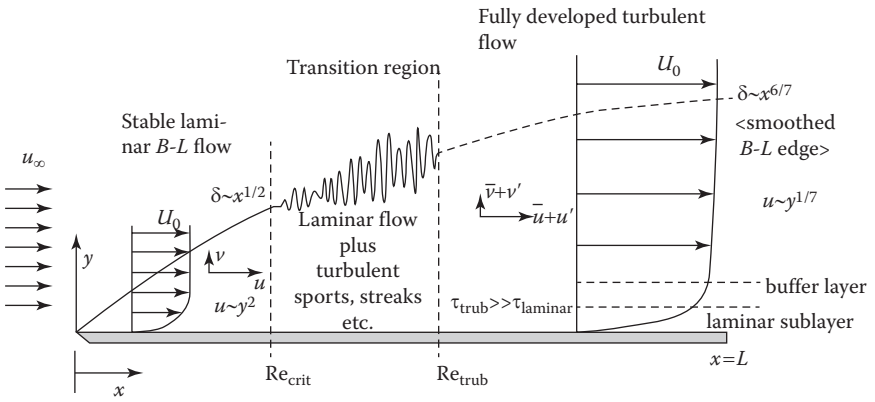


**FIGURE 3.5**
Flat-plate laminar and turbulent boundary layers with velocity profiles.

Based on this,

$$\frac{\partial^2}{\partial x^2} \ll \frac{\partial^2}{\partial y^2} \tag{3.33b}$$

Equation 3.33b implies that *axial* momentum diffusion, $\nu\partial^2 u/\partial x^2$, is negligible. However, the convective term $v\partial u/\partial y$ has to be retained, because, although $v$ is quite small, the normal gradient $\partial u/\partial y$ is very large inside the boundary layer. Employing Equation 3.33 and scale analysis with the scales $X = x/l$, $Y = y/\delta(x)$, $U = u/U_0$, $V = v/V_0$, and $P = p/P_0$, the steady 2-D N-S equations then reduce to (see HWA Section 3.4)

$$\frac{\partial u}{\partial x} + \frac{\partial v}{\partial y} = 0 \tag{3.34}$$

$$u\frac{\partial u}{\partial x} + v\frac{\partial u}{\partial y} = -\frac{1}{\rho}\frac{\partial p}{\partial x} + \nu\frac{\partial^2 u}{\partial y^2} \tag{3.35}$$

and

$$0 = -\frac{1}{\rho}\frac{\partial p}{\partial y} \tag{3.36}$$

Clearly, continuity, that is, fluid-mass conservation, is fully preserved, the $x$-momentum equation is slightly simplified, and the $y$-momentum equation collapses to $\partial p/\partial y = 0$. Equation 3.36 implies that the pressure is constant *across* the boundary layer, and hence, $p(x)$ can be determined with the Euler equation just outside the boundary layer. Clearly, in reality, there is no "edge", but for practical purposes, we postulate that $\delta(x)$ has been reached when the ratio $u(y)/U_0$ differs less than 1% from unity there, and all velocity gradients are basically zero at $y = \delta(x)$ (see Figure 3.4).

### 3.2.1 Momentum Boundary-Layer Flow

While Prandtl's B-L theory will prevail as an educational tool to gain physical insight and explain special fluid flow phenomena, solutions to the B-L equations (outside aerodynamics) have become largely superfluous. The reason is that nowadays, commercial as well as open-source N-S equation solvers, which run on basic workstations, are being routinely employed to tackle simulation problems in academia and industry. In any case, the mother of all B-L flows is flow past a (razor-thin) horizontal flat plate, of which only the upper half is usually shown (see Figure 3.5).

#### *3.2.1.1 Solution Methods for Flat-Plate Boundary-Layer Flows*

Other than direct numerical solutions of Equations 3.34 through 3.36, B-L flows are solved with the similarity analysis (for B-Ls with steady laminar self-similar velocity profiles) and the integral method (for both laminar and turbulent B-Ls).

##### *3.2.1.1.1 Similarity Analysis for Laminar Boundary-Layer Flows*

One elegant solution of Equations 3.34 and 3.35 relies on the *similarity* of the axial velocity profiles $u(x, y)$. Employing the stream-function approach, $u \equiv \partial\psi/\partial y$ and $v \equiv -\partial\psi/\partial x$, Equation 3.34 is automatically fulfilled. Similarly to Stokes' First Problem solution in

Section 3.1.4, a similarity variable $\eta = \eta(x, y) = y(U_0/\nu x)^{1/2}$ is postulated, which combines both independent variables $x$ and $y$. Now, setting $u/U_0 = f'(\eta) = df/d\eta$, the PDE Equation 3.35 can be transformed into a third-order ODE for $f(\eta)$, as illustrated with a HW Assignment (see Section 3.4). Specifically, we obtain

$$2f''' + ff'' = 0 \tag{3.37}$$

subject to

$$f'(0) = u(x,0)/U_0 = 0,\ f'(\infty) = 1,\ \text{and}\ \ f(0) = v(x,0) = 0 \tag{3.38a through c}$$

The derivation of Equation 3.37 starts with the determination of both the similarity variable

$$\eta(x,y) = y\sqrt{\frac{U_0}{\nu x}} \tag{3.39}$$

and the similarity function in terms of the stream function, which automatically fulfills continuity:

$$\psi(x,y) = \sqrt{\nu U_0 x}\, f(\eta) \tag{3.40}$$

The velocity components are then

$$u \equiv \frac{\partial \psi}{\partial y} = \frac{\partial \eta}{\partial y}\frac{\partial \psi}{\partial \eta} = \sqrt{\frac{U_0}{\nu x}}\sqrt{\nu U_0 x}\, f' = U_0 f' \tag{3.41a}$$

$$v \equiv -\frac{\partial \psi}{\partial x} = -\frac{1}{2}\sqrt{\frac{\nu U_0}{x}} f + \sqrt{\nu U_0 x}\,\frac{\partial f}{\partial \eta}\frac{\partial \eta}{\partial x} = \frac{1}{2}\sqrt{\frac{\nu U_0}{x}}\left(\eta f' - f\right) \tag{3.41b}$$

Differentiating produces

$$\frac{\partial u}{\partial x} = \frac{\partial}{\partial x}\left[U_0 f'\right] = U_0\frac{\partial \eta}{\partial x}\frac{\partial f'}{\partial \eta} = -\frac{U_0}{2} y\sqrt{\frac{U_0}{\nu}}\frac{1}{x^{\frac{3}{2}}} f'' = -\frac{U_0 \eta}{2x} f'' \tag{3.42a}$$

$$\frac{\partial u}{\partial y} = \frac{\partial}{\partial y}\left(U_0 f'\right) = U_0\frac{\partial \eta}{\partial y}\frac{\partial f'}{\partial \eta} = \frac{U_0^{\frac{3}{2}}}{\sqrt{\nu x}} f'' \tag{3.42b}$$

$$\frac{\partial^2 u}{\partial y^2} = \frac{\partial}{\partial y}\left(\frac{\partial u}{\partial y}\right) = \frac{U_0^{\frac{3}{2}}}{\sqrt{\nu x}}\frac{\partial \eta}{\partial y}\frac{\partial f''}{\partial y} = \frac{U_0^2}{\nu x} f''' \tag{3.42c}$$

Since $\partial p/\partial y = 0$, the pressure outside of the B-L at any given $x$-location must equal the pressure inside the B-L at that $x$-location. Outside of the B-L, it is known that $u = U_0 = \text{constant}$ and $v = 0$. Evaluating the $x$-momentum equation under these conditions show

$$\frac{dp}{dx} = 0, \tag{3.43}$$

That is, $p$ = constant. Substituting Equations 3.41 through 3.43 into the momentum Equation 3.35 yields

$$U_0 f'\left[-\frac{U_0\eta}{2x}f''\right]+\frac{1}{2}\sqrt{\frac{\nu U_0}{x}}\left(\eta f'-f\right)\left[\frac{U_0^{\frac{3}{2}}}{\sqrt{\nu x}}f''\right]=\nu\left[\frac{U_0^2}{\nu x}f'''\right]$$

$$-\frac{U_0^2\eta}{2x}f'f''+\frac{U_0^2\eta}{2x}ff''-\frac{U_0^2}{2x}ff''=\frac{U_0^2}{x}f''' \qquad \text{(3.43a through c)}$$

$$\frac{U_0^2}{x}f'''+\frac{U_0^2}{2x}ff''=0$$

Dividing through by $U_0^2/2x$ yields $2f''' + f'' = 0$, which is exactly the third-order ODE in terms of $f(\eta)$ given as Equation 3.37. This equation can then be numerically solved to yield key properties of the B-L; for example, the B-L thickness, $\delta$, and skin-friction coefficient, $C_f$ Tabulated values for $\eta(x, y)$, $f$, $f'$, $f''$, and $f'''$ are given in Table 3.2.

The numerical (Runge-Kutta) solution of this system includes the following results:

$$\frac{\delta}{x}=\frac{5.0}{\sqrt{\mathrm{Re}_x}} \tag{3.45}$$

and

$$C_f \equiv \frac{\tau_{\text{wall}}}{\rho/2U_0^2}=\frac{0.664}{\sqrt{\mathrm{Re}_x}} \tag{3.46}$$

where:

$$\mathrm{Re}_x=\frac{U_0\ x}{\nu} \qquad 3.47$$

**TABLE 3.2**

Tabulated Values from Numerical Solution to Blasius Equation

| $\eta(x, y)$ | $f(\eta)$ | $f'(\eta)$ | $f''(\eta)$ | $f'''(\eta)$ |
|---|---|---|---|---|
| 0.0000 | 0.0000 | 0.0000 | 0.3321 | 0.0000 |
| 1.0000 | 0.1656 | 0.3298 | 0.3230 | −0.0267 |
| 2.0000 | 0.6500 | 0.6298 | 0.2668 | −0.0867 |
| 3.0000 | 1.3968 | 0.8460 | 0.1614 | −0.1127 |
| 4.0000 | 2.3058 | 0.9555 | 0.0642 | −0.0741 |
| 5.0000 | 3.2833 | 0.9915 | 0.0159 | −0.0261 |
| 6.0000 | 4.2796 | 0.9990 | 0.0024 | −0.0051 |
| 7.0000 | 5.2792 | 0.9999 | 0.0002 | −0.0006 |
| 8.0000 | 6.2792 | 1.0000 | 0.0000 | 0.0000 |
| 9.0000 | 7.2792 | 1.0000 | 0.0000 | 0.0000 |
| 10.000 | 8.2792 | 1.0000 | 0.0000 | 0.0000 |

and

$$\tau_w = \mu \left.\frac{\partial u}{\partial y}\right|_{y=0} \tag{3.48}$$

Equation 3.45 reveals that $\delta(x) \sim \sqrt{x}$ and that even for laminar B-L flow, the Reynolds number has to be very large for hypothesis Equation 3.32b to hold. Nevertheless, it should be noted that at the leading edge, $x = 0$, we have a singular point/line as $\mathrm{Re}_x = 0$. Another interesting observation can be made when evaluating Equation 3.35 at the wall, where $u = v = 0$. Thus, at the wall,

$$\left.\frac{\partial^2 u}{\partial y^2}\right|_{y=0} = \frac{1}{\mu}\frac{\partial p}{\partial x} \tag{3.49}$$

Equation 3.49 indicates that the magnitude of the pressure gradient determines qualitatively the velocity profile near the wall. Clearly, for constant-pressure flow (Blasius, 1908), $\partial^2 u/\partial y^2 = 0$, and hence, the profile is linear at the wall. However, a negative (or favorable) pressure gradient causes a fuller profile because of the negative curvature, while a positive (or adverse) pressure gradient with positive curvature (i.e., $\partial^2 u/\partial y^2 > 0$) may generate B-L separation and reverse flow.

When $u(y) = U_0 df(\eta)/d\eta$ is plotted at any $x$-station, it could be well approximated by a parabolic function (or something locally similar, e.g., an exponential function or a sine- or tanh-function). Indeed, that idea of approximating the (unknown) $u(x, y)$ -profile, subject to appropriate boundary conditions, is the kernel of the *momentum integral relation* (MIR) after Von Kármán (1921).

*3.2.1.1.2 Integral Method for Laminar or Turbulent Boundary-Layer Flows*

For all kinds of similar or non-similar, laminar or turbulent B-L type flows, the Von Kármán (1921) MIR may be most appropriate. The approximate solutions provide local as well as global system parameters such as the B-L thickness, wall shear stress, flow rates, fluxes, drag coefficients, and forces, in addition to realistic velocity profiles. Specifically, suitable velocity functions are postulated, subject to standard boundary conditions, and then, momentum conservation is preserved. Clearly, the more accurate the assumed tangential/axial velocity profiles, the better are the results for the system parameters. To best illustrate the integral method, we focus on the steady laminar (or turbulent) 2-D flat-plate B-L problem (see Figure 3.4).

Along the B-L edge, Euler's equation holds, so that

$$-\frac{1}{\rho}\frac{\partial p}{\partial x} = U\frac{\partial U}{\partial x} \tag{3.50}$$

and hence, Equation 3.34 can be rewritten, with $\mu \partial u/\partial y = \tau_{xy}$, as

$$u\frac{\partial u}{\partial x} + v\frac{\partial u}{\partial y} = U\frac{\partial U}{\partial x} + \frac{1}{\rho}\frac{\partial \tau_{yx}}{\partial y} \tag{3.51}$$

From Equation 3.33, we obtain

$$v(x, y) = -\int \frac{\partial u}{\partial x}\,dy + f(x) \qquad \text{or} \qquad v = -\int_0^y \frac{\partial u}{\partial x}\,dy \tag{3.52a, b}$$

which will be used to eliminate the normal (vertical) velocity $v$ in Equation 3.51. Now, integrating Equation 3.51 across the B-L yields

$$\int_{y=0}^{y=\delta(x)} \left( u\frac{\partial u}{\partial x} + v\frac{\partial u}{\partial y} - U\frac{dU}{dx} \right) dy = \frac{1}{\rho}\int_0^{\delta} \frac{\partial \tau_{yx}}{\partial y}\, dy = -\frac{\tau_{\text{wall}}}{\rho} \tag{3.53}$$

Integration by parts of the $v\partial u/\partial y$ term with Equation 3.52b inserted results in

$$-\int_0^{\delta} \left\{ \frac{\partial u}{\partial x}\int_0^{y} \frac{\partial u}{\partial x}\, dy \right\} dy = -\left[ U\int_0^{\delta} \frac{\partial u}{\partial x}\, dy - \int u\frac{\partial u}{\partial x}\, dy \right] \tag{3.54}$$

so that Equation 3.53 finally reads:

$$\int_0^{\delta} \frac{\partial}{\partial x}\left[u(U-u)\right] dy + \frac{dU}{dx}\int_0^{\delta} (U-u)\, dy = \frac{\tau_w}{\rho} \tag{3.55}$$

As mentioned, with the right choice of $u(x, y)$, both sides of the momentum balance (Equation 3.55) have to be matched (see Example 3.8 or Appendix AI.4.3).

**Example 3.8: Blasius Flow**

Consider steady laminar high–Reynolds number flow past a horizontal flat plate with zero pressure gradient, that is, given $u_\infty \equiv U = \text{constant}$ Employing the MIR with a basic polynomial for $u(x, y)$, find $\delta(x)$ and $\vec{\mathbf{v}} = (u, v, 0)$ .

| **Sketch 10** | **Assumptions** | **Method** |
|---|---|---|
| 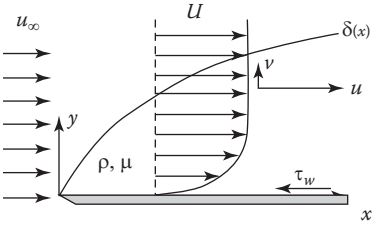 | • As stated<br>• Constant fluid properties<br>• Mass-less plate with upper B-L only | • Integral B-L Equation 3.55 with $U = u_\infty = \not\subset$<br>• *Postulate:*<br>• $u(x, y) = a + by + cy^2$<br>• where the coefficients are functions of $x$ |

*Solution:*

With $U = \not\subset$ and invoking Leibniz' rule, Equation 3.55 reduces to

$$\rho\frac{d}{dx}\int_0^{\delta} u(u_\infty - u)\, dy = \tau_w = \mu\left.\frac{\partial u}{\partial y}\right|_{y=0} \tag{E.3.8.1}$$

where $u_\infty = U$ is given and we employ the postulate

$$u(x, y) = a + by + cy^2 \tag{E.3.8.2a}$$

Clearly, the three $x$-dependent coefficients are determined by the following BCs:

$$u(y=0)=0, \qquad u(y=\delta)=u_\infty, \quad \text{and} \quad \left.\frac{\partial u}{\partial y}\right|_{y=\delta}=0 \qquad \text{(E.3.8.2b through d)}$$

*Note:* A simple *linear* velocity profile postulate would have missed incorporating the third B.C.
(Equation E.3.8.2d) and hence, would have generated an incorrect result.
Using Equations E.3.8.2a through d yields

$$a=0, \qquad b=u_\infty/\delta, \quad \text{and} \quad c=-u_\infty/(2\delta^2)$$

so that only $\delta(x)$ remains as an unknown:

$$u(x,y)=u_\infty\left[\frac{y}{\delta(x)}-\frac{1}{2}\left(\frac{y}{\delta(x)}\right)^2\right] \qquad \text{(E.3.8.3)}$$

Inserting Equations E.3.8.3 into E.3.8.1, carrying out the integration, and evaluating $\tau_{wall}$ yields

$$0.0666\,\bar{\rho}\,u_\infty^2\,\frac{d\delta}{dx}=\mu\frac{u_\infty}{\delta} \qquad \text{(E.3.8.4a)}$$

or

$$\delta\frac{d\delta}{dx}=K\equiv\frac{\mu}{0.0666\,\bar{\rho}\,u_\infty} \qquad \text{(E.3.8.4b)}$$

subject to $\delta(x=0)=0$. Thus,

$$\frac{\delta^2}{2}=Kx \qquad \text{(E.3.8.4c)}$$

or

$$\frac{\delta(x)}{x}=\frac{5.477}{\sqrt{\mathrm{Re}_x}} \qquad \text{(E.3.8.5)}$$

*Comments:*

- The expected $\delta(x)\sim\sqrt{x}$ is depicted in Figure 3.5.
- Compared with the "exact" solution (Equation 3.45), this simple approximation for $u(x, y)$ is off by just under 10%.

### *3.2.2 Thermal Boundary-Layer Flow*

In most natural and industrial scenarios, the wall-surface temperature differs from the fluid temperature. Hence, in such cases of *forced convection heat transfer*, momentum as well as thermal B-L developments have to be considered. The major concerns include:

- Are the fluid properties constant or not (see degree of coupling in Figure 3.2)?

- Is the B-L flow laminar or turbulent, or a mixture of both with a significant zone of transitional flow?
- Is the value of the Prandtl number, $\mathrm{Pr} = \delta_{\text{momentum}}/\delta_{\text{themal}}$, equal to one, or less or greater than unity?

In general, the modeling equations for *one-way coupled, steady laminar thermal B-L flow in 2-D rectangular coordinates* read:

$$\frac{\partial u}{\partial x} + \frac{\partial v}{\partial y} = 0 \tag{3.56}$$

$$u\frac{\partial u}{\partial x} + v\frac{\partial u}{\partial y} = -\frac{1}{\rho}\frac{dp_\infty}{dx} + \nu\frac{\partial^2 u}{\partial y^2} \tag{3.57}$$

and

$$u\frac{\partial T}{\partial x} + v\frac{\partial T}{\partial y} = \alpha\frac{\partial^2 T}{\partial y^2} \tag{3.58}$$

Clearly, the general convection heat transfer problem (see Section 2.4) has been reduced to solve three equations for three unknowns ($u$,$v$,$T$) when dealing with (laminar) B-L flows. It is insightful to start with scale analysis (Section 1.4.1). With reference to Figures 3.3 and 3.4, we select:

$$u \sim u_\infty \equiv U_0,\ v \sim V_0,\ x \sim L,\ y = \delta \text{ or } \delta_{th}, \text{ and } T \sim \Delta T = T_{\text{wall}} - T_\infty.$$

While continuity is balanced, that is, $\frac{U_\infty}{L} \sim \frac{V_0}{\delta}$, Equation 3.57 carries the proportionality between the inertia terms and the viscous terms. As both inertia terms are equivalent, that is,

$$\frac{u_\infty^2}{L} \triangleq \frac{V_0 u_\infty}{\delta} \quad \text{as} \quad \frac{V_0}{\delta} \sim \frac{u_\infty}{L},$$

we compare

$$\frac{u_\infty^2}{L} \sim \nu\frac{u_\infty}{\delta^2}$$

which implies, as shown in Example 3.8, that

$$\delta \sim \sqrt{\frac{\nu L}{u_\infty}} \quad \text{or} \quad \frac{\delta}{L} \sim \frac{1}{\sqrt{\mathrm{Re}_L}} \tag{3.59a, b}$$

With the shear stress $\vec{\vec{\tau}} = \mu\left(\nabla\vec{v} + \nabla\vec{v}^{tr}\right)$, that is, $\tau \sim \mu\frac{u_\infty}{\delta}$, we have for the skin-friction coefficient

$$C_f = \frac{2\tau}{\rho u_\infty^2} \tag{3.60a}$$

the same relation:

$$C_f \sim \frac{\mu u_\infty \sqrt{\mathrm{Re}_L}}{L\rho u_\infty^2} = \frac{1}{\sqrt{\mathrm{Re}_L}} \tag{3.60b}$$

In Equation 3.58, the convection terms $u\Delta T/L$ and $V_\theta \Delta T/\delta_{th}$ are balanced by thermal diffusion; that is, we compare

$$u_\theta \frac{\Delta T}{L} \sim \alpha \frac{\Delta T}{\delta_{th}^2}$$

because within the momentum B-L, we scale $u \sim u_\infty = ¢$, which yields

$$\frac{\delta_{th}}{L} \sim \frac{1}{\sqrt{Pe_L}}; \quad Pe_L = \frac{u_\infty L}{\alpha} = \mathrm{Pr}\,\mathrm{Re}_L \tag{3.61a through c}$$

#### *3.2.2.1 Thick Thermal Boundary Layers*

Dividing Equation 3.61 by 3.59b yields for *thick thermal* B-Ls, such as liquid metals ($\mathrm{Pr} \ll 1$),

$$\frac{\delta_{th}}{\delta} \sim \frac{1}{\sqrt{\mathrm{Pr}}} > 1$$

#### *3.2.2.2 Thin Thermal Boundary Layers*

For water and oil, where $\mathrm{Pr} > 1$ (i.e., $\delta_{th} < \delta$), the thermal B-L exhibits $u = u(y)$, and hence, the axial velocity has to be scaled as

$$u \sim u_\infty \frac{\delta_{th}}{\delta} \tag{3.62a}$$

Scaling of the convection-diffusion terms in Equation 3.58 yields

$$u \frac{\Delta T}{L} \sim \alpha \frac{\Delta T}{\delta_{th}^2} \tag{3.62b}$$

Combining both:

$$u_\infty \frac{\delta_{th}}{L} \sim \alpha \frac{\delta}{\delta_{th}^2} \text{ or } \frac{\delta_{th}}{L} \sim \frac{\alpha}{u_\infty L}\left(\frac{L}{\delta_{th}}\right)^2 \frac{\delta}{L} \tag{3.63a, b}$$

Using $\frac{\delta}{L} \sim \mathrm{Re}_L^{-\frac{1}{2}}$, we obtain

$$\left(\frac{\delta_{th}}{L}\right) \sim \mathrm{Re}_L^{-1/2}\,\mathrm{Pr}^{-1} \tag{3.64a}$$

Hence,

$$\left(\frac{\delta_{th}}{L}\right)^3 \sim \mathrm{Re}_L^{-1/2}\,\mathrm{Pr}^{-1/3} \tag{3.64b}$$

Using again $\mathrm{Re}_L^{-1/2} \sim \delta / L$, we obtain for *thin thermal B-L flow*

$$\frac{\delta_{th}}{\delta} \sim \mathrm{Pr}^{-\frac{1}{3}} < 1 \tag{3.65}$$

#### *3.2.2.3 Nusselt Number Correlations*

Now, recalling that the convection heat transfer coefficient is defined as

$$h = \frac{q_w}{T_w - T_\infty} = \frac{k\left.\dfrac{\delta T}{\partial y}\right|_{y=0}}{T_w - T_\infty} \sim \frac{k\dfrac{\Delta T}{\delta_{th}}}{\Delta T} = \frac{k}{\delta_{th}} \tag{3.66}$$

we have with proportionality Equation 3.64b:

$$h \sim \frac{k}{L}\mathrm{Re}_L^{1/2}\,\mathrm{Pr}^{1/3} \tag{3.67}$$

Hence, the Nusselt number $Nu_L = \dfrac{\text{convection}}{\text{conduction}} = \dfrac{hL}{k}$ exhibits the dependence

$$Nu_L \sim \mathrm{Re}_L^{1/2}\,\mathrm{Pr}^{1/3} \tag{3.68}$$

Indeed, based on experience, the averaged Nusselt number for flat plates of length $L$ have the form

$$\overline{Nu} = Nu_L = C\,\mathrm{Re}_L^m\,\mathrm{Pr}^n \tag{3.69}$$

For example, measurements of *laminar B-L flows* ($\mathrm{Pr} > 0.6$) yield

$$\overline{Nu} = 0.664\,\mathrm{Re}_L^{1/2}\,\mathrm{Pr}^{1/3} \tag{3.70}$$

and for *turbulent B-L flows* ($0.6 \le \mathrm{Pr} \le 60$; $5\times10^5 \le \mathrm{Re}_L \le 10^7$)

$$\overline{Nu} = 0.037\,\mathrm{Re}_L^{4/5}\,\mathrm{Pr}^{1/3} \tag{3.71}$$

**Example 3.9: Analysis of Thermal Blasius Flow**

Assuming that the basic thermal B-L flow is decoupled from the momentum B-L flow (see Example 3.8) and $\mathrm{Pr} > 1$, that is, $\delta_{th} < \delta$, find numerically $q_{\mathrm{wall}}(x)$, $Nu(x)$, and $\delta/\delta_{th}$.

| Sketch 11 | Assumptions | Method |
|---|---|---|
| 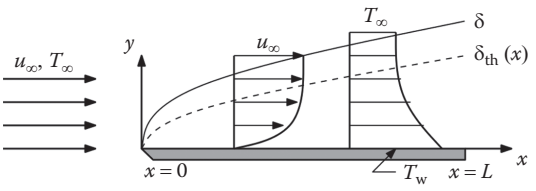 | • Constant pressure $(\therefore U_{outer} = u_\infty)$<br>• Constant properties | • Use similarity results $f(\eta)$, $\eta = y\sqrt{u_\infty / \nu x}$, for Blasius flow |

*Previous numerical Blasius B-L flow results* (see Table 3.2):

| $\eta = y\sqrt{\frac{u_\infty}{\nu x}}$ | 0 | 0.4 | 0.8 | 1.2 | 1.6 | 2.0 | 2.4 | 2.8 | 3.2 | 5.0 |
|---|---|---|---|---|---|---|---|---|---|---|
| $f(\eta)$ | 0 | 0.027 | 0.106 | 0.238 | 0.420 | 0.65 | 0.92 | 1.31 | 1.57 | 3.2 |
| $\frac{df}{d\eta} = \frac{u}{u_\infty}$ | 0 | 0.133 | 0.265 | 0.394 | 0.517 | 0.63 | 0.73 | 0.81 | 0.88 | 0.99 |

*Solution:*

Assuming a similarity solution $\theta(\eta)$, Equation 3.58 can be transformed with

$$\theta = \frac{T - T_w}{T_\infty - T_w} \text{ and } \eta = \frac{y}{\sqrt{x}}\sqrt{\frac{u_\infty}{\nu}} \tag{E.3.9.1a, b}$$

This yields (see Section 3.2.1 and HWA in Section 3.4.2)

$$\frac{d^2\theta}{d\eta^2} + \frac{\Pr}{2} f(y)\frac{d\theta}{d\eta} = 0 \tag{E.3.9.2}$$

subject to

$$\theta(\eta = 0) = 0 \text{ and } \theta(\eta \to \infty) = 1 \tag{E.3.9.3a, b}$$

Of special interest is the dimensionless temperature gradient at the plate surface, which directly relates to $q_w(x)$, $h(x)$, and $Nu(x)$. The numerical result shows that

$$\left.\frac{d\theta}{d\eta}\right|_{\eta=0} = 0.332\Pr^{1/3} \quad \text{for} \quad \Pr > 0.6 \tag{E.3.9.4}$$

Now,

$$h(x) \equiv \frac{q_w}{T_w - T_\infty} = \frac{T_\infty - T_w}{T_w - T_\infty} k \left.\frac{\partial\theta}{\partial y}\right|_{y=0} = k\sqrt{\frac{u_\infty}{\nu x}} \left.\frac{d\theta}{d\eta}\right|_{\eta=0} \tag{E.3.9.5}$$

so that

$$Nu(x) \equiv Nu_x = \frac{h_x x}{k} = 0.332\,\mathrm{Re}_x^{\frac{1}{2}}\Pr^{\frac{1}{3}} \sim x^{1/2} \tag{E.3.9.6}$$

while

$$q_w(x) = 0.332\frac{\Delta T k}{x}\mathrm{Re}_x^{1/2}\Pr^{1/3} \sim x^{-1/2} \tag{E.3.9.7}$$

Note that $\overline{Nu} = 2Nu_L = 0.664\,\mathrm{Re}_L^{1/2}\,\mathrm{Pr}^{1/3}$ (see Equation 3.63). The numerical solution of Equation E.3.9.2 also yields

$$\frac{\delta}{\delta_{th}} \approx \mathrm{Pr}^{1/3} \tag{E.3.9.8}$$

where $\delta = 5.477x/\sqrt{\mathrm{Re}_x}$ based on the integral analysis of Example 3.8, or $\delta = 5x/\sqrt{\mathrm{Re}_x}$ based on the (exact) similarity solution.

*Comments:*

- The convective term $u\partial T/\partial x$ in Equation 3.51 made the solution more challenging.
- Scaling produced all the basic dependencies for $\delta/\delta_{th}$, $h$ and $Nu$, obtained with just some algebra.

While the solution to Example 3.9 required numerical analysis using computer software, the next example illustrates basic thermal B-L flow solutions using only algebra based on the Reynolds-Colburn analogy. Even if the local skin-friction coefficient $C_f(x)$ is numerically not known, the dependence of key thermal quantities, such as the wall heat flux, can be evaluated.

**Example 3.10: Reynolds-Colburn Analogy Applied to Laminar Boundary-Layer Flow**

Consider a heated plate of length $L$ and constant wall temperature $T_w$, subject to a cooling air-stream ($u_\infty$, $T_\infty$). Find a functional dependence for $q_w(x)$.

| **Sketch 12** | **Assumptions** | **Method** |
|---|---|---|
| 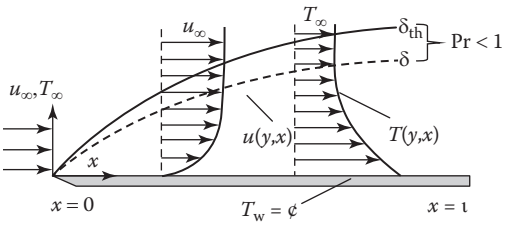 | • Thermal Blasius flow (see also Section 3.2.1)<br>• Constant properties | Reynolds-Colburn analogy |



*Solution:*

Rewriting Equation 3.20, we have

$$\frac{q_w(x)}{\rho\, c_p\, u_\infty (T_w - T_\infty)} = C_f\,\mathrm{Pr}^{-2/3} \tag{E.3.10.1}$$

From Section 3.2.2 or Example 3.8, we know that

$$C_f \sim \mathrm{Re}_x^{-1/2} \tag{E.3.10.2}$$

where actually $C_f = 0.664/\sqrt{\mathrm{Re}_x}$, as shown in Section 3.2.1. Now, with everything else being constant,

$$q_w(x) \sim \frac{K}{\sqrt{x}},\quad K = ¢ \tag{E.3.10.3a, b}$$

*Graph 12:*

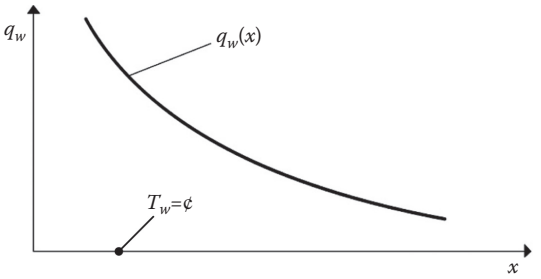


*Comments:*

- The wall heat flux from the plate surface decreases nonlinearly with plate distance because of the increasing Re($x$) as well as the growth of the thermal B-L thickness $\delta_{th}(x)$, leading to milder wall temperature gradients.
- Clearly, it was easier to obtain this result using the R-C analogy than to solve the actual PDEs describing fluid flow and heat transfer in thin wall layers (see Examples 3.8 and 3.9).

### 3.2.3 Drag and Lift Computations

Drag and lift computations are naturally most important in aerodynamics as part of any aircraft design (see Bertin, 2002, among others). In general, fluid flow around a submerged body, for example, an airplane, a submarine, a race car, or a cruising bird, or fixed objects such as weather balloons, commercial signs, buildings, and large trees, produces a resulting force. It can be decomposed into a component parallel to the object motion (or free-stream), called the *drag*, and in the vertical direction, that is, against gravity, called *lift*. Both the total drag and lift are due to frictional and net pressure effects, and hence, the surface force exerted by a fluid on the object is (see Figure 3.6)

$$\sigma\vec{\mathbf{F}}_{\text{surface}} = \vec{\mathbf{F}}_{\text{pressure}} + \vec{\mathbf{F}}_{\text{viscous}} \tag{3.72a}$$

That is,

$$\vec{\mathbf{F}}_S = \oiint\left[-\left(p - p_\infty\right)\hat{n} + \tau_w\,\hat{t}\right] dS \tag{3.72b}$$

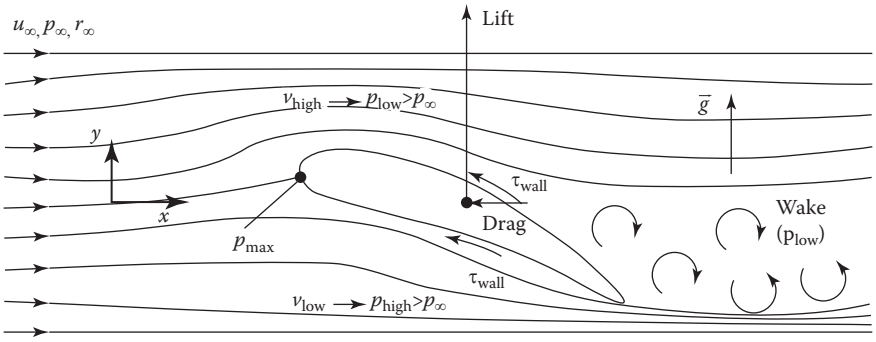


**FIGURE 3.6**
Pressure and wall shear stress around an airfoil causing lift and drag.

where:

$\hat{n}$ is the normal unit vector

$\hat{t}$ is the tangential unit vector

Assuming that the free-stream is parallel to the $x$-axis (see Figure 3.5), then from Equation 3.72a,

$$\vec{\mathbf{F}}_{\text{Drag}} \equiv \vec{\mathbf{F}}_{\text{form}} + \vec{\mathbf{F}}_{\text{friction}} = \hat{i}\ F_S \qquad \text{and} \qquad \vec{\mathbf{F}}_{\text{Lift}} = \hat{j}\ F_S \qquad \text{(3.73a through c)}$$

Considering the streamlines around an idealized airplane wing (see Figure 3.6), we detect accelerating airflow above the wing. This, according to Bernoulli's equation (see Section 2.3.3), translates into a low (i.e., suction) pressure, while the opposite is true beneath the wing. The difference, $\Delta p.\ A_{\text{horizontal}}$, generates almost entirely the lift force, $F_{\text{lift}}$, in Equation 3.73c. In contrast, the total drag results from the front-and-back pressure difference times projected vertical area, also called *form drag*, as well as the net wall shear stress on the object's surface area (see Equation 3.73c in conjunction with Equation 3.73b), called *frictional drag.*

In general, detailed $p$ and $\tau_w$ distributions from numerical (computational fluid dynamics) simulations have to be known to solve the closed surface integral Equation 3.72b. Alternative approaches for finding $\vec{\mathbf{F}}_S$ are

1. Analytic solutions, employing the momentum RTT, as discussed in Section 2.3
2. Measurements of drag and lift coefficients based on dimensional analysis

Specifically, Method (ii) relies on empirical values of the lift and drag coefficients, defined, respectively, as

$$C_L \equiv \frac{F_L}{\frac{\rho}{2}\, u_\infty^2\, A_p} \tag{3.74}$$

and

$$C_D \equiv \frac{F_D}{\frac{\rho}{2}\, u_\infty^2\, A_p} \tag{3.75}$$

where:

$u_\infty$ is the free-stream velocity

$\rho$ is the fluid density

$A_p$ is the projected area, that is, either the frontal (plane normal) or the mid-plane area

Figure 3.7a,b depict typical force coefficients for an airfoil and a sphere, respectively.

The $C_D(\text{Re}_D)$ curve for spheres shown in Figure 3.7b encapsulates different flow structures and regimes:

- For $\text{Re} \leq 1$, we are in the Stokes regime, and $C_D = \text{Re}_D$ without any flow separation, which starts at $\text{Re}_D \approx 10$ and vortex shedding at $\text{Re}_D \approx 90$.
- At about $\text{Re}_D = 10^3$, the drag is 95% due to net pressure (i.e., form drag).

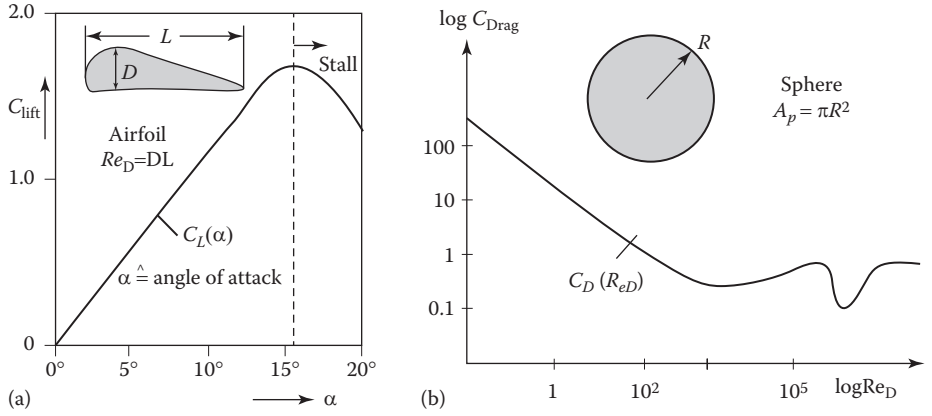


**FIGURE 3.7**
Lift and drag coefficients. (a) Airfoil lift coefficient as a function of inclined angle, where $C_L(\alpha_{critical})$ decreases because of upper boundary-layer separation, called "stall." (b) Average drag coefficient for a smooth sphere in uniform flow (see Appendix II).

- *Note:* $C_D \sim v$ may decrease, but $F_D \sim v^2$ increases.
- Between $10^5 < \mathrm{Re}_D < 10^6$, the B-L becomes turbulent, and flow separation is delayed from angle $\theta_{\text{separation}}^{\text{laminar}} \approx 80^\circ$ to $\theta_{\text{separation}}^{\text{turbulent}} \approx 140^\circ$.
- At about $\mathrm{Re}_D = 2 \times 10^5$, $C_D(\mathrm{Re}_D)$ dips, that is, a sudden drag reduction leading to instabilities at high speeds or, on a positive note, longer travel distances of, say, dimpled golf balls.

Because of the flow field complexities around submerged bodies, analytical solutions are not available. A famous exception is Stokes' equation for flow around a sphere when $\mathrm{Re}_D \leq 1.0$, as discussed in Panton (2013) and its derivation assigned in Section 3.4.2.

$$F_{\text{total}} = \underbrace{\int_A \tau_w \, dA}_{\substack{\text{frictional} \\ \text{drag}}} + \underbrace{\int_A p \, dA}_{\text{form drag}} = 4\pi\mu UR + 2\pi\mu UR = 6\pi\mu UR \tag{3.76}$$

where:

$U$ is the free-stream velocity
$R$ is the sphere's radius

*Equation 3.76 will be frequently applied in Section 4.3.1.*

Curve-fitted correlations (see Figure 3.7b) have been proposed for a wide range of Reynolds numbers. For example, for a sphere up to the "drag crisis" of $\mathrm{Re}_D \approx 2 \times 10^5$,

$$C_{D,\text{sphere}} \equiv \frac{F_{\text{total}}}{\frac{\rho}{2} U^2 A_{\text{proj}}} = \frac{24}{\mathrm{Re}_D} + \frac{6}{1 + \sqrt{\mathrm{Re}_D}} + 0.4 \tag{3.77a,b}$$

In contrast, a simple drag coefficient for a cylinder in laminar cross flow reads (White, 1974):

$$C_{D,\text{cylinder}} \approx 1 + \frac{10}{\text{Re}_D^{2/3}} \tag{3.78}$$

**Example 3.11: Commercial Passenger Jet**

Consider a cruising airplane ($m = 70 \times 10^3$ kg, $A_p = 150$ m$^2$, $v = 350$ mph) at 12 km altitude ($\rho_{air} = 0.312$ kg/m$^3$). What are the necessary angle of attack, lift-to-drag ratio, and engine power requirement to maintain the cruising speed? How would you estimate the minimum take-off velocity?

*Note:* For modern aircraft, $C_{L,\max} = 3.5$ <double-flapped wings> and $C_{D,\text{cruising}} \approx 0.03$.

| Sketch 13 | Assumptions | Method |
|---|---|---|
| 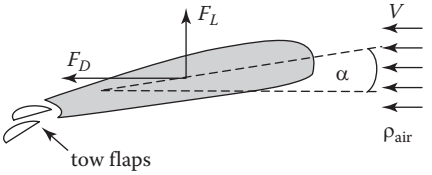 | • Only the wings generate $F_D$ and $F_L$<br>• Steady (2-D) incompressible flow | • 1-D force balance<br>• Power = $F_D \cdot v$<br>• Use of lift/drag coefficients |

*Solution:*

- Force coefficients:

$$C_i = \frac{F_i}{\frac{\rho}{2} v^2 A_p}; \; i = L \text{ or } D \tag{E.3.11.1}$$

- Force balance:

$$F_{\text{weight}} = F_{\text{lift}} \tag{E.3.11.2}$$

- Power:

$$P = F_{\text{drag}} \times \text{velocity} \tag{E.3.11.3}$$

- Angle of attack: $C_L = C_L(\alpha)$, knowing that

$$C_L = \frac{F_L}{\frac{\rho}{2} v^2 A_p} \tag{E.3.11.4}$$

With $F_L = W = m \cdot g = 686.7$ kN in this case, as well as the conversion $1 \text{ mph} \triangleq 0.447 \text{ m/s}$ and $A_p = 150$ m$^2$, we have $C_L = 1.20$. Hence, from Figure 3.8a (or a handbook), $\alpha \approx 10°$.
Furthermore,

- Lift-to-drag ratio and power requirement:

$$P = F_D \cdot v \text{ where } F_D = C_D \, A_p \frac{\rho}{2} v^2 := 17.2 \text{ kN} \tag{E.3.11.5a through c}$$

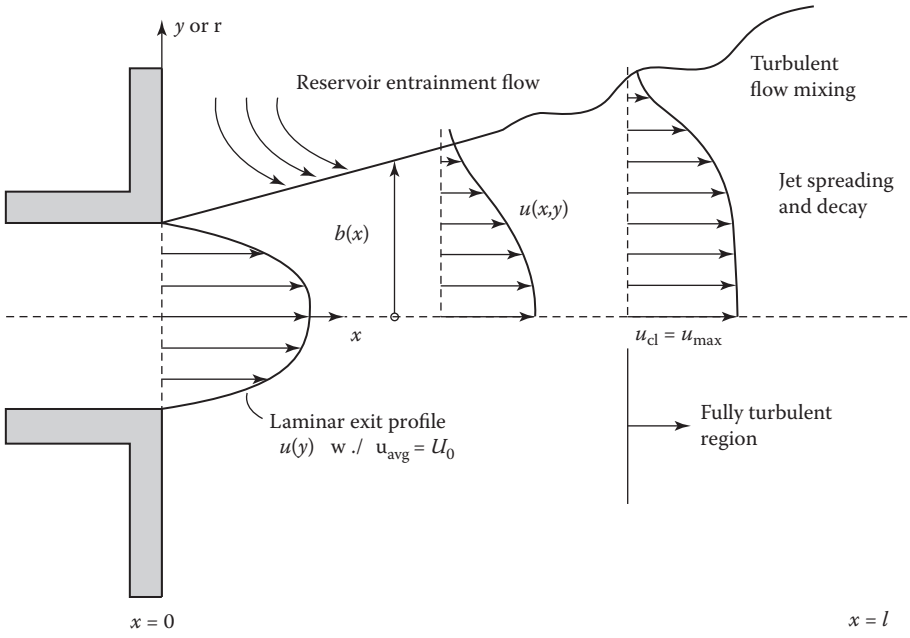


**FIGURE 3.8**
Half-jet development and flow regions.

Thus,

$$\kappa = \frac{F_L}{F_D} \approx 40 \qquad \text{and} \qquad P = 2620\,\text{kW} \tag{E.3.11.6a, b}$$

- Minimum take-off speed $v_{\min}$=*fct.*($C_L$,max):
  Take-off requires $F_L\big|_{\max} \geq W$, that is,

$$C_{L,\max}\ A_p\ \frac{\rho}{2}\ v_{\min}^2 \geq\ mg \equiv W_{\text{plane}} \tag{E.3.11.7a through c}$$

or

$$v_{\min} \geq \sqrt{\frac{2\ mg}{\rho\ C_{L,\max}\ A_p}} := 46.8\ \text{m/s}$$

*Comment:*

Clearly, a take-off speed exceeding $v_{\min}$, say, $v = 150$ mph may be safer.

### 3.2.4 Steady Planar and Round Jets

Free jets are distinct, relatively fast streams of a fluid or fluid-particle mixture, emanating from a nozzle and dispersing into a reservoir of the same or a different fluid, or into a vacuum. They appear ubiquitously in nature and industrial applications, ranging from ink-jet printers to fuel-injection pumps and spray-coating devices. The stream-ejector is either a simple pipe-end or a controllable nozzle. While for a basic analysis, it is assumed

that the jet is steady, laminar, planar 2-D, or round; however, in reality turbulence rapidly develops—first in the high-stress regions around the jet-edges away from the exit plane and then in the entire jet (see Figure 3.8). *Turbulent* jets are discussed in Pope (2011), Bogey and Bailly (2010), and many others.

Assuming steady laminar incompressible jets evolving at constant pressure in a boundless environment, the present analysis relates to the fundamentals of B-L theory and the similarity method (see Section 3.2.1). Specifically, with $\partial p/\partial x = 0$, Prandtl's $x$-momentum equation can be written in the form

$$\frac{\partial u^2}{\partial x} + \frac{\partial (uv)}{\partial y} - \underbrace{u\left(\frac{\partial u}{\partial x} + \frac{\partial v}{\partial y}\right)}_{\equiv 0} = \nu \frac{\partial^2 u}{\partial y^2} \tag{3.79}$$

Integrating each term from $y = -\infty$ to $y = \infty$ for any axial location $x$ yields with the Leibniz rule

$$\frac{\partial}{\partial x}\int_{-\infty}^{\infty} u^2\, dy + uv\int_{-\infty}^{\infty} \frac{\partial}{\partial y} dy = \nu \frac{\partial u}{\partial y}\int_{-\infty}^{\infty} \frac{\partial u}{\partial y} dy \tag{3.80}$$

Noting that $u(y = \pm\infty) = 0$ and $\left.\frac{\partial u}{\partial y}\right|_{y=\pm\infty} = 0$, we obtain

$$\frac{\partial}{\partial x}\int_{-\infty}^{\infty} u^2\, dy = 0 \tag{3.81}$$

Hence,

$$\int_{-\infty}^{\infty} u^2\, dy = \text{constant} \tag{3.82}$$

Multiplying Equation 3.82 by the fluid density, ρ, yields the (constant) $x$-momentum flux $J_g$:

$$J_g = \rho \int_{-\infty}^{\infty} u^2\, dy = \text{constant} \tag{3.83}$$

At the exit ($x = 0$) with average injection velocity $U_0$ and slit height $H$,

$$J = J_0 = \rho U_0^2 H \tag{3.84}$$

Now, of interest are the jet velocity field ($u$, $u_L \equiv u_{\max,}$ and $_v$), the spreading ($b(x)$), the mass flow rate $\left(\dot{m}(x)\right)$, and the momentum flux ($J(Re)$). As mentioned, the starting point for the mathematical analysis are the steady, 2-D laminar B-L equations:

$$\frac{\partial u}{\partial x} + \frac{\partial v}{\partial y} = 0 \tag{3.85}$$

and

$$u\frac{\partial u}{\partial x}+v\frac{\partial u}{\partial y}=\nu\frac{\partial^2 u}{\partial y^2} \tag{3.86}$$

subject to

$$u\left(y=\pm\infty\right)=0,\ \left.\frac{\partial u}{\partial y}\right|_{y=0}=0\ \ v\left(0\right)=0 \tag{3.87a, b}$$

As the developing axial velocity profiles are similar, we postulate

$$\psi=C_1x^p f\left(\eta\right) \tag{3.88}$$

$$\eta=C_2yx^{-q} \tag{3.89}$$

where $x^q$ indicates the scale of the jet thickness $b(x)$. To determine the four unknown constants, $p$, $q$, $C_1$, and $C_2$, we proceed as follows. Using the stream function and considering momentum flux, $J_g$, $p$, and $q$ can be determined.

$$u=\frac{\partial\psi}{\partial\eta}=C_1x^p f'\left(\eta\right)\frac{\partial\eta}{\partial y} \tag{3.90}$$

Also, from $\partial\eta/\partial y=C_2x^{-q}$,

$$dy=\frac{x^q d\eta}{C_2} \tag{3.91}$$

Applying Equations 3.90 and 3.91 into the momentum flux equation yields

$$J=\rho\int_{-\infty}^{+\infty}u^2\,dy=\rho C_1^2C_2^2\int_{-\infty}^{+\infty}x^{2p-2q}f'^2\left(\eta\right)\frac{x^q}{C_2}d\eta=\text{constant}\times x^{2p-q}\int_{-\infty}^{+\infty}f'^2\left(\eta\right)d\eta \tag{3.92}$$

In this equation, $f'(\eta)$ is only a function of $\eta$ and hence, not a function of $x$. Thus, we obtain the relation for $p$ and $q$ as

$$x^{2p-q}=\text{constant}$$

or

$$2p-q=0 \tag{3.93}$$

To find a second equation for $p$ and $q$, we consider the $x$-momentum Equation 3.86:

$$u\frac{\partial u}{\partial x}+v\frac{\partial u}{\partial y}=\nu\frac{\partial^2 u}{\partial y^2}$$

where

$$v=-\frac{\partial\psi}{\partial x}=-C_1px^{p-1}f\left(\eta\right)-C_1x^p\frac{\partial f}{\partial x} \tag{3.94}$$

and

$$\frac{\partial f}{\partial x} = \frac{\partial f}{\partial \eta}\frac{\partial \eta}{\partial x} = qf'\, C_2 y x^{-q-1} \tag{3.95}$$

Using the expression for $\partial f/\partial x$, Equation 3.94 now reads:

$$v = -C_1 p x^{p-1} f + C_1 C_2 q y x^{p-q-1} f' \tag{3.96}$$

and hence, the $x$-momentum equation can be converted to

$$C_1^2 C_2^2 \left(p-q\right) x^{2p-2q-1} f'^2 - C_1^2 C_2^2 p x^{2p-2q-1} f f'' = \nu C_1 C_2^3 x^{p-3q} f''' \tag{3.97}$$

To achieve similarity, the $x$-dependence has to vanish; that is, we have to set the exponents of $x$ equal. As a result,

$$2p - 2q - 1 = p - 3q$$

or

$$p + q = 1 \tag{3.98}$$

Combining Equations 3.93 and 3.98 yields

$$p = \frac{1}{3} \qquad \text{and} \qquad q = \frac{2}{3} \tag{3.99a, b}$$

Now, the stream function and $\eta$ can be written as

$$\psi = C_1 x^{1/3} f\left(\eta\right) \tag{3.100}$$

and

$$\eta = C_2 y x^{-2/3} \tag{3.101}$$

Inserting in Equation 3.97 the $p$ and $q$ values and dividing through by $C_1$ and $C_2^2$ yields

$$-\frac{1}{3} C_1 \left(f'\left(\eta\right)\right)^2 - \frac{1}{3} C_1 f f'' = \nu C_2 f''' \tag{3.102}$$

where $C_1$ and $C_2$ are arbitrary constants. Dimensional homogeneity requires that

$$\frac{1}{3} C_1 = \nu C_2 \tag{3.103}$$

That is,

$$\psi = C_1 x^{\frac{1}{3}} f\left(\eta\right) \tag{3.104a}$$

$$\text{where} \quad [\psi] = \left[\frac{L^2}{t}\right] \left(\therefore \psi \sim udy\right) \tag{3.104b}$$

so that

$$C_1 = \left[L^{5/3}/t\right]$$

And hence, with $[\nu] = \left[L^2/t\right]$

$$C_2 = \frac{1}{3\nu} C_1 = \frac{1}{3} \frac{1}{\nu^{1/2}}$$

which implies that

$$[C_2] = \left[L^{-1/3}\right]$$

Finally,

$$C_1 = \nu^{1/2}, \ \left[L^{5/3}/t\right] \tag{3.105}$$

and

$$C_2 = \frac{1}{3}\nu^{-1/2}, \ \left[L^{-1/3}\right] \tag{3.106}$$

The resulting ODE for this jet problem can be written as

$$f'^2 + ff'' + f''' = 0 \tag{3.107}$$

Now,

$$\psi = \nu^{-1/2} x^{1/3} f(\eta) \tag{3.108}$$

and

$$\eta = \frac{1}{3}\nu^{-1/2} x^{-2/3} y \tag{3.109}$$

The boundary conditions are symmetry about the *x*-axis and a quiescent ambient fluid. This translates for the similarity variables to

$$f(0) = f''(0) = 0 \tag{3.110a}$$

and

$$f'(\infty) = 0 \tag{3.110b}$$

#### 3.2.4.1 Exact Solution

A suitable trial profile matching the axial jet-velocities is in dimensionless form (Schlichting and Gersten, 2014):

$$f(\eta) = 2a \tanh(a\eta) \tag{3.111}$$

so that

$$f'(\eta) = 2a^2 \operatorname{sech}_2(a\eta) \tag{3.112}$$

The solution for the axial velocity then reads:

$$u = \frac{\partial \psi}{\partial y} = C_1 C_2 x^{p-q} f'(\eta) = \frac{1}{3x^{1/3}} f'(\eta) = \frac{2}{3}\left(\frac{a^2}{x^{1/3}}\right)\operatorname{sech}^2(a\eta) \tag{3.113}$$

The coefficient $a$ can be obtained by using the momentum flux, $J$.

$$J = const. = \rho \int_{-\infty}^{+\infty} u^2 dy = \frac{4\rho\nu^{1/2}a^3}{3} \int_{-\infty}^{+\infty} \operatorname{sech}^4(a\eta)\, d(a\eta) \tag{3.114}$$

so that with $J = J_0 = \rho U_0^2 H$,

$$a = \left(\frac{9J_0}{16\rho\sqrt{\nu}}\right)^{\frac{1}{3}} \tag{3.115}$$

Using this expression for $a$ together with Equations 3.109 and 3.113, the axial velocity in the jet is

$$u = \frac{2}{3}\left(\frac{9J_0}{16\rho\sqrt{\nu}}\right)^{\frac{2}{3}} \frac{1}{x^{1/3}} \operatorname{sech}^2\left[\left(\frac{9J_0}{16\rho\sqrt{\nu}}\right)^{\frac{1}{3}} \frac{y}{3\nu^{1/2}x^{2/3}}\right] \tag{3.116}$$

At the centerline, $y = \eta = 0$ and $\operatorname{sech}(0) = 1$, so that the maximum $x$-velocity is

$$u_{\max} = \frac{2}{3}\left(\frac{9}{16}\right)^{2/3}\left(\frac{J_0^{2/3}}{(\rho\mu x)^{1/3}}\right) \tag{3.117}$$

The jet thickness, $2b(x)$, can then be defined as twice the distance $y$ where $u = 0.01u_{\max}$. Noting that

$$\left.\frac{u}{u_{\max}}\right|_{\text{boundary}} = \operatorname{sech}^2\left[\left(\frac{9J_0}{16\rho\sqrt{\nu}}\right)^{\frac{1}{3}} \frac{b(x)}{3\nu^{1/2}x^{2/3}}\right] = 0.01, \tag{3.118}$$

the boundary of the jet can be written as

$$\text{Jet boundary} = 2b(x) = 2y\big|_{1\%} = 21.8\left(\frac{x^2\mu^2}{J_0\rho}\right)^{1/3} \tag{3.119}$$

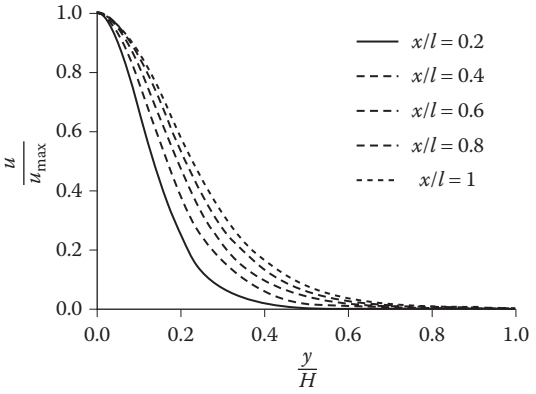


**FIGURE 3.9**
Velocity profiles for axisymmetric jet.

in the laminar, self-similar region $b \sim x^{\frac{2}{3}}$. Considering the Reynolds number based on the half-boundary of the jet, the Reynolds number is described as

$$\mathrm{Re} = \frac{u_{\max} b}{\nu} \sim x^{-1/3} x^{2/3} \sim x^{1/3} \tag{3.120}$$

Mass flow rate per unit width away from the jet exit can be written as

$$\dot{m} = \int_{-\infty}^{+\infty} \rho u \, dy = \left(36 J_0 \rho x\right)^{1/3} \sim x^{1/3} \tag{3.121}$$

Due to fluid entrainment from the ambient, the mass flow rate increases with $x$. This implies that a larger momentum flux can entrain more ambient fluid from the reservoir. The non-dimensionalized jet velocity profiles at various $x$-locations are shown in Figure 3.9.

## 3.3 Turbulent Flows

When a critical (flat-plate) Reynolds number of about $\mathrm{Re}_L = 5 \times 10^5$ has been reached, the B-L flow becomes fully turbulent after undergoing transition, as indicated in Figure 3.5. In contrast, for flow in straight smooth pipes, the flow field may become turbulent when the inlet Reynolds number exceeds 2000, based on the tube diameter. Because of the very high wall shear stresses, fully developed turbulent velocity profiles look quite different from laminar velocity distributions. For example, in laminar flow, the axial velocity follows $u \sim y^2$ (or $v_z \sim r^2$ in pipe flow), whereas for turbulent flow, $u \sim \ln y^+$ (the log law) or $v_z \sim r^{1/n}$, with $n = n(\mathrm{Re}_D)$, as tabulated in Appendix AI.7.3.2.

The traditional approach for tackling turbulent flow problems is the numerical solution of the *Reynolds-averaged Navier–Stokes* (*RANS*) equations. Such turbulence modeling is necessary because present computational resources are insufficient to solve the actual (i.e., instantaneous) variables directly. So, the *instantaneous* dependent variables,

here $v$ representing pressure, velocity, temperature, and so on, are decomposed according to Reynolds as

$$v = \overline{v} + v' \; ; \qquad \overline{v} = \frac{1}{\Delta t}\int_{t_1}^{t_2} v \; dt \tag{3.122a, b}$$

where:

$\overline{v}$ is the time-averaged (i.e., smoothed) variable
$v'$ is the randomly fluctuating part

This time-smoothing (or filtering) procedure applied to the N-S equations (see Section 2.3.2 and Appendix AI.5) generates *apparent (or Reynolds) stresses*, $-\rho\,\overline{\vec{\mathbf{v}}'\vec{\mathbf{v}}'}$, caused by the 3-D velocity fluctuations $\vec{\mathbf{v}}' = (u', v', w')$. Clearly, the off-diagonal entries of the $\overline{\vec{\mathbf{v}}'\vec{\mathbf{v}}'}$ tensor (see Appendix AI.1.2 for the dyadic product) may cause large (turbulent) shear stresses. The sum of the diagonal, using the Einstein convention of repeated indices, is called the *turbulence kinetic energy*:

$$\frac{1}{2}\left(\overline{u'^2} + \overline{v'^2} + \overline{w'^2}\right) \equiv k = \frac{1}{2}\,\overline{v_i' v_i'} \tag{3.123a, b}$$

The RANS equations then read in index notation (with the Einstein convention of term-summation with repeated indices):

$$\frac{\partial \overline{v}_i}{\partial x_i} = 0 \tag{3.124}$$

and

$$\frac{\partial \overline{v}_i}{\partial t} + \overline{v}_j \frac{\partial \overline{v}_i}{\partial x_j} = -\frac{1}{\rho}\frac{\partial \overline{p}}{\partial x_i} + \underbrace{\nu \frac{\partial^2 \overline{v}_i}{\partial x_j\, \partial x_j}}_{\sim \nabla\cdot\tau_{ij}^{\text{lam}}} - \underbrace{\frac{\partial}{\partial x_j}\left(\overline{v_i' v_j'}\right)}_{\sim \nabla\cdot\tau_{ij}^{\text{turb}}} \tag{3.125}$$

The new (unknown) stress tensor $\tau_{ij}^{\text{turb}} = -\,\rho\,\overline{v_i'\, v_j'}$ is expressed, following Boussinesq's idea, as

$$\frac{\tau_{ij}^{\text{turb}}}{\rho} = \nu_{\text{turb}} \frac{\partial \overline{v}_i}{\partial x_j} \tag{3.126}$$

The *turbulent eddy viscosity* $\nu_t$ is a complex function of the turbulence kinetic energy, turbulence energy dissipation, turbulence time and length scales, velocity gradients, flow-system geometry, fluid viscosity, and so on. Starting with Boussinesq (1877) and Kolmogorov (1942), numerous $\nu_t$-models have been postulated (see Wilcox, 2006; Pope, 2011; Libby, 1996, among others), each only applicable to a rather small class of (fully) turbulent flows. For example,

$$\nu_{\text{turbulence}} \sim \begin{cases} l_{\text{mix}}^2 \left|\dfrac{d\overline{u}}{dy}\right|; \; l_{\text{mix}} = \kappa y \\ k-\omega; \quad k = 1/2\,\Sigma(v_i')^2, \; \omega = \varepsilon/k \\ \text{Large Eddy Simulation (LES)} \end{cases} \tag{3.127a through d}$$

The simplest eddy-viscosity model is Prandtl's mixing-length hypothesis, in which the size-change of the interacting eddies, as measured from the wall, is $l_{\text{mix}} = ky$, with $k = 0.41$ being the von Karman constant. Quite popular is the $k$-ω turbulence model, where in addition to the RANS equations, PDEs for turbulence kinetic energy $k$ and dissipation function ε have to be solved iteratively to gain a suitable $\nu_t$- expression (see Wilcox, 2006). In large eddy simulation (LES), the large eddies are simulated directly, but a suitable turbulence model is required for the small, near-wall eddies. While the future belongs to direct numerical simulation (DNS), whereby the N-S equations are solved without any turbulence modeling, DNS still cannot be used for actual turbulent flow problem solutions, because it requires numerical time and mesh-length scales smaller than the eddies appearing in a given turbulent flow field.

In any case, engineers have always found a way to bypass tasks that are mathematically or numerically difficult—as is the case in turbulence modeling. One simple approach is to forego the solution of the RANS equations and directly *postulate turbulent velocity profiles* for B-L flow (see Section 3.3.1) or pipe flow (see Section 3.3.2). Even easier and more powerful is the use of the *extended Bernoulli equation* to solve *steady, fully developed turbulent flow in horizontal pipes*:

$$\frac{\Delta p}{\rho g} = h_f = \frac{4\tau_{\text{wall}}}{\rho g}\left(\frac{L}{D}\right) = f\left(\frac{L}{D}\right)\frac{v^2}{2g} \qquad \text{(3.128a through c)}$$

where:

$h_f$ is the frictional loss (in meters), while the Darcy friction factor $f = f(\text{Re}_D, \varepsilon/D)$ encapsulates turbulence effects in pipes with surface roughness ε (see Moody Chart in Appendix II)

To illuminate Equation 3.128b, a 1-D force balance for pipe flow relates pressure drop to wall stress (see HWA in Section 3.4):

$$\Delta p\big|_{\max} = \frac{2}{r_0}\tau_{\text{wall}} L \qquad (3.129)$$

Hence, the friction factor in horizontal pipes with $D = 2r_0$ reads:

$$f = \frac{8\tau_w}{\rho v^2} \qquad (3.130)$$

In terms of the "friction velocity," defined as

$$u_\tau = \sqrt{\frac{\tau_w}{\rho}} \qquad (3.131)$$

we can express $f$ as

$$f = 8\left(\frac{u_\tau}{v}\right)^2 \qquad (3.132)$$

### 3.3.1 External Flows

As mentioned in Section 3.2, turbulent flow past submerged bodies is traditionally modeled based on B-L theory, that is, interactions between potential flow outside the boundary layer and the thin-shear layer. Specifically, a solution to Euler's equation for the assumed outer ideal flow yields the pressure field that is imposed on the thin-shear layer described by Prandtl's B-L equations. However, present-day use of software and workstations allows direct solutions of the RANS equations with suitable turbulence models (Pope, 2011). Alternatively, turbulent velocity profiles, representing the thin-shear layers for different conditions, are discussed and applied in subsequent examples.

#### *3.3.1.1 Boundary-Layer Velocity Profiles*

Clearly, postulating semi-empirical turbulent velocity profiles directly bypasses any solution of the RANS equations. The one-seventh law $\bar{u}/U = (y/\delta)^{1/7}$ (see Example 3.12) is a very popular one. More accurate is a "composite profile," consisting of the (linear) laminar sublayer and the log law, for which the *inner variables* $u^+ \equiv \bar{u}/u_\tau$ and $y^+ \equiv yu_\tau/v$ are employed (see Figure 3.10). Here, $u_\tau = \sqrt{\tau_{\text{wall}}/\rho}$ is the "friction velocity," while $y^+$ represents a "wall Reynolds number."

In the *viscous sublayer*, the velocity profile at the wall is linear:

$$u^+ = y^+ \text{ for } 0 \le y^+ \le 5 \tag{3.133a}$$

The *log law* describing the "overlap layer" reads:

$$u^+ = \frac{1}{\kappa} \ln y^+ + B \quad \text{for} \quad 20 \text{ to } 30 \le y^+ = 500 \tag{3.133b}$$

Where based on measurements, $\kappa = 0.41$ and $B = 5.0$. There is a buffer region $5 < y^+ < 30$ where another log law may be needed:

$$u^+ = 5.0 \ln y^+ - 3.0 \tag{3.133c}$$

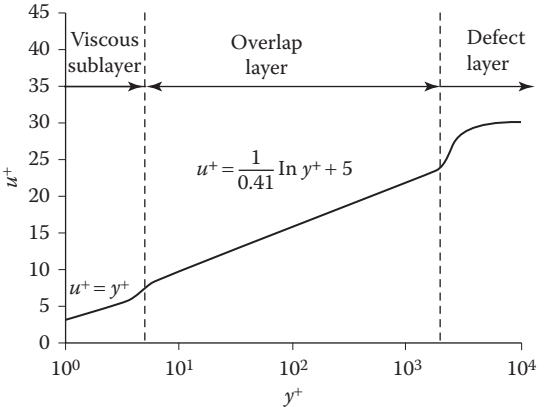


**FIGURE 3.10**
Semi-log plot of a composite velocity profile for turbulent boundary-layer flow.

Finally, the *wake (or defect) layer* has also the natural-log form:

$$u^+ = \frac{1}{\kappa}\ln y^+ + C + \frac{2\Pi}{\kappa}\sin^2\left(\frac{\pi}{2}\frac{y}{\delta}\right) \tag{3.133d}$$

where:

$k = 0.41$
$C = 5-8$
$\Pi \approx 0.6$

It is of interest to note the percentage fractions of the three "layers" in relation to the B-L thickness $\delta(x)$. For example, with $y^+_{\text{sublayer}} = 20$, $y^+_{\log} = 500$, $y^+_{\text{core}} = 6200$, and hence, with $\delta^+_{\text{sublayer}} \approx 20$, $\delta^+_{\log} = 500$, and $\delta^+_{\text{core}} = 5700$, the extents of the three regions are as follows:

- 0.3% occupy the viscous sublayer
- 7.7% are part of the log-buffer zone
- 92% constitute the turbulent core

Clearly, for some calculations, it is sufficient to only employ the log law. In general, basic turbulent velocity profiles covering the entire B-L can be efficiently used with the *integral method* (Section 3.2.1 or Appendix AI.3.4), as illustrated in Example 3.12.

**Example 3.12: Steady Turbulent Boundary-Layer Flow past a Flat Plate with $u_\infty = U =$ constant**

For this Blasius-flow problem, we assume $\dfrac{\bar{u}}{U} = \left[\dfrac{y}{\delta}\right]^{1/n}$ with measured $\tau_w = \dfrac{f}{8}\left(\rho v^2\right)$, where:

$$v = \bar{u}_{\text{avg}}$$

$\mathcal{O}$the friction factor is $f \approx 0.3164\,\text{Re}_\delta^{-1/4}$ (Blasius) with $\text{Re}_\delta = v(2\delta)/\nu = \mathcal{O}(10^7)$

Find $v(n, U)$ and hence $\tau_w$, as well as $\delta/x$ for $5\times10^8 \le \text{Re} \le 10^8$. Determine also the skin-friction coefficient.

| Sketch 14 | Assumptions | Method |
|---|---|---|
| 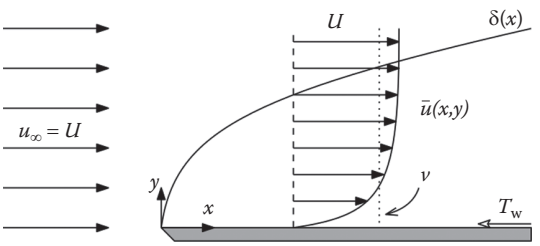 | • As stated in Example 3.12<br>• Laminar B-L portion is negligible | • Use integral method<br>• Solve ODE for $\delta(x)$ |



*Solution:*

The averaged axial velocity is

$$v = \frac{1}{A}\int_A \bar{u}\left(y, \delta; U, n\right) dA \tag{E.3.12.1}$$

With $\eta = y/\delta(x)$ and $dA = w dy = w\delta d\eta$; $A = w\delta$, the averaged velocity can be expressed as

$$v = \frac{U}{w\delta}\int_0^1 \eta^{1/n}\delta w\, dy = U\int_0^1 \eta^{1/n}\, d\eta = \frac{U}{1+1/n}\eta^{1/n+1}\Big|_0^1 = \frac{nU}{n+1} \tag{E.3.12.2}$$

We derived (see Equation 3.55) for $u_\infty = U = \text{constant}$ that

$$\frac{\partial}{\partial x}\int_0^\delta \left[\bar{u}(U-\bar{u})\right] dy = \frac{\tau_w}{\rho} \tag{E.3.12.3}$$

Here, after inserting the given $f$ and $\text{Re}_\delta$,

$$\tau_w = 0.03325\rho v^{7/4}\left(\frac{\nu}{\delta}\right)^{1/4} \tag{E.3.12.4}$$

The LHS of Equation E.3.12.3 can be rewritten as

$$U^2\frac{\partial}{\partial x}\int_0^\delta\left[\frac{\bar{u}}{U}-\left(\frac{\bar{u}}{U}\right)^2\right]dy = U^2\frac{\partial}{\partial x}\left\{\int_0^1\left[\frac{\bar{u}}{U}\left(1-\frac{\bar{u}}{U}\right)\right]d\left(\frac{y}{\delta}\right)\right\} \tag{E.3.12.5}$$

Using $n = 7$ and with $y/\delta = \eta$, we have to solve

$$\frac{d}{dx}\left[\delta(x)\int_0^1 \eta^{1/7}\left(1-\eta^{1/7}\right)d\eta\right] = \frac{\tau_w}{\rho U^2} = 0.03325\left(\frac{\nu}{U\delta}\right)^{1/4} \tag{E.3.12.6}$$

Integration yields an ODE for $\delta(x)$:

$$\delta^{1/4}\frac{d\delta}{dx} = 0.24\left(\frac{\nu}{U}\right)^{1/4} \quad \text{subject to} \quad \delta(x=0) = 0 \tag{E.3.12.7}$$

Hence,

$$\delta = 0.38\left(\frac{\nu}{U}\right)^{1/5}x^{4/5} \tag{E.3.12.8}$$

or

$$\frac{\delta}{x} = \frac{0.38}{\text{Re}_x^{1/5}} \tag{E.3.12.9}$$

Thus,

$$c_f(x) = \frac{\tau_w}{\frac{\rho}{2}U^2} = 0.0847v^{7/4}\,\text{Re}_x^{-1/5} \tag{E.3.12.10}$$

Recalling that $\delta_{\text{laminar}} \sim x^{1/2}$, while $\delta_{\text{turb}} \sim x^{4/5}$, the turbulent boundary-layer thickness grows, almost linearly, much faster than in the laminar case.

**Example 3.13: Drag of a Ship Based on Turbulent Boundary-Layer Flow Analysis**

Evaluate the B-L thicknesses above and below the waterline and the maximum frictional drag for a ship 50 m long and 10 m high) traveling at 15 mph. The kinematic viscosities are $v_{\text{air}} = 1.5\times10^{-5}$ m$^2$/s (at 20°C) and $v_{\text{water}} = 1.3\times10^{-6}$ m$^2$/s (at 10°C) for 5 m of ship surface below the waterline.

| Sketch 15 | Assumptions | Method |
|---|---|---|
| 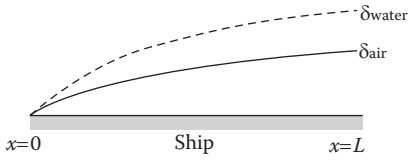 | • Fully turbulent flow for $0 \le x \le L$<br>• Constant pressure<br>• Straight ship walls | • Use of correlations for $\delta(x)$ and $C_F(x)$ |

*Solutions:*

From Section 3.3.1, for turbulent B-L flow in the range $5\times10^5 < \mathrm{Re}_x < 10^9$, we have

$$\frac{\delta(x)}{x} \approx 0.14\ \mathrm{Re}_x^{-1/7} \tag{E.3.13.1}$$

and

$$c_f(x) = \frac{\tau_w(x)}{\frac{\rho}{2}U^2} \approx 0.025\ \mathrm{Re}_x^{-1/7} \tag{E.3.13.2}$$

Here, $\mathrm{Re}_L\big|_{\min} = UL/\nu_{\text{air}} := 2.22\times10^7$, while $\mathrm{Re}_L\big|_{\text{water}} = 2.56\times10^8$ ; that is, both are turbulent B-L flows. Hence,

$$\delta(x=L) = \begin{cases} 0.625\ \text{m} & \text{for air} \\ 0.44\ \text{m} & \text{for water} \end{cases} \tag{E.3.13.3a, b}$$

Now, the drag force is

$$F_D = \int_0^L \tau_w(x)\, h\, dx \tag{E.3.13.4a}$$

or

$$\frac{F_D}{\frac{\rho}{2}U^2 Lh} = \int_0^L c_f(x)\, d\left(\frac{x}{L}\right) \approx 0.03\ \mathrm{Re}_L^{-1/7} \tag{E.3.13.4b}$$

$$\therefore \quad F_D = 0.03\ \mathrm{Re}_L^{-1/7}\frac{\rho}{2}U^2\ Lh := 2.1\times10^4\ \text{N} \tag{E.3.13.4c}$$

and hence

$$P_{\text{ship}} = F_D\ U\ 1.4\times10^5\ \text{N}\ \frac{\text{m}}{\text{s}} \ge 0.14\ \text{MW} \tag{E.3.13.5}$$

*Comment:*
Clearly, the *actual* power required to maintain a speed of 15 mph through calm seas is larger because the two-fluid form drags were not considered.

### 3.3.1.2 Summary of Modeling Results

Employing the integral method of Section 3.2.1 (or see Appendix AI.3.4), a turbulent B-L flow analysis based on a *logarithmic velocity profile* (see Equation 3.133b) can provide some good results within the range of $10^5 \leq \mathrm{Re}_x \leq 10^9$ (see HW Assignment in Section 3.4):

$$\frac{\delta(x)}{x} \approx 0.14\,\mathrm{Re}_x^{-\frac{1}{7}} \tag{3.134}$$

$$\tau_w \approx 0.0125\rho U^2\,\mathrm{Re}_x^{-\frac{1}{7}} \tag{3.135}$$

$$c_f \approx 0.025\,\mathrm{Re}_x^{-\frac{1}{7}} \tag{3.136}$$

$$F_D \approx 0.015\rho U^2 LW\ \mathrm{Re}_x^{-\frac{1}{7}} \tag{3.137}$$

and

$$c_D \approx 0.030\,\mathrm{Re}_x^{-\frac{1}{7}} \tag{3.138}$$

Compared with laminar B-L flow, in turbulent flat-plate B-L flow, $\delta(x)$ grows almost linearly rather than in a quadratic manner (see Equation 3.134 and Figure 3.5). As expected, the wall shear stress is much larger due to the steeper velocity gradients at the plate surface. The behavior of the skin-friction coefficient for flat-plate flow in the laminar-transitional-turbulent regimes is shown in Figure 3.11 for a restricted Reynolds number range. Clearly, industrial operations in the chaotic, highly nonlinear *transitional regime* should be avoided.

Other skin-friction correlations for turbulent flow past a flat plate (Wilcox, 2006) include

$$C_f = 0.0576\,\mathrm{Re}_x^{-1/5} \tag{3.139}$$

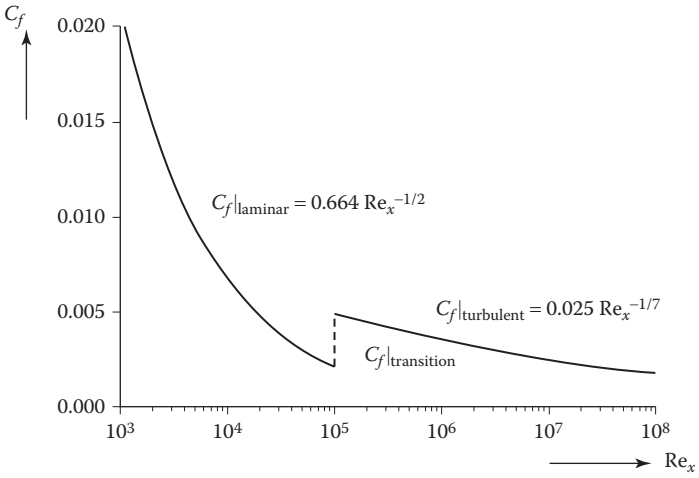


**FIGURE 3.11**
Flat-plate skin-friction coefficient $C_f(\mathrm{Re}_x)$.

and from White (2006)

$$C_f = \frac{0.455}{\left[\log_{10}\left(\mathrm{Re}_x\right)\right]^{2.58}} \tag{3.140}$$

For example, considering turbulent flow past a razor-like flat plate with zero pressure gradient, the form drag is negligible, and hence, the total drag on the plate of length $L$ and width $w$ is due only to viscous effects. Specifically,

$$F_{\text{drag}} = F_{\text{viscous}} = \int_0^L \tau_{\text{wall}}\left(x\right) dA; dA = wdx \tag{3.141}$$

or

$$F_D = \left(\frac{\rho}{2} u_\infty^2 Lw\right) \int_0^1 C_f\left(x\right) d\left(\frac{x}{L}\right) \tag{3.142}$$

When selecting for $C_f$ using Equation 3.138, we obtain

$$C_D = \frac{F_D}{\rho / 2 u_\infty^2 Lw} = 0.031 \mathrm{Re}_L^{-1/7} = \frac{7}{6} C_f\left(L\right) \tag{3.143a through c}$$

When using Equation 3.140, the result is

$$C_D = \frac{0.523}{[\ln\left(0.06\mathrm{Re}_L\right)]^2} \approx 1.15 C_f\left(L\right) \tag{3.144a, b}$$

### 3.3.2 Internal Flows

The B-L results of Section 3.3.1 can be directly related to internal turbulent flows. For example, we recall the following for turbulent pipe flow:

- Shear layers develop in the entrance region of length $L \approx 10D$, being shorter than in laminar pipe flow due to the rapid cross-mixing.
- Again, for fully developed flow, the velocity profile is rather blunt; that is, the average velocity is near (81.7%) the maximum flow at the center.
- Also, the shear-stress field is very much larger than in laminar flow.
- The Reynolds analogy holds for turbulent pipe flow as well.

Starting with semi-empirical (time-smoothed) velocity profiles for *turbulent pipe flow*, the convenient power law are frequently employed:

$$\frac{\overline{u}}{u_{\max}} = \left(1 - \frac{r}{R}\right)^{1/n} \qquad \text{and} \qquad \frac{\overline{u}}{u_\tau} = 8.74 \left(\frac{y u_\tau}{\nu}\right)^{1/n} \tag{3.145a, b}$$

where:
$R$ is the pipe radius
$n$ (typically 7) is a function of $\mathrm{Re}_D$ (see Appendix AI.7.3.2)
the friction velocity $u_\tau \equiv \sqrt{\tau_w / \rho}$
the wall coordinate $y = R - r$

While Equation 3.145a matches the BCs $u(r=R)=0$ and $u(r=0)=u_{max}$, its derivative at $r=0$ is *not* zero (see HWA in Section 3.4). Equation 3.145b can be rewritten in terms of inner variables $u^+$ and $y^+$, as introduced in Section 3.3.1. When using just Equation 3.145b, the viscous sublayer $u^+ = y^+$ is ignored, which is permissible, because the turbulent core covers 92% of the tubular cross section (see Section 3.3.1 and HWA in Section 3.4).

**Example 3.15: Fully Turbulent Flow Characteristics in a Smooth Pipe**

Water at 20°C flows through a horizontal pipe ($D=0.1$ m, $Q=4\times10^{-2}$ m$^3$/s) driven by $\Delta p/l = 2.59$ kPa/m. Of interest are the "laminar sublayer thickness" $\delta_s$; the ratio of centerline to average velocity; and, for radial position $r_p = 0.025$ m, the ratio of turbulent-to-laminar shear stresses, where $\tau_{laminar}$ is the laminar stress portion of the turbulent flow field at $r = r_p$.

**Sketch 16**

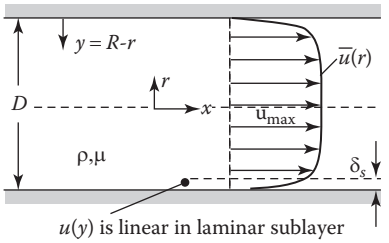


**Assumptions**

- Steady fully developed turbulent flow
- Smooth pipe
- Constant properties
- $\tau_{total} = \tau_{laminar} + \tau_{turbulent}$
- Extent of laminar sublayer is $0 \le y^+ \le 5$ (see Equation 3.133a)

**Method**

- Mass conservation $Q = \int_A \vec{\mathbf{v}} \cdot d\vec{\mathbf{A}} = u_{avg}\, A$
- A 1-D force balance on a C.∀. of $\pi R^2 \Delta x$ yields $\Delta p \approx 4\tau_{wall} l/D$
- Turbulent velocity profiles:

(i) Pipe flow: $\dfrac{\bar{u}}{u_{max}} = \left(1 - \dfrac{r}{R}\right)^{1/n}$ ; $n = n(\mathrm{Re})$

Here, we have $\mathrm{Re}_D = \dfrac{u_{avg} D}{\nu} = 5.07 \times 10^5$ and hence, $n = 8.4$ (see Appendix AI.7.3.2 or Schlichting and Gersten, 2014)

(ii) Pipe wall: $u^+ = y^+$ for $0 \le y^+ \le 5$ and friction velocity $u_\tau \equiv \sqrt{\tau_w / \rho}$

*Properties:* For water at 20°C, $\rho = 998$ kg/m$^3$, and $v = 10^{-6}$ m$^2$/s (see Appendix II).

*Solution:*
(a) Sublayer thickness $\delta_s$:

$$y^+(y=\delta_s) \equiv \frac{u_\tau \delta_s}{\nu} = 5.0 \qquad \text{(E.3.15.1)}$$

$$\therefore \qquad \delta_s = 5\nu\sqrt{\tau_w / \rho}\ ; \qquad \tau_w = \frac{D}{4}\left(\frac{\Delta p}{\ell}\right) \tag{E.3.15.2a, b}$$

Hence, numerically,

$$\tau_w = 64.8\ \mathrm{N/m^2} \qquad \text{and} \qquad u_\tau = 0.255\ \mathrm{m/s}$$

so that

$$\delta_s = 0.02\ \mathrm{mm}$$

(b) With $n \approx 8.4$ for $\mathrm{Re}_D = 5.07 \times 10^5$, we have

$$Q = v_{\mathrm{avg}}\left(\pi R^2\right) = v_{\max}\int_0^R \left(1 - \frac{r}{R}\right)^{1/8.4} \left(2\pi r dr\right) \tag{E.3.15.3a, b}$$

or

$$\frac{u_{\max}}{u_{\mathrm{avg}}} = \frac{R^2}{2}\left[\int_0^R \left(1 - \frac{r}{R}\right)^{1/8.4} r\ dr\right]^{-1} := 1.186 \tag{E.3.15.4}$$

while $u_{\max} = 6.04$ m/s.

(c) Anywhere in the pipe, we have

$$\tau_{rx} \equiv \tau_{\mathrm{total}} = \tau_{\mathrm{turb}} + \tau_{\mathrm{lam}} \tag{E.3.15.5}$$

A 1-D force balance (or the momentum RTT) for fully developed flow yields

$$\frac{\Delta p}{\ell} = \frac{2\tau_{rx}}{r} = \not\subset, \text{ or with } \tau\left(r = \frac{D}{2}\right) = \tau_{\mathrm{wall}} \tag{E.3.15.6a, b}$$

$$\tau_{\mathrm{total}} = \frac{2\tau_w}{D}\, r \tag{E.3.15.6c}$$

Numerically,

$$\tau_{\mathrm{total}}\left(r = r_p = 0.025\ \mathrm{m}\right) = 32.4\ \mathrm{N/m^2}$$

Recalling

$$\tau_{\mathrm{lam}} = \mu\frac{d\bar{u}}{dr} := \frac{\mu\, u_{\max}}{r\ R}\left(1 - \frac{r}{R}\right)^{\frac{1-n}{n}} \tag{E.3.15.7a, b}$$

We have numerically

$$\tau_{\mathrm{lam}}\left(r = r_p\right) = \left(\nu\rho\right)\left.\frac{d\bar{u}}{dr}\right|_{r=r_p} := 0.0266\,\mathrm{N/m^2} \tag{E.3.15.8}$$

Finally,

$$\kappa \equiv \frac{\tau_{\mathrm{turb}}}{\tau_{\mathrm{lam}}} = \frac{\tau_{\mathrm{total}} - \tau_{\mathrm{lam}}}{\tau_{\mathrm{lam}}} := 1220 \tag{E.3.15.9a through c}$$

*Comments:*

- The laminar sublayer, only 20 μm thick, exhibits a very steep velocity gradient and hence a very large wall shear stress.
- While $u_{max}/u_{avg} = 2.0$ for laminar flow because of the parabolic velocity profile, the ratio is only 1.186 for turbulent pipe flow.
- Midway between pipe centerline and wall, the turbulent shear-stress portion is an astonishing $1220 \times \tau_{laminar}$.

**Example 3.16: Log-Law Applications for Turbulent Couette Flow**

Consider two parallel plates with spacing h, upper-plate velocity $u_0$, and $\Delta p = 0$. Employing the standard log law, that is, Equation 3.133b, find the following, assuming that the turbulent shear-stress distribution is approximately equal to the wall shear stress:

1. Turbulent stress and eddy-viscosity expressions based on the Boussinesq and Prandtl postulates, respectively
2. Upper-plate velocity for water at 20°C with the measured data $h = 0.03$ m and $\tau_{wall} = 15$ Pa
3. Velocity profile $u(y)$

| Sketch 17 | Assumptions | Method |
|---|---|---|
| 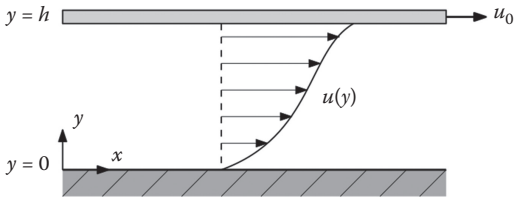 | • Steady 1-D flow<br>• No pressure gradient<br>• $T_{turb} \approx \tau_{wall}$ for $0 \le y \le h$<br>• Constant density | • Log law, that is, Equation 3.133b<br>• Boussinesq: $\tau_t = \nu_t \rho \frac{d\bar{u}}{dy}$<br>• Prandtl: $\nu_t = \rho \kappa^2 y^2 \left\lvert \frac{d\bar{u}}{dy} \right\rvert$ |

Solution:

Given $\frac{\bar{u}}{u_\tau} = \frac{1}{\kappa} \ln \frac{y u_\tau}{\nu} + B$ where $k = 0.41$ and $B = 5.0$, with Boussinesq's postulate is $\tau_t = v_t \rho (du/dy)$ and $du/dy = u_\tau / ky$, we have for the case where $\tau_t = \tau_w$

$$\tau_t = \nu_t \rho \frac{u_\tau}{\kappa y} \approx \tau_w = \rho u_\tau^2 \tag{E.3.16.1}$$

or

$$\nu_t = \kappa u_\tau y \tag{E.3.16.2}$$

With the Prandtl model, the Boussinesq hypothesis reads:

$$\tau_t = \left[ \rho \kappa^2 y^2 \left| \frac{du}{dy} \right| \right] \frac{du}{dy} \tag{E.3.16.3}$$

where $\kappa y = l_m$ is the eddy mixing length. Again, $\tau_t \approx \tau_w = \rho u_\tau^2 = \nu_t \rho \, du/dy$, where $du/dy = u_\tau / \kappa y$. Substitution yields

$$\rho u_\tau^2 = \left[\rho \kappa^2 y^2 \frac{u_\tau}{\kappa y}\right]\frac{du}{dy} \tag{E.3.16.4}$$

or

$$u_\tau = \kappa y \frac{du}{dy} \tag{E.3.16.5}$$

Now, we can integrate

$$\int du = \frac{u_\tau}{\kappa}\int \frac{dy}{y} \tag{E.3.16.6}$$

resulting in another log-law expression:

$$u = \bar{u} = \frac{u_\tau}{\kappa}\ln y + C_1 \tag{E.3.16.7}$$

With $\bar{u}(y = 0.5h) = u_{\max} = u_0/2$ due to symmetry, we can rewrite Equation 3.133b as

$$\frac{u_0}{2u_\tau} = \frac{1}{\kappa}\ln\left(\frac{hu_\tau}{2\nu}\right) + B; \quad B = 5 \text{ and } \kappa = 0.41 \tag{E.3.16.8}$$

With the numerical values,

$$u_\tau = \sqrt{\tau_w/\rho} = \sqrt{15/998} = 0.123 \text{ m/s} \tag{E.3.16.9a}$$

$$u_0 = \frac{2u_\tau}{\kappa}\ln\left(\frac{hu_\tau}{2\nu}\right) + 2u_\tau B = 5.72 \text{ m/s} \tag{E.3.16.9b}$$

Note that

$$\text{Re}_h = \frac{0.5u_0 h}{\nu} = 85{,}628 \tag{E.3.16.10}$$

*Comments:*

- The assumption that $\tau_t = \tau_w$ in the entire gap distorts the results, implying a quasi-linear velocity profile.
- Nevertheless, the numerical values for the very different velocities are of interest.

### *3.3.2.1 Turbulent Convection Heat Transfer*

In most industrial applications, turbulent pipe flow is non-isothermal; that is, heat conduction and forced convection have to be considered as well. Again, what has been learned from thermal turbulent B-L flow can be adopted for internal flow analysis. Specifically, of major interest are the transport phenomena occurring at the wall, that is, wall friction and wall heat transfer. So, we can normalize the two wall fluxes for fully developed thermal flow with fluids at Prandtl number, $\text{Pr} = \nu/\alpha$, of unity when momentum and heat transfer are the same. This implies that the wall gradients of the dimensionless velocity and temperature are identical; thus, the Reynolds analogy reads:

$$C_f \ \mathrm{Re} \sim Nu \ \text{ or } \ C_f \sim Nu/(\mathrm{Re}\ \mathrm{Pr}) = St(\text{Stanton number}) \tag{3.146a, b}$$

where $C_f$ is known as the *friction coefficient* (or the Fanning friction factor). Much more frequently used is the Darcy friction factor $f = 4C_f$, defined as

$$f \equiv \frac{8\tau_{\text{wall}}}{\rho u_m^2} = \frac{2(\Delta p/L)D}{\rho u_m^2} \tag{3.147a, b}$$

where:

| | |
|---|---|
| $\Delta p/L$ | is the constant pressure gradient |
| $D$ | is the tube diameter |
| $\rho$ | is the fluid density |
| $u_m$ | is the mean (or average) velocity |

Clearly, for Poiseuille flow,

$$f_{\text{laminar}} = \frac{64}{\mathrm{Re}_D} \tag{3.148}$$

However, for turbulent pipe flow, semi-equational correlations are necessary (see also Moody chart in Appendix II). For example, Petukhov and Zhilin (1970) suggested

$$f_{\text{turbulent}} = (0.79 \ln \mathrm{Re}_D - 1.64)^{-2} \tag{3.149}$$

covering the range $3000 < \mathrm{Re} < 5 \times 10^6$. Furuichi et al. (2015) reviewed friction factors for pipe flow at high Reynolds numbers. More importantly, they measured and proposed an accurate friction factor up to $\mathrm{Re}_D = 1.8 \times 10^7$.

Again, connecting momentum transfer in pipes to convection heat transfer (see Reynolds-Colburn analogy of Equations 3.20 and 3.21a through c) results in an empirical extension of Equation 3.146b as

$$\frac{C_f}{2} = \frac{f}{8} = St\,\mathrm{Pr}^{2/3} = \frac{Nu_D}{\mathrm{Re}_D\,\mathrm{Pr}^{1/3}} \tag{3.150a through c}$$

Equation 3.150 combined with Equation 3.149 yields

$$Nu_D = 0.023\,\mathrm{Re}_D^{4/5}\,\mathrm{Pr}^{1/3} \tag{3.151}$$

Equation 3.151 is very similar to the empirical Dittus-Boelter equation (see Incropera et al., 2007) for $0.6 \le \mathrm{Pr} \le 160$ and $\mathrm{Re}_D > 10^4$, when assuming $L/D \ge 10$. For a broader range of Pr # and Re # applications, Gnielinski (1976) postulated:

$$Nu_D = \frac{(f/8)(\mathrm{Re}_D - 10^3)\mathrm{Pr}}{1 + 12.7(f/8)^{1/2}(\mathrm{Pr}^{2/3} - 1)} \tag{3.152}$$

which holds for $0.5 \le \mathrm{Pr} \le 2000$ and $3000 \le \mathrm{Re}_D \le 5 \times 10^6$.

In summary, there are basically three methods for solving fully developed thermal flow in conduits:

1. Solve the turbulent momentum and heat transfer equations directly, or the RANS forms with suitable turbulence models for $\tau_{ij,\,\text{apparent}}$ and $q_{i,\,\text{apparent}}$.
2. Employ the integral method by postulating smart turbulent $v$- and $T$-profiles that satisfy the BCs.
3. Use the Reynolds-Colburn analogy to obtain typically the Nusselt number, given the friction coefficient $C_f$ or the Darcy friction factor $f$.
4. In terms of the axial coordinate $x$, the *local friction coefficient* is (see Equation 3.150)

$$C_f(x) = 2St_x \,\text{Pr}^{1/3} \tag{3.153}$$

The next four examples illustrate the use of the derived equations/correlations and highlight characteristics of internal turbulent flow, typically in contrast to laminar pipe flow.

**Example 3.17: Derivation of Friction Factor and Nusselt Number Correlation for Turbulent Pipe Flow with Constant Wall Heat Flux and Unit Prandtl Number**

Consider steady fully developed turbulent pipe flow. Given measured flow rate, pipe geometry, pressure drop over pipe length, and fluid properties, find expressions for the friction factor and the Nusselt number based on the Reynolds-Colburn analogy. Summarize three basic solution methods for this problem category.

**Sketch 18**

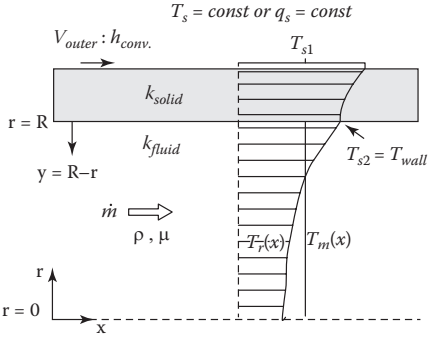


**Assumptions**

- $Nu_x = \dfrac{hx}{k} = \dfrac{q_w x}{k\Delta T}$ or $Nu_D = hD/k$

**Method**

- $T_m(x) = \dfrac{1}{\dot{m}} \iint_A \rho v T \, dA$
- $\vec{q} = -k\nabla T$, where $q_s = \dfrac{\dot{Q}_s}{A_{surf.}}$
- $h \equiv \dfrac{q_s}{T_s - T_{\text{ref}}}$; $T_{\text{ref}} = T_m$; $T_s = T_{\text{wall}}$ $q_s = q_{\text{wall}} = -k_{\text{fluid}} \left.\dfrac{\partial T}{\partial y}\right|_{y=0}$
- $\tau_w = \mu \left.\dfrac{\partial v}{\partial y}\right|_{y=0} = \dfrac{f}{8}\rho v_{\text{mean}}^2$

*Solution:*

Rearranging, that is, normalizing the wall fluxes due to friction and heat transfer, we have:

- Wall friction:

$$\left.\frac{d\left(v/v_{\text{avg}}\right)}{d\left(y/L\right)}\right|_{y=0} = \frac{f}{4}\frac{\rho v_{\text{avg}} L}{\mu} = \frac{f}{4}\text{Re}_L \tag{E.3.17.1}$$

- Wall heat transfer:

$$\left.\frac{d\left[\left(T - T_w\right)/\left(T_m - T_w\right)\right]}{d\left(y/L\right)}\right|_{y=0} = \frac{hL}{k} = Nu \tag{E.3.17.2}$$

Note that for $\mathrm{Pr} \approx 1$, $\nu = \alpha$ (same diffusivities, say for a gas), wall momentum and heat transfer are the same (since the LHS slopes/gradients are identical); hence, we have the Reynolds analogy:

$$\frac{f}{4}\mathrm{Re} = Nu \quad \text{or} \quad \frac{f}{4} = \frac{Nu}{\mathrm{Re}\,\mathrm{Pr}} \equiv St \tag{E.3.17.3a, b}$$

Empirical extension with the Reynolds-Colburn analogy then reads:

$$\frac{f}{4} \equiv \frac{\tau_w}{\frac{\rho}{2}v_{\text{avg}}^2} \equiv c_f = 2\overline{St}_D\,\mathrm{Pr}^{2/3}; \quad \overline{St}_D = \overline{Nu}_D/\left(\mathrm{Re}_D\,\mathrm{Pr}\right) \tag{E.3.17.4a, b}$$

For example, from turbulent pipe flow experiments,

$$f = 0.184\,\mathrm{Re}_D^{-0.2}; \quad 2\times10^4 \le \mathrm{Re}_D \le 10^6 \tag{E.3.17.5}$$

so that

$$\overline{Nu}_D = 0.023\,\mathrm{Re}_D^{0.8}\,\mathrm{Pr}^{1/3} \tag{E.3.17.5}$$

for $\mathrm{Re}_D > 10^4$; $0.7 \le \mathrm{Pr} \le 160$; and $L/D > 60$. Equation E.3.17.5 matches the purely empirical Dittus-Boelter correlation. *Note:* use $f = 0.3164\,\mathrm{Re}_D^{-0.25}$ when $4\times10^3 \le \mathrm{Re}_D \le 10^5$.

*Summary of solution methods:*

1. Solve the turbulent momentum and heat transfer equations directly or the RANS forms ($\vec{\mathbf{v}} = \bar{\vec{\mathbf{v}}} + \vec{\mathbf{v}}'$ and $T = \bar{T} + T'$) with turbulence models for $\tau_{ij}^{\text{apparent}}$ and $q_i^{\text{apparent}}$.
2. Employ turbulent $v$- and $T$-profiles with the integral method.
3. Use the Reynolds-Colburn analogy.

**Example 3.18: Turbulent Thermal Pipe Flow**

Consider fully developed hot air flow in a metal tube ($\dot{m} = 0.05$ kg/s; $L = 5$ m; $D = 0.15$ m). Because of the cold ambient ($T_\infty = 0°\mathrm{C}$, $h_{\text{ambient}} = 6\ \mathrm{W/m^2k}$), the air inlet temperature $T_1 = 103°\mathrm{C}$ drops to $T_2 = 77°\mathrm{C}$ at the tube outlet. Find the heat loss and surface temperature at $x = L$.

| Sketch 19 | Assumptions | Method |
|---|---|---|
| 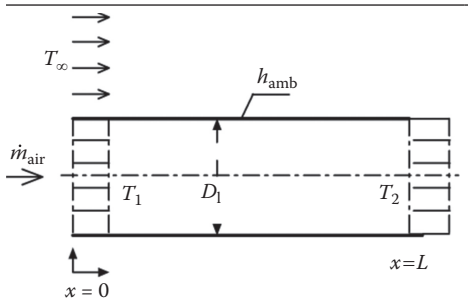 | • Steady-state<br>• Air $\triangleq$ Ideal gas<br>• Constant properties and parameters<br>• Tube-wall effects negligible | • Energy balance $\dot{Q} = \dot{m}c_p\left(T_1 - T_2\right)$<br>• Radial heat loss modeled as *resistance in series*<br>• $Nu_D$-correlation Equation 3.151 |

*Solution:*

- Properties (Appendix II) for $T_{\text{ref}} \approx 360$ K, $\mathrm{Pr} = 0.7$, $c_p = 1010$ J/kg·K, $k = 0.03$ W/m·k, $\mu = 208.2\times10^{-7}$ N·s/m²

- Reynolds number $\mathrm{Re}_D = \dfrac{4\dot{m}}{\mu\pi D} := 20{,}384$ (i.e., turbulent)
- Heat loss over entire tube: $\dot{Q} = \dot{m}c_p\left(T_1 - T_2\right) = 1313\ \mathrm{W}$
- Tube surface temperature $T_s$ at $x = L$ (see thermal resistance network, which implies $Q_{\text{heat}} = \Delta T / R_{\text{thermal}}$)

$q_s\,(x = L) \quad \Rightarrow$
(Radial heat flux)

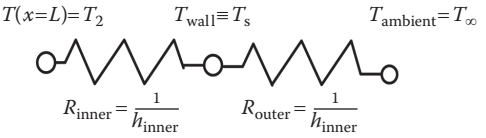


Hence, we can write:

$$q_s\left(x = L\right) = \frac{T_2 - T_\infty}{\dfrac{1}{h_i} + \dfrac{1}{h_{\text{amb.}}}} \tag{E.3.18.1}$$

where:

$$h_i = h\left(x = L\right) = Nu_D \frac{k}{D}$$

$$Nu_D = 0.023\,\mathrm{Re}_D^{4/5}\,\mathrm{Pr}^{1/3}$$

Finally, with $Nu_D = 57.22$ and hence $h_i = 11.44\ \mathrm{W/m^2\text{-}K}$, we have

$$q_s\left(x = L\right) = 305\,\frac{J}{m^2 \cdot s} \tag{E.3.18.2}$$

Now, applying again

$$q_s = h_i\left(T_2 - T_s\right) \tag{E.3.18.3}$$

we obtain

$$T_s = 77 - \frac{305}{11.44} = 50.34^{\circ}C \tag{E.3.18.4}$$

*Comments:*

- As just an end-point temperature (i.e., $T_{\text{mean}}$) was required, only a global (or whole-system) analysis was necessary. Thus, the combination of overall energy balance plus a radial resistance network representing the radial heat flux yielded the desired result.
- A differential analysis, that is, reduced forms of the N-S and convection heat transfer (CHT) equations with appropriate closure models, would make an interesting Course Project (see Chapter 10).

**Example 3.19*:* Mean Temperature Development for Thermal Turbulent Pipe Flow**

The mean fluid temperature is very useful; for example, as used in the dimensionless temperature profile, which is a function of the pipe radius only. Consider fully developed turbulent flow in a tube of diameter *D*. Find an expression for $T_m(x)$, given the mean inlet temperature, wall temperature, average heat transfer

coefficient, and mass flow rate. What is $T_m(x)$ when the tube is subjected to a constant wall heat flux $q_w$?

| Sketch 20 | Assumptions | Method |
|---|---|---|
| 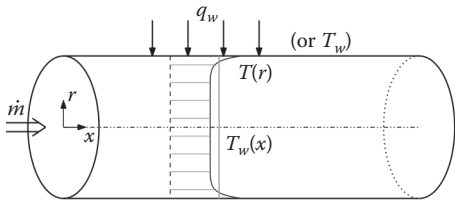 | • Steady fully developed tubular flow with thermal B.C.<br>• Constant fluid properties | • 1-D energy balance for an $RE\forall$ (i.e., $\pi R^2 \Delta x$) in terms of $T_{mean}$<br>• $\dot{Q}_{wall,in} = \dot{Q}_{flow,out}$ |



*Solution:*

For the uniform heat flux case with $q_{wall}$ given, the overall energy balance $\dot{Q}_{wall,in} = \dot{Q}_{flow,out}$ can be written for an arbitrary pipe section $\Delta x = x_2 - x_1$ as

$$\frac{q_w(\pi D \Delta x)}{\dot{m} c_p} = T_m(x_2) - T_m(x_1) \tag{E.3.19.1}$$

in the limit

$$\frac{dT_m}{dx} = \frac{q_w(\pi D)}{\dot{m} c_p} \tag{E.3.19.2}$$

or

$$T_m(x) = T_{m,0} + \frac{\pi D q_w}{\dot{m} c_p} x \tag{E.3.19.3}$$

The two classic cases, that is, $T_w = \text{const.}$ and $q_w = \text{const.}$, are depicted in Graph 8a and b, respectively.

*Graph 8:*

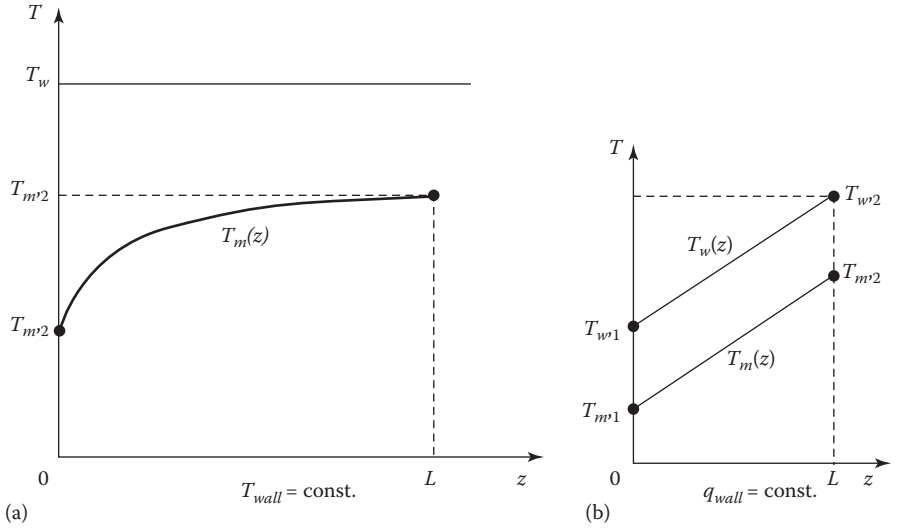

**Example 3.20: Falling Film Where the Film Thickness Is $h = h(z,t)$**

| Sketch 21 | Assumptions | Method |
|---|---|---|
| 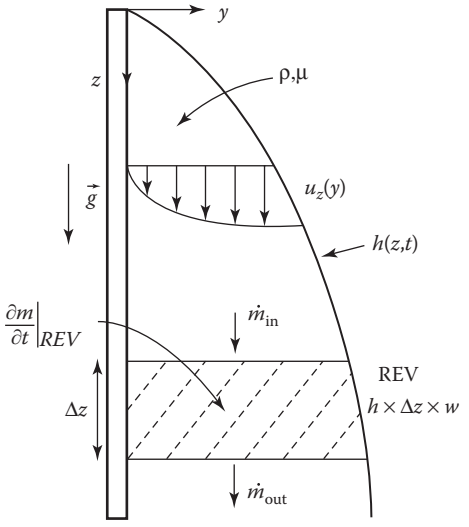 | • Transient, laminar, --D flow<br>• $v_z(y)$ is steady and fully developed<br>• Constant fluid properties | • 1-D fluid mass balance, that is, PDE for $h(z, t)$<br>• Determination of vavg via the reduced N-S equation<br>• Trial solution $h = A\sqrt{z/t}$ with $t > 0$ |



*Solution:*

Considering the 1-D global mass balance

$$\frac{\partial m}{\partial t} = \dot{m}_{\text{in}} - \dot{m}_{\text{out}} \tag{E.3.20.1}$$

Then, with depth $w = 1$ and $v = v_{\text{avg}} = \dfrac{1}{A}\displaystyle\int_A v_z(y)\, dA$, we have

$$\rho \Delta z \frac{\partial h}{\partial t} = \rho v h\big|_z - \rho v h\big|_{z+\Delta z} \tag{E.3.20.2}$$

Dividing by $\Delta z$ and taking the limit, that is,

$$\frac{\partial h}{\partial t} = -v\frac{\partial h}{\partial z} \tag{E.3.20.3}$$

leads to the expression

$$\frac{\partial h}{\partial t} + v_{\text{avg}}\frac{\partial h}{\partial z} = 0 \tag{E.3.20.4}$$

The average film velocity, $v_{\text{avg}}$, is obtained from the velocity profile, $v_z(y)$, which is the solution of the reduced N-S equation:

$$0 = \mu\frac{d^2v}{dy^2} + \rho g \tag{E.3.20.5}$$

Invoking the boundary conditions

$$v(y=0) = 0 \qquad \text{and} \qquad \left.\frac{dv}{dy}\right|_{y=h} \approx 0 \tag{E.3.20.6}$$

after double integration yields

$$v(y) = \frac{\rho g h^2}{2\mu}\left[2\left(\frac{y}{h}\right) - \left(\frac{y}{h}\right)^2\right] \tag{E.3.20.7}$$

The average film velocity is therefore

$$v_{avg} = \frac{1}{A}\int_A v_z(y)\, dA := \frac{\rho g}{3\mu} h^2 \tag{E.3.20.8}$$

Using the trial solution $h(z, t) = A\sqrt{z/t}$ as well as the $v_{avg}$ result in the PDE (Equation E.3.20.4) yields an equation that may be used to determine the unknown coefficient, $A$:

$$A\frac{\partial}{\partial t}\left[\left(\frac{z}{t}\right)^{1/2}\right] + \frac{\rho g}{3\mu}A^2\left(\frac{z}{t}\right)A\frac{\partial}{\partial z}\left[\left(\frac{z}{t}\right)^{1/2}\right] = 0 \tag{E.3.20.9}$$

Hence,

$$\frac{\rho g}{3\mu}A^2 - A = 0 \qquad \text{or} \qquad A = \begin{cases} 0 \\ \dfrac{3\mu}{\rho g} \end{cases} \tag{E.3.20.10}$$

Finally, we obtain the solution for the film height as

$$h(z, t) = \frac{3\mu}{\rho g}\sqrt{\frac{z}{t}} \tag{E.3.20.11}$$

*Graph 9:*

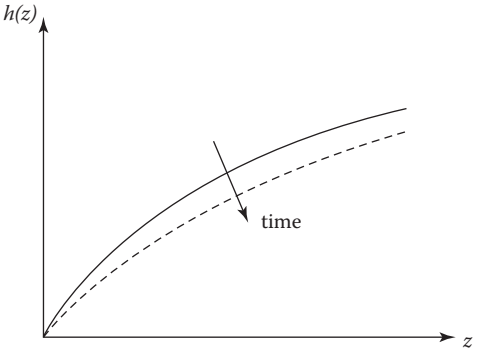


*Comments:*

- $h(z,t) \to h(z)$ as $t \to \infty$
- $h(z=0) = 0$ for $t \geq 0$
- $\mathrm{Re}_h < 1$ to avoid ripple effect

## 3.4 Homework Assignments

As mentioned, homework problems done ultimately independently should help to further illustrate fluid dynamics concepts as well as approaches to problem solving and, in conjunction with Appendix I, can sharpen the reader's math skills. The key word is

"independence"; that is, the student should be able to (1) satisfactorily answer all concept questions and (2) solve correctly all basic fluid dynamics problems.

The "Insight" questions emerged directly out of the Chapter 3 text, while some "Problems" were taken from lecture notes in modified form when using White (2006), Cimbala and Cengel (2008) and Incropera et al. (2007) over the years. Additional examples, concept questions, and problems may be found in any undergraduate fluid mechanics and heat transfer text, or on the Web (see websites of MIT, Stanford, Cornell, Penn State, University of Michigan, etc.)

### 3.4.1 Physical Insight

Whenever possible, answers to *Physical Insight* questions should feature a sample illustration (or system sketch), a brief description/explanation, and some math in terms of definitions or derivations.

3.1 Concerning Table 3.1, provide additional examples with sketches illustrating the different flow assumptions and associated math descriptions.

3.2 Show that Equation 3.3 also holds for basic flows in cylindrical coordinates, and discuss the impact on the velocity field in the case of cylinder rotation.

3.3 For Case A in Example 3.3, determine the location of the maximum velocity. Knowing Q from measurements, what can Equation E.3.3.7 be used for?

3.4 Consider steady laminar flow of the Von Karman pump, where a thin disk rotating in a reservoir (i.e., an infinite body of a quiescent viscous fluid) sucks the fluid in, swirls it, and distributes it radially. Sketch the system, set up the reduced momentum equations plus BCs based on sound postulates, and discuss an application.

3.5 Revisiting Section 3.1.2, develop a criterion that sets the limit for the "nearly parallel-flow" assumption.

3.6 Why is there a minus sign in Equation 3.9?

3.7 Provide practical applications when the viscous dissipation function in Equation 3.10 is important.

3.8 In an extension of Example 3.5, evaluate $T_{mean}$ and find $h$. Comment!

3.9 How do heat conduction and convection heat transfer differ? How do $T_{surface}$, $T_{wall}$, $T_{mean}$, $T_{ref}$, $T_{bulk}$, and $T_{\infty}$ differ?

3.10 The convective heat transfer coefficient $h = q_{wall}/(T_{wall} - T_{ref})$ is considered by some researchers as an artifact that masks the actual physics of convection heat transfer. Discuss this topic.

3.11 Why is the Nusselt number for the isothermal wall condition larger than for the constant heat flux case?

3.12 Derive Equation 3.20 and comment on the advantages of heat-momentum transfer and heat-mass transfer analogies.

3.13 Revisit Example 3.6 and discuss the case of high-speed spindle rotation, that is, $\omega_i \gg 1$ and $q_{wall} \neq 0$.

3.14 Considering problem solutions to linear momentum or convection heat transfer, it is evident that the flow rate of fluids or heat can be expressed as the ratio of "driving force"/resistance; for example,

$$Q = \begin{cases} \dfrac{\Delta p}{\sum R_{\text{fluid}}} & \text{for momentum transfer} \\ \dfrac{\Delta T}{\sum R_{\text{thermal}}} & \text{for heat transfer} \end{cases}$$

Write a report on the derivations and multitude of applications of such correlations. Is there something similar for species-mass transfer?

3.15 List examples of transient flows in industry and nature. Why is Stokes' First Problem solution so important? For which applications does it provide math models?

3.16 Discuss the three figures of Example 3.8; that is, explain the time-lag between pressure-profile and resulting flow rate as well the reason for the *M*-profile formation.

3.17 Draw representative streamlines through the boundary layer of steady laminar flow past a flat plate. Comment!

3.18 In Example 3.8, why is the basic polynomial such a good choice for the axial velocity profile in Blasius flow? Find an expression for the normal velocity $v(x, y)$ and graph $v(y)$ at different $x$-stations.

3.19 Summarize and discuss 2-D problems described by PDEs that can be transformed to ODEs with suitable "combined variables."

3.20 Why is the velocity above an airfoil (or wing) much higher than below (see Figure 3.5)? What are the implications?

3.21 While ups and downs of the drag curve $C_{\text{drag}}(\text{Re}_D)$ for a sphere of diameter $D$ are *described* (see Figure 3.6), now provide explanations for the $C_{\text{drag}} \sim \text{Re}_D$ decrease and dip, as well as the flow-separation delay when moving from laminar to turbulent flow.

3.22 Check out the details in the open literature of the Stokes Equation 3.76. Why is the form drag twice the frictional drag? Discuss a system where it is the opposite.

3.23 Generate a review report on laminar and turbulent jets with industrial applications (see Section 3.2.4).

3.24 List causes of turbulence in natural and industrial settings, and show that turbulent flow is always transient, 3-D, and chaotic.

3.25 Derive the RANS Equations 3.124 and 3.125.

3.26 Write a report on *practical* turbulence models to gain closure (see Equations 3.127a through c).

3.27 Turbulent pipe velocity profiles: (a) Plot Equation 3.145a for exponents $n = 7$ and 10, and discuss the pros and cons of this $\overline{u}(r)$-profile correlation. (b) Compare Equation 3.145a with Equation 3.145b. (c) Derive an expression for $u_{\text{avg.}}/u_{\max}$ as a function of exponent $n$.

3.28 Derive Equation 3.128, list useful expressions for friction factor f(Re), and comment.

3.29 Derive, plot, and discuss the results given with Equations 3.1.34 through 3.138. Why are all dependent variables a function of $\text{Re}_x^{-1/7}$ ?

3.30 Derive and explain the connection between $C_{drag}$ and $C_{skin-friction}$ (see Equations 3.143 and 3.144).

3.31 Graph and compare carefully Equation 3.145a versus Equation 3.145b, take the derivatives at $r=0$, $R$ (or $y=R$, 0), and comment on the results.

3.32 Discuss the pros and cons of the different solution methods for turbulent CHT in pipes. For what (dimensionless) temperature does the temperature field appear to be thermally fully developed, that is, the $T$-profile does not change in the axial direction?

3.33 Considering the $T_{wall} = ¢$ case, develop an equation for $T_m(z)$, mentioned in Example 3.19.

### 3.4.2 Engineering Problems

Before launching into an engineering-problem solution, three preliminary tasks should be carefully executed:

1. A system *Sketch* with coordinates, expected velocity/temperature profiles, and given/unknown parameters in symbolic form
2. A detailed list of *Assumptions* concerning flow field characteristics, system simplifications, submodels, and fluid properties
3. Solution *Method* in terms of concepts and approach, expressed as brief mathematical statements

3.34 Consider horizontal tubular flow ($D_1 \equiv D_{tube} \equiv 5$ cm, $\rho = 10^3$ kg/m$^3$) for which a Venturi meter ($D_2 = D_{throat} = 3$ cm and $K = 0.98$) with a differential pressure gage measures $\Delta p = p_1 - p_2$. (a) Develop an equation for the mass flow rate $\dot{m}$, and plot $\dot{m}(\Delta p)$ for $1 \le \Delta p \le 10$ kPa. (b) Compute the average tube velocity for $\Delta p = 5$ kPa.

3.35 A 50 hp air-compressor sucks in ambient air ($Q = 0.3$ m$^3$/s, $p = 100$ kPa, $\rho = 1.15$ kg/m$^3$, $\mu = 1.8 \times 10^{-5} \frac{\text{kg}}{\text{m} \cdot \text{s}}$) through a long pipe ($D = 20$ cm, $L = 20$ m, $\varepsilon = 0.15$ mm). What percentage of the compressor power is lost due to the (frictional) pipe resistance?

3.36 Consider two parallel-connected pipes, both of diameter $D$ and of the same material but of lengths $L$ and $X^L$, where $1 < X < 4$. Find and plot the flow rate ratio $Q_1/Q_2$ as a function of $X$.

3.37 A typical industrial process is the discharge of a highly viscous liquid from a tank [$D$, $h(t=0) = H$] via a horizontal long small pipe ($d$,L). Assuming laminar flow and negligible losses (e.g., pipe entrance, etc.), derive an ODE for $h(t)$, which is the fluid depth. Solve for $t = t(h; L, d; D, H)$, and graph $h(t)$.

3.38 Consider steady fully developed flow of a power-law fluid ($m$, $n$) in a slit of small spacing $2h$ formed by two plates ($L \times W$).

(a) Compare your velocity profile with the Poiseuille solution ($m = \mu$, $n = 1$):

$$u(y) = \frac{h^2}{2\mu}\left(\frac{\Delta p}{L}\right)\left[1 - \left(\frac{x}{h}\right)^2\right]$$

(b) Show that the mass flow rate is

$$\dot{m} = \frac{2\rho W h^2}{(1/n)+2}\left[\frac{h}{m}\left(\frac{\Delta p}{L}\right)\right]^{1/n}$$

(c) How would your results change if the plates were vertical, that is, 100% downward flow, and still subject to a pressure gradient?

3.39 Commercial capillary viscometers (see Bird et al., 2002) can be modeled as cylindrical Couette flow. Assuming that the inner cylinder (radius $\kappa R$, $0<\kappa<1$) is stationary and the outer one (radius $R$, forming a small gap of filled with an unknown power-law fluid) rotating at low angular velocity $\omega_0$ due to a measured torque, how would you obtain the power-law fluid parameters $m$ and $n$? $R-\kappa R$

3.40 Consider flow of a power-law fluid ($m$,$n$; $\rho$) in a horizontal annulus ($\kappa R$ and $R$). The fluid is kept in motion due to the translatory motion ($u_0$) of the inner cylinder ($\kappa R$).

(a) Derive the velocity profile $v_z(r;v_0,\kappa,R;n)$ and show that it simplifies to $\dfrac{v_z}{v_0}=\dfrac{\ln(r/R)}{\ln\kappa}$ for $n\to 1$.

(b) Find an expression for the mass flow rate $\dot{m}$ for $n\neq 1/3$; what is $\dot{m}$ $(n\neq 1/3)$?

3.41 Consider flow of two immiscible fluids (viscosities $\mu_1$ and $\mu_2$ with different densities) between parallel horizontal plates a small distance $2h$ apart, driven by $\Delta p/L=$ constant. Assuming that the interface stays planar and each fluid takes up half the channel, find the shear stress $\tau_{yx}$ and velocities $u_1(y)$ for $-h\le y\le 0$ and $u_2(y)$ for $0\le y\le h$.

3.42 An inverted U-tube acts as a water siphon (see Schematic 1). The bend in the tube is 1 m above the water surface; the tube outlet is 7 m below the water surface. The water issues from the bottom of the siphon as a free jet at atmospheric pressure. Determine (after listing the necessary assumptions) the speed of the free jet and the minimum absolute pressure of the water in the bend (see Point A). *Note:* $p_{atm}=1.01\times10^5$ N/m$^2$ and $\rho=999$ kg/m$^3$.

*Schematic 1*

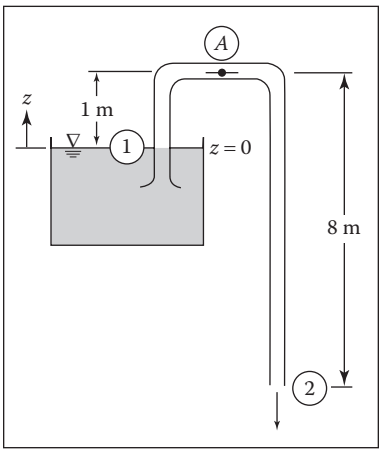

3.43 Consider steady fully developed airflow in a smooth tube where a Pitot-static pressure arrangement measures $p_{static}$ and $P_{stagnation}$ as shown. Estimate (a) the centerline velocity; (b) the volumetric flow rate; and (c) the wall shear stress.

*Schematic 2*

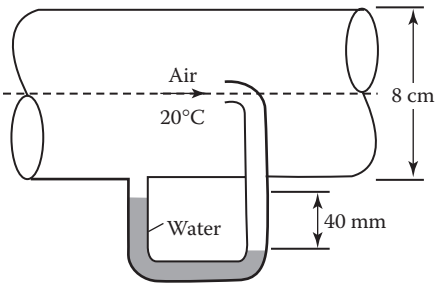


*Properties:*
$\rho_{air} = 1.2$ kg/m$^3$
$\mu_{air} = 1.8\times10^{-5}$ kg/(ms)
$\rho_{water} = 998$ kg/m$^3$
$\mu_{water} = 0.001$ kg/(ms)

3.44 Draw very carefully a gravity-driven vertical velocity profile, $v_z(r)$, in an annulus, that is, a ring-like gap formed by a cylinder placed concentrically in a pipe. Is the profile symmetric with respect to the gap's center? If not, why not? With a slight fluid-dynamic system change, can the ratio of the wall shear stresses ever be one?

3.45 Consider a viscometer consisting of two concentric cylinders ($R_1$ and $R_2$) where the inner one is fixed and the outer one rotates with $\omega_0 = \text{const}$. The gap, $\Delta R = R_2 - R_1$, is filled with a viscous (unknown) fluid. Solve for the velocity profile in the annular gap $R_1 \le r \le R_2$, and find an expression for the shear stress at the surface of the inner cylinder.

3.46 A (wide, vertical) moving belt drags upward at velocity $v_0$ a viscous fluid layer of thickness $h$. Develop expressions for the film's velocity profile, the average fluid velocity, the shear-stress distribution, and the volumetric flow rate per unit width. What is the condition for the minimum belt speed to achieve net upward flow?

3.47 A horizontal disk of mass $M$ and face area $A$ can move vertically when a water jet ($d$,$v_0$) strikes the disk from below. Obtain a differential equation for the disk height $h(t)$ above the jet exit plane when the disk is initially released at $H > h_0$, where $h_0$ is the equilibrium height. Find an expression for $h_0$, sketch $h(t)$, and explain.

3.48 Consider two inclined (angle $\theta$) parallel plates a distance $d$ apart, where the upper plate moves at $u_0 = ¢$ and a constant pressure gradient is applied to the viscous fluid ($\rho$, $\mu$). Derive an expression for the velocity, and graph typical profiles for different $dp/dx$ values. Evaluate $\tau_{wall}$ and graph $\tau_{yx}(y)$.

3.49 Expanding on the modeling equations for the Von Karman pump (see Problem 3), solve for the velocity field and plot the results.

3.50 The axial velocity of an incompressible fluid flowing between parallel plates is given as $u(y) = \text{fct.}(Ay, By^2)$.

(i) Determine $v(x, y)$.

(ii) When and where is $u = u(x, y)$?

(iii) Draw a velocity profile for each case.

3.51 Convection heat transfer: Consider a well-insulated tube ($D_i = 20$ mm, $D_o = 40$ mm) with an electric wall heater providing $q_{el} = 10^6$ W/m$^2$ to increase the average water temperature $T_i(x=0) = 20°C$ to $T_0(x=L) = 60°C$ when $\dot{m}_{water} = 0.1\,\mathrm{kg/s}$ with $C_p = 4.179$ J/kg K.

(a) Find the necessary tube length.

(b) Assuming a constant convection coefficient $h = 1500$ J/m$^2 \cdot$K, find the inner-surface inlet and exit temperatures.

3.52 Consider a well-insulated counter-flow heat exchanger (i.e., a thin-walled, double pipe system), which connects a water heater to a shower. Specifically, cold water ($c_p = 4.18$ kJ/kg°C) enters at 15°C at a rate of 0.25 kg/s and is heated to 45°C by hot water ($c_p = 4.19$kJ/kg°C) that enters at 100°C with 3 kg/s. Determine (a) the rate of heat transfer and (b) the rate of entropy generation in the heat exchanger.

3.53 Expand Example 3.19 by solving the CHT problem for the isothermal wall case.

3.54 Consider a mixing chamber where liquid water at 200 kPa and 20°C is mixed with superheated steam at 200 kPa and 150°C, and the mixture leaves at 60°C and 200 kPa. The chamber loses heat at a rate of 1200 kJ/min to the ambient ($T_{ambient} = 25°C$). Find $S_{total} = S_{gen}$.

# Part B

# Modern Fluid Dynamics Topics

The fundamentals of fluid mechanics and convection heat transfer were discussed in the first three chapters, that is, Part A. From there, it seems to be a bit of a jump to start Part B with two-phase flow applications, such as flow through saturated porous media, mixture and non-Newtonian fluid flows, as well as fluid-particle dynamics. However, sticking to simple but essential aspects of these modern topics, the new material is presented as a logical extension of what has been discussed in Part A. In Chapter 4 for example, "two-phase flow" is reduced to laminar fully developed flow in: either tiny straight tubes (or pores), or homogeneous mixture flows, or flow of well-dispersed particle suspensions. Thus, in Part B, the system geometries, basic assumptions, and governing equations stay the same for the most part, although the math requirements may go up a notch. The same holds for the material given in Chapters 5 through 7. Chapter 8 then adds some solid mechanics essentials to analyze fluid–structure interaction phenomena. While almost all problems posed in Chapters 1 through 8 have analytic (or simple approximate) solutions, Chapter 9 deals with numerical solutions of more complex systems and hence, discusses more challenging fluid-particle dynamics problems.

It is very important as part of an in-depth education and for a professional career to learn how to carry out detailed problem solutions and subsequently proper report-writing. For that purpose, Chapter 10 provides a guide to accomplishing such assignments as they may be encountered in industrial, governmental, and/or academic environments.

Taylor & Francis
Taylor & Francis Group
http://taylorandfrancis.com

# 4

# *Mixture Flows*

By definition, a mixture flow, typically with two phases, is the interactive flow of two distinct phases with common interfaces in, say, a conduit or around a submerged body. Each phase, representing a volume fraction (or mass fraction) of solid, liquid, or gaseous matter, has its own properties, velocities, and temperatures. Typical examples are dilute (or dense) particle suspension flows, which include droplets in gas flow, air-bubbles or vapors in liquid flow, as well as liquid/gas flow with solid particles. Thus, such mixtures may form various two-phase combinations, including solid–gas or solid–liquid flows as well as liquid–gas or gas–liquid flows. In addition to the flow-system geometry plus inlet conditions, the characteristics of the particulate matter, mainly particle size, shape, density, and concentration, together with the type of carrier fluid, determine the two-phase flow behavior and hence, the type of solution approach. In addition to predicting the volume or mass fractions of the flow phases, it is also important to know the flow regimes, that is, characteristic flow patterns based on the interfaces formed between the phases (see Figure 4.1). Two-phase systems can be grouped into flows of separated phases, mixed phases, and dispersed phases. Examples of *separated* flows include liquid layers on a wall in gas flow, for example, an oil film on water, the mucus layer in lung airways, and liquid jets in gas flow (or vice versa). *Mixed-phase* flows are encountered in phase-change processes, such as boiling fluid flow channels and steam pipes with vapor core and annular liquid wall film, as well as heat pipes with large vapor bubbles and evaporating liquid layers on heated surfaces. A frequent occurrence of *dispersed flows* is solid particle distributions in a liquid or gaseous stream. Traditionally, two-phase flow theories and applications were the domains of applied mathematicians as well as chemical and environmental engineers. However, for pipe-network design, pump sizing, and applied force evaluation, mechanical engineers have to know basic two-phase flow modeling techniques. The reason is that many industrial fluids to be conveyed may actually be non-Newtonian fluids, such as polymeric liquids, slurries, foodstuff, synthetic oils, and so on. Furthermore, biomedical engineers encounter fluid-particle dynamics problems in both the cardiovascular and the pulmonary systems, especially during drug delivery. Interacting multi-component droplet-vapor mixtures, which may appear in electronic cigarette smoke and welding fumes, as well as during fuel-handling, spray operations, and combustion processes, to name a few, are highly complex. In any case, a more direct two-phase flow classification would be that the particles, droplets, or bubbles are the *dispersed (or "particle") phase*, while the carrier fluid is the *continuous (or fluid) phase.* The degree of *phase-coupling* may vary from one-way for very *dilute particle suspensions* to four-way in *dense multi-particle suspensions*. In the latter case, not only does fluid flow affect (as always) particle motion, but particles also alter the local flow field. Furthermore, particle-particle as well as particle-wall interactions occur due to collisions, and particle-induced flow fields may affect other particles, which can be solid and/or liquid.

In the frequent case of solid spheres in gas or liquid flow, there are two basic solution options when it can be assumed that the particle suspension is *dilute*:

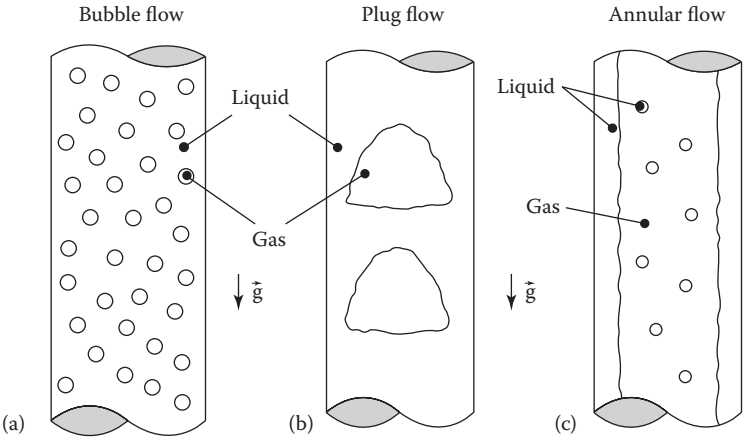


**FIGURE 4.1**
Flow regimes in vertical pipes with co-current gas–liquid flows.

1. For flows of nanoparticles dispersed at low-volume concentrations in a carrier fluid, the Navier–Stokes (N-S) and one-way coupled mass transfer equations are solved within the Euler–Euler framework.
2. Particles with measurable inertia (say, $d_p > 100$ nm), after solving the N-S equations for the fluid flow field, are tracked with Newton's Second Law of Motion within the Euler–Lagrange framework.

These modeling approaches are discussed and illustrated with examples throughout this chapter.

Critical *heat transfer* may change the thermodynamic state of a phase or may generate two-phase flow in the first place, as discussed by Naterer (2002) and Faghri and Zhang (2006). Other recent two-phase or multiphase books include the texts by Crowe et al. (1998) and Kleinstreuer (2003), and the handbook edited by Crowe (2006).

It should be evident from reading the brief introduction that a very dilute suspension of uniformly distributed (micron or nano) particles, which only slightly affect the mixture properties, constitutes the simplest two-phase flow problem and hence, the easiest case to solve. Such well-mixed particle suspensions, which are actually *pseudo* two-phase flows, can be described with the single-fluid mechanics equations and fall into the category of *flow mixture models* (see left box in Figure 4.2). In contrast, when a distinct particle phase interacts with the continuous phase, more complex *separate flow models* are needed to describe the two-phase dynamics (see right box in Figure 4.2).

One "two-phase flow" application is flow through a *saturated porous medium*, where the dispersed phase is actually a rigid porous structure forming small irregular conduits in which a fluid flows. Thus, in most cases, it is actually (steady, laminar) single-phase flow. So, we start with "porous media flow," describing it as a special case of Poiseuille flow in a network of very small tubes (see Section 4.1). Then in Section 4.2, two groups of pseudo two-phase flows are discussed, that is, quasi-homogeneous mixture flows and non-Newtonian fluid flows. Again, they are treated as extensions of solutions to Newtonian fluid flows given in Chapters 2 and 3. Section 4.3 (see right box in Figure 4.2) provides problem solutions of *separated flows*, for example, solid spheres moving in air, water, or oil.

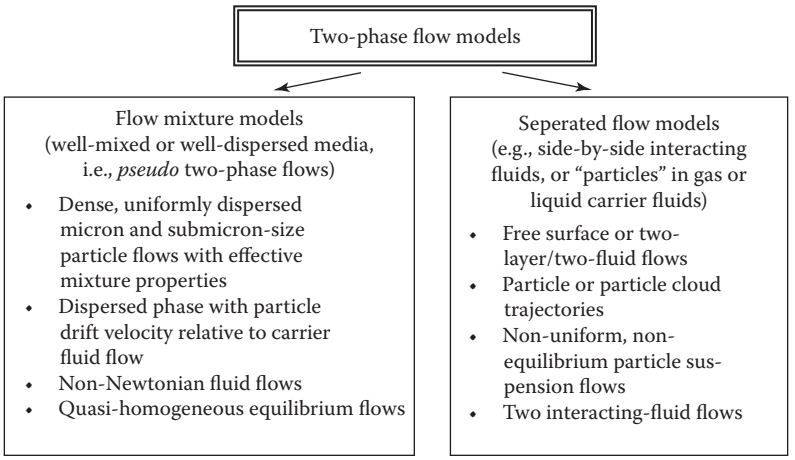


**FIGURE 4.2**
Two-phase flow modeling categories.

## 4.1 Porous Medium Flow

A porous medium is typically a *fixed solid matrix* with a connected void space, which is either 100% filled with a moving fluid (i.e., saturated flow of, say, water) or filled with a liquid–gas combination, known as *unsaturated flow*. The fraction of void space to total volume is the *porosity*, which may go up to 0.6 in nature and up to 0.99 in industry, such as for metallic foams. The *permeability k* (in meters squared), depending greatly on the medium's effective pore diameter and porosity, indicates the ease with which a fluid is flowing through a porous medium. Darcy in 1856 established for groundwater flow a 1-D linear proportionality between the driving force (say, $d_p/d_x$, and/or gravity) and the flow resistance, $\mu v/k$, where $v$ is the superficial (or volume-averaged) velocity. This correlation only holds for small, volume-averaged "filtration" velocities; that is, the Reynolds number based on the pore (or particle) diameter has to be less than 1. A major extension of Darcy's law is the Brinkman-Forchheimer equation, discussed in the next section. Materials with flow-through-porous-media applications include soils, rocks, and sands as well as foams, composites, fibers, and tissues and also membranes, filters and packed beds. A review on convection in porous media is given by Nield and Kuznetsov (2013).

### 4.1.1 Saturated Porous Medium Flow

In numerous natural and industrial processes, a fluid flows (or just seeps or migrates) through a *fully saturated* porous medium. Examples include blood flow through tissue, groundwater flow through geologic media, oil or steam dispersion through sand and porous rock, fluid flow through a container packed with spheres, pellets, or granular material (with upward flow known as "fluidized beds"), moisture migration through a porous composite, mixture flow across membranes or filters, coolant flow through nano-channels, and so on. In any case, as indicated in Figure 4.3, the local velocity field through conduits packed with spheres, pellets, cylinders, fibers, cells, or granular material is very complicated. The same holds for flow in capillaries, pores, fissures, and nanochannels.

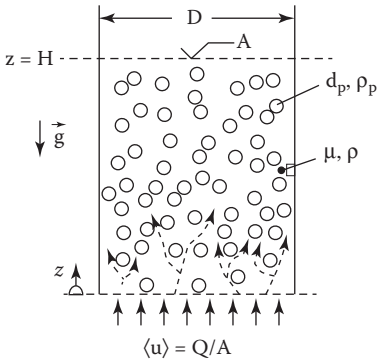


**FIGURE 4.3**
Upward flow through a porous medium column.

For that reason, a volume-averaged, that is, *superficial velocity* has been introduced (see Figure 4.3) as

$$\langle \vec{u} \rangle = \frac{1}{\forall} \int \vec{u} d\forall = \frac{Q}{A} \tag{4.1a,b}$$

where, assuming incompressible fluids:
$Q$ is the volumetric flow rate
$A$ is the cross-sectional area of the porous medium

It should be noted that the length-scale of the control volume, $\forall^{1/3}$, is smaller than the characteristic length of the system, say, channel height or pipe diameter; but also, $\forall^{1/3} \gg d_p$, that is, the pore (or pellet) diameter, so that we have $d_p \ll \forall^{1/3} \ll L_{\text{system}}$. Note, the integral extends over the volume space occupied by the fluid. Clearly, $\langle \vec{u} \rangle$ is a function of the driving forces (e.g., pressure gradient and/or gravity) and fluid properties (i.e., viscosity and density) as well as the porous medium structure and type of material. As with all complicated fluid flow problems, possible solutions start with dimensional analysis and experimental investigations. Specifically, based on Darcy's observations in 1856, the uniform superficial one-dimensional (1-D) velocity of a viscous fluid through a homogeneous porous medium is (Figure 4.3)

$$\langle u \rangle = -\frac{æ}{\mu}\left(\frac{dp}{dz} + \rho g_z\right) \tag{4.2}$$

where æ [$L^2$] is the permeability, that is, $\sqrt{æ}$ [L] can be used as a length-scale representative of the effective pore diameter.

Note that $æ/\mu \equiv K$ is the "hydraulic conductivity." Not surprisingly, æ has been correlated to the porosity ε; for example, by Ergun (1952) as

$$æ = \frac{\varepsilon^3 d_p^2}{C(1-\varepsilon)^2} \tag{4.3}$$

where $C = 150 - 180$.

Assuming negligible gravitational effects, Equation 4.2 can be used to determine the key driving force, that is, the pressure gradient, as

$$\frac{dp}{dz} = \frac{C\mu\langle u\rangle}{d_p^2}\frac{(1-\varepsilon)^2}{\varepsilon^3} \tag{4.5}$$

The porosity, or void fraction, is a volume ratio; that is, $\varepsilon = \forall_{\text{void}}/\forall_{\text{total}} \approx \forall_{\text{particles}}/\forall_{\text{total}}$. It can be employed to construct a particle Reynolds number; for example, for a uniformly packed bed of spheres,

$$\text{Re}_p = \frac{\rho\langle u\rangle d_p}{(1-\varepsilon)\mu} \tag{4.6a}$$

Alternatively, the Reynolds number is based on $\sqrt{æ}$, that is,

$$\text{Re} = \frac{\langle u\rangle\sqrt{æ}}{\nu} \tag{4.6b}$$

In any case, Equation 4.2 holds for $\text{Re} < 1$, but it is often used up to $\text{Re} \approx 10$. When Equation 4.2 without the gravitational term is compared with the Poiseuille flow result for a horizontal tube of radius $R$, that is,

$$u_{\text{average}} = \frac{R^2}{8\mu}\left(-\frac{dp}{dx}\right) \tag{4.7}$$

the similarity is obvious. Thus, it is conducive that a homogeneous porous medium could be modeled as an assemblage of tiny (straight) tubes (i.e., pores) with steady laminar fully developed flow of a viscous fluid (see Example 4.2).

Because of the obvious shortcomings of Equation 4.2—for example, $\text{Re} \leq \mathcal{O}(1)$, 1-D flow only, the no-slip condition cannot be enforced, local variations in the flow field and porous material structure are averaged out—several additions to Equation 4.2 have been proposed. As mentioned, the two most famous ones are the Brinkman (1947) and the Forchheimer (1901) extensions to Darcy's law, where in three dimensions (3-D)

$$\nabla p = -\frac{\mu}{æ}\vec{\mathbf{u}} - \underbrace{C_F\frac{\rho\vec{\mathbf{u}}|\vec{\mathbf{u}}}{\sqrt{æ}}}_{\substack{\text{Forchheimer}\\ \text{term}}} + \underbrace{\hat{\mu}\nabla^2\vec{\mathbf{u}}}_{\substack{\text{Brinkman}\\ \text{term}}} \tag{4.8}$$

where:

$\vec{\mathbf{u}} \hat{=} \langle\vec{\mathbf{u}}\rangle$

$C_F$ is a dimensionless form-drag constant, which depends on the characteristics of the porous medium and the bounding walls, if any; typically, $C_F \approx 0.55$

the effective viscosity $\hat{\mu} \approx \mu$; however, the ratio $\hat{\mu}/\mu$ can depend again on the nature of the porous medium

When comparing Equation 4.8 with the N-S Equation 2.33, it is apparent that the nonlinear Forchheimer term relates to the inertia force. It is a necessary addition for porous media flow with $\text{Re} > 10$, that is, when the pore-flow is still laminar but the form drag posed by the porous material structure becomes important. The second-order Brinkman term relates to the viscous drag term. It is necessary to enforce no-slip boundary conditions; that is, the term is significant in thin wall shear layers, typically of thickness $\sqrt{æ} << L_{\text{system}}$.

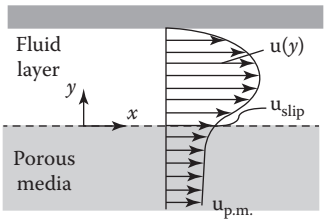


**FIGURE 4.4**
Unidirectional channel flow with porous medium flow.

Quite frequently, channel flow interacts with (saturated) porous medium flow (see Figure 4.4) where the magnitude and gradient of the velocity have to match at the interface between fluid layer and medium. As a first approximation, Beavers and Joseph (1967) suggested

$$\left.\frac{\partial u}{\partial y}\right|_{y=0} = \frac{\alpha}{\sqrt{æ}}\left(u_{slip} - u_{p.m.}\right) \tag{4.9}$$

where:
$u_{\text{slip}} = u(y=0)$
$u_{p.m.}$ is the averaged superficial velocity well below the interface

More realistic interface conditions are given by Ochoa-Tapia and Whitaker (1995):

$$u = v \tag{4.10a}$$

and

$$\frac{1}{\varepsilon}\frac{du}{dy} - \frac{dv}{dy} = \frac{\beta}{\sqrt{æ}}u \tag{4.10b}$$

where æ, β and ε are measured coefficients.

### 4.1.2 Modeling of Flow through Saturated Porous Media

Two examples illustrate the background of Darcy's law (see Example 4.1) and a possible derivation of the hydraulic conductivity $K$ (Example 4.2), while Examples 4.3 and 4.4 demonstrate the application of extensions to Darcy's law.

**Example 4.1: Darcy's Experiment**

Sketch 1 depicts the basic setup of Darcy's experiment. In terms of the form factor $\phi \equiv A/l$ of the porous slab, find the flow rate for the given data, that is, $A = 10$ m$^2$, $l = 1.5$ m, $h = 1.0$ m, and the Darcy coefficient $k = \gamma K = 0.5$ cm/s, where $\gamma \equiv \rho g$. Derive also Darcy's law.

**Sketch 1**

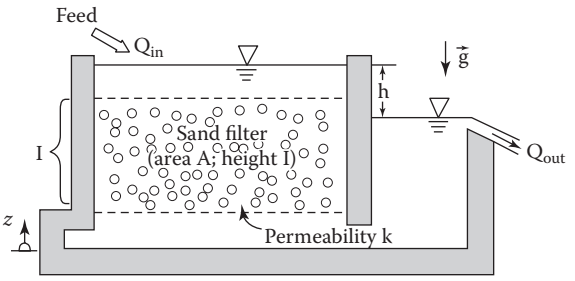


**Assumptions**

- Steady laminar flow with $Re \leq 1.0$
- Height $h$ kept constant
- Constant properties
- Homogeneous "sand-filter" without wall effects

*Method:*

- Bernoulli and mass conservation

*Solution:*

- Based on dimensional analysis, we can state:

$$Q = Q\left(\underbrace{æ, \mu}_{\sim k \text{ or } K}; v; A; \underbrace{h, l}_{\sim \Delta p}\right) \tag{E.4.1.1}$$

- From laboratory observations:

$$\frac{Q}{A} \sim \frac{h}{l} \quad \text{or} \quad \frac{Q}{A} \sim \frac{\Delta p}{\rho g L} \quad \text{after Bernoulli} \qquad \text{(see Equation 2.41)}$$

Darcy employed a coefficient of proportionality $k$, so that

$$Q = \left(k\frac{h}{l}\right)A = u_{\text{avg}}A \tag{E.4.1.2}$$

That coefficient depends on both the porous matrix and the fluid properties, that is,

$$k = æ\rho g/\mu \equiv \gamma K \tag{E.4.1.3a,b}$$

where:

| | |
|---|---|
| æ | is the permeability |
| $\gamma = \rho g$ | is the specific weight |
| $K$ | is the *hydraulic permeability* |

From these findings, the previous equations can be formulated, that is,

$$u_{avg} \equiv \langle u \rangle = -K\frac{\partial p}{\partial z} \tag{E.4.1.4}$$

and as a 3-D extension:

$$\nabla p = -\frac{\mu}{æ}\vec{v} \tag{E.4.1.5}$$

For the present problem,

$$\phi \equiv \frac{A}{l} := 6.6 \text{ m and } Q = kh\phi := 0.033 \text{ m}^3/\text{s}$$

*Note:* Typical Darcy coefficients, with $[k] \hat{=} \text{length/time}$, for averaged grain sizes and different soil types are given as follows:

| Soil Type | Clean Gravel | Fine Gravel | Coarse Sand | Fine Sand | Clay |
|---|---|---|---|---|---|
| Grain size (mm) | 4–7 | 2–4 | 0.5 | 0.1 | 0.002 |
| *k*-range (cm/s) | 2.5–4.0 | 1.0–3.5 | 0.01–1.0 | 0.001–0.05 | $10^{-9}$–$10^{-6}$ |

**Example 4.2: Evaluation of the Hydraulic Conductivity**

As discussed, a possible porous-medium model is a structure with $n$ parallel tubes of diameter $d$, representing straight pores or capillaries. Assuming steady laminar fully developed flow in horizontal tubes, find an expression for the hydraulic conductivity $K = æ/\mu$.

| Sketch 2 | Method |
|---|---|
| 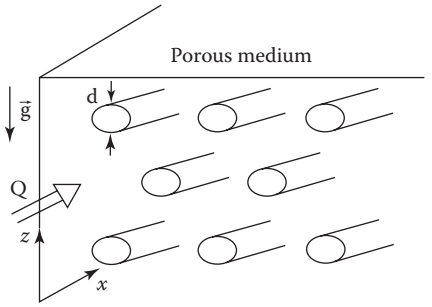  | Equate volumetric flow rate obtained from Poiseuille flow with Darcy's law, where $dp/dx \approx ¢$ and $\langle u \rangle = \frac{Q}{A} = -K\frac{dp}{dx}$ |

*Solution:* Using the Poiseuille-flow result of Equation E.2.6 to obtain the flow rate per pore (or tube) $n$, we have

$$\frac{Q}{n} = v_{av} A_{tube} = -\frac{\pi d^4}{128\mu}\left(\frac{dp}{dx}\right) \tag{E.4.2.1a}$$

As indicated in Figure 4.3, $\langle u \rangle = Q/A := \varepsilon v_{av}$, so that $A = n/\varepsilon\, A_{\text{tube}}$.
Hence,

$$\frac{Q}{n} = \langle u \rangle \frac{1}{\varepsilon} A_{tube} = -K\left(\frac{dp}{dx}\right)\frac{d^2\pi}{4\varepsilon} \tag{E.4.2.1b}$$

so that by inspection,

$$K = \frac{d^2\varepsilon}{32\mu} \tag{E.4.2.2}$$

where the porosity range is $0 < \varepsilon < 1.0$.

*Comments:*

- Once the average pore diameter has been estimated and setting $\varepsilon = 0.5$–$0.7$, with the known fluid viscosity, K and æ can be calculated, and hence, suitable porous medium flow analyses can be carried out.
- Equation E.4.2.2 can be compared to the semi-empirical correlation by Ergun (see Equation 4.3); that is, in both cases, K~$d^2$ and ε.

**Example 4.3: Creeping Flow in a Channel Filled with a Porous Medium**

A slab of homogeneous porous medium of thickness h, bound by impermeable channel walls, represents a good base case for axial flow through porous insulation, a filter, a catalytic converter, tissue, and so on.

| Sketch 3 | Assumptions | Method |
|---|---|---|
| 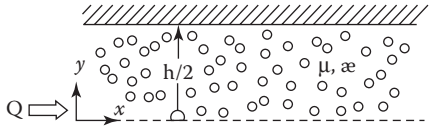 | • Creeping flow, that is, $\langle u \rangle \equiv u$, where $u = u(y)$ only<br>• $\partial p/\partial x = ¢$<br>• Constant properties<br>• Symmetry | Use of the Darcy–Brinkman equation to invoke no slip at channel walls |

*Solution:*
For the present case, the 1-D form of Equation 4.8 without the "high-speed" Forchheimer term reads:

$$\frac{dp}{dx} = -\frac{\mu}{æ}u + \mu\frac{d^2u}{dy^2} = ¢ \tag{E.4.3.1a}$$

or

$$\frac{d^2u}{dy^2} - \frac{1}{æ}u = \frac{1}{\mu}\left(\frac{dp}{dx}\right) = ¢ \tag{E.4.3.1b}$$

subject to $u\left(y = \frac{h}{2}\right) = 0$ and $du/dy = 0$ at $y = 0$.
The homogeneous solution to Equation E.4.3.1b can be found on page 130 of Polyanin and Zaitsev (1995) or in other math handbooks:

$$u(y) = -\frac{æh}{\mu}\left(\frac{dp}{dx}\right)\left[1 - \frac{\cosh\left(y/\sqrt{æ}\right)}{\cosh\left(h/\sqrt{æ}\right)}\right] \tag{E.4.3.2}$$

An *effective* hydraulic conductivity can be estimated, given the channel flow rate per unit depth, that is,

$$\hat{Q} = 2\int_0^{h/2} u\,dy := -\frac{æh}{\mu}\left(\frac{dp}{dx}\right)\left[1 - \frac{2\sqrt{æ}}{h}\tanh\left(\frac{h}{2\sqrt{æ}}\right)\right] \tag{E.4.3.3}$$

Defining $K_{eff}$ as $\bar{u}/(dp/dx) = -\dfrac{\hat{Q}/h}{dp/dx}$ we obtain

$$\frac{K_{eff}}{æ/\mu} \equiv \frac{K_{eff}}{K} = 1 - \frac{2\sqrt{æ}}{h}\tanh\left(\frac{h}{2\sqrt{æ}}\right) \tag{E.4.3.4}$$

*Graphs 1:*

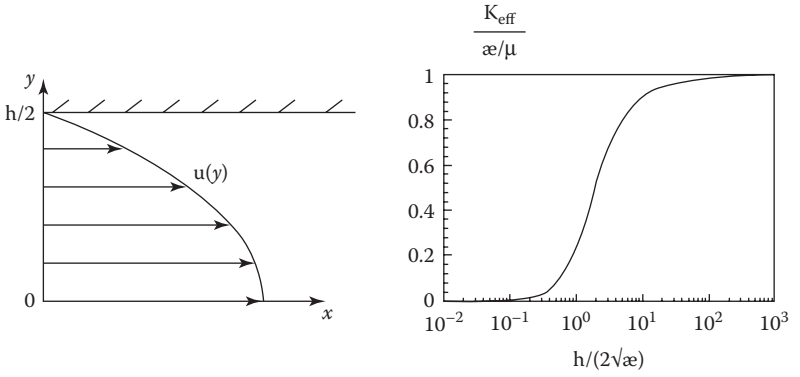


*Comments:*

- The left-hand graph depicts a $u(y)$-profile determined by the (1–cosh $y$)-function, to be compared to Equation E.4.3.1b with Equation E.2.6 for Poiseuille-type flow without gravitational effect.
- The right-hand graph shows the expected nonlinear increase of the non-dimensionalized $K_{eff}$ with channel height $h$.

**Example 4.4: Radial Flow through a Porous-Walled Tube**

Consider pressure-driven flow in the radial direction through a porous tubular wall. Applications include radial flow in a porous pipe, ultrafiltration, tubular filter or membrane, seepage into a lymph vessel, and so on. For the given system (see Sketch 4), find the radial $p(r)$ distribution and $v(r)$ profile as well as the added mass flow rate over the tube length $L$.

| Sketch 4 | Assumptions | Method |
|---|---|---|
| 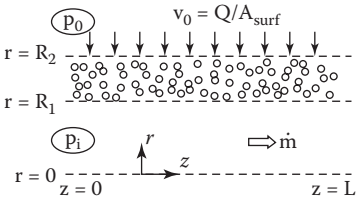  | • Steady radial seepage in $R_1 \le r \le R_2$<br>• Constant pressures and properties<br>• No gravity effect | • Darcy's law: $\vec{\mathbf{v}} = -\frac{\kappa}{\mu}\nabla p$ where $\vec{\mathbf{v}} = (0,\ v,\ 0)$ and $v = v(r)$<br>• Mass balance |

*Solution:*
Writing Equation 4.8 in reduced form (see Assumptions and Method),

$$\vec{\mathbf{v}} = -\frac{æ}{\mu}\nabla p \tag{E.4.4.1}$$

Taking the divergence of Equation E.4.4.1, we have with $\nabla \cdot \vec{\mathbf{v}} = 0$ (see continuity equation for incompressible fluids)

$$0 = -\frac{æ}{\mu}\nabla^2 p \tag{E.4.4.2}$$

where $\nabla^2$ is the Laplacian operator (Appendix AI.1.2).
For our 1-D case in cylindrical coordinates, Equation 4.4.2 is simply

$$\frac{1}{r}\frac{d}{dr}\left(r\frac{dp}{dr}\right)=0 \tag{E.4.4.3}$$

subject to $p(r=R_1)=p_i$ and $p(r=R_2)=p_0$. Note that the internal pressure $p_i$ is a constant value averaged over the tube length.
Double integration leads to

$$p(r) = C_1 \ln r + C_2 \tag{E.4.4.4a}$$

Invoking the boundary conditions (BCs) where $p_0 > p_i$, we have

$$\frac{p-p_i}{p_o-p_i}=\frac{\ln(r/R_1)}{\ln(R_2/R_1)} \tag{E.4.4.4b}$$

Now, with Darcy's law in the $r$-direction, that is,

$$v=-\frac{æ}{\mu}\left(\frac{dp}{dr}\right) \tag{E.4.4.5a}$$

we obtain with the given $p(r)$ and $\Delta p \equiv p_0 - p_i$

$$v(r)=-\frac{æ}{\mu}\frac{\Delta p}{\ln(R_2/R_1)}\frac{1}{r} \tag{E.4.4.5b}$$

A radial mass balance provides the added mass flow rate

$$\Delta\dot{m}=-\rho v\big|_{r=R_1} A_{\text{surface}} \tag{E.4.4.6a}$$

where $A_{\text{surface}}=2\pi R_1 L$, so that

$$\Delta\dot{m}=\frac{2\pi æ\rho\Delta p}{\mu\ln(R_2/R_1)}L \tag{E.4.4.6b}$$

*Graph 2:*

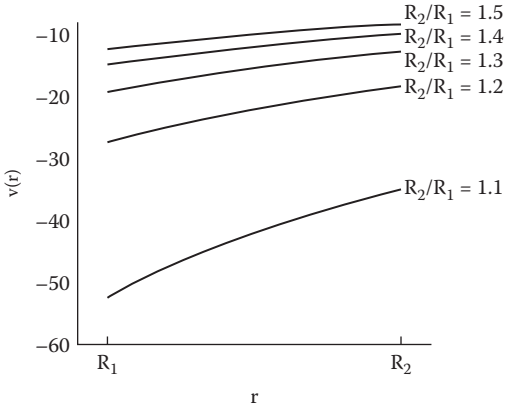


*Comments:*

- The $v(r)$-function Equation E.4.4.5b is hyperbolic; that is, for a given $\Delta p$, æ, μ, and geometry, $v$ decreases inversely with $r$; however, as $A_{surface} = A(r)$ as well, the product $Av = Q$ is constant everywhere.
- As expected, radial mass influx increases with wall permeability, tube length, and pressure difference.
- This simple example may relate to radial flow through capillary tissue or across a tubular membrane, filter, and so on.

## 4.2 Pseudo Two-Phase Flows

As demonstrated in Section 4.2.1, with some nifty assumptions/concepts, solving quasi-homogeneous flow problems is rather straightforward. The requirement is that the two phases form a near-perfect mixture with effective properties and that the phases are in thermodynamic equilibrium, that is, no velocity-slip between particles and fluid as well as locally equal temperatures. Similarly, basic non-Newtonian fluids as well as flows with drift flux (Kleinstreuer, 2003) fall also into the category of flow mixture models and hence can be solved as single-phase flows. However, when a given fluid-particle system deviates from the underlying assumptions of "quasi-homogeneous flow," alternative solution methods should be considered (see Figure 4.2 and Section 4.3).

### 4.2.1 Quasi-Homogeneous Mixture Flows

Of the various modeling and simulation approaches outlined, the easiest one is based on the assumption of a *quasi-homogeneous mixture*, for which, in straight conduits, analytic or approximate solutions exist. Focusing on such mixture flows with well-dispersed particles, the dispersed phase is characterized by the particle volume fraction, mass concentration, and loading. In light of the continuum assumption (see Section 1.1), all quantities are defined as volume ratios. For these ratios, the mixture volume sample cannot approach zero but a small volume $\delta\forall'$, so that the molecular range is excluded. It should be noted that in the open literature, *subscripts c, f, or 1* all indicate the continuous phase or carrier fluid, while *subscripts p, d, or 2* all refer to the particle or dispersed phase. For example, the volume (or void) fraction of the dispersed phase is

$$\alpha_d \equiv \alpha = \lim_{\delta\forall \to \delta\forall'} \frac{\delta\forall_d}{\delta\forall} := \frac{\forall_{\text{particles}}}{\forall_{\text{mixture}}} \tag{4.11}$$

Then, the volume fraction of the continuous fluid phase is

$$\alpha_c = \lim_{\delta\forall \to \delta\forall'} \frac{\delta\forall_c}{\delta\forall} := \frac{\forall_{\text{fluid}}}{\forall_{\text{mixture}}} \tag{4.12a,b}$$

so that

$$\alpha_d + \alpha_c = 1 \tag{4.13}$$

With the two-phase volume fractions defined, the mixture (or effective) density is

$$\rho_m = \alpha_c \rho_c + \alpha_d \rho_d \approx \bar{\rho}_c + \bar{\rho}_d \tag{4.14a,b}$$

where $\overline{\rho}_d = n\, m_p$, with $n$ being the number of particles per unit volume and $m_p$ being the particle's mass. The dispersed-phase concentration is given as

$$c = \frac{\overline{\rho}_d}{\overline{\rho}_c} \tag{4.15}$$

The local loading is the mass-flux ratio:

$$r = \frac{\overline{\rho}_d \overline{v}_p}{\overline{\rho}_c \overline{v}_c} \tag{4.16a}$$

while the total loading is

$$\kappa = \dot{m}_d / \dot{m}_c \approx \overline{\rho}_d / \overline{\rho}_c = c \tag{4.16b}$$

This implies that $k$ is approximately equal to the concentration $c$. Clearly, the mixture mass flow rate, important for internal flows, is

$$\dot{m}_m = \dot{m}_c + \dot{m}_d = (\rho Q)_c + (\rho Q)_d \tag{4.17a,b}$$

which leads to the "quality" (i.e., particle mass concentration)

$$x = \dot{m}_d / \dot{m}_m \tag{4.18}$$

In contrast, the mixture mass flux is

$$G_m = \frac{\dot{m}_m}{A} = G_c + G_d \tag{4.19a,b}$$

and the volume flux is

$$j_m = \frac{G_m}{\rho_m} = \frac{Q_c + Q_d}{A} = j_c + j_d = v_m \tag{4.20a through d}$$

where $v_\mathrm{m}$ is the superficial velocity of the mixture, which is composed of the phase superficial velocities

$$v_{c,s} = \alpha_c\, v_c \quad \text{and} \quad v_{d,s} = \alpha_d\, v_d \tag{4.21a,b}$$

while the actual phase velocities are

$$v_c = j_c / \alpha_c \quad \text{and} \quad v_d = j_d / \alpha_d \tag{4.22a,b}$$

Finally, the relative (or slip) velocity between the two phases is

$$v_r = v_c - v_d \tag{4.23}$$

The drift velocity, which indicates deviatory motion of the particle phase from the mixture flow, is

$$v^{\text{drift}} = v_d - v_m \tag{4.24}$$

With these basic phase definitions established, we can now consider mixture properties, such as density $\rho_m$ and dynamic viscosity $\mu_m$ (see Figure 4.5). Specifically,

$$\rho_m = \alpha\rho_2 + (1-\alpha)\rho_1 \tag{4.25a}$$

or

$$\frac{1}{\rho_m} = \frac{x}{\rho_2} + \frac{1-x}{\rho_1} \tag{4.26b}$$

where $\alpha \equiv \alpha_2 = \forall_2 / \forall = \forall_d / \forall_m$ and $x = \dot{m}_2 / \dot{m}$. At low-volume fractions of spherical particles (say, $\alpha \leq 0.05$), the mixture viscosity is (Soo, 1990; Zapryanov and Tabakova, 1999)

$$\mu_m = \mu_1\left(1 + 2.5\alpha\frac{\mu_2 + 0.4\mu_1}{\mu_2 + \mu_1}\right) \tag{4.27}$$

which for $\mu_2 \gg \mu_1$ reduces to

$$\mu_m\big|_{\text{solid spheres}} = \mu_1(1 + 2.5\alpha) \tag{4.28}$$

where range for the particle volume fraction is $0 < \alpha < 0.05$. Now, with $\mu_1 \gg \mu_2$ and again $0 < \alpha < 0.05$,

$$\mu_m\big|_{\text{gas bubbles}} = \mu_1(1 + \alpha) \tag{4.29}$$

Similarly to Equation 4.26b, for well-dispersed gas–liquid flows, for example, droplets in air or bubbles in liquid flow, we have

$$\frac{1}{\mu_m} = \frac{x}{\mu_2} + \frac{1-x}{\mu_1} \tag{4.30}$$

or

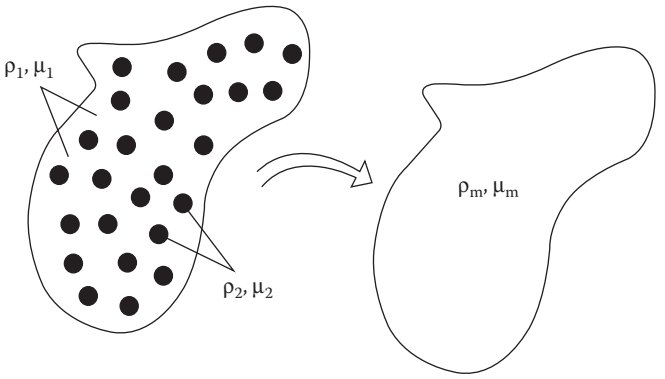


**FIGURE 4.5**
Approximation of two-phase (dispersed particle) flow to a uniform mixture flow.

$$\mu_m = \alpha\mu_2 + (1-\alpha)\mu_1 \tag{4.31}$$

The next two examples deal with quasi-homogeneous mixture flows as extensions to the single-fluid flow solutions discussed in Chapter 3.

**Example 4.5: Poiseuille-Type Mixture Flow**

Consider steady laminar fully developed pipe flow (radius $R$, length $L$) where the "void" fraction of solid particles in air ranges from $\alpha = 0$ to $\alpha = 0.05$. Find $u(r)$ and plot $u/u_{max}$ vs. $r/R$.

| Sketch 5 | Assumptions | Method and Postulates |
|---|---|---|
| 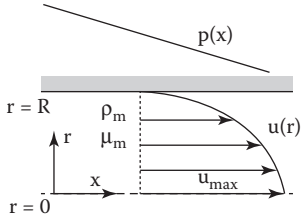 | • Poiseuille flow<br>• One-way coupling<br>• Quasi-homogeneous mixture flow<br>• Constant mixture properties<br>• Particles and fluid elements are in thermodynamic equilibrium | • Reduced N-S equations<br>• Constant $-dp/dx = \Delta p/L$<br>• Axial velocity $u = u(r)$ only<br>• Mixture viscosity: $\mu_m = \mu_1(1-2.5\alpha)$<br>• where $\alpha \equiv \frac{\forall_{\text{particles}}}{\forall_{\text{mixture}}}$ |

*Solution:* Based on the assumptions, continuity is fulfilled, and the $x$-momentum equation reduces to (see Example 3.2)

$$0 = -\frac{dp}{dx} + \frac{\mu}{r}\frac{d}{dr}\left(r\frac{d}{dr}\right) \tag{E.4.5.1}$$

subject to $u(r=R)=0$ and $du/dr\big|_{r=0} = 0$. Hence,

$$u(r) = \underbrace{\frac{R^2}{4\mu_m}\left(\frac{\Delta p}{L}\right)}_{u_{\max}}\left[1-\left(\frac{r}{R}\right)^2\right] \tag{E.4.5.2}$$

where, according to Equation 4.28,

$$\mu_m = (1+2.5\alpha)\mu_{\text{fluid}} \quad \text{for} \quad 0 \le \alpha \le 0.05 \tag{E.4.5.3}$$

*Graph 3:*

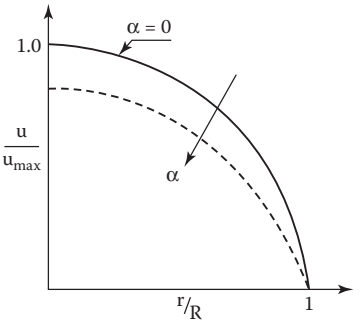


*Comments:*

- Clearly, for $\alpha = 0$, the original Poiseuille flow is recovered.
- Note that Equation E.4.5.2 looks the same as the Poiseuille-flow solution, except for $u_{max}$ being dependent on $\mu_m$, which in turn, is a function of $\alpha$.
- When $\alpha > 0$, the flow rate decreases for the same (given) pressure drop because of the higher resistance, and hence, the velocity profile is flatter.

**Example 4.6: Bubbly Pipe Flow**

Of interest are the total pressure drop and void fraction of steady turbulent bubbly flow in a vertical pipe ($D = 25$ mm, $L = 45$ cm). The upward flow is a mixture of water ($m_l = 0.42$ kg/s, $\rho_l = 10^3$ kg/m$^3$) and air bubbles ($m_g = 0.01$ kg/s, $\rho_g = 1.1777$ kg/m$^3$).

| Sketch 6 | Assumptions | Method/Concepts |
|---|---|---|
| 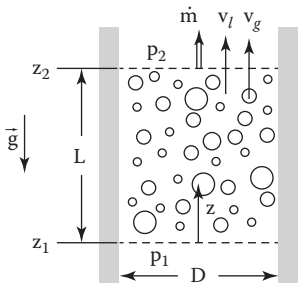  | • Steady fully developed turbulent flow with near-uniform velocities<br>• Thermodynamic equilibrium, that is, $v_g = v_l$ and $T = \not\in$ | • Constant mixture properties $\rho_m$ and $\mu_m$<br>• Extended Bernoulli equation<br>• Blasius friction factor for smooth pipes $f = 0.316\,\mathrm{Re}_D^{-1/4}$<br>• Void fraction $\alpha = Q_g/Q$ |

*Solution*:

Mass Conservation: $\dot{m} = \dot{m}_\ell + \dot{m}_g$ and hence, $v = v_\ell = v_g = \dot{m}/(\rho_m A)$, while quality $x = \dot{m}_g / \dot{m}$

- Mixture Properties (see Equations 4.26b and 4.30):

$$\rho_m = \left( \frac{x}{\rho_g} + \frac{1-x}{\rho_\ell} \right)^{-1} \quad \text{and} \quad \mu_m = \left( \frac{x}{\mu_g} + \frac{1-x}{\mu_\ell} \right)^{-1} \qquad \text{(E.4.6.1 and 2)}$$

Thus, the numerical property values with $x = 0.023$ and $v = 17.65$ m/s are as follows:

$$\rho_m \equiv \rho = 49.64 \text{ kg/m}^3,\ \mu_m \equiv \mu = 4.435 \times 10^{-4} \text{ kg/(m s)},\ \text{and } \mathrm{Re}_D = \rho v D/\mu = 49{,}388$$

- After Blasius (see Section 3.2.1), the pipe friction factor for turbulent flow is

$$f = \frac{0.316}{\mathrm{Re}_D^{0.25}} = 0.0212 \qquad \text{(E.4.6.3)}$$

- The extended Bernoulli equation reads (see Section 2.33):

$$\frac{p_1}{\rho g} + \frac{v_1^2}{2g} + z_1 = \frac{p_2}{\rho g} + \frac{v_2^2}{2g} + z_2 + h_f \qquad \text{(E.4.6.4)}$$

where

$$h_f = f\left(\frac{L}{D}\right)\frac{v^2}{2g} \qquad \text{(E.4.6.5)}$$

Hence,

$$\Delta p = \Delta z + h_f := 31.7\,\text{kN/m}^2 \tag{E.4.6.6}$$

- The volumetric flow rates for the two phases are

$$Q_i = \left(\frac{\dot{m}}{\rho}\right)_i := \begin{cases} 0.00833\ \text{m}^3/\text{s} & <\text{bubbles}> \\ 0.00042\ \text{m}^3/\text{s} & <\text{water}> \end{cases} \tag{E.4.6.7a,b}$$

- Hence, the void fraction is

$$\alpha = \frac{\forall_g}{\forall} = \frac{Q_g}{Q} := 0.96 \tag{E.4.6.8}$$

*Comments:*

- Although the quality ($x = 0.023$) is rather low, the almost 1000-fold density difference between the carrier fluid and the air-bubbles generates 20× the volumetric flow rate for air when compared with water flow.
- As a result, $\alpha = 0.96$; that is, the pipe is mainly filled with air bubbles, under the assumption of homogeneous equilibrium flow.

As discussed and illustrated, certain two-phase flows can be treated as a single-phase flow if both phases are in quasi-thermodynamic equilibrium; that is, their properties, velocities, and temperatures do not deviate measurably. The flow regimes for gas–liquid flows are typically bubbly or misty flows, while for solid-particle-suspension flows, the void fraction is assumed to be very low—say, less than 5%—and the relative velocity, $u_{\text{fluid}} - v_{\text{particle}}$, being minor. *Area-averaging of both phases and the use of mixture properties result in 1-D transport equations.* Specifically, for a conduit of area $A$ and inclined angle $\theta$, we obtain the following flow-system equations (see homework assignment [HA] in Section 4.4):

*Continuity:*

$$A\frac{\partial \rho}{\partial \rho} + \frac{\partial}{\partial x}(\rho\, v\, A) = 0 \tag{4.32}$$

*Momentum:*

$$A\frac{\partial(\rho v)}{\partial t} + \frac{\partial}{\partial x}(\rho\, v\, v\, A) = -\frac{\partial(pA)}{\partial x} + \tau_w\, P + \rho\, g\, A \sin\theta \tag{4.33}$$

*Energy:*

$$\frac{\partial(\rho e)}{\partial t} + \frac{1}{A}\frac{\partial}{\partial x}(v\, A\, \rho\, e) = \frac{P}{A} q_w + q_{\text{gen}} + \frac{\partial P}{\partial t} \tag{4.34}$$

where:

$\tau_w$ is the wall shear stress
$P$ is the conduit perimeter
the specific energy is $e = h + v^2/2 + g_x \sin\theta$, with $h = u + p/\rho = h_c + x(h_\alpha - h_c)$ being the enthalpy
$q_w$ is the wall heat flux
$q_{\text{gen}}$ is the internal heat generation, say, due to viscous effects or chemical reaction

For steady homogeneous mixture flow in a rigid pipe of diameter $D$, the momentum Equation 4.33 reduces to

$$-\frac{dp}{dx} = \frac{\Delta p}{L} = \frac{\partial}{\partial x}(\rho\, v\, v) + \frac{4\tau_w}{D} + \rho\, g\, \sin\theta \tag{4.35}$$

while the energy Equation 4.34 becomes with $dh = c_p dT$ the heat transfer equation:

$$\rho c_p \frac{dT}{dx} = -\frac{d}{dx}\left(\frac{\rho}{2} v^2\right) + \frac{4q_w}{vD} + \frac{q_{\text{gen}}}{v} - \rho g \sin\theta \tag{4.36}$$

Knowing the quality $x = \dot{m}_d / \dot{m}$, we can express the mixture density as

$$\rho = \frac{\rho_d\, \rho_c}{\rho_c x + \rho_d (1 - x)} \tag{4.37}$$

and the void fraction as

$$\alpha = \frac{x}{x + (1 - x)\rho_d / \rho_c} \tag{4.38}$$

while the momentum flux is

$$\rho v = (\dot{m}_c + \dot{m}_d) / A = \dot{m} / A \tag{4.39}$$

Now, omitting the inertial and gravitational forces, Equation 4.35 can be greatly simplified. Specifically, for the wall shear stress, we recall $\tau_w \sim \Delta p/L \sim h_f = h_f(f, L/D, v^2)$, as discussed in Section 2.3.3. Hence,

$$-\left.\frac{dp}{dx}\right|_{\text{friction}} = \frac{4\tau_w}{D} = \frac{2f\, \rho\, v^2}{D} \tag{4.40}$$

where Beattie and Whalley (1982) suggested for the annular and bubbly regimes (see Figure 4.4)

$$f^{-1/2} = 3.48 - 4\log_{10}\left[2\left(\frac{\varepsilon}{D}\right) + \frac{9.35}{\text{Re}\sqrt{f}}\right] \tag{4.41}$$

The Reynolds number $\text{Re}_D = \rho_{vD}/\mu$ requires the evaluation of the dynamic viscosity, for example,

$$\mu = \left( \frac{x}{\mu_d} + \frac{1-x}{\mu_c} \right) \tag{4.42}$$

An application of 1-D homogeneous mixture flow is given in Umbarkar and Kleinstreuer (2015), among others.

### 4.2.2 Non-Newtonian Fluid Flow

We recall that gases and small-molecule liquids (e.g., water and basic oils) are Newtonian. The main reason is that the random, thermally driven molecular actions (i.e., spin, vibration, and translation, as well as collision) within such fluids are very strong. Such vigorous kinetics completely overcomes any tendency of any applied forces to produce a molecular configuration state (i.e., local molecular restructuring) that differs significantly from the isotropic, homogeneous state of statistical equilibrium. So, as a result of any externally induced shear stress ($F_{\text{tangential}}/A$), fluid mass displaces, that is, it flows continuously without changing the fluid configuration on the molecular level. *Non-Newtonian* fluids behave quite differently. They are macro-molecule fluids (MW > 400); for example, toothpaste, foodstuffs, paints, exotic oils, polymeric liquids, and multi-fluid blends, as well as particle suspensions, including blood (when $\dot{\gamma} < 200\ \text{s}^{-1}$), and slurries.

For Newtonian fluids, such as air, water, and basic oils, Stokes' hypothesis of a *linear* relationship between shear stress and shear rate holds (Section 2.3). In contrast, non-Newtonian fluids exhibit nonlinear viscous effects (see Figure 4.6). Shear-rate dependence and/or memory of the viscosity of such fluids is due to their component make-up and/or molecular structure (Tanner and Walters, 1998; Macosko, 1994; Bird et al., 1987). Assuming steady incompressible isothermal fluid flow, only shear rate- (or shear stress)-dependent liquids are considered; that is,

$$\tau_{ij} = \mu\, \dot{\gamma}_{ij} \text{ is now replaced by } \tau_{ij} = \eta\left(\dot{\gamma}, \tau\right)\dot{\gamma}_{ij} \tag{4.43, 4.44}$$

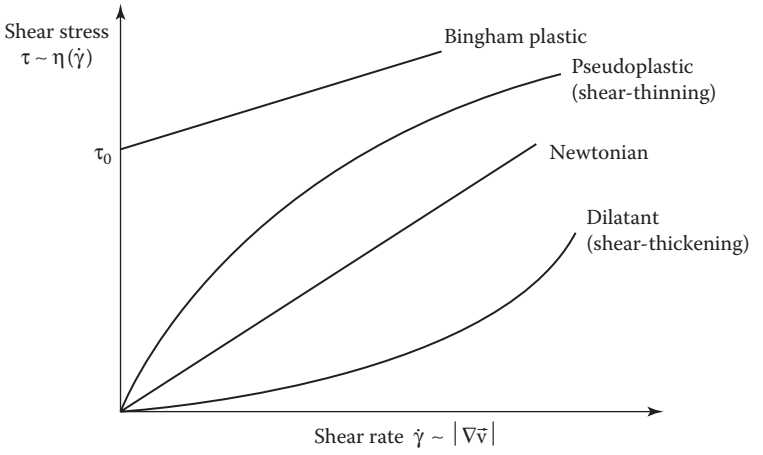


**FIGURE 4.6**
Stress/shear rate–dependent behavior of fluids.

Here, η is the non-Newtonian (or apparent) viscosity. Clearly, complex non-Newtonian fluid flow phenomena such as rotating-rod climbing and jet-swelling after extrusion or the visco-elastic effect of fluid recoil, stress relaxation, and overshoot are not discussed (see Tanner and Walters, 1998).

#### 4.2.2.1 Internal Flow of Power-Law Fluids

As is deducible from Equation 4.43 versus Equation 4.44, viscous inelastic liquids are also labeled *generalized Newtonian fluids* because of their similar constitutive equations. The simplest empiricism for $\eta(\dot{\gamma})$ is the two-parameter power law expression:

$$\eta = m\dot{\gamma}^{n-1} \tag{4.45}$$

where the constants $m$ and $n$ characterize the fluid. Clearly, when $n=1$, then $m=\mu$, and Equation 4.43 is recovered. If $n<1$, the fluid exhibits shear-thinning (i.e., pseudo-plastic) behavior, while for $n>1$ the fluid is called dilatant (or shear-thickening) as shown in Figure 4.6. Although the power law is widely used, the parameters $m$ and $n$ are not actual fluid properties, and it cannot describe the viscosity at very low shear rates (e.g., blood). When Equation 4.45 is used to model viscous inelastic liquid flows, the point of departure is the reduced *equation of motion* (i.e., the Cauchy equation of Appendix AI.5.2), not the N-S equation, which implies constant fluid properties. For example, considering steady unidirectional flow, the simplified forms of Equation 2.26 read:

$$0 = -\frac{dp}{dx} + \frac{d\tau_{yx}}{dy} \quad \text{for planar Couette flows} \tag{4.46}$$

$$0 = \frac{d\tau_{yx}}{dy} + \rho g \sin\theta \quad \text{for thin-film flow} \tag{4.47}$$

$$0 = -\frac{dp}{dx} + \frac{1}{r}\frac{d}{dr}\left(r\tau_{rx}\right) \quad \text{for tubular Poiseuille flow} \tag{4.48}$$

Examples 4.7 and 4.8 illustrate the use of Equations 4.46 through 4.48; that is, problem solutions of Chapters 2 and 3 are extended with applications to power-law fluids.

**Example 4.7: Power-Law Fluid Flow in a Slightly Tapered Tube**

| Sketch 7 | Assumptions and Postulates | Method |
|---|---|---|
| 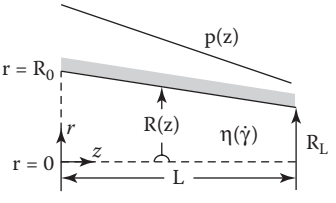 | • Steady laminar unidirectional flow<br>• Power-law fluid<br>*Postulates:*<br>• $\vec{v}=\left[v_z(r,z);0;0\right]$<br>• $-\partial p/\partial z = \Delta p/L = \not\subset$ | • Solve Equation 4.48 with reduced form of $\tau_{rz}$, assuming $v_z = v_z(r)$ only<br>• However, $v_z(r, z)$ dependence appears via no-slip condition |

*Solution:*

- Slightly tapered tube:

$$R(z) = R_0 - \frac{R_0 - R_L}{L} z \tag{E.4.7.1}$$

- Shear stress and power law (Appendix AI.6.6):

$$\tau_{rz} = \eta \frac{dv_z}{dr} \text{ and } \eta = m\dot{\gamma}^{n-1} = m\left(\frac{dv_z}{dr}\right)^{n-1}$$

so that

$$\tau_{rz} = m\left(-\frac{dv_z}{dr}\right)^n \tag{E.4.7.2}$$

where the negative sign ensures that $\dot{\gamma}$ stays a positive quantity.

- $z$-momentum Equation 4.48:

$$\frac{1}{r}\frac{d}{dr}(r\,\tau_{rz}) = -\frac{p_0 - p_L}{L} \tag{E.4.7.3a}$$

or after integration

$$\tau_{rz} = -\frac{\Delta p}{2L} r + \frac{C_1}{r} \tag{E.4.7.3b}$$

- Clearly, $C_1 \equiv 0$, because at the centerline $r = 0$, but $\tau_{rz}$ is finite; actually, $\tau_{rz}(r=0) = 0$, as can be seen from a 1-D force balance for fully developed flow:

$$\tau_{rz} = -\frac{\Delta p}{2L} r = \tau_w \frac{r}{R} \tag{E.4.7.4a,b}$$

Combining Equations E.4.7.3b with E.4.7.2 and E.4.7.4b yields

$$m\left(-\frac{dv_z}{dr}\right)^n = \tau_w \frac{r}{R} \tag{E.4.7.5}$$

Taking the $n$th root of both sides and integrating results in

$$v_z = -\left(\frac{\tau_w}{mR}\right)^{1/n} \frac{n\, r^{\frac{n+1}{n}}}{n+1} + C_2 \text{ subject to } v_z\left[r = R(z) \;=\; R_0 - \frac{R_0 - R_L}{L} z\right] = 0$$

Thus,

$$v_z(r,z) = \underbrace{\left[\left(\frac{\tau_W}{mR(z)}\right)^{1/n} \frac{n\,R(z)}{n+1}\right]}_{v_{\max}} \left[1 - \left(\frac{r}{R(z)}\right)^{\frac{n+1}{n}}\right] \tag{E.4.7.6}$$

where $\tau_w = -\frac{\Delta p}{2L} R$ from Equation E.4.7.5.

- Pressure drop based on volumetric flow rate given a Q-value and with

$$Q = \int_A \vec{v} \cdot d\vec{A} = 2\pi \int_0^R v_z(r, z) r dr$$

we obtain

$$\Delta p = \frac{2mL}{3n}\left[\frac{Q}{n\pi}(3n+1)\right]^n \left(\frac{R_L^{-3n} - R_0^{-3n}}{R_0 - R_L}\right) \tag{E.4.7.7}$$

*Graph 4:*

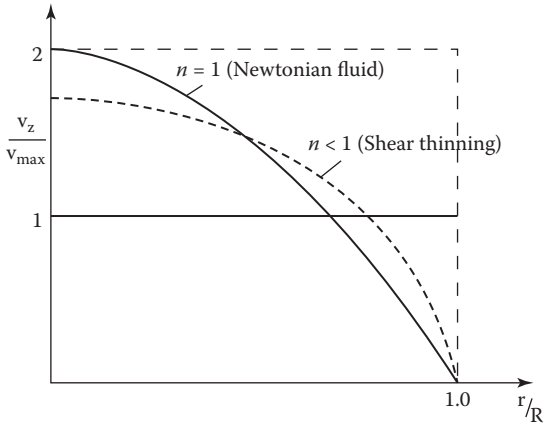


*Comments:*

- With $n < 1.0$, the axial velocity profile becomes flatter because of the shear-thinning effect.
- It is of interest to compare these profiles with the results of Example 4.5 for dilute homogeneous particle suspension flows.

**Example 4.8: Film Thickness of a Flowing Polymer**

Consider a steady laminar thin layer ($h = \not<$) of a power-law fluid ($m$, $n$) moving down an incline (angle θ, width $w$) with a volumetric flow rate $Q$. Find the film thickness $h$.

| Sketch 8 | Assumptions | Method |
|---|---|---|
| 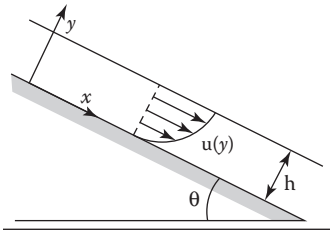  | • Steady laminar unidirectional flow<br>• No surface ripples, that is, $h$ = constant | • Equation 4.47 subject to no-slip and zero interface stress conditions<br>• Power law |

*Solution:*

Integration of Equation 4.47 subject to $\tau_{interface} = \tau_{yz}(y = h) = 0$ yields

$$\tau_{yx} = \rho g h \sin\theta \left(1 - \frac{y}{h}\right) \tag{E.4.8.1}$$

Equation E4.8.1 implies that $\tau_{xz}(y=0)=\tau_{\text{wall}}=\rho g h \sin\theta$. Now, with $\tau_{yx}=m\left(-\frac{du}{dy}\right)^n$ and after taking the $n$th root yields

$$-\frac{du}{dy}=\left[\frac{\rho\, g\, h\sin\theta}{m}\left(1-\frac{y}{h}\right)\right]^{1/n} \tag{E.4.8.2a}$$

Integration subject to $u(y=0)=0$ results in

$$u(y)=C\left[1-\left(1-\frac{y}{h}\right)^{\frac{n+1}{n}}\right] \tag{E.4.8.2b}$$

where

$$C\equiv\left(\frac{\rho\, g\, h\sin\theta}{m}\right)^{1/n}\frac{n\,h}{n+1} \tag{E.4.8.2c}$$

The volumetric flow rate is

$$Q=w\int_0^h u(y)\,dy=w\,h\,C\left(1-\frac{n}{2n+1}\right) \tag{E.4.8.3a}$$

$$Q=\frac{w\,h^2\,n}{2n+1}\left(\frac{\rho\, g\, h\sin\theta}{m}\right)^{1/n} \tag{E.4.8.3b}$$

Given $Q$, we can solve for the film thickness, that is,

$$h=\left(\frac{m}{\rho\, g\sin\theta}\right)^{1/(2n+1)}\left[\frac{(2n+1)Q}{n\,w}\right]^{n/(2n+1)} \tag{E.4.8.4}$$

*Graph 5:*

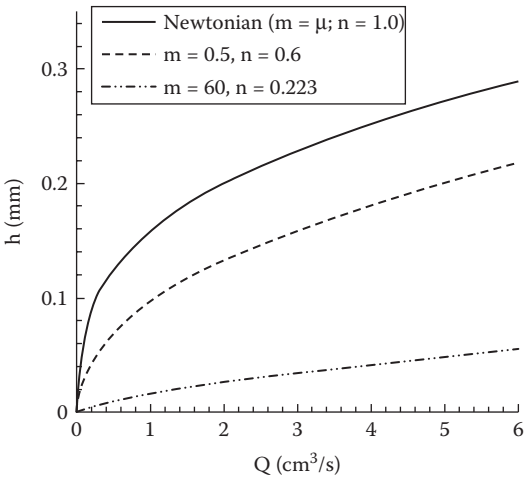

*Comments:*

- As expected, $h(Q)$ is a nonlinearly increasing function.
- As mentioned, power-law fluids with $n < 1.0$ are shear-thinning, which generates a blunter velocity profile (see Example 4.5); thus, the film thickness decreases with lower $n$-values.

### 4.2.3 Internal Flow of Bingham Plastics

For thick suspensions and pastes (e.g., ketchup and toothpaste), no flow occurs until a certain critical stress, called the *yield stress* $\tau_0$, is reached. So, only after a sufficient force is applied does the mixture flow like a Newtonian fluid (see Figure 4.6). Such action is described by the two-parameter Bingham model:

$$\eta = \begin{cases} \infty & for \quad \tau < \tau_0 \\ \mu_0 + \dfrac{\tau_0}{\dot{\gamma}} & for \quad \tau \geq \tau_0 \end{cases} \tag{4.49a,b}$$

Equation 4.49 is an illustration of a constitutive equation for a "viscoplastic" material. Example 4.9 illustrates the use of the Bingham model. More accurate but also more complex non-Newtonian fluid models for specific applications are discussed in Bird et al. (1987), Macosko (1994) and Tanner and Walters (1998), among other texts. Convection heat transfer results in terms of Nusselt number correlations for pipe and slit flows with power-law fluids are summarized in Bird et al. (2002).

**Example 4.9: Cylindrical Couette Flow with a Bingham Plastic**

Consider two *concentric* cylinders (length $L$, $R_{inner} = kR$, and $R_{outer} = R$) where the outer one rotates at angular velocity $\omega_0$ due to torque $T$, maintaining the steady laminar flow of a Bingham fluid ($\tau_0$, $\mu_0$). Develop a relationship for $T = T(\omega_0; R, k, L; \tau_0, \mu_0)$.

| Sketch 9 | Assumptions/Postulates | Method |
|---|---|---|
| 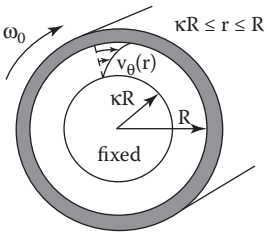 | • Two cases depending on $\tau_{wall} \leq \tau_0$ or $\tau_{wall} > \tau_0$<br>• Constant torque on outer cylinder and slow rotation<br>*Postulates:*<br>• $\vec{v} = \left[0, v_\theta(r), 0\right]$<br>• $\nabla p \Rightarrow \dfrac{dp}{dr}$ only | • Reduced θ-momentum equation with only $\tau_{r,\theta}$ Being non-zero<br>• Bingham fluid model $\eta(\tau)$<br>• Two cases depending on $\tau_{wall}$ relative to $\tau_0$ |

*Solution:*

Note that for Case I, there are actually two scenarios, that is, $\tau(r = R) = \tau_{wall} < \tau_0$ and $\tau_{r,\theta} > \tau_0$ for $r \leq r_0$. For Case II, there will be $\tau_{wall} > \tau_0$ in the entire gap. While continuity is preserved, the θ-momentum equation in cylindrical coordinates (see Appendix AI.6.2) reduces to

$$0 = \frac{1}{r^2}\frac{d}{dr}\left(r^2 \tau_{r\theta}\right) \tag{E.4.9.1}$$

Integration yields

$$\tau_{r\theta} = \frac{C}{r^2} \tag{E.4.9.2}$$

implying two unknowns. Thus, recall

$$\tau_{r\theta}(r = R) = \tau_{\text{wall}} = \frac{T}{2\pi L R^2} = \frac{C}{R^2} \tag{E.4.9.3a through c}$$

and hence, with $C = T/2\pi L$,

$$\tau_{r\theta} = \frac{T}{2\pi L} r^{-2} = \eta\dot{\gamma}_{r\theta} \text{ for } \kappa R < r < R \tag{E.4.9.4a,b}$$

As indicated with Equation 4.49a, b, there is a radial location $r_0$ where $\tau_{r\theta}(r = r_0) = \tau_0$, being the yield stress. So, from Equation E.4.9.4,

$$\tau_0 = \frac{T}{2\pi L r_0^2} \tag{E.4.9.5}$$

Clearly, $r_0$ has to be between $kR$ and $R$ for some form of fluid flow to be observed (see Equation E.4.9.4). Specifically, for $kR < r < r_0$, there will be nonlinear viscous flow and for $r_0 \le r \le R$, there will be uniform (or plug) flow.

Using the shear rate component $\dot{\gamma}_{r\theta} = r\dfrac{d}{dr}\left(\dfrac{v_\theta}{r}\right)$ (see Appendix AI.6.6), we rewrite Equation 4.49b as

$$\tau_{r\theta} = \eta\left[r\frac{d}{dr}\left(\frac{v_\theta}{r}\right)\right] \tag{E.4.9.6}$$

With Equation 4.49b, we have

$$\eta = \mu_0 + \frac{\tau_0}{\dot{\gamma}} = \mu_0 + \frac{\tau_0}{r\dfrac{d}{dr}\left(\dfrac{v_\theta}{r}\right)} \tag{E.4.9.7a, b}$$

so that

$$\tau_{r\theta} = \tau_0 + \mu_0\, r\frac{d}{dr}\left(\frac{v_\theta}{r}\right) \tag{E.4.9.8}$$

Combining Equations E.4.9.8 and E.4.9.5 to solve for $v_\theta(r)$ when $kR < r \le R$, we obtain

$$\frac{d}{dr}\left(\frac{v_\theta}{r}\right) = \frac{T}{2\pi L\mu_0} r^{-3} - \frac{\tau_0}{\mu_0} r^{-1} \tag{E.4.9.9}$$

Integration, assuming that $v_\theta(r = r_0) = r_0\omega_0$, yields for $kR \le r \le r_0$

$$v_\theta(r) = \omega_0 r + \frac{T}{4\pi L\mu_0 r_0}\left(\frac{r}{r_0}\right)\left[1 - \left(\frac{r_0}{r}\right)^2\right] - \frac{\tau_0 r}{\mu_0}\ln\frac{r}{r_0} \tag{E.4.9.10}$$

while for $r_0 \le r \le R$

$$v_\theta = \omega_0 \, r_0 \tag{E.4.9.11}$$

Graph 6 shows schematically the impact regions of Equation E.4.9.10 in light of the $\tau_{r\theta}(r)$ function given by Equation E.4.9.8.

*Graph 6:*

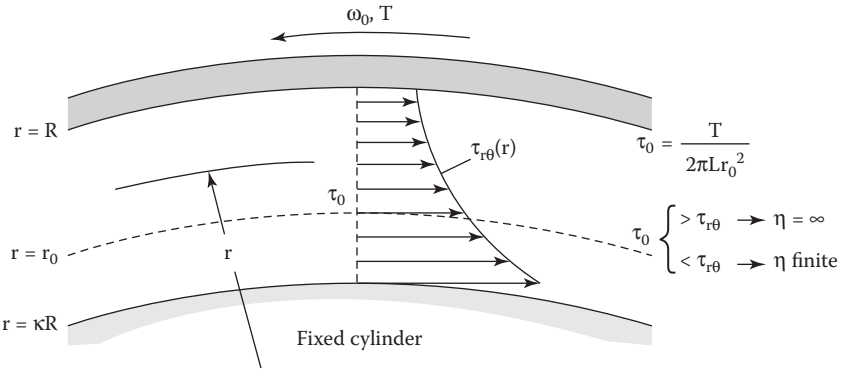


Graph 7 depicts $\nu_\theta(r)$ when $T_0$ is between $\kappa R$ and $R$ (see Graph 6).

*Graph 7:*

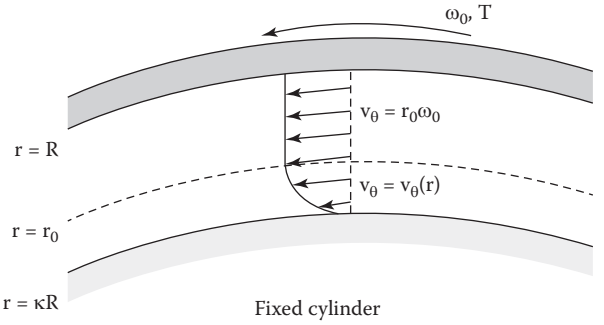


Now, if the yield stress $\tau_0$ is exceeded in the entire gap, that is, $\tau_{wall} > \tau_0$ if $r_0 \ge R$, Equation E.4.9.10 yields with the B.C. $\nu_\theta(r = R) = \omega_0 R$

$$\nu_\theta(r) = \omega_0 \, r + \frac{T}{4\pi L \mu_0 R}\left(\frac{r}{R}\right)\left[1 - \left(\frac{R}{r}\right)^2\right] - \frac{\tau_0 r}{\mu_0}\ln\frac{r}{R} \tag{E.4.9.12}$$

Invoking the no-slip condition $\nu_\theta(r = \kappa R) = 0$ yields the desired expression for the torque:

$$T = \frac{4\pi L \mu_0 (\kappa R)^2}{1 - \kappa^2}\left[\omega_0 - \frac{\tau_0}{\mu_0}\ln\kappa\right] \tag{E.4.9.13}$$

*Comments:*

- Equation E.4.7.13 is known as the (80-year-old) Reiner–Rivlin equation. With the geometry of the "concentric-cylinder viscometer" given and $T$ and $\omega_0$ measured, the Bingham plastic parameters $\mu_0$ and $\tau_0$ can be determined.

## 4.3 Fluid-Particle Dynamics

As mentioned, naturally occurring and industrial two-phase flows are all around us, ranging from dust-storms in arid regions to bubbly flows in pipes, air-fuel injection in internal combustion engines, and drug delivery via inhalation or injection. Such particulate matter forms *a discrete phase moving separately from the continuous phase* (see right box in Figure 4.2).

For separated flow models, two size-dependent categories are of interest, where microspheres are typically described with the Euler–Lagrange approach (see Section 4.3.1). In contrast, nanoparticles (i.e., $d_p < 100$ nm) in liquid flow are modeled in the Euler–Euler frame (see Section 4.3.2). Here, *Euler* implies continuum solution of the conservation laws and *Lagrange* means particle tracking, that is, the solution of Newton's second law. Consequently, *two separate sets of equations* are needed, where in general, both transport equations may contain coupling terms in the case that two-phase interactions are important (see Michaelides, 1997). However, quite frequently the dispersed phase, that is, solid particles, droplets, or bubbles, is *uncoupled* from the continuous phase (or carrier fluid). Especially solid, non-rotating spheres with $d_p > 1$ μm and a high particle-to-fluid-density ratio simplify the trajectory equation significantly when the flow field is laminar.

### 4.3.1 Micron-Particle Transport and Deposition

Considering relatively small, quasi-spherical particles as well as low particle and shear Reynolds numbers, that is, $\mathrm{Re}_p = d_p \left| v - v_p \right| / \nu \ll 1$ and $\mathrm{Re}_s = v\, d_p^2 / (\nu L) \ll 1$, respectively, Newton's second law of motion is applicable in the form (Michaelides, 1997; Crowe et al., 1998; Kleinstreuer, 2003, among others)

$$m_p \frac{d\vec{\mathbf{v}}_p}{dt} = \vec{\mathbf{F}}_{\text{drag}} + \vec{\mathbf{F}}_{\text{pressure}} + \vec{\mathbf{F}}_{\text{interactive}} + \vec{\mathbf{F}}_{\text{lift}} + \vec{\mathbf{F}}_{\text{Basset}} + \underbrace{\vec{\mathbf{F}}_{\text{gravity}} + \vec{\mathbf{F}}_{\text{virtual mass}}}_{\sum \vec{\mathbf{F}}_{\text{body}}} \tag{4.50}$$

where:

$m_p$ is the particle mass

$\vec{\mathbf{v}}_p = d\vec{\mathbf{x}} / dt$ is the particle velocity vector

while all external forces are *point forces* acting on the particle's mass center

While drag, gravity, and lift are the most common ones, the pressure force is due to fluid acceleration because of the pressure gradient in the absence of the particle; particle-particle interaction forces are important in dense particle suspensions, while particle-wall interactions have to be simulated when determining particle deposition; the Basset force is a an "unsteady-drag force" accounting for temporal development of the fluid flow near the particle; and the "virtual mass" term accounts for the work required to change the momentum of the surrounding fluid as the particle accelerates.

Now, for laminar flow with negligible particle lift ($\omega_p \approx 0$), one-way coupling prevails; that is, the particle presence does not influence the fluid flow. A high-density ratio, that is, $\rho_p/\rho_c \gg 1$, ensures that only $\vec{\mathbf{F}}_{\text{drag}}$ and perhaps $\vec{\mathbf{F}}_{\text{gravity}}$ are important (see Crowe et al., 1998; Buchanan et al., 2000, among others). For cases with particle rotation, the Saffman lift force and/or the Magnus effect have to be considered (see Loth and Dorgan, 2009, among others). For example, soccer and tennis balls receive intentionally significant rotations when kicked/hit to generate unusual ball trajectories that may confuse the goalie/opponent. Even stranger trajectories can be produced via sphere-rotation and sphere-surface unevenness in baseball, cricket, and golf. Following Bernoulli, crowding of streamlines above the rotating sphere causes locally higher velocities and hence, lower pressures when compared with the sphere's underside. This net pressure differential generates a force perpendicular to the flight path and the axis of rotation, known as the *Magnus effect* (see HWA in Section 4.4).

Back to the simplified case when only drag and gravity accelerate the sphere, we have

$$m_p \frac{d\vec{\mathbf{v}}_p}{dt} = \vec{\mathbf{F}}_D + \vec{\mathbf{F}}_G \tag{4.51}$$

where

$$\vec{\mathbf{F}}_D = \frac{\pi}{8} \rho d_p^2 C_{Dp} (\vec{\mathbf{v}}_p - \vec{\mathbf{v}}) \left| \vec{\mathbf{v}}_p - \vec{\mathbf{v}} \right| \tag{4.52}$$

which always keeps $F_{\text{drag}}$ opposite to the flow direction. Furthermore,

$$\vec{\mathbf{F}}_G = m_p \, \vec{\mathbf{g}} \tag{4.53}$$

with the particle mass being $m_p = \rho_p \pi \, d_p^3/6$. The particle drag coefficient is given as

$$C_{D_p} = C_D / C_{\text{slip}} \tag{4.54}$$

where $C_{\text{slip}}$ is the slip correction factor, being of $\mathcal{O}(1)$ after Clift et al. (1978).

The drag coefficient is defined as

$$C_D = \frac{F_D}{0.5 \rho v^2 A_{\text{projected}}} \tag{4.55}$$

One should recall that $F_D$ is actually the total drag, consisting of the form drag due to pressure differences around the particle and the viscous drag because of the net wall shear effect. The projected particle-area for a sphere is $\pi R^2$. For example, Stokes obtained for uniform flow of velocity $v$ at $\text{Re}_p < 1$ around a stationary sphere of radius $R$ (see HWA Section 4.4)

$$F_D = 6 \mu \pi v R \tag{4.56}$$

Clearly, for particle Reynolds numbers $\text{Re}_p = \rho d_p \left| v - v_p \right| / \mu < 1$, Equation 4.55 combined with Equation 4.56, using $v_{rel} = v_{\text{fluid}} - v_{\text{particle}}$, yields

$$C_D = 24/\mathrm{Re}_p \tag{4.57}$$

Quite accurate $C_D$-correlations for solid spheres and droplets exposed to higher–Reynolds number flows are

$$C_{D_{\text{sphere}}} \approx \frac{24}{\mathrm{Re}} + \frac{6}{1+\sqrt{\mathrm{Re}}} + 0.4,\ 0 \le \mathrm{Re} \le 2\times 10^5 \tag{4.58}$$

$$C_{D_{\text{droplet}}} \approx 27\,\mathrm{Re}^{-0.84} \tag{4.59}$$

It should be noted that for spherical, non-interacting *droplets*, the $C_D$-values are somewhat lower because of the friction-induced internal circulation, known as *Hill's vortices*.

An insightful application of the base case is the derivation of the Stokes particle equation. Starting with Equation 4.51, where the key quantities are depicted in Figure 4.7, we have

$$\frac{\rho_p \pi d_p^3}{6}\frac{d\vec{\mathbf{v}}_p}{dt} = \frac{\pi}{8}\rho d_p^2 \frac{24}{Re_p}\left(\vec{\mathbf{v}} - \vec{\mathbf{v}}_p\right)\left|\vec{\mathbf{v}} - \vec{\mathbf{v}}_p\right| + \frac{\rho_p \pi d_p^3}{6}\vec{\mathbf{g}} \tag{4.60a}$$

or, after inserting $Re_p = \rho d_p \left|\vec{\mathbf{v}} - \vec{\mathbf{v}}_p\right| / \mu$,

$$\frac{d\vec{\mathbf{v}}_p}{dt} = \frac{18\mu}{\rho_p d_p^3}\left(\vec{\mathbf{v}} - \vec{\mathbf{v}}_p\right) + \vec{\mathbf{g}} \tag{4.60b}$$

Multiplying through with $\rho_p d_p^2 / 18\mu$ and expanding the resulting coefficient on the left-hand side with $(D/U)(U/D)$, where $U$ is a representative system velocity, say $u_{\text{average}}$ in tubular flow, and $D$ is a length scale, such as the tube diameter, we have

$$\left(\frac{D}{U}\right)\underbrace{\frac{\rho_p d_p^2 U}{18\mu D}}_{\substack{\text{Stokes}\\ \text{Number}}}\frac{d\vec{\mathbf{v}}_p}{dt} = \left(\vec{\mathbf{v}} - \vec{\mathbf{v}}_p\right) + \frac{\rho_p d_p^2}{18\mu}\vec{\mathbf{g}} \tag{4.61}$$

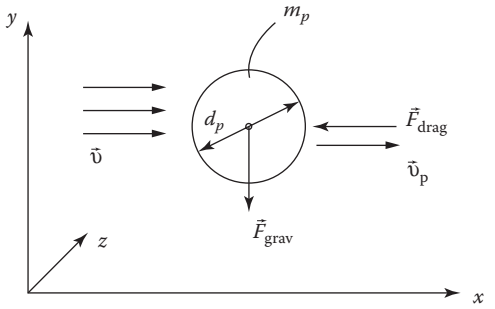


**FIGURE 4.7**
Illustration of key quantities for determining spherical particle dynamics.

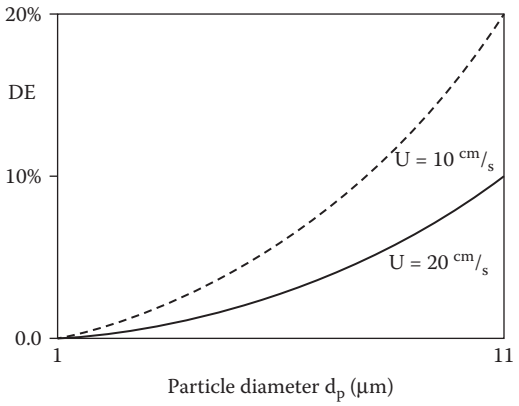


**FIGURE 4.8**
Deposition efficiency (DE) of micron-particles in a horizontal pipe, assuming Stokes flow.

Thus,

$$\frac{D}{U} St_D \frac{d\vec{\mathbf{v}}_p}{dt} = \left(\vec{\mathbf{v}} - \vec{\mathbf{v}}_p\right) + v_{\text{terminal}}\, g\hat{\mathbf{k}} \tag{4.62}$$

It should be noted that as $\left.\frac{d\vec{\mathbf{v}}_p}{dt}\right|_{t=t_{\text{term}}} = 0$ with $\vec{\mathbf{v}} = 0$, that is, a quiescent body of viscous fluid, $\vec{v}_p \Rightarrow v_{\text{terminal}} = \rho_p d_p^2 g / 18\mu$.

Clearly, the magnitude of the Stokes number

$$St_D = \frac{\rho_p d_p^2 U}{18\mu D} \tag{4.63}$$

indicates particle behavior in shear flow as follows:

1. $St_D \gg 1$ implies streamline crossing of larger particles having significant inertia.
2. In contrast, for $St_D \ll 1$, the small nanoparticles with $d_p < 100$ nm follow the streamlines.

Knowing the flow field $\vec{\mathbf{v}}(\vec{\mathbf{x}}, t)$, the individual particle velocities $\vec{\mathbf{v}}_p(t)$ can be obtained, subject to given initial conditions. A second integration, $\vec{\mathbf{x}} = \int \vec{\mathbf{v}}_p\, dt$, then provides the particle locations, that is, trajectories. It is typically assumed that a particle has deposited on a surface when it approaches within one radius, that is, the particle touches the wall. An application of Equation 4.62 for microsphere suspension flow in a horizontal pipe ($D = 0.2$ cm and $L = 1$ cm) is shown in Figure 4.8 for $U = 10$ and 20 m/s. The deposition efficiency (DE) is defined as the ratio of the number of particles deposited in a specific region to the number of particles that have entered this region (Kleinstreuer et al., 2007). Not surprisingly, the deposition efficiency increases with larger particles at lower inlet velocities.

**Example 4.10: Analyze the Dynamics of a Falling Sphere from Rest in a Reservoir of a Newtonian Fluid**

| Sketch 10 | Assumptions | Method |
|---|---|---|
| 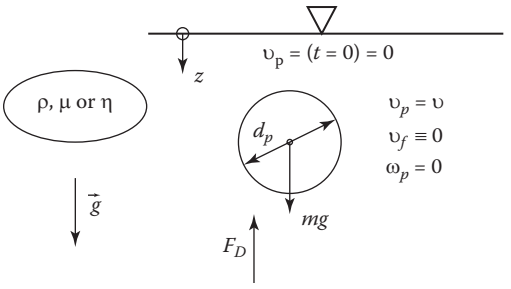 | • 1-D analysis<br>• Newtonian or non-Newtonian fluid reservoir<br>• $\rho_p \gg \rho_f$; $\omega_p = 0$ | • 1-D Newton's second law with $F_{drag}$ and $F_{gravity}$<br>• Stokes flow with $C_D = 24/\mathrm{Re}_p$<br>• Newtonian vs. power-law fluid flow |

*Solution:*

Using Equation 4.51 with $m_p = m = \frac{\pi}{6}\rho_p d_p^3$ and $F_D = C_D\left(\frac{\rho}{2}v^2 A_{\text{projected}}\right)$, we have

$$m\frac{dv}{dt} = F_{\text{grav}} - F_{\text{drag}} \tag{E.4.10.1}$$

or

$$\frac{\pi}{6}\rho_p d_p^3 \frac{dv}{dt} = \frac{\pi}{6}\rho_p g d^3 - \frac{\pi}{8}\rho d^2 C_D v^2;\ C_D \approx \frac{24}{\mathrm{Re}_p} \tag{E.4.10.2a,b}$$

In compact form,

$$\frac{dv}{dt} = g - \frac{18\mu}{\rho_p d_p^2} v \tag{E.4.10.3}$$

Note that this is a linear, homogeneous, first-order ordinary differential equation (ODE) of the form

$$\dot{v} + Av + B = 0, \tag{E.4.10.4a}$$

subject to the initial and steady-state conditions

$$v(t=0) = 0 \text{ and } \left.\frac{dv}{dt}\right|_{v_{\text{terminal}}} = 0 \tag{E.4.10.4b,c}$$

Inserting the proposed solution $v(t) = Ce^{at} + \frac{B}{A}$ _ with _ $\dot{v} = aCe^{at}$ into the ODE yields

$$a + A = 0 \text{ or } a = -A = -18\frac{\nu_f}{d^2}$$

Using the initial condition $v(t=0) = 0$,

$$C = -\frac{B}{A} = -\frac{\rho_p g d^2}{18\mu}$$

Finally,

$$v(t) = -\frac{gd^2}{18\nu_f} e^{-\frac{t}{\tau}} + \frac{\rho_p g d^2}{18\mu_f} \text{ or } v(t) = \underbrace{\frac{\rho_p g d^2}{18\mu_f}}_{v_{\text{terminal}}} \left(1 - e^{-\frac{t}{\tau}}\right) \qquad \text{(E.4.10.5a,b)}$$

where $\tau = \rho_p d^2/18\mu_f$ is the characteristic time constant.

*Graph 8:*

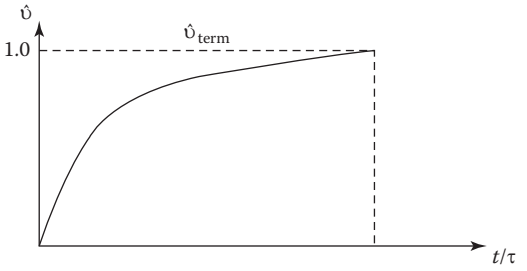


*Comments:*

- Following an exponential function, the particle approaches the terminal velocity when $t = \tau$.
- Clearly, the particle diameter and density as well as the type of fluid greatly determine when steady-state is reached.

**Example 4.11: Particle Being Accelerated from Rest by a Steady Uniform Air-Stream**

| Sketch 11 | Assumptions | Concepts |
|---|---|---|
| 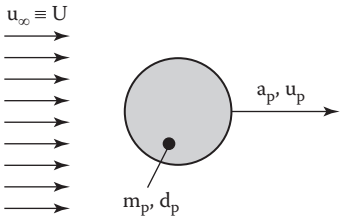  | • Spherical particle<br>• Steady unidirectional (air)flow with $\rho_p \gg \rho$<br>• Drag is the dominant point force | • Carrier fluid<br>$\vec{\mathbf{v}} = (u \equiv U, 0, 0)$<br>• Particle trajectory:<br>$m_p \frac{du_p}{dt} = F_D$;<br>$F_D \sim C_D A_{\text{projected}}$ |

*Solution:*

Using Equation 4.51 with $\vec{F}_G = 0$, the 1-D form reads:

$$m_p \frac{du_p}{dt} = \frac{\rho}{2} A C_D (u - u_p)\left|u - u_p\right| \qquad \text{(E.4.11.1)}$$

where:

$u\_u_p = u_{\text{relative}} \equiv u_r$
$C_D$ is given with Equation 4.58
$A_{\text{proj}} = d_p^2 \pi / 4$
$m_p = \rho_p \pi d_p^3 / 6$

With $u \equiv U = ¢$, $du_r/dt = -du_p/dt$, and hence, Equation E.4.11.1 can be rewritten as

$$-\frac{du_r}{dt}=\frac{18\mu}{\rho_p d_p{}^2}\left[1+0.15\left(\frac{\rho\, d_p}{\mu}\right)^{0.687}u_r^{0.687}\right]u_r \qquad \text{(E.4.11.2a,b)}$$

or

$$\frac{du_r}{dt}=A\left[1+Bu_r^{0.687}\right]u_r$$

where:

$$A=-\frac{18\mu}{\rho_p d_p{}^2}$$

$$B=0.15\left(\frac{\rho\, d_p}{\mu}\right)^{0.687}$$

Subject to $u_p(t=0)=0$, that is, $u_r(t=0)=u\equiv U$. Separation of variables and integration yields

$$u_r=U-u_p=\left[\left(B\ +\ U^{-0.687}\right)\cdot\exp\left(-0.687\,At\right)-B\right]^{-1/0.687} \qquad \text{(E.4.11.3)}$$

*Graph 9:*

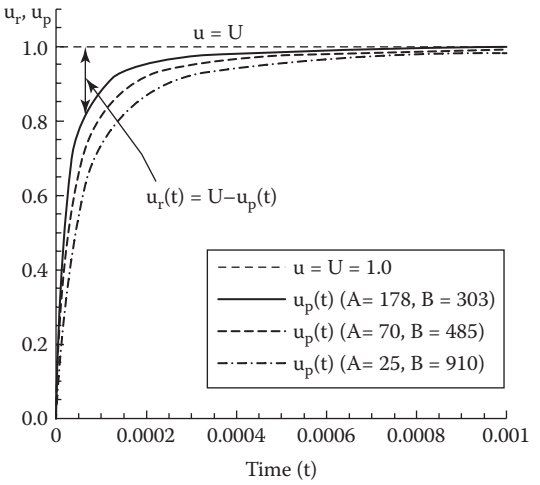


*Comment:*

Pushed by the free-stream, the particle accelerates from rest and exponentially reaches the fluid velocity at a point in time that depends on $A=18f/(\rho d^2)$, that is, $t_e=\ln[1/(0.6878A)]$.

### 4.3.2 Nanoparticle Transport

Nanoparticles, practically $10^{-8}$ m$<d_p<10^{-5}$ m, and their transport in micro/nanochannels deal with a key system parameter in micro/nanofluidics, that is, $\epsilon = A_{\text{surface}}/V_{\text{system}} = l^{-1} \gg 1$, where the system length-scale $l$ could be the hydraulic diameter (Kleinstreuer, 2014). To illustrate how tiny a nanosphere actually is, consider the equivalent ratios: nanosphere/soccer ball = soccer ball/Planet Earth! For submicron particles, Brownian motion becomes

effective, that is, random particle motion due to molecular bombardment by the surrounding fluid. That results in particle diffusion with decreasing nanoparticle diameter. Thus, rather than employing the Euler–Lagrange modeling approach (i.e., solving the fluid flow equations and then the particle trajectory equation), nanomaterial transport is best described in the Eulerian–Eulerian frame, certainly when the particle diameter is less than 100 nm. Again, assuming laminar flow with low nanoparticle loading, say, below 6% by volume, and hence, only one-way coupling, the momentum equation is solved first and then the mass transfer equation:

$$\frac{\partial Y}{\partial t}+\frac{\partial}{x_i}(u_i Y)=\frac{\partial}{\partial x_i}\left[\mathcal{D}_{\text{nano}}\frac{\partial Y}{\partial x_i}\right]\pm S_y \tag{4.64}$$

where:

$Y\equiv C/C_0$ is the nanoparticle mass fraction
$u_i$ is the fluid velocity vector
$\mathcal{D}_{\text{nano}}$ is the nanomaterial diffusion coefficient
$S_y$ is a possible nanoparticle sink or source

Specifically, according to Stokes–Einstein,

$$\mathcal{D}_{\text{nano}}=\frac{k_B T C_{\text{slip}}}{3\pi\mu d_p} \tag{4.65}$$

where:

$k_B=1.38\times10^{-23}$ J K$^{-1}$ is the Boltzmann constant
$T$ is the temperature in Kelvin
$C_{\text{slip}}=\mathcal{O}(1)$ is the Cunningham slip correction factor (Clift et al., 1978)

Based on Fick's law, the regional deposition efficiency can be computed as

$$DE=\left(\mathcal{D}\frac{\partial Y}{\partial n}\bigg|_{n=0}A\right)\Big/\left(Q_{in}\ Y_{in}\right) \tag{4.66}$$

where:

$n$ is the surface normal
$A$ is the surface area
$Q_{in}$ is the inlet volumetric flow rate
$Y_{in}$ is the inlet mass fraction

Theories on nanofluid flow and sample problem solutions are given in Kleinstreuer (2014), while applications of nanoparticle transport and deposition related to biomedical engineering are discussed in Kleinstreuer (2006).

**Example 4.12: Nanoparticle Convection, Diffusion and Uptake from a Planar Source**

Consider steady 1-D flow of a liquid through a porous plug that releases a low, constant concentration of nanoparticles, which disperse and dissolve/vanish according to a first-order reaction.

| Sketch 12 | Assumptions | Method |
|---|---|---|
| 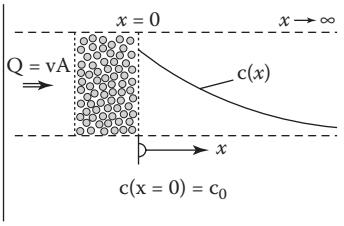 | • Steady 1-D isothermal plug flow<br>• Constant properties<br>• Low-volume nanoparticle release<br>• Idealized nanoparticle sink | • Uniform flow<br>$v = \frac{Q}{A} = \mathcal{C}$<br>• Reduced form of Equation 4.64 with axial diffusion only |

*Solution*:

In light of the assumptions, Equation 4.64 can be reduced, with $y \to c$, $u \to v$, and $S_c \to kc$, to

$$v\frac{dc}{dx} = \mathcal{D}\frac{d^2c}{dx^2} - kc \tag{E.4.12.1}$$

where:

$v = Q/A$

the binary diffusion coefficient $\mathcal{D}$ is given with Equation 4.65

$k$ is a constant reaction coefficient

Equation E.4.12.1 can be recast as

$$c'' - \frac{v}{\mathcal{D}}c' - \frac{k}{\mathcal{D}}c = 0 \tag{E.4.12.2}$$

subject to the BCs

$$c(x=0) = c_0 \quad \text{and} \quad c(x \to \infty) \to 0 \tag{E.4.12.3a,b}$$

The trial solution $c(x) = Ce^{(-ax)}$ satisfies Equation E.4.12.2, where

$$a = \frac{v}{2\mathcal{D}}\left[1 - \sqrt{1 + \frac{4k\mathcal{D}}{v^2}}\right] \tag{E.4.12.3a,b}$$

to match the BCs. Hence,

$$c(x) = c_0 \exp\left[-\frac{vx}{2\mathcal{D}}\left(\sqrt{1 + \frac{4k\mathcal{D}}{v^2}} - 1\right)\right] \tag{E.4.12.3a,b}$$

Parameter values:

- The nanoparticle diffusion coefficient for $T = 300$ K, $C_{slip} \approx 1$, $\mu_{water} = 0.9 \times 10^{-3}$ kg m/s, and $d_p = 10$ nm is

$$\mathcal{D} = 4.88 \times 10^{-10} \text{ m}^2/\text{s}$$

- Assuming the ratio $4k\mathcal{D}/v^2$ in Equation E.4.12.4 to be in the range of

$$0.1 \le \frac{4k\mathcal{D}}{v^2} \le 10 \quad ,$$

we can now graph a family of curves:

$$\frac{c(x)}{c_0} \quad \text{vs.} \quad \frac{v}{2\mathcal{D}}x$$

*Graph 10:*

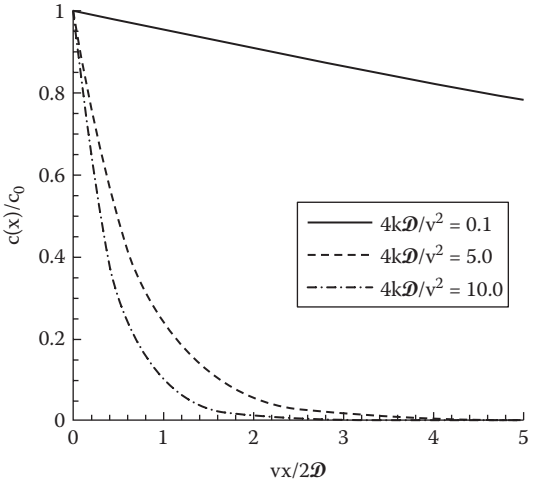


*Comment:*

As expected, $c(x)$ decays swiftly for $\frac{4k\mathcal{D}}{v^2} > 1.0$ because of the stronger first-order uptake.

## 4.4 Homework Assignments

Solutions to homework problems done individually or in, say, three-person groups should help to further illustrate fluid dynamics concepts as well as approaches to problem solving, and in conjunction with Appendix I, sharpen the reader's math skills. Unfortunately, there is no substantial correlation between good homework results and fine test performances, only vice versa. Table 1.1 summarizes three suggestions for students to achieve a good grade in fluid dynamics—for that matter, in any engineering subject. The key word is "independence"; that is, equipped with an equation sheet (see Appendix I), the student should be able: (1) to satisfactorily answer all concept questions and (2) to solve correctly all basic fluid dynamics problems.

### 4.4.1 Physical Insight

4.1 Discuss the underlying physics of Equation 4.2 as well as its extensions (see Equation 4.8).

4.2 Compare, for actual porous media flow, porosity vs. permeability vs. hydraulic conductivity vs. the Darcy drag coefficient. Provide real-world applications.

4.3 List examples of natural and man-made (i.e., industrial) flows in terms of (1) quasi-homogeneous mixture flows and (2) separated (or truly two-phase) flows.

4.4 Concerning Example 4.1, justify Equation E.4.1.1 and derive Equation E.4.1.2 to confirm Equation E.4.1.5.

4.5 Extend Example 4.2 by (1) estimating hydraulic conductivity $K$ and permeability æ based on realistic p-m flow values and (2) comparing Equation E.4.2.1b with the 1-D version of Equation E.4.1.5.

4.6 Concerning Example 4.3, derive the solution (Equation E.4.3.2) and plot the dimensionless velocity for different (realistic) permeability (i.e., æ) values. Comment!

4.7 Relate the results from Example 4.4 to different tubular filtration processes.

4.8 Definitions: (a) What are the underlying assumptions for $\kappa \approx c$ to hold (see Equation 4.16b)? (b) Is Equation 4.18 related to the definition of "steam quality" in thermodynamics? (c) Give an example with sketch and explanation for the particle drift velocity (see Equation 4.24). (d) Derive and discuss Equation 4.28 vs. Equation 4.31.

4.9 Derive Equations 4.32 through 4.34 from first principles and set up a typical application.

4.10 Discuss the reduction of Equations 4.35 through 4.40 and set up a specific problem, that is, modeling equations with realistic p-m coefficient values.

4.11 Set up the governing equations and boundary conditions for power-law fluid flow in an annulus formed by a stationary (cylindrical) housing and a rotating and translating shaft.

4.12 In Graph 6 of Example 4.9, the shear stress $\tau_{r\theta}$ varies inside the gap; however, $v_\theta = r_0\omega_0 = ¢$ (see Graph 7). Explain this mathematically and physically.

4.13 Devise an experiment, based on Equation E.4.9.13, by which both unknown Bingham plastic parameters $\tau_0$ and $\mu_0$ can be determined.

4.14 Derive and discuss the different Reynolds numbers in fluid-particle flows.

4.15 The forces in Equation 4.50 are so-called *point forces*; what does that mean? Discuss alternative (numerical) methods to solve for (spherical) particle trajectories.

4.16 What does the correction factor $C_{slip}$ accomplish?

4.17 Derive Equation 4.41, interpret Equation 4.63, and discuss the steady-state particle velocity.

4.18 Solve the falling sphere problem and plot $v_p(t)$ for different fluids, for example, oil, syrup, and a power-law fluid.

4.19 Discuss Equation 4.65 for $d_p < 100$ nm; that is, research its derivation and state its limits of application.

4.20 Plot the results of Example 4.7 for $n > 1$ and comment.

### 4.4.2 Engineering Problems

4.21 Find $v_z(r)$ for creeping flow through a porous-medium tube of radius $r_0$ (see Example 4.3). List possible applications.

4.22 Consider steady fully developed flow of a power-law fluid ($m$, $n$) in a slit of small spacing $2h$ formed by two plates ($L \times W$).

(a) Show that the mass flow rate is

$$\dot{m} = \frac{2\rho W h^2}{(1/n) + 2}\left[\frac{h}{m}\left(\frac{\Delta p}{L}\right)\right]^{1/n}$$

(b) How would your results change if the plates were vertical, that is, 100% downward flow?

4.23 Commercial capillary viscometers can be modeled as cylindrical Couette flow. The inner cylinder (radius $kR$, $0 < k < 1$) is stationary, and the outer one (radius $R$) rotates at low angular velocity $\omega_0$ due to a measured torque. A small gap of $R–kR$ is filled with an unknown power-law fluid. How would you obtain the power-law fluid parameters $m$ and $n$?

4.24 Consider the flow of a power-law fluid ($m$, $n$; $\rho$) in a horizontal annulus ($kR$ and $R$). The fluid is kept in motion due to the translatory motion ($v_0$) of the inner cylinder ($kR$).

(a) Derive the velocity profile $v_z(r;v_0,k,R;n)$ and show that it simplifies to $\dfrac{v_z}{v_0} = \dfrac{\ln(r/R)}{\ln \kappa}$ for $n \to 1$.

(b) Find an expression for the mass flow rate $\dot{m}$ for $n \neq 1/3$; what is $\dot{m}$ $(n \neq 1/3)$?

4.25 Consider the flow of two immiscible fluids (viscosities $\mu_1$ and $\mu_2$ with different densities) between parallel horizontal plates a small distance $2h$ apart, driven by $\Delta p/L = \text{const}$. Assuming that the interface stays planar and each fluid takes up half the channel, find the shear stress $\tau_{yx}$ and velocities $u_1(y)$ for $-h \le y \le 0$ and $u_2(y)$ for $0 \le y \le h$.

4.26 Consider steady laminar flow in a network of 12 tubes forming a cube, driven by an effective pressure drop $\Delta p = p(1) - p(8)$, where (1) is the (corner) inlet and (8) is the diagonally opposite outlet.

(a) Find an expression for the mass flow rate $\dot{m} = \dot{m}(\Delta p;\ \rho, \mu,\ R,\ L)$, where $R$ and $L$ are the same radius and length of each of the 12 tubes.

(b) Convert this system to a simple "flow-through porous media" model by extracting Darcy's velocity. Comment!

4.27 Provide definitions, characteristics, differences, and applications of *constitutive* equations vs. *closure* models in two-phase flow analysis.

4.28 Red blood cells (RBCs) in tubular flow appear to congregate in the tube's central core, resulting in a cell-free plasma layer along the vessel wall. Thus, there are two regions: a constant plasma layer of thickness $\delta$ with viscosity $\mu_p$ and a homogeneous mixture region, $0 \le r \le (R-\delta)$ with $\mu_m$. Typical parameter values are $R = 10$ μm, $\delta = 1$ μm, and $\mu_p/\mu_m = 0.25$.

(a) Find $u(r)$ for each of the two domains.

(b) Find $Q = Q_p + Q_M$ and compare the result with the Hagen–Poiseuille expression:

$$Q = \frac{\pi R^4 \Delta p}{8\mu L}$$

Relate $\mu$ to $\mu_p/\mu_m$ for $\delta/R \ll 1$.

(c) Plot for the given numerical data $u_p(r) + u_M(r)$ as well as Poiseuille's $u(r)$.

4.29 A spherical particle of mass $m$ is released at the upper plate corner ($x = 0$; $y = h$) in Poiseuille flow between two horizontal parallel plates, a small distance $2h$ apart. For $\mathrm{Re} \leq 1.0$, find the minimum channel length when the particle just touches the lower plate (i.e., $x = L_{\min}$, $y = -h$).

4.30 A sphere ($D$, $\rho_s$), submerged in a viscous fluid ($\rho$,$\mu$), is released from rest, that is, $v(t = 0) = 0$. Assuming a constant drag coefficient, derive the ODE for $v(t)$, using the specific gravity $S = \rho_s/\rho$ as a system parameter.

(a) Without solving the ODE, provide graphs for $v(t)$ and $a(t)$. Comment!

(b) Solve the ODE, check the influence of the sphere's buoyancy, and discuss the assumption of $c_D = \text{¢}$.

Taylor & Francis
Taylor & Francis Group
http://taylorandfrancis.com

# 5

# *Basic Lubrication Systems*

Lubrication is a subset of *tribology*, the theory of friction, lubrication, wear and damage. It also deals with the replacement of mechanical or biological systems, such as gliding/rotating machine parts or movable joints. For two solids to slide relative to each other, a tangential resistance, that is, a frictional force, $F$, has to be overcome:

$$F = f \cdot N \tag{5.1}$$

where:

$N$ is the normal load

$f$ is the friction coefficient, with a typical range of $0.01 < f < 1.0$

Low *friction coefficients* can be achieved when the two solid body surfaces stay separated at all times via a suitable lubricant. Load-carrying lubrication relies on the *wedge-film* effect to work, where a minimum angled surface/plate velocity is required to generate a load-carrying pressure field (see Figure 5.1a). Water-skiing and hydroplaning are just two practical examples of the amazing impact of the wedge effect. In any case, *hydrodynamic lubrication* greatly reduces wear and hence, surface damage. Clearly, friction and wear should be considered as separate phenomena, as in the case of *"boundary" lubrication*, when friction and wear are determined by the surface properties of the *solids and the chemical nature of the lubricant* rather than just its viscosity. Specifically, wear is the removal of one material by another due to sliding contact. Wear debris may ultimately cause device/machine (or human-joint) failure. Other lubrication modes include *squeeze-film and elasto-hydrodynamic lubrication*. In the latter of which bounding material deformation, for example, cartilage in joints, is considered as well (see Figure 5.1a through d).

The basic mechanism of *squeeze-film* lubrication is shown in Figure 5.1b, while the human knee joint (Figure 5.1d) is an illustrative example of coupled hydrodynamic lubrication with squeeze-film material deformation, labeled *elasto-hydrodynamic lubrication*. For example, for the problem of human-joint replacement, selection of the right cup-and-ball material (e.g., polyethylene, metal alloys, or ceramics) and lubricant, as well as perfect sphericity and surface finish, is important. Also of concern are the minimum sustained radial clearance and constant properties of the pseudo-synovial fluid in light of realistic load changes during walking, running, and so on. In any case, problems may arise when particles are entrained due to wear, or boundary lubrication occurs when the fluid film breaks.

In summary, this chapter on lubrication starts in Section 5.1.1 with simple slot flow, that is, flow between slightly converging plates (see also Section 3.1.2). It then expands to squeeze-film and planar lubrication (Sections 5.1.2 and 5.1.3), which are special cases of the *Reynolds lubrication equation* (Section 5.2). A more recent direction in tribology is the use of *nanoparticles in lubricants* to reduce friction and avoid/mitigate wear (Section 5.3). For some background information on that topic, see Section 4.3.2, discussing the transport and applications of nanoparticle-liquid mixtures.

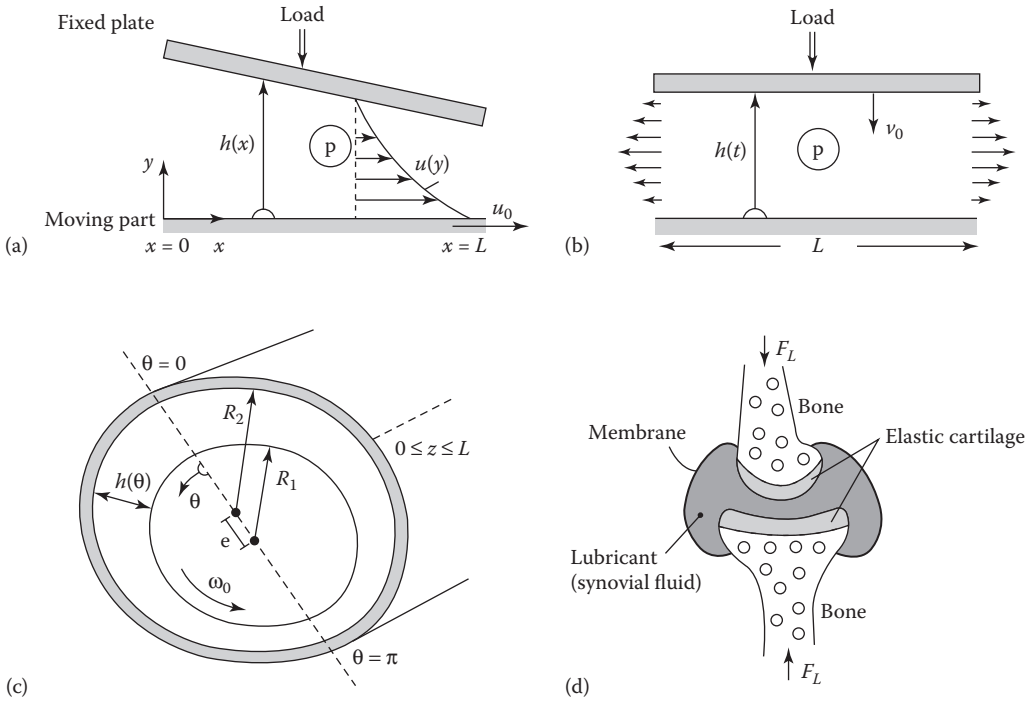


**FIGURE 5.1**
Lubrication models: (a) hydrodynamic model of a slider bearing; (b) squeeze-film model; (c) journal bearing; and (d) knee-joint bearing (i.e., elasto-hydrodynamic model).

## 5.1 Lubrication Approximations

Underlying aspects of lubrication approximations are that geometrically the spacing (or lubricating film thickness) $h(x)$ is much less than the system's length scale $l$; that is, $h \ll l$, or $\varepsilon = h/l \to 0$; and, the Reynolds number $\mathrm{Re} = u_0 h_0/v$ is small, allowing the use of the Stokes equation (see Section 2.3.3), where typically the flow field is laminar, quasi-steady, and two-dimensional (2-D). Several lubrication approximations are introduced and illustrated, starting with simple slot flow (see Figure 5.2) and ending with the more encompassing Reynolds lubrication equation in Section 5.2.

For 2-D slot flow, the continuity equation reads:

$$\frac{\partial u}{\partial x} + \frac{\partial v}{\partial y} = 0 \tag{5.2a}$$

It can be scaled (see Section 1.4), resulting in

$$\frac{u_0}{l} + \frac{v_0}{h_0} = 0 \tag{5.2b}$$

or

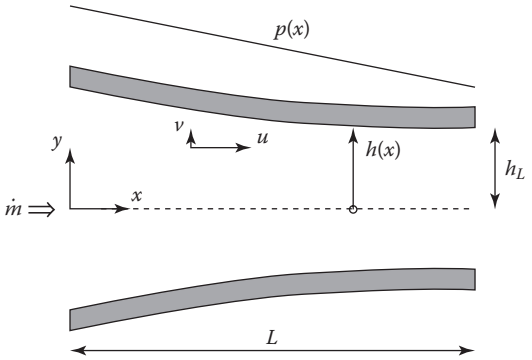


**FIGURE 5.2**
Axisymmetric slot flow with mildly varying height.

$$v_0 = \frac{h}{l} u_0 = \varepsilon u_0 \tag{5.3}$$

where $\varepsilon = h/l \ll 1$. Based on the condition $h \ll l$, the normal velocity $v$ is much less than the axial velocity $u$.

### 5.1.1 Slot-Flow Analysis

As a preliminary task, we analyze flow between slightly converging plates (see Figure 5.2), known as *slot flow*. Following the approach outlined in Section 3.1.2, first, (steady laminar) *unidirectional* flow is assumed. Thus, starting with Stokes' steady 2-D equation (see Equation 2.36) and applying scale analysis, the $y$-momentum component collapses to

$$0 = -\frac{\partial p}{\partial y} \tag{5.4}$$

The $x$-momentum reduces to

$$0 = -\frac{dp}{dx} + \mu \frac{\partial^2 u}{\partial y^2} \tag{5.5}$$

Considering such slot flow with locally varying clearance $h(x)$, we have as the solution to Equation 5.5 (see Section 3.1.2 and Figure 5.2)

$$u(x, y) = -\frac{h^2}{2\mu}\left(\frac{dp}{dx}\right)\left[1 - \left(\frac{y}{h}\right)^2\right] \tag{5.6}$$

This is Poiseuille-type flow, depending on the local height $h(x)$ and the local pressure gradient. Clearly, via the boundary condition $u(y = h(x) = 0)$, the axial velocity is not only a function of $y$ (as in Poiseuille flow) but also dependent on $x$. To complete the slot-flow analysis, global continuity, $\dot{m} = \rho \bar{v} A = \rho Q = \text{constant}$, requires for incompressible flow

$$Q = \int_A v_n \, dA = 2 \int_0^{h(x)} u \, dy := \frac{h^3}{2\mu}\left(\frac{\Delta p}{L}\right) \tag{5.7a through c}$$

Given the flow rate per unit depth, the quasi-constant pressure gradient, $dp/dx \cong -\Delta p/L$, can be eliminated in Equation 5.6. Alternatively, Equation 5.7c delivers the overall pressure drop, that is,

$$p_1 - p_2 = 2\mu Q \int_0^L \frac{dx}{h^3} \tag{5.8}$$

Clearly, Equation 5.8 is based on the geometric fact that $\varepsilon = h/L \ll 1$, that is, the *lubrication approximation*. This underlying assumption is used to describe numerous other applications; for example, slightly expanding/contracting flows in narrow channels, thin films, small blood vessels, filter pores, and so on.

### 5.1.2 Squeeze-Film Lubrication

A unique application in lubrication are squeeze-film systems (see Figure 5.1b). Here, $h = h(t)$ only, and of major interest (again) is the pressure field $p(r,t)$ due to the closing gap. Example 5.1 considers a basic case with first a Newtonian fluid and then a power-law fluid as well as a visco-elastic fluid as lubricants.

**Example 5.1: Sample Squeeze-Film System**

Consider squeeze-film lubrication under a constant load L for different fluids: Newtonian, power-law, and linear visco-elastic.

| Model Schematic 1 | Assumptions | Method/Approach |
|---|---|---|
| 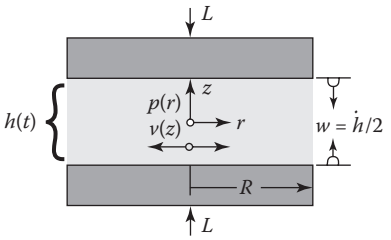 | • Transient 2-D axisymmetric incompressible fluid flow<br>• Gap height $h \ll R$ and $\dot{h} \ll \bar{v}$<br>• Normal stresses are negligible<br>• Neglect end effects | • Reduced continuity and equation of motion<br>• Insert appropriate rheology models for $\tau_{rz}$<br>• Average $v(r, z, t)$ over $z$:<br>• $\bar{v} = \frac{2}{h}\int_0^{h/2} v\, dz$ |

*Solution:*

Based on the *postulates* $\vec{v} = \left[0;\ v = v(r,\ z,\ t);\ w = \dot{h}/2\right]$ and $\nabla p = dp/dr$, we reduce the continuity equation (Appendix AI.5.1) to

$$\frac{1}{r}\frac{\partial(rv)}{\partial r} + \frac{\partial w}{\partial z} = 0 \tag{E.5.1.1}$$

and the equation of motion (Appendix AI.5.2) to

$$\frac{\partial}{\partial r} p(r,t) = \frac{\partial}{\partial z}\tau_{rz} \tag{E.5.1.2}$$

Integration of Equation E.5.1.1 across the gap $-h/z \le z \le h/2$ requires

$$\int dw = -\int \frac{1}{r}\frac{\partial(r\ v)}{\partial r} dz \tag{E.5.1.3}$$

Specifically,

$$\int_{-h/2}^{h/2} dw = w\left(\frac{h}{2}\right) - w\left(-\frac{h}{2}\right) = \frac{\dot{h}}{2} - \left(-\frac{h}{2}\right) = \dot{h} \tag{E.5.1.4a}$$

and

$$-\int_{-h/2}^{h/2} \frac{1}{r}\frac{\partial(rv)}{\partial r} dz = \frac{1}{r}\frac{d(r\bar{v})}{dr}\int_{-h/2}^{h/2} dz = -\frac{1}{r}\frac{d}{dr}(r\bar{v})h \tag{E.5.1.4b}$$

so that

$$\dot{h} \equiv \frac{dh}{dt} = -\frac{1}{r}\frac{d}{dr}(rh\bar{v}) \tag{E.5.1.5}$$

where

$$\bar{v} = \frac{2}{h}\int_0^{h/2} v(r, z; t) dz \tag{E.5.1.6}$$

Before integrating Equation E.5.1.2 across the gap, $\tau_{rz}$ has to be defined.

i. *Newtonian fluid:*

$$\tau_{rz} \approx \mu\frac{\partial v}{\partial z} \tag{E.5.1.7}$$

Thus, Equation E.5.1.2 reads:

$$\mu\frac{\partial^2 v}{\partial z^2} = \frac{dp}{dr} \tag{E.5.1.8}$$

subject to $v(z = \pm h/2) = 0$.
Integration across the gap yields

$$v = \frac{h^2}{2\mu}\left(\frac{dp}{dr}\right)\left[\left(\frac{z}{h}\right)^2 - \frac{1}{4}\right] \tag{E.5.1.9}$$

Evaluating the average radial velocity (i.e., Equation E.5.1.6), as needed in Equation E.5.1.5, we have

$$h\bar{v} = \frac{1}{\mu}\left(\frac{dp}{dr}\right)\int_0^{h/2}\left(z^2 - \frac{h^2}{4}\right) dz \coloneqq \frac{-h^3}{12\mu}\frac{dp}{dr} \tag{E.5.1.10}$$

so that

$$\frac{1}{r}\frac{d}{dr}\left(r\frac{dp}{dr}\right) = \frac{12\mu}{h^3}\frac{dh}{dt} \tag{E.5.1.11}$$

subject to $p(r = R) = 0$ and $dp/dr = 0$. Thus, double integration yields

$$p = \frac{3\mu R^2}{h^3}\dot{h}\left[\left(\frac{r}{R}\right)^2 - 1\right] \tag{E.5.1.12}$$

Now, the load can be evaluated as

$$L = \int_0^R pdA = 2\pi \int_0^R prdr := \frac{3\pi}{2}\mu R^4 \dot{h}/h^3 \tag{E.5.1.13}$$

Clearly, $p(r)$ and hence $L$ are proportional to $h^{-3}$, which indicates the significance of the "small-gap-wedge effect"

ii. *Power-law fluid:*

$$\tau_{rz} = K\left(\frac{\partial u}{\partial z}\right)^{n-1} \tau_{rz} = K\left(\frac{\partial v}{\partial z}\right)^n \tag{E.5.1.14}$$

Starting over with Equation E.5.1.2 for this basic non-Newtonian fluid, the load is (see Section 4.2.2)

$$L = \frac{2\pi(2+1/n)^n}{n+3} K\ \mathrm{sgn}(\dot{h})|\dot{h}|^n h^{-(2n+1)} R^{n+3} \tag{E.5.1.15}$$

As expected, when $n = 1$ and hence, $K = \mu$, Equation E.5.1.13 for Newtonian fluid flow is recovered.

iii. *Linear visco-elastic fluid:*

$$\tau_{rz} = \int_{-\infty}^{t} G(t-t')\frac{\partial u(t')}{\partial z} dt' \tag{E.5.1.16}$$

This closure model leads to (see homework assignments in Section 5.3.2)

$$L = \frac{3\pi R^4}{2} \int_0^t Q(t-t')\left(\dot{h}/h^3\right) dt' \tag{E.5.1.17}$$

*Graphs 1 (for Case (i) "Newtonian fluid flow"):*

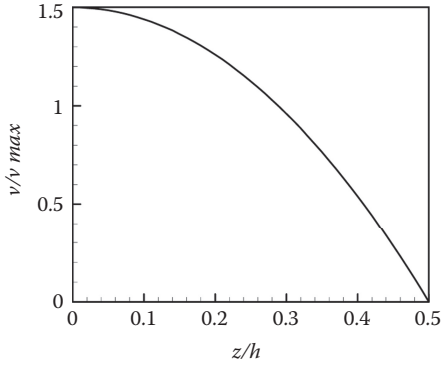


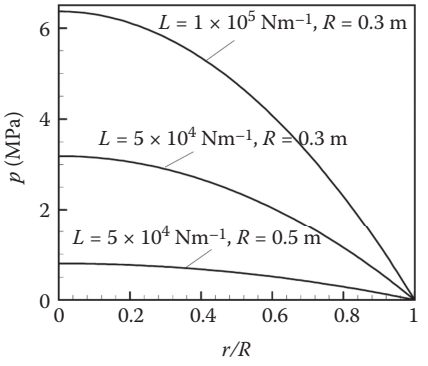

*Comments:*

- As expected, the radial squeeze-film velocity $v(z)$ is parabolic due to the approaching disks.
- At a given time $t$ with $w \sim \dot{h}_{disk}$, a pressure gradient $dp/dr$ is created, which is driving the fluid outward.
- The pressure distribution (see Equation E.5.1.12) clearly depends on the disk-approach speed $\dot{h}_{disk} = \dot{h}(L)$ and the disk radius $R$. In turn, the load $L$ determines the disk speed (see Equation E.5.1.13).
- A *Course Project* (see Section 10.2) would be a good venue to further explore the impact of non-Newtonian lubricants.

### 5.1.3 Planar Lubrication

As pointed out a few times, for steady fully developed internal flows (e.g., Couette and Poiseuille), the pressure gradient is constant, and hence, parabolic velocity profiles are ensured. When one stationary wall is slanted (or curved), and the other flat surface drags viscous fluid into the narrowing passage, the lubrication approximation $\varepsilon = h/L \ll 1$, discussed in Section 5.1.1, can be applied. In such planar bearings, the local pressure builds up, capable of sustaining a significant load exerted on the fixed wall, that is, $L = p_{\text{mean}} \cdot A_{\text{surface}}$ (see Figure 5.3).

Very similar to the slot-flow analysis of Section 5.1.1, that is, assuming a small, only slightly varying gap $h(x)$, it can be shown that the viscous forces are dominant. Clearly,

$$v \ll u, \quad \frac{\partial^2 u}{\partial x^2} \ll \frac{\partial^2 u}{\partial y^2}, \quad \text{and} \quad \frac{\partial p}{\partial y} \approx 0 \qquad \text{(5.9a through c)}$$

Specifically,

$$\frac{F_{\text{inertia}}}{F_{\text{viscous}}} = \frac{u\,\partial u/\partial x}{\nu\left(\partial^2 u\right)/\left(\partial y^2\right)} \sim \frac{U^2/l}{\nu U/h^2} = \text{Re}_l \left(\frac{h}{l}\right)^2 < 1 \qquad \text{(5.10a through c)}$$

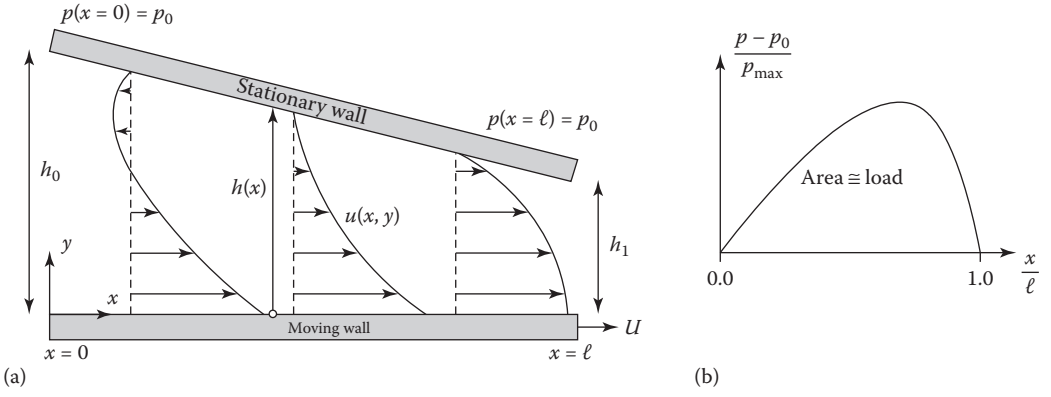


**FIGURE 5.3**
Slider bearing: (a) velocity profiles and (b) pressure distribution.

*Notes:*

- Although $\mathrm{Re}_l \equiv Ul/v$ may be relatively high in lubrication, $\mathrm{Re}_l(h/l)^2 \ll 1$. To illustrate that fact numerically, assume $U = 10$ m/s, $h_{\mathrm{avg}} = 0.1$ mm, $l = 4$ cm, and $\nu_{\mathrm{oil}} = 7 \times 10^{-4}$ m$^2$/s. As a result, $\mathrm{Re}_l = 570$, but $\mathrm{Re}_l(h/l)^2 = 0.004$ (see White, 2006).
- As discussed, the two major forces in lubrication are the viscous and the pressure force. Their ratio forms a dimensionless group called the "bearing number," $B = (\mu Ul)/(p_0 h^2)$, which is of the order of one for typical slider bearings.

With the simplifications, the scaled Navier–Stokes (N-S) equations then reduce to the Reynolds lubrication equations as

$$\nabla \cdot \vec{v} = 0 \quad \text{and} \quad \nabla p = \mu \nabla^2 \vec{v} + \rho \vec{g} \tag{5.11a, b}$$

For the given 2-D system with a very mild $h(x)$-variation (Figure 5.3), these equations are simplified to

$$\frac{\partial u}{\partial x} \approx 0 \text{ and } \frac{dp}{dx} = \mu \frac{\partial^2 u}{\partial y^2} \tag{5.12a, b}$$

subject to

$$u(y = 0) = U; \quad u\left[y = h(x)\right] = 0 \tag{5.13a, b}$$

and

$$p(x = 0) = p, \text{ and } p(x = \ell) = p_0 \tag{5.13c, d}$$

Integration with respect to $y$ yields

$$u(x, y) = U\left(1 - \frac{y}{h(x)}\right) - \frac{\left[h(x)\right]^2}{2\mu}\left(\frac{dp}{dx}\right)\frac{y}{h(x)}\left(1 - \frac{y}{h(x)}\right) \tag{5.14}$$

Clearly, the velocity field in Equation 5.14 is a combination of simple Couette and basic Poiseuille flow. Now, the pressure gradient is obtained via the (given) flow rate:

$$Q = \int_0^{h(x)} u(x, y)\, dy = -\frac{\left[h(x)\right]^3}{12\mu}\left(\frac{dp}{dx}\right) + \frac{hU}{2} \tag{5.15}$$

so that

$$p(x) = p_0 + 6\mu U \int_0^x \frac{dx}{\left[h(x)\right]^2} - 12\mu Q \int_0^x \frac{dx}{\left[h(x)\right]^3} \tag{5.16}$$

*Note:* $h(x)$ is a design function where the stationary surface is usually slightly curved. Clearly, the last term in Equation 5.16 indicates that (see also Equation E.5.1.12)

$$p(x) \sim h^{-3}$$

This implies that very small gap sizes may produce very high pressure levels and hence, load-carrying capacities. As this can be interpreted as a "safety measure" (i.e., $L \to \infty$ as $h \to 0$), very thin lubrication films may rupture or get perturbed by entrained wear-particles.

**Example 5.2: Simple Slider Bearing with a Given Volumetric Flow Rate**

| Sketch 1 | Assumptions | Method |
|---|---|---|
| 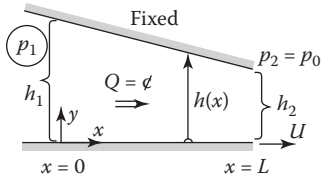 | • Steady quasi-unidirectional laminar flow in a very small gap<br>• Negligible inertia terms<br>• No end effects<br>• Constant fluid properties | • Planar lubrication equation<br>• Conservation of mass<br>• $\lvert h_2 - h_1 \rvert \ll L$ |

*Solution:*

Again, the basic problem solution is a combination of Couette flow and Poiseuille flow (see Equation 5.14):

$$u(x,\ y) = U\left(1 - \frac{y}{h}\right) - \frac{h^2}{2\mu}\left(\frac{dp}{dx}\right)\frac{y}{h}\left(1 - \frac{y}{h}\right) \tag{E.5.2.1}$$

Here, we suggest a linear $h(x)$:

$$h \equiv h(x) = h_1 + \frac{h_2 - h_1}{L}x \tag{E.5.2.2}$$

So, the flow rate $Q$ is

$$Q = \int_0^{h(x)} u(x,\ y)dy = \frac{h_1 h_2}{h_1 + h_2}U = ? \tag{E.5.2.3}$$

From Equation 5.15, we have

$$\frac{dp}{dx} = -\frac{12\mu}{h^3}\left(Q - \frac{hU}{2}\right) \tag{E.5.2.4}$$

The maximum pressure occurs at an $x$-location where $dp/dx = 0$, that is,

$$h_{\text{opt}} = \frac{2Q}{U} = \frac{2h_1 h_2}{h_1 + h_2} = h_1 + \frac{h_2 - h_1}{L}x_{\text{opt}} \tag{E.5.2.5a}$$

Thus,

$$x_{\text{opt}} = \frac{h_1 L}{h_1 + h_2} \tag{E.5.2.5b}$$

The sustaining force per unit width, that is, the load, is

$$F = \int_0^L (p - p_0)dx \tag{E.5.2.6}$$

where with Equation E.5.2.4, we obtain

$$p(x) = p_0 + 6\mu U \int_0^x \frac{dx}{h^2} - 12\,\mu Q \int_0^x \frac{dx}{h^3} \tag{E.5.2.7}$$

*Tasks:*

- Solve Equations E.5.2.7 and E.5.2.6 with $h(x) = h_1 + \dfrac{h_2 - h_1}{L} x$
- Plot $p(x)$ and indicate $x_{opt}$ and $p_{max}$ for a reasonable geometry (see Graph 2a).
- Plot velocity profiles of Equation E.5.2.1, similar to Graph 2b.

*Graphs 2:*

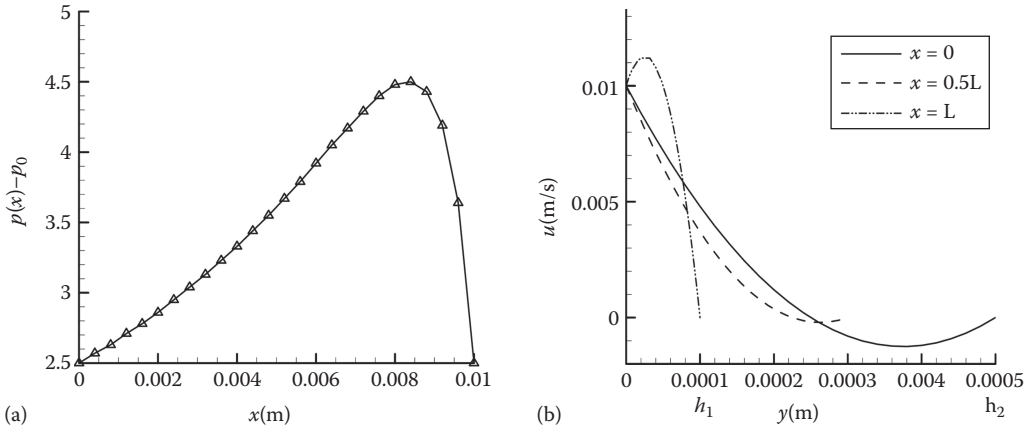


*Comments:*

1. When $x = x_{opt} = h_1 L/(h_1 + h_2)$, $p(x)$ reaches its maximum $p_{max}$
2. The $u(x,y)$ -distributions vary greatly relative to the $x$ position; as $x$ increases, the backflow region decreases.

## 5.2 The Reynolds Lubrication Equation

To generalize the "planar (or slider) bearing" of Section 5.1.3, we now consider that the upper slanted (or curved wall) also moves downward with a vertical velocity (see Example 5.1 and Figure 5.4):

$$v(t) = -\frac{\partial h}{\partial t} \cong -V \tag{5.17}$$

Now, $h = h(x,t)$, and the squeezing effect will produce flow in the $z$-direction as well. Hence, with the following scales:

$$x, z \sim L; \quad y \sim h_0; \quad t \sim \frac{L}{U}; \quad u, w \sim U; \quad v \sim \frac{h_0}{L}; \quad p \sim \mu \frac{uL}{h_0}$$

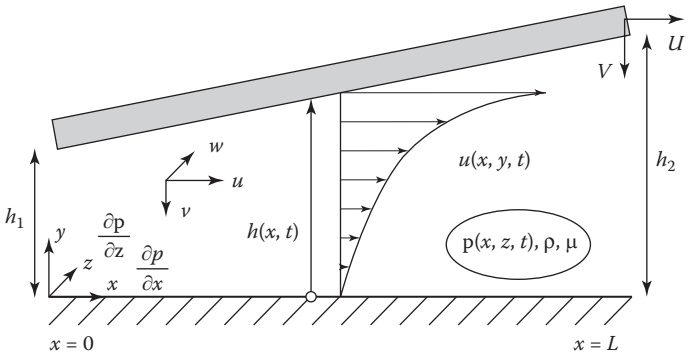


**FIGURE 5.4**
Generalized slider bearing.

we have to solve

$$0 = -\frac{\partial p}{\partial x} + \mu \frac{\partial^2 u}{\partial y^2} \tag{5.18}$$

and

$$0 = -\frac{\partial p}{\partial z} + \mu \frac{\partial^2 w}{\partial y^2} \tag{5.19}$$

subject to the no-slip conditions at $y = 0$ and $y = h(x, t)$. The results are (see HWA in Section 5.3) for the axial flow

$$u(x, y; t) = \frac{h^2}{2\mu}\left(\frac{\partial p}{\partial x}\right)\left[\left(\frac{y}{h}\right)^2 - \left(\frac{y}{h}\right)\right] + \left(1 - \frac{y}{h}\right)U \tag{5.20}$$

If the pressure gradient is zero, simple Couette flow is recovered. For the film flow in the $z$-direction, that is, due to the squeeze effect, we have

$$w(x, y, z; t) = \frac{h^2}{2\mu}\left(\frac{\partial p}{\partial z}\right)\left[\left(\frac{y}{h}\right)^2 - \left(\frac{y}{h}\right)\right] \tag{5.21}$$

Knowing the velocity field of the lubrication film, we now can develop an equation with a varying spacing $h(x, t)$ for the pressure gradients in the $x$-direction and $z$-direction (see Figure 5.4). We start out with the continuity equation, that is,

$$-\frac{\partial v}{\partial y} = \frac{\partial u}{\partial x} + \frac{\partial w}{\partial z} \tag{5.22}$$

Integrating Equation 5.22 across the gap, recalling that $V = \partial h / \partial t = \int_0^h \frac{\partial v}{\partial y} dy$ and applying the Leibniz rule (see Appendix AI.3.2), we obtain

$$-\frac{\partial h}{\partial t} = -V = \frac{\partial}{\partial x}\int_0^h u\,dy - \frac{\partial u(h)}{\partial x} + \frac{\partial}{\partial z}\int_0^h w\,dy \qquad \text{(5.23a through c)}$$

where

$$u(h) = U \quad \text{and hence,} \quad \frac{\partial\{u(h)\}}{\partial x} = 0$$

In detail:

$$\int_0^h u\,dy = \int_0^h \left[\frac{h^2}{2\mu}\left(\frac{\partial p}{\partial x}\right)\left(\frac{y^2}{h^2} - \frac{y}{h}\right) + U\frac{y}{h}\right]dy \qquad (5.24a)$$

$$\int_0^h u\,dy = \frac{h^2}{2\mu}\left(\frac{\partial p}{\partial x}\right)\left[\frac{y^3}{3h^2} - \frac{y^2}{2h}\right]_0^h + U\left[\frac{y^2}{2h}\right]_0^h = -\frac{h^3}{12\mu}\left(\frac{\partial p}{\partial x}\right) + \frac{Uh}{2} \qquad (5.24b)$$

and

$$\int_0^h w\,dy = \int_0^h \left[\frac{h^2}{2\mu}\left(\frac{\partial p}{\partial z}\right)\left(\frac{y^2}{h^2} - \frac{y}{h}\right)\right]dy \qquad (5.25a)$$

$$\int_0^h w\,dy = \frac{h^2}{2\mu}\left(\frac{\partial p}{\partial z}\right)\left[\frac{y^3}{3h^2} - \frac{y^2}{2h}\right]_0^h = -\frac{h^3}{12\mu}\left(\frac{\partial p}{\partial z}\right) \qquad (5.25b)$$

With the given results of the integral expressions, the continuity equation now reads:

$$-\frac{\partial h}{\partial t} = -\frac{\partial}{\partial x}\left[\frac{h^3}{12\mu}\left(\frac{\partial p}{\partial x}\right) + \frac{Uh}{2}\right] - \frac{\partial}{\partial z}\left[\frac{h^3}{12\mu}\left(\frac{\partial p}{\partial z}\right)\right] \qquad (5.26a)$$

or

$$\frac{\partial h}{\partial t} = \frac{\partial}{\partial x}\left[\frac{h^3}{12\mu}\left(\frac{\partial p}{\partial x}\right)\right] + \frac{U}{2}\frac{\partial h}{\partial x} + \frac{\partial}{\partial z}\left[\frac{h^3}{12\mu}\left(\frac{\partial p}{\partial z}\right)\right] \qquad (5.26b)$$

For *planar bearings*, the geometry condition is $\partial h/\partial z = 0$, so that Equation 5.26b reduces to

$$\frac{\partial h}{\partial t} = \frac{\partial}{\partial x}\left[\frac{h^3}{12\mu}\left(\frac{\partial p}{\partial x}\right)\right] + \frac{U}{2}\frac{\partial h}{\partial x} \qquad (5.27a)$$

It can be rewritten in three dimensions (3-D) as

$$\frac{\partial h}{\partial t} = \nabla\cdot\left[\frac{h^3}{12}\nabla p + \frac{h}{2}\vec{U}\right] \qquad (5.27b)$$

In non-dimensional form, with

$$\hat{p} = \frac{p - p_0}{\frac{\mu UL}{h_1^2}}, \qquad d\hat{p} = \frac{h_1^2}{\mu UL} dp, \hat{x} = \frac{x}{L}, \qquad d\hat{x} = \frac{dx}{L}$$

and a linear gap

$$\hat{h} = \frac{h(x)}{h_1} = 1 + \left( \frac{h_2}{h_1} - 1 \right) \hat{x},$$

we have

$$d\hat{h} = \frac{1}{h_1} dh \quad \text{and} \quad \frac{\partial \hat{h}}{\partial \hat{x}} = \left( \frac{h_2}{h_1} - 1 \right)$$

Without squeezing action, $V = \partial h/\partial t = \partial h(x)/\partial t = 0$, we obtain

$$0 = \frac{1}{L} \frac{\partial}{\partial \hat{x}} \left[ \frac{\hat{h}^3}{12\mu} h_1^3 \frac{\mu UL}{h_1^2 L} \left( \frac{\partial \hat{p}}{\partial \hat{x}} \right) \right] + \frac{U h_1}{2L} \left( \frac{h_2}{h_1} - 1 \right) \tag{5.28}$$

which in compact form reads:

$$\frac{\partial}{\partial \hat{x}} \left[ \hat{h}^3 \left( \frac{\partial \hat{p}}{\partial \hat{x}} \right) \right] = 6 \left( 1 - \frac{h_2}{h_1} \right) \tag{5.29}$$

**Example 5.3: Find the Pressure Build-Up in a Basic Slider Bearing with a Linearly Increasing Gap, $U$ = Constant and Atmospheric Inlet and Outlet Pressures**

| Sketch 2 | Assumptions | Method |
|---|---|---|
| 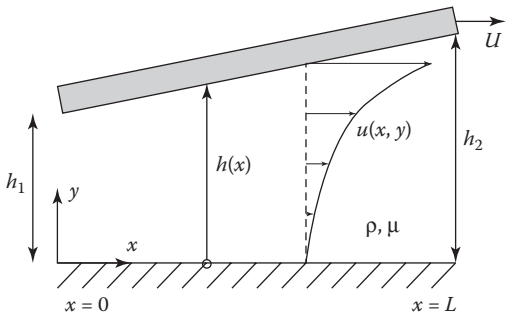 | • Laminar flow<br>• Lubrication approximation<br>• Constant fluid properties<br>• No end effects<br>• Linear $h(x)$ | • Continuity equation<br>• Reduced N-S equation<br>• $\vec{v} = \left[ u(y); 0; w(y) \right]$<br>• $\nabla p = \left[ \frac{\partial p}{\partial x}; 0; \frac{\partial p}{\partial z} \right]$<br>• $h(x) = h_1 + \left( \frac{h_2 - h_1}{L} \right) x$ |



*Solution:* Equation 5.29 is first rewritten in terms of the dimensionless pressure gradient, where at $x = x_m$ (or $h = h_m$), the film pressure has the mean value of $p_m$:

$$\frac{\partial}{\partial \hat{x}} \left[ \hat{h}^3 \left( \frac{\partial \hat{p}}{\partial \hat{x}} \right) \right] = 6 \left( 1 - \frac{h_2}{h_1} \right), \tag{E.5.3.1}$$

$$\hat{h}_m = \frac{\hat{h}(\hat{x}_m)}{h_1} = 1 + \left(\frac{h_2}{h_1} - 1\right)\hat{x}_m \tag{E.5.3.2}$$

$$\hat{h}^3\left(\frac{\partial \hat{p}}{\partial \hat{x}}\right) = 6\left(\hat{h} - \hat{h}_m\right) \tag{E.5.3.3}$$

$$\frac{\partial \hat{p}}{\partial \hat{x}} = 6\left(\frac{1}{\hat{h}^2} - \frac{\hat{h}_m}{\hat{h}^3}\right) \tag{E.5.3.4}$$

Integration in the axial direction yields

$$\hat{p} = \int_0^{\hat{x}} 6\left(\frac{1}{\hat{h}^2} - \frac{\hat{h}_m}{\hat{h}^3}\right) d\hat{x} \tag{E.5.3.5}$$

At either end of the channel, the pressure is a minimum. Thus, the appropriate boundary conditions for the pressure in the channel are $\hat{p}(\hat{x}=0)=0$ and $\hat{p}(\hat{x}=1)=0$.

Applying these boundary conditions yields the following pressure distribution:

$$p(x) - p_0 = -6U\frac{\mu\hat{x}}{h_1^2\left[1-\left(\frac{h_2}{h_1}-1\right)\frac{x}{L}\right]}\left\{\frac{1-\left(\frac{h_2}{h_1}-1\right)}{2-\left(\frac{h_2}{h_1}-1\right)}\right\}\left\{\frac{2-\left(\frac{h_2}{h_1}-1\right)}{1-\left(\frac{h_2}{h_1}-1\right)}\right\}(1-\hat{x}) \tag{E.5.3.6}$$

Or in a more compact form:

$$\frac{p(x)-p_0}{6\left(\frac{h_2-h_1}{h_2+h_1}\right)} = \frac{\mu U x}{\left[h_1 + (h_2-h_1)\frac{x}{L}\right]^2}\left(1-\frac{x}{L}\right) \tag{E.5.3.7}$$

It should be noted that the "wedge effect," that is, $h_2 > h_1$, has to be preserved. In other words, Equation E.5.3.7 is not applicable to Couette-type flows.

*Graph 3:*

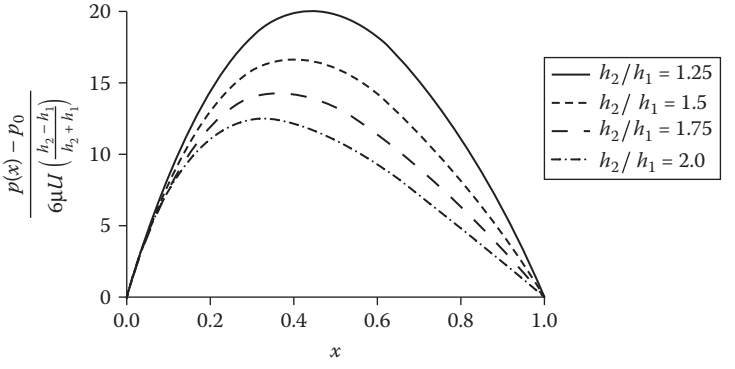

*Comments:*

- As the geometry parameter $h_1/h_2$ increases, the hydraulic resistance goes up, and the load-carrying capacity diminishes.
- With larger $h_1/h_2$-ratios, the peak-pressure location shifts toward the slider front-end.

As in (planar) slider bearings, a wedge effect for high-load lubrication can be generated when a rotating cylinder is placed *eccentrically* in a stationary housing (see Figure 5.1c). This is called a *journal bearing*, as it appears in most rotating machinery (see Example 5.4).

**Example 5.4: Long, Eccentric Journal Bearing**

Consider a rotating shaft of radius $R_1$ inside a stationary housing of inner radius $R_2$, both of length $L$. The difference $R_2 - R_1 \equiv c$ is the *variable clearance*, and the ratio $e/c = \varepsilon$ is the eccentricity, where $e$ is the off-center distance (see Sketch 3). Again, it is the "confined wedge-flow effect" that generates the high, load-bearing pressure distribution. Different from the clearance is the *very small gap h*. Here, $h \approx c(1+\varepsilon\cos\theta) \ll 1$, which implies $h(\theta=0) = h_{max} = c(1+\varepsilon) = c + e$ and $h(\theta=\pi) = h_{min} = c - e$.

Derive an expression for the internal pressure in the form $\hat{p}(\theta)$, where $\hat{p} = \dfrac{p - p_0}{\mu\omega_0 (R_1/c)^2}$.

| Sketch 3 | Assumptions | Method |
|---|---|---|
| 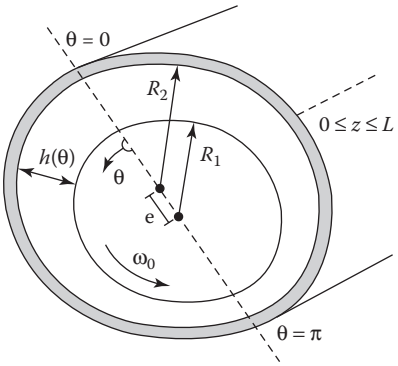 | • Steady laminar flow<br>• Slow shaft rotation<br>• $h/R_1 \ll 1$; $R_1/L \ll 1$<br>• $h = h(e, \theta)$ as given<br>• Stretched coordinate $x = R_1\theta$<br>• Constant properties<br>• No end effects | • Reduced lubrication equation (Equation 5.24)<br>• Reynolds pressure conditions at $\theta = \theta_{cavity}$: $p = 0$ and $dp/d\theta = 0$ |

*Solution:* Non-dimensionalization yields

$$\theta = \frac{x}{R_1},\ \hat{h} = \frac{h}{c},\ \hat{z} = \frac{z}{L/2},\ \text{and}\ \ \hat{p} = (p - p_0) / \left[\mu\omega_0 (R_1/c)^2\right]$$

Employing Equation 5.29 with $h = h(x)$ becoming $h(\theta)$ and $(R_1/L)^2 \approx 0$, we have

$$\frac{\partial}{\partial\theta}\left(\hat{h}^3 \frac{\partial\hat{p}}{\partial\theta}\right) = 6\frac{\partial\hat{h}}{\partial\theta} \qquad \text{(E.5.4.1)}$$

Integrating twice yields

$$\hat{p}(\theta) = 6\int_0^\theta \frac{\hat{h} - C}{\hat{h}^3}\, d\theta \qquad \text{(E.5.4.2a)}$$

where the integration constant $C$ depends on the assumed pressure boundary conditions. For example, setting $p=0$ and $dp/d\theta=0$ when a vapor cavity starts to form at $\theta=\theta_{cav}$, we get (Szeri, 1980)

$$C = \hat{h}(\theta_{cav}) \tag{E.5.4.2b}$$

Typical $\theta_{cav}$-values are 249.2° when $\varepsilon=0.1$ and 219.7° when $\varepsilon=0.5$. For the latter case, the $\hat{p}(\theta)$ distribution is given in Graph 4.

*Graph 4:*

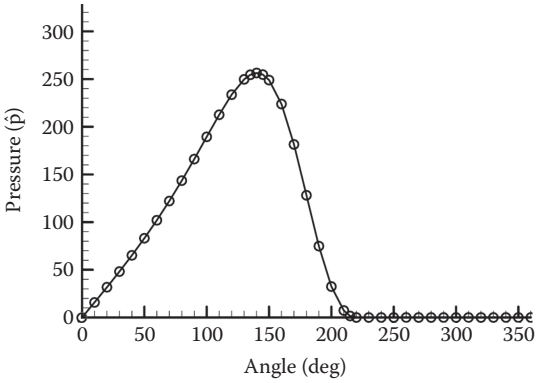


*Comments:*

- The pressure distribution in the journal bearing follows qualitatively that of planar bearings (see Example 5.2).
- Again, the magnitude of $h$ and the pressure boundary conditions greatly determine $\hat{p}(\theta)$ and hence the load-carrying capacity of the journal bearing.

## 5.3 Lubricants with Nanoparticles

Nanofluids, being very dilute suspensions of nanospheres or short carbon-nanotubes in a liquid, have numerous applications in microsystem cooling, drug delivery, and enhanced lubrication, to name just a few (Kleinstreuer and Xu, 2016; Kleinstreuer, 2014, among others). Adding either soft or hard nanoparticles to lubricants can significantly reduce friction and wear and increase the load-carrying capacity of bearings (see Figure 5.5). Typically, such nanoparticles are metal or metal oxides, sulfides, or non-metals, which are well suspended at around 1% in volume.

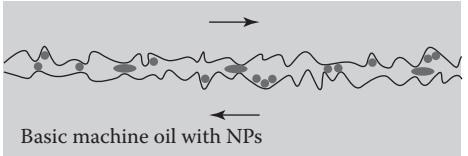


**FIGURE 5.5**
Boundary lubrication with a nanofluid.

Under boundary nano-lubricating conditions, the nanoparticles first nestle into the rubbing surfaces, generating a surface-polishing effect. In addition, they separate the asperities of the moving surfaces, preventing their direct contact, and hence, may act like a ball-bearing. The friction-related mechanisms of lubricants with nanoparticles can be deduced by analyzing scanning electron microscopy images and energy-dispersive spectrometry patterns of the wear surface. Clearly, using nanofluids as lubricants can provide improved efficiency in energy use and reliability of mechanical systems.

There are very few numerical studies of enhanced lubrication when using nanoparticles. This can be attributed to the fact that the lubrication process often involves the deformation of nanoparticles, which is difficult to model. Nevertheless, some studies have revealed lubrication characteristics using numerical methods. For example, Lv et al. (2011) used molecular dynamics (MD) simulations to study the frictional mechanisms of nanofluid lubricants. They showed nanoparticle rotations under low pressure as well as trapping and aggregation of nanoparticles under higher pressures. These effects separated the friction surfaces and led to enhanced lubrication properties. The MD simulations of Hu et al. (2014) demonstrated that phase transition took place under high load, while the transition pressure of a nanoparticle-added lubricant was higher than that of the base lubricant. Nanoparticles could effectively increase the load-carrying capacity, especially for nanoparticles with smaller sizes, due to stronger micro-motions and volume effects. The authors demonstrated that the improved load-carrying capacity is due to the organized molecular structures of the lubricant near the nanoparticles and to the deformation of nanoparticles. Shenoy et al. (2012) used a modified Reynolds equation to numerically investigate the effect of a nanoparticle additive on the fluid film of a journal bearing. The results indicated that dispersing $TiO_2$ nanoparticles in engine oil can reduce end-leakage as well as friction, thus improving the load capacity of the bearing. Binu et al. (2014) used a modified viscosity model to incorporate the nanoparticle effect on the rheology of the fluid-particle mixture, that is, a $TiO_2$-based lubricant. They introduced coupled stresses to the Reynolds equation to account for the impact of nanoparticles. The model predicted a significant increase in load-carrying capacity of the journal bearing. Nicoletti (2014) found that adding nanoparticles to the base oil modified the volumetric heat capacity of the lubricant, resulting in a lower temperature and hence, a larger viscosity, implying an improved load-carrying capacity.

In summary, using nanoparticles as additives to lubricants can greatly enhance their tribological properties by reducing friction and wear as well as increasing the load-carrying capacity. Low weight percentages of nanoparticles seem to provide the best performance. The mechanisms for enhanced lubrication performance are manifold and depend on the material structure of the nanoparticles. Under film-lubrication conditions, where the load is supported by the lubricant and any solid-solid contact is avoided, the potential increase of the lubricant's viscosity due to nanoparticle addition needs to be considered. Again, a homogeneous suspension of nanoparticles in lubricants is vital for proper applications, as large aggregates of nanoparticles may be detrimental to the lubrication process.

## 5.4 Homework Assignments

The "Insight" questions emerged directly out of the Chapter 5 text. Some "Problems" were taken from lecture notes based on the open literature after content modification and enhancement. Additional examples, concept questions, and problems may be found in

good undergraduate fluid mechanics and heat transfer texts or on the Web (see websites of MIT, Stanford, Cornell, Penn State, University of Michigan, etc.).

### 5.4.1 Physical Insight

5.1 Interpret and illustrate Equation 5.1 (1) mathematically and (2) physically, especially the extreme cases of $f = 0.01$ and $f = 1.0$.

5.2 Derive via scale analysis Equations 5.4 to 5.7c.

5.3 Find an expression for $p(x)$ based on a linear $h(x)$ in slot flow. Plot the pressure distribution for different system parameters and comment.

5.4 Derive in Example 5.1 the load-expression Equation E.5.1.15. Plot for reasonable $h(t)$-functions the loads given with Equations E.5.1.13 and E.5.1.15 for different μ- and $(n < 1)$-values.

5.5 Develop an equation for (1) the reactive force in slot flow (see Figure 5.2) and (2) the load in squeeze-film lubrication (see Example 5.1).

5.6 Why is there possibly backflow in a slider bearing (see Figure 5.3)?

5.7 Compare the slot-flow analysis of Section 5.1.1 with planar lubrication (Section 5.1.3) in terms of 2-D modeling equations and the expected results for $u(x,y)$ and $p(x)$.

5.8 Extend Example 5.2 by implementing the following tasks: (1) Solve Equations E.5.2.7 and E.5.2.6 with $h(x) = h_1 + (h_2 - h_1/L)x$; (2) Plot $p(x)$ and indicate $x_{opt}$ and $p_{max}$ for a reasonable geometry; (3) Plot velocity profiles of Equation E.5.2.1.

5.9 Concerning Example 5.4, derive Equation E.5.4.1 and solve Equation E.5.4.2a with the given information for $C$ and $h(\theta)$.

5.10 Derive Equations 5.20 and 5.21 with examples.

### 5.4.2 Engineering Problems

5.11 Consider a basic slider-block as shown:

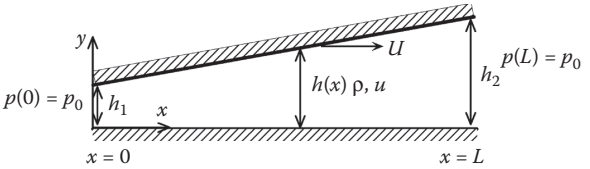


To apply the Reynolds Lubrication Theory, we recall that $h_2 \ll L$ and $U = ¢$, so that due to the "wedge effect," a high pressure in the lubrication layer generates a large lift, that is, load-carrying capacity of the planar bearing.

$$\frac{\partial h}{\partial t} = \nabla \cdot \left[ \frac{h^3}{12} \nabla p + \frac{h}{2} \vec{U} \right] \quad \text{to} \quad \frac{d}{dx}\left( h^3 \frac{dp}{dx} \right) = 6\left( 1 - \frac{h_2}{h_1} \right)$$

which is now in dimensionless form with $U = 1$ (unity).

a. Solve for $p(x) - p_0$ and $dp/dx$.

b. Plot $\dfrac{p(x)-p_0}{6\left(\dfrac{h_2-h_1}{h_2+h_1}\right)}$, find the location for $p_{\max}$, and comment.

c. Find the velocity field, $\vec{v} = \nabla p\left(\dfrac{y^2}{2\mu}-\dfrac{yh}{2\mu}\right) + \vec{U}\left(\dfrac{y}{h}-1\right)$, and indicate how to compute the hydrodynamic forces, that is,

$$\vec{F} = -\int_A \hat{n}\left[p(x)-p_0\right]dA + \int_A \hat{n}\cdot\vec{\tau}_w dA$$

5.12 Consider a sphere of radius $R$ approaching a horizontal wall vertically under force $F_z$ in a viscous fluid $\mu$. Note that the distance $h(t,x)$; that is, the sphere-wall gap function is small: $\varepsilon = h_0/R \ll 1$. Thus, the film-lubrication region is of interest. Specifically,

a. Show that the Reynolds equation (see Equation 5.27a) reduces to

$$12\mu\frac{\partial h}{\partial t} = \frac{1}{x}\frac{\partial}{\partial x}\left(xh^3\frac{\partial p}{\partial x}\right)$$

and determine the gap function $h(x,t) = h_0(t) + f(x, R)$, where $h_0(t)$ is the smallest clearance.

The reference pressure at the film's outer boundaries, $\pm x_b$, is $p(x = \pm x_b) = p_b$.

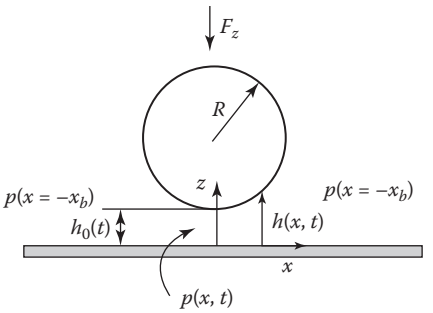


b. Find $\partial p/\partial x = 6\mu\dfrac{x}{h^3}\dfrac{dh}{dt}$ as well as an expression for $p(x) - p_b$.

c. Assuming that only the film pressure contributes to the vertical force, develop an equation for

$$F_z = 2\pi\int_0^{x_b}\left[p(x)-p_b\right]x\,dx$$

d. With the approximation $\dfrac{x_b^2}{2h_0R} \gg 1$, show that $F_z \approx 6\pi\mu R^2\dfrac{dh_0/dt}{h_0}$, and discuss various scenarios for

$$F_z \sim \left(h_0^{-1} \text{ and } \frac{dh}{dt} = \text{const.}, \text{ etc.}\right)$$

e. Given a constant $F_z$ (e.g., the sphere's weight), find $h_0(t)$ subject to $h_0(t=0) = h_{\text{initial}}$, plot $dh_0/dt$ as well as $h_0(t)$ and comment.

f. The result of (e) indicates that the sphere will not touch the wall within a finite time interval, which contradicts experimental observations. What happens?

5.13 Consider a nanofluid as a lubricant in the planar bearing of Example 5.3 and compare the pressure results for nanofluid flow (i.e., mixture flow) versus oil (i.e., a Newtonian fluid).

# 6

# *Fluid Spreading, Film Drawing, and Surface Coating*

## 6.1 Introduction

Pressure, viscous, and gravitational forces, as well as surface tension for free-surface problems play key roles in planar fluid spreading, surface coating, slit flow, lubrication systems, and film drawing. Typically, *nearly parallel flow* and one-dimensional (1-D) free-surface force balances are assumed to solve basic thin-film problems. The underlying fluid-interface assumptions are that the free-surface curvature $C = R^{-1}$ relates to the second derivative of the film thickness $h$, which is very small, that is, $h/L \ll 1$. Such a geometric simplification entails a negligible normal velocity component, and consequently, $\partial u/\partial x \approx 0$ from continuity and $\partial p/\partial y \approx 0$ from the $y$-momentum equation. Hence, the $x$-momentum equation can be reduced to

$$0 = -\frac{dp}{dx} + \mu \frac{\partial^2 u}{\partial y^2} + \rho g_x \; + f_{\text{surface - tension}} \tag{6.1}$$

In general, for free-surface flows, $p = p(x, y, t)$; but for many practical applications, one can assume a hydrostatic pressure, that is, $p = \rho g h$. For thin-film or device geometries with slightly non-parallel boundaries, $u = u(x, y)$.

Section 6.2 deals with the mechanics of gas–liquid interfaces that are formed when net pressure and surface-tension forces are in equilibrium. Of major interest are the static interface function $z = z(x)$ and the interface angle with a solid surface. Section 6.3 provides an introduction to film-drawing and coating processes, which are illustrated with several examples. The chapter closes with a brief summary of spray-coating systems.

## 6.2 Fluid-Interface Mechanics

Meniscus and droplet formation are two static examples involving fluid-interface mechanics, while gravity-spreading of a pool of fluid is a dynamic example of free-surface flow. For a more general case, consider two immiscible, relatively moving fluids A and B, forming interface $S$ of mean curvature $\overline{C}$. Ignoring surfactant and temperature gradients, the equilibrium forces are net total stress tensor $T$ and surface tension $\sigma = F/l$ (Figure 6.1).

The force vector balance reads:

$$\hat{n} \cdot (T_B - T_A) + \hat{n}\overline{C}\,\sigma = \vec{0} \tag{6.2}$$

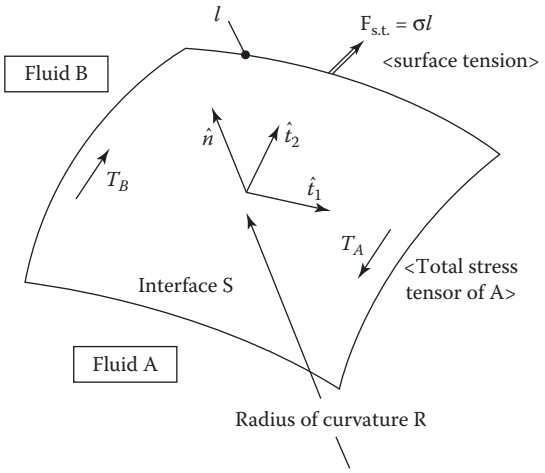


**FIGURE 6.1**
Free-body diagram for interface between two immiscible fluids A and B.

where:

| | |
|---|---|
| $\overline{C} \equiv R^{-1}$ | is the mean curvature of the interface $S$ |
| $\sigma$ | is a given fluid surface tension |
| $T \equiv \vec{\vec{\tau}}_{\text{total}} = -p\hat{I} + \vec{\vec{\tau}}$ , $p$ | is the thermodynamic pressure |
| $\hat{I}$ | is the unit tensor |
| $\vec{\vec{\tau}}$ | combines the normal and tangential (i.e., shear) stresses |

Under static, that is, no-flow conditions, Equation 6.3 reduces to the Young–Laplace equation:

$$-\Delta p + \overline{C}\sigma = 0 \tag{6.3}$$

where $\Delta p$ is the static pressure difference between the two fluids. The mean surface curvature has to be determined based on the interface geometry:

$$\overline{C}\hat{n} = \frac{d\hat{t}}{ds} \tag{6.4}$$

where:

$\hat{n}$ is the normal unit vector
$\hat{t}$ is the tangent unit vector
$s$ is the interface arc length

Specifically, for a cylindrically symmetric surface described by $h(x)$, with $h'$ and $h''$ being the contour derivatives (see Homework Assignments in Section 6.5),

$$\overline{C} = \frac{h''}{\sqrt{[1+(h')^2]^{3/2}}} \tag{6.5}$$

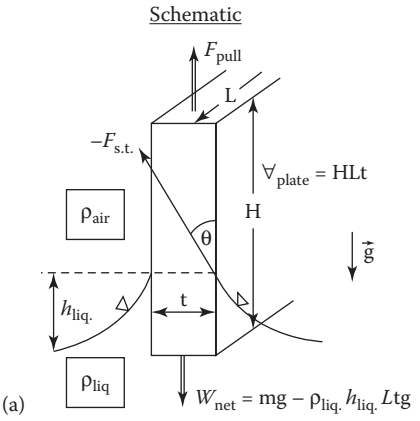


**FIGURE 6.2**
(a) System schematic and (b) Force balance.

Usually, $h'$ in Equation 6.5 is very small, so that the radius of curvature becomes $R = 1/h''$. When applied to standard gas–liquid configurations, we have

$$\overline{C} = \begin{cases} 0 & \text{for planar surfaces} \\ 2/R & \text{for spheres of radius } R \\ 1/R & \text{for cylinders of radius } R \end{cases}$$

If a meniscus forms between a rising liquid (on a vertical wall as shown in Example 6.1) and air, a 1-D force balance between surface tension and gravity yields (see Equation 6.3)

$$\frac{\sigma}{R} + \rho g h = 0 \tag{6.6}$$

where:
σ (N/m) is the surface tension
$R \sim 1/h''$ is the meniscus curvature
$\rho g h$ is the fluid static pressure

**Example 6.1: Meniscus at a Vertical Wall**

Consider a gas–liquid interface with capillary rise $h$ at a vertical wall forming the contact angle θ, which is the inclination angle $\varphi = \pi/2 - \theta$. Find $h$ and θ.

| Sketch 1 | Assumptions | Method |
|---|---|---|
| 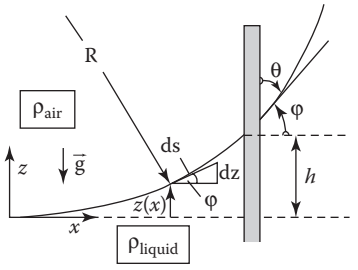  | • Cylindrically symmetric surface<br>• 1-D static analysis: surface-tension force balances gravity | • Young–Laplace equation with $\overline{C} = 1/R$ and $\Delta p = -\Delta\rho g z$ from fluid statics, where Δρ is the two-fluid density change |

*Solution*: Equation 6.3 now reads:

$$\Delta\rho g z + \bar{C}\sigma = 0 \tag{E.6.1.1}$$

With Equation 6.5, we now have

$$\bar{C} \equiv \frac{1}{R} = \frac{z''}{[1+(z')^2]^{3/2}} = -\frac{\Delta\rho g}{\sigma} z = -Kz \tag{E.6.1.2a through d}$$

subject to $z(x = 0) = 0$ and $z'(x = 0) = \tan(\varphi) = 0$. Instead of solving this nonlinear ordinary differential equation (ODE) numerically, we start with the simplification $\bar{C} = R^{-1}$, that is, $z' \approx 0$. Now, the circular arc length $\Delta s = R\Delta\varphi$, or

$$\frac{1}{R} = \frac{d\varphi}{ds} \tag{E.6.1.3}$$

Eliminating $ds$, we recall $\sin\varphi = \dfrac{dz}{ds}$, so that

$$\frac{1}{R} = \frac{d\varphi}{dz}\frac{dz}{ds} = \frac{d\varphi}{dz}\sin\varphi = -Kz$$

Integrating

$$\sin\varphi \cdot d\varphi = -Kz dz \tag{E.6.1.4}$$

yields

$$\cos\varphi = -\frac{K}{2}z^2 + C_1 \tag{E.6.1.5}$$

where at $z = 0$, we have the incline angle $\varphi = 0°$, that is, $\cos\varphi = 1$ and $C_1 = 1$. Thus,

$$\cos\varphi - 1 = -2\sin^2\left(\frac{\varphi}{2}\right) = -\frac{K}{2}z^2$$

or

$$z = \pm 2\sqrt{\frac{\sigma}{\Delta\rho g}}\sin\left(\frac{\varphi}{2}\right) \tag{E.6.1.6}$$

Finally, $z = h$ when the contact angle is $\theta$, or $\varphi = \pi/2 - \theta$.
Hence,

$$h = 2\sqrt{\frac{\sigma}{\Delta\rho g}}\sin\left(\frac{\pi}{4} - \frac{\theta}{2}\right) \tag{E.6.1.7}$$

where $\theta < \pi/2$ for $h$ to be positive.

*Graph 1:*

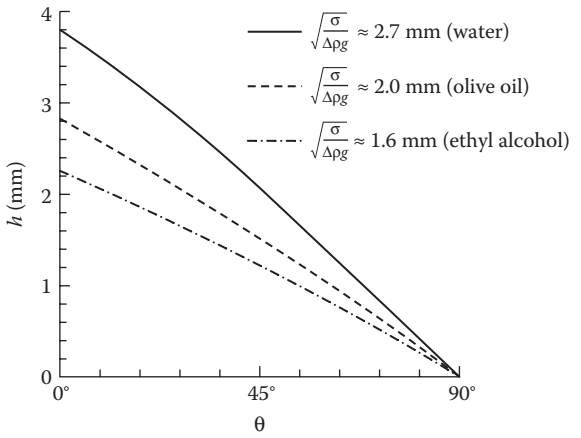


*Comments:*

- As expected, $h \sim \sigma$; that is, with increasing parameter $\sqrt{\frac{\sigma}{\Delta\rho g}}$, the (pulling) surface-tension force $\vec{F}_\sigma$ gets larger, and hence, $h$ increases.
- The magnitude of the vertical component of $\vec{F}_\sigma$ depends greatly on $\theta$, that is, $0° \le \theta \le 90°$, implying that for $\theta = 0°$, $F_{vertical} = F_{max}$, and hence, $h = h_{max}$, while for $\theta = 90°$, $F_{vertical} = 0$.

Clearly, the key parameter in air–liquid interface mechanics is the surface tension $\sigma$. Example 6.1 indicates that, if not known beforehand, $\sigma$-values can be obtained from a vertical-plate force balance measuring the upward pulling force, the fluid densities, and the contact angle, as shown in Figure 6.2.

Thus, ignoring the buoyance effect on the plate portion in the air,

$$F_{\text{pull}} = 2\sigma(L+t)\cos\theta + (\rho H - \rho_{\text{liq.}} h_{\text{liq.}})Ltg \tag{6.7}$$

With $h_{\text{liq}}$ from the net-weight expression (see Figure 6.2) and the plate geometry plus density known, only the pulling force and the contact angle have to be measured to compute the surface tension from Equation 6.7.

**Example 6.2: Surface Coating**

In contrast to the falling film of constant thickness (see Example 2.7), we now consider more realistic surface coating. A thin plate is being submerged into a finite reservoir of a coating solution and then vertically withdrawn at a constant velocity.
The interplay of drag force, gravitational effect, and surface tension is described by the Reynolds lubrication equation (see Section 5.2.1) combining pressure gradient, drag force, and gravity, while the Young–Laplace equation (Equation 6.6) relates pressure gradient and surface tension.

*Solution*: Based on the stated assumptions, Stokes' equation reduces to

$$-\frac{dp}{dy} + \mu\frac{d^2u}{dx^2} - \rho g = 0 \tag{E.6.2.1}$$

| Sketch 2 | Assumptions | Method |
|---|---|---|
| 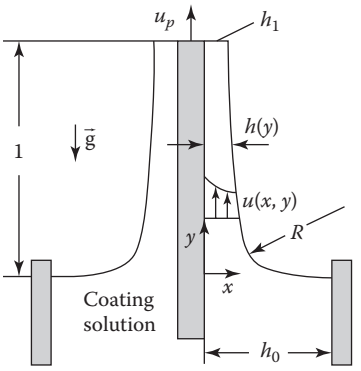 | • Steady laminar, quasi-unidirectional flow<br>• Constant properties<br>• Smooth film surface<br>• Negligible shear stress at the air–liquid interface<br>• Plug flow $u(y=1)=u_p=\not<$ and $Q=u_p h_1$; that is, $h_1$ is the final coat thickness<br>• Film solidification at $y=1$, that is, $h_1=\not<$, and $u\approx u_p$ | • Differential approach<br>• Reduced Stokes equation (Equation 2.36)<br>• Static force balance at plane interface<br>• Free surface meniscus radius:<br>$R=\dfrac{[1-(h')^2]^{3/2}}{h''}$ |

subject to

$$u(x=0)=u_p \quad \text{and} \quad \left.\frac{du}{dx}\right|_{x=h(y)}=0 \tag{E.6.2.2a, b}$$

Double integration yields

$$u(x,y)=u_p+P[h(y)]^2\left[\left(\frac{x}{h}\right)^2-2\left(\frac{x}{h}\right)\right] \tag{E.6.2.3a}$$

where

$$P\equiv\left(\frac{dp}{dy}+\rho g\right)\Big/(2\mu) \tag{E.6.2.3b}$$

Recall from Example 6.1 that a meniscus is formed between a rising liquid on a vertical wall and air, where a 1-D force balance between surface tension and gravity yields (see Equation 6.6)

$$\frac{\sigma}{R}+\rho g h=0 \tag{E.6.2.4}$$

where:

$\rho g h=p$ is the hydrostatic pressure

meniscus radius $R=\left[1-(h')^2\right]^{3/2}\Big/h''$

Hence, recognizing that $(h')^2\ll 1$, we obtain after differentiation

$$\frac{dp}{dy}=-\sigma\frac{d^3h}{dy^3} \tag{E.6.2.5}$$

Now, the flow rate per unit depth is

$$Q=\int_0^h u\,dx=-\frac{h^3}{3\mu}\left(\frac{dp}{dy}+\rho g\right)+u_p h=u_p h_1 \tag{E.6.2.6a through c}$$

Substituting $dp/dy$ and then rearranging Equation E.6.2.6c results in

$$\frac{h^3}{3}\left(\frac{d^3h}{dy^3}-\frac{\rho g}{\sigma}\right)+\frac{\mu u_p}{\sigma}(h-h_1)=0 \tag{E.6.2.7}$$

Introducing the capillary number $Ca=u_p\mu/\sigma$ and Stokes number $St=\mu u_p/(\rho g h_1^2)$, we recast Equation E.6.2.7 in the form:

$$\frac{d^3h}{dy^3}-\frac{Ca}{h_1^2\,St}+\frac{3Ca}{h^2}\left(1-\frac{h_1}{h}\right)=0 \tag{E.6.2.8}$$

Note that $Ca$ and $St$ may vary within the limiting assumptions of laminar ripple-free film flow; that is, $Ca\sim10^{-5}$, and $St$ is in the range of 0.1–1.0.

Numerical solution of Equation E.6.2.6b, subject to $h(y=l)=h_1$, $h(y=0)=h_0$, and $dh/dy(y=1)=0$, could be achieved with a Runge-Kutta ODE solver. Alternatively, combining Equation E.6.2.5 with Equation E.6.2.8 yields

$$\begin{aligned}\frac{dp}{dy}&=-\sigma\frac{d^3h}{dy^3}=-\sigma\frac{Ca}{h_1^2St}+\sigma\frac{3Ca}{h^2}\left(1-\frac{h_1}{h}\right)\\&=-\rho g+\frac{3u_p\mu}{h^2}\left(1-\frac{h_1}{h}\right)\end{aligned} \tag{E.6.2.9a through c}$$

Now, we have

$$P\equiv\left(\frac{dp}{dy}+\rho g\right)/(2\mu)=\frac{3u_p}{h^2}\left(1-\frac{h_1}{h}\right) \tag{E.6.2.10}$$

where $h=(y)$. We substitute $P$ into Equation E.6.2.3a, and rearranging yields

$$\frac{u(x,y)}{u_p}=1+\frac{3}{2}\left(1-\frac{h_1}{h}\right)\left[\left(\frac{x}{h}\right)^2-2\left(\frac{x}{h}\right)\right] \tag{E.6.2.11}$$

Assuming realistic film thicknesses $h$ (i.e., different $y$-stations) in the range $h_1\le h\le h_0$, we can plot Equation E.6.2.11 as follows.

*Graphs 2:*

(a) Vertical film velocity $u[x, h(y)]$

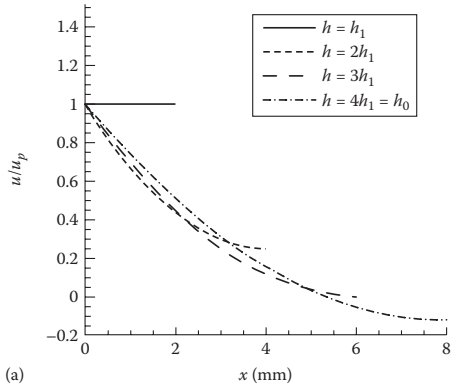


(a)

(b) Emerging film thickness $h(y)$

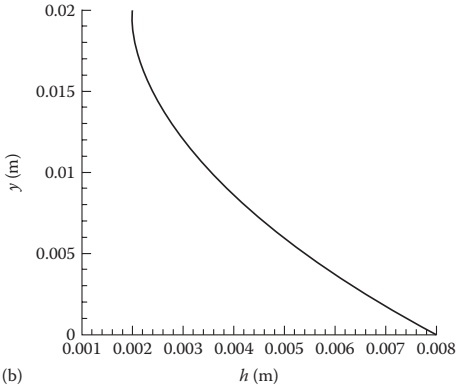


*Comments:*

- For various assumed $h$-values, that is, $y$-stations, Graph 2a depicts the local film velocity profiles at $h_1 \le h \le h_0$ according to Equation E.6.2.11.
- Numerical solution of Equation E.6.2.8 is shown in Graph 2b as $h(y)$ for $h_0 = 8$ mm and $h_1 = 2$ mm, to coat a plate of 20 mm length.

## 6.3 Drawing and Coating Processes

For certain drawing processes in which an applied force pulls the film out of an extruder, the normal stresses are more important than the shear stresses, and hence, Equation 6.1 has to be updated (see Figure 6.3a and Example 6.3). A classic example surface coating is

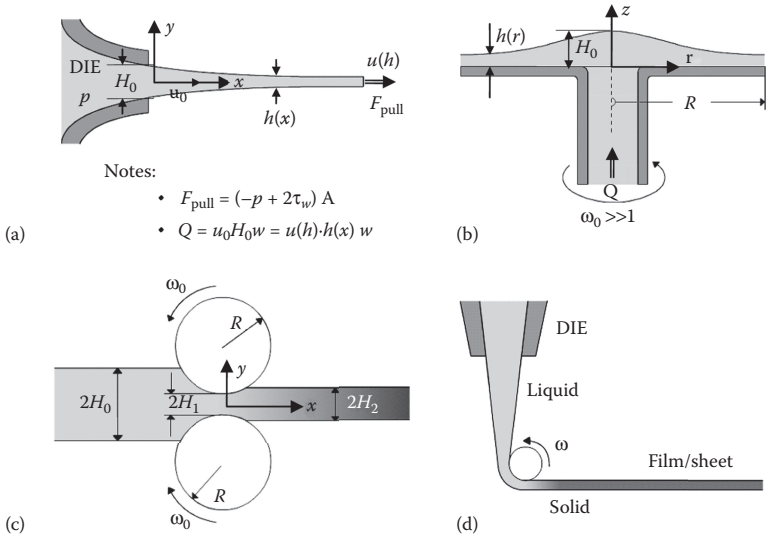


**FIGURE 6.3**
Thin-film drawing and coating processes. (a) Film drawing, (b) spin coating, (c) calendaring, and (d) film casting.

dip-coating (Example 6.2). Other thin-film applications include spin coating, calendering (or extrusion coating), and sheet casting (see Figure 6.3b through d). In most cases, the material is non-Newtonian, such as polymers or melts, and its thermodynamic state changes from liquid (in the die) to solid (as the end product). Specifically, in *film drawing*, molten material is drawn out of a die and pulled up as a solid, thin sheet/film onto a large roll (see Figure 6.3a). For *spin* coating (see Figure 6.3b), a polymeric liquid is fed through the center of a fast-spinning disk, which then spreads radially and coats the disk surface. In polymer processing via *calendering* operation (see Figure 6.3c), a relatively thick sheet is reduced to a final thickness determined by the clearance of the two counter-rotating rollers. In addition, such rollers can impart any surface pattern onto the sheet. *Film casting* is another extrusion process, whereby a liquid film from a die is turned into a solid thin sheet via a cooled, rotating roller (see Figure 6.3d).

**Example 6.3: Film Drawing**

Consider an ultimately solidified thin sheet/film being drawn out of a die with force $F_{pull}$ (see Figure 6.3a). Assuming a steady, slow extrusion process, find expressions for $h(x)$ and $u(x)$ for a given pulling force, volumetric material flow rate, and die-exit velocity and opening.

| Sketch 3 | Assumptions | Method |
|---|---|---|
| 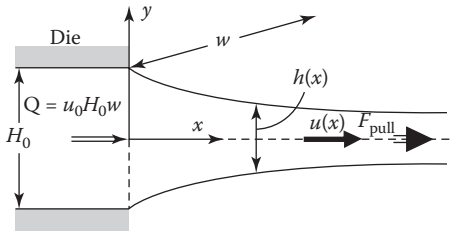 | • Steady two-dimensional (2-D) flow<br>• Constant properties<br>• Thin film for which $H \ll L$, $v \ll u$, and $F_{pull} = \infty$<br>• Normal stresses are important | • Mass conservation with $Q = u(hw)$ and $\frac{\partial u}{\partial x} + \frac{\partial v}{\partial y} = 0$<br>• Dynamic boundary conditions (BCs)<br>• Reduced Navier–Stokes (N-S) equation where $\tau_{normal} \gg \tau_{tangential}$ |

*Solution:*

$$\bullet \quad \text{Continuity:} \quad \frac{\partial u}{\partial x} + \frac{\partial v}{\partial y} = 0 \tag{E.6.3.1}$$

$$\bullet \quad x\text{-momentum:} \quad 0 = -\frac{\partial p}{\partial x} + \mu\left(2\frac{\partial^2 u}{\partial x^2} + \frac{\partial^2 u}{\partial y^2}\right) \tag{E.6.3.2}$$

net normal stress changes

$$\bullet \quad y\text{-momentum:} \quad 0 = -\frac{\partial p}{\partial y} + \mu\left(2\frac{\partial^2 v}{\partial x^2} + \frac{\partial^2 v}{\partial y^2}\right) \tag{E.6.3.3}$$

- Free-surface boundary conditions

$$x\text{-direction}: \quad \tau_{yx}\Big|_{y=\pm h/2} = 0 \tag{E.6.3.4a}$$

$$y\text{ - direction:}\quad \left[-p+\tau_{yy}\right]\Big|_{y=\pm h/2}=0 \tag{E.6.3.4b}$$

- Dynamic B.C.: $$\underbrace{-p+2\mu\frac{\partial u}{\partial x}}_{\substack{\text{pressure plus}\\ \text{normal stress}}}=\underbrace{\frac{F_{\text{pull}}}{hw}}_{\substack{\text{external}\\ \text{force/area}}} \tag{E.6.3.5}$$

With Equation (E.6.3.4a), we assume throughout the film that the shear stress is negligible, implying that

$$\tau_{yx}=\mu\left(\frac{\partial v}{\partial x}+\frac{\partial u}{\partial y}\right)=0$$

Hence, one solution is that $\partial v/\partial x=\partial u/\partial y=0$, so that Equations E.6.3.2 and E.6.3.3 reduce to

$$\frac{\partial}{\partial x}\left(-p+2\mu\frac{\partial u}{\partial x}\right)=0 \tag{E.6.3.6}$$

and

$$\frac{\partial}{\partial y}\left(-p+2\mu\frac{\partial v}{\partial y}\right)=0 \tag{E.6.3.7}$$

Integrating Equation E.6.3.6 subject to B.C. (Equation E.6.3.5) yields

$$-p+2\mu\frac{\partial u}{\partial x}=\frac{F}{hw} \tag{E.6.3.8}$$

Integrating Equation E.6.3.7 subject to B.C. (Equation E.6.3.4b) yields

$$-p+2\mu\frac{\partial v}{\partial y}=0$$

From the assumption $\tau_{yx}=0$, we also have $\partial v/\partial y=-\partial u/\partial x$, so that $p=-2\mu(\partial u/\partial x)$ and hence, Equation E.6.3.8 now read:

$$\frac{du}{dx}=\frac{F}{4\mu hw} \tag{E.6.3.9}$$

To replace $du/dx$, we use $Q=U_0\left(H_0w\right)=uhw=\not{\alpha}$ and differentiate the expression $uh=\not{\alpha}$ to obtain

$$u\frac{dh}{dx}+h\frac{du}{dx}=0 \tag{E.6.3.10}$$

Now, with $u=Q/(hw)$ and Equation E.6.3.9, an ODE for $h(x)$ appears:

$$\frac{Q}{hw}\frac{dh}{dx}+h\frac{F}{4\mu hw}=0 \tag{E.6.3.11a}$$

or

$$\frac{dh}{dx} + \frac{F}{4\mu Q} h = 0 \tag{E.6.3.11b}$$

subject to $h(x=0) = h_0$.

Separation of variables and integration leads to:

$$h(x) = H_0 \exp\left[ -\frac{F}{4\mu Q} x \right] \tag{E.6.3.12}$$

The constant flow rate $u_0 H_0 = hu$ implies that

$$u(x) = U_0 \exp\left[ \frac{F}{4\mu Q} x \right] \tag{E.6.3.13}$$

*Graphs 3:*

(a) Film-thickness developments for different extrusion forces

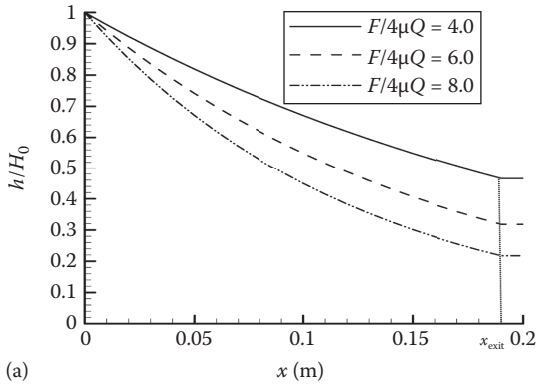


(a)

(b) Developing film velocity for different driving forces

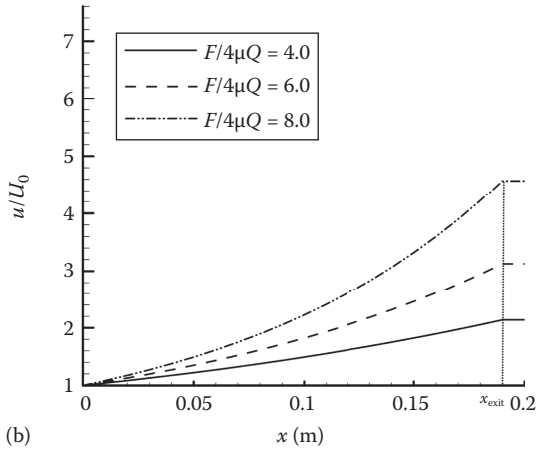


(b)

*Comments:*

- The film thickness decreases exponentially with distance, with the film-thinning greatly influenced by the magnitude of the pulling force (see Graph 3.a). Of course, at a certain axial location $x = x_{exit}$, the film has been solidified, and hence, $h$ = constant.
- The axial film velocity increases exponentially with distance and pulling force (see Graph 3.b). Again, at a critical distance $x$, the solid film moves with a constant velocity $u_p$.

**Example 6.4: Spin Coating**

A material supplied by steady flow from the center is radially spread and thinned on a horizontal, fast-spinning disk (see Figure 6.3b). Assuming lubrication-type flow, derive the radial velocity profile $v_r(r, z)$ and film thickness $h(r)$ during the material-application stage for a given material flow rate $Q$ and disk angular velocity $\omega_0$ (after Papanastasiou, 1994).

| Sketch 4 | Assumptions | Method |
|---|---|---|
| 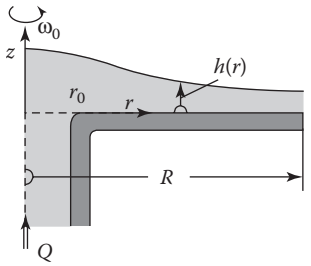 | • Steady 2-D axisymmetric flow, where<br>• $\vec{\mathbf{v}} = [v_r, v_\theta = r w_0, 0]$<br>• Constant properties<br>• $v_r = v_r(r, z)$<br>• where $\partial v_r/\partial r \ll \partial v_r/\partial z$<br>• *Note:* $\nabla p \approx 0$ | • Differential approach<br>• Reduced continuity and N-S equations<br>• Use assumed postulates for $\vec{\mathbf{v}}$ and $\nabla p$ |

*Solution*: Based on the stated assumptions/postulates, the 2-D continuity equation in cylindrical coordinates reduces to

$$\frac{1}{r}\frac{\partial}{\partial r}(r v_r) = 0 \tag{E.6.4.1a}$$

which implies that

$$v_r = \frac{f(z)}{r} \tag{E.6.4.1b}$$

The $r$-momentum equation reduces to

$$v_r \frac{\partial v_r}{\partial r} - \frac{v_\theta^2}{r} = \nu \frac{\partial^2 v_r}{\partial z^2} \tag{E.6.4.2a}$$

With the "lubrication assumption" of Section 5.1.3, that is, $\partial v_r/\partial r \ll \partial v_r/\partial z$, and $v_\theta = r\omega_0$, Equation E.6.4.2a becomes

$$\frac{\partial^2 v_r}{\partial z^2} = -\frac{\omega_0^2}{\nu} r \tag{E.6.4.2b}$$

subject to $v_r(z = 0) = 0$ (no slip) and $\left.\dfrac{\partial v_r}{\partial z}\right|_{z=h} = 0$ (no stress).

Double integration yields

$$v_r(r,z)=\frac{\omega_0^2}{\nu}\left[h(r)z-\frac{z^2}{2}\right]r \tag{E.6.4.3}$$

The film thickness $h(r)$ can be obtained via the constant supply-rate condition:

$$Q=\bar{v}A=\int_0^{h(r)} v_r(r,z)dA;\quad dA=2\pi r\,dz \tag{E.6.4.4a, b}$$

Hence,

$$Q=\frac{2}{3}\frac{\pi\omega_0^2 r^2}{\nu}h^3 \tag{E.6.4.5}$$

so that

$$h(r)=\left(\frac{3\nu Q}{2\pi\omega_0^2 r^2}\right)^{1/3} \tag{E.6.4.6a}$$

or with $\frac{r}{R}\equiv\hat{r}$

$$\hat{h}=\frac{h}{R}=\left(\frac{3\nu Q}{2\pi\omega_0^2 R\hat{r}^2}\right)^{1/3}=K\left(\frac{r}{R}\right)^{2/3} \tag{E.6.4.6b}$$

*Graph 4:*

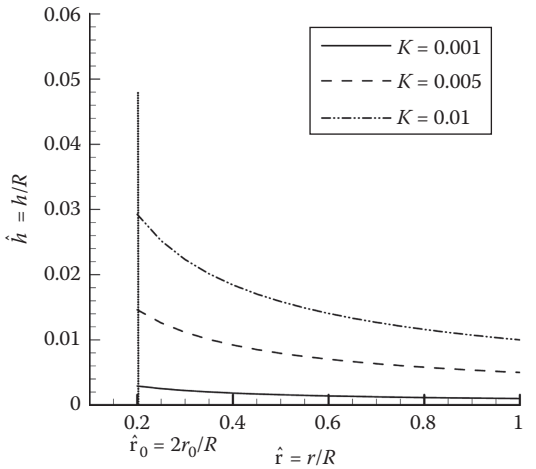


*Comments:*

The film thins in radial direction in balance with the two key parameters, that is, material supply rate $Q$ and disk rotation $\omega_0$, where $h \sim (Q^{1/3}$ and $\omega^{-2/3})$. Note that the region $0\le\hat{r}\le 0.2$ was not considered in this model.

**Example 6.5: Calendering Operation**

Consider a rolling process whereby a relatively thick sheet ($2H_0$) is pressed into a thin sheet of $2H$ (see Figure 6.2c). While the material gage pressure is zero upstream of the rollers until $x=x_{in}$, it rapidly peaks inside the gap $x_{in}<x<x_{out}$ and then returns to

atmospheric pressure for $x \geq x_{out}$ when the sheet takes on the final thickness $2H$. Thus, the focus is on $h(x)$ for $-x_{in} \leq x \leq x_{out}$. Given the roller separation $2H_1$, the roller data ($R$, $\omega_0$) and sheet thicknesses ($2H_0$ and $2H$) as well as the constant material supply rate $Q$, find the pressure distribution along the calendered sheet.

| Sketch 5 | Assumptions | Method |
|---|---|---|
| 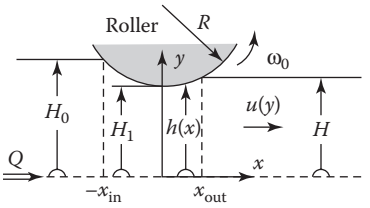 | • Steady operation where $H(x \geq x_{out}) = \infty$<br>• Ratio $x/R \ll 1$<br>• Unit width or depth $w$<br>• Stated pressure developments<br>• Axisymmetric process | • Lubrication equation<br>• Mass conservation<br>• Geometric correlations<br>• Symmetry |

*Solution:* We start with basic geometric considerations, where the inlet-to-outlet height between rollers is

$$h(x) = (R + H_1) - \sqrt{R^2 - x^2} \tag{E.6.5.1}$$

With $x/R \ll 1$,

$$h(x) = (R + H_1) - R\left[1 - \left(\frac{x}{R}\right)^2\right]^{1/2} = H_1 + \frac{x^2}{2R} \tag{E.6.5.2a, b}$$

Thus,

$$h(x = x_{in}) = H_0 = H_1 + \frac{x_{in}^2}{2R} \tag{E.6.5.3}$$

and

$$h(x = x_{out}) = H = H_1 + \frac{x_{out}^2}{2R} \tag{E.6.5.4}$$

The volumetric material supply rate is

$$Q = \int_A u(y)dA = \bar{v}A = (R\omega_0)(2H_1 w) \tag{E.6.5.5a through c}$$

Thin-film equation (or lubrication theory) reads:

$$0 = -\frac{dp}{dx} + \mu\frac{\partial^2 u}{\partial y^2} \tag{E.6.5.6}$$

subject to

$$u[y = h(x = 0)] = R\omega_0 \quad \text{and} \quad \left.\frac{\partial u}{\partial y}\right|_{y=0} = 0 \tag{E.6.5.7a, b}$$

Double integration yields

$$u(x,y) = R\omega_0 - \frac{h^2}{2\mu}\left[\frac{dp(x)}{dx}\right]\left[1-\left(\frac{y}{h}\right)^2\right] \tag{E.6.5.8}$$

Again, the pressure gradient is deduced from $Q = \not{\alpha}$, that is,

$$\begin{aligned} Q &= 2\int_0^h u\,dy = 2h\left[R\omega_0 - \frac{h^2}{3\mu}\left(\frac{dp}{dx}\right)\right] \\ &= 2R\omega_0 H_1 \end{aligned} \tag{E.6.5.9a through c}$$

Now, solving for the pressure gradient:

$$\frac{dp}{dx} = \frac{3\mu R\omega_0 (h - H_1)}{h^3} \tag{E.6.5.10}$$

where

$$h(x) = H_1 + \frac{x^2}{2R} \quad \text{for} \quad -x_{\text{in}} \le x \le x_{\text{out}} \tag{E.6.5.11}$$

and

$$p(x = x_{\text{out}}) = 0,$$

non-dimensionalization of Equation E.6.5.8 yields with $\hat{x} = \dfrac{x}{(2H_1R)^{1/2}}$, $\hat{y} = y / H_1$, $\hat{u} = u / U = u / R\omega_0$, and $\hat{h} = h / H_1$,

$$\hat{u}(\hat{x},\hat{y}) = 1 - \frac{3\hat{x}^2}{2(1+\hat{x}^2)}\left[1-\left(\frac{\hat{y}}{1+\hat{x}^2}\right)^2\right] \tag{E.6.5.12}$$

*Graph 5:*

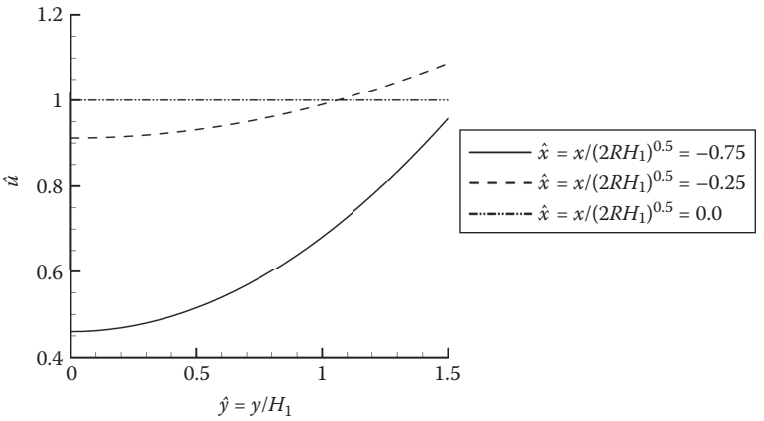

*Comments:*

- As the deformable sheet approaches the roller, that is, $-x_{in} < x < 0$, the highly nonlinear material velocity profile flattens out and becomes uniform at $x = 0$.
- Because the axial coordinate appears as $\hat{x}^2$ in Equation E.6.5.9, the same velocity development occurs for $0 < x < x_{out}$.

## 6.4 Spray-Coating

Simple spray-coating of surfaces requires atomization of a liquid, forming a spray of droplets of different sizes. The underlying theory still relies on Rayleigh's instability analysis of inviscid jet break-up and Weber's extension to viscous liquids. Specifically,

$$\left(\frac{d}{D}\right)^3 = \frac{3\pi}{\sqrt{2}}\left(1 + \frac{3\mu}{\sqrt{\rho\sigma D}}\right)^{1/2} \tag{6.8}$$

where:

$d$ is the droplet diameter
$D$ is the jet diameter
$\mu$, $\rho$, and $\sigma$ are the fluid properties (see Figure 6.4)

Basic spray processes are greatly dependent on the atomizer design and function. More elaborate techniques, collectively known as *thermal spraying*, are surface-coating processes whereby melted (or just heated) coating material, such as metals, ceramics, or plastics in powder or liquid form, are sprayed over large surfaces, generating micrometer to millimeter thicknesses. A common variant of thermal spraying is *plasma spraying*, in which a high-temperature (>10,000 K), high-velocity (>100 m/s) fluid-particle stream is generated by mixing the coating material into a plasma jet emanating from a plasma torch (Pawlowski, 2009). In contrast, *cold spraying*, in which coating particles are accelerated by the carrier gas through a converging-diverging (de Laval) nozzle, has gained numerous applications. If the powder-particle impact velocity exceeds a threshold value (300–1200 m/s), these particles deform and adhere to the target surface. Using kinetic energy

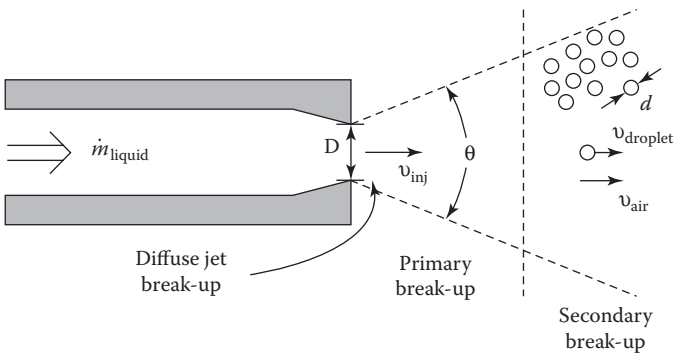


**FIGURE 6.4**
Spray-coating nozzle and droplet evolution.

(rather than heat) for deposition, thermal stresses, surface-oxidation, and certain chemical reactions can be avoided (see Moridi et al., 2014 for details). More recently, simple one-step spray-coating processes have been developed, using a spraying gun loaded with stearates or silica nanoparticles, to create (artificial) super-hydrophobic surfaces. Such coated (metal or plastic) surfaces can be self-cleaning, antifogging, or anticorrosion, or can separate two fluids (Li et al., 2015).

## 6.5 Homework Assignments

Solutions to homework problems done individually or in, say, three-person groups should help to further illustrate fluid dynamics concepts as well as approaches to problem solving, and in conjunction with Appendix I, sharpen the reader's math skills. Ultimately, work "independence" should be achieved. Specifically, after studying the text and equipped with Appendix AI, the student should be able (1) to satisfactorily answer all concept questions, and (2) to solve correctly all basic fluid dynamics problems.

### 6.5.1 Physical Insight

6.1 What is the physical reason for the surface-tension force, and in which type of systems may it become dominant?

6.2 The thin-film analysis assumes no rippling of the free surface, that is, low Reynolds numbers. Discuss conditions, characteristics, and potential solution methods for more realistic cases with $\mathrm{Re}_h > \mathrm{Re}_{\mathrm{critical}}$.

6.3 Derive Equation 6.1; how does it differ from the thin-film equation of Section 2.3.2 and the planar lubrication equation in Section 5.1.3?

6.4 In conjunction with Figure 6.1, derive Equation 6.2, and rewrite Equations 6.3 and 6.4 for a cylindrical interface.

6.5 Connect Equation 6.7 with the result of Example 6.1 to provide an expression for $F_{\mathrm{pull}}$, to be evaluated with some practical parameter values from the open literature.

6.6 Write tutorial reports on (1) film-drawing or (2) coating processes. Specifically, illustrate the basics with process videos, empirical correlations, and math modeling/simulation results.

6.7 Concerning Example 6.3, justify the assumption $Q/w = uh = \text{constant}$, and discuss its implications.

6.8 Revisiting Example 6.3, set up a more rigorous math model plus BCs, and suggest a solution method with expected results.

6.9 Revisiting Example 6.4, set up a more rigorous math model plus BCs, which includes the region $0 \leq \hat{r} \leq 0.2$, and suggest a solution method with expected results.

6.10 Revisiting Example 6.5, derive Equation E.6.5.1, and determine the final sheet thickness $H_1$.

6.11 Write a tutorial report on spray-coating (see Section 6.4).

### 6.5.2 Engineering Problems

6.12 In Example 6.2, solve Equation E.6.2.8 numerically using MATLAB®. With some practical data, compare the result graphically with Equation E.6.2.11. Comment!

6.13 Derive Equation 6.5 and apply the result to a cylinder of radius $R$.

6.14 In an extension of Task 6.8, solve numerically the complete problem given in Example 6.4.

6.15 Thin film on an incline (see Leal, 2007): Consider gravity-driven flow of a thin layer of a Newtonian fluid on a flat slope with angle θ and fluid width $W$.

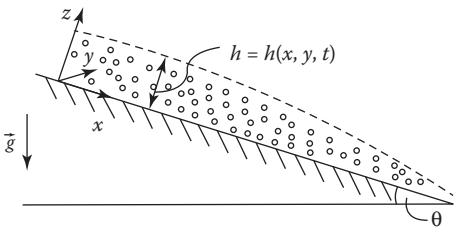


(a) Based on suitable assumptions/postulates, derive the governing equation for $h(x, y, t)$, that is,

$$\frac{\partial h}{\partial t}+\frac{g\sin\theta}{3\nu}\frac{\partial h^3}{\partial x}=\frac{g\cos\theta}{3\nu}\left[\frac{\partial}{\partial x}\left(h^3\frac{\partial h}{\partial x}\right)+\frac{\partial}{\partial y}\left(h^3\frac{\partial h}{\partial y}\right)\right] \tag{1}$$

where $v \equiv \mu/\rho$ is the kinematic viscosity.

(b) Assuming steady-state and a constant material supply $Q[L^3/T]$, consider a downstream test section where $h$ is still $h=h(x,y)$, but $\bar{h} \ll \bar{y}(x) \ll x$, where $\bar{h}$ and $\bar{y}$ are characteristic lengths, that is, film thickness and cross-slope extent, respectively. Show that now

$$\frac{\partial h^3}{\partial x}=(\cot\theta)\frac{\partial}{\partial y}\left(h^3\frac{\partial h}{\partial y}\right) \tag{2}$$

where it is postulated that $h(x, y)=\bar{h}(x)\cdot H(\eta)$, $\eta=\dfrac{y}{\bar{y}(x)}$, that is,

$$H(\eta)=\frac{3}{14}(\bar{\eta}^2-\eta^2) \tag{3}$$

$$\bar{h}(x)\sim\left(\frac{\nu Q}{g\sin\theta}\right)^{2/7}(x\cot\theta)^{-1/7} \tag{4}$$

and

$$\bar{y}(x) \sim \left( \frac{\nu Q}{g \sin\theta} \right)^{1/7} (x \cot\theta)^{3/7} \tag{5}$$

(c) Confirm Equations 3 through 5, solve for Equation (2), plot $h(x,y)$ for reasonable parameters $\theta$ and $vQ/(g\sin\theta)$, and comment.

Taylor & Francis
Taylor & Francis Group
http://taylorandfrancis.com

# 7

# *Microscale Fluid Dynamics*

## 7.1 Introduction

In the age of device miniaturization, for example, microelectromechanical systems (MEMS) or laboratory on a chip (LoC), the fluid-particle dynamics in such devices has to be modeled/simulated down from the macro-scale to the microscale or even the nano-scale. Fortunately, the *continuum mechanics hypothesis* is valid for fluid flow in most microchannels and microtubes (see Section 1.1). In fact, it may even hold for gas flow in nano-size conduits if the Knudsen number is small enough, that is, $Kn = \lambda_{mfp}/D_{hydraulic} < 0.1$, where $\lambda_{mfp}$ is the mean-free-path of the gas molecules (see Section 7.3.2). Thus, the fundamentals described in Part A can be employed to solve almost all problems in the research area of microscale fluid dynamics, which is also known as *microfluidics* (Kleinstreuer, 2014).

Microfluidics encompasses the science and technology of systems that process/manipulate small amounts of fluids, say $10^{-12}$ to $10^{-9}$ L, and probe the nano/microparticle dynamics in microchannels with characteristic "length" scales of, say, $L = 10$–$500$ μm. Here, $L$ represents a hydraulic diameter or channel height or width. Appendix AI.7.3 lists unit prefixes from "femto" ($10^{-15}$) to "peta" ($10^{15}$) as well as length-scales from nano- to macro-systems. To appreciate microconduit sizes, one should recall that *the diameter of a human hair is about 80 μm*. More impressive is a relative-size illustration of the *nanoworld*, equating two ratios in the form

$$\text{Nanosphere-to-soccer-ball} = \text{Soccer-ball-to-planet-earth}.$$

Of major interest are gas and liquid flows, as well as the fluid-particle dynamics in microchannels plus the associated drivers (i.e., "pumps"), mixers, and heaters. Other microsystem components, such as fluid-particle reservoirs, actuators, valves, sensors, and controllers, as well as microchannel materials and fabrication techniques, are discussed elsewhere (see Lee and Sundararajan, 2010; Meng, 2011, among others). Presently, the main focus in microscale research and development (R&D) is on device fabrication and expansion of microsystem applications. This implies innovative advances in the material sciences and manufacturing technology as well as the creation of the necessary design software. Supportive of these R&D activities are the fluid flow, heat/mass transfer, and particle transport aspects of microsystems, which are introduced in this chapter. However, phase changes such as boiling and condensation as well as thermal radiation are excluded; for boiling and radiation processes, see Tong and Tang (1997) and Zhang (2007), among others.

Clearly, the very high surface-to-volume ratio of microsystems forms the foundation of their many advantages over macro-scale devices and processes. Specifically, the implications of such *geometric scaling*, known as the "size-reduction effect," can be illustrated in terms of the area-to-volume ratio of a simple fluid conduit, or for that matter, for an entire device:

**TABLE 7.1**

Macrochannel versus Microchannel Flows

| Condition/Phenomenon | Flow in Macroconduits | Flow in Microconduits |
|---|---|---|
| Continuum mechanics hypothesis | Each fluid is a continuum | Continuum assumption fully holds for most liquid flows when $D_h \geq 10$ μm and for gases when $D_h \geq 100$ μm |
| Type of fluid (i.e., liquid vs. gas) | • Special considerations for compressible and/or rarefied gases<br>• Differentiate between Newtonian and non-Newtonian liquids | May have to treat gas flow and liquid flow differently because of the impact of a given fluid's molecular structure and behavioral characteristics |
| No-slip condition | Can generally be assumed | Velocity-slip may occur on solid hydrophobic, rough surfaces. Temperature jumps at a heated/cooled wall may occur in rarefied gas flows |
| Entrance effects | Entrance length is usually negligible when compared with the length of the conduit | Entrance lengths may be on the order of a microchannel length. Stronger mixing may occur in that region |
| Reynolds number | Important to evaluate laminar versus transitional versus turbulent flows | Typically, $\mathrm{Re}_{D_h} \leq \mathcal{O}(1)$ justifies Stokes flow and allows for non-mechanical pumps driving fluid flow |
| Turbulence | Transition varies with geometry of domain, but often requires larger Re-numbers than in microchannel flow. Example, $\mathrm{Re}_D\big\|_{\text{pipe}} \approx 2000$ | Transition to turbulence may occur earlier, for example, at $\mathrm{Re}_{D_h} \geq 1200$. Although turbulent flow is desirable for mixing, it is avoided for controlled (i.e., laminar) conditions |
| Surface roughness | Is often negligible or included in the friction factor (see Moody chart in Appendix II) | May need to be considered due to manufacturing limitations at this small scale. It may cause complex flow fields near walls |
| Viscous heating | Is often small/negligible | May become a major heat source due to high-velocity gradients in tiny channels with viscous fluids |
| Wall-temperature condition | Usually, thermodynamic equilibrium is assumed | For rarefied gas flows, there may be a temperature jump between the solid wall and the gas |
| Diffusion | Present, but very slow; therefore, often negligible | Due to the small channel size, diffusion is important and is part of mixing processes |
| Surface tension | Is negligible outside capillaries under fluid static conditions | May become a major contributing force, and hence, is being used for small fluid-volume transfer |
| Electro-hydrodynamic effects, such as electro-osmosis (EO) | Negligible | In a liquid electrolyte, an electric double layer (EDL) can be formed, which is set into motion via an applied electric field ($\vec{E}$): $E_x \Rightarrow EDL \rightarrow f_{\text{coulomb}} \rightarrow u_{\text{EO}} \approx u_{\text{slip}}$ |

*Source:* After Kleinstreuer, C. *Microfluidics and Nanofluidics: Theory and Selected Applications*, John Wiley & Sons, Hoboken, NJ, 2014.

$$\frac{\text{Device surface area}}{\text{Device volume}} = \frac{A}{\forall} \sim \frac{l^2}{l^3} = l^{-1} \tag{7.1}$$

where $l$ is the system length-scale, such as the hydraulic diameter, channel height, or width. So, in the micro/nano-size limit, the ratio becomes very large, which implies that in micro/nanofluidics, a system's *surface area–related quantities* become dominant, which typically include the pressure force and shear stresses, as well as surface tension. Table 7.1 provides a quick look at other size-related aspects, contrasting important flow conditions and phenomena in macro-scale conduits of the order of meters and millimeters with those in microchannels that are of the order of micrometers.

While this chapter is based on the first edition of the book, some parts are revised and updated versions of previous book material (Kleinstreuer, 2014) and a review article (Kleinstreuer 2016).

## 7.2 Microscale Flow Systems

In any microfluidics system, the *microchannel* forms the central element, which is typically connected to necessary accessories such as a pump, a valve, a mixer, and/or a heater. Figures 7.1a, b depict a general flowchart of a microfluidics system as well as an application for microscale biochemical production (LoC).

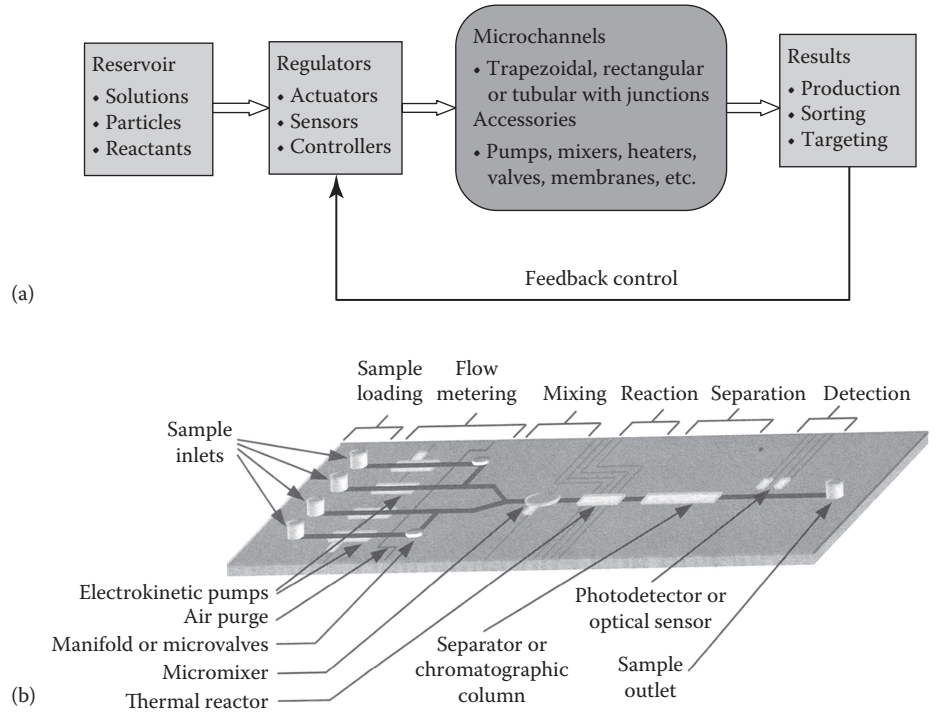


**FIGURE 7.1**
(a) Key components and interactions of microfluidic systems and (b) microfluidic system example. (From Chang and Yeo, 2010.)

Microfluidic devices are manufactured using planar substrates such as silicon wafers, glass slides, ceramic blocks, stainless steel, polymer, or even paper chips. The type of material selected affects not only device architecture, cost, and fabrication method (e.g., micromachining or soft lithography) but also microscale phenomena (e.g., surface roughness or heat transfer effects). Polydimethylsiloxane (PDMS) is the most frequently used material to fabricate microsystems. When uncured, PDMS flows freely at room temperature, and once cured, it produces a mechanically strong and optically transparent substrate.

Clearly, it is an interdisciplinary undertaking to produce a desired outcome with, say, an LoC, a diagnostics system, a drug-delivery device, or a special MEMS. The underlying functionalities of such micro-devices may be based on mechanical, electrical, thermal, magnetic, optical, chemical, and/or biological transport phenomena, all obeying the three conservation laws. For example, electro-mechanical, say, piezo-electric actuators are used for micro-valve or micro-pump displacements, while electric motors or syringe pumps provide angular or linear displacements. In contrast, not having to deal with moving parts, electro-osmosis allows fluid pumping, while electrophoresis allows particle manipulation. Thermal energy transfer via electric heaters is used for temperature-driven gas expansion, finite liquid volume displacement, and/or control of chemical reactions (Zhang 2007). Applications of microfluidic technologies can be most frequently found in chemistry, biology, and medicine as well as in chemical, biomedical, and mechanical engineering. As mentioned, the advantages of microfluidic devices over conventional-size equipment are largely based on the very high surface-to-volume ratio. In addition to the implied savings in space, material, energy, and hence, cost, miniaturized process devices feature:

- Higher heat and mass transfer rates
- Safer handling of hazardous/toxic chemicals
- Integrated analytic platforms (e.g., chips), such as LoC and micro-total analysis systems (μ-TAS) for biochemical and biomedical processing
- Simplified flow and screening process control
- *In vivo* robotic diagnostics and treatment; for example, as in image-guided surgery or drug delivery

While microfluidics and microsystem applications can be very advantageous, they may also face a number of problems, as already alluded to with some entries in Table 7.1. Specifically, critical considerations associated with microfluidics systems include

- Possible violation of the Continuum Mechanics Hypothesis, especially when dealing with rarefied gases in micro/nanoconduits
- Malfunctioning of accessories, for example, tiny pumps, valves, heaters, actuators, sensors, controllers, and so on
- Slip flow for liquids on hydrophobic and rough surfaces, or more generally for rarefied gases
- Need for wall-temperature jump condition in the case of rarefied gases
- Impact of microchannel entrance flow in small devices
- Microchannel-wall effects, such as roughness, electric charge, and so on
- Air bubbles and/or impurities in microchannel flow
- Particle/cell aggregation and bio-fouling leading to clogging

- Temperature rise due to Joule heating (see electro-osmosis) or viscous dissipation
- Evaporation effects impairing especially digital microfluidics operation
- Macro-scale to microscale flow connection problems
- Early onset of chaotic flow and hence, turbulence effects
- Compressibility of rarefied gases

Detailed fluid-particle dynamics modeling and simulation can greatly assist in analyzing the key transport phenomena, determine ways to avoid the listed problems associated with microsystems, and evaluate methodologies for achieving optimal end-products or goals.

## 7.3 Fluid Flow in Microconduits

### 7.3.1 Scale Analysis

As implied in Section 1.4 and mentioned in Section 7.1, the scaling laws are fundamental to system, device, or process miniaturization. We start again with the geometric ratio:

$$\kappa \equiv \frac{\text{Surface area}}{\text{System volume}} \sim \frac{l^2}{l^3} = l^{-1} \tag{7.2}$$

Clearly, in the limit as $l \to 0$, $\kappa \to \infty$, implying that *surface-related* forces, fluxes, and process characteristics can become dominant in microfluidics over volume-based quantities, such as gravity. Scaling some basic dimensionless groups illustrates the length dependence of common transport phenomena. For example, considering capillary rise of height in a liquid column of diameter D:

$$\frac{F_{\text{surface tension}}}{F_{\text{weight}}} = \frac{(4D\pi)\gamma}{D^2\pi h\rho g} = \frac{1}{hD}\frac{\gamma}{\rho g} \sim l^{-2} \tag{7.3}$$

In contrast, the Stokes number, a ratio of particle travel and fluid flow residence times, can be scaled as

$$St = \frac{\tau_{\text{particle}}}{\tau_{\text{fluid}}} = \frac{v\rho_p d_p^2}{18\mu D} \sim \frac{l \cdot l^2}{l} = l^2 \tag{7.4}$$

The result is the same for the Reynolds number, that is, the ratio of inertia to viscous forces:

$$\text{Re} = \frac{vD_h}{\nu} \sim l^2 \tag{7.5}$$

Trickier is the Peclet number, Pe = Convection/Diffusion, which scales as

$$Pe = \frac{vD_h}{\mathcal{D}} \text{ or } \sim \frac{vD_h}{\alpha} \sim l^2 \tag{7.6}$$

for a *constant* diffusivity $\mathcal{D}$ (or thermal diffusivity α). However, as shown with Equation 7.7, when the diffusivity scales as $\mathcal{D} \sim l^{-1}$, the result is $\text{Pe} \sim l^3$.

It is apparent that the length-scale dependence of forces, fluxes, and dimensionless groups varies with the given system dynamics, so one has to decide which parameters can be kept constant or not. In any case, it is most important to note that in microchannel flow, very different forces may become significant. For example, as shown directly with Equation 7.3, surface tension can be more important than gravity or viscous forces, and mass or momentum diffusion may trump convection or inertia for devices with $l \ll 1$.

**Example 7.1: Evaluate the Dominant Forces in the Navier–Stokes (N-S) Equation for Microchannel Flow as $L_{system} \to 0$**

| Sketch 1 | Assumptions | Method |
|---|---|---|
| 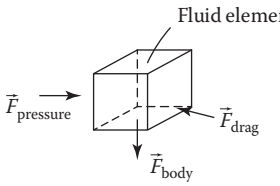  | • Constant fluid properties<br>• Additive *net* surface and body forces | • Extended N-S equation<br>• Characteristic length scaling |

*Solution:* The linear momentum equation for a fluid-element of mass m reads:

$$m\frac{D\vec{v}}{Dt} = \vec{F}_{\text{pressure}} + \vec{F}_{\text{viscous}} + \vec{F}_{\text{gravity}} + \vec{F}_{\text{surface tension}} + \vec{F}_{\text{electro-static}} + \cdots \tag{E.7.1.1}$$

Equation E.7.1.1 can be rewritten with relative length scales associated with each term as

$$\underbrace{m\frac{\partial\vec{v}}{\partial t}}_{\substack{L^4\\1}} + \underbrace{m(\vec{v}\cdot\nabla)\vec{v}}_{\substack{L^4\\1}} = \underbrace{-\nabla p\forall}_{\substack{L^3\\L^{-1}}} + \underbrace{\nabla\cdot\vec{\tau}\forall}_{\substack{L^3\\L^{-1}}} + \underbrace{m\vec{g}}_{\substack{L^4\\1}} + \underbrace{\vec{\gamma}l}_{\substack{L\\L^{-3}}} + \underbrace{\rho_{el}\vec{E}\forall}_{\substack{L^2\\L^{-2}}} \quad |*L^{-4} \tag{E.7.1.2}$$

The relative $L$-scale of each term indicates that for $L \to 0$ only four terms remain important, that is, mainly surface tension force as well as Coulomb's (electrostatic) force, but also the net pressure and viscous forces. So, in summary,

- Fluid acceleration is negligible, that is, $\vec{a} = D\vec{v}/Dt \ll 1$.
- Gravity, being a body-force term, has a minimal effect, if any.
- Next to surface tension and electrostatic (or Coulomb) force, surface forces such as pressure and drag are most important.

The surface-area to body-volume ratio (see Equation 7.2) indicates that previously ignored mechanisms to travel distances and associated time scales become important in very narrow channels. Specifically, in a microsystem, diffusion, rather than convection, may be the dominant transport mechanism at very small time levels. Material migration via diffusion and associated times needed, as well as time scales in momentum/heat/mass transfer, can be illustrated as follows.

- *Diffusion scaling*: For molecular or nanoparticle transport, diffusional effects become important in microfluidics. The suitable Stokes–Einstein equation for the binary diffusion coefficient reads:

$$\mathcal{D} = \frac{k_B T}{3\pi\mu d} \sim l^{-1} \tag{7.7}$$

where the Boltzmann constant $k_B = 1.38 \times 10^{-23}$ J/K, T is in degrees Kelvin and μ in kilograms per meter per second, while the particle diameter $d$ is in meters.

Based on Einstein's random-walk analysis, the diffusion length of a molecule in solution is

$$x = \sqrt{2\mathcal{D}\tau} \tag{7.8a}$$

So, assuming $\mathcal{D} = \text{const.}$, the diffusion time can be estimated as

$$\tau = \frac{x^2}{2\mathcal{D}} \sim l^2 \tag{7.8b}$$

For a typical binary diffusivity of $\mathcal{D} = 10^{-9}$ m²/s, the nanoparticle diffusion times decrease rapidly as, say, the channel width or height $x$ decreases. Specifically, when

- $x = 1\,\text{mm} \Rightarrow \tau = 500\,\text{s}$
- $x = 10\,\mu\text{m} \Rightarrow \tau = 0.05\,\text{s}$
- $x = 1\,\mu\text{m} \Rightarrow \tau = 0.5\,\text{ms}$
- $x = 100\,\text{nm} \Rightarrow \tau = 0.05\,\text{ms}$

As an example, it takes only one-twentieth of a second for a small nanoparticle to cross a channel of 10 μm width.

*Time scales*: Flow fields are transient due to (sudden) operational system changes. Examples include start-up, on-and-off switching, and periodic boundary conditions, such as pulsatile (blood) flow, inlet pressure waveforms, vibrating walls, and so on. In general, momentum, energy, and species-mass transfer phenomena have to adjust to those time-dependent changes.

Considering a flow field, for the *velocity* field to adjust, the characteristic time is (see Example 7.2)

$$\tau_v = \frac{\rho L^2}{\mu} \tag{7.9}$$

For the *temperature* field:

$$\tau_T = \frac{\rho c_p L^2}{k} \tag{7.10}$$

while for the *species-mass* field:

$$\tau_c = \frac{L^2}{\mathcal{D}} \tag{7.11}$$

where:

- $L$ is the system's characteristic length
- $k$ is the fluid conductivity
- $\mathcal{D}$ is the binary diffusion coefficient

For example, using water flow at $T = 20°C$ in a microchannel of $h = L = 100\ \mu m$, the adjustment times to reach a new equilibrium (i.e., steady-state), after a sudden change in flow conditions, are:

$$\tau_v = 10\,\text{ms},\ \tau_T = 100\,\text{ms},\ \text{and}\ \tau_c = 10\,\text{s}$$

Clearly, the relatively large species-diffusion time is rate limiting.

**Example 7.2: Characteristic Time Scale for Momentum Transfer**

Given transient liquid flow ($\rho$, $\mu$) in a microchannel of height $h$ and mean velocity $U$, derive the momentum time scale $\tau_v$. Calculate its value for $\rho = 10^3\ kg/m^3$, $\mu = 10^{-3}\ Ns/m^2$, $h = 10\ \mu m$, and $u_{avg.} = U = 0.1\ m/s$.

| Sketch 2 | Assumptions | Method |
|---|---|---|
| 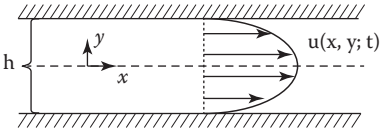  | • Transient laminar two-dimensional flow with constant properties | • Reduced N-S equation<br>• Non-dimensionalization |

*Solution:*

The N-S equation without body forces states:

$$\rho\left[\frac{\partial \vec{v}}{\partial t} + (\vec{v}\cdot\nabla)\vec{v}\right] = -\nabla p + \mu\nabla^2\vec{v} \tag{E.7.2.1}$$

With $\tilde{\mathbf{v}} = \vec{v}/U$; $\tilde{p} = p/p_0$; $\tilde{t} = t/\tau$; and $\tilde{\nabla} = \nabla h$, we rewrite the momentum equation as

$$\rho\frac{U}{\tau}\frac{\partial \tilde{\mathbf{v}}}{\partial \tilde{t}} + \frac{\rho U^2}{h}\left(\tilde{\mathbf{v}}\cdot\tilde{\nabla}\right)\tilde{\mathbf{v}} = -\frac{p_0}{h}\tilde{\nabla}\tilde{p} + \frac{\mu}{h^2}U\tilde{\nabla}^2\tilde{\mathbf{v}} \tag{E.7.2.2a}$$

or

$$\frac{\rho h^2}{\mu\tau}\frac{\partial \tilde{\mathbf{v}}}{\partial \tilde{t}} + \frac{\rho U h}{\mu}\left(\tilde{\mathbf{v}}\cdot\tilde{\nabla}\right)\tilde{\mathbf{v}} = -\frac{p_0 h}{\mu U}\tilde{\nabla}\tilde{p} + \tilde{\nabla}^2\tilde{\mathbf{v}} \tag{E.7.2.2b}$$

Setting the coefficient of the transient term equal to one (unity), we obtain

$$\tau = \tau_v = \frac{\rho h^2}{\mu} \tag{E.7.2.3}$$

while the coefficient of the inertial term is, as expected,

$$\text{Re}_h = \frac{Uh}{\nu} \tag{E.7.2.4}$$

with the given system values,

$$\tau_v = 100\ \mu s \text{ and } \mathrm{Re}_h\ 1.0 \text{ (i.e., Stokes flow).}$$

*Comments:*

A frequent application of transient microchannel flow is periodic flow due to changes in inlet pressure (e.g., in hemodynamics) or in electric potential (e.g., electrokinetic flow driven by alternating current fields). Then, $\tau_v = f^{-1}$, and the dimensionless group is the Strouhal number, $Str = fh/U$, where $f$ is the frequency.

As in macrosystem analyses, it is quite often sufficient to estimate global quantities that are characteristic of fluid flow or heat transfer processes in microconduits. One is the *hydraulic resistance*, and it is of interest to see how it scales with a representative geometric parameter of a microsystem. Specifically,

$$R_{\text{hydraulic}} = \Delta p / Q \tag{7.12}$$

where:
$\Delta p$ is the pressure drop across the flow conduits
$Q$ is the volumetric flow rate

As shown in Example 7.3, $R_{\text{hydraulic}}$ scales typically with $l^{-3}$, implying a significant flow resistance when $L \ll 1$ for any microscale flow system. Table 3.4 in Kleinstreuer (2014) lists the velocity, flow rate, and hydraulic resistance results for most common flow conduits.

**Example 7.3: Parallel-Plate Hydraulic Resistance**

Consider Poiseuille-type flow between two horizontal parallel plates (i.e., micro-spacing $h$, length $L$, and infinite width $w$) forming a microchannel, where $\Delta p = p(0) - p(L)$.

| Sketch 3 | Assumptions | Method |
|---|---|---|
| 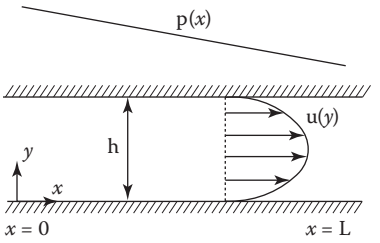 | • Poiseuille-type flow<br>• Constant fluid properties | • Reduced N-S equation<br>*Postulates:*<br>• $-\nabla p = \Delta p / L = \text{¢}$<br>• $\vec{v} = [u(y); 0; 0]$<br>See Equation E.3.1.4 in Example 3.1 |

*Solution:*

- Based on the postulates, the $x$-momentum equation reduces to

$$0 = \frac{\Delta p}{L} + \mu \frac{d^2 u}{dy^2} \tag{E.7.3.1}$$

while continuity is satisfied. The boundary conditions (BCs) are

$$u(0) = 0 \quad \text{and} \quad u(h) = 0 \tag{E.7.3.2a, b}$$

Hence,

$$u(y) = \frac{\Delta p}{2\mu L}(h-y)y = \frac{\Delta p}{2\mu L}h^2\left[\frac{y}{h} - \left(\frac{y}{h}\right)^2\right] \qquad \text{(E.7.3.3a, b)}$$

- Flow rate $Q = \int_A u(y)dA$; $dA = wdy$, so that

$$Q = \frac{h^3 w}{12\mu}\left(\frac{\Delta p}{L}\right) \qquad \text{(E.7.3.4)}$$

- Here, the hydraulic resistance $R_{\text{hydr.}} = \Delta p/Q$ leads to

$$R_{\text{hydr.}} = \frac{12\mu L}{wh^3} \sim l^{-3} \qquad \text{(E.7.3.5)}$$

*Comments:*

- Clearly, for microchannel flow, let alone flow in nanochannels, the hydraulic resistance can be large, which may present a challenge to micro-pumping.
- It should be noted that in complex conduits, for example, suddenly expanding/contracting channels, the Hagen–Poiseuille law (Equation [E.7.3.4]) does not hold. For example, considering three different flow regions in series, we have $Q = Q_{\text{I}} = Q_{\text{II}} = Q_{\text{III}}$; but, $\Delta p \neq (R_{\text{I}} + R_{\text{II}} + R_{\text{III}})Q$.

*Notes*:

Similarly, a *thermal resistance* concept, $R = \Delta T/Q$, can be defined for solutions of convection heat transfer problems, where here $Q = q \cdot A$ is the heat transfer rate (Joules/second):

1. For conduction across a wall of thickness $L$ and area $A$, it is $R_{\text{cond}} = L/(kA)$.
2. For convection with $\Delta T = T_{\text{surface}} - T\infty$, it would be $R_{\text{conv}} = 1/(hA)$, where $h$ is the heat transfer coefficient (see Section 2.4.2).

### 7.3.2 Fluid Properties and Flow Conditions

It has been established that the surface-to-volume ratio $\kappa \equiv S/\forall = L^{-1}$ may imply a significant shift in the importance of certain forces, fluxes, and processes as $L \to 0$. Impressive length-scale examples include the human-hair diameter being about 80 μm and a DNA strand being around 2.5 nm. They may serve as geometric yardsticks in microfluidics and nanofluidics, respectively.

Clearly, as fluid flow systems get smaller and smaller, one has to consider the micro-structure of liquids and gases. Especially for rarefied gases, the channel width may be of the order of the mean-free-path of a representative molecule, or even the average distance between two molecules. With *liquids*, groups of molecules move about each other, and the internal energy is a function of microscopic activities, including sensible and bonding energies. In *gases*, however, molecules exhibit random, highly temperature-dependent motion. Specifically, for gases, elevated sensible energy (and hence, a large part of the internal energy) may cause gas molecules to travel relatively large distances before collision. Based on kinetic theory, assuming ideal hard-sphere collision, the mean-free-path is (Probstein 1994)

$$\lambda_{\text{mfp}} = \frac{\mu}{\rho}\sqrt{\frac{\pi RT}{2}} = \frac{1}{\sqrt{2}\pi n_i {d_c}^2} = \frac{m_g}{\sqrt{2}\pi\rho\, {d_c}^2} \qquad \text{(7.13a through c)}$$

as a statistical average,

where:

$R$ is the specific gas constant for ideal gases
$n_i$ is the number of molecules per unit volume
$d_c = d$ is the molecular (collision) diameter
$m_g$ is the mass of a gas molecule

The associated ideal gas expressions read:

$$p = \rho RT = nk_BT \tag{7.14a, b}$$

Of special interest is the mean intermolecular distance:

$$\delta_{IM} \approx n^{-1/3} \tag{7.14c}$$

where:

$n$ is the number of molecules per cubic meter
$\delta_{IM}$ is in meters
$T$ is the temperature in degrees Kelvin
$k_B$ is the Boltzmann constant ($1.38 \times 10^{-23}$ J/K)

For all practical purposes, the conditions when the *continuum assumption* holds are as follows.

***For liquids:***

- $D_{\text{hydr.}}$ or $L_{\text{system}} \geq 10$ μm, where $D_{\text{hydr.}} = 4A/P$
  and/or
- $\delta_{IM}/L_{\text{system}} \leq 3.0 \times 10^{-5}$, where $\delta_{IM} \hat{=}$ intermolecular spacing

***For gases:***

- $D_{\text{hydr.}}$ or $L_{\text{system}} \geq 100$ μm and/or
- The Knudsen number, $Kn = \lambda_{\text{mfp}}/L_{\text{system}} < 0.01$, where $\lambda_{\text{mfp}} \hat{=}$ mean-free-path.

*Note:* $0.01 \leq Kn \leq 0.1$ is the "slip-flow" regime, where the N-S equations still hold, but with velocity-slip and temperature-jump BCs.

To contrast liquid and gas property values, here are a few data for air and water at standard temperature and pressure conditions.

| | |
|---|---|
| • *Water:* | Intermolecular distance $\delta_{IM} \approx 0.3$–$0.4$ nm |
| | Molecular diameter $d \approx 0.3$ nm |
| | Number density $n \approx 3.34 \times 10^{19}$ mm$^{-3}$ |
| • *Air:* | Mean spacing $\delta_{IM} \approx 3.3$ nm |
| | Mean-free-path $\lambda_{\text{mfp}} \approx 65$ nm |
| | Typical diameter $d \approx 0.375$ nm ($N_2$ molecule) |
| | Number density $n \approx 2.69 \times 10^{19}$ cm$^{-3}$ (air) |

As indicated, the Knudsen number value for *gas flow* in micro/nanoconduits determines the "modeling regime." Specifically,

$$\begin{cases} \text{Fluid continuum} \\ \text{(Cauchy or N-S equations)} \end{cases} \leftarrow \begin{cases} \underbrace{0.01 \le Kn = \dfrac{\lambda}{L} < 0.1}_{\substack{\text{Slip-flow regime} \\ \text{(N-S equations with slip BCs)}}} \\ \underbrace{0.1 < Kn < 10}_{\substack{\text{Transitional flow regime} \\ \text{(Lattice-Boltzmann or direct} \\ \text{simulation Monte Carlo methods)}}} \end{cases} \rightarrow \begin{cases} \text{Rarefied gases of free} \\ \text{molecular flow} \\ \text{(molecular dynamics} \\ \text{simulation)} \end{cases} \tag{7.15}$$

It should be noted that $Kn = \lambda/L$ depends on the definition of $L$, for example, $L \hat{=} D_{\text{hydr.}}$, $h_{\text{channel}}$, $\delta_{\text{spacing}}$, and so on, and may vary with conduit length, because $\lambda$ varies with axial temperature changes. A simple length-scale application for gas flow is given with Example 7.4.

**Example 7.4: Gas Flow Characteristics**

Consider nitrogen ($N_2$) gas flow at $v = 100$ m/s, $p = 200$ kPa, and $T = 350$ K in a microconduit of $D_h = 1$ μm.

*Given:* $M_{N_2} = 28\,\text{kg/kmole}$, $d_{N_2} = 3.75 \times 10^{-10}\,\text{m}$, $\lambda_{\text{mfp}} = 64$ nm, $R_u = 8.3145$ kJ/(kmol K), $\kappa = c_p/c_v = 1.4$, $v = 2 \times 10^{-4}$ m$^2$/s, and $k_B = 1.38 \times 10^{-23}$ J/K,

*Find*:

- $\delta/d$ to determine whether the gas is rarefied, where $\delta/d \gg 1$ (say, at least $\delta/d \gg 7$) implies a "dilute" gas
  where:
  $\delta \equiv \delta_{lM}$ is the intermolecular distance
  $d$ is the molecular diameter
- $Kn = \lambda/L$
  where:
  $\lambda = \lambda_{\text{mfp}}$
  $L \hat{=} D_h$

  to determine the modeling regime (see Equation 7.15)
- $\text{Re} = vD_h/v$ to determine the flow regime, recalling that $\text{Re}_{D_h} \le 1200$ to ensure laminar flow (see Table 7.1)
- $Ma = v/c_{\text{sound}}$; $c = \sqrt{\kappa RT}$ to check whether the gas is incompressible, that is, $Ma < 0.3$

| Sketch 4 | Assumptions | Method |
|---|---|---|
| 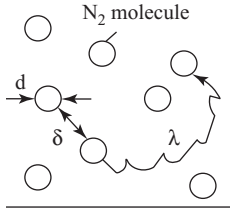  | • Ideal gas law<br>• Averaged, constant properties | • Correlations based on kinetics theory, that is, Equations 7.13 through 7.15 |

*Solution:*

Gas constant $R_{N_2} = R_u / M_{N_2} := 0.2968\ \mathrm{kJ/(kg \cdot K)}$, where $R_u$ is the universal gas constant
Number of molecules $n = p/k_B T := 4.14 \times 10^{25}\ /\ \mathrm{m}^3$, so that the intermolecular distance is $\delta \approx n^{-1/3} := 2.89 \times 10^{-9}\mathrm{m}$
Speed of sound in $N_2$ gas: $c_s = \sqrt{\kappa RT} := 381\mathrm{m/s}$
Hence,

- $\delta/d := 7.7$, that is, here $N_2$ is a rarefied gas, because $\delta/d > 7$
- $Kn = \lambda/D_h := 0.064$, that is, the N-S equations with no-slip wall condition are applicable, mainly because $N_2$ is a borderline "rarefied gas"
- $\mathrm{Re} = vD_h/\nu := 92$, that is, laminar flow
- $Ma = v/c_s := 0.26$, that is, incompressible gas, because $Ma < 0.3$

### 7.3.3 Wall Slip Velocity and Temperature Jump

The standard wall-boundary condition in vector form, including no-slip velocity and impermeable wall, is

$$\vec{v}_{\text{fluid}} = \vec{v}_{\text{wall}} \tag{7.16}$$

It is correct for macro-scale flows and is applicable for most microscale flows. However, in many natural and industrial microfluidics cases, effective or apparent slip velocities can be observed. Examples include

- Rarefied *gases* on actual solid surfaces, where due to the large molecular spacing, an apparent gas motion occurs at the wall
- *Liquids* on rough and hydrophobic surfaces, labeled "super-hydrophobic" surfaces, where entrained gas/air molecules in the wall crevices assist the liquid to slide effectively over the wall
- Liquid flow in microconduits with molecule-depletion layer, which is a math modeling concept for certain fluids that exhibit a very low viscosity at the wall
- Electro-osmotic flow of electrolytes with ultra-thin electric double layers (EDLs), which is discussed in the next Section 7.3.4
- Porous wall-layer flow, which again is a math modeling concept

Sticking with the first two examples, the underlying physics for velocity-slip differs greatly between rarefied gas molecules and liquid molecules. Due to the very low number density of *rarefied gas* molecules and the associated large mean-free-path, the near-wall molecules hardly collide with the solid surface, which, statistically averaged, results in an effective slip velocity. As mentioned, the mean-free-path, $\lambda_{\text{mfp}} = KnD_h$, is often taken as the key model parameter when gas flow is in the "slip range," that is, $0.01 \le Kn \le 0.1$.

For *liquid flow* in micro- or nanochannels, the average intermolecular distance $\delta_{IM}$ is employed to assure fluid continuum, that is, $\delta_{IM}/D_h > 3 \times 10^{-5}$. Nevertheless, the slip length $L_s$ can be from $\mathcal{O}(10\,\mathrm{nm})$ to $\mathcal{O}(100\,\mu\mathrm{m})$. Relatively high apparent $L_s$-values may be encountered when rough hydrophobic surfaces with air/vapor pockets allow liquids to "glide" over the wall with minimum resistance (see Figure 7.2). Alternatively, a depletion of liquid molecules, or particles in the case of suspensions, causes much lower viscosities in a thin

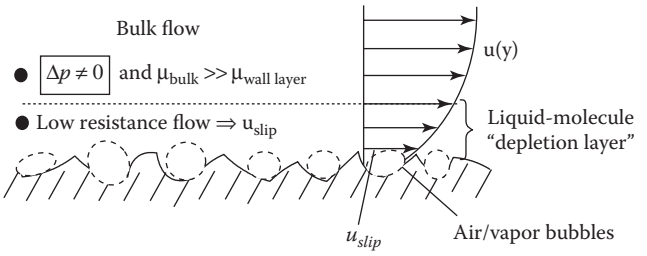


**FIGURE 7.2**
Example of effective velocity-slip of liquids at a rough and hydrophobic surface.

wall layer. This may lead to apparent velocity-slip, as has been demonstrated for liquid flow in carbon nanotubes. For *non-Newtonian fluids* (Section 4.2.2), a determination of the degree of true or apparent velocity-slip is more complicated. In addition to the physical and chemical characteristics of the conduit surface, the properties of the non-Newtonian fluid or nanoparticle suspension have to be known. Thus, one has to simulate the effects of wall characteristics as well as apparent density, complex viscosity, yield stress, elastic modulus, particle concentration, and electric charge.

### *7.3.3.1 Velocity-Slip Models*

For *rarefied gas flow*, Maxwell suggested a wall velocity-slip dependent on the mean-free-path and the wall velocity gradient. In contrast, for *liquid flow* with wall slip, Navier postulated the "slip length" $L_s$, a hypothetical linear extension of the velocity profile into the wall (Figure 7.3).

Specifically, as a first-order approximation, Maxwell suggested for *rarefied gas flow* in the Knudsen number range of $0.01 \leq Kn = \lambda_{mfp}/D_h \leq 0.1$:

$$u_{slip} = \lambda_{mfp} \left. \frac{\partial u}{\partial y} \right|_{\hat{n}=0} \tag{7.17}$$

where:

$\lambda_{mfp}$ is the mean-free-path
$D_h = 4A/P$ is the hydraulic diameter
$\hat{n}$ is the wall-normal vector

For *liquid flow*, the Navier model envisions a linear extension of the velocity profile into the wall, generating a slip length $L_s$. Again,

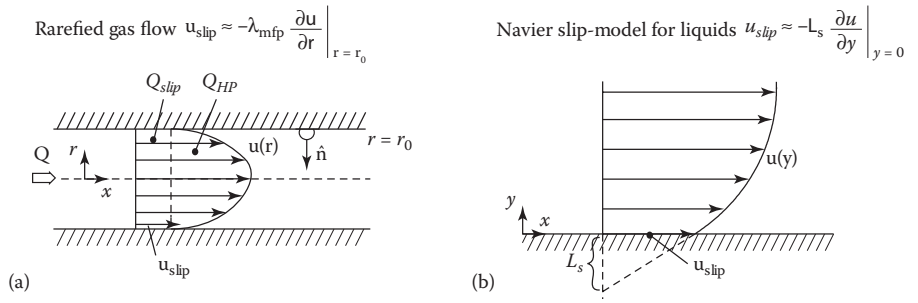


**FIGURE 7.3**
Slip-flow schematics for (a) gas flow (Maxwell) and (b) liquid flow (Navier).

$$u_{\text{slip}} = L_s \left.\frac{\partial u}{\partial y}\right|_{\hat{n}=0} \tag{7.18}$$

Clearly, such "slip flows" generate higher volumetric flow rates than no-slip flows. For example, in reference to basic Hagen–Poiseuille flow (see Section 2.3.4), that is,

$$Q_{HP} = \frac{\pi r_0^4}{8\mu}\left(\frac{\Delta p}{L}\right) \tag{7.19}$$

the flow rate enhancement ratio $\kappa$ is greater than one (see Figure 7.3a):

$$\kappa = \frac{Q}{Q_{HP}} \tag{7.20a}$$

where

$$Q = Q_{HP} + u_{\text{slip}}(\pi r_0^2) = Q_{HP} + Q_{\text{slip}} \tag{7.20b, c}$$

In fact, for Poiseuille-type flow in carbon nanotubes (CNTs), $\kappa \leq 8$ has been measured.

### *7.3.3.2 Temperature-Jump Model*

For cooled or heated *rarefied gases*, deviations from the wall temperature have been observed due to thermal non-equilibrium conditions in the wall region. Example 7.5 illustrates the case of an elevated fluid temperature due to viscous heating remaining higher than the wall temperature, that is, $T_{\text{jump}} = T_{\text{gas}} - T_{\text{wall}}$. Specifically, the relatively few gas molecules near/at the wall cannot attain instantaneously the exact wall temperature. Hence, as a first-order approximation,

$$T_{\text{gas}}(x, \hat{n}=0) = T_{\text{wall}} + T_{\text{jump}} \approx T_{\text{wall}} + \frac{2\kappa\lambda_{\text{mfp}}}{\text{Pr}(\kappa+1)} \left.\frac{\partial u}{\partial y}\right|_{\hat{n}} \tag{7.21a, b}$$

where the heat-capacity ratio $\kappa = c_p/c_v$ and the Prandtl number $\text{Pr} = \nu/\alpha$.

**Example 7.5: Nitrogen-Gas Flow with Viscous Heating and Velocity-Slip**

Consider thermal micro-Couette gas flow with viscous heating in the slip regime. $0.01 \leq Kn \leq 0.1$.

*System Description:*

- Nitrogen at $T_{\text{in}} = T_{\text{wall}} = 300$ K and $\lambda_{\text{mfp}} \approx 64$ nm
- Channel parameters: $h = 0.8$ μm and $U = 100$ m/s

| Sketch 5 | Assumptions | Method |
|---|---|---|
| 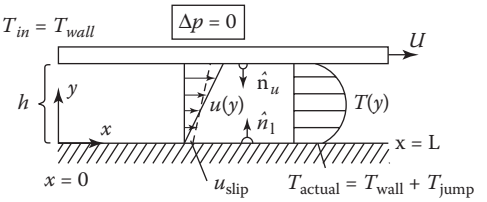 | • Slip regime: $Kn \equiv \lambda/h = 0.08$<br>• One-dimensional (1-D) conduction, *neglecting convection*, with viscous heating | • Reduced N-S equations<br>• Viscous heating<br>• Slip-flow regime<br>*Postulates:*<br>• $u = u(y)$ only<br>• $\nabla p = 0$<br>• $\mu\Phi \approx \mu(du/dy)^2$ |

*Solution:*

*Fluid flow*: The reduced *x*-momentum equation reads:

$$0 = \mu \frac{d^2u}{dy^2};\ \text{or integrated}\ u(y) = C_1 y + C_2 \tag{E.7.5.1a, b}$$

*BCs:* $u(y=0) = u_{slip} = \lambda_{mfp} du/dy|_{y=0} = C_2$ and at $y = h$ (see negative unit vector for the moving surface):

$$u(y=h) = U - u_{slip} = U - \lambda \left.\frac{du}{dy}\right|_{y=0};\quad \text{where}\ \lambda = hKn \tag{E.7.5.2a, b}$$

With $du/dy = C_1$ from the basic solution, we have with the first B.C.,

$$C_2 = hKnC_1 \tag{E.7.5.3a}$$

and with the second B.C.,

$$U - hKnC_1 = C_1 h + C_2 \tag{E.7.5.3b}$$

Hence,

$$C_1 = \frac{U}{h(1+2Kn)} \tag{E.7.5.3c}$$

Finally,

$$u(y) = \frac{U}{1+2Kn}\left[\left(\frac{y}{h}\right) + Kn\right] \tag{E.7.5.4}$$

*Check:* For $Kn \to 0$, that is, $L_{system} \equiv h \ggg \lambda_{mfp}$, $u(y) = U\, y/h$ (i.e., simple shear flow)

*Heat transfer:* The reduced energy equation reads:

$$0 = k\frac{d^2T}{dy^2} + \mu\left(\frac{du}{dy}\right)^2 \text{ or } \frac{d^2T}{dy^2} + \underbrace{\frac{\mu}{k}\left[\frac{U}{h(1+2Kn)}\right]^2}_{\equiv A} = 0 \tag{E.7.5.5a, b}$$

subject to (see Equation 7.21b)

$$T(y=0) = T_w + T_{jump} = T_w + \frac{2\kappa}{\kappa+1}\frac{hKn}{\mathrm{Pr}}\left.\frac{dT}{dy}\right|_{y=0} \tag{E.7.5.6a, b}$$

where:

$$\kappa = \frac{c_p}{c_v}$$

$$\mathrm{Pr} = \frac{\nu}{\alpha}$$

Employing symmetry, that is, $dT/dy|_{y=h/2} = 0$, we have after double integration

$$\frac{dT}{dy} = -Ay + C_1 \succ C_1 = A\frac{h}{2} \qquad \text{(E.7.5.7a, b)}$$

and

$$T(y) = -\frac{A}{2}y^2 + C_1 y + C_2 \qquad \text{(E.7.5.8)}$$

Hence, at $y = 0$,

$$T_w + \frac{2\kappa}{\kappa+1}\frac{hKn}{\mathrm{Pr}}\overbrace{\left(\frac{h}{2}A\right)}^{\equiv C_1} = C_2 \qquad \text{(E.7.5.9)}$$

and finally,

$$T(y) = T_w + \frac{A}{2}h^2\left[-\left(\frac{y}{h}\right)^2 + \left(\frac{y}{h}\right) + \frac{2\kappa}{\kappa+1}\frac{Kn}{\mathrm{Pr}}\right] \qquad \text{(E.7.5.10)}$$

With the numbers for nitrogen, that is, $\kappa = 1.4$, $Pr = 0.72$, and $\mu = 1.656 \times 10^{-5}\ N \times s/m^2$, as well as $Kn = 0.08$, $U = 100$ m/s, and $h = 0.8$ μm, we can calculate the theoretical temperature jump as $T_{\text{jump}} = T_{\text{gas}} - T_{\text{wall}} \approx 0.3$ K.

| **Graph 1** | **Comment** |
|---|---|
| 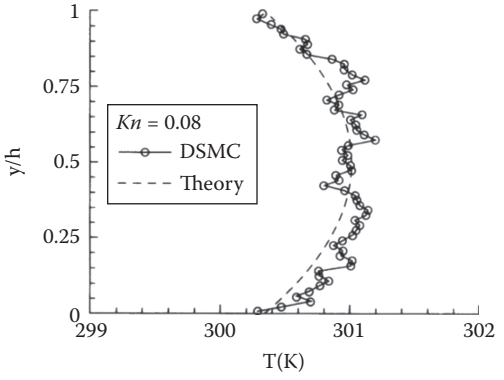 | • $T_{\text{jump}}$ is minimal, as confirmed by direct simulation Monte Carlo (DSMC) results of Fang and Liou (2002).<br>• *Recall:* DSMC is a numerical method for modeling rarefied gases (typically $Kn = \mathcal{O}(1)$) by solving the Boltzmann equation by tracking simulation molecules, which represent a large number of real gas molecules. |



### 7.3.4 Electro-Osmotic Flow

As briefly mentioned in Section 7.3.3, an electrolyte (e.g., saltwater) subject to an electrostatic field exhibits an apparent slip velocity at the charged conduit wall. In general, surface-modulated driving forces, such as surface tension and especially electro-osmosis, are often employed for *liquid flow* in micro- and nanochannels in the Stokes-flow regime ($\mathrm{Re} \leq 1.0$). The advantages of such "pumps" include minimal space requirements, no moving parts, and low costs. Movement of *charged particles* is accomplished via *electrophoresis*. In fact, there are four distinct electrokinetic phenomena (i.e., electro-osmosis, electrophoresis, streaming, and sedimentation), of which two are depicted in Figure 7.4.

In electro-osmosis, when a solid surface, for example, plastic or glass, contacts an electrolyte, such as salt water, the solid surface is already charged or becomes naturally charged.

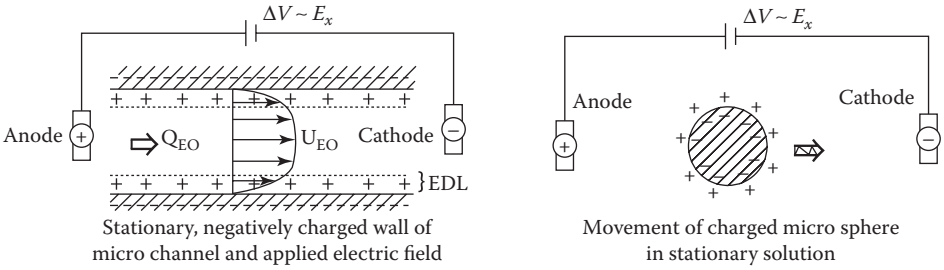


**FIGURE 7.4**
Electrokinetic phenomena: (a) electro-osmotic (EO) flow; (b) particle movement due to electrophoresis.

The latter occurs due to the difference of electron (or ion) affinities between the solid surface and the solution. As a result, the surface charge, being either negative or positive depending on the type of solid-electrolyte pairing, causes a special layered ion-structure at the solid–liquid interface. This is labeled the EDL, which has a net mobile electric charge. The EDL consists of the stationary Stern mono-layer and the diffuse layer. Now, applying externally an electric field, $\vec{E}$, between the channel inlet and outlet induces a Coulomb force, which causes a major part of the EDL to move; for example, the positive ions moving toward the cathode (see Figures 7.4a and b, 7.5, and 7.6). This moving fluid layer of typically nanometer thickness $\lambda_D$ (known as the *Debye length*) is also known as the diffuse layer. It drags with it via viscous effects the adjacent layers and hence, practically the entire quasi-neutral bulk fluid. This phenomenon is known as *electro-osmotic flow*. Thus, electro-osmosis works like a (non-mechanical) *pump*. It is most desirable in devices where the length-scales are in micrometers to nanometers, the flow rates are very low ($\mathrm{Re} \leq 1.0$), or the fluid-volumes to be conveyed are in the nanoliter and picoliter range, as in digital microfluidics.

Before discussing the underlying physics of electro-osmosis, a few definitions are in order:

- *Ion*: An atom or molecule for which the total number of electrons (–) does not match the total number of protons (+) will result in a net positive charge (i.e., cations) or net negative charge (anions). The process of gaining or losing electrons from a neutral atom/molecule is called *ionization*. This electron-transfer process is driven by the tendency to attain a stable electronic configuration, that is, a "closed shell."

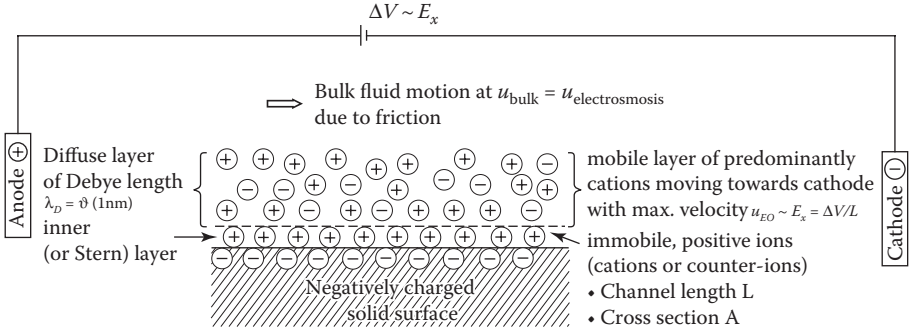


**FIGURE 7.5**
Moving diffuse layer generating microchannel flow rate $Q_{EO} = u_{EO}A$.

For example, sodium is stable when it loses an (extra) electron and hence, becomes a cation: $Na \rightarrow Na^{+} + e^{-}$. The opposite holds for the chlorine atom, where gaining an electron, that is, $Cl + e^{-} \rightarrow Cl^{-}$, yields an anion. As an aside, being oppositely charged, ionic bonds are formed: $Na^{+} + Cl^{-} \rightarrow NaCl$ (salt).

- *Electrolyte*: A substance containing free ions that make the medium electrically conductive. For example, salt in water forms an ionic solution; that is, solid salt dissolves into component elements: $\mathrm{NaCl}|_{\mathrm{solid}} \rightarrow \mathrm{Na}^{+}{}_{\mathrm{aq.}} + \mathrm{Cl}^{-}{}_{\mathrm{aq.}}$

  Another example is $CO_2$ dissolving in water, producing $H_3O^{+}$, $CO_3^{2-}$, and $HCO_3^{-}$ ions. As an aside, all higher life forms require a subtle electrolyte balance between the intracellular and extracellular milieu for proper body hydration, blood pH, and nerve and muscle functions.
- *EDL*: As mentioned, an electrolyte (e.g., salt water) in contact with a plastic or glass wall forms a double layer of ions. For example, a negatively charged surface attracts and immobilizes cations (also called counter-ions), forming an inner sublayer, that is, the Stern layer of net electric surface potential $\phi_{\mathrm{wall}} = \phi_{\mathrm{stern}} - \phi_{\mathrm{bulk}}$. The adjacent larger layer, known as the *movable diffuse layer* of thickness $\lambda_D$, also contains mainly cations. It typically exhibits an exponentially decaying electric potential (see Figure 7.6).
- In 1-D, as indicated in Figure 7.6 and with Equation 7.43, the electric potential can be approximated as

$$\phi(y) \approx \phi_w e^{-y/\lambda_D} \tag{7.22}$$

where:

$y$ is the wall-normal coordinate

$\lambda_D$ is the Debye length in the range $1 \leq \lambda_D \leq 50$ nm, with typically $25 \leq \phi_w \leq 100$ mV

For example, ion concentrations of 1–100 mM may generate $\lambda_D$–values of $10^{-1}$ nm, respectively. Clearly, there is a "slipping plane" (i.e., the shear surface) that separates potentially moving fluid, that is, the electrolyte, from the ion (or Stern) layer attached to the (charged, typically solid) surface.

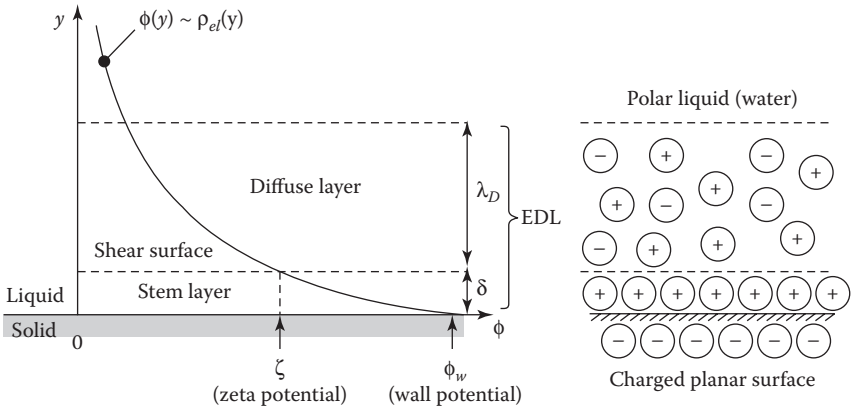


**FIGURE 7.6**
Decay of the electric potential in an electric double layer (EDL): ions, the resulting electric potential, and the electrical double layer with zeta potential $\zeta \leq \phi_{\mathrm{wall}}$.

Although electro-osmosis deals with moving fluid layers driven by forces, the laws of electrostatics (i.e., Coulomb, Gauss, Poisson, etc.) are applicable. In other words, although resulting observations/laws hold strictly only for static charges (e.g., ions in a quiescent electrolyte), they actually describe slowly moving charges as well; say, conducting liquids at $\mathrm{Re} \leq 1.0$. In general, electrostatics deals with phenomena involving time-independent distributions of electric point charges and resulting electric fields. Coulomb's law, concerning the interactive force between charged bodies at rest, is fundamental. The Coulomb (or electrostatic) force between two point charges $q_i$ and $q_j$ a distance $r_{ij}$ apart reads:

$$\vec{F}_{ji} = -\vec{F}_{ij} = \frac{1}{4\pi\varepsilon_0}\frac{q_i q_j}{r_{ij}^2}\hat{e}_{ij} \quad (\text{Coulomb}) \tag{7.23a}$$

where:

$\vec{F}_{ji}$ is the force exerted on $q_j$ by charge $q_i$
$\varepsilon_0$ is the permittivity in a vacuum
$\hat{e}_{ij}$ is the unit vector

Typical values of the *relative permittivity* (or dielectric constant) are

$$\varepsilon_r = \frac{\varepsilon}{\varepsilon_0} = \begin{cases} 1 & \text{in a vacuum} \\ 1.0005 & \text{in dry air} \\ 6 & \text{in glass} \\ 12 & \text{in silicon} \\ 80 & \text{in water} \end{cases}$$

where:

$\varepsilon$ is in [C/(Vm)]
$\varepsilon_0 = 8.85\times10^{-12}\,\mathrm{C/(Vm)}$

Clearly, 1 Coulomb (C) = 1 Nm/V. The electric permittivity indicates how much electric field is caused by a source charge (see Gauss's law).

Clearly, oppositely charged particles cause attractive forces, while equally charged particles generate repulsive forces. For example, the repulsive electrostatic force increases as particle-charge $+q_1$ moves toward particle-charge $+q_2$. The associated electric fields are due to electromagnetic waves traveling outward at the speed of light.

Rewriting Coulomb's law as

$$\left|\vec{F}\right| = F_{\text{Coulomb}} = k\frac{|q_1||q_2|}{r^2} \tag{7.23b}$$

where $k = 8.99\times10^9\ \mathrm{N\times m^2/C^2}$ is the electrostatic constant, Equation 7.23a is similar to Newton's gravitational force between two objects of masses $m_1$ and $m_2$ a distance r apart.

Now, the electric field vector $\vec{E}[N/C \triangleq V/m]$ is defined as

$$\vec{E} \equiv \frac{\vec{F}_{ji}}{q_j} = \frac{1}{4\pi\varepsilon_0}\frac{q_i}{r_{ij}^2}\hat{e}_{ij} \tag{7.24a, b}$$

where unit vector $\hat{e}_{ij} \equiv \dfrac{\vec{r}_{ij}}{r_{ij}}$. Thus, for a continuous spatial distribution of charges,

$$\vec{E} = \frac{1}{4\pi\varepsilon_0}\int \frac{\vec{r}}{r^3}dq := \frac{1}{4\pi\varepsilon_0}\int_{\forall} \frac{\rho_{el}\vec{r}}{r^3}d\forall \tag{7.25a, b}$$

where $\rho_{el}$ is the *volume-charge density*, that is,

$$\rho_{el} \equiv \lim_{\Delta\forall\to 0}\frac{\Delta q}{\Delta\forall} \quad \left[\frac{C}{m^3}\right] \tag{7.26}$$

For an ensemble of point charges $q_i$, as in an electrolyte, we have

$$\sum q_i = \int_{\forall} \rho_{el} d\forall \tag{7.27}$$

The electric field $\vec{E}$ being conservative (see Chang and Yeo 2010) and irrotational (i.e., $\nabla\times\vec{E} = 0$), it can be derived from a scalar potential function $\phi$ [$V$]:

$$\vec{E} = -\nabla\phi \left[\frac{V}{m}\right] or \left[\frac{N}{C}\right] \tag{7.28}$$

Clearly, $\phi$ is the electric potential (or net voltage), while typical values for the electric field $\vec{E}$ are

- $3\times10^{21}$ *N/C* at the surface of a uranium nucleus
- $5\times10^{4}$ *N/C* within a hydrogen atom
- $10^{3}$ *N/C* near a charged plastic rod
- $10^{-2}$ *N/C* inside a copper wire

The flux of the electric field through a (spherical) surface $A$ surrounding a point charge is

$$\int_S \vec{E}\cdot d\vec{A} = \int_S \vec{E}\cdot\hat{n}dA = 4\pi r^2\left(\frac{1}{4\pi\varepsilon_0}\frac{q}{r^2}\right) = \frac{q}{\varepsilon_0} \tag{7.29a through c}$$

For an ensemble of point charges in an electrolyte, i.e., $\Sigma q_i$, we have

$$\int_S \vec{E}\cdot\hat{n}dA = \frac{1}{\varepsilon_0}\sum q_i = \frac{1}{\varepsilon_0}\int_{\forall}\rho_{el}d\forall \ (\text{Gauss}) \tag{7.30}$$

Applying the divergence theorem (Appendix AI.3.1), $\int_S \vec{E}\cdot\hat{n}dA = \int_{\forall}\nabla\cdot\vec{E}d\forall$, we have

$$\int_{\forall}\nabla\cdot\vec{E}d\forall = \int_{\forall}\frac{\rho_{el}}{\varepsilon_0}d\forall \ or \ \int_{\forall}\left[-\nabla^2\phi - \frac{\rho_{el}}{\varepsilon_0}\right]d\forall = 0 \tag{7.31}$$

Hence,

$$\nabla\cdot\vec{E} = -\nabla^2\phi = \frac{\rho_{el}}{\varepsilon_0} \ (\text{Poisson}) \tag{7.32}$$

or for a heterogeneous dielectric, that is, insulating, medium,

$$-\nabla\cdot(\varepsilon\nabla\phi)=\rho_{el}\quad\xrightarrow[\text{uniform}]{\varepsilon=\not{c}}\quad-\varepsilon\nabla^2\phi=\rho_{el};\ \varepsilon=\varepsilon_r\varepsilon_0 \tag{7.33a through c}$$

*Note:* Actual microfluidics materials are typically "weak electrical conductors" and hence, have finite permittivities ε ranging from low (e.g., insulators such as glass or polymers or silicon) to high (e.g., electrodes), with aqueous solutions being in-between.

Now, from the definition $\vec{E}=\vec{F}/q$ and with $\rho_{el}=q/\forall$, we have the Coulomb *electric force per unit volume*:

$$\vec{f}_C\equiv\vec{f}_{el}=\rho_{el}\vec{E}=-(-\varepsilon\nabla^2\phi)\nabla\phi \tag{7.34}$$

Thus, when an electric field ($\vec{E}_{\text{ext.}}$) is externally applied to an electrolyte ($\rho_{el}$) in, say, a micro-channel, a new body force $\vec{f}_{el}$ has to be added to the N-S equation:

$$\rho\frac{\partial\vec{v}}{\partial t}+\rho(\vec{v}\cdot\nabla)\vec{v}=-\nabla p+\mu\nabla^2\vec{v}+\rho\vec{g}+\rho_{el}\vec{E}_{\text{ext.}} \tag{7.35}$$

The expression for the new body force is then

$$\vec{f}_{el}=\rho_{el}\vec{E}=-\varepsilon\nabla^2\phi\vec{E} \tag{7.36}$$

In summary:

- An applied voltage difference or electric potential, $\Delta V=\phi_{\text{ext.}}$, results in an external electric field $\vec{E}_{\text{ext.}}=-\nabla\phi_{\text{ext.}}$ [V/m].
- For a continuous medium, Maxwell showed that the charge density is

$$\rho_{el}=-\nabla\cdot(\varepsilon\vec{E})\xrightarrow{\varepsilon=\not{c}}=-\varepsilon\nabla^2\phi_{\text{ext.}}\left[C/m^3\right] \tag{7.37a, b}$$

  where $\varepsilon=\varepsilon_r\varepsilon_0$ is the dielectric constant (or permittivity).
- The charge density $\rho_{el}$ along the wall is confined to the EDL $\approx\lambda_D$ thick, that is, $\rho_{el}\sim\phi_{\text{ext}}$. Specifically, based on statistical thermodynamics analysis (Boltzmann) and following the Debye-Hückel linear approximation,

$$\rho_{el}=-\frac{\varepsilon}{\lambda_D^2}\phi_{\text{ext.}} \tag{7.38}$$

Hence,

$$-\frac{\varepsilon}{\lambda_D^2}\phi_{\text{ext.}}=-\varepsilon\nabla^2\phi_{\text{ext.}}\ \text{ or }\ \nabla^2\phi=\frac{\phi}{\lambda_D^2}\ (\text{Poisson}-\text{Boltzmann}) \tag{7.39a, b}$$

so that

$$\vec{f}_{el}=\rho_{el}\vec{E}=-\varepsilon\nabla^2\phi\vec{E}=-\frac{\varepsilon}{\lambda_D^2}\phi\vec{E} \tag{7.40a through c}$$

For axial (1-D) flow:

$$f_x^{el} = -\varepsilon \frac{d^2\phi}{dy^2} E_x \tag{7.41}$$

For the 1-D case, the Poisson–Boltzmann equation reads:

$$\frac{d^2\phi}{dy^2} = \frac{\phi(y)}{\lambda_D^2} \tag{7.42}$$

Equation 7.42 is now integrated for the two extreme cases in terms of channel geometry, that is, a single wall, as in a very wide channel, and a narrow microchannel.

*Case I:* Equation 7.42 is subject to two BCs, that is, $\phi(y=0) = \phi_{\text{wall}} \approx \zeta$ (zeta potential) and $\phi(y \to \infty$, i.e., $y = \lambda_D) = 0$ (zero bulk potential), resulting in

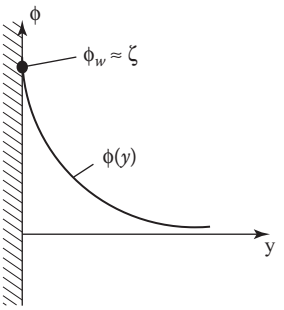


$$\phi(y) = \phi_w \exp\left(-\frac{y}{\lambda_D}\right) \tag{7.43}$$

*Note:* Equation 7.43 is suitable for a single charged surface or very wide channels where the focus is on one charged wall.

*Case II:* For the sketched microchannel flow, we impose $\varphi(y=h) = \phi_{\text{wall}} \approx \zeta$ and $d\phi/dy = 0$ at $y = 0$. Then, the solution of Equation 7.42 is

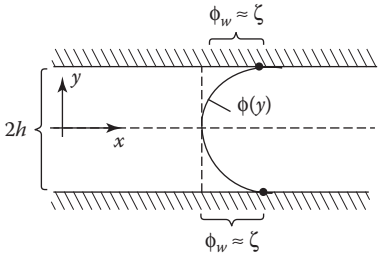


$$\phi(y) = \phi_w \frac{\cosh\left(\frac{y}{\lambda_D}\right)}{\cosh\left(\frac{h}{\lambda_D}\right)} \tag{7.44}$$

*Notes:*

- These 1-D solutions hold for relatively low $\phi_{wall} \approx \zeta$ values, say, $\zeta \leq 50$ mV.
- To avoid Joule heating, the applied electric current $I \sim E_{ext.}$ should be low as well.

**Example 7.6: Electro-osmotic Flow of an Electrolyte in a Microchannel with Charged Surfaces**

Consider saltwater ($\mu$) in a microchannel (height $h$, length $L$, and permittivity $\varepsilon$) with zeta potential $\zeta \approx \phi_{wall}$ and Debye length $\lambda_D$, subject to an electric field $Ex = -\Delta\phi/\Delta x = -\Delta V/L$. Find the induced velocity $u(y)$ and plot several non-dimensional velocity profiles. Discuss the interpretation of $u(y=\lambda_D) = u_{EO} \approx u_{slip}$ when $\lambda_D/h \lll 1$.

| **Sketch 6** | **Assumptions** | **Method** |
|---|---|---|
| 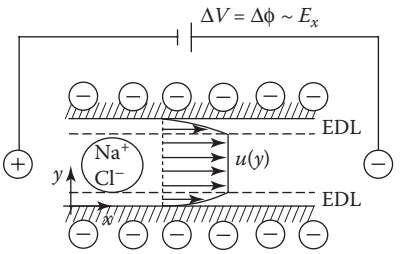 | • Steady laminar fully developed flow<br>• Constant properties/ parameters<br>• $\phi_{wall} \approx \zeta$ and $\phi(y \geq \lambda_D) \approx 0$<br>• No viscous heating | • Reduced N-S equation with $\vec{f}_{coulomb} = \rho_{el}\vec{E}_{ext.} = -\varepsilon\nabla^2\phi\vec{E}_{ext.}$; $\therefore f_x = -\varepsilon(d^2\phi/dy^2)E_x$<br>• $\phi(y) \approx \zeta\exp(-y/\lambda_D)$<br>*Postulates:*<br>• $\nabla p = 0$ and $\vec{v} \to u(y)$<br>• Employ wall BCs at $y=0$ and $y=h$ for both $u(y)$ and $\phi(y)$ |

*Solution:* Based on the assumptions and postulates, a reduced form of Equation 7.35 in conjunction with Equation 7.41 yields the $x$-momentum equation:

$$0 = \mu\frac{d^2u}{dy^2} - \varepsilon\frac{d^2\phi}{dy^2}E_x \quad \text{or} \quad \frac{d^2u}{dy^2} - K\frac{d^2\phi}{dy^2} = 0 \qquad \text{(E.7.6.1a, b)}$$

where $K = \varepsilon E_x/\mu = ¢$ as $E_x = -d\phi/dy \approx \Delta V/L$.

Integrating Equation E.7.6.1b twice yields $u(y) - K\phi(y) = Ay + B$, which is subject to the $u$- and $\phi$- conditions at $y=0$ and $y=h$, that is, $u=0$ and $\phi \approx \zeta$. Hence,

$$u(y) = \frac{\varepsilon E_x}{\mu}\left[\phi(y) - \zeta\right] \qquad \text{(E.7.6.2)}$$

Clearly, only $\phi(y)$ creates the electrolyte flow. Specifically, in the wall region $0 < y < \lambda_D$, $\phi(y) \approx \zeta\exp(-y/\lambda_D)$, and hence, Equation E.7.6.2 reads with the non-dimensionalized $P \equiv h/2\lambda_D$ and $\hat{y} = y/h$ and $E_x = \Delta V/L$:

$$\hat{u} \equiv \frac{u(y)\mu L}{\varepsilon\zeta\Delta V} = 1 - \exp\left[-2P\hat{y}\right] \qquad \text{(E.7.6.3)}$$

Outside the EDL, when $\lambda_D \lll 1$, at $y > \lambda_D$, the exponential term is approximately zero, and we have

$$u = u_{EO} = u_{slip} = \varepsilon\Delta V\zeta/(\mu L) \qquad \text{(E.7.6.4a through c)}$$

In summary, the $u(y)$-profile has to be pieced together by adjusting the $\phi(y)$-function between the two EDLs at the walls and the microchannel center.

*Graphs 2:*

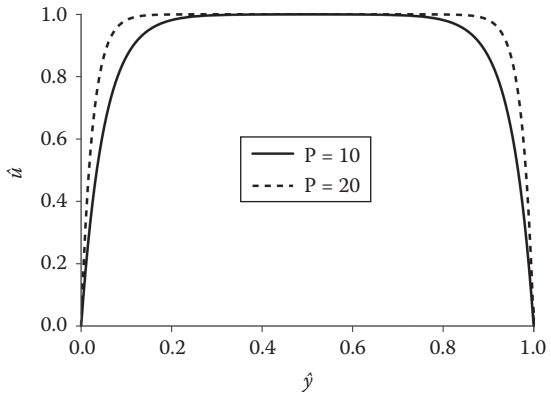


*Comments:*

- For very thin EDLs, we have $u_{\text{EO}} \hat{=} u_{\text{slip}} = u_{\text{bulk}} \equiv \mu_{\text{EO}} E_x$ for $\lambda_D < y < h - \lambda_D$, where $\mu_{\text{EO}} \equiv \varepsilon/\mu\phi \approx \varepsilon/\mu\zeta$ is the *electro-osmotic mobility*.
- Measuring $u_{EO}$ and knowing $E_x = \Delta V/L$ yield $\mu_{EO}$ and hence, $\phi_{\text{wall}} \approx \zeta = \mu_{EO}\mu/\varepsilon$.

### *7.3.4.1 Summary*

Assuming *steady* electrolyte flow with constant fluid properties and uniform zeta potential, we have shown the following:

- Continuity:

$$\nabla \cdot \vec{v} = 0 \tag{7.45}$$

- Momentum transfer:

$$\rho(\vec{v} \cdot \nabla)\vec{v} + \nabla p - \mu\nabla^2\vec{v} - \rho_{el}\vec{E} = 0 \tag{7.46}$$

and by deduction,

- Energy transfer:

$$\rho c_p(\vec{v} \cdot \nabla)T + \nabla \cdot (k\nabla T) - \mu\Phi - \sigma_{el}(\vec{E} \cdot \vec{E}) = 0 \tag{7.47}$$

where the term $\sigma_{el}(\vec{E} \cdot \vec{E})$ indicates Joule heating. The applied electric potential can be obtained from

$$\nabla^2\phi = -\frac{\rho_{el}}{\varepsilon} \tag{7.48}$$

As shown with Example 7.6, for a microchannel of height $2h$ where the driving Coulomb force balances the viscous resistance force, we have for $\phi_{\text{wall}} \approx \zeta$

$$u = u_{\text{EO}}\left(1 - \frac{\phi}{\zeta}\right) \tag{7.49}$$

Following Dutta and Beskok (2001), the electric potential $\phi(y)$ is

$$\phi = \frac{4k_BT}{ez}\tanh^{-1}\left[\tanh\left(\frac{ez\zeta}{4k_BT}\right)\exp\left[\frac{|y|-h}{\lambda_D}\right]\right] \tag{7.50}$$

Horiuchi and Dutta (2004) showed that the ratio of Joule heating to viscous dissipation for 1-D microchannel flow is

$$\kappa \approx \frac{\sigma_{el}\delta h}{\zeta^2}\frac{\mu}{\varepsilon^2} \tag{7.51}$$

Here, $\delta \leq 5\lambda_D$ is the wall layer, where $\varphi(y) \neq 0 (0 \leq y \leq \delta)$, and typical parameter values are $\sigma_{el} = 10^{-3}$ S/m, $\lambda_D = -100$ mV, $h \gg \delta$, $\mu = 10^{-3}$ Ns/m$^2$, and permittivity $\varepsilon = \varepsilon_0\varepsilon_r$ (see previous list of $\varepsilon$-values). It should be noted that $\kappa = \kappa(h, \lambda_D, \zeta^{-2}$; plus medium parameter values) but is not explicitly dependent on $E_x = \Delta V/L$.

Clearly, Section 7.3.4 is only a very brief introduction to steady creeping flow of simple electrolytes in microchannels. More may be found in texts by Tabeling (2005), Nguyen and Wereley (2006), Kirby (2013), and Kleinstreuer (2014).

## 7.4 Homework Assignments

As always, two types of homework problems, that is, text-illuminating questions and basic microscale engineering problems, are suggested. The problems in Section 7.4.2 were taken in modified and extended form from the open literature as well as previous homework and test assignments of the author's fluid dynamics as well as micro/nanofluidics courses.

### 7.4.1 Physical Insight

7.1 Using Figure 7.1a as a guide, develop a flowchart for a microfluidic system, such as an LoC (see Figure 7.1b), or a MEMS (e.g., ink-jet printer), or a PoC (point-of-care) device, for example, for blood-sugar analysis.

7.2 Select a specific microfluidics system and provide images and descriptions of major system aspects from fabrication to application.

7.3 Discuss major functions and applications of microscale systems in mechanical (or chemical or biomedical) engineering.

7.4 After reading Sections 7.1 and 7.2 plus Table 7.1, select five microscale problem areas, and provide real-world microsystem examples.

7.5 Most dimensionless groups (see Section 7.3.1) scale with $L^2$, that is, appearing to be "irrelevant as $L \to 0$." Nevertheless, considering the three conservation laws, discuss the reduced modeling equations most useful for micro/nanosystem analysis in light of dominant forces, fluxes, time scales, and/or transport phenomena.

7.6 Consider a square microchannel of width and height $h$ and length $10h$. Form $\kappa = S/\forall$ and plot $\kappa(h)$ for $0 < h < 4$ units.

7.7 Redo Example 7.1 for heat transfer and species-mass transfer.

7.8 Contrast the Strouhal number, $St = fL/v$, with the Womersley number, $Wo = L(\omega\rho/\mu)^{1/2}$, and provide applications.

7.9 Redo Example 7.2 for heat transfer and species-mass transfer with suitable parameter values.

7.10 Similarly to the analysis shown in Example 7.3, derive $R_{\text{thermal}} = \Delta T/Q_{\text{heat}}$ and $R_{\text{species-mass}} = \Delta c/\dot{m}$.

7.11 Show that for steady fully developed flow in an ellipsoidal tube with $u = u(y, z)$, the hydraulic resistance is again $R_{\text{hydr.}} \sim l^{-3}$ (see Example 7.3).

7.12 In light of Section 7.3.2, select, illustrate, and discuss one flow device with important applications for all three geometric system scales, that is, from macro- to nano-scale.

7.13 Section 7.3.2 provides *gas flow*–modeling regimes in terms of the Knudsen number $Kn = \lambda_{\text{mfp}}/l_{\text{system}}$. Why is there not a sound theory for *liquid flows* in microconduits? Discuss ideas for developing such liquid flow–modeling regimes.

7.14 Obtain a specific data set for argon from the open literature, and redo Example 7.4.

7.15 Review gas versus liquid properties (i.e., density, viscosity, and conductivity), contrasting macro-scale with nano-scale phenomena and resulting property values.

7.16 Provide an updated literature review on wall slip velocity and wall-temperature jump models with applications (see Section 7.3.3). What is the underlying nano-scale physics?

7.17 Concerning Section 7.3.4, research the differences between electrophoresis and dielectrophoresis, and give applications of other electrokinetic phenomena.

7.18 Research the impact of the diffuse layer on electro-osmosis in microchannel flow.

7.19 Derive, illustrate, and explain Equation 7.21 and then Equations 7.34, 7.36, and 7.40.

7.20 Derive Equation 7.44 of Case II. Estimate Joule heating, $\sigma_{el}(\vec{E}\cdot\vec{E})$, and compare it with viscous heating, $\mu\Phi$, for a reasonable set of parameter values.

7.21 Redo Example 7.6 for $P < 10$, that is, using Equation 7.44.

7.22 Review the paper by Dutta and Beskok (2001), derive Equation 7.50, and contrast it with Equation 3.57a.

7.23 Review the paper by Horiuchi and Dutta (2004) and derive/discuss Equation 7.51. Cite practical applications where $\kappa > 1$, that is, Joule heating is important.

### 7.4.2 Engineering Problems

7.24 Consider a quasi-spherical drop ($D_d$, $\sigma$, $\theta$) about to fall from the tip of a capillary ($D_c$). It is assumed that the contact angle $\theta = 0$ when the drop actually falls. Based on a 1-D force balance, that is, $F_z\cos\theta = (\sigma\pi D_c)\cos\theta = m_d g$, find the falling-drop volume $\forall_{\max}$ and an expression for the diameter ratio $D_d/D_c$. Introducing the Bond number ( $Bo \equiv D_c^2\rho g/\sigma$ ), show that $D_d/D_c = 1.82Bo^{-1/3}$.

7.25 As a correction to $\forall_{max}$ of Problem 7.24, Harkins and Brown (1919) suggested $\forall_{drop} = \forall_{max} C$, where $C = 0.6 + 0.4(1 - 0.488Bo^{1/3})^{2.2}$. Estimate $\forall_{drop}$ for $D_c = 1$ mm, $\sigma = 0.06$ N/m, and $\rho = 1000$ kg/m$^3$.

7.26 Consider spherical micro-bubble growth (radius $R$) in a very viscous fluid.

a. Using the reduced continuity equation and the dynamic boundary condition $v_r[r = R(t)] = dR/dt \equiv \dot{R}$, show that $v_r(r) = \dot{R}R^2/r^2$.

b. With only the pressure and viscous forces being dominant, show that the internal bubble pressure is

$$p(t) = p_\infty + 4\mu\dot{R}R$$

c. Find $R(t)/R_0$, where $R_0 = R(t=0)$, $\Delta p = p - p\infty$, and compute/graph $R(t)/R_0$ for $R_0 = 100$ μm, $\Delta p = 900$ kPa, $\rho = 1000$ kg/m$^3$, and $\mu = 100$ Pa·s.

7.27 Consider a rod ($\kappa R.\ L$) falling with velocity $v_0$ in a tall, liquid-filled cylinder (radius $R$) with a closed bottom. Assuming axisymmetric steady laminar fully developed flow between these cylinders, find the velocity distribution $v_z(r)$ in the micro-gap.

7.28 Consider radial flow between horizontal parallel micro-disks of inner radius $R_i$, outer radius $R_0$, and spacing $2h$. Given inlet flow rate $Q = 4\pi R_i h u_{mean}$,

a. Show that $v_r(r,z) = \left(\dfrac{3Q}{8\pi h}\right)\dfrac{1}{r}\left[1 - \left(\dfrac{z}{h}\right)^2\right]$

b. Show that $\Delta p = -\dfrac{3\mu Q}{4\pi h^3}\ln(R_i/R_0)$

c. Plot $v_r$ and $\Delta p$ using the base values $Q = 10^{-4}$m$^3$/s, $R_i = 5$ mm, $R_0 = 50$ mm, $h = 200$ μm, $\rho = 1000$ kg/m$^3$, and $\mu = 10$ Pa·s. Check whether $\mathrm{Re}_h < 1.0$!

7.29 Consider 2-D flow in a microchannel ($h$, $L$) with the bottom wall being porous where fluid is being withdrawn at velocity as $v_{wall}(x)$.

a. Show that for $\varepsilon \equiv h/L \ll 1$ and $\mathrm{Re}_h = u_{in}h/v \le 1.0$ (Stokes flow), the N-S equations reduced to

$$\frac{\partial u}{\partial x} + \frac{\partial v}{\partial y} = 0; \quad \frac{\partial p}{\partial y} = 0 \quad \text{and} \quad 0 = -\frac{\partial p}{\partial x} + \nu\frac{\partial^2 u}{\partial y^2}$$

b. Using the dimensionless variables $\hat{x} = x/L$, $\hat{y} = y/h$, $\hat{u} = u/u_{in}$, $\hat{v} = v/(\varepsilon u_{in})$, and $\hat{p} = (p - p_{ref.})/[\mu u_{in}/(\varepsilon h)]$, show that

$$\hat{u}(\hat{x},\hat{y}) = 6\hat{u}_{avg.}(\hat{x})[\hat{y} - \hat{y}^2],$$

where $\hat{u}_{avg.}(0) = 1$.

c. Employing the continuity equation, show that

$$\hat{v}(\hat{x},\hat{y}) = v_w(\hat{x})[1 - 3\hat{y}^2 + 2\hat{y}^3]$$

d. Plot the velocity profiles and comment!

7.30 For Poiseuille flow with velocity-slip between parallel plates a distance $h$ apart or in a tube of radius $r_0$,

a. Show that $u(y) = 4u_c[(y/h) - (y/h)^2] + u_{\text{slip}}$ for microtube flow. Interpret $u_c$ and $v_c$!

b. Derive expressions for the mass flow rates $\dot{m}_{\text{plate}}$ and $\dot{m}_{\text{tube}}$, plot $\dot{m}_p(h)$ and $\dot{m}_t(r_0)$, and comment.

7.31. Consider thermal micro-Couette flow of a gas ($U$, $h$; $\Delta p = 0$; $T(y=0) = T_w = ¢$; and $q(y=h) = q_w = 0$)) in the slip-flow regime $0.01 < Kn \equiv \lambda/2h < 0.1$. Assume 1-D fluid flow and only thermal diffusion with viscous heating.

a. Show that, indeed, $Kn = \lambda/2h$.

b. Derive the velocity profile and temperature distribution.

c. Graph $T(y/h)$ for $U = 100$ m/s, $T_{\text{wall}} = 300$ K, $h = 500$ μm, $\kappa = 1.4$, and $\text{Pr} = 0.7$ by selecting $Kn = 0.0$, 0.01, and 0.1.

d. Comment and explain!

7.32. Consider electro-osmotic microchannel flow characterized by $h$; $\lambda_D$; μ, ε, ζ, and $E_x$. Derive and graph $\hat{u} = u(y)/u_{\text{bulk}}$ as a function of $y/\lambda_D$ for two different sets of BCs with regard to the linearized ϕ(y)-distribution. Comment!

7.33. Consider pressure-driven flow ( $\Delta p/L = ¢$ ) of a particle suspension, which can be described by a power-law fluid ($m$, $n$) in a microchannel of height $2h$.

a. Obtain the velocity profile, and check your answer for $n = 1$ and $m = \mu$, that is,

$$u(y) = \frac{h^2}{2\mu}\left(\frac{\Delta p}{L}\right)\left[1 - \left(\frac{y}{h}\right)^2\right]$$

b. Graph $u(y)$ for $n = 0.2$ and 1, where $u_{\max} = 0.8$ and 1 m/s, respectively.

7.34. Consider a tube of diameter $D = 5$ μm and length $L = 10$ cm, filled with an electrolyte ($\varepsilon = 7.08 \times 10^{-10}$C/(V·m); $\mu = 10^{-3}$Pa·s). The wall potential, that is, approximately the zeta potential, is $\zeta = -100$ mV, based on a voltage of 1 kV, which is applied across the tube length. Calculate the pressure drop required to achieve the same volumetric flow rate as $Q_{EO}$. Plot the velocity profiles and comment!

Taylor & Francis
Taylor & Francis Group
http://taylorandfrancis.com

# 8

# *Fluid–Structure Interaction*

## 8.1 Introduction

Almost all problems solved in the previous chapters dealt with *static* fluid–structure scenarios. Geometric configurations of solid structures at rest, or with independently moving surfaces, largely determined the fluid flow fields. Examples include internal flow through a conduit or external flow past submerged bodies. Both the flow field along the static structure as well as the fluid stresses and forces on the structure walls could be readily determined. This included cases of independently *moving surfaces*, as in planar and rotational Couette flows.

In contrast to the static cases, *dynamic fluid–structure interactions* (FSIs) are characterized by the following two-way coupled mechanisms (see Figure 8.1):

(i) Transient, typically fluctuating displacements of a structure wall induce fluid motion, where the fluid stays in contact with the moving wall.

(ii) The unsteady flow field imposes varying shear stresses and pressure loads onto a fluid–solid interface and hence, initiates or modifies the motion of the structure, as in vortex shedding.

Clearly, most often, such dynamic coupling occurs when transient fluid flow causes structure movement (or even structure reconfiguration). Examples include blood flow past heart valves and in elastic arteries, turbulent flow causing conduit or machine-part vibration, container or structure motion due to surface waves, vibro-acoustic coupling in speakers, wind effects on wires, towers, and bridges, or ocean waves affecting offshore structures. Specifically, high winds, strong river currents, major ocean waves, and atmospheric explosions can cause severe damage to all kinds of structures, while on a microscale, fluid flow–induced vibration may lead to material fatigue, internal/external cracks, and ultimately, structure collapse.

FSIs are modeled based on the equation of motion (Section 2.3) and the dynamic equations of deformable solids (Section 8.2). Suitable coupling conditions at the fluid–structure interface have to be enforced. Specifically, the fluid and solid wall have the same motion (i.e., wetted surface), and the fluid and structural stresses exerted on the wall are balanced; that is, they are locally in dynamic equilibrium.

Section 8.2 deals briefly with stress fields in solids, conditions of equilibrium, stress–strain relations, and compatibility conditions. Subsequently, applications to slender-body dynamics and flow-induced vibrations in terms of mass-spring-damper systems are discussed in Sections 8.3 and 8.4, respectively.

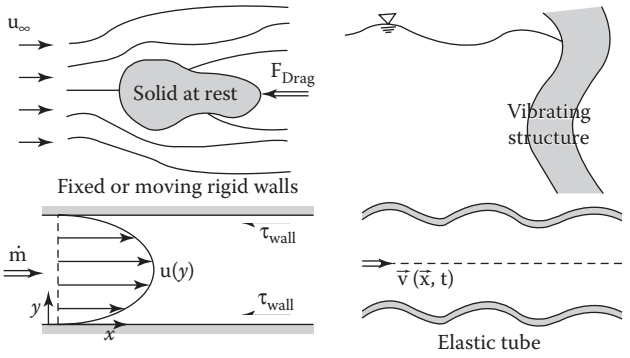


**FIGURE 8.1**
Fluid–structure interactions: (a) static cases and (b) dynamic examples.

## 8.2 Solid Mechanics Review

As mentioned in Section 8.1, FSI is an integral part of most transport phenomena in biological, environmental, and industrial systems. In this section, the basic solid mechanics equations are reviewed. They are needed to solve FSI problems in conjunction with the conservation laws (Chapter 2). Typically, a pressure due to fluid flow generates a load on a structure, which results in wall stress, strain, and deformation.

### 8.2.1 Stresses in Solid Structures

As outlined in Section 2.3, the state of material interaction at any point in a body is specified by the stress tensor (see also Appendix AI.1.2):

$$\sigma_{ij} = \begin{bmatrix} \sigma_{11} & \sigma_{12} & \sigma_{13} \\ \sigma_{21} & \sigma_{22} & \sigma_{23} \\ \sigma_{31} & \sigma_{32} & \sigma_{33} \end{bmatrix} = \begin{bmatrix} \sigma_{xx} & \tau_{xy} & \tau_{xz} \\ \tau_{yx} & \sigma_{yy} & \tau_{yz} \\ \tau_{zx} & \tau_{zy} & \sigma_{zz} \end{bmatrix} \tag{8.1a, b}$$

where $\sigma_{ii}$ (no sum on $i$) are the normal stresses, that is, generated by forces $F_i$ perpendicular to surfaces $A_i$, while the shearing stresses $\sigma_{ij} \hat{=} \tau_{ij}$ $(i \neq j)$ are caused by tangential forces $F_j$ acting on surfaces $A_i$ $(i \neq j)$ with normal vector $\hat{\boldsymbol{n}}_i$ (see Figure 8.2).

As alluded to in Section 2.3, the stress tensor is symmetric, that is, $\sigma_{ij} = \sigma_{ji}$. This equality of shearing stresses can be readily shown in applying to the solid cube of Figure 8.2a the static conditions $\sum \vec{\mathbf{M}} = \mathbf{I}\,\vec{\boldsymbol{\alpha}} \equiv 0$,

where:

| | |
|---|---|
| $\vec{\mathbf{M}} = \vec{\mathbf{r}} \times \vec{\mathbf{F}}$ | is the applied moment or torque, that is, force times lever distance |
| $\mathbf{I}$ | is the moment of inertia |
| $\vec{\boldsymbol{\alpha}}$ | is the angular acceleration vector |

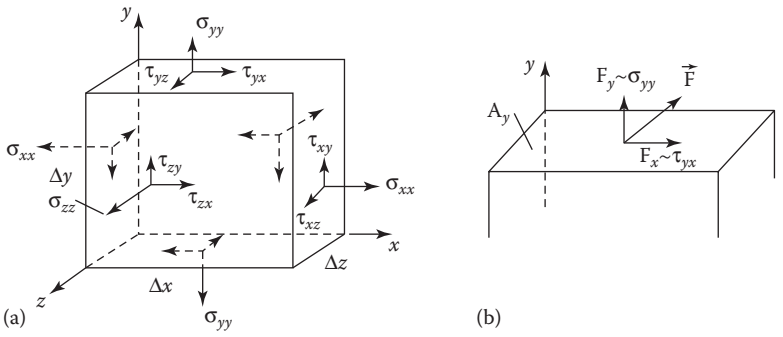


**FIGURE 8.2**
Stresses and forces: (a) 3-D solid element with positive stresses; (b) 2-D force components and stresses in the $A_y$-plane.

The normal and shearing stresses relate to the following forces and moments (Figure 8.2b):

- *Axial force* $\sim \int \sigma_{ii} dA$ , where $h_{ij}$ (no sum on $i$) are either tensile or compressive stresses
- *Shear force* $\sim \int \tau_{ij} dA \;\; (i \neq j)$, which try to move (shear) adjacent parts of a solid
- *Moments* (or torques), which may bend a beam, for example, $M_y = \int \sigma_{xx} z dA$,

  $M_z = -\int \sigma_{xx} y dA$, and so on, or may twist a body, for example, $T = \int (\tau_{xz} y - \tau_{xy} z) z dA$

Clearly, the symmetric stress tensor has six independent components. These can be further reduced to three principal stresses, which act in mutually perpendicular, principal directions. They act normal to three principal planes on which all shearing stresses are zero. Thus, Equation 8.1a now reads after the coordinate transformation from $\sigma_{ij}$ to $\sigma_{ii}$:

$$\sigma_{ij} = \begin{bmatrix} \sigma_1 & & 0 \\ & \sigma_2 & \\ 0 & & \sigma_3 \end{bmatrix} \tag{8.1c}$$

where $\sigma_1$, $\sigma_2$, $\sigma_3$ are the principal stresses. The principal stresses can be combined according to von Mises' deformational theory in terms of an effective stress $\sigma_e$, known as the *von Mises stress*.

$$\sigma_e = \frac{1}{\sqrt{2}} \left[ (\sigma_1 - \sigma_2)^2 + (\sigma_2 - \sigma_3)^2 + (\sigma_3 - \sigma_1)^2 \right]^{1/2} \tag{8.2}$$

Equation 8.2 is typically used to determine the locations and magnitudes of maximum stresses in human hard or soft tissues as well as medical devices and implants.

The next two examples illustrate how internal stresses are computed for two-dimensional (2-D) plate bending and cylinder twisting (Example 8.1) as well as internal stress distributions, including principal stresses, for a bar under axial tension (Example 8.2).

**Example 8.1: Simple Bending and Torsion Formulas for 2-D Solids of Linearly Elastic Material**

Consider a 2-D beam subject to pure bending and then a cylinder subject to simple torsion. Show that $\sigma_{xx} = -M_z y/I$, where $I$ is the moment of inertia, and $\tau_{\rho\theta} = Tr / J$, where $J$ is the polar moment of inertia.

Sketches 1a and 1b

(a) Bending

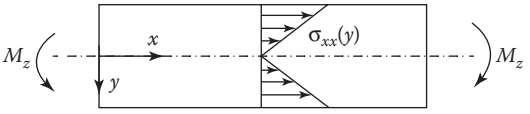


(b) Torsion

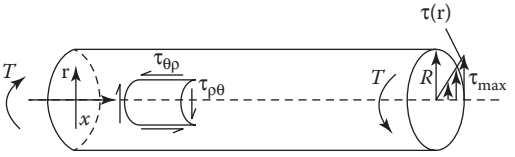


*Assumptions:*

- The normal stress $\sigma_{xx}(y)$ is linear in $y$, and all other stresses in the beam are zero (pure bending).
- The resultant of the internal force of the beam is zero, that is, $\int_A \sigma_{xx} dA = 0$.
- The torsional loading does not reshape or re-orientate the cross-sectional planes of the cylinder.

*Solution:*

**Bending**

The moments of the internal forces about the beam's centerline (i.e., normal axis) are equal to the applied moment around the $z$-axis (see Sketch 1a):

$$M_z = -\int_A y\sigma_{xx} dA \tag{E.8.1.1}$$

With $\sigma_{xx} = ky$, where $k$ is a constant, we have

$$M_z = -k\int_A y dA := -kI_z \tag{E.8.1.2}$$

where $I_x$ is the moment of inertia of the cross section $A$ about the $z$-axis; for example, $I_x = bh^3/12$ for a rectangular beam with $A = bh$ and $I_z = \pi R^4/4$ for a cylinder of radius R, that is, $A_0 = \pi R^2$.

Thus, with $k = -M_z/I_z$

$$\sigma_{xx} = -M_z y / I_z \tag{E.8.1.3}$$

**Torsion**

The resultant of the shearing stress distribution being equal to the applied torque yields (see Sketch 1b)

$$T = r\tau dA; \quad \tau(r) = \frac{r}{R}\tau_{\max} \tag{E.8.1.4a, b}$$

Thus,

$$T = \frac{\tau_{\max}}{R}\int_A r^2 dA := \frac{\tau_{\max}}{R} J \tag{E.8.1.5a, b}$$

where $J = \pi R^4/2$ is the polar moment of inertia of the cylinder's cross section. Finally, with $\tau_{\max}/R = \tau/r$, we obtain

$$\tau = \tau_{\rho\theta} = Tr/J \tag{E.8.1.6}$$

**Example 8.2: Stresses on an Inclined Plane of a Bar under Uniaxial Tension**

Consider a bar ($A = 10^3$ mm$^2$) subject to a tensile load of $N = 100$ kN. Determine the stress in a plane slanted by $\alpha = 35°$ and verify stress symmetry and the existence of a principal plane.

| **Sketch 2** | **Assumption** |
|---|---|
| 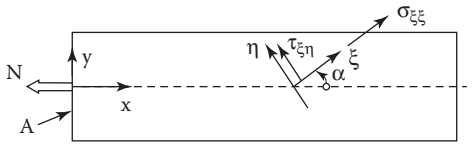 | • Uniform stress distributions in/on every plane |



*Solution*:

With respect to the incline, the loading force $N$ generates a tensile stress $\sigma_{\xi\xi}$ because of the normal $N\cos\alpha$ and a shearing stress $\tau_{\xi\eta}$ because of the tangential $N\sin\alpha$. Thus, with $\sigma_{xx} = N/A$, we have

$$\sigma_{\xi\xi} = \frac{N\cos\alpha}{A/\cos\alpha} = \sigma_{xx}\cos^2\alpha \tag{E.8.2.1}$$

and

$$\tau_{\xi\eta} = -\frac{N\sin\alpha}{A/\cos\alpha} = -\sigma_{xx}\sin\alpha\cos\alpha \tag{E.8.2.2}$$

In letting the "cutting angle" vary, that is, $0° \le \alpha \le 180°$, $\sigma_{\xi\xi}$ and $\tau_{\xi\eta}$ undergo maxima and minima. For example,

$$\sigma_{\xi\xi}\ (\alpha = 0°, 180°) = \sigma_{xx} = \sigma_{\max} \text{ when } \tau_{\xi\eta} = 0$$

and

$$\tau_{\xi\eta}\ (\alpha = 45°, 135°) = \tau_{\max} \text{ when } \sigma_{\xi\xi} = \pm\frac{1}{2}\sigma_{xx}$$

*Graph 1:*

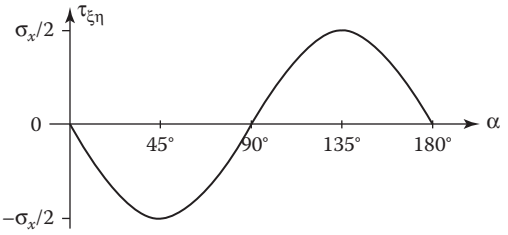


*Comments:*

On plotting $\tau_{\xi\eta}$, it is revealed that both symmetry of the stress tensor (see Equation 8.1a) and principal planes or axes (see Equation 8.1b) actually exist. Specifically,

$$\left|\tau_{\xi\eta}(\theta)\right| = \left|\tau_{\xi\eta}(\theta + 90°)\right|$$

and at $\alpha = 0°$ and 180°

$$\sigma_{\xi\xi} = \alpha_{\max} = \sigma_{xx} \text{ when } \tau_{\xi\eta} = 0$$

With the given data,

$$\sigma_{xx} = \frac{N}{A} = 100\ MPa,\ \sigma_{\xi\xi} = \sigma_{xx}\cos^2\alpha = 67.11\ MPa, \text{ and } \tau_{\xi\eta} = -\sigma_{xx}\sin\theta\cos\theta = -47\ MPa$$

### 8.2.2 Equilibrium Conditions

So far, we have assumed uniformly distributed stresses across each surface caused by an external load. It is more likely that stress components will vary from point to point in a body. Nevertheless, all external forces and internal stresses have to be in static equilibrium, that is,

$$\sum \vec{\mathbf{F}} = 0 \tag{8.3}$$

$$\sum \vec{\mathbf{M}} = 0 \tag{8.4}$$

For example, considering a thin 2-D solid element of differential area $dA_z = dxdy$ (see Figure 8.3), we take the moments about the origin (see Equation 8.4) and can show that $\tau_{xy} = \tau_{yx}$. Now, employing $\sum F_x = 0$ (see Equation 8.3), we obtain

$$\left(\sigma_{xx} + \frac{\partial\sigma_{xx}}{\partial x}\,dx\right)dy - \sigma_{xx}dy + \left(\tau_{xy} + \frac{\partial\tau_{xy}}{\partial y}\,dy\right)dx - \tau_{xy}dx + f_s dxdy = 0$$

or

$$\frac{\partial\sigma_{xx}}{\partial x} + \frac{\partial\tau_{xy}}{\partial y} + f_x = 0$$

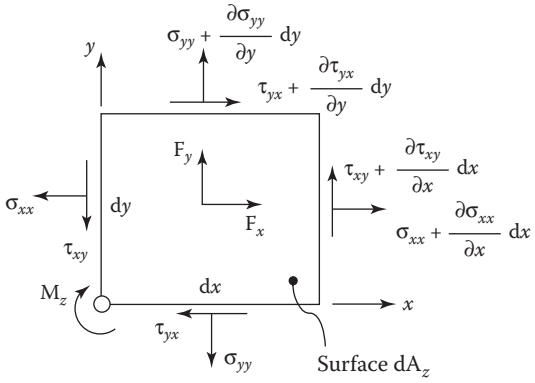


**FIGURE 8.3**
Differential 2-D solid element with varying forces and stresses.

Similarly,

$$\frac{\partial \sigma_{yy}}{\partial y} + \frac{\partial \tau_{xy}}{\partial x} + f_y = 0$$

In three dimensions (3-D), using tensor notation with the summation convection of repeated indices, we have the equilibrium condition:

$$\frac{\partial \sigma_{ij}}{\partial x_j} + f_i = 0 \tag{8.5}$$

with $i, j = x, y, z$ and $\sigma_{ij} \neq \sigma_{ji}$ $(i \neq j)$.

Clearly, given the external forces per unit volume $f_i$, Equation 8.5 contains six unknown stress components; that is, three additional equations have to be found. This brings us to the three basic principles for solving solid mechanics problems:

1. *Conditions of equilibrium* (see Equation 8.5)
2. *Stress–strain relations*, where material properties in terms of constitutive equations correlate forces, causing stresses in a given solid with body displacements
3. *Conditions of compatibility*, where body continuity is everywhere preserved, consistently with local strain distributions and deformations

Equation 8.5 can be readily extended to *dynamic structures*, where in general (see Newton's second law of motion),

$$\rho a_i = \sigma_{ij,j} + f_i \qquad \text{in } \Omega(t) \tag{8.6}$$

where:

| | |
|---|---|
| $a_i = dv_i/dt$ | is the acceleration of a material point in the domain $\Omega$ at time $t$ |
| $f_i$ | are the external forces per unit volume |
| $\rho$ | is the mass density |

Equation 8.6 is subject to appropriate boundary conditions and necessary stress–strain relations, as discussed in the next section.

### 8.2.3 Stress–Strain Relationships

When a force and/or moment is applied to an object, material deformation may occur in the form of body elongation/contraction, beam bending, rod twisting, and/or simple shearing. In all these cases, body elements undergo shape changes. In contrast, during rigid-body motion, no stress is induced. This is the case for translatory displacement due to an axial force, such as for any flying/moving, non-deforming object, such as balls, cars, planes, and ships. In summary, deformation relates directly to stress when body element distortions, that is, shape changes, occur, say, due to stretching, compression, and/or twisting.

#### *8.2.3.1 Deformation Analysis*

As illustrated in Fung (1994) and other texts, a line element in a 3-D body, $\overline{AA'} = ds_A$, translates, stretches, and rotates, because of body deformation, to $\overline{BB'} = ds_B$ (see Figure 8.4).

Clearly, with point A at $(a_1, a_2, a_3)$ and point B at $(b_1, b_2, b_3)$, the distance to the neighboring point $A'(a_1 + da_1, a_2 + da_2, a_3 + da_3)$ is, after Pythagoras,

$$(ds_A)^2 = (da_1)^2 + (da_2)^2 + (da_3)^2$$

Similarly,

$$(ds_B)^2 = (db_1)^2 + (db_2)^2 + (db_3)^2$$

Now, the determination of any continuous body deformation requires known mapping functions

$$b_i = b_i(a_1, a_2\ a_3) \quad \text{or} \quad a_i = a_i(b_1, b_2\ b_3)$$

for every point in the body. The components of the displacement vector $\vec{\mathbf{u}} = \Delta\vec{\mathbf{r}}$ (see Figure 8.4) are then

$$u_i = b_i - a_i$$

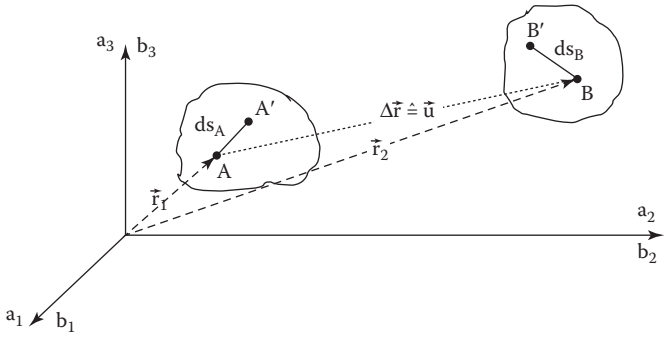


**FIGURE 8.4**
Line element changes during body deformation. (After Fung, Y., *A First Course in Continuum Mechanics: For Physical and Biological Engineers and Scientists*, Prentice Hall, Englewood Cliffs, NJ, 1994.)

Given the mapping functions, we can write

$$db_i = \frac{\partial b_i}{\partial a_j}\, da_j \quad \text{and} \quad da_i = \frac{\partial a_i}{\partial b_j}\, db_j$$

so that the displacements can be expressed, using the Kronecker delta, as

$$ds_A^2 = \delta_{ij} da_i da_i = \delta_{ij} \frac{\partial a_i}{\partial b_l} \frac{\partial a_j}{\partial b_m}\, db_l\, db_m$$

and

$$ds_B^2 = \delta_{ij} db_i db_i = \delta_{ij} \frac{\partial b_i}{\partial a_l} \frac{\partial b_j}{\partial a_m}\, da_l\, da_m$$

Forming the difference, that is, *a measure of body deformation*, we obtain

$$ds_B^2 - ds_A^2 = \begin{cases} 2E_{ij} da_i da_j \\ \text{or} \\ 2\varepsilon_{ij} db_i db_j \end{cases}$$

where the symmetric tensor $E_{ij}$ is the Lagrangian (or Green's) strain tensor, and the tensor $\varepsilon_{ij}$ is the Eulerian (or Cauchy's) strain tensor. Clearly, if the length of each line element stays the same, $ds_B^2 - ds_A^2 = 0$, implying that $E_{ij} = \varepsilon_{ij} = 0$, and the body is at rest or undergoing rigid-body motion.

Using the displacement vector $u_i = b_i - a_i$, we can form

$$\frac{\partial b_i}{\partial a_j} = \frac{\partial u_i}{\partial a_j} + \delta_{ij} \quad \text{and} \quad \frac{\partial a_i}{\partial b_j} = \delta_{ij} - \frac{\partial u_i}{\partial b_j}$$

where $u_i = (u_1, u_2, u_3)$ and $b_i = (x_1, x_2, x_3)$. Thus, inserting these relations into the displacement expression and neglecting squares and products of the derivatives of the displacement components $u_i$, the Cauchy infinitesimal strain terms reduce to

$$\varepsilon_{ij} = \frac{1}{2}\left( \frac{\partial u_j}{\partial x_i} + \frac{\partial u_i}{\partial x_j} \right) \tag{8.7}$$

or in terms of the engineering shearing strain (i.e., the shear-rate tensor of Section 2.4):

$$\gamma_{ij} = \frac{\partial u_i}{\partial x_j} + \frac{\partial u_j}{\partial x_i} \quad (i \neq j) \tag{8.8}$$

Equation 8.7 can be written as

$$\varepsilon_{ij} = \begin{bmatrix} \varepsilon_{xx} & \frac{1}{2}\gamma_{xy} & \frac{1}{2}\gamma_{xz} \\ \frac{1}{2}\gamma_{yx} & \varepsilon_{yy} & \frac{1}{2}\gamma_{yz} \\ \frac{1}{2}\gamma_{zx} & \frac{1}{2}\gamma_{zy} & \varepsilon_{zz} \end{bmatrix} \tag{8.9}$$

Clearly, for infinitesimal displacements, $E_{ij} \approx \varepsilon_{ij}$, because it is immaterial whether the derivatives $u_{i,j}$ are calculated at the position of a point before or after deformation.

Now, the cause of displacements, that is, stresses, has to be correlated to strain. Specifically, a stress–strain relationship describes the mechanical property of a material and is therefore a *constitutive equation*. For linear elastic materials, for example, hard tissue (bones) and basic metals, *Hooke's law* holds:

$$\sigma_{ij} = C_{ijkl}\varepsilon_{kl} \tag{8.10}$$

The tensor of rank four, $C_{ijkl}$, is symmetric; that is, the $3^4 = 81$ elastic constants (or moduli) can be reduced to 36 (Fung, 1994). For an *isotropic* elastic solid, that is, when the properties are identical in all directions, Equation 8.10 reduces to

$$\sigma_{ij} = \lambda\varepsilon_{kk}\delta_{ij} + 2\mu\varepsilon_{ij} \tag{8.11}$$

Clearly, instead of 36 material values, only two, that is, the *Lamé constants* $\lambda$ and $\mu$, are needed (see Section 1.2.4 for comparison with viscous flow). Writing Equation 8.11 out and solving for the six $\varepsilon$-components, we obtain

$$\varepsilon_{ij} = \frac{1+v}{E}\sigma_{ij} - \frac{v}{E}\sigma_{kk}\delta_{ij} = \begin{cases} \dfrac{1}{2}\left(\dfrac{\partial u_i}{\partial x_j} + \dfrac{\partial u_j}{\partial x_i}\right) \\ \dfrac{1}{2}\gamma_{ij} \end{cases} \tag{8.12a through c}$$

where:

the "shearing strain" $\gamma_{ij} = \tau_{ij}/G$,

$E$ is *Young's modulus*

$v = -\varepsilon_{yy}/\varepsilon_{xx} = -\varepsilon_{zz}/\varepsilon_{xx}$ is the *Poisson ratio* expressing (lateral strain)/(axial strain)

$G \equiv \mu$ is the *shear modulus*

Because only two independent constants are needed for homogeneous isotropic elastic materials (see Equation 8.11), $E$, $v$, and $G$ are related, that is,

$$G = \frac{E}{2(1+v)} \tag{8.13}$$

Actual materials, such as biological soft and most hard tissues, rubber, and shape memory alloys (SMAs), do not follow Hooke's law. Clearly, compared with metals, these other materials exhibit nonlinear relationships and hysteresis; that is, the nonlinear loading and unloading curves differ. Mechanical models, a combination of (linear) springs and viscous dashpots, mimic some visco-elastic behavior. For example, as outlined in Humphrey and Delange (2004) and other solid mechanics books, the *Kelvin model* relates the load $F$ to the deflection (or displacement) $u(t)$ as

$$F + a\dot{F} = b(u + c\dot{u}) \tag{8.14a}$$

subject to

$$aF(t=0) = bcu(t=0) \tag{8.14b}$$

where $a$ to $c$ are constant system parameters.

#### *8.2.3.2 Simplifications*

Hooke's law, for a linear elastic, isotropic material, that is, Equation 8.12, can be rewritten as

$$\varepsilon_{xx} = \frac{1}{E}[\sigma_{xx} - v(\sigma_{yy} + \sigma_{zz})] \tag{8.15a}$$

$$\varepsilon_{yy} = \frac{1}{E}[\sigma_{yy} - v(\sigma_{xx} + \sigma_{zz})] \tag{8.15b}$$

$$\varepsilon_{zz} = \frac{1}{E}[\sigma_{zz} - v(\sigma_{xx} + \sigma_{yy})] \tag{8.15c}$$

$$\varepsilon_{xy} = \frac{1+v}{E}\tau_{xy} = \frac{1}{2G}\tau_{xy} := \frac{1}{2}\gamma_{xy} \tag{8.15d}$$

$$\varepsilon_{yz} = \frac{1+v}{E}\tau_{yz} = \frac{1}{2G}\tau_{yz} := \frac{1}{2}\gamma_{yz} \tag{8.15e}$$

$$\varepsilon_{zx} = \frac{1+v}{E}\tau_{zx} = \frac{1}{2G}\tau_{zx} := \frac{1}{2}\gamma_{zx} \tag{8.15f}$$

Clearly, for plane stress analysis, $\sigma_z = 0$, and the remaining normal stresses are:

| in rectangular coordinates | in polar coordinates |
|---|---|
| $\sigma_{xx} = \frac{E}{1-v^2}(\varepsilon_{xx} + v\varepsilon_{yy})$ | $\sigma_{rr} = \frac{E}{1-v^2}(\varepsilon_{rr} + v\varepsilon_{\theta\theta})$ |
| $\sigma_{yy} = \frac{E}{1-v^2}(\varepsilon_{yy} + v\varepsilon_{xx})$ | $\sigma_{\theta\theta} = \frac{E}{1-v^2}(\varepsilon_{\theta\theta} + v\varepsilon_{rr})$ |

(8.16a through d)

Provided that Young's modulus $E$ and Poisson's ratio $v$ are known, each of these equations contains extra unknowns; thus, equilibrium equations have to be established first, which relate forces to stresses, as illustrated next.

**Example 8.3: Displacement of a Non-Uniform Rod under Axial Stress**

Consider a vertical, axially loaded rod with suddenly changing cross section and material property as shown (cf. bone with implanted metal segment). Find the total axial displacement $u$.

| Sketch 3 | Assumptions | Method |
|---|---|---|
| 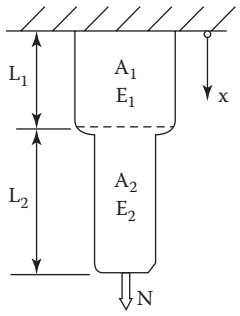 | • Segmentally constant $A_i$ and $E_i$<br>• Only normal, that is, axial force $N$ applied<br>• Hooke's law holds | Use of Equation 8.15a, where $\sigma_{yy}=\sigma_{zz}=0$ |

*Solution:*

The reduced governing equations read:

$$\varepsilon_{xx}=\frac{\sigma_{xx}}{E} \quad \text{and} \quad \Delta u=\int_0^L \varepsilon_{xx}dx, \quad \text{where } \sigma_{xx}=\frac{N}{A} \quad \text{(E.8.3.1a through c)}$$

Specifically, with axial displacement $u(x=0)=0$,

$$u_{total}=\int_0^{L_1}\frac{N}{A_1E_1}\,dx+\int_{L_1}^{L}\frac{N}{A_2E_2}\,dx; \quad L=L_1+L_2 \qquad \text{(E.8.3.2a)}$$

and hence,

$$u_{total}=N\left(\frac{L_1}{A_1E_1}+\frac{L_2}{A_2E_2}\right)=\frac{NL_1}{A_1E_1}\left(1+\frac{L_2}{L_1}\frac{A_1}{A_2}\frac{E_1}{E_2}\right)$$

### *8.2.3.3 Plane Stress Analysis*

If the body force $F_z=0$, then $\sigma_{zz}=\tau_{xz}=\tau_{yz}=0$ (cf. "thin plate problem"). Thus, three equations are necessary to calculate $\sigma_{xx}$, $\sigma_{yy}$, and $\tau_{xy}$, subject to *surface tractions*, that is, surface forces per unit area:

$$p_x=\sigma_{xx}l+\tau_{xy}m \qquad (8.17a)$$

and

$$p_y=\tau_{xy}l+\sigma_{yy}m \qquad (8.17b)$$

where $l=\cos(\hat{n},x)$ and $m=\cos(\hat{n},y)$ are the direction cosines for the normal vector $\hat{n}$. The first two equations for $\sigma_{xx}$, $\sigma_{yy}$, and $\tau_{xy}$ are obtained from Equation 8.5:

$$\frac{\partial\sigma_{xx}}{\partial x}+\frac{\partial\tau_{xy}}{\partial y}+f_x=0 \qquad (8.18a)$$

$$\frac{\partial\sigma_{yy}}{\partial y}+\frac{\partial\tau_{xy}}{\partial x}+f_y=0 \qquad (8.18b)$$

The third one is the equation of compatibility in terms of stress:

$$\left(\frac{\partial^2}{\partial x^2}+\frac{\partial^2}{\partial y^2}\right)(\sigma_{xx}+\sigma_{yy})=-\frac{1}{1-v}\left(\frac{\partial f_x}{\partial x}+\frac{\partial f_y}{\partial y}\right) \tag{8.19a}$$

and strain:

$$\frac{\partial^2 \varepsilon_{xx}}{\partial y^2}+\frac{\partial^2 \varepsilon_{yy}}{\partial x^2}=\frac{\partial^2 \gamma_{xy}}{\partial x \partial y} \tag{8.19b}$$

Equation 8.19a, b can be derived from the compatibility condition for strain components that directly relate to the displacements $u$ and $v$.

When the body forces $f_x$ and $f_y$ are zero, the task of evaluating planar stress, strain, and displacement subject to Equation 8.17a, b is less challenging. Similarly to the stream function $\Psi(x, y)$ satisfying the continuity condition, $\nabla \cdot \vec{v} = 0$, automatically, a *stress function* $\Phi(x, y)$ is introduced, where

$$\sigma_{xx} \equiv \frac{\partial^2 \Phi}{\partial y^2}, \sigma_{yy} \equiv \frac{\partial^2 \Phi}{\partial x^2}, \quad \text{and} \quad \tau_{xy} \equiv -\frac{\partial^2 \Phi}{\partial x \partial y}$$

Now, the balance of Equations 8.18a, b with Equation 8.19a yields

$$\frac{\partial^4 \Phi}{\partial x^4}+\frac{2\partial^4 \Phi}{\partial x^2 \partial y^2}+\frac{\partial^4 \Phi}{\partial y^4}=0 \tag{8.20}$$

Traditionally, the biharmonic Equation 8.20 has been approximately solved, subject to Equation 8.17a, b, with polynomial functions of various degrees (see Ugural and Fenster, 2003).

## 8.3 Slender-Body Dynamics

Structure vibrations caused by fluid flow may lead to noise, material fatigue, system damage, or even total destruction. However, controlled fluid-induced vibration can be desirable, as with music using wind instruments, as well as for enhanced mixing or particle sorting.

A body, subject to a flow field, experiences surface pressures and stresses, resulting in surface forces such as drag and lift (see Section 3.2.3). In turn, the body may not only move but also deform under these exerted forces. Such body deflections change the flow boundary conditions and hence the flow field, which again alters the surface forces. Thus, fluid-dynamic forces and structural motions may interact significantly. In any case, *flow instabilities*, such as vortex shedding from a fixed body (see Figure 8.5a and Section 2.3.5), as well as elastic instabilities, are of interest. They may cause structure oscillations or even the coupled FSIs of both (see Figure 8.5b). As mentioned, the fundamental aspects of coupled fluid-flow and elastic-body phenomena are important for the safe design of tall buildings, suspension bridges, towers, off-shore structures, piping systems, and power lines on a large scale, as well as medical implants, such as stent-grafts, and microelectromechanical systems (MEMS) for cooling or drug delivery on a small scale.

Classification of flow-induced vibration has been done in terms of the sources of excitation, according to the nature of the vibration, or via the type of fluid flow, that is, steady or unsteady (see Païdoussis, 1998). Specifically, steady flows may cause instabilities in terms of self-excited vibrations and vortex-induced vibrations. An example of self-excited oscillations (or flutter) is the thrashing, shaking motion of a garden-hose when dropped on the ground. Transient flows causing structure vibrations include random/chaotic (i.e., turbulent) flows as well as wavy and oscillatory flows. A commonly observed phenomenon of internal oscillatory flow is the water hammer, a quite noisy occurrence of pressure waves in pipe networks after sudden valve opening.

### 8.3.1 Flow-Induced Slender-Body Oscillations

Consider planar isothermal fluid flow ($u_{mean} \equiv U$) in a flexible pipe (elasticity-module $E$ and mass moment of inertia $I$) with lateral deflection $w(x, t)$ of small amplitude and long wavelength compared with the pipe diameter (see Figure 8.5c). For a representative elementary volume $A\Delta s$ (Figure 8.6) with accelerating fluid mass $m_f$, the following forces have to be taken into account: net pressure, gravity, and fluid–pipe interaction forces, that is, tangential (wall shear stress) and normal (reaction) forces. Thus, applying Newton's second law in the $x$- and $z$-direction, where $\partial s \approx \partial x$ and the deflections $w$ are small, we have per unit length $\Delta s$:

$$-A\frac{\partial p}{\partial x} - \tau_w S + m_f g + R\frac{\partial w}{\partial x} = m_f a_{f,x} \tag{8.21a}$$

and

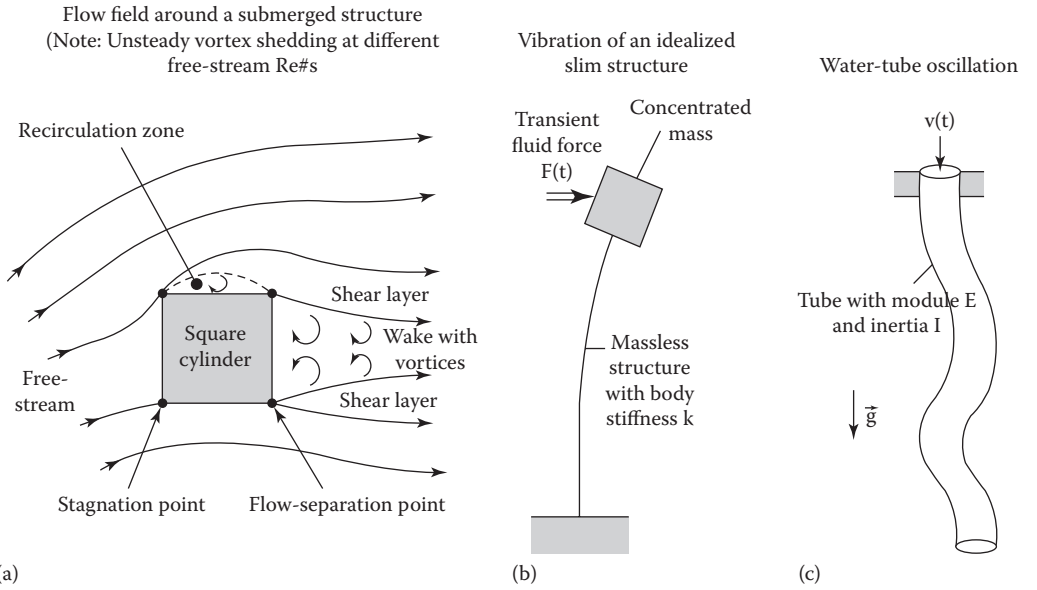


**FIGURE 8.5**
Example of fluid–structure transients: (a) flow field around a square cylinder submerged in an angled free-stream; (b) 1-D cantilever vibration; and (c) oscillation of an elastic tube caused by fluid flow.

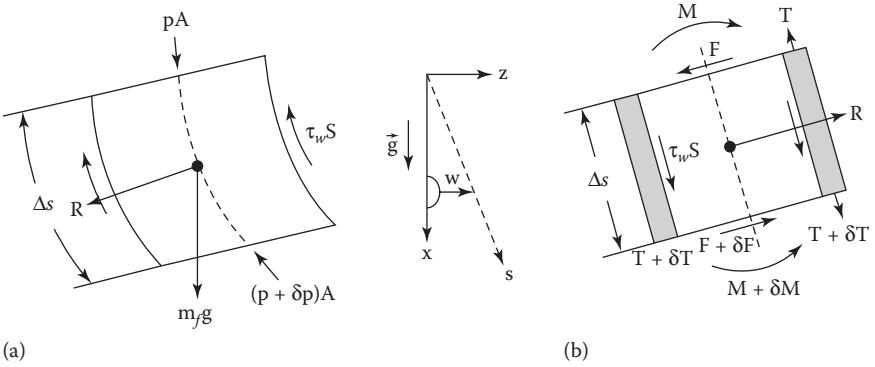


**FIGURE 8.6**
Forces on (a) accelerating fluid element and (b) coupled pipe segment.

$$-R - A\,\frac{\partial}{\partial x}\left(p\,\frac{\partial w}{\partial x}\right) - \tau_w\,S\,\frac{\partial w}{\partial x} = m_f\,a_{f,z} \tag{8.21b}$$

where:

- $A$ is the cross-sectional area
- $p$ is the gage pressure
- $\tau_w$ is the wall shear stress
- $S$ is the wall surface
- $R$ is the reaction force
- $m$ is the mass, where subscript $f$ denotes fluid and $p$ indicates pipe

The pipe segment is subject to longitudinal tension $T$ and a transverse shear force $F$, that is,

$$F = \frac{\partial M}{\partial x} \approx EI\,\frac{\partial^3 w}{\partial x^3}. \tag{8.22}$$

Thus, following Païdoussis (1998),

$$\frac{\partial T}{\partial x} + \tau_w\,S - m_p\,g - R\,\frac{\partial w}{\partial x} = m_p\,a_{p,x} \approx 0 \tag{8.23a}$$

and

$$\frac{\partial F}{\partial x} + R + \frac{\partial}{\partial x}\left(T\,\frac{\partial w}{\partial x}\right) + \tau_w\,S\,\frac{\partial w}{\partial x} = m_p a_{p,z} \tag{8.23b}$$

Recalling that $a_p = \dfrac{\partial^2 w}{\partial t^2}$, while $a_{f,x} = \dfrac{dU}{dt}$ and $a_{f,z} \approx \left[\dfrac{\partial}{\partial t} + U\,\dfrac{\partial}{\partial x}\right]^2 w$, substituting Equation 8.22, $F \approx EI\,\dfrac{\partial^3 w}{\partial x^3}$, using Equation 8.21a, b to eliminate $R$, and combining terms yields a partial differential equation (PDE) for small lateral motion of a vertical pipe with axial uniform flow $U(t)$:

$$EI\frac{\partial^4 w}{\partial x^4}+\left\{m_f U^2-\bar{T}+\bar{p}\,A(1-2\nu\delta)-\left[(m_f+m_p)g-M\frac{dU}{dt}\right](L-x)\right\}\frac{\partial^2 w}{\partial x^2}$$
$$+2m_f U\frac{\partial^2 w}{\partial x\partial t}+(m_f+m_p)g\frac{\partial w}{\partial x}+(m_f+m_p)\frac{\partial^2 w}{\partial t^2}=0 \tag{8.24a}$$

For Equation 8.24a, averaged tension and pressure over pipe length $L$ were assumed, while $v$ is the Poisson ratio, and $\delta=0$ implies no pipe constraint to axial motion at $x=L$. Neglecting gravity, pressure, and wall tension effects, and assuming $U=$ constant, Equation 8.24a reduces to

$$\underbrace{EI\frac{\partial^4 w}{\partial x^4}}_{\substack{\text{Flexural}\\ \text{restoring force}}}+\underbrace{m_f U^2\frac{\partial^2 w}{\partial x^2}}_{\text{Centrifugal force}}+\underbrace{2m_f U\frac{\partial^2 w}{\partial x\partial t}}_{\text{Coriolis force}}$$
$$+\underbrace{(m_f+m_p)\frac{\partial^2 w}{\partial t^2}}_{\text{Inertial force}}=0 \tag{8.24b}$$

Clearly, Equation 8.24b subject to appropriate initial/boundary conditions has to be solved numerically for $w(x, t)$, representing "free vibration" (see Section 8.4).

### 8.3.2 Flow-Induced Concentrated-Mass Oscillations

In the previous section, we considered the lateral small-scale deflection, $w=w(x, t)$, of a flexible pipe, induced by transient or steady axial flow. The described fourth-order PDE for $w(x, t)$ is essentially the same as for an oscillating cantilever. In fact, a cantilevered tube conveying fluid at sufficiently high velocities may exhibit flutter of the single-mode type (see Païdoussis, 1998, among others), as seen with wings and beams.

In this section, we focus on a (vertical) elastic cantilever, for example, a tower or high-rise, where the mass of the structure is concentrated at the end point, and the displacement $x(t)$ is caused by a transient load $F(t)$, say, a gusty wind. Figure 8.7 depicts this single-degree-of-freedom system (see also Figure 8.5b). Specifically, in response to the excitation force $F(t)$, the body mass $m$ accelerates, $\ddot{x}$, and moves, $x(t)$, while it is opposed to a restoring force $R=kx$ and slowed down by a damping force $D=c\dot{x}$. Thus, Newton's second law of motion, $\sum \vec{F}_{\text{ext}}=m\vec{a}$, describes the basic mass-spring-damper system in the form:

$$F(t)-kx-c\dot{x}=m\ddot{x} \tag{8.25}$$

Here, for linear systems, $k$ (the "spring" constant or body stiffness) and $c$ (the damping coefficient combining internal body friction and external fluid resistance) are independent of the displacement.

As shown in the next section, Equation 8.25 is commonly written in more "vibrational terms" as

$$\ddot{x}+2\kappa\,\omega_N\,\dot{x}+\omega_N^2\,x=\frac{F(t)}{m} \tag{8.26}$$

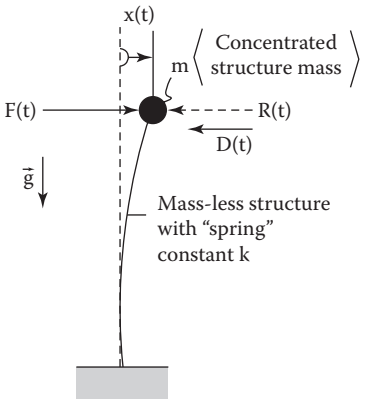


**FIGURE 8.7**
Mass-spring-damper model representing slender-elastic-body dynamics.

where:

$\kappa \equiv \dfrac{c}{2\sqrt{km}}$ is the damping ratio

$\omega_N \equiv 2\pi f_N = \sqrt{\dfrac{k}{m}}$ is the system's natural angular velocity (or circular frequency)

For $K = 1$, free motion of the system is non-oscillatory; but, when $\kappa \ll 1$ and $\omega_{\text{forced}} = \omega_N$ (or $F_{\text{forced}} = F_{\text{natural}}$), resonance oscillation may occur, leading potentially to system destruction.

Example 8.4 summarizes a vibrating slender-body application, illustrating a solution to Equation 8.26. Section 8.4 then provides in more detail the theoretical background for both translatory and rotational vibration induced by unbalanced forces.

**Example 8.4: Slender-Body Oscillations Caused by a Harmonic Load**

Consider an excitation function of the form $F(t) = F_0 \cos \omega t$, although in reality, $F(t)$ is non-harmonic when structures are subject to, say, turbulent flow or vortex shedding.

| Sketch 4 | Model 1 | Assumption | Method |
|---|---|---|---|
| 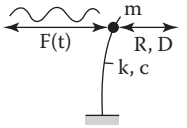  | 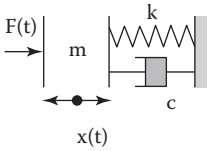  | • Linear, single-degree-of-freedom system | Newton's second law of motion |

*Solution*:
Equation 8.26 with $F(t) = F_0 \cos \omega t$, $\omega = 2\pi f$, has the solution (see Polyanin and Zaitsev, 1995, p. 130):

$$x(t) = F_0 \, H(\omega) \cos(\omega t - \varphi) \tag{E. 8.4.1}$$

where

$$H(\omega) = \left\{ m^2 \, \omega_N^4 \left[ \left( 1 - \left( \frac{\omega}{\omega_N} \right)^2 \right)^2 + 4\kappa^2 \left( \frac{\omega}{\omega_N} \right)^2 \right] \right\}^{-1/2} \tag{E.8.4.2}$$

The damping ratio is

$$\kappa \equiv \frac{c}{2\sqrt{mk}} \tag{E.8.4.3}$$

and the phase angle is

$$\varphi = \tan^{-1}\left[\frac{2\kappa\left(\frac{\omega}{\omega_N}\right)}{1-\left(\frac{\omega}{\omega_N}\right)^2}\right] \tag{E.8.4.5}$$

*Graphs 2a and 2b:*

- Resonance example with damping
- Forced oscillation with damping effects

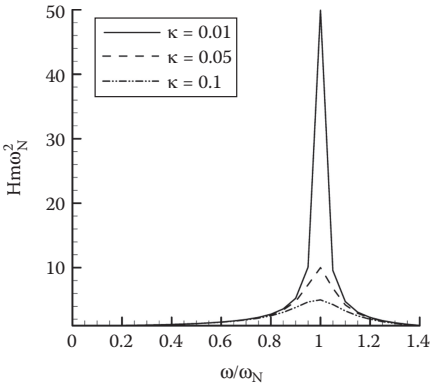


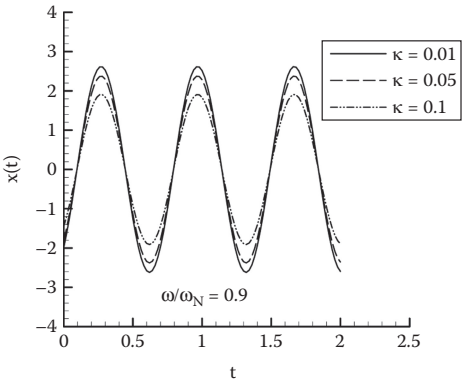


*Comments:*

- As expected, the amplitude of the resulting forced vibration spikes at $\omega = \omega_{natural}$ with values greatly dependent on $\kappa \sim c$, the damping coefficient (Graph 2a).
- Forced oscillations are strong when $\omega$ is near $\omega_{natural}$. Again, $\kappa \sim c$ has a measurable effect on the amplitude $F_0H$ (see Equation E.8.4.1 and Graph 2b).

## 8.4 Flow-Induced Vibration

Dynamics, that is, body (or fluid) motion caused by forces, encompasses (1) kinematics, that is, the study of motion disregarding the forces, and (2) kinetics, that is, the relationship between forces and the resulting motion. As indicated in Section 8.3.1, the dynamic response to forced vibration (or oscillation) of a linear, single-degree-of-freedom system is the solution to

$$m\ddot{x} + c\dot{x} + kx = F(t) \quad \text{and} \quad I\ddot{\theta} + c\dot{\theta} + k\theta = T(t) \tag{8.27a, b}$$

where $F(t)$ in Equation 8.27a can be any transient input, such as a harmonic forcing function $F(t) = F_0 \sin(\omega t)$ or displacement $x(t)$, while $T(t)$ is a moment or torque. As mentioned, such excitations may be caused by gusty winds, unbalanced rotary parts, earthquakes, or uneven surfaces. The homogeneous solution of Equation 8.27a and b, that is, $F(t) = T(t) = 0$, is known as the free response (or free vibration), triggered solely by the initial conditions. The particular solutions of Equation 8.27a and b have the form of the forcing function plus its derivative to match the second-order ordinary differential equation (ODE).

Numerous applications of Equation 8.27a and b and their solutions are discussed in mechanical-vibration texts (e.g., Palm, 2007). In the framework of FSIs, of special interest are the different forms of the damping coefficient $c$, as related to viscous flow. The (linear) spring constants, $k$, are given in strength-of-material books or deduced from experiments (see Roark et al., 2001). In general,

$$k = \begin{cases} dF/dx & \text{for force} - \text{deflection elements} \\ dT/d\theta & \text{for torque} - \text{angular} - \text{twist elements} \end{cases} \tag{8.28a, b}$$

Damping is the fluid resistance force or torque, that is,

$$F = c\,\bar{v} \quad \text{or} \quad T = c\,\omega \tag{8.29a, b}$$

where:

$c$ is the damping coefficient
$\bar{v}$ is the mean velocity of the moving part
$\omega = 2\pi f$ is the angular velocity in radians per unit time, while the frequency $f$ is in cycles per unit time (Hertz)

Figure 8.8 summarizes the two basic damping elements: translational and rotational (or torsional) dampers. Oscillating machine-part lubrication, shock absorbers, and door closers are just a few sample applications. Example 8.5 discusses the associated damping coefficients.

**Example 8.5: Derivations of Damping Coefficients**

Correlations for $c = F/\bar{v}$ are derived, considering translatory and rotational Couette flows with approximately linear velocity profiles, as well as a basic piston-orifice-cylinder system.
Simple Couette flow (e.g., basic thin-film lubrication):

| **Sketch 5** | **Method** |
|---|---|
| 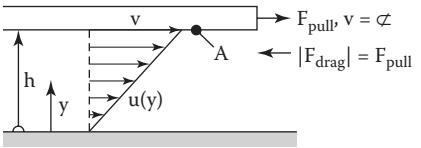 | • Linear velocity profile $u(y) = v\,\frac{y}{h}$<br>• $F = \tau_{wall} \cdot A;\ \tau_{wall} = \mu \left.\frac{du}{dy}\right\|_{y=h}$ |

*Solution:*

By definition,

$$c = \frac{F}{\bar{v}} \tag{E.8.5.1}$$

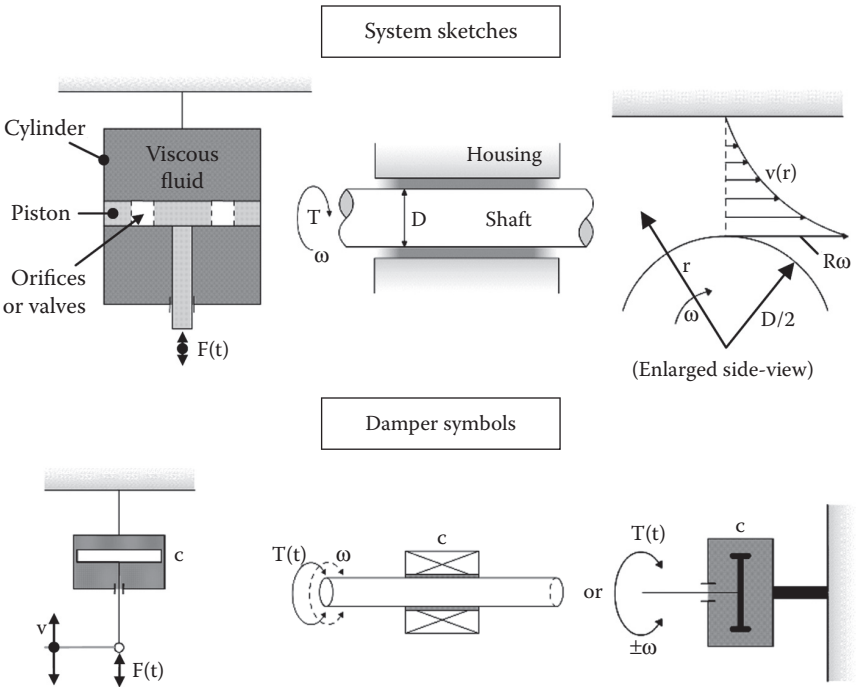


**FIGURE 8.8**
Basic viscous flow systems and associated damper/dashpot symbols.

$$F = \tau_w A = \mu \left.\frac{du}{dy}\right|_{y=h} \cdot A = \mu\, A \frac{\mathrm{v}}{h} \qquad \text{(E.8.5.2a through c)}$$

Hence, with $v \equiv \bar{v}$,

$$c = \frac{F}{\bar{\mathrm{v}}} = \frac{\mu\, A}{h} \qquad \text{(E.8.5.3)}$$

Cylindrical Couette flow (e.g., journal bearing)

| Sketch 6 | Method |
|---|---|
| 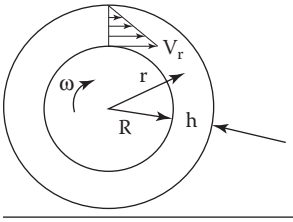 | • Shaft ($R$, $L$) and housing ($R+h$) forming a small gap, so that $v(r) \approx v_R \frac{r}{h}$<br>• Torque $T = F_{\text{drag}} \mathrm{R} = A\, \tau_w R$ |



*Solution:*
By definition (Equation 8.29b),

$$c = \frac{T}{\omega} \qquad \text{(E.8.5.4)}$$

$$T = A\,\tau_w\,R = (2\pi\,L\,R)\left(\mu\,\frac{dv_\theta}{dr}\bigg|_{r=R}\right)R \qquad \text{(E.8.5.5a, b)}$$

$$\tau_w = \mu\,\frac{du}{dr}\bigg|_{r=R} = \mu\,\frac{v_R}{h};\quad v_R = \omega\,R \qquad \text{(E.8.5.6a through c)}$$

Thus,

$$T = \frac{2\pi\,\mu L\,R^3}{h}\,\omega \qquad \text{(E.8.5.7)}$$

and hence,

$$c = \frac{T}{\omega} = 2\pi\,\mu\,R^3\,\frac{L}{h} \qquad \text{(E.8.5.8)}$$

Piston-orifice-cylinder damper (i.e., part of a suspension system)

| Sketch 7 | Method |
|---|---|
| 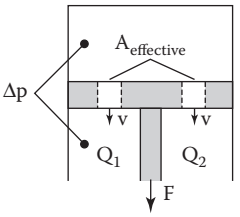  | • Effective orifice area $A$<br>• Constant flow rate $Q = \Sigma Q_i$<br>• $Q = \frac{\sqrt{\Delta p}}{R}$ from Poiseuille flow where R is the flow resistance<br>• $F = \Delta p A$<br>• Establish $F(v)$ relation |

*Solution:*

$$F = \Delta pA = (QR)^2\,A = (v\,A\,R)^2\,A \qquad \text{(E.8.5.9a through c)}$$

or

$$F = R^2\,A^3\,v^2 \qquad \text{(E.8.5.10)}$$

Hence,

$$c = \frac{F}{v} = R^2\,A^3\,v \qquad \text{(E.8.5.11)}$$

Now, with the fluid–structure damping coefficient illuminated and "spring constant" $k$ given based on structure properties (see Roark et al., 2001, among others), Equation 8.27a and b can be solved step-by-step, starting with the free-response case, that is, when $F(t)$ or $T(t)$ are zero.

### 8.4.1 Harmonic Response to Free Vibration

#### *8.4.1.1 Undamped Vibration Case*

Clearly, when there is zero (or negligible) damping, the system oscillates at its natural frequency, that is, the case of *free undamped vibration*, and Equation 8.27a and b reduce to

$$m\ddot{x} + kx = 0 \text{ and } I\ddot{\theta} + k\theta = 0 \tag{8.30a, b}$$

where the translatory mass $m$ is equivalent to the mass moment of inertia $I$. With the trial solution $x = A\sin(\omega t)$ and hence, $\ddot{x} = -\omega^2 A \sin \omega t$ , Equation 8.30a reads:

$$(-m\omega^2 + k)\left(A \sin \omega t\right) = 0$$

This implies

$$-m\omega^2 + k = 0$$

As a result, the frequency of the free response is the natural frequency:

$$\omega = \omega_N = \begin{cases} \sqrt{k/m} & \text{for linear oscillations} \\ \sqrt{k/I} & \text{for rotational oscillations} \end{cases}$$

#### *8.4.1.2 Damped Vibration Case*

1-D free vibration with damping is described by

$$m\ddot{x} + c\dot{x} + kx = 0 \text{ and } I\ddot{\theta} + c\dot{\theta} + k\theta = 0 \tag{8.31a, b}$$

With the trial solution $x = A$est for Equation 8.31a, the characteristic equation reads:

$$ms^2 + cs + k = 0 \tag{8.32a}$$

Hence,

$$s_{1,2} = \frac{-c \pm \sqrt{c^2 - 4mk}}{2m} \tag{8.32b}$$

Equation 8.32b implies three distinct cases depending on the character of the roots $s_{1,2}$, that is, $s_1 = s_2$ real, $s_1 \neq s_2$ real, or $s_{1,2}$ complex. Specifically, Equation 8.32b implies:

(i) Critical damping when $c^2 - 4km = 0$, that is,

$$c_{\text{crit}} = 2\sqrt{km} \tag{8.33}$$

(ii) Overdamping when $c > c_{\text{crit}}$ <real roots>
(iii) Underdamping when $c > c_{\text{crit}}$ <real roots>

The three cases are summarized via the damping ratio, which is defined as

$$\kappa \equiv \frac{c}{c_{\text{crit}}} \begin{cases} = 1 \text{ .....critically damped system} \\ > 1 \text{ .....exponential behavior occurs} \\ < 1 \text{ ..... oscillation occurs} \end{cases} \tag{8.34a through c}$$

Now, with $\kappa = \frac{c}{2\sqrt{km}}$ and $\omega_N = \sqrt{\frac{k}{m}}$ (see Equation 8.26), $c = 2\kappa\sqrt{km} = 2\kappa\, m\, \omega_N$, and Equation 8.32b can be rewritten as ($i \equiv \sqrt{-1}$)

$$s = \frac{-2\kappa\, m\, \omega_N \pm i\, 2\sqrt{km}\, \sqrt{1 - \left(\frac{c}{2\sqrt{km}}\right)^2}}{2m} \tag{8.35}$$

Hence,

$$s = -\kappa\, \omega_N \pm i\, \omega_N \sqrt{1-\kappa^2}$$

or

$$s_{1,\,2} = a \pm ib$$

The inverse of the first term is a time constant, that is, $\tau = a^{-1}$ (see the trial solution $x = Ae^{st}$), and the second term is the system's damped (natural) frequency:

$$\omega_D = \omega_N \sqrt{1-\kappa^2} \tag{8.36}$$

Clearly, we always have $\omega_D < \omega_N$, which implies that only the underdamped case with $\kappa < 1$ lends physical meaning to these frequencies $\omega_D$ and $\omega_N$. With the two roots of the characteristic equation, the general solution is a linear combination of the postulate $x = Ae^{st}$, that is,

$$x = A_1\, e^{s_1 t} + A_2\, e^{s_2 t}$$

With the initial conditions $x(t=0) = x_0$ and $\dot{x}(t=0) = \mathrm{v}_0$, the coefficients are

$$A_1 = \frac{v_0 - s_2\, x_0}{s_1 - s_2} \quad \text{and} \quad A_2 = x_0 - A_1$$

For the underdamped case, $\kappa < 1$, $s_1 = a + ib$, and $s_2 = a - ib$, so that

$$x = A_1\, e^{(a+ib)t} + A_2\, e^{(a-ib)t} = e^{at}(A_1 e^{ibt} + A_2 e^{-ibt})$$

or in equivalent form, employing Euler's identities (see Section AI.2.4 of Appendix I),

$$x = B\, e^{at}\, \sin(bt + \varphi) \tag{8.37}$$

where:

B is the amplitude
ϕ is the phase angle

Applying the initial conditions (ICs), $x(t=0) \equiv x_0 = B\, \sin\varphi$ and $\dot{x}(t=0) \equiv v_0 = a\, B \sin\varphi + b\, B \cos\varphi$, yields

$$\sin\varphi = \frac{x_0}{B} \quad \text{and} \quad \cos\varphi = \frac{v_0 - a\, x_0}{b\, B}$$

so that the phase angle

$$\varphi = \tan^{-1}\left(\frac{b\, x_0}{v_0 - a\, x_0}\right) \tag{8.38}$$

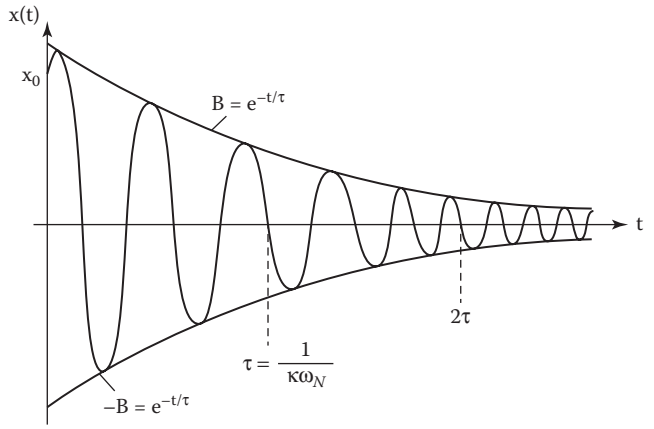


**FIGURE 8.9**
Free response oscillations of an underdamped case.

while the amplitude $B$ can be deduced via the identity $\sin^2\varphi + \cos^2\varphi = 1$. The free response of the mass-spring-damper system to the ICs $x = x_0$ and $\dot{x} = v_0$ at $t = 0$ is shown in Figure 8.9. Here, $a \equiv -\kappa\,\omega_N < 0$ and $b \equiv \omega_N$ in radians per unit time is the natural frequency. Clearly, due to the damping effect ($\kappa \neq 0$), the amplitude of the oscillations decays exponentially to zero, and the system mass gains a stable equilibrium.

**Example 8.6: Torsion Viscometer**

Consider a thin disk of diameter $D$ and inertia $I$, suspended by a torsion wire of "spring constant" $k$, oscillating in a viscous fluid layer of height $h$ and damping coefficient $c$. Develop an equation for the fluid viscosity $\mu = \mu(D, h, I, \omega_N, \text{and } \omega)$.

| Sketch 8 | Assumptions | Method |
|---|---|---|
| 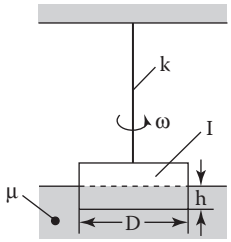 | Free response, single-degree-of-freedom mass-damper-spring system for rotating disk | • Newton's second law of motion<br>• Rotational damper $T = c\omega$ |



*Solution:*
The equation of motion of the "freely" oscillating disk is (see Equation 8.27b)

$$I\ddot{\theta} + c\dot{\theta} + k\theta = 0 \qquad \text{(E.8.6.1)}$$

where:
- $I$ is the disk inertia
- $c$ is the damping coefficient
- $k$ is the wire (spring) constant

Similarly to Example 8.1B, the damping constant can be derived as (see also Von Karman's "rotating disk in an infinite fluid reservoir" in, for example, Kleinstreuer, 1997)

$$c = \frac{\mu \pi D^4}{32h} \tag{E.8.6.2a}$$

or

$$\mu = 32hc/(\pi D^4) \tag{E.8.6.2b}$$

With the trial solution $\theta = Ae^{st}$, the characteristic equation of (E.8.6.1) reads:

$$Is^2 + cs + k = 0 \tag{E.8.6.3a}$$

Hence,

$$s_{1,2} = \frac{-c \pm \sqrt{c^2 - 4kI}}{2I} \tag{E.8.6.3b}$$

As shown (see Equations 8.33 and 8.34):

$$\kappa = \frac{c}{2\sqrt{kI}} \quad \text{and} \quad \omega_D = \omega_N \sqrt{1 - \kappa^2}$$

or

$$\kappa = \sqrt{1 - \left(\frac{\omega_D}{\omega_N}\right)^2} = \frac{c}{2\sqrt{kI}} \tag{E.8.6.4a}$$

so that

$$c = 2\sqrt{kI}\sqrt{1 - \left(\frac{\omega_D}{\omega_N}\right)^2} \tag{E.8.6.4b}$$

With $k = I\,\omega_N^2$,

$$c = 2\,I\,\omega_N \sqrt{1 - \left(\frac{\omega_D}{\omega_N}\right)^2} \tag{E.8.6.5}$$

and finally with Equation E8.6.2b:

$$\mu = \frac{64hI}{\pi D^4}\,\omega_N \sqrt{1 - \left(\frac{\omega_D}{\omega_N}\right)^2} \tag{E.8.6.6}$$

**Example 8.7: Free Response to a Linear Mass-Damper-Spring System, $2\ddot{x} + 6\dot{x} + 18x = 0$, Based on the Initial Body Displacement $x(0) = 2$**

| Sketch 9 | Assumptions | Method |
|---|---|---|
| 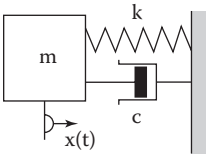 | As stated: 1-D, underdamped system | • Newton's second law<br>• Parameter identification by comparing Equation 8.27a with the given ODE |

*Solution:*

- Compare given ODE with Equation 8.27a; thus, $m=2$, $c=6$, and $k=18$. Hence, $\kappa = \dfrac{c}{2\sqrt{km}} = 0.5$, that is, underdamped, $\omega_N = \sqrt{k/m} = 3\ \text{rad/s}$, and $\omega_D = \omega_N\sqrt{1-\kappa^2} = 2.6\ \text{rad/s}$
- The roots of the characteristic equation

$$2s^2 + 6s + 18 = 0$$

are

$$s_{1,2} = -1.5 \pm 2.6i = a \pm bi$$

which implies: $\tau = a^{-1} = 2/3s$; $\omega = b = 2.6$ rad/s; and period $p = \dfrac{2\pi}{\omega_N} = 2.42\ s$

- Hence, in comparison with Equation 8.37,

$$x(t) = Be^{-1.5t}\sin(2.6t + \varphi)$$

where the parameters $B$ and $\phi$ depend on the initial conditions.

- ICs: $x(t=0)=2$ and $\dot{x}(t=0)=0$, so that $\sin\varphi = \dfrac{x_0}{B} = \dfrac{2}{B}$ and $\cos\varphi = \dfrac{v_0 - a\,x_0}{b\,B} = \dfrac{3}{2.6B}$. Employing the identity $\sin^2\varphi+\cos^2\varphi=1$, we have $\dfrac{4}{B^2} + \dfrac{9}{6.76B^2} = 1$ or $B=2.31$. Hence, $\varphi = \tan^{-1}\left(\dfrac{bx_0}{v_0 - ax_0}\right) = 1.04$ (or $1.04+\pi$); but, with $\sin\varphi = \dfrac{2}{2.31} > 0$ and $\cos\varphi = \dfrac{3}{2.6-2.31} > 0$, $\phi$ is in the first quadrant.
- Finally,

$$x(t) = 2.31e^{-1.5t}\sin(2.6t + 1.04) \qquad \text{(E.8.7.1)}$$

*Graph 3:*

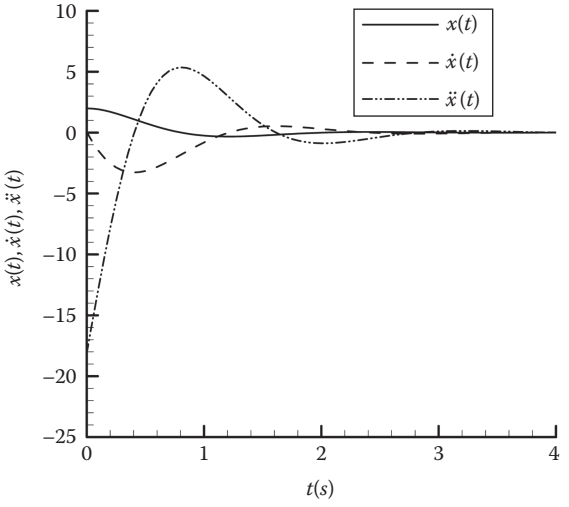

*Comments:*

- For the given system values, say, $m = 2$ kg, $k = 18$ kg/s$^2$ and $c = 6 \times 10^2$ N × s/cm the initial displacement, that is, $x_0 = x(t=0) = 2$ cm, is damped out after $t \approx 2$ s.
- This causes within the start-up period of, say, $0 \le t \le 1.4$ s rather large mass velocities $\dot{x}(t)$ and accelerations $\ddot{x}(t)$.

### 8.4.2 Harmonic Response to Forced Vibration

*Free vibration* implies *one-way* fluid–structure coupling where a mass-spring system, set into oscillatory motion via initial conditions, is damped due to the interaction with a viscous fluid. If in addition to the initial conditions $x(t=0) = x_0$ and $\dot{x}(t=0) = v_0$, the system is subjected to a *forcing function*, say, $F(t) = F_0 \sin \omega t$ caused by a periodic stream, we have a *two-way coupled* FSI case:

$$m\ddot{x} + c\dot{x} + kx = F_0 \sin \omega t \tag{8.39}$$

The trial solution reads:

$$x(t) = \underbrace{Ae^{at} \sin(bt + \varphi)}_{\text{free response}} + \underbrace{B \sin \omega t + C \cos \omega t}_{\text{forced response plus derivation}} \tag{8.40}$$

For the underdamped case, we have two complex conjugate roots $s_1 = a + ib$ and $s_2 = a - ib$, where

$$a = -\frac{c}{2m} \quad \text{and} \quad b = \frac{\sqrt{4mk - c^2}}{2m} \tag{8.41a, b}$$

implying that $4mk - c^2 > 0$. As before, the phase angle $\phi$ depends on the ICs. With the ICs $x(0) = \dot{x}(0) = 0$, we obtain the forced response as

$$\begin{aligned} x(t) = \frac{F_0}{(k - m\omega^2)^2 + (c\omega)^2} \Bigg\{ e^{at} \left[ -\frac{\omega}{b} (ac + k - m\omega^2) \sin bt + c\omega \cos bt \right] \\ + \left[ (k - m\omega^2) \sin \omega t - c\omega \cos \omega t \right] \Bigg\} \end{aligned} \tag{8.42}$$

With $a \equiv \tau^{-1} = -\frac{c}{2m} = -\kappa\, \omega_N < 0$, the terms multiplied by $e^{at}$ vanish with time; that is, the first bracket is the disappearing transient response. What remain with time are the sin $\omega t$ and cos $\omega t$ terms, known as the "steady-state", that is, periodic, response:

$$x_{ss}(t) = \frac{F_0}{(k - m\omega^2)^2 + (c\omega)^2} \left[ (k - m\omega^2) \sin \omega t - c\omega \cos \omega t \right] \tag{8.43}$$

**Example 8.8: Harmonic Response of an Underdamped System**

Consider the forced response to the mass-damper-spring system described by

$$\ddot{x} + \dot{x} + x = \sin \omega t$$

for the two imposed frequencies $\omega_1 = 1$ and $\omega_2 = 2$.

| Sketch 10 | Assumptions | Method |
|---|---|---|
| 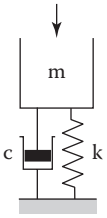 | • Linear, single-degree-of-freedom, second-order system<br>• Zero initial conditions<br>• One-way coupled FSI | • Identification of coefficients $m$, $c$, $k$, and $F_0$ by comparison with Equations 8.39 and 8.42<br>• Solution $x(t)$ given by Equation 8.42 |

*Solution:*

- Comparison of the given ODE with Equation 8.39 yields $m = c = k = F_0 = 1$, so that for both cases

$$\kappa = \frac{c}{2\sqrt{km}} = 0.5 \quad \text{that is, we have an underdamped system.}$$

- The roots are $s_{1,2} = a \pm bi$, where

$$a = -\frac{c}{2m} = -0.5\ \text{s}^{-1} \equiv \tau^{-1}$$

$$\text{and} \quad b = \frac{\sqrt{4mk - c^2}}{2m} = \frac{\sqrt{3}}{2} = 0.866\ \text{rad/s} \equiv \omega_N$$

- Case I ($\omega_1 = 1$):
  Thus, in comparison with Equation 8.42:

$$x(t) = e^{-0.5t}[0.5774\sin(0.866t) + \cos(0.866t)] - \cos t \tag{E.8.8.1}$$

*Note:* With $\tau = \frac{1}{a} = -2$, $\left. e^{-\frac{t}{2}} \right|_{t=8} \approx 0$, and hence, the "steady-state" response is

$$x_{ss}(t) = -\cos t \tag{E.8.8.2}$$

- Case II ($\omega_2 = 2$):
  Again in comparison with Equation 8.42:

$$x(t) = 0.0769\left\{e^{-0.5t}\left[8.0829\sin(0.866t) + 2\cos(0.866t)\right]\right.$$
$$\left. -\left[3\sin 2t + 2\cos 2t\right]\right\} \tag{E.8.8.3}$$

*Graph 4:*

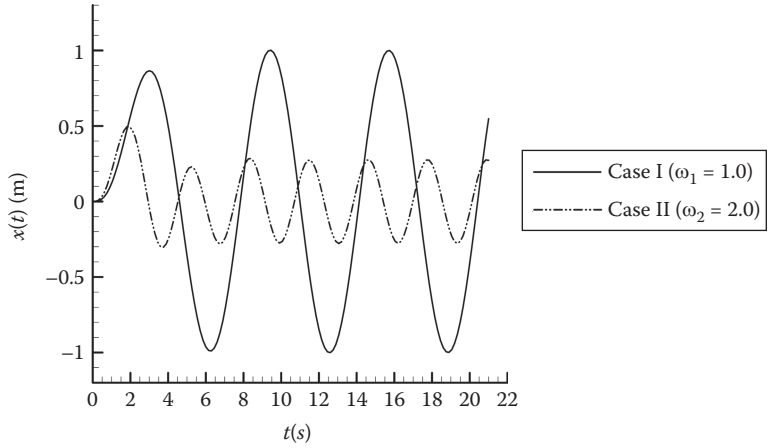


*Comments:*

- Case I (i.e., $\omega_1 = 1$) with forcing function sin(*t*): The forced oscillation is damped during $0 \le t \le 8$ s; then, Equation E.8.8.2, that is, the "steady" oscillations, takes over.
- Case II (i.e., $\omega_2 = 2$) with forcing function sin(2t): At the higher frequency, the initial "overshoot" is damped, and then at $t \approx 6$ s, $x_{ss}(t) = 0.0769(-3 \sin 2t - 2 \cos 2t)$ prevails.

## 8.5 Homework Assignments

The following questions and assigned tasks, all directly relating to the text, should enhance the reader's knowledge base and skill level.

8.1 Why are Couette-flow and lubrication systems, despite having moving surfaces, categorized as *static* FSI cases?

8.2 Prove that $\sigma_{ij} = \sigma_{ji}$, that is, $\vec{\vec{\sigma}}$ being a symmetric tensor (see Section 8.2.1 and Appendix AI.1.2).

8.3 Show how to transform Equation 8.1a for $\sigma_{ij} = \sigma_{ji}$ to Equation 8.1b, and express $\sigma_1$ to $\sigma_3$ in Equation 8.1c.

8.4 Derive Equation 8.2, and discuss its usefulness.

8.5 Provide a fluid dynamics application (i.e., sketch, physics, and math model) that would cause the scenario/result of Example 8.1.

8.6 Provide a fluid dynamics application (i.e., sketch, physics, and math model) that would cause the scenario/result of Example 8.2.

8.7 Relate Equations 8.3 and 8.4, as well as Equation 8.6, to fluid mechanics.

8.8 Derive Equation 8.12a through c, and discuss how they relate to (similar) fluid flow equations.

8.9 Following the introduction to Section 8.3 as a guide, research "structure vibration" with applications from the macro-scale, for example, visible effects, to the nano-scale, explaining slender-body cracks, break-up, and destruction.

8.10 Sketch, derive, and discuss the Kelvin model for visco-elastic material behavior. Graph $F(t)$, $u(t)$, and $F(u)$.

8.11 Describe the causes of elastic tube oscillation as validated in Figure 8.5c. What happens when the inlet velocity $v$ = constant?

8.12 The period ($P$) of vibration of a beam is a function of its length ($L$), moment of inertia ($I$), elasticity ($E$), Poisson ratio $\sigma$, and density $\rho$. Find via inspection the Pi-parameters where the dimensionless $\sigma$ already is a dimensionless group (DG). Express your results in terms of (elascity) × (inetia), that is, the EI-product.

8.13 Derive Equation 8.22 as well as Equation 8.23a, b.

8.14 Derive Equation 8.26, and discuss the system parameters $\kappa$ and $\omega_N$. Provide an FSI example that illustrates $c$, $\kappa$ and $\omega_N$.

8.15 Discuss Equations 8.28a, b and 8.29a, b with FSI examples.

8.16 Redo Example 8.8 with higher damping, that is, $c = 1.5$.

8.17 The natural frequency $f$ of vibration of a mass $m$ attached to a vertical rod (length L and stiffness EI) depends only on $m$, $L$, and EI.

(i) Determine the constant Pi-group.

(ii) Given $m = 2$ kg and for steel $E = 2 \times 10^{11}$ Pa, $L = 40$ cm, and $D = 12$ mm as well as a measured $f = 0.9$ Hz, find the frequency for $m = 1$ kg attached to an aluminum rod ($E = 7.4 \times 10^{10}$ Pa) of the same $D$ and $L$.

8.18 A 4 mm car-antenna vibrates strongly at 8 Hz while the car travels at 45 mph over an uneven road, which can be approximated as a sine-wave of amplitude 2 cm and wavelength 2.5 m. So, either vortex shedding due to the wind or the forced road-frequency causes the antenna vibration. Recalling that the Strouhal $\# = fd/v \approx 0.2$ for a wide range of Reynolds numbers (i.e., $2 \times 10^2$ to $2 \times 10^5$), determine the cause of vibration.

# 9

# *Computational Fluid Dynamics Modeling and Simulation*

## 9.1 Introduction

The laws of physics describe all natural and anthropogenic occurrences, ranging from post-Big-Bang phenomena to transport and conversion processes in fluid dynamics, mechanics, biology, chemistry, brain-functions, and much more. In the broader field of modern fluid dynamics, math modeling describes transport phenomena based on the conservation laws, while computer programs solve the related partial differential equations (PDEs) to simulate, say, fluid flow, convective heat transfer, fluid-particle dynamics, and fluid–structure interaction (FSI). So far, the conservation laws in the form of such PDEs have been reduced to ODEs for analytic or approximate solutions in specific problem areas (see Chapters 2–8 and AppendixI). Now, to obtain more realistic solutions to actual transport phenomena, the PDEs for mass, momentum, and energy transfer have to be solved numerically, subject to appropriate initial and boundary conditions. Computational fluid dynamics (CFD) is a technique in which PDEs are replaced by a system of algebraic equations that can be solved using computers. The resulting CFD software, which runs on engineering workstations or supercomputers, can be licensed, or free open-source software can be downloaded for problem adaptation (see Table 9.1). With CFD-simulation results, *distributed* fluid flow, particle trajectory, and convection heat transfer quantities, such as the velocity, pressure, position, and temperature, can all be analyzed in time and space. The derivations or integrations of these results then yield stresses and fluxes or flow rates and forces. CFD methods are well documented in Versteeg and Malalasekera (1996), Ferziger and Peric (2002), Tu et al. (2008), Zikanov (2010), Pletcher and Tannehill (2011), and White (2016), to name a few. They are routinely applied to gain new physical insight and to improve engineering system design and hence, performance. Nowadays in aircraft, automobile, and machine-part design, CFD simulations have replaced wind-tunnel or other experimental tests, relying often on either general-purpose or problem-specific commercial CFD-software tools. Such software has to run efficiently on suitable computer platforms, considering important aspects such as parallel processing, overall computer-run time, and numerical accuracy. It is needless to mention that experimental analysis will remain important for obtaining new discoveries, verifying theories, and validating computer models. Salient features of any math model with CFD simulation are depicted in Figure 9.1, where next to "results", in-depth problem formulation is most important. Especially for modern *multi-scale problems*, the spatial and temporal scales involved have to be considered (Figure 9.2). An example of multi-scale geometric structure would be fluid flow in a microchannel with nano-scale wall-roughness, as appears in micro-electromechanical systems (MEMS) and laboratory on a chip (LoC) devices.

**TABLE 9.1**

Popular General-Purpose Navier–Stokes Equation Solvers

| N-S Equation Solver | Discretization Scheme | Provider | Pros | Cons |
|---|---|---|---|---|
| CFX | Element-based finite volume method | ANSYS, Inc. | • Robust in convergence<br>• Better tolerance on grid quality<br>• Easy to define parameters and functions for advanced modeling<br>• Multiphase flow modeling | • Limited ability in multi-physics coupling<br>• High memory cost in transient simulations |
| Fluent | Finite volume method | ANSYS, Inc. | • Flexible in adding user-defined functions<br>• Solution accuracy<br>• Dedicated to CFD modeling with built-in advanced features<br>• Good online forum resource | • Limited ability in multi-physics coupling<br>• Difficult in setting up fluid–structure interaction simulations |
| COMSOL multiphysics | Finite element method | COMSOL, Inc. | • Easy coupling for multi-physics simulations<br>• Great flexibility, easy to define/modify equations<br>• User-friendly graphic interface<br>• Link with external tools such as SolidWorks, MatLab®<br>• Comprehensive tutorial | • Limited grid generation capabilities<br>• Limited performance in complex and multiphase CFD problems<br>• Computational efficiency<br>• Limited run-time control<br>• High licensing fees |
| STAR-CCM+ | Finite volume method | CD-adapco | • Robust and easy meshing<br>• Solution accuracy<br>• Powerful in turbomachinery simulation | • Computational cost<br>• User-friendliness |
| OpenFOAM | Finite volume method | Open source | • Free of charge and direct portability<br>• Flexible in modifying code for problem-specific simulations<br>• Good online forum support | • No graphic user interface (GUI)<br>• Steep learning curve<br>• Meshing and post-processing<br>• Solution stability and accuracy |

Before undertaking any mathematical modeling and subsequent CFD work for flow-system simulation, three basic questions have to be answered for each new engineering problem:

- Are sufficient project/system information and data sets for input and validation available, so that all important problem aspects are fully recognized, and the modeling objectives can be achieved (see Figure 9.1)?

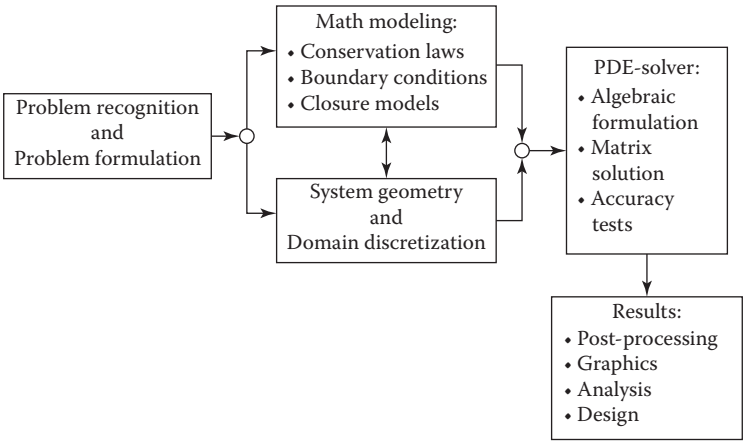


**FIGURE 9.1**
Key elements of math modeling and computer simulation.

- In the age of multi-scale modeling and computation of complex transport phenomena, can the most suitable solution method and fast computers be identified in light of the project-specific space-time scales (see Figure 9.2)?
- Is it cost-effective and manageable to develop an accurate and predictive computer simulation model (or license commercial CFD software), which leads toward useful discoveries and practical applications (see Figure 9.1)?

The next sections deal with major aspects of mathematical modeling and computer simulations of engineering transport phenomena (Section 9.2) as well as examples of computer simulations in modern fluid dynamics (Section 9.3).

## 9.2 Modeling Objectives and Numerical Tools

As already alluded to in Part A, math modeling objectives include an understanding of the system-specific transport phenomena and the ability to improve the design/function of a flow system or device. To achieve these goals, powerful, flexible, and accurate numerical tools, that is, *CFD software*, in conjunction with fast, large-memory, multi-processor *computer hardware* are necessary. Figure 9.1 provides the sequential steps from the given problem to its solution for any CFD technique after considering the best modeling approach as indicated in Figure 9.2. Selecting the continuum mechanics approach, Figure 9.3 depicts the development phases of a numerical model to execute CFD simulations with the goals of new physical insight and possible device improvement.

The implications of the content of each of the four development phases depicted in Figure 9.3 are discussed next.

### 9.2.1 Problem Recognition and Modeling Scale

To diagnose the cause of a problem correctly is especially challenging in the industrial environment when the system at hand is large and/or complex. For example, what is the cause of the periodic noise in a pipe network: component vibration due to sudden

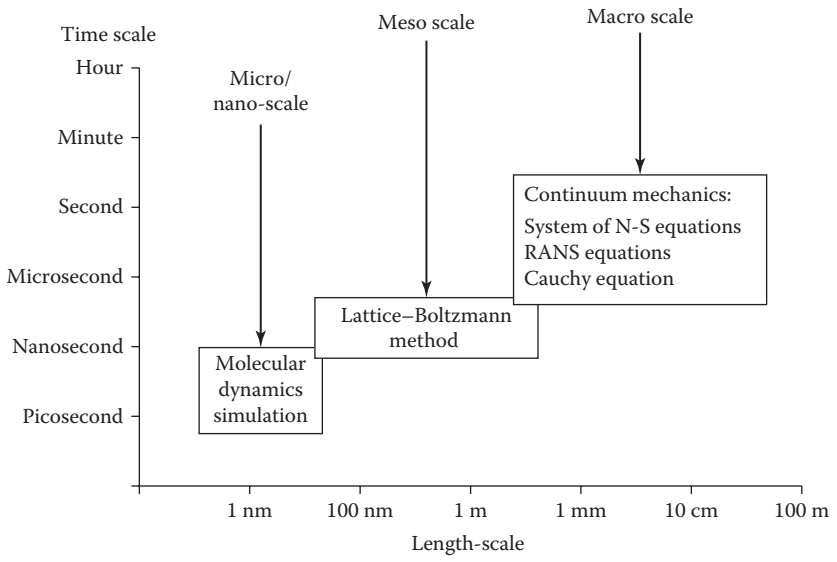


**FIGURE 9.2**
Modeling/simulation approaches for different spatial and temporal scales.

transient flow (also known as *water hammer*) or turbulent flow? What is the cause of malfunction of an electronic device: a local "hot spot" temperature exceeding a thermal material tolerance? Why did a medical stent implant break: fatigue micro-cracks caused by pulsatile fluid-pressure loads? What is the cause of excessive local particle deposition in a pipe network: a flow recirculation zone right after a sudden pipe expansion? Once the nature of a problem is known, the type and characteristics of a system can be identified. As a follow-up to these four sample problems, the CFD-system categories would

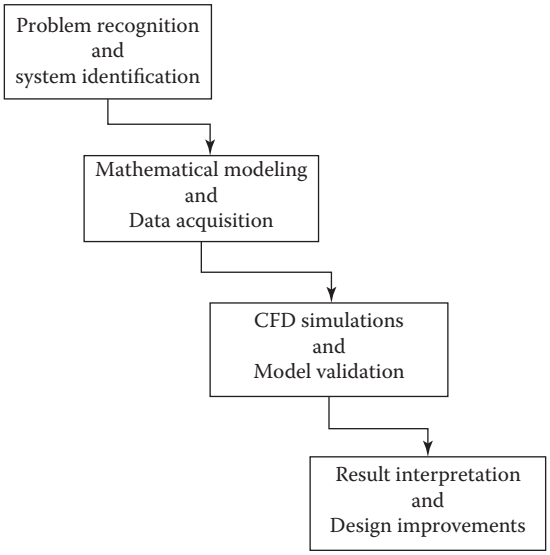


**FIGURE 9.3**
Theoretical and computational modeling steps.

be transient turbulent flow, convection-conduction heat transfer, FSI, and fluid-particle dynamics, respectively.

Throughout the text, it is assumed that the continuum mechanics hypothesis is valid; hence, (reduced) forms of the system of Navier–Stokes (N-S) equations describe almost all scales of fluid flow phenomena (see Section 1.1). However, at very small scales, fluids are subject to interfacial phenomena (e.g., wall-roughness, hydrophobic fluid–solid behavior, and charged surfaces), which significantly affect the main portion of the flow field in MEMS, LoCs, microchannel heat sinks, and nano-electronic devices. So, to achieve solutions to certain multi-scale problems, a *hybrid molecular-continuum simulation* approach is necessary (see Figure 9.2). It combines computer resources–intensive molecular dynamics (MD) simulations with conventional continuum mechanics analyses based on the N-S equations; thus, coupled MD and N-S solvers exchange information. Less expensive, but also with lower resolution, are *meso-scale models* (e.g., based on the lattice-Boltzmann equation), which comprise a single solver.

### 9.2.2 Mathematical Modeling and Data Needs

Models may be classified as

- Verbal, that is, a theory or concept
- Physical, for example, a laboratory set-up or electric analog
- Mathematical/computational, which could be deterministic analytical or numerical, stochastic, empirical, molecular discrete, multi-scale, or problem specific; where the last one is the common model identifier

Thus, a physical or mathematical model represents a real process or several transport phenomena. After math model completion, the descriptive equations are then discretized following a specific numerical scheme, for example, the finite difference, control volume, or finite element method. This is documented in the form of a numerical program, which is then executed on a computer to generate simulation results.

To construct a model, data sets have to be made available concerning the given system's geometry and hence, dimensionality, initial (if transient) and boundary (or operational) conditions, fluid properties, and necessary closure models in the case of turbulent flow, heat and mass transfer, fluid-structure-interaction (FSI), and/or fluid-particle dynamics. Typically, the system's geometry plus the simulation-input conditions largely determine the results. In addition, an independent set of reliable experimental and/or benchmark numerical data is needed for computer model validation.

### 9.2.3 Computational Fluid Dynamics

The first and very important step for geometrically complex systems is generating a grid (or mesh) that defines cells (or control volumes). For such two-dimensional (2-D) or three-dimensional (3-D) cells, all dependent variables (e.g., velocity, pressure, temperature, and/or species concentration) are computed throughout the system domain. Computational meshes are either *structured*, where the domain is discretized into large blocks made up of cells, or *unstructured*, where more variable cells directly accommodate complex geometric domains (see Figure 9.4). Simply put, a mesh that fills the flow region, bounded by walls or free surfaces, is the underlying grid for the discrete representation of the governing equations, typically PDEs. Mesh refinements are necessary until the results, typically in terms of velocity profiles, are independent of the cell density.

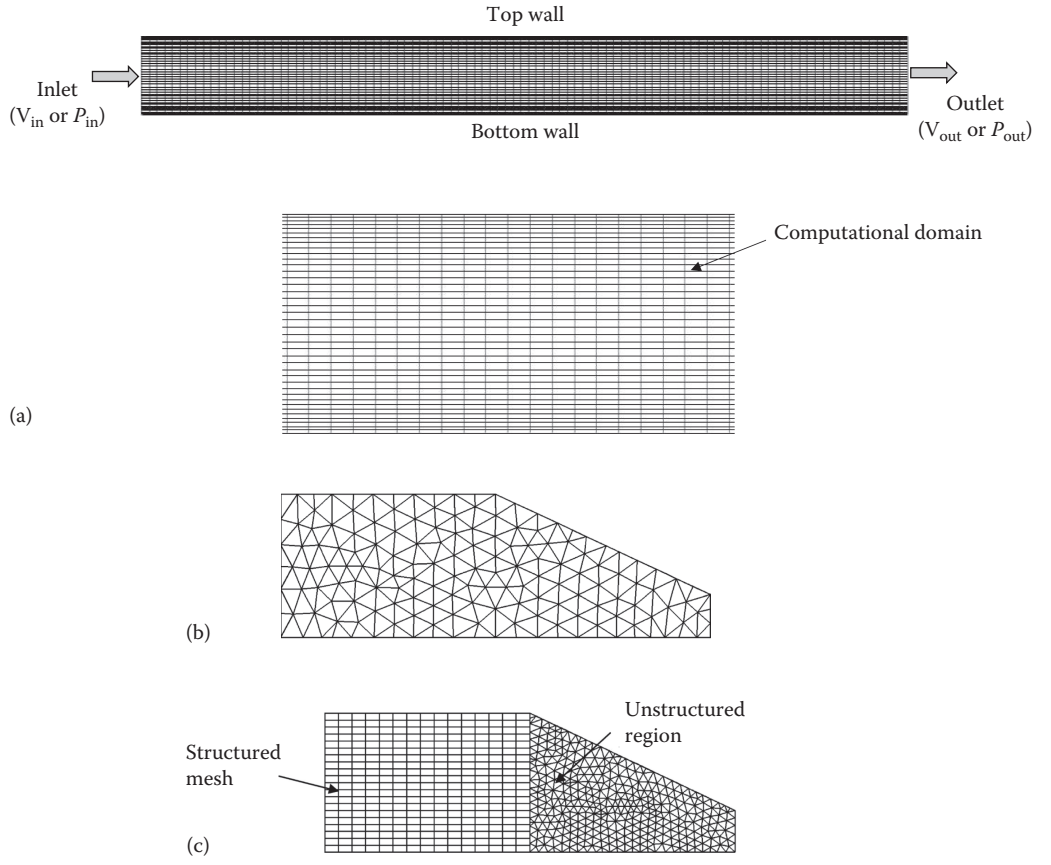


**FIGURE 9.4**
Types of 2-D meshes. (a) Structured quadrilateral mesh. (b) Unstructured triangular mesh. (c) Hybrid mesh. Notes: To (b): triangles of different sizes accommodate more easily complex domains; identifiable grid lines discretize the computational domain; cell (in 3-D) has volume ∀ and surface S. To (c): structured cell blocks are combined with a triangular grid in the more complex region or near walls.

Boundary conditions are specified on each edge of the 2-D system or on each face of the 3-D domain. Values of material properties (e.g., fluid density and viscosity and/or Young's modulus and Poisson ratio) and submodels in the case of turbulent flow or particle suspension flows have to be given as well.

Starting with initial guesses for all dependent variables, the discretized forms of the governing equations are solved interactively, usually at each cell center. Various numerical methods (e.g., finite difference, finite volume, finite element) are available to discretize the system operations, typically coupled PDEs (see Chapter 2), into a set of algebraic equations. A suitable matrix solution algorithm and associated convergence parameters are then activated to obtain the solution. Clearly, a numerical solution is reached when, after hundreds (or thousands) of *iterations*, the mass and momentum residuals have decreased to, say, $10^{-4}$ or less.

#### *9.2.3.1 Simulation Accuracy*

Computer model validation has a numerical part and a comparison part. Numerical validation includes a refined mesh, so that the results are just independent of the mesh density,

where mass and momentum residuals should be less than $10^{-6}$, or at least $10^{-4}$. The comparison part involves matching of simulation results with exact (analytical) solutions and/or benchmark experimental data sets. If there is no confidence in the accuracy (and realism) of the simulation results, there is no reason to talk/write about predictive model capability, new physical insight, or quantitative data for system/device improvement. In this context, the article by Roache (2009) on computer model validation versus numerical code verification is of interest.

Computer simulation results are never exact, usually for four reasons:

- Incomplete mathematical description
- Simplified geometry
- Incomplete flow data
- Numerical errors

Potentially, the most severe error sources are shortcomings in modeling when the physics of complex transport phenomena or property functions are mathematically not fully described. This may very well be the case when modeling turbulence, multiphase reactive flows, and FSIs. Input data as well as critical and/or boundary conditions can be erroneous when the system geometry inlet/outlet flows and fluid properties are only assumed and not measured for realistic scenarios. Intrinsic to all numerical methods is the discretization error, which depends mainly on the degree of flow domain resolution with a fine mesh as well as the type and accuracy of the numerical method employed.

Obviously, the finer the mesh, the better the representation of the system geometry and the local flow field. Indicative of a mesh (or grid) is the grid spacing $h$, that is, the characteristic length scale of a 2-D or 3-D mesh element or cell. In fact, the order of numerical code accuracy is directly related to the power of $h$. Most numerical algorithms are second-order approximations of the governing equations. For convergence of explicit time-integration schemes, the grid-size and time-step are coupled via the Courant number, $C = \Delta t \Sigma (u/h)_i < C_{\max} = 1$, where $i = 1, 2, 3$.

As mentioned, there are basically structured and unstructured meshes (Thompson et al. 1999; Durbin and Medic, 2007, among others). Structured meshes feature identifiable grid lines, which can be numbered sequentially, say, in 3-D: $i, j, k$, forming grid points $x(i, j, k)$, $y(i, j, k)$, and $z(i, j, k)$. Cells (or elements) of structured grids may be quite distorted when geometrically complex flow domains are meshed, that is, discretized. However, straight wall geometries can be easily accommodated, and boundary conditions can be readily enforced. In contrast, unstructured meshes, typically triangles for 2-D and tetrahedral elements for 3-D flow domains, map faithfully any physical space to the computational space (see Figure 9.4).

#### *9.2.3.2 Equation Discretization*

Along with flow domain discretization, that is, meshing, it is required to discretize the governing equations, typically the N-S equations, subject to given initial/boundary conditions. Most codes use the finite (or control) volume method (FVM), as indicated in Table 9.1, employing either structured grids or unstructured meshes. The mesh decomposes the fluid flow domain into connected cells. The flow variables are assigned to each cell; typically, velocity and pressure are stored at the center of each cell, that is, the

individual control volume. Specifically, integral forms of the conservation equations (see the Reynolds Transport Theorem [RTT] in Section 2.1) are solved via an iteration method of successive approximations (see Durbin and Medic, 2007, among others). For example, the linear momentum equation integrated over a cell (see Figure 9.4) of "control volume" $\forall$ with the "control surface" S and individual (inter)faces reads:

$$\frac{\partial}{\partial t}\left(\forall \rho \vec{\mathbf{v}}\right)_{\text{cell}} = -\sum_{f_i}\left(\rho \vec{\mathbf{v}}\vec{\mathbf{v}} \cdot \hat{n}S\right)_i - \sum_{f_i}\left(p\hat{n}S\right)_i + \sum_{f_i}\left(\mu \nabla \vec{\mathbf{v}} \cdot \hat{n}S\right)_i \tag{9.1}$$

The left-hand side (LHS) is the time-rate-of-change of momentum inside the cell (i.e., control volume) due to net momentum efflux across the cell (inter)faces $f_i$ as well as all the pressure and viscous forces acting on the cell faces $f_i$. Clearly, the equations of each cell are coupled with all neighboring cells, because the interface values needed are interpolated between the cell centers, and so is the velocity gradient in the viscous force term generated with adjacent center velocity values. Furthermore, the local time derivative (see LHS. of Equation 9.1) is also replaced by a second-order (Euler) approximation. Discretization of the nonlinear convection term, $\rho\vec{\mathbf{v}}\vec{\mathbf{v}}$, is most crucial, requiring usually second-order (or higher) up-winding, such as the numerical QUICK scheme (see Patankar, 1980 or Hoffman 2001).

Focusing on numerical solutions of fluid dynamics problems, general-purpose software codes, known as *Navier–Stokes equation solvers*, are either commercial or open-source. Table 9.1 summarizes the features of the *most popular* commercial as well as open-source CFD codes.

#### *9.2.3.3 Boundary Conditions*

The most common boundary conditions are prescribed velocity inlet, no velocity-slip on walls, and zero-gage pressure outlet conditions (see Figure 9.4a). Alternatively, the inlet pressure is prescribed, and a zero-velocity gradient, that is, via a long exit conduit, is assumed at the extended outlet, implying fully developed flow. Across a line/plane of symmetry, the gradients of all field variables are zero. For systems with repetitive geometries, such as turbine blades or heat exchanger tubes, periodic boundary conditions are imposed.

Mathematically, parabolic PDEs, for example, Prandtl's boundary-layer equation, have solutions that march forward toward the open end, guided by the wall or edge boundary conditions. In contrast, for elliptic PDEs, for example, the Laplace heat conduction equation, the domain-surrounding boundary conditions greatly determine the solution. *If the magnitude of any field variable on a boundary (or inlet/outlet) is assigned, it is called a* Dirichlet condition, *while if enforcing the gradient of a dependent variable, it is labeled a* Neumann condition *(or* Neumann problem*).*

### 9.2.4 Result Interpretation and Data Management Plan

Smartly depicting and then interpreting results from predictive (i.e., realistic and accurate) computer simulations is the final step. As part of post-processing, functional forms of dependent versus independent variables (or dimensionless groups) are graphed in figures, or flow fields are visualized via videos, for physical insight report/manuscript writing and conference presentation. Specifically, to gain new physical insight and for useful applications, it is important that the flood of data sets is turned into smart 2-D or 3-D

color figures (see Section 9.3). Useful plotting software includes Tecplot, ParaView, Ensight, and FieldView, as well as built-in post-processing tools in CFD-equation solvers such as Fluent-Post (ANSYS) or Post-processing (COMSOL). Clearly, after successful computer simulations and result graphing, a comprehensive research report should be written, which is the point of departure for conference papers, journal articles, theses, and dissertations (see Chapter 10). In summary, result interpretation is the scientific part of a research project, while result application as part of, say, device/process improvement or new design is the engineering part (see Section 9.2.5).

In this computer age, engineers and scientists have to cope with floods of data (even mega-data) sets, which for proper management and dissemination, require an efficient and effective plan, known as the *data management plan* (DMP). Federal funding agencies (e.g., the National Science Foundation, Department of Defense), companies (e.g., IBM, Microsoft), and universities (e.g., Massachusetts Institute of Technology, University of California San Diego) have developed extensive guidelines, examples, and associated software to generate personalized DMPs.

#### *9.2.4.1 Data Management Plan*

All aspects of the DMP have to be addressed for the computational results generated at home computer labs or centers and displayed in accordance with project-sponsored funding agencies.

1. Types of data, samples, and other materials to be produced in the course of the project

   Gigabytes of computer simulation data will be generated when applied to the problem solutions. Figures, graphs, and correlations will be produced, and the fundamental and applied research results will be published in archival journals and in book chapters and presented at conferences. New numerical algorithms will be coded in C++ for the extension and improvement of the OpenFOAM engineering software and made available to the public.

2. Standards to be used for data and metadata format and content

   All computer-generated data are in digital form and securely stored and safely networked between all project participants.

3. Methods and policies for providing access and enabling sharing

   There is no disaster recovery plan required, because all data used and generated are in digital form, and there is no sensitive information, such as human subjects concerns. Also, all data will be stored in a computer that is securely networked. All data will be transferred within a secure virtual network between all collaborators. The data generated from computational modeling and simulation studies are for publications, including conference presentations, journal articles, and book chapters. The intellectual property and copyrights are owned by the home university.

4. Provisions for re-use, re-distribution, and the production of derivatives

   There is no limitation on the data requestor's ability to re-use or re-distribute the data or materials. However, any person who downloads the data will be required to read an agreement by which it is understood that the data may only be used for nonprofit problem-solution or instructional purposes.

5. Methods for archiving and preserving access to data and materials

   After data publication in the form of conference presentations, journal articles, book chapters, and numerical codes, the data will be shown on the university website. Also, the programs, user's manual, and tutorials for setting up and running OpenFOAM software will be uploaded on university and sponsor websites and hence, made available free-of-charge.

### 9.2.5 Computational Design Aspects

After gaining sufficient physical insight into the mechanics of fluid flow, convection heat transfer, fluid-particle dynamics, and/or FSIs, the next major task is new (or improved) engineering system design. This is accomplished via *virtual prototyping*, that is, on the computer rather than in the laboratory or wind tunnel, where *scaled* physical models would have to be employed. The flow chart in Figure 9.5 lists the major steps from innovative idea (via computer simulation and lab testing) to prototype commercialization.

Clearly, some of the activities and tasks can be executed in parallel. Typically, the university functions as a major supporter concerning the protection of intellectual property rights, financial research support, and contacts with industry for licensing and commercialization. In any case, "Theoretical Proof-of-Concept" and "Numerical System Design" are of major interest within modern fluid dynamics.

#### *9.2.5.1 Computer Simulations*

In general, validated computer simulations and computational design analysis assist in evaluating the performance of a system described by a set of extensions and/or differences in geometric design, material properties, thermodynamic loads, and operational requirements. *Typically, best system geometry and optimal operational conditions are the key design goals.* A well-planned *parametric sensitivity analysis* (PSA), for example, varying the values of input parameters or even boundary conditions, may generate results that describe a flow system's behavior within realistic bounds. PSA can be either deterministic or probabilistic. In the deterministic case, all parameters change continuously within the expected design/operational space, resulting in continuous responses, that is, actual system performance. However, quite often, device dimensions and positioning, material properties, and loads are not deterministic parameters, which poses the question of "design robustness." Again, computational analysis can swiftly assess how significant fluctuations in system parameter values may influence the design performance, including potential device failure.

In summary, for device/system improvement, first, the transport phenomena have to be fully understood via CFD analysis; that is, geometric and operational changes can be tested via computer experiments. Examples include automobile or aircraft design for drag reduction and/or (downward) lift modification, heat exchangers with improved mixing and reduced size/weight, fuel-injection systems generating higher combustion efficiencies, bio-MEMS for targeted drug delivery, medical implants to improve the quality of life, green-energy converters of high efficiency and reliability, and so on.

#### *9.2.5.2 Computer-Aided Design*

Historically, computer-aided design (CAD) software emerged in response to the needs of architects as well as urban and industrial complex planners. Fluid dynamics–related CAD applications focusing on optimal design in terms of system shape and function,

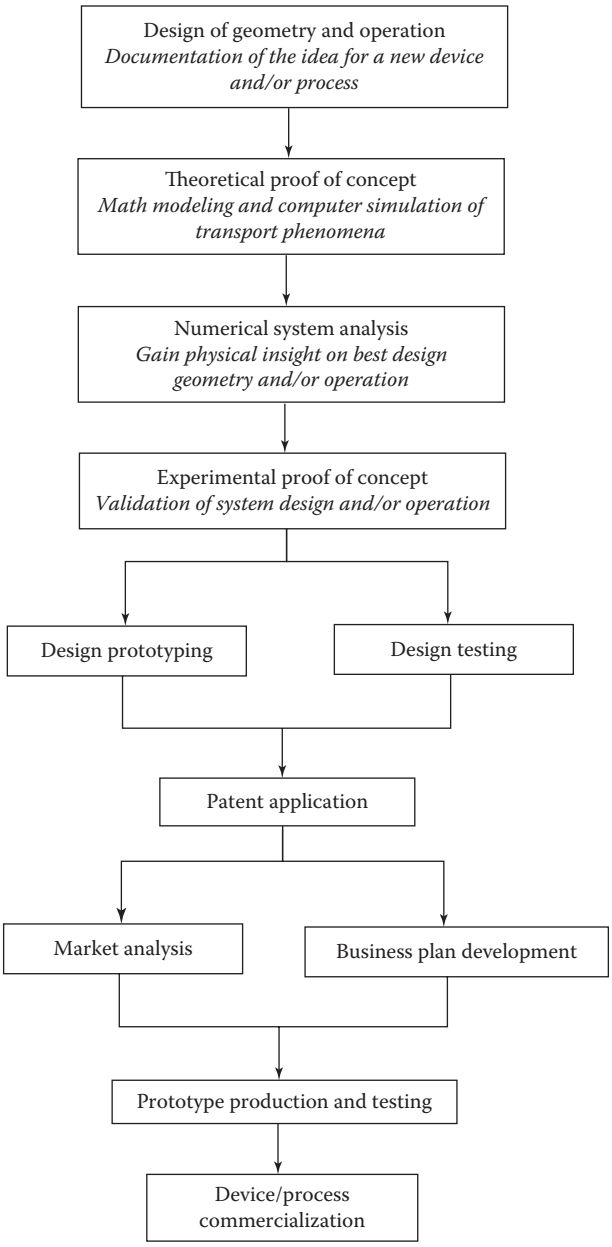


**FIGURE 9.5**
Aspects of engineering system design and prototyping.

that is, *best geometric and operational features*, range from automotive and aerospace vehicles to heat exchangers and microfluidics systems. Two of the author's research projects may serve as illustrative examples. A patented methodology for *direct drug delivery* from a particle-release point to a diseased site has led to new designs of both a smart inhaler system and a smart micro-catheter. First, the underlying idea of direct lung- or liver-tumor targeting was tested via computer simulations of controlled fluid-particle

streams on a patient-specific basis (see Kleinstreuer and Zhang 2003; Kleinstreuer et al., 2008a,b, 2014; Kleinstreuer 2015). Then, the best operational conditions for device improvement were computed and analyzed (see Xu et al. 2016; Kolanjiyil et al. 2016). Another example is uniform nanoparticle transport and mixing for micro-cooling devices or nanomedicine systems (see Kleinstreuer et al., 2008a, b; Kleinstreuer et al., 2014). Still, for inventions to be acceptable, laboratory proof-of-concept has to follow any convincing computer simulation result (see Richards et al. 2012), while for medical devices clinical outcome is the ultimate litmus test.

## 9.3 Computer Simulation Examples

The previous sections mentioned the importance of *validation studies* prior to a detailed computational analysis of a system. Computer model validation can be achieved via detailed comparisons with an analytic solution, considering a simplified version of the computer model, or reliable experimental data sets, or benchmark numerical results, for example, from direct numerical simulations (Section 9.3.1). Establishing an acceptable match between the output of the computer model and reliable data sets, typically the velocity field, gives confidence that the new model is indeed a predictive tool for engineering analysis.

The remaining sections deal with additional examples of computer model validation as well as sample case studies of internal flow and external flow (i.e., Sections 9.3.2 and 9.3.3).

### 9.3.1 Computer Model Validations

A straightforward way to validate the computer model is to directly compare the predicted velocity distribution with measured data. The latter can be obtained using such methods as particle image velocimetry, laser Doppler velocimetry, and hot-wire anemometry (see Tavoularis; among others). For example, Lieber and Zhao (1998) measured the instantaneous flow velocity distribution at different sites of a bifurcation geometry representative of physiological conditions of human airways. Figure 9.6 compares predictions of velocity profiles using CFX12 (Ansys, Canonsburg, PA) with the measurement at two locations of the geometry.

The computer simulation was transient, with a fully developed inlet velocity profile given as

$$u = U_{\max}\left(1 - \frac{z^2 + y^2}{R^2}\right)\sin(0.327t) \tag{9.2}$$

where:

$U_{\max}$ is the maximum flow velocity
$R$ is the radius of the parent tube
$y$ and $z$ are the coordinates with the origin positioned at the center of the inlet plane
$t$ is the time

Opening boundary condition was imposed at the outlets, and no-slip boundary conditions were assigned to the walls. The simulation was run from $t = 0$ s to $t = 19.2$ s with

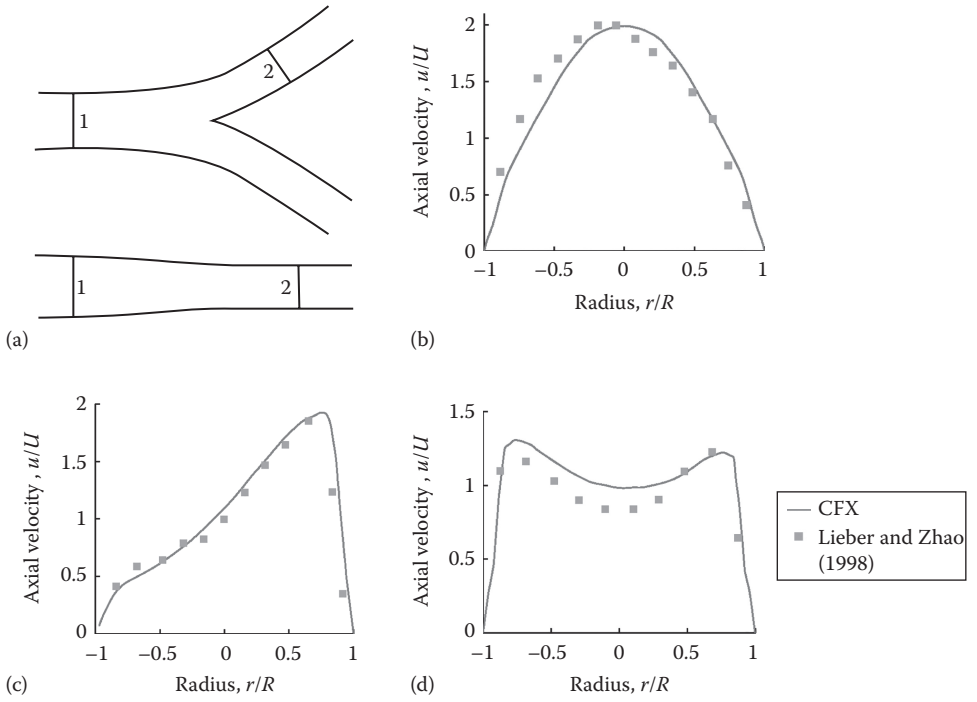


**FIGURE 9.6**
Comparison between computational and experimental flow velocity data at $Re_D = 1278$: (a) model geometry with location of velocity measurements; (b) Cross section 1 aligned with bifurcation plane; (c) Cross section 2 aligned with bifurcation plane; (d) Cross section 2 perpendicular to bifurcation plane.

a time step of 0.02 s. The comparison was performed at a moment when the instantaneous Reynolds number was 1278. Overall, Figure 9.6 indicates that good comparisons were achieved between model predictions and measurements. Specifically, Figure 9.6b shows a near-parabolic inlet profile at Station 1, known from Poiseuille flow in straight tubes. At Station 2, viewed in the bifurcation plane, the velocity profile is highly skewed due to the inertia effect forming a boundary-layer along the inner wall of the daughter tube (see Figure 9.6c). Still at Station 2 but from a 90°-shifted angle, Figure 9.6d depicts an M-shaped velocity profile; again, because of 3-D boundary-layer formation. An additional check relates to "mass conservation"; that is, the integral over the velocity profiles at any cross sectional plane should be the same; clearly, the mass flow rate results in Figure 9.6d for experimental versus numerical profile-integration differ a little.

Turning to an example in fluid-particle dynamics, multiple experiments have been conducted on particle deposition in a symmetric double-bifurcation geometry. Thus, comparisons between the computationally predicted deposition efficiencies and experimental results are a common validation study. The computational procedure normally uses nondimensional parameters such as the Reynolds number and Stokes number to develop a simulation model that mimics the experimental conditions. For example, Figure 9.7 compares predictions of the commercial finite volume solver CFX11 (Ansys, Canonsburg, PA) of particle depositions in a double bifurcation with the experimental analysis of Kim and Fisher (1999).

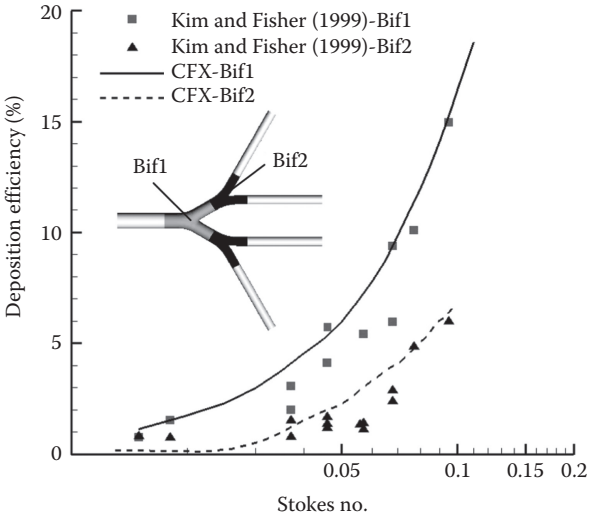


**FIGURE 9.7**
Comparison between computational and experimental particle-deposition data.

The computational simulations were conducted with varying particle diameters and at a constant Reynolds number (i.e., 3.1 μm $\leq d_p \leq$ 8.4 μm and Re = 1200) to match the experimental Stokes numbers $St = \dfrac{\rho_p d_p^2 U_0}{18\mu D}$ where:

- $D$ is the inlet tube diameter
- $d_p$ is the particle diameter
- $\rho_p$ is the particle density
- $\mu$ is the fluid dynamics viscosity
- $U_0$ is the average velocity at the inlet defined by the definition of Reynolds number ($\text{Re}_D = U_0 D/v$) where $v$ is the fluid kinematic viscosity

The deposition efficiency ($DE = \#\ of\ deposited\ particles / \#\ of\ incoming\ particles$) results illustrate a good match with the experimental data using dimensionless parameters.

As expected, the first bifurcation region has higher DE values than the second one due to impaction. For both regions, the DE numbers increase exponentially with larger Stokes numbers.

A variation of the previous particle-deposition validation is the evaluation of the number of particles that exit the daughter branches of a bifurcation (see Figure 9.8a). For the case of a symmetric bifurcation with different daughter branch diameters, the proportion of particles exiting each branch for different flow ratios between the branches was measured by Bushi et al. (2005) in an attempt to model embolism trajectories through the human cardiovascular system. The exit percentages of neutrally buoyant solid particles of 0.6 mm diameter were obtained for a symmetric bifurcation where one daughter branch had the same diameter as the parent vessel, and the other daughter branch had a diameter of 2/3 of the parent vessel. Different ratios of flow ($Q_1/Q_2$) were established by varying the downstream resistance (i.e., outlet pressure) at the daughter branch outlets. Figure 9.8b illustrates the close match of the experimental and numerical data sets.

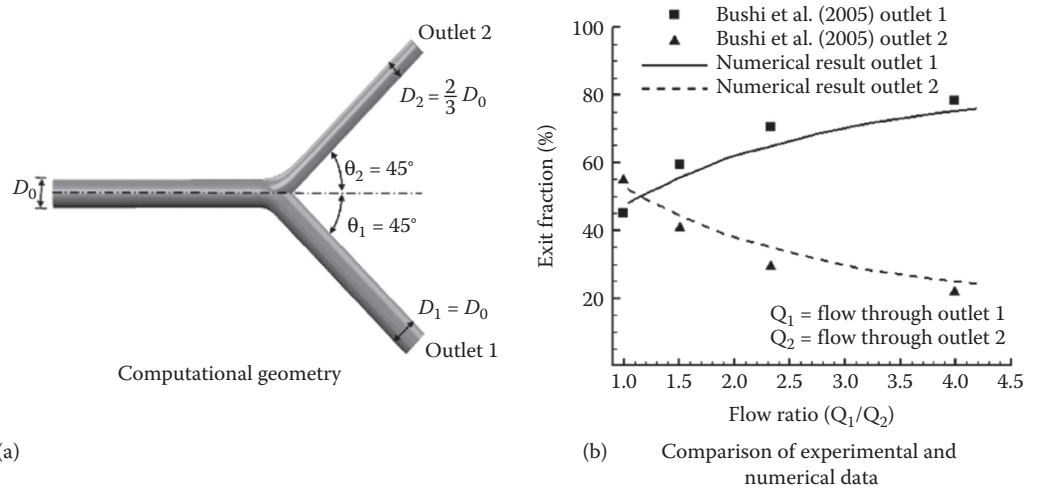


**FIGURE 9.8**
Comparison of numerical and experimental data concerning particle-exit percentages. (a) Computational geometry. (b) Comparison of experimental and numerical data.

With the smaller Outlet 2 posing a larger flow resistance, more particles exit Outlet 1 and in larger amounts as $Q_1/Q_2$ increases. In addition to validating the computational modeling methodology, the experimental comparison also provides vital information and experience in determining appropriate meshes that result in a stable solution that is independent of further mesh refinements.

### 9.3.2 Sample Case Studies

The computational case studies range from a basic comparison of internal Newtonian versus non-Newtonian fluid flow to an FSI example. Additional case studies are presented in Chapter 10, following the guidelines discussed in Section 10.2.

#### *9.3.2.1 Steady Laminar Newtonian versus Non-Newtonian Fluid Flows in a Constricted Tube*

##### *9.3.2.1.1 Introduction*

Laminar fluid flow in a locally constricted conduit has numerous natural and industrial applications. Examples include the Venturi tube, or fouling in pipes due to deposition of constituents in the fluid, and airway or blood-vessel restrictions in the human body. Selecting math modeling and simulation of pathological cardiovascular conditions (constrictions, stenoses, aneurysms, atherosclerosis, etc.) as an example, evaluating the resulting hemodynamics (flow of blood) continues to increase understanding of the various conditions and in turn, improve healthcare (Kleinstreuer, 2006, among others). One fundamental example is the transport properties of human blood. This report documents a fundamental investigation of three different models of human blood (Newtonian, Quemada, and a modified model proposed by De Gruttola et al., 2005) and their influence on the resulting hemodynamics of laminar flow separation and recirculation.

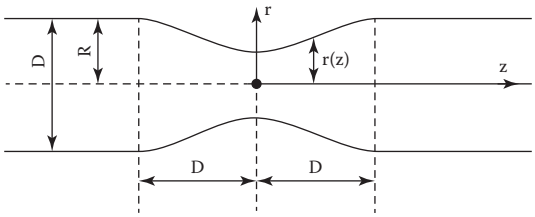


**FIGURE 9.9**
Computational domain used in this study.

A geometry containing a symmetric constriction of the vessel was used to determine the effects of blood viscosity models on flow separation and recirculation after the constriction. The constriction was modeled as a 75% area reduction in cardiovascular stenosis and matched the dimensions used in Zhang and Kleinstreuer (2003). Figure 9.9 provides a visual representation of the geometry and its corresponding dimensions.

The minimum point of the vessel radius is $R/2$, which occurs at the $z$-coordinate of zero. A structured grid was used for the 3-D mesh, implementing an "O-Grid" orientation and clustering several layers of elements near the walls to capture high gradients of flow. Mesh independence was ensured by testing the velocity profiles of multiple locations throughout the domain for meshes of different element densities (cf. Zhang and Kleinstreuer, 2003).

The governing equations for the analysis were the conservation of momentum and the constitutive viscosity law relating shear stress and apparent viscosity. Equation 9.3a and b list the conservation of momentum for an incompressible fluid with a non-accelerating control volume and no body forces along with the constitutive relation between viscosity and shear stress. Specifically,

$$\rho\left[\frac{\partial v_i}{\partial t}+v_j\frac{\partial v_i}{\partial x_j}\right]=-\frac{\partial p}{\partial x_i}+\frac{\partial \tau_{ij}}{\partial x_j} \tag{9.3a}$$

with

$$\tau_{ij}=\eta\left[\frac{\partial v_i}{\partial x_j}+\frac{\partial v_j}{\partial x_i}\right] \tag{9.3b}$$

where:

- $x_i$ are the three orthogonal coordinate directions
- $t$ represents time
- $\rho$ is the fluid domain density
- $v_i$ is the fluid velocity vector
- $p$ is the fluid pressure
- $\tau_{ij}$ is the fluid shear stress tensor
- $\eta$ is the apparent dynamic viscosity of the fluid

The domain is governed by the function

$$r(z)=\begin{cases}R-\dfrac{R}{2}\cos\left(\dfrac{\pi z}{2D}\right) & \text{if} \quad |z|\le D\\ R & \text{if} \quad |z|>D\end{cases} \tag{9.4}$$

where:

*R* is the non-constricted radius
*D* is the non-constricted diameter of the vessel

The computational domain has its origin at the center of the constricted portion of the vessel, a pre-constriction length of 7*D*, and a post-constriction length of 17*D*. At the inlet, a uniform velocity profile was applied, whereas a zero gauge pressure was used for the outlet condition. Three different models for the apparent viscosity of blood were used in this study. The first one is a Newtonian viscosity, which is approximated based on the experimental data of Merrill (1969); the second is the Quemada model with parameters given by Buchanan et al. (2000) that were fitted to the Merrill (1969) experimental data; and the third one is an exponential form presented by De Gruttola et al. (2005). The Newtonian model is just Equation 9.5a; the full Quemada model can be simplified to a modified Casson model, whose simplified form is shown in Equation 9.5b; and the DGBP model (after De Gruttola et al., 2005) is given with Equation 9.5c and d.

$$\eta = \mu_{\text{Newt}}$$

$$\eta = \eta_Q = \left( \sqrt{\eta_\infty} + \frac{\sqrt{\tau_0}}{\sqrt{\lambda} + \sqrt{\dot{\gamma}}} \right)^2$$

$$\eta \equiv \eta_{\text{DGBP}} = \mu_{\text{plasma}} \beta (1 - Ht) \exp\left( \frac{4.1 Ht}{1.64 - Ht} \right) \qquad \text{(9.5a through d)}$$

$$\beta = 1 + \frac{b}{\dot{\gamma}^n}$$

where:

$\dot{\gamma}$ is the shear rate of the fluid
*Ht* is the blood hematocrit

Table 9.2 lists the parameters and their corresponding values for each viscosity model (see Figure 9.10). An important note is that De Gruttola et al. (2005) listed the units of the curve-fitted parameter *b* as ($s^{-1}$). However, that is inconsistent with exponential units of the shear rate and has been adjusted in Table 9.2.

The other transport property of blood is the density. Both the Newtonian and Quemada models used a constant density of 1060 kg/$m^3$, while the DGBP model included an equation

**TABLE 9.2**

Parameters of the Different Viscosity Models

| | |
|---|---|
| Newtonian | $\mu_{\text{Newt}} = 0.0309 \left[ \frac{g}{m \cdot s} \right]$ |
| Quemada | $\eta_\infty = 0.02654 \left[ \frac{g}{m \cdot s} \right], \tau_0 = 0.04360 \left[ \frac{g}{m \cdot s^2} \right], \lambda = 0.02181 \left[ s^{-1} \right]$ |
| DGBP | $\mu_{\text{plasma}} = 0.014 \left[ \frac{g}{m \cdot s} \right]; Ht = 0.25, 0.45, 0.65; b = 6.0 \left[ s^{-0.75} \right]; n = 0.75$ |

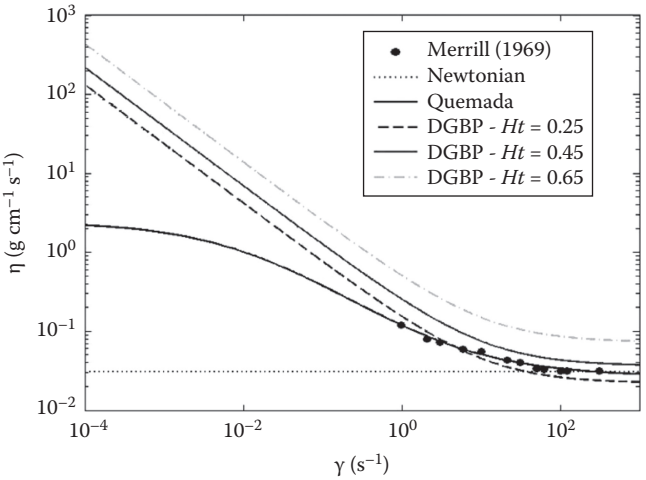


**FIGURE 9.10**
The different viscosity models versus shear rate.

for the density based on the *Ht* level and volume fractions of white blood cells (WBCs) and platelets. The DGBP density model is given as Equation 9.6, with parameter values listed in Table 9.2:

$$\rho_{DGBP} = \rho_{plasma}(1 - Ht) + \rho_{RBC} Ht + Vf_{WBC}\rho_{WBC} + Vf_{platelet}\rho_{platelet} \tag{9.6}$$

where:

$\rho_{plasma}$, $\rho_{RBC}$, $\rho_{WBC}$, and $\rho_{platelet}$ are the density of plasma, red blood cells (RBCs), WBCs, and platelets, respectively

$Vf_{WBC}$ and $Vf_{platelet}$ are the volume fraction of WBCs and platelets (Table 9.3)

Simulations of steady flow through the domain (see Figure 9.9) at different Reynolds numbers were conducted to analyze laminar flow separation and recirculation in regions downstream of the vessel constriction. Fluid flow was introduced at the inlet with a parabolic velocity profile, and inlet Reynolds numbers of 250, 500, and 750 were selected for the analysis. The range was based on physiological Re values in the carotid artery (a common location of stenoses), which has an approximate mean Re of 250 and a maximum Re of about 1100. Using the conservation of mass and volume flow rate, the Re value in the constriction can be calculated to be twice that of the upstream Re value for this geometry.

**TABLE 9.3**
Parameters of the DGBP Density Model

| | |
|---|---|
| $\rho_{plasma}$ | 1030 kg/m$^3$ |
| $\rho_{RBC}$ | 1096.5 kg/m$^3$ |
| $\rho_{WBC}$ | 1077.5 kg/m$^3$ |
| $\rho_{platelet}$ | 1040 kg/m$^3$ |
| *Ht* | 0.25, 0.45, 0.65 |
| $Vf_{WBC}$ | $6.8293 \times 10^{-3}$ |
| $Vf_{platelet}$ | $1.707 \times 10^{-4}$ |

Thus, the selected Re values ensured that the Re in the vessel constriction was well below 2000 for each Re specified at the inlet to avoid turbulent flow effects.

The commercial finite volume solver CFX11 (ANSYS Inc., Canonsburg, PA) was used to solve the governing and constitutive equations. A high-resolution advection scheme was specified for the solver, where simulations concluded when root mean square error residuals were less than $10^{-5}$. Simulations were run using a single Intel 3.59 GHz processor on a Dell Precision 670 workstation with 8 GB of RAM. Run times varied between 13 min (for the Newtonian Re = 250 case) to 1.5 h (for the Re = 750 cases).

*9.3.2.1.2 Apparent Viscosity*

The viscosity models were first plotted to illustrate their different behavior at the same shear strain rates. Figure 9.10 depicts each viscosity model as a function of shear rate; it illustrates significantly different responses of the apparent viscosity models. When specific regions of the viscosity model behavior are examined, when $\dot{\gamma}_{\text{blood}}$ is greater than 200 $s^{-1}$, the different models all predict a nearly constant behavior, suggesting a Newtonian fluid flow response. The two-phase nature of blood suggests that under high shear rates, the particles move away from the high–shear rate regions, leaving primarily plasma, a Newtonian fluid with a lower viscosity than whole blood. Conversely, the models (see Nichols et al., 2011) all predict an increase in viscosity as $\dot{\gamma}_{\text{blood}} \to 0$, which further illustrates shear-thinning behavior. However, the Quemada model more correctly levels off to a maximum viscosity, whereas the DGBP model continues to exponentially increase in value with no upper limit. Another important point is the influence of *Ht* on the different viscosity models. Figure 9.10 reveals similar overall shapes to the viscosity versus $\dot{\gamma}$ curves, yet the multiple *Ht* values offset the different graphs to illustrate that an increase in particle concentration is met with an increased baseline viscosity, and vice versa.

*9.3.2.1.3 Model Validation*

A model validation was conducted by comparing the primary reattachment length of laminar flow over a backward-facing step with experimental and previously validated computational data sets (see Figure 9.11).

The discrepancy between the experimental data and the computational simulations at higher Reynolds numbers is due to the fact that the experiment encountered 3-D physics, whereas the simulation was only 2-D. Such a trend is also seen with the 2-D simulations of Biswas et al. (2004). The stenosis geometry is a full 3-D geometry and enables the range of Reynolds numbers to be modeled with confidence for accurate predictions of their reattachment lengths.

*9.3.2.1.4 Recirculation Regions*

The length of the recirculation after the vessel constriction is an important parameter for blood particle trajectories and future cardiovascular disease development. Different models of blood viscosity can have a pronounced effect on the recirculation zone and its length. Figure 9.12 illustrates the different lengths of flow separation calculated with the different viscosity models for different Reynolds numbers.

The reattachment length trends of the different viscosity models are a direct result of the viscosity values of each model illustrated in Figure 9.10. Recirculation regions tend to have a very low shear rate, which increases the viscosity of a shear-thinning fluid (e.g., blood) in these regions of recirculation. An elevated viscosity provides an increased resistance to flow and limits the vortex development in the regions of flow separation when compared

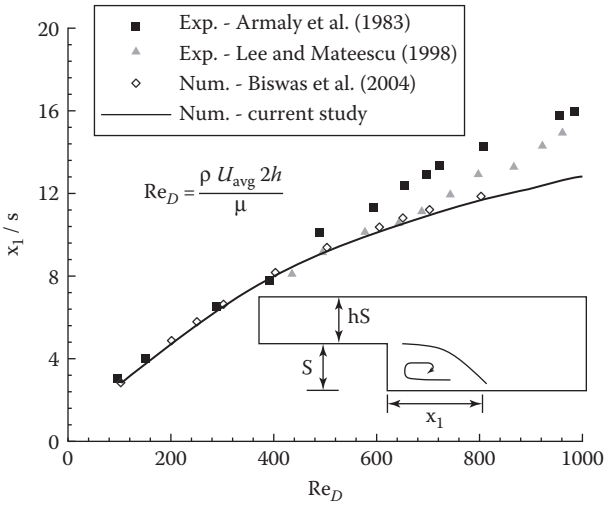


**FIGURE 9.11**
Comparison of reattachment lengths for 2-D flow over back-step.

with Newtonian fluids. Both the Quemada and DGBP viscosity models capture the shear-thinning behavior of blood, and hence, produce higher viscosities in this region than the Newtonian fluid, and consequently, have lower reattachment lengths than the Newtonian model. Moreover, the DGBP model with $Ht = 0.45$ has a visibly higher viscosity than the Quemada model for almost all shear strain rates, and consequently, has a smaller reattachment length than the Quemada model.

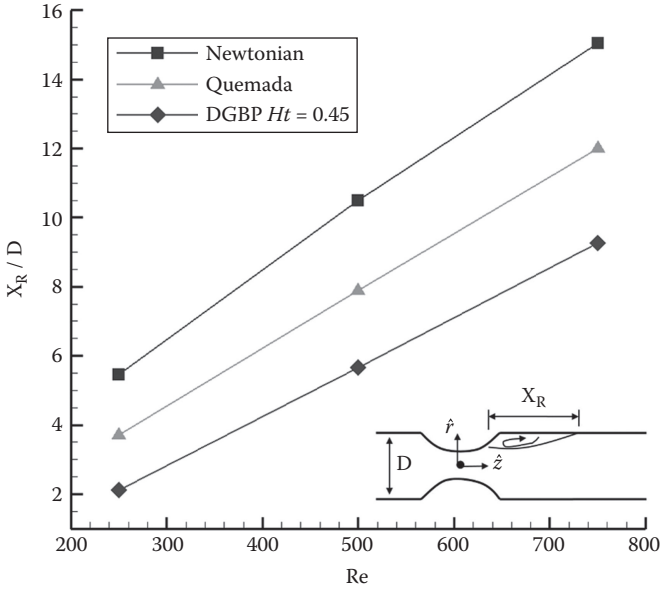


**FIGURE 9.12**
Reattachment lengths of different viscosity models at different Reynolds numbers.

*9.3.2.1.5 Velocity Fields*

Velocity profiles (see Figure 9.13) at three locations downstream of the vessel constriction reveal a growing discrepancy between the viscosity models as the (axial) $z$-coordinate increases. Such a trend is again related to the impact of the type of viscosity, with the Newtonian viscosity having the lowest value and thus providing the lowest flow resistance at the vessel centerline and near the wall.

It should be noted that the velocity profiles near the constriction are practically identical except for the centerline velocity. This is due to the high velocity of the fluid exiting the constriction, thereby overcoming the elevated viscosity of the non-Newtonian models.

An interesting result is observed when plotting the wall shear stress (WSS) through the vessel constriction up to the 5D location ($z$-coordinate = 10) downstream. The Quemada model actually predicts a peak-WSS lower than the Newtonian model, while the DGBP $Ht = 0.45$ model has the highest peak-WSS value. Figure 9.14 depicts the WSS trends over the specified range.

The reason for these WSS distributions is that a lower limit was not placed on the Quemada model, and at shear rates above $10^2$ $s^{-1}$, the Quemada model may actually predict a lower viscosity than the Newtonian model, due to its shear-thinning behavior. The

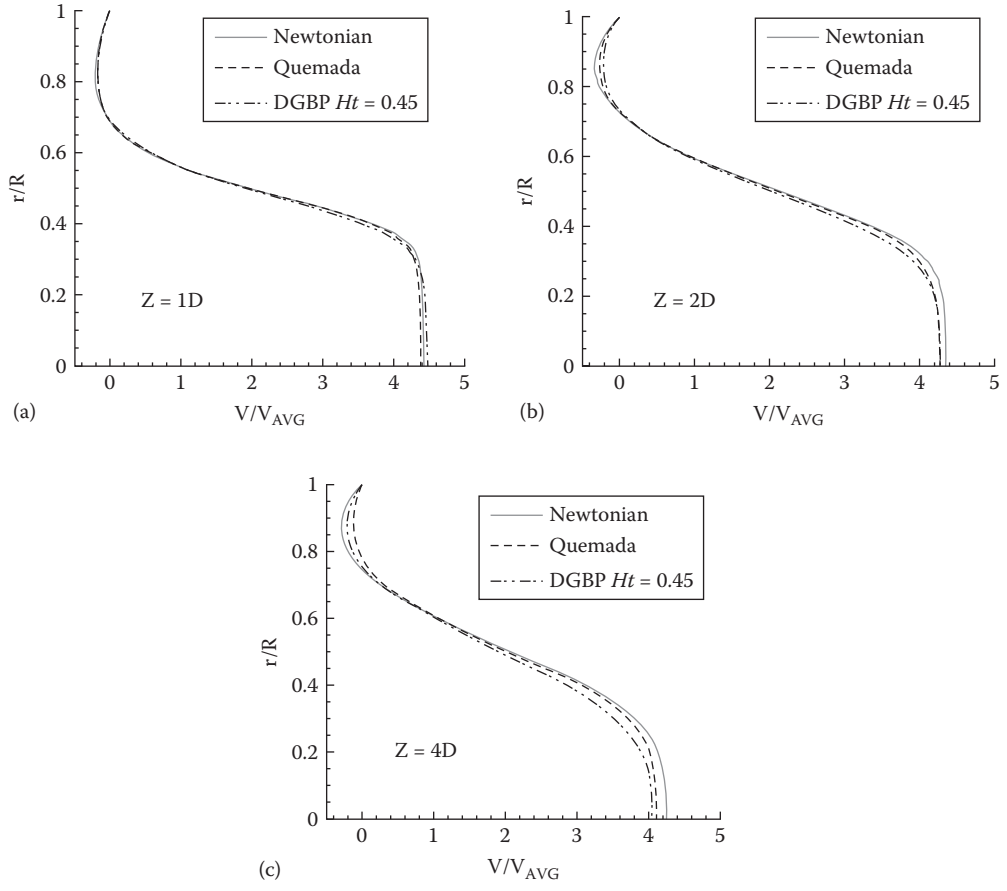


**FIGURE 9.13**
Velocity profiles of the three viscosity models: (a) $z = D$, (b) $z = 2.5D$, (c) $z = 4D$.

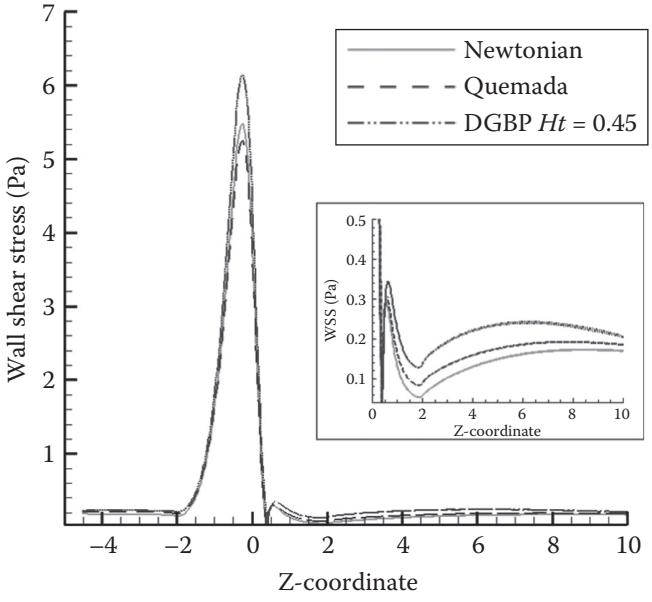


**FIGURE 9.14**
WSS distributions in the constricted tube for each viscosity model.

DGBP $Ht = 0.45$ model will not predict a viscosity lower than the Newtonian value until higher shear rates occur. The magnified window of Figure 9.14 reveals that in regions where the Quemada model would predict a higher viscosity than the Newtonian model, the WSS is greater than with the Newtonian model. It is important to note that the varying WSS values of each viscosity model do not violate the conservation of momentum, because the velocity is not fully developed at this point. The presence of the additional terms (specifically, the dependence on the $z$-coordinate) creates discrepancies between the Newtonian and the non-Newtonian WSS values.

*9.3.2.1.6 Conclusions*

The study analyzed the effects of non-Newtonian versus Newtonian viscosity models on the local flow parameters in a constricted tube. As expected, the local fluid dynamics are influenced by the non-Newtonian viscosity models. Specifically, the reattachment lengths, peak-WSS values, and regions of the velocity field are measurably affected. The pressure gradient of the different viscosity models did not reveal significantly different distributions, which implies that the pressure drop in the constricted portion of the vessel is unchanged for each model. The recirculation zones proved to be highly dependent on the viscosity of the fluid, and such knowledge should be taken into consideration when simulating pathological conditions where large recirculation regions occur (i.e., in aneurysms, the carotid artery, etc.).

De Gruttola et al. (2005) have shown that their DGBP model accurately predicts local concentrations of RBCs, WBCs, and platelets. However, when compared with the whole blood behavior as a function of shear rate, the model exhibits similar results to the validated Quemada model only in elevated–shear rate regions, but is offset from the Quemada model by a factor related to the assumed *Ht* value. The low–shear rate regions yield vast differences between all three models. In particular, the DGBP model predicts a much higher viscosity for

the lower-shear regions than the Quemada model. More experimental data on whole blood behavior in this low–shear and strain rate region is needed to determine which model best predicts actual blood behavior. An advantage of the DGBP model is the ability to incorporate a locally varying *Ht* value in future work, whereas the simplified Quemada model has the *Ht* term lumped in as one of its parameters. For the experimental data used, the Quemada model still appears to be a more accurate predictor of whole blood behavior, but the DGBP model has the potential to come close to the Quemada model predictions given the right parameters, both curve-fitted and operational. Not surprisingly, the Newtonian model was the easiest to implement, but it did not match the whole blood behavior under various shear rates.

In conclusion, the current study highlights specific effects of non-Newtonian viscosity models on the local fluid dynamics. Physical insight gained from this study illustrates the need to incorporate non-Newtonian effects of blood where significant amounts of recirculation exist, regardless of the vessel size. Therefore, future analyses should incorporate and continue to investigate the non-Newtonian behavior of whole blood within low shear regions and for different pathological conditions. In reality, the hematocrit is a function of time and space within the flow domain; thus, for future analyses, a scalar transport equation for $Ht(\bar{x},t)$ should be developed and validated, taking into account both RBC diffusion and convection.

### *9.3.2.2 Transient Laminar Flow Past a Tall Obstacle*

#### *9.3.2.2.1 Background Information*

An excellent example of external flow, relying on Chapters 2, 3, and 8, is the multi-physics phenomenon of FSI. As discussed in Chapter 8, FSI implies the coupling of solid and fluid dynamics as either two-way or one-way coupling. In one-way coupling, results are only passed on to one system. A common example is water flowing through a rigid pipe, where the flow of water results in pressure loading of the pipe, but the pipe does not deform and thus does not affect the fluid flow. Conversely, in two-way coupling, the results are passed between both system components. An example is transient flow through a flexible tube, say, an artery. In such a case, the pulsatile blood flow causes a varying pressure load, which causes arterial wall deformation, and the changing geometry measurably affects the fluid flow field. Figure 9.15 contains diagrams illustrating the different coupling of one and two-way fluid–structure interactions.

Important considerations of FSI simulations are the computational mesh and time-step iterations. Often, FSI simulations are computationally demanding and require fine-tuned parameters to achieve desired accuracy and manageable simulation time.

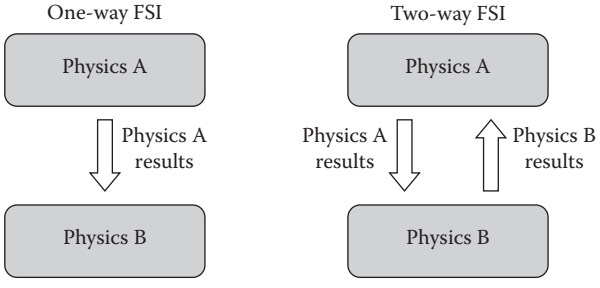


**FIGURE 9.15**
Coupling diagrams of one- and two-way FSI.

*9.3.2.2.2 Theory*

The ultimate governing equations of most FSI systems are the conservation of momentum and mass for fluid flow coupled with the conservation of momentum (Newton's second law) for solid bodies and equations of mechanical equilibrium for solid bodies. The unknown quantities of the first set of equations include fluid pressure, orthogonal fluid velocity components, solid displacement/deformation, and solid forces/stresses. To solve for these unknowns, additional equations are needed, called *constitutive* equations. They link the fluid forces with fluid motion and solid forces with solid displacement/deformation. These equations often describe the material properties/parameters of the fluid or solid and have a wide range of complexities (i.e., Newtonian vs. non-Newtonian viscosity models; isotropic Hooke's law vs. anisotropic strain-energy functions). Specifically, Equations 9.7a through e and 9.8a and b provide the fluid, solid, and mesh displacement governing equations. They were solved with the commercial simulation product CFX11 (Ansys, Canonsburg, PA).

Fluid domain-continuity:

$$\frac{\partial \rho_f}{\partial t} + \frac{\partial \left(\rho_f v_i\right)}{\partial x_i} = 0$$

Fluid domain-momentum:

$$\frac{\partial \left(\rho_f v_i\right)}{\partial t} + \left(v_j - v_j{}^m\right)\frac{\partial \left(\rho_f v_i\right)}{\partial x_j} = -\frac{\partial p}{\partial x_i} + \frac{\partial \tau_{ij}}{\partial x_j} + f_i{}^V$$

Fluid domain-constitutive law: (9.7a through e)

$$\tau_{ij} = \eta\left[\frac{\partial v_i}{\partial x_j} + \frac{\partial v_j}{\partial x_i}\right]$$

Fluid domain-mesh displacement:

$$\nabla \cdot \left(\Gamma_{\text{disp}} \nabla \delta\right) = 0$$

$$\Gamma_{\text{disp}} = f\left(\forall\right)$$

Solid domain-mechanical equilibrium:

$$\frac{\partial \sigma_{ij}}{\partial x_j} + \rho_s f_i{}^{Vs} = \rho_s a_i$$

Solid domain-constitutive laws:

(9.8a through d)

$$\text{Hooke's law}\left(\sigma_{ij} = C_{ijkl} E_{kl}\right)$$

$$\text{Strain-energy function}\left(\sigma_{ij} = \frac{\partial \psi}{\partial E_{ij}},\ \psi = \psi(E_{ij})\right)$$

$$\text{Visco-elastic model}\left(\sigma_{ij} = f(E_{ij}, t)\right)$$

where:

- $x_i$ is the three orthogonal coordinate directions
- $t$ represents time
- $\rho_f$ is the fluid domain density
- $v_i$ is the fluid velocity vector
- $v_i^m$ is the mesh velocity vector
- $p$ is the fluid pressure
- $\tau_{ij}$ is the fluid shear stress tensor
- $\eta$ is the apparent dynamic viscosity of the fluid
- $\delta$ is the displacement relative to the previous mesh position
- $\forall$ is the cell/element control volume
- $f_i^v$ is a volumetric body force vector acting on the fluid domain
- $\sigma_{ij}$ is the solid stress tensor
- $f_i^{Vs}$ is a volumetric body force vector acting on the solid domain
- $\rho_s$ is the solid domain density
- $a_i$ is the acceleration vector of the solid domain
- $C_{ijkl}$ is the general stiffness matrix
- $E_{ij}$ is the Lagrange strain tensor

It is noteworthy that the convective terms in the fluid conservation of momentum are the most altered, as convective terms must take into account the deformable mesh and its velocity.

Further description is needed to understand the mesh displacement equations listed in Equation 9.7d and e. The overall methodology is to use a diffusion transport equation to define mesh displacement at every control volume point throughout the domain. Mesh displacement relative to the previous mesh locations ($\delta$) is the variable that is acted on by a gradient and divergence operation, and $\Gamma_{disp}$ is a stiffness function that enables the option of a non-uniform diffusion of displacement throughout the computational fluid domain. Often, the stiffness parameter is a function of the element control volume, which enables the mesh to have different stiffness values at different points in time for transient analyses. Such a function is very important to prevent mesh folding and negative volume elements from forming during FSI analyses with large displacements. It is important to note that Equation 9.7d and e are used in CFX11 and should not be regarded as the only method to transfer the deformations calculated by the solid domain to the fluid mesh.

Two primary forms of coupling methodologies exist between the solid and fluid domains. The first is a direct coupling method, which solves both fluid and solid physics in a single computational step. The second is an iterative coupling methodology that solves the fluid and solid physics in a sequential process (i.e., fluid physics are solved first, fluid loads are passed on as inputs to the solid physics simulation, resulting solid displacements are then mapped to the fluid domain mesh, fluid physics are then solved on the deformed mesh). Iterative coupling is more prevalently used in most situations in attempts to control the nonlinearities of both the fluid domains and ensure that physics are not eliminated through the coupling procedure. Figure 9.16 provides a flowchart illustrating the computational algorithm of the iterative coupling methodology per time step, where the fluid domain is solved prior to the solid domain.

#### *9.3.2.2.3 System Description*

An example of one-way FSI is the wind loading of a tall building, where building displacements do not significantly alter the surrounding airflow. A simplified 2-D simulation of flow over a building is used for this illustration. Recent simulations of wind-loaded

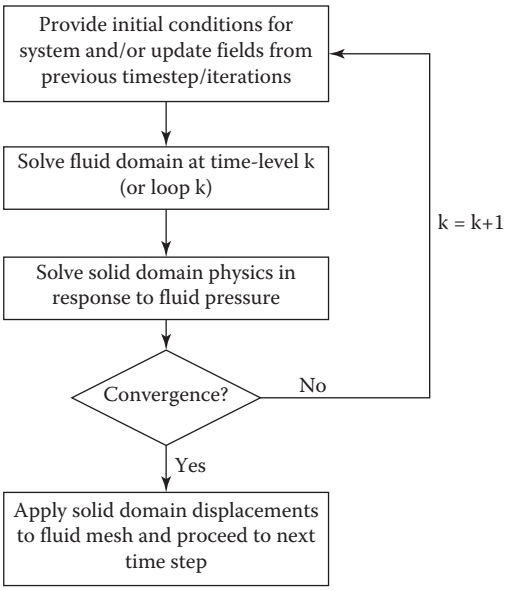


**FIGURE 9.16**
Iterative coupling procedure per time step with fluid physics being solved first.

structures have shown the increased importance of 3-D simulations to capture all the physical phenomena; thus, the following analysis is used for illustration purposes and should not be used for more complex structural health design considerations. Figure 9.17 summarizes the preliminary steps, that is, system sketch, assumptions, and concepts.

*9.3.2.2.4 Simulation Implementation*

ANSYS products along with SolidWorks 2008 were used to develop the example. SolidWorks was used to create the fluid and solid domain geometry files, ANSYS ICEM CFD generated the fluid mesh, ANSYS CFX carried out the fluid calculations, and ANSYS Workbench generated the solid mesh and carried out the solid calculations. Figure 9.18 illustrates the system dimensions and computational mesh. Notice regions of mesh refinement, which correspond to high gradients of the simulation variables (velocity, pressure, stress, and displacement). A caveat must be made when conducting FSI analyses; that is,

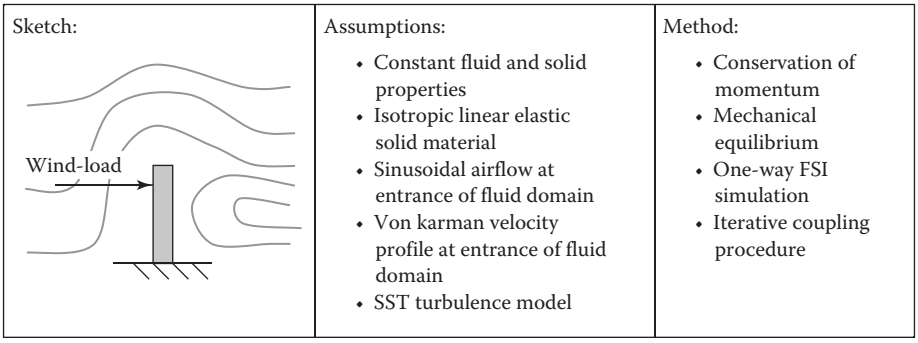


**FIGURE 9.17**
Sketch, assumptions, and concepts of 2-D flow over obstacle.

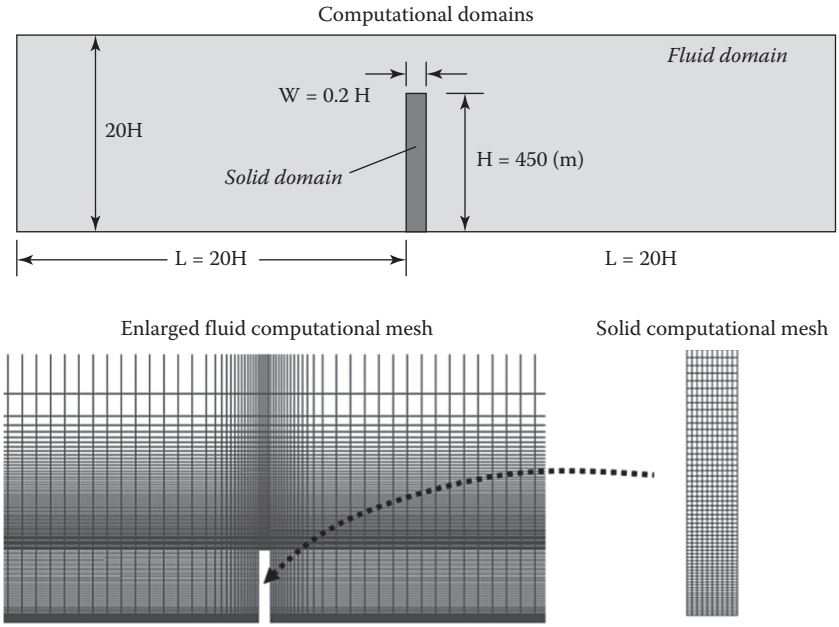


**FIGURE 9.18**
Fluid and solid computational domains and meshes.

mesh refinement is a very sensitive parameter, which can have a prominent effect on the final FSI solutions. In simulations where large displacements occur, the fluid mesh can be stretched and/or skewed in ways that cause mesh folding (negative volume elements) or can cause regions of originally sufficient mesh refinement to be stretched in ways that negate the mesh refinement and cause inaccurate solutions to regions of high gradients. Ways around these problems include knowledge of the system physics, using adaptive mesh refinement with element death throughout the solution procedure, or specifying a function of the mesh element size that diffuses the displacements to regions of the fluid mesh that can handle these displacements (cf. Equation 9.6e).

The computational settings applied to the coupled systems are summarized in Table 9.4, while the boundary conditions of each domain are illustrated in Figure 9.19.

**TABLE 9.4**

Computational Settings of the Coupled Systems

| **Fluid Domain** | **Solid Domain** |
|---|---|
| Air at 25°C:<br>• $\mu_{air} = 1.831 \times 10^{-5}$ Pa*s<br>• $\rho_{air} = 1.185$ kg/m$^3$ | Mixture of concrete and steel<br>• $E_{bldg} \approx 6.00 \times 10^{10}$ Pa<br>• $v_{bldg} = 0.23$ |
| RMS residual $<1 \times 10^{-4}$ | 2 norm convergence for force and displacement |
| von Karman inlet velocity profile<br>• $V_0\left(2\frac{y}{\delta} - \left(\frac{y}{\delta}\right)^2\right),\ 0 \le y \le \delta,\ \delta = 0.2\text{H}$<br>• $V_0 = 15[\text{m/s}]\cdot\sin(\omega\cdot t)$ | |

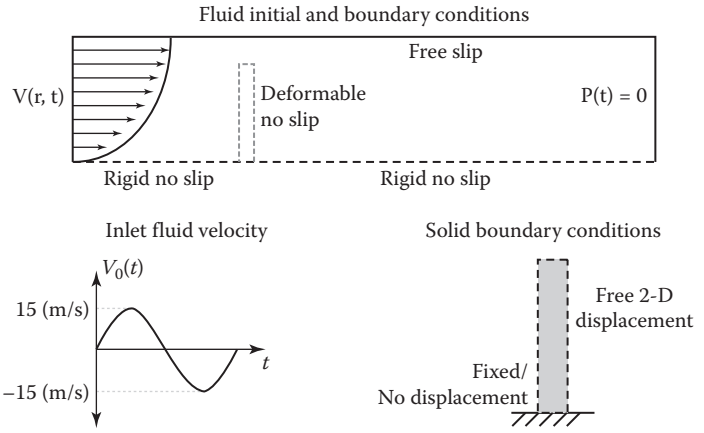


**FIGURE 9.19**
Boundary conditions of fluid and solid system.

For this simulation, the iterative coupling methodology is implemented, which requires additional parameters to be specified that are related to the number of internal loops (*k* in Figure 9.16) and the convergence criteria of the variables passed between the two physical domains. The conditions are:

- Max. number of iteration loops is 10
- Min. number of iteration loops is 2
- Iteration loops repeat until both domains' local physics converge *and* the coupling variables (fluid mesh displacement and applied loads) residuals $< 1 \times 10^{-3}$

Three types of simulations were conducted, and the results of two studies are shown. The first was a steady-state simulation with the inlet velocity at 15 m/s, and the second was a transient simulation that simulated developing flow until a near–steady-state point was reached. The third case was a transient simulation with a time-step of 5 s for a total time of 180 s. The amplitude and frequency of the inlet sinusoidal velocity for the transient cases were set at 15 m/s and 2π rad/min, respectively.

Again, prior to the full solution of the FSI system, a validation comparison with flow over a back-step (see Figure 9.20a) was completed to ensure the solver's ability to predict vortex behavior and reattachment lengths. Specifically, 2-D simulations of steady flow over a back-step using ANSYS CFX11 were compared with the experimental data from Armaly et al. (1983) and Lee and Mateescu (1998) along with the numerical data of Biswas et al. (2004). The results are presented in Figure 9.20b.

The additional vortices only develop at $Re_D$ values larger than 400, which is where the 3-D effects begin to have a prominent influence on the 2-D simulation accuracy. Despite the growing discrepancy illustrated in Figure 9.20b for the $x_2$-reattachment length, the $x_2$-reattachment length data sets reveal a good match for all simulated Reynolds numbers.

*9.3.2.2.5 Simulation Results*

The steady flow simulation can be compared against specific time points of the developing flow simulations to illustrate the characteristic time when the system's physics can be modeled as a pure time-independent process. Figure 9.21 illustrates the difference between the steady solutions and the developing flow simulations.

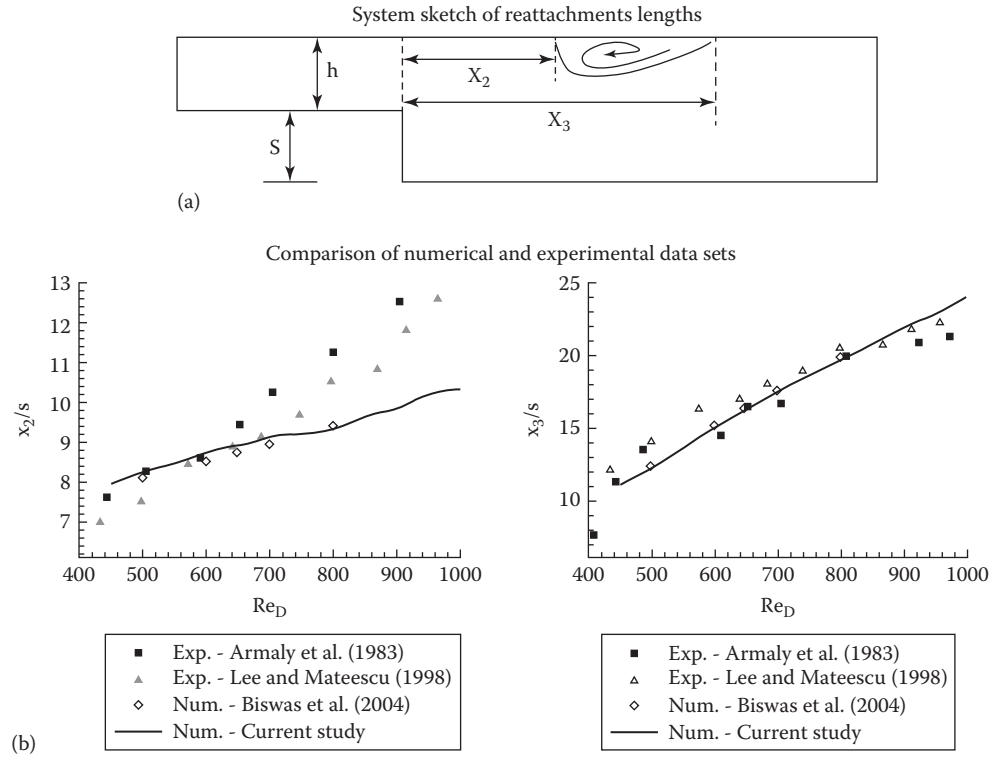


**FIGURE 9.20**
(a) System sketch of reattachment lengths $x_2$ and $x_3$; (b) comparison of experimental and numerical reattachment lengths for steady laminar flow over a back-step.

The different plots in Figure 9.21 are on different length scales to provide a clear view of each time point's regions of recirculation. A measurable vortex develops immediately downstream the building after 55 s of a constant inlet velocity and continues to increase in length and height during a continuous inflow of fluid for 300 s. Additionally, at around 300 s, a small recirculation zone, directly upstream of the building, is noticeable at the base of the building structure. Despite the length of time simulated with constant inflow velocity, the dimensions of the 300 s recirculation zones are much lower than the dimensions of the steady-state recirculation zones. Therefore, the time needed to establish steady-state physics of fluid flow is greater than 5 min of constant inflow velocity.

Interestingly, the stress fields for the developing flow simulations also show some differences from the stress fields of the steady flow simulations. Figure 9.22 highlights the maximum von Mises stress at different time levels of all simulations.

Figure 9.22 clearly illustrates that even if the flow over the building is constant, the resulting loads applied to the building vary with time and are the cause of the varying stress values with respect to passing time. Furthermore, an approximately 400% difference exists between the maximum von Mises stress level calculated by the steady flow simulation and the developing flow simulation. Thus, time effects should be a significant consideration when conducting analyses of flow over structures, and questions regarding the validity of steady-state simulations to estimate structure loading should be investigated prior to using steady-state simulations for detailed analyses of structures.

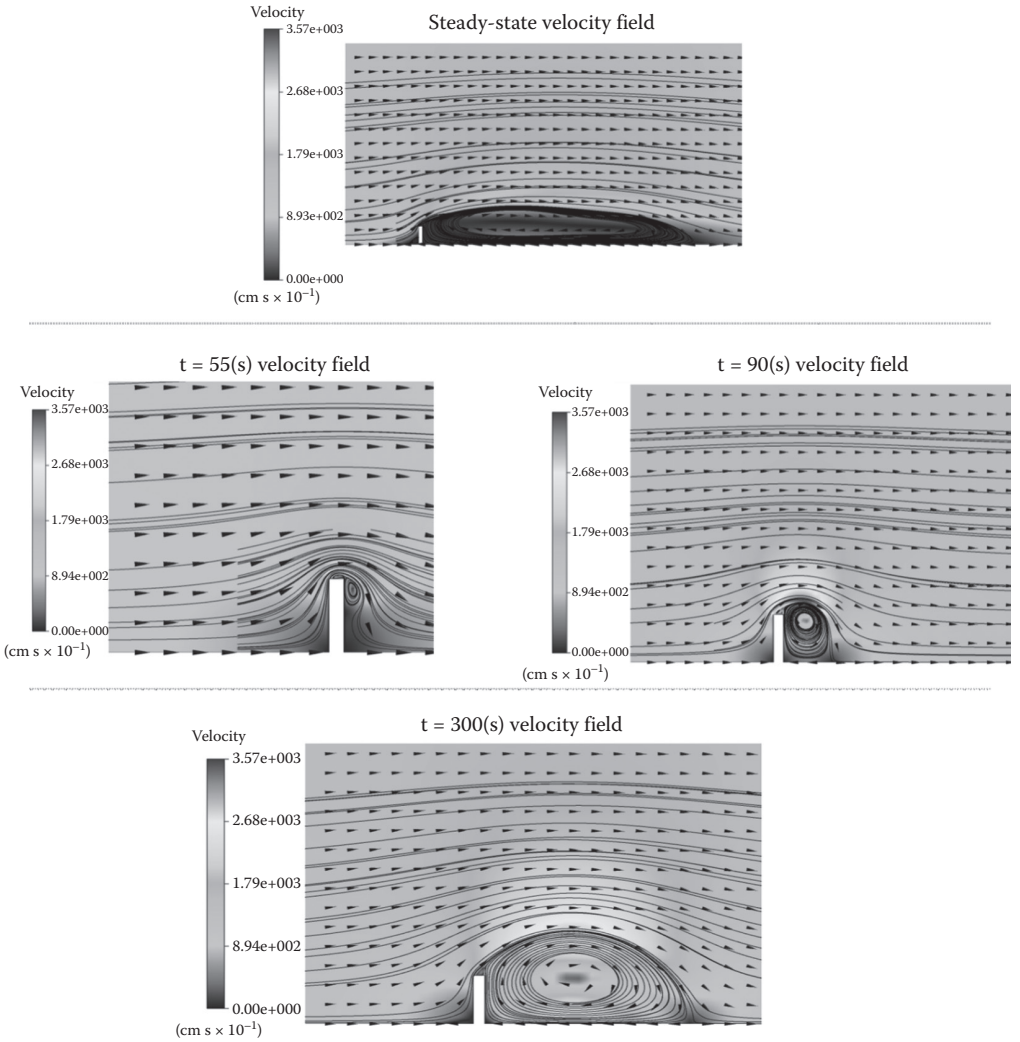


**FIGURE 9.21**
Steady flow simulation data compared with developing flow simulation data.

The time scales of all simulations varied significantly. Table 9.5 lists the different completion times of the various simulations completed for the external flow study. All simulations were completed using a single Intel 3.59 GHz processor on a Dell Precision 670 workstation with 8 GB of RAM using a 64 bit Windows operating system.

Results of the transient computational simulations exhibit measurable differences from the constant inlet velocity simulation results. Specifically, vortices develop at different locations and primarily during deceleration phases of the inlet velocity. Figure 9.23 illustrates the velocity fields around the building at different time points during the third period. Only the third period is shown, since the previous two periods do not exhibit visible dynamic equilibrium/cyclic repetition, whereas a visible amount of dynamic equilibrium/cyclic repetition is observed in the third period.

An interesting result of the transient simulations is the development of multiple vortices at both upstream and downstream locations of the building. During the maximum levels

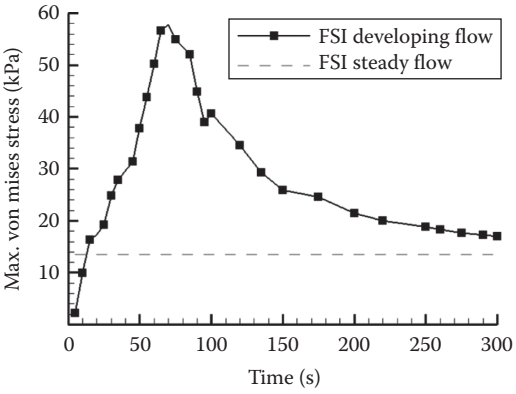


**FIGURE 9.22**
Maximum von Mises stress versus time.

**TABLE 9.5**
Simulation Run Times

| One-Way FSI Simulation | Run Time |
|---|---|
| 2-D steady flow | 40 min |
| 2-D developing flow with constant inflow velocity | 6 h and 38 min |

of retrograde flow, the vortices significantly diminish, and they begin to return during the deceleration portion of negative inflow velocity, continuing to be present at the beginning of the acceleration of positive inflow velocity. Throughout both the positive and the negative inflow velocities, a recirculation zone the size of the steady-state recirculation never develops during the three periods of oscillating flow.

Figure 9.24 illustrates the oscillatory behavior of the average force applied to the building's side surface.

The plot in Figure 9.24 reveals that the average force applied to the building is approximately shifted 90° behind the average inlet fluid flow velocity. A cosine function can be used to fit the discrete force with an amplitude of $0.36 \times 10^9$ N and a frequency of $2\pi$ rad/min. Mesh position, velocity, and acceleration can also be calculated at the center-point of the building's upper surface. Mesh position is a direct output of the FSI simulations, whereas mesh velocity and acceleration are calculated using a first-order forward-difference Taylor series expansion of the discrete position data of the fitted FSI position data.

*9.3.2.2.6 Summary and Conclusions*

Simulations of steady flow and developing flow over a simple structure, using one-way iterative FSI coupling, have been documented. An understanding regarding the characteristic time needed to reach steady-state has been investigated. The characteristic time required is greater than 5 min, where the potential to underestimate the maximum stress

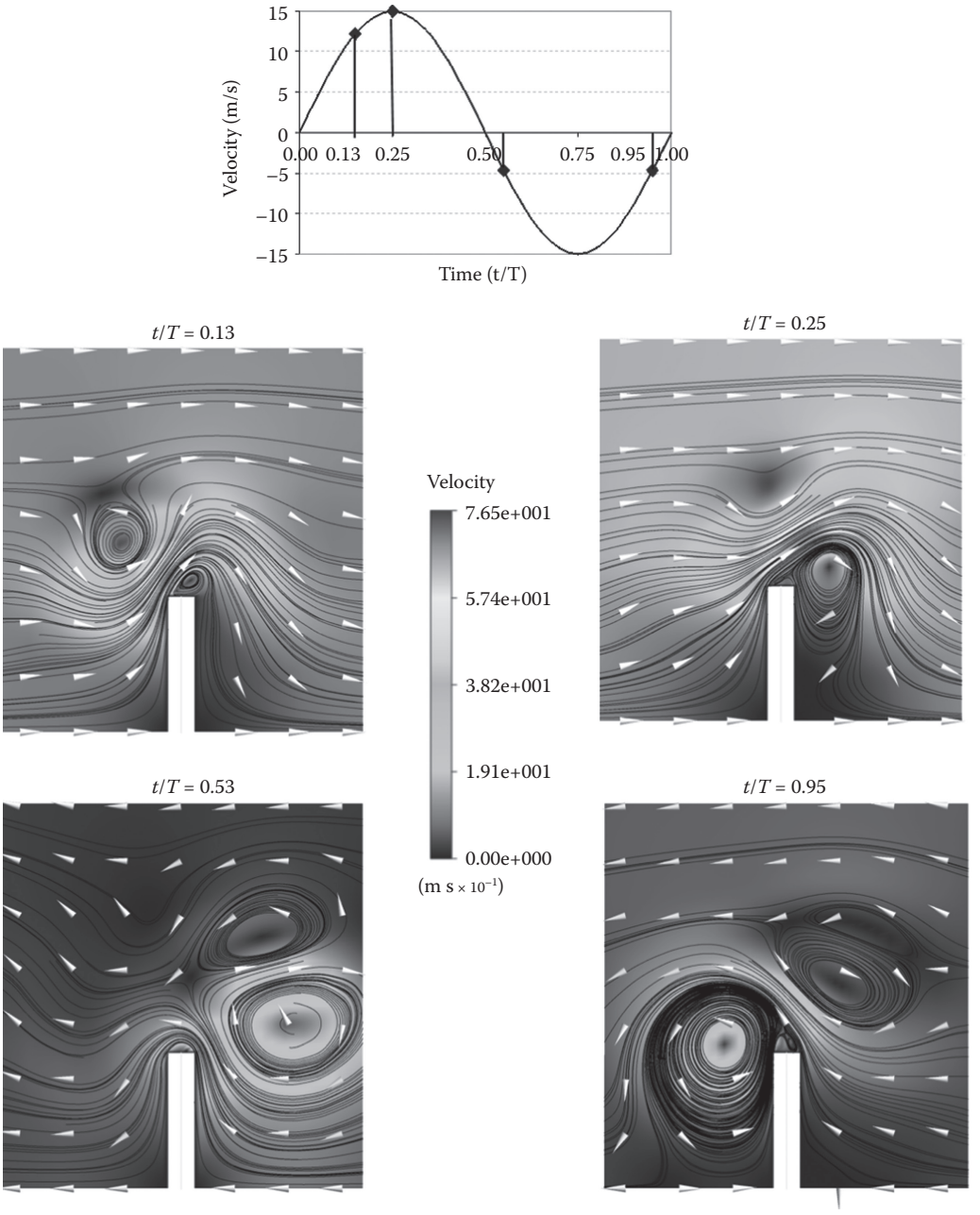


**FIGURE 9.23**
Velocity fields around building at time points during the third period.

in the structure can be by a factor of 400% when using a steady-state simulation. Clearly, oscillatory inlet flows produce more complex velocity fields and resulting oscillatory loads that are not captured in any constant velocity simulation.

The present study illustrates the utility of one-way FSI analyses and their ability to provide useful insight and understanding of complex physical phenomena that may not be

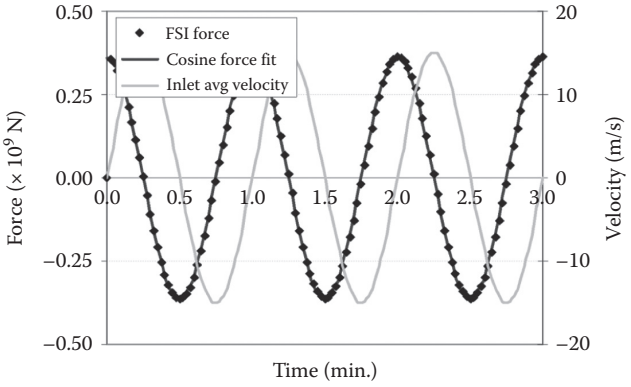


**FIGURE 9.24** Fitted FSI position, velocity and acceleration data.

possible with experimental analyses alone. It should be noted that to accurately determine the natural frequency and damping ratio of a system, additional experiments/simulations should be conducted to ensure that the fitted parameters enable the system behavior to be matched in more than a single implementation. Additionally, the oscillatory loads and displacement of the vibrating structure should include an analysis of fatigue to ensure that the strength of the structure under oscillatory loads does not decrease to a level that makes fatigue failure a possibility.

Taylor & Francis
Taylor & Francis Group
http://taylorandfrancis.com

# 10

# *Course Projects*

## 10.1 Introduction

There are significantly different end-of-the-semester approaches for testing to what degree students have learned the fundamentals plus applications in a challenging subject, say, fluid dynamics. The common approach is to take *a final exam*, which has the merits of uniformity as well as a certain comprehensiveness, fairness, and simplicity (at least for the instructor). Doing a *course project, presenting in-class some preliminary results and writing a research report* is an alternative (or complementary) way of demonstrating a good understanding of the fundamentals and practical application skills. If proper, subject-specific research topics have been selected, such course project–related activities may probe a student's knowledge base and skill level more thoroughly and could certainly be a better preparation for future job assignments in engineering and technology. Of course, the chosen topic should not be too narrow, or too complicated, or one for which a detailed solution can be readily found in the public domain.

This chapter starts out showing how to write a research report; that is, it provides guidelines that are applicable to standard assignments in industry, government, and academia as well (Section 10.2). Then, features of and some suggestions for different types of course projects are listed, relying on the material previously presented (Section 10.3). Actual course projects with some interesting physical insight are given for the two project categories: those with a strong tutorial component and those that require computer simulations. On rare occasions, an exceptional research report may form the basis for a journal article.

## 10.2 Guidelines for Project Report Writing

A course project is more than a homework problem. As a starter, it typically requires a brief literature review to document the state-of-the-art for the given task. The antagonistic interplay between a rather accurate mathematical description of an assigned problem and finding a tractable solution method puts a premium on making the right assumptions and selecting a suitable equation solver, often in terms of available software and hardware. The resulting work has to be documented in an appropriate format, that is, a *project report*, which should have the following features:

- *ToC*: There should be a table of contents with page numbers (if needed for lengthy reports).

- *Nomenclature*: This is optional but recommended for complex problem solutions.
- *Abstract*: This is a summary of the fluid dynamics problem analyzed, solution method employed, and novel results with physical insight presented.
- *Introduction*: This should include project objectives and task justification, a system sketch with state-of-the-art description, the basic approach or concept, and references of the literature review in terms of "author (year)," for example, "White (1998)"; succinctly list the differences between the published system/problem and your results.
- *Theory*: This should include basic assumptions, governing equations, inlet/boundary conditions, property values in the form of a data table, ranges of dimensionless groups, closure models, and references.
- *Solution method and model validations*: On a first-year graduate level, it is always recommended to devise an interesting flow system for which an analytic/approximate solution is available. Still, linear partial differential equations (PDEs) and most ordinary differential equations (ODEs) can be solved with the popular MatLab software. In many cases, numerical equation solvers (e.g., OpenFOAM or commercial software) are needed to obtain realistic results. For model validation, the two basic approaches are (1) numerical accuracy checks, that is, mesh independence of the results as well as mass and momentum residuals less than, say, $10^{-4}$ and (2) quantitative proof, for example, comparison with an exact solution of a (typically much) simpler system, and/or experimental data comparisons, or (at least) qualitative justification that the solution is correct.
- *Results and discussion*: Results should include graphs with interpretations; that is, explain physical insight (note: number the figures and discuss them concisely), draw conclusions, and provide applications.
- *Conclusions and future work*: Conclusions are an extended form of the Abstract, listing what novel contributions have been made and what their significance is while adding limitations of the study as well as future work.
- *References*: All sources (e.g., websites) and literature must be cited in alphabetical order, following the format: Author (year), or first author and second author (year), or first author et al. (year).
- *Appendices*: These should include lengthy derivations, computer programs, and so on.

## 10.3 Course Project Suggestions

Course projects may range from the basic type, that is, the *tutorial* kind, to the more challenging *advanced research* kind. What type of project to select depends on the student's interest, learning experience, and skill level. In any case, for course project topics to be acceptable, they should have the following requirements:

- They should cover a major topic in fluid dynamics, that is, fluid flow, fluid-particle dynamics, and/or convection heat transfer, stressing fundamental aspects as well as an application.

- They must be doable within the given time frame, such that preliminary results should be available for in-class presentation at the end of the semester.
- Except for combined theoretical-experimental studies, all projects are done individually.
- Student-initiated topics have to be approved by the instructor based on a brief write-up addressing/proposing the flow problem or system, a brief literature review, a list of assumptions, the modeling equations with boundary conditions and input data, the solution method (with identification of the software/computer, if needed), anticipated results with possible application, and ways to validate the expected results.

Expanding on the given guidelines for writing a course project report, there are several basic tasks to be accomplished:

a) As a first step, a thorough literature review is necessary, taking up the major part of the *Introduction*. Clearly, all topics are well documented in the open literature, and videos illuminating the unique flow phenomena plus nifty applications are readily available.

b) A challenge is to set up a specific system/problem by which the fundamentals can be explained and thereby, natural as well as man-made applications can be illustrated. The necessary math model builds on and expands the material learned from Part A and/or Part B. Some problem solutions can be gained via analytical means, while others require computational tools. In any case, as with all reports, the course project should be a fine balance between math and physics of fluid dynamics.

c) The *Theory* section connects the chosen flow system with its solution method by describing the expected fluid flow field mathematically and hence, indicates a suitable solution method. If the flow (or fluid-particle, or convection heat transfer) equations appear to be too difficult, the project objectives will have to be curtailed and a revised, well-posed math model developed. Next, necessary input data sets have to be collected, and the expected value-ranges of key dimensionless groups (definitely including the Reynolds number) have to be determined.

d) A prime course project choice should be an interesting flow system for which an *analytic/approximate solution* is available. The popular MatLab software can be part of this approach when linear PDEs or ODEs have to be solved. In many cases, however, *numerical equation solvers* (e.g., the free OpenFOAM library or commercial software) are needed to obtain realistic results. For *model validation*, the two basic approaches are (1) numerical accuracy checks, that is, mesh independence of the results as well as mass and momentum residuals less than, say, $10^{-4}$ and (2) quantitative proof, for example, comparison with an exact solution of a (typically much) simpler system, and/or experimental data comparisons, or (at least) qualitative justification that the solution is correct.

e) *Results*, in terms of figures, tables, and/or correlations, should be displayed in dimensionless form. Once the velocity, pressure, and temperature distributions are known, their derivatives (or integrations) generate all the practical answers in terms of shear stresses, flow rates, and forces. Then, with parametric sensitivity analysis (PSA), the full range of flow-system behavior can be explored, intriguing flow field structures uncovered, and flow rates and forces evaluated. Figures with their captions and legends should be largely self-explanatory. The related

*discussions* explain the reasons for unusual trends and summarize new physical insight, expanding on scientific implications and/or on practical applications.

f) *Conclusions* are an extended form of the abstract, listing what novel contributions have been made and what their significance is while adding limitations of the study as well as future work.

### 10.3.1 Tutorial Project with Analytic Solutions

By definition, *tutorial* projects provide interesting material for students to learn the essentials plus applications in *Modern Fluid Dynamics*. Thus, after topic selection, the main focus is on a comprehensive literature review, canvasing appropriate textbooks, journal articles, university websites, and internet videos/tutorials. *Just copying literature sources is tempting but not at all the main objective of a tutorial course project report! Here, the goals are to first understand the relevant research papers, book chapters, and videos and then consider a variation to the selected flow system or assemble something novel to produce new physical insight based on new figures, tables, and/or a video.*

Examples in this project category may include

1. Couette flow variations and particle transport analysis
2. Comparison of Poiseuille, annular, and slit flow phenomena
3. The Reynolds lubrication equation applied to slider and journal bearings
4. Illustration and applications of the Magnus effect
5. The occurrence and implications of Dean's flow
6. Depiction and discussion of exotic non-Newtonian fluid flow behavior
7. Fluid-particle flow for small versus large Stokes numbers in tubes
8. Hiemenz flow with different fluids
9. Evaluation of the Nusselt number for laminar versus turbulent pipe flow
10. Laminar vortex shedding behind a cylinder in cross flow (the von Karman vortex street)

It is no accident that each topic title carries the name of a major contributor to fluid dynamics, implying that the main focus of these projects is on the understanding of the essentials. Tutorial Projects #2 and #10 were selected to illustrate the basic tasks outlined in the previous section. While Project #2 summarizes and extends the in-class material of Chapters 2 and 3, Project #10 focuses on the wake formation caused by laminar flow perpendicular to a horizontal (or vertical), infinitely long cylinder. Note: a course project report for tutorial Project #10 *requiring computer simulations* appears in Section 10.3.2.

Up front, using Project #2 as an example, the physical insight that could be gained includes:

- The three Poiseuille-type flow characteristics are very similar; however, with some distinct aspects because of the geometric differences.
- The normalized velocity and shear-stress profiles of tubular flow and slit flow are the same. However, the $u_{max}/V$ ratio is different.
- The friction factor of slit flow is greater than that of tubular flow for the same Reynolds number, indicating a higher head loss due to the elevated shear stress.

- Tubular flow and slit flow can be seen as two limiting cases of annular flow. This is because annular flow characteristics approach those of tubular flow when $R_1/R_2 \to 0$ and approach those of slit flow when $R_1/R_2 \to 1$.
- The volumetric flow rates of the three Poiseuille-type flows all scale with the pressure drop, the reciprocal of viscosity, and the channel length. However, they scale with conduit radius (or height/width) to the fourth power.

*Notes:*

- All Course Project Reports are displayed as self-contained documents, that is, with their own numbering systems for sections, equations, tables, and figures as well as nomenclature and references.
- Course Project Report #2 was done by Zelin (Luke) Xu.

### 10.3.2 Computer Simulation and Design Projects Using Open-Source Software

As indicated, problems amenable to analytic/approximate solutions have all been documented in textbooks or review articles. Thus, the modern focus is on numerical solutions as discussed in Chapter 9. The major goal is to develop a computer simulation model that is predictive, that is, realistic and accurate. Such a reliable tool can then be used to display interesting flow phenomena, gain new insight, expand on a basic theory, and improve engineering devices. The typical objectives for device design are both optimal geometry and operation, leading to improved performance, cost savings, and enhanced reliability.

The sample course project reports presented are the two tutorial projects #2 and #10 as well as Design Project #11 which is on improved nanofluid flow mixing in microchannels forming a Y-junction. Course projects #10 and #11 were done by Sriram V. Chari.

Concerning Tutorial Project #10, "Laminar Vortex Shedding behind a Cylinder in Cross Flow," the most notable observations are as follows:

- For Reynolds numbers less than unity, the flow field front and aft of the cylinder is the same, known as *Stokes flow*; however, for $\mathrm{Re} > 1$, flow separation occurs, and hence, a wake starts to form.
- Although the approaching flow is *uniform and steady*, after a critical Reynolds number ($\mathrm{Re} > 45$) is reached, the *wake field becomes unsteady* and vortex shedding starts.
- The oscillating flow field can rattle structures in the cylinder's wake, as happened with a cooling tower on the west coast of England.

## Appendix 1: Comparison of Poiseuille, Annular, and Slit Flow Phenomena

***Course Project Report of Tutorial Category #2***

### A1.1 Introduction

Poiseuille-type flow is steady laminar fully developed fluid flow caused by a constant pressure gradient or gravity. For internal flows, the conduit is a pipe with circular cross section,

a narrow slit, or an annulus formed by a cylinder inside a concentric tube. An example of external Poiseuille-type flow is a moving thin film on an incline. In any case, the streamlines are parallel to the walls, and the fluid is Newtonian with viscosity μ.

Poiseuille-type flow is one of the few cases in fluid dynamics where exact solutions can be obtained. Sample applications include airflow in lungs, flow through a drinking straw or a hypodermic needle, microfluidics and nanofluidics (Kleinstreuer, 2014), and blood flow in arteries. It has also been used in various studies as a baseline case to validate measurements or simulations.

In this tutorial, the analytical solutions of three kinds of Poiseuille-type flow are derived and compared. Specifically, tubular flow, slit flow, and annular flow solutions are presented for velocity profiles, wall shear stresses, volumetric flow rates, hydraulic resistances, and pressure drops.

## A1.2 Poiseuille Flow in a Pipe

A pipe with radius $R$ and length $L$ is considered (see Figure A1.1), where flow is in the fully developed regime. The Navier–Stokes equation can be conveniently solved in a cylindrical coordinate system. Let $u$ represent the velocity in the flow direction.

### *A1.2.1 Assumptions*

- Fully developed flow: $\dfrac{\partial u}{\partial x} = 0$
- Steady-state: $\dfrac{\partial u}{\partial t} = 0$
- Flow is steady and unidirectional with parallel streamlines, that is, $\vec{v} = u(r)$ only
- Flow is axisymmetric: $\dfrac{\partial^2 u}{\partial \theta^2} = 0$

With the stated assumptions, the $x$-component of the Navier–Stokes (N–S) equation becomes

$$\frac{1}{\mu}\frac{\partial p}{\partial x} = \frac{\partial^2 u}{\partial r^2} + \frac{1}{r}\frac{\partial u}{\partial r} \tag{A1.1}$$

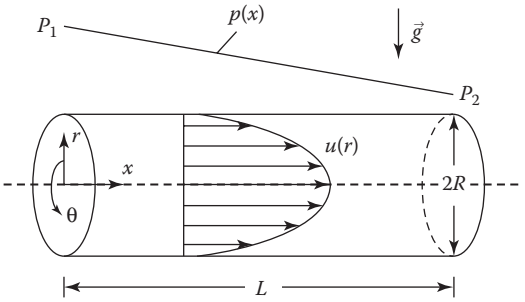


**FIGURE A1.1**
Fully developed flow through a tube.

The left-hand side is a function of $x$ only, and the right-hand side is a function of $r$ only. Since $x$ and $r$ are independent, the two sides of the equation must equal the same constant:

$$\frac{1}{r}\frac{d}{dr}\left(r\frac{du}{dr}\right)=C=\frac{1}{\mu}\frac{\partial p}{\partial x} \tag{A1.2}$$

Here, the two terms on the right-hand side of Equation A1.1 have been combined. Integrating twice, we obtain

$$u(r)=\frac{C}{4}r^2+C_1\ln r+C_2 \tag{A1.3}$$

The constants $C_1$ and $C_2$ can be obtained using the following conditions:

$$\begin{aligned} &u=0 \; at \; r=R \\ &u<\infty \; at \; r=0 \\ &C=\frac{1}{\mu}\frac{dp}{dx} \end{aligned} \tag{A1.4}$$

Finally, the velocity profile can be obtained as

$$u(r)=-\frac{R^2}{4\mu}\frac{dp}{dx}\left(1-\frac{r^2}{R^2}\right) \tag{A1.5}$$

where

$$\frac{\partial p}{\partial x}=-\frac{\Delta P}{L} \tag{A1.6}$$

The normalized velocity profile is shown in Figure A1.2. It is a parabolic profile, where the maximum velocity appears at the center line of the pipe:

$$u_{\max}=\frac{R^2}{4\mu}\frac{\Delta P}{L} \tag{A1.7}$$

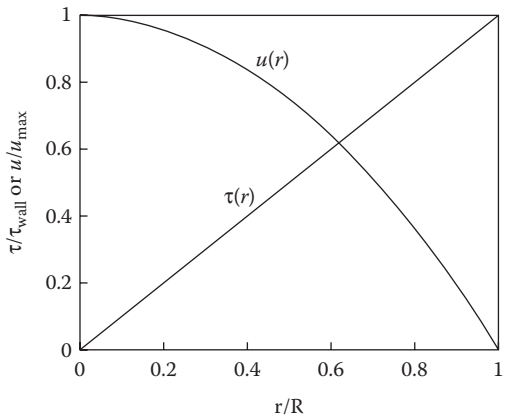


**FIGURE A1.2**
Velocity and shear stress profiles of Poiseuille flow in a pipe.

The average velocity is found as

$$V = \frac{\int_0^R u(r)2\pi r dr}{\pi R^2} = \frac{\Delta P R^2}{8\mu L} = \frac{1}{2}u_{\max} \tag{A1.8}$$

Hence, the volumetric flow rate is

$$Q = \int_0^R u(r)2\pi r dr = \frac{\pi \Delta P R^4}{8\mu L} = V A_{\text{cross section}} \tag{A1.9}$$

For a horizontal tube, the pressure drop can be easily obtained to be

$$\Delta P = \frac{8\mu L Q}{\pi R^4} \tag{A1.10}$$

It is also of interest to compute the shear-stress distribution of the flow, that is,

$$\tau = \left|\mu \frac{du}{dr}\right| = \frac{r}{2}\frac{\Delta P}{L} = C \cdot r \tag{A1.11}$$

Equation A1.11 indicates that shear stress varies linearly with $r$ (see Figure A1.2).

### A1.3 Pressure-Driven Flow in a Narrow Slit

Slit flow is three-dimensional due to the existence of the side walls. However, it can be simplified when the aspect ratio of the cross section is very large, that is, $W/d \gg 1$. In this case, the flow can be treated as two-dimensional, whereby the edge effects are neglected. The three components of the velocity vector are $u$, $v$, and $w$ (Figure A1.3).

#### *A1.3.1 Assumptions*

- Fully developed flow: $\dfrac{\partial u}{\partial x} = 0$
- Steady-state: $\dfrac{\partial u}{\partial t} = 0$
- Flow is unidirectional and parallel to the wall: $v = 0,\ w = 0,\ \vec{v} = u(y)$ only
- Negligible edge effects: $\dfrac{\partial^2 u}{\partial z^2} = 0$

With the above assumptions, the $x$-component of the N–S equation becomes

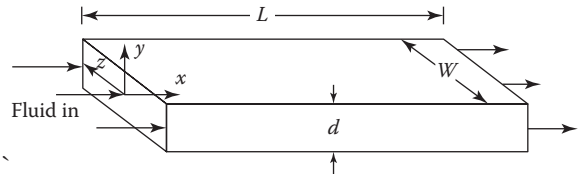


**FIGURE A1.3**
Fully developed flow through a rectangular channel with slit cross section.

$$\frac{1}{\mu}\frac{dp}{dx}=\frac{\partial^2 u}{\partial y^2} \tag{A1.12}$$

Similarly, for the equation to hold, the two sides of the equation must equal the same constant $C$. It is easy to obtain that

$$\frac{dp}{dx}=-\frac{\Delta P}{L} \tag{A1.13}$$

After integration, Equation A1.6 becomes

$$u(y)=\frac{\Delta P}{2\mu L}y^2+C_1 y+C_2 \tag{A1.14}$$

Applying the no-slip boundary conditions

$$u=0 \text{ at } y=d/2$$

and

$$u=0 \text{ at } y=-d/2 \tag{A1.15}$$

the velocity profile can then be obtained as

$$u(y)=\frac{\Delta P d^2}{8\mu L}\left[1-\left(\frac{2y}{d}\right)^2\right] \tag{A1.16}$$

Similarly to Poiseuille flow in tubes, the velocity profile of slit flow is also parabolic. The maximum velocity appears at the mid-plane where $y=0$:

$$u_{\max}=\frac{\Delta P d^2}{8\mu L} \tag{A1.17}$$

The average velocity is found to be

$$V=\frac{\Delta P d^2}{12\mu L}=\frac{2}{3}u_{\max} \tag{A1.18}$$

It should be noted that in contrast to Poiseuille flow in a tube, where $V=0.5u_{\max}$, the average velocity of slit flow is two-thirds of its maximum velocity due to the different shape of the flow cross section.

The volumetric flow rate of slit flow can be calculated as

$$Q=\int_{-d/2}^{d/2}u(y)W dy=\frac{\Delta P d^3 W}{12\mu L} \tag{A1.19}$$

So, the pressure drop across the length $L$ will be

$$\Delta P=\frac{12\mu L Q}{d^3 W} \tag{A1.20}$$

The shear-stress distribution can be obtained as

$$\tau=\left|\mu\frac{du}{dy}\right|=\frac{\Delta P}{L}y \tag{A1.21}$$

*Note:* With the assumption that $W \gg 1$ to assure one-dimensional flow, the results given with Equations A1.19 through A1.21 are reported as Q/W in square meters per second, that is, volumetric flow rate per unit width.

## A1.4 Pressure-Driven Flow in an Annulus

Annular flow features an asymmetric velocity profile. However, analytical solution is still possible in a cylindrical coordinate system. Again, let $u$ represent the velocity in the flow direction (Figure A1.4).

### *A1.4.1 Assumptions*

- Fully developed flow: $\dfrac{\partial u}{\partial x} = 0$
- Steady-state: $\dfrac{\partial u}{\partial t} = 0$
- Flow is unidirectional and parallel to the wall: $\vec{v} = u(r)$ only
- Flow is axisymmetric: $\dfrac{\partial^2 u}{\partial \theta^2} = 0$

Under these assumptions, the $x$-component of the N–S equation becomes

$$\frac{1}{\mu}\frac{\partial p}{\partial z} = C = \frac{1}{r}\frac{\partial}{\partial r}\left(r\frac{\partial u}{\partial r}\right) \tag{A1.22}$$

where $C$ is a constant. After integration, it becomes

$$u(r) = \frac{\Delta P}{4\mu L}r^2 + C_1 \ln r + C_2 \tag{A1.23}$$

The boundary conditions are

$$u = 0 \text{ at } r = R_1$$

and

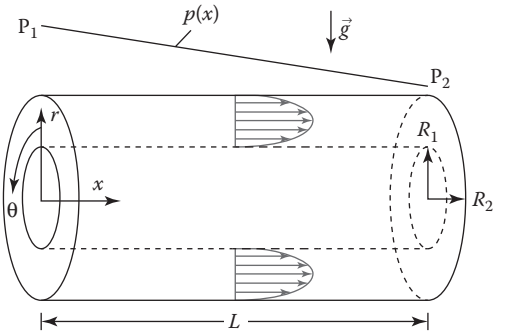


**FIGURE A1.4**
The two velocity profiles should be clearly asymmetric, that is, the max velocities have to be closer to the inner (dashed) surfaces.

$$u = 0 \text{ at } r = R_2 \tag{A1.24}$$

Substituting Equation A1.22 into Equation A1.21, we obtain

$$u(r) = \frac{\Delta P R_2^2}{4\mu L}\left[1 - \frac{r^2}{R_2^2} - \frac{\left(1 - R_1^2/R_2^2\right)}{\ln\left(R_2/R_1\right)}\ln\left(R_2/r\right)\right] \tag{A1.25}$$

The maximum velocity can be found by differentiating $u(r)$ with respect to $r$ and setting the value to be zero. The corresponding radial position is found to be

$$r_0 = \left[\frac{\left(R_2^2 - R_1^2\right)}{2\ln\left(R_2/R_1\right)}\right]^{1/2} \tag{A1.26}$$

and

$$u_{\max} = \frac{\Delta P R_2^2}{4\mu L}\left[1 - \frac{\left(1 - R_1^2/R_2^2\right)}{\ln\left(R_2/R_1\right)}\left(\frac{1}{2} + \ln\left(R_2/r_0\right)\right)\right] \tag{A1.27}$$

The maximum is closer to the inner radius but approaches the midpoint between cylinders as the clearance $R_2 - R_1$ becomes small. Three normalized velocity profiles with different $R_1/R_2$ ratios are compared in Figure A1.5.

The volumetric flow rate can be obtained as

$$Q = \int_{R_1}^{R_2} u(r) 2\pi r dr = \frac{\pi \Delta P R_2^4}{8\mu L}\left[1 - \left(\frac{R_1}{R_2}\right)^4 - \frac{\left(1 - \left(R_1/R_2\right)^2\right)^2}{\ln\left(R_2/R_1\right)}\right] \tag{A1.28}$$

and the average flow rate is simply Equation A1.26 divided by the cross-sectional area:

$$Q = \frac{R_2^2 \Delta P}{8\mu L}\left[1 + \left(\frac{R_1}{R_2}\right)^2 - \frac{1 - \left(R_1/R_2\right)^2}{\ln\left(R_2/R_1\right)}\right] \tag{A1.29}$$

The shear-stress distribution can be obtained as

$$\tau = \left|\mu \frac{du}{dr}\right| = \frac{\Delta P}{4L}\left[2r - \frac{\left(R_2^2 - R_1^2\right)}{\ln\left(R_2/R_1\right)}\frac{1}{r}\right] \tag{A1.30}$$

Clearly, it is no longer a linear function of $r$ because of the more complex flow geometry. In addition, the shear stress at the inner wall is larger than at the outer wall due to the greater curvature effect of the smaller inner cylinder. As a result, the velocity profile is no longer symmetric inside the gap; that is, it is skewed toward the inner cylinder. As $R_1 \longrightarrow R_2$, the second term in the bracket approaches zero, and the velocity profile approaches a symmetric one (see Figure A1.5).

Table A1.1 provides a comparison of the flow characteristics of the three Poiseuille-type flows.

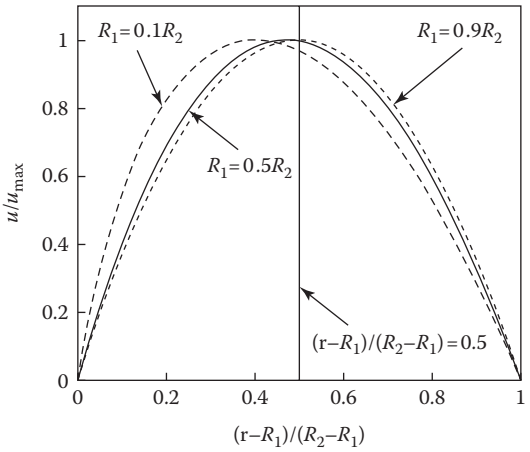


**FIGURE A1.5**
Velocity profiles of annular flow.

## A1.5 Friction Factor

The wall shear stress can be computed from the velocity gradient at the wall. For Poiseuille flow in a tube,

$$\tau_w = \left|\mu \frac{du}{dr}\right|_{r=R} \tag{A1.31}$$

According to its definition, the Darcy friction factor can be expressed as

$$f = \frac{8\tau_w}{\rho V^2} \tag{A1.32}$$

Therefore, the Darcy friction factor can be obtained for all of the flows discussed here. For Poiseuille flow in a tube,

$$f = \frac{8}{\rho V^2} \cdot \frac{R}{2} \frac{\Delta P}{L} = \frac{8}{\rho V^2} \cdot \frac{8\mu V}{d} = \frac{64\mu}{\rho V d} = \frac{64}{\mathrm{Re}} \tag{A1.33}$$

where $\mathrm{Re} = V\mathrm{d}/v$ is the Reynolds number. Similarly, for slit flow, we have

$$f = \frac{48\mu}{\rho V d} = \frac{96}{\mathrm{Re}_{D_h}} \tag{A1.34}$$

where $D_h$ is the hydraulic diameter, defined as

$$D_h = \frac{4 \times \text{area}}{\text{wetted perimeter}} \tag{A1.35}$$

**TABLE A1.1**

Comparison between Poiseuille Flow, Slit Flow, and Annular Flow

| | Velocity Profile | Maximum Velocity | Average Velocity | Flow Rate | Pressure Drop | Shear Stress |
|---|---|---|---|---|---|---|
| Poiseuille Flow | $u_{max}\left(1-\frac{r^2}{R^2}\right)$ | $\frac{R^2}{4\mu}\frac{\Delta P}{L}$ | $\frac{1}{2}u_{max}$ | $\frac{\pi\Delta P R^4}{8\mu L}$ | $\frac{8\mu LQ}{\pi R^4}$ | $\frac{\Delta P}{2L}r$ |
| Slit Flow | $u_{max}\left[1-\left(\frac{2y}{d}\right)^2\right]$ | $\frac{d^2}{8\mu}\frac{\Delta P}{L}$ | $\frac{2}{3}u_{max}$ | $\frac{\Delta P d^3 W}{12\mu L}$ | $\frac{12\mu LQ}{d^3 W}$ | $\frac{\Delta P}{L}y$ |
| Annular Flow | $\frac{\Delta P R_2^2}{4\mu L}\left[1-\frac{r^2}{R_2^2}-\frac{\left(1-R_1^2/R_2^2\right)}{\ln\left(R_2/R_1\right)}\ln\frac{R_2}{r}\right]$ | $\frac{\Delta P R_2^2}{4\mu L}f\left(\frac{R_2}{R_1}\right)$ | – | $\frac{\pi\Delta P R_2^4}{8\mu L}f\left(\frac{R_2}{R_1}\right)$ | – | $\frac{\Delta P}{4L}\left[2r-\frac{\left(R_2^2-R_1^2\right)}{\ln\left(R_2/R_1\right)}\frac{1}{r}\right]$ |

For annular flow, where the two shear stresses at the inner and outer walls are different, a friction factor can be defined using the head loss (White, 1999):

$$f = h_f \frac{D_h}{L} \frac{2g}{V^2} \tag{A1.36}$$

where, for a horizontal annular, the heat loss $h_f = \Delta P/\rho g$. Substituting $h_f$, $D_h$, and $V$ into Equation A1.33, the friction factor for laminar flow in a concentric annulus can be obtained as

$$f = \frac{64\zeta}{\mathrm{Re}_{D_h}}; \quad \zeta = \frac{\left(R_2 - R_1\right)^2}{R_2^2 + R_1^2 - \left(R_2^2 - R_1^2\right)/\ln\left(R_2/R_1\right)} \tag{A1.37}$$

where $\zeta$ is a dimensionless correction factor for the hydraulic diameter.

An interesting observation is that the friction factor of annular flow approaches that of Poiseuille flow when $R_1/R_2 \to 0$, and it approaches slit flow when $R_1/R_2 \to 1$.

### A1.6 Conclusions and Limitations

The three Poiseuille-type flow characteristics are very similar; however, there are some distinct aspects because of the geometric differences. The normalized velocity and shear-stress profiles of tubular flow and slit flow are the same. However, the $u_{\max}/V$ ratio is different. The friction factor of slit flow is greater than that of tubular flow for the same Reynolds number, indicating a higher head loss due to the elevated shear stress. Tubular flow and slit flow can be seen as two limiting cases of annular flow. This is because annular flow characteristics approach those of tubular flow when $R_1/R_2 \to 0$ and approach those of slit flow when $R_1/R_2 \to 1$.

The volumetric flow rates of the three Poiseuille-type flows all scale with the pressure drop, the reciprocal of viscosity, and the channel length. However, they scale with conduit radius (or height/width) to the fourth power. Therefore, it is expected that changing channel size will have a very strong effect on the flow rate, indicating distinct fluid flow behavior in micro- or nanochannels compared with regular-size conduits (Kleinstreuer, 2014).

The derivations assumed that the conduits are horizontal, thus avoiding the gravity effect on the flow field. If the conduits are inclined, the pressure term should be augmented to $p + \rho g z \sin\theta$ to reflect the effect of gravity. Its derivative being a constant, this will not alter the velocity profile of the flow.

The derivation of these solutions is limited to flow in the laminar regime. As the Reynolds number of the flow increases, instabilities will arise due to wall-roughness effects, and transition to turbulent flow will occur. The velocity profile will be blunted in this case, and the friction factor will be significantly larger than the one for laminar flow.

*Critique:* This project in Category #2 is a nice analytical tutorial, which highlights the fundamentals and mentions some applications of Poiseuille-type flows. Thin-film flow analysis and the equations for the hydraulic resistances, $R_{\mathrm{hydr}} = \Delta p/Q$, are missing as well as a discussion of the limitations when applying Poiseuille-type flow results to computer model validations and real-world internal flow scenarios. An abstract summarizing the essentials of the project should have been included.

Nevertheless, this report may serve as a guide to tackle some of the other tutorial course projects.

## Appendix 2: A Circular Cylinder in Laminar Cross Flow

***Course Project Report of Tutorial Category # 10***

### A2.1 Introduction

Flow past a circular cylinder is a classic problem in fluid dynamics, which has practical applications: wind blowing past the columns of a suspension bridge, construction cables and electric wires exposed to the wind, tall structures such as chimneys obstructing the wind, and so on. The type of flow past a cylinder is governed by the Reynolds number, which is the ratio of the inertia force and the viscous force $\left(\mathrm{Re} = F_{\text{inertia}}/F_{\text{viscous}} = U_\infty x D/\nu\right)$. Experimental studies show that as the Reynolds number increases, the flow shows a series of different flow structures, even when the approaching flow is steady and uniform. The flow Reynolds number determines whether the flow is steady or unsteady. At $\mathrm{Re} \approx 45$, the flow becomes unsteady, and a unique phenomenon called *vortex shedding* is observed. Vortex shedding has been a topic of interest to physicists and engineers studying fluid flow phenomena. The unsteady wake that is formed has been the cause of catastrophic structural failures in the past. Vortex-induced vibration problems are often encountered while designing bridges, cooling towers, oil rigs, and so on. Considering the impact vortex shedding can have, it is imperative to take this into account while designing structures.

Table A2.1 shows the flow structures at different Reynolds numbers. For $\mathrm{Re} < 1$, the viscous forces are more dominant than the inertia forces. This type of flow is called *creeping flow*. The pressure distribution is symmetric about the horizontal axis. Also, the streamlines are symmetric about the vertical and horizontal axes. As the Reynolds number increases, the effect of the viscous forces diminishes. At $\mathrm{Re} \approx 1$, the inertia forces are as important as the viscous forces. At $\mathrm{Re} \approx 10$, the flow separates at the cylinder surface, generating a pair of standing vortices behind the cylinder. With increasing Re, the length of the recirculation region increases linearly until the wake becomes unstable at $\mathrm{Re} \approx 45$, resulting in the onset of the Von Kármán vortex street by Hopf bifurcation [See Carlsson, n.d.].

In this tutorial, laminar cross flow over a circular cylinder has been simulated in the open-source computational fluid dynamics (CFD) software OpenFOAM to visualize the different flow characteristics at different Reynolds numbers in the laminar regime. With complex phenomena such as boundary-layer separation and oscillatory effects dominant in this regime beyond a certain Reynolds number, it is difficult to find an analytical solution. In such circumstances, CFD simulation becomes an effective means of simulating and understanding the nature of such complex phenomena. This tutorial deals with two different Re values ($\mathrm{Re} = 20$ and 200). The aim is to plot the velocity contours, the streamlines, and the lift and drag coefficients with respect to time and calculate the Strouhal number corresponding to the vortex shedding frequency. The Strouhal number (St) is a non-dimensional number that gives the frequency of vortices that are shed downstream in the wake, and it is non-dimensionalized by the diameter ($D$) and the free-stream velocity ($U_\infty$). Also, a comparison of the evolution of streamlines over time is shown for $\mathrm{Re} = 20$ and $\mathrm{Re} = 200$. The post-processing has been done using ParaView and Tecplot 360.

**TABLE A2.1**

Flow Patterns at Different Reynolds Numbers

| | | |
|---|---|---|
| 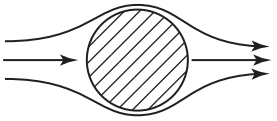 | No separation | $Re < 1$ |
| 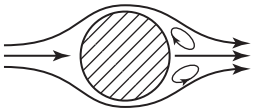 | A pair of standing vortices are formed in the wake | $5 < Re < 45$ |
| 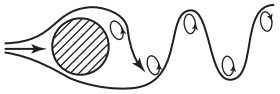 | Laminar vortex shedding | $45 < Re < 200$ |
| 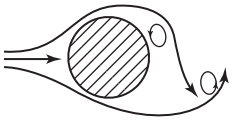 | Transition to turbulence in the wake | $200 < Re < 300$ |
| 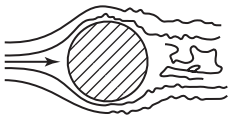 | Wake is fully turbulent | $300 < Re < 3 \times 10^5$ |
|  | Turbulent vortex shedding | $Re \gg 3 \times 10^5$ |

## A2.2 Mathematical Model

### *A2.2.1 System Sketch*

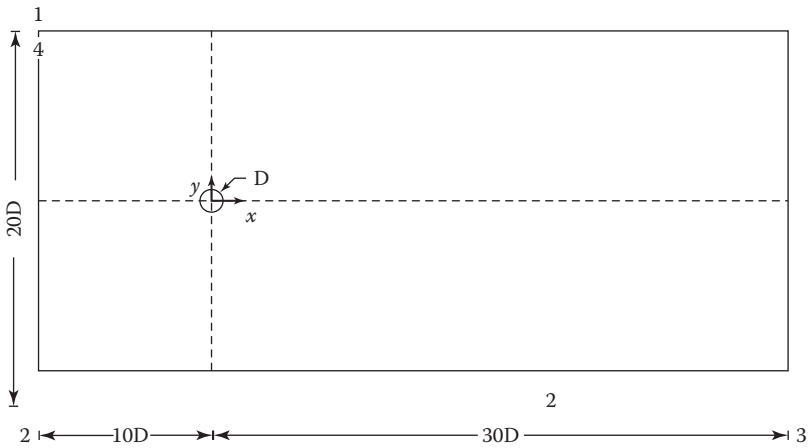


**FIGURE A2.1**
System sketch.

A cylinder of diameter unity is considered for this tutorial. The selection of the computational domain is an important part of any numerical simulation. This arbitrarily selected domain is only an approximation of the actual physical space around the cylinder. Most of the boundary conditions used in simulations can be accurately applied only if they are sufficiently removed from the region where the flow physics is being studied. The purpose behind keeping the domain large is that the inflow and outflow boundary conditions should not adversely affect the accuracy of the simulation. On the other hand, maintaining a very large domain size increases the computational cost of the simulation. Keeping this in mind, an upstream length of 10 times the diameter of the cylinder (10D) and a downstream length of 30 times the diameter of the cylinder (30D) have been maintained. A uniform velocity boundary condition is applied at the inlet. The upstream length of 10D has been selected to ensure that the velocity profile becomes fully developed by the time the flow reaches the cylinder. A downstream length of 30D has been selected to ensure that the flow field immediately after the cylinder is not influenced by the outflow boundary condition. If this is not the case, then the calculated lift and drag coefficients and the Strouhal number will have inordinately high values. The width of the flow domain is maintained at 20 times the cylinder diameter (20D) to eliminate the effect of the side boundaries on the flow field near the region of interest, which is the cylinder (Figure A2.1).

### *A2.2.2 Assumptions and Postulates*

Laminar 2-D flow of a Newtonian fluid:

$$\vec{v} = \vec{v}(x;y;t)$$

$$p = p(x;y;t)$$

*Notes:*

1. Transient $\left(\frac{\partial}{\partial t} \neq 0\right)$
2. Incompressible $(\rho = \not\subset)$
3. Negligible effect of gravity

### *A2.2.3 Boundary Conditions*

A uniform velocity $U\infty$ enters the domain at the inlet (1–2) at $x = 10D$. The outlet of the domain is defined by the face 3–4. The flow exit is treated as a pressure outlet. The walls of the domain are defined by the boundaries 1–4 and 2–3. The velocity at the cylinder wall is zero to satisfy the no-slip condition (Table A2.2).

### *A2.2.4 Describing Equations*

Based on the assumptions and postulates, the continuity and momentum equations for an incompressible, laminar, fully developed flow can be reduced as follows.

**TABLE A2.2**

Boundary Conditions

| Boundary | Boundary Condition |
|---|---|
| Inlet | $u(-10D, y) = U\infty$ |
| Side Walls | $u(x, 10D) = u(x, -10D) = 0 v(x, 10D) = v(x, -10D) = 0$ |
| Cylinder Wall | $u = v = 0$ |
| Outlet | $\left.\frac{\partial p}{\partial x}\right\|_{x=30D} = 0$ |

#### *A2.2.4.1 The Continuity Equation*

$$\nabla \cdot \vec{v} = 0 \tag{A2.1}$$

#### *A2.2.4.2 The Momentum Equation*

$$\frac{\partial \vec{v}}{\partial t} + \vec{v} \cdot \nabla \vec{v} = -\frac{1}{\rho} \cdot \nabla p + \frac{\mu}{\rho} \nabla^2 \vec{v} \tag{A2.2}$$

### A2.3 Case Setup: Cylinder in Cross Flow

#### *A2.3.1 Mesh*

Generating a good mesh is perhaps the most important and time-consuming part of setting up the simulation. If the mesh is not fine enough, the solution may not be accurate, and if the mesh is too fine, then it becomes computationally expensive, and it will take a long time for the solution to converge. The mesh can be generated in OpenFOAM itself by specifying the geometry and mesh parameters in the blockMeshDict file in the polyMesh folder. For this tutorial, the mesh has been generated in ANSYS ICEM. Care should be taken to ensure that the elements in the boundary layer must be fine and must gradually increase in size as we move away from the boundary layer. This helps capture the features in the boundary layer. This has been achieved using the O—Grid feature in ANSYS ICEM (Figure A2.2).

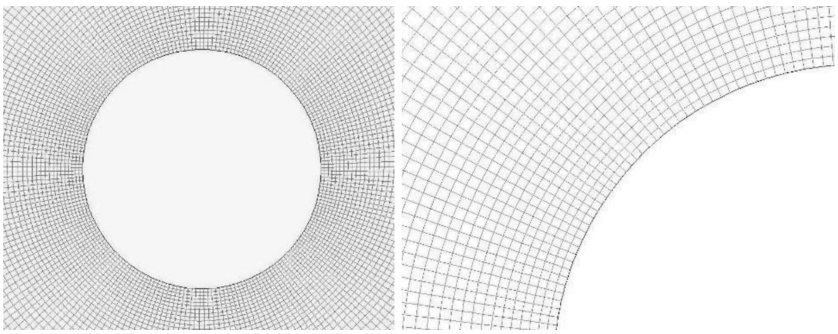

**FIGURE A2.2**
O-Grid.

Since this mesh has been created in ANSYS ICEM, it needs to be converted into OpenFOAM format. This is done by the command fluentMeshToFoam "name-of-mesh". msh. For example, if the mesh file is saved as cylinder.msh, the command will be fluentMeshToFoam cylinder.msh.

### *A2.3.2 Mesh-Independence Test*

A mesh-independence test has been performed to analyze the effect of mesh refinement on the accuracy of the solution. Representative results for three meshes are presented in Table A2.3 for Re = 200. The solution is considered to have converged when the residuals resulting from solving the mass and momentum equations fall below $10^{-5}$.

From Table A2.3, it can be seen that as the number of hexahedral elements is increased from 118,312 to 224,134, there is no appreciable change in the values of the lift and drag coefficients or the Strouhal number. So, to reduce the computational cost without compromising the accuracy of the result, Mesh 2 with 118312 hexahedral elements has been chosen for all computer simulations.

### *A2.3.3 Boundary Conditions*

The boundary conditions are set in the "0" folder. For the sake of simplicity, the kinematic viscosity ($\nu$) in the transportProperties has been set as 0.01. The diameter of the cylinder is 1 m. So for a Reynolds number of 200, the velocity has been set as 2 m/s. The boundary conditions for pressure have been set in the p file in the "0" folder. Note that the pressure in OpenFOAM is the kinematic pressure $\left(p/\rho\right)$ and has units of meters squared per second squared. The dimensions of a physical quantity in OpenFOAM are specified in square brackets. Each element inside the square brackets corresponds to the exponent of a fundamental unit: mass, length, time, temperature, quantity, current, luminous intensity (Table A2.4).

**TABLE A2.3**

Meshes used in Mesh-Independence Study

| Mesh No. | Cell Size | $C_{lrms}$ | $C_{davg}$ | Str |
|---|---|---|---|---|
| 1 | 88,087 | 0.3959 | 1.2626 | 0.2046 |
| 2 | 118,312 | 0.4549 | 1.3499 | 0.2050 |
| 3 | 220,484 | 0.4578 | 1.3516 | 0.2052 |

**TABLE A2.4**

Fundamental Units in OpenFOAM

| No. | Property | SI Unit |
|---|---|---|
| 1 | Mass | Kilogram (kg) |
| 2 | Length | Meter (m) |
| 3 | Time | Second (s) |
| 4 | Temperature | Kelvin (K) |
| 5 | Quantity | Kilogram-mole (kgmol) |
| 6 | Current | Ampere (A) |
| 7 | Luminous intensity | Candela (cd) |

### *A2.3.3 Control Dictionary*

The control dictionary contains parameters such as the type of solver, start time, end time, time steps, and so on. In our case, since the lift and drag forces have to be calculated, a separate function block has been defined at the end. The forces function computes the forces and moments acting on the patch CYLINDER, while the forceCoeffs function calculates the lift, drag, and pitching moment coefficients. The solver used is icoFoam, which is *a transient solver for incompressible laminar flow of Newtonian fluids*. It makes use of the PISO algorithm, which couples the pressure and momentum equations to resolve the flow field.

### *A2.3.4 Numerical Schemes*

The N–S equations are converted from PDEs to algebraic form using the different discretization schemes. These should be chosen properly to suit the case that is being solved. For example, first-order schemes are too diffusive and underpredict the forces and gradients, but at the same time, the solution converges faster using a first-order scheme.

#### *A2.3.4.1 Time Schemes*

A number of temporal discretization schemes are available in OpenFOAM. When specifying time schemes, care must be taken to ensure that an appropriate discretization scheme is used. To specify first time derivative terms, the keyword ddtSchemes is used. The commonly used discretization schemes are Euler, which is a first-order bounded implicit scheme, and crankNicholson ψ, which is a second-order bounded implicit scheme. Other schemes are also available.

#### *A2.3.4.2 Laplacian Schemes*

Laplacian terms are computed using Gauss integration over the cell. To do this, the gradient values must be calculated first, which is done via interpolation schemes using cell and face center data. It requires the selection of both an interpolation scheme and a surface normal gradient scheme. The keyword laplacianSchemes is used to specify Laplacian schemes. Some of the commonly used interpolation schemes are linear, upwind, linearUpwind, and limited Linear.

#### *A2.3.4.3 Gradient Schemes*

Gradient terms are calculated using the Gauss integration or least squares method. Other methods are also available although not commonly used. The Gauss integration method requires an interpolation scheme. Gradient limiters can be used to handle fluctuations in the solution flow field. The keyword gradSchemes is used to specify gradient schemes.

#### *A2.3.4.4 Divergence Schemes*

The easiest method for calculating divergence is the central difference method, which makes use of the Gauss Linear interpolation schemes. These are specified by using the keyword divSchemes.

### *A2.3.5 Solution and Algorithm Control*

The specifications of the linear solution solver, tolerances, and other algorithm controls are specified in the fvSolution file. The solvers in OpenFOAM can distinguish between

symmetric and asymmetric matrices. The symmetry depends on the structure of the equation being.

## A2.4 Post-Processing: Results and Discussion

In this section, the velocity contours and streamlines at different time intervals are shown for Re = 200. Initially, two standing vortices are formed behind the cylinder, eventually leading to the onset of oscillatory effects, resulting in the phenomenon called *Von Ka´rma´n vortex street*. The periodic shedding of vortices into the wake produces an oscillating lift and drag force on the cylinder. The variation in $C_d$ and $C_l$ with respect to time is plotted, and the non-dimensional Strouhal number is calculated.

### *A2.4.1 Comparison between Re = 20 and Re = 200*

In this section, a comparison is made between the evolution of streamlines at Re = 20 and Re = 200 with time. As shown in Table A2.1, for Re = 20, the two standing vortices do not detach from the cylinder wall, and hence, vortex shedding does not occur. At Re = 200, however, the two standing vortices elongate with time and eventually break away from the cylinder wall and start shedding alternately into the wake downstream of the cylinder (Figure A2.3).

### *A2.4.2 Velocity Contours*

The evolution of the velocity field over time is shown for Re = 200.

### *A2.4.3 Streamlines*

The evolution of streamlines over time for Re = 200 is shown in Figures A2.4 through A2.18.

These figures depict the temporal evolution of the velocity contours and streamlines at Re = 200. At $t \approx 0.1$ s, the boundary layer remains attached to the cylinder. Since there is no separation, there is no wake formed downstream of the cylinder. Figure A2.11 shows a pair of symmetric standing vortices formed near the cylinder wall. These vortices elongate with time, as shown in Figures A2.12 through A2.14, exhibiting an irregular growth. With the passage of time, the detachment of vortices from the cylinder wall takes place, and the vortex due to flow over the upper part of the cylinder sheds and starts traveling downstream into the wake. In the next instant, the lower vortex breaks away from the cylinder wall and starts traveling downstream into the wake. This oscillatory motion continues as the flow proceeds over the cylinder, as shown in Figures A2.9 through A2.18.

### *A2.4.4 Plot of Lift and Drag Coefficients*

The periodic shedding of vortices into the wake results in an oscillating lift and drag force on the cylinder, which is an indication of the onset of the Von Ka´ rma´ n vortex street. As the flow proceeds over the cylinder, the vortex shedding causes the drag and lift coefficients to oscillate about a mean value, as shown in Figures A2.19 and A2.20.

*A2.4.4.1 Plots of Cl and Cd with time*

The coefficients of lift and drag are calculated using the following formulae:

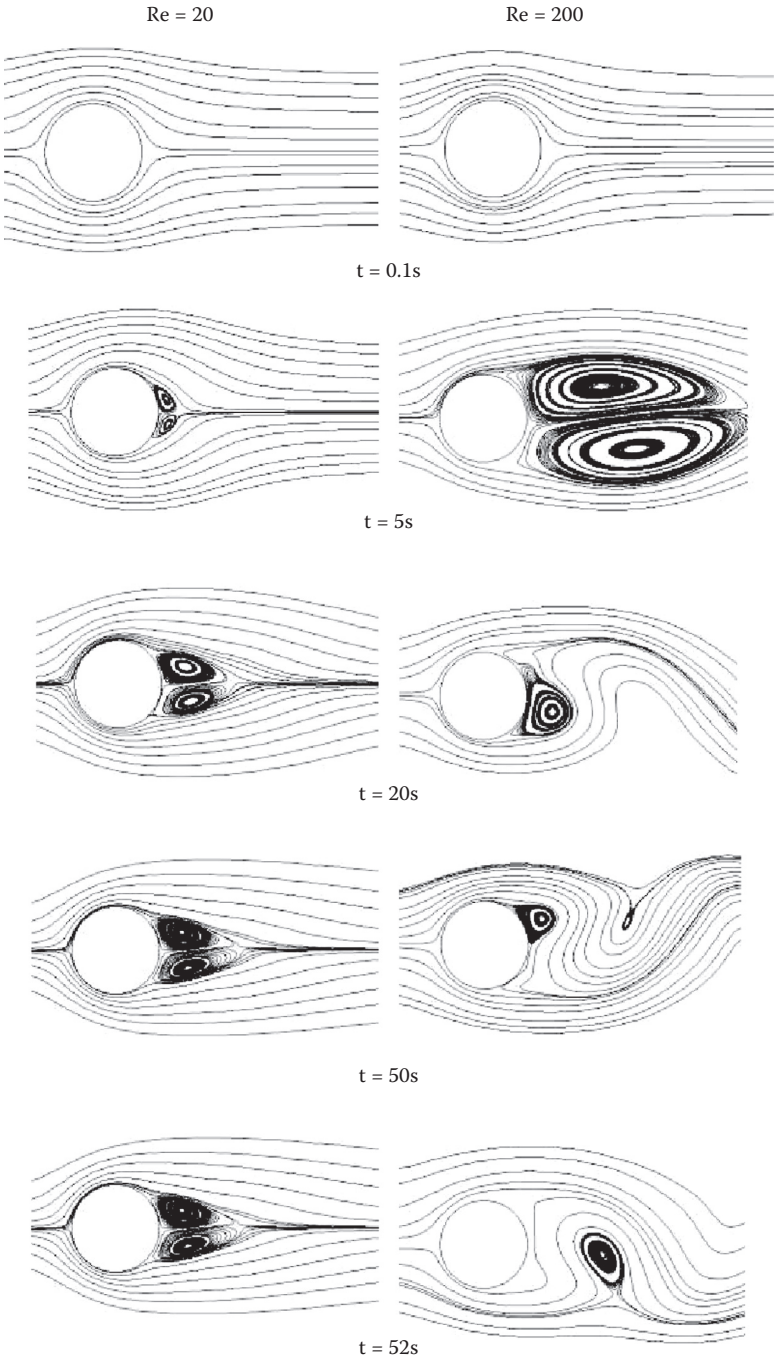


**FIGURE A2.3**
Evolution of streamlines at Re = 20 and Re = 200.

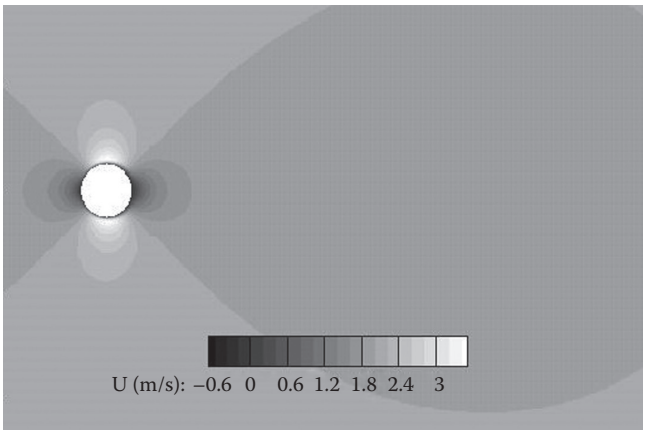


**FIGURE A2.4**
Velocity field at $t \approx 0.1$ s.

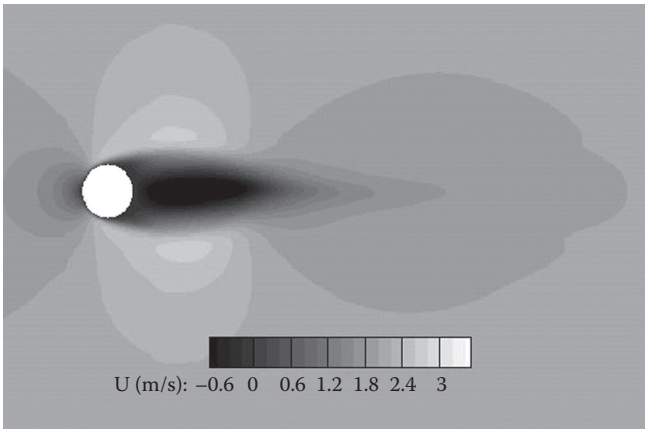


**FIGURE A2.5**
Velocity field at $t \approx 5$ s.

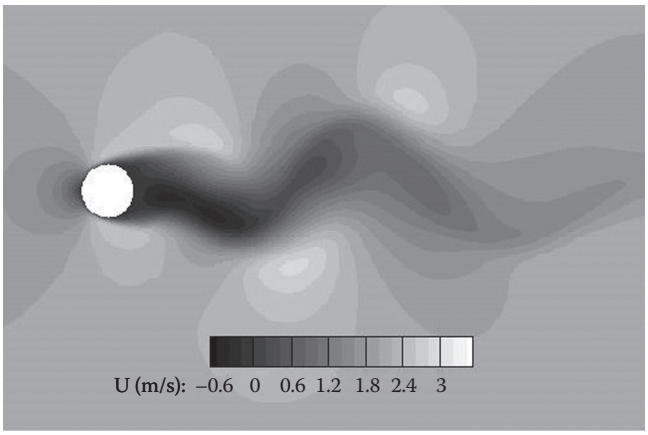


**FIGURE A2.6**
Velocity field at $t \approx 10$ s.

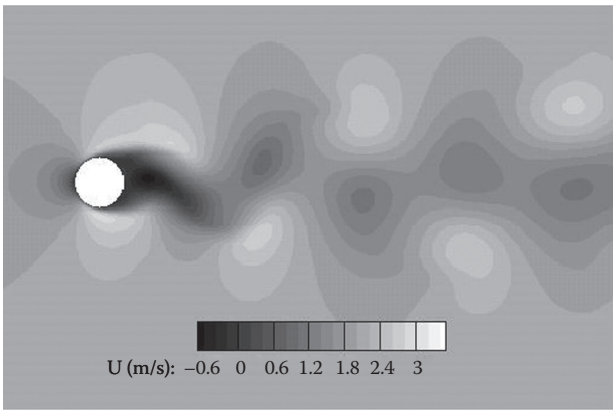


**FIGURE A2.7**
Velocity field at $t \approx 20$ s.

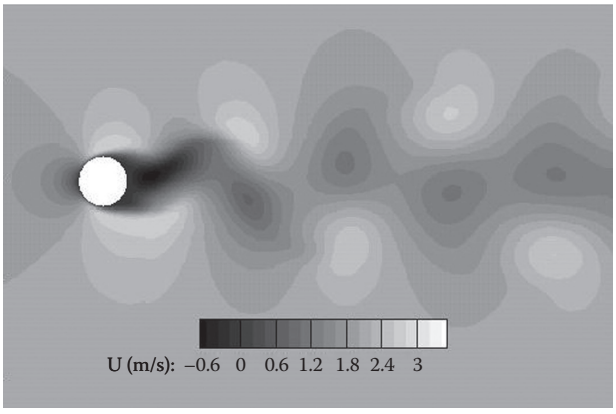


**FIGURE A2.8**
Velocity field at $t \approx 21$ s

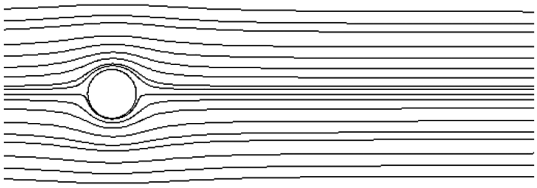

**FIGURE A2.9**
Streamlines at $t \approx 0.1$ s.

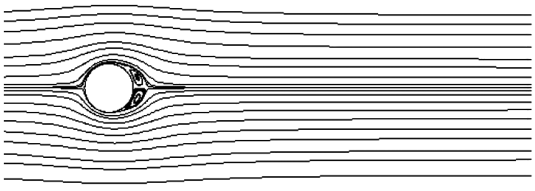

**FIGURE A2.10**
Streamlines at $t \approx 0.5$ s.

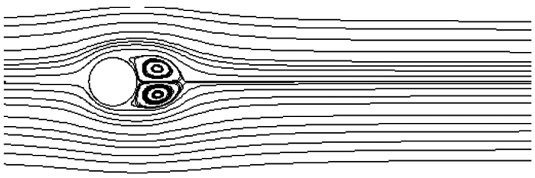

**FIGURE A2.11**
Streamlines at $t \approx 1$ s.

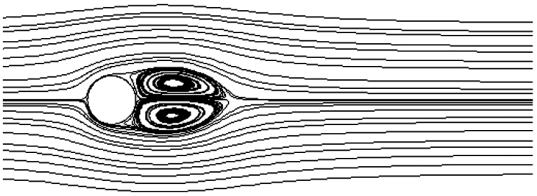

**FIGURE A2.12**
Streamlines at $t \approx 3$ s.

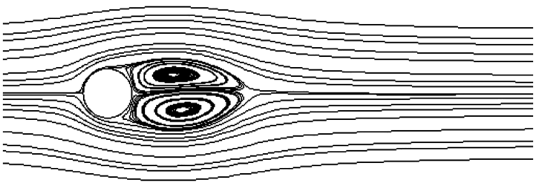

**FIGURE A2.13**
Streamlines at $t \approx 4$ s.

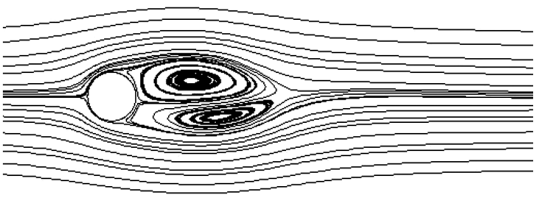

**FIGURE A2.14**
Streamlines at $t \approx 5$ s.

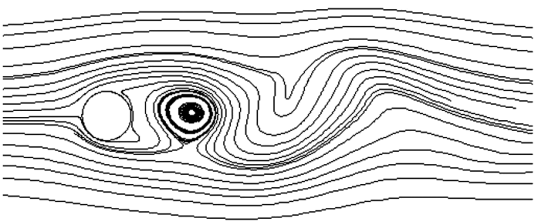

**FIGURE A2.15**
Streamlines at $t \approx 9$ s.

**FIGURE A2.16**
Streamlines at $t \approx 10$ s.

**FIGURE A2.17**
Streamlines at $t \approx 21$ s.

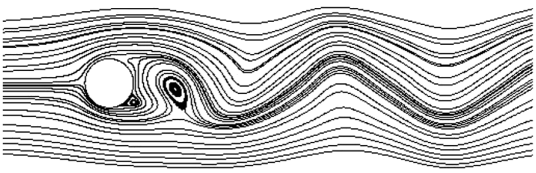

**FIGURE A2.18**
Streamlines at $t \approx 22$ s.

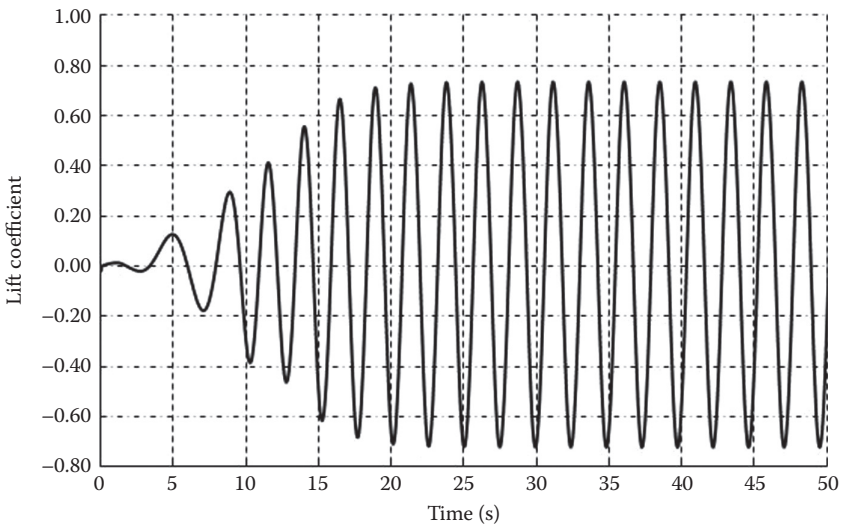


**FIGURE A2.19**
Plot of $C_l$ over time.

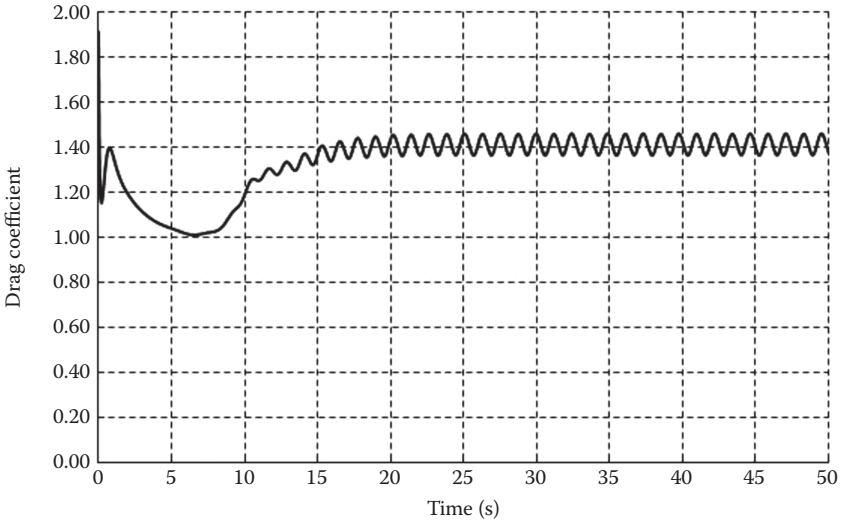


**FIGURE A2.20**
Plot of $C_d$ over time.

$$C_l = \frac{F_l}{\frac{1}{2}\rho A U_\infty{}^2} \tag{A2.3}$$

$$C_d = \frac{F_d}{\frac{1}{2}\rho A U_\infty{}^2} \tag{A2.4}$$

OpenFOAM calculates $F_l$ and $F_d$ acting on the cylinder by integrating the pressure and shear forces acting on it. This is specified in the function block in the controlDict file. The lift force acts perpendicular to the direction of the relative motion of the fluid; in this case, in the vertical direction. The drag force, on the other hand, is the resistive force acting on a body moving through a fluid. The drag force is generated parallel and opposite to the direction of motion of the body through the fluid. These directions are specified in the function block in the controlDict file.

A Fast Fourier Transform (FFT) of the plot of $C_l$ versus time can be used to ascertain the dominant frequency of vortex shedding.

Using this frequency, the non-dimensional Strouhal number (Str) can be calculated. The Strouhal number is defined as

$$Str = \frac{f \times l}{U_\infty} \tag{A2.5a}$$

Experiments have shown that the Strouhal number for large Reynolds numbers is approximately equal to 0.2 (Str $\approx$ 0.2). From Figure A2.21, it can be seen that the dominant frequency is 0.41 Hz. The corresponding Strouhal number is

$$Str = \frac{0.41 \times 1}{2} = 0.205 \tag{A2.5b}$$

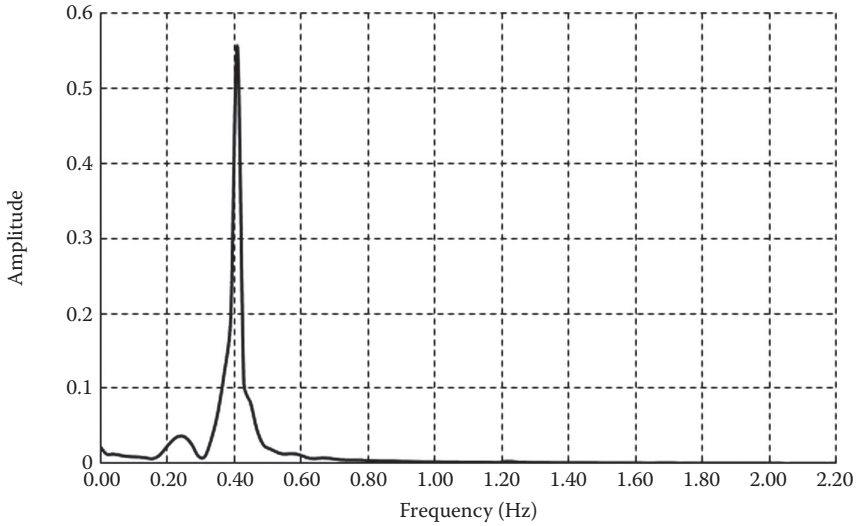


**FIGURE A2.21**
Fast Fourier Transform of $C_l$.

In Table A2.5, the $C_d$, $C_l$, and Str corresponding to Re = 100, 200 and 300 have been computed. The simulations for the same have been performed in OpenFOAM, which matches the values found in literature (see Majumdar et al., 2009; Davidson et al., 2013).

Table A2.6 lists the necessary computer resources, that is, the storage and typical run times for the simulations at different Reynolds numbers.

From Table A2.6, it can be seen that the computational time and storage for Re = 300 are very large when compared with Re = 200, and the same can be observed when comparing requirements for Re = 200 and Re = 100. This is because with higher Reynolds numbers, the velocity increases, and so does the non-dimensional Courant number (*Co*). The Courant number is defined as

**TABLE A2.5**
Lift and Drag Coefficients and Strouhal Number at Different Reynolds Numbers

| | $C_{lrms}$ | | $C_{davg}$ | | St | |
|---|---|---|---|---|---|---|
| Re | OpenFOAM | Literature (Majumdar et al., 2009) | OpenFOAM | Literature (Majumdar et al., 2009) | OpenFOAM | Literature (Majumdar et al., 2009) |
| 100 | 0.1821 | 0.1792 | 1.3484 | 1.3353 | 0.1662 | 0.1569 |
| 200 | 0.4549 | 0.4244 | 1.3499 | 1.3365 | 0.2050 | 0.1957 |
| 300 | 0.6337 | 0.6041 | 1.3981 | 1.3667 | 0.2214 | 0.2150 |

**TABLE A2.6**
Typical Computer Resources Required to Run the Simulations

| Re | CPU Time (s) | CPU Storage (GB) |
|---|---|---|
| 100 | 2,691 | 12.5 |
| 200 | 8,880 | 13.7 |
| 300 | 17,250 | 25.1 |

$$Co = \frac{U \times \delta t}{\delta x} \tag{A2.6}$$

where:

| | |
|---|---|
| $U$ | is the mean or local velocity |
| $\delta t$ | is the time step |
| $\delta x$ | is the distance traveled |

The Courant number indicates how the fluid is moving in the domain through the computational cells. If Co < 1, the fluid elements move from one cell to another within one time step. If Co > 1, the fluid particles move through more than one cell during each time step, and this may negatively impact the convergence of the solution. It is therefore advisable to maintain a Courant number less than one. Since the mesh is fixed, and the velocity has to be increased to increase the Reynolds number, the only way to keep a check on the Courant number is to reduce the time step ($\delta$t). Thus, for the same end time, more data is written by the solver, which increases the central processing unit (CPU) time and storage.

*Critique:* Project #10 provides a lot of physical insight into the fluid-flow structures at different laminar Re#s behind a cylinder in cross flow. Still, a brief discussion of laminar boundary-layer development as well as locations of flow separation at critical laminar versus turbulent Re#s would have been nice. Using open-source library functions, this report may help students to master OpenFOAM (see Appendix AI.7.4) and extend the analysis to convection heat transfer, turbulent flow, and/or flow past other submerged objects.

## Appendix 3: Enhancement of microfluidic mixing through optimization of microchannel geometry and inlet flow conditions

***Course Project of Category # 11***

This report deals with the fluid-particle dynamics simulations as well as design suggestions for "improved mixing of nanofluids in microchannels forming a Y-junction." Again using OpenFOAM (see Appendix AI.7.4), the merging of two different nanoparticle streams in wavy wall–shaped microchannels under oscillatory flow conditions is simulated and discussed. Specifically, inlet conditions and the basic microchannel geometry are changed with the goal of improving nanoparticle mixing, which is especially important in chemical and biomedical engineering.

***Nomenclature***

| | |
|---|---|
| δt | Time step |
| δx | Cell size |
| $C_d$ | Coefficient of drag |
| $C_l$ | Coefficient of lift |
| Cdavg | Average value of drag coefficient |
| $C_{lrms}$ | Root mean square (RMS) value of lift coefficient |
| Co | Courant number |
| U∞ | Free-stream velocity (m/s) |
| $\nu$ | Kinematic viscosity |
| φ | Diameter (m) |

| | |
|---|---|
| $\rho$ | Density (kg/m$^3$) |
| $f$ | Frequency of vortex shedding |
| FFT | Fast Fourier Transform |
| $p$ | Pressure (m$^2$/ s$^2$) |
| Re | Reynolds number |
| Str | Strouhal number |
| U | Velocity (m/s) |

### A3.1 Introduction

The efficient mixing of two or more species is of particular importance in the areas of chemical engineering and biomedical processing. Microfluidic devices are used for this purpose. As the characteristic dimensions of these flow channels are in the microscale, the Reynolds number is typically of $O(0.1)$ . In such laminar Re# regimes, the mixing process is largely governed by molecular diffusion, which is an inherently slow process. Consequently, many strategies have been devised to ensure effective mixing. The mixing efficiency is characterized in terms of the degree of mixing (Cheaib et al., 2016; Glasgow and Aubry, 2003). One of the common ways of achieving this is by increasing the contact area between the two species to be mixed. Many active and passive mixing methods are employed to achieve this. Typically, *active mixing methods* leverage the ability of external forces to accelerate the molecular diffusion process. For example, ultrasound transducers are integrated into the microfluidic device to generate acoustic waves to enhance mixing between the two incoming fluids or solutions. However, it has been shown that these acoustic vibrations can be a source of heat generation, resulting in undesirable reaction between the incoming fluid streams. Also, from a manufacturing standpoint, it becomes difficult to embed these tiny auxiliary devices into a micromixer. In *passive mixing*, however, the geometry of the microchannel itself is modified to create flow patterns that aid in rapid mixing. Passive micromixers do not require external energy, and the mixing process depends entirely on the chaotic advection process triggered by flow instabilities, which can be created by geometry modifications. This helps to distort or elongate the interface between the streams to be mixed.

In this Design Project #11, the effects of geometry modification and inlet flow variation are studied. Specifically, the following system parameters are computed:

1. The temporal average of the degree of mixing after the pulsating flow reaches a quasi-steady-state
2. The mixing length, which is the location down the outlet channel at which a desired level of mixing is obtained

Based on these goals, the microchannel geometry and inlet flow conditions that yield the highest average degree of mixing with the smallest mixing length are selected. Specifically, the average degree of mixing is explored, as it depends on geometric and inlet flow parameters such as the angle between the two inlet streams, the amplitude and frequency of pulsations, and the phase difference between the two inlet streams. The frequency is represented in terms of the Strouhal number. First, the geometry is optimized before the inlet flow parameters are varied. The report considers different phase shifts of the wavy walls of the microchannels. Once the phase shift that yields the highest degree of mixing is selected, the angle between the two inlet streams is increased for three different values of $\alpha$. It is shown that as $\alpha$ increases, the average degree of mixing also increases. Extending this analysis, it can be argued that purely from a mixing standpoint, a T-junction, which is a special case

of a Y-junction with $\alpha = 90°$, would yield the highest average degree of mixing. However, in most of the applications where such microchannels are used, space constraints necessitate the need for a compact geometry that does not occupy a lot of space. For this reason, the included angle between the two inlet channels is increased only up to 60°.

Once the microchannel geometry that yields the highest degree of mixing is selected, the inlet flow parameters are varied. The degree of mixing, which is undergoing spatial variations in the exit channel as well as temporal fluctuations over one pulsation cycle, is shown to be most sensitive to the amplitude and frequency of pulsation. For a fixed amplitude, the average degree of mixing increases with higher Strouhal (St) numbers. It reaches a peak at a particular St-value and then decreases with further St-increases. Finally, a microchannel with both optimized geometry and inlet flow conditions is proposed, which takes advantage of the flow instabilities created by the modified geometry and pulsating flow to yield the highest degree of mixing within the constraints mentioned earlier.

The geometry modifications are done in two distinct parts. First, the phase shift between the wavy walls of the Y-channel is varied for three different shift values (0°, 90°, and 180°). Once the shift that yields the highest degree of mixing has been determined, the bifurcation angle between the input streams is varied (30°, 45°, and 60°). After the geometry is optimized, the impact of changing the inlet flow conditions using time pulsing is explored. The pulsating flow is achieved by imposing a velocity of the form $V + \delta V \sin(\omega t + \phi)$ , where $V$, $\delta V$, $\omega$, and $\phi$ are the average velocity, pulse amplitude, pulse frequency, and phase shift, respectively. For inlet flow modification, pulsations with different phase shifts (30°, 45°, and 60°) and different phase amplitudes (0.5, 1, 1.2 mm) have been considered.

This report is organized in three distinct parts, as follows. First, the geometry of the Y-shaped microchannel is described, and the criteria for effective mixing are outlined. Then, the governing equations are presented along with the modified material properties due to the addition of nanoparticles. Finally, the computational aspects of the simulation are discussed, followed by a presentation of the results.

The average degree of mixing, as formulated by Glasgow and Aubry (2003), is expressed as

$$\zeta = 1 - \sqrt{\frac{\int_A \left(\xi - \xi_{\max}\right)^2 v \cdot \hat{n}\, dA}{\int_A \xi_{\max}^2 v \cdot \hat{n}\, dA}} \tag{A3.2.1}$$

where:

- $A$ is the channel cross section
- $\hat{n}$ is the unit vector normal to $dA$
- $v$ is the velocity vector
- $\xi$ is the mass fraction
- $\xi_{\max}$ is the mass fraction when perfect mixing occurs ($\xi_{\max} = 0.5$). $\zeta = 1$ denotes complete mixing, and $\zeta = 0$ indicates no mixing

## A3.2 Mathematical model

### A3.2.1 System sketch

The bifurcating microchannel geometry is schematically represented in Figure A3.1, where the length of the outlet channel is $L = 175$ μm, and $H = 100$ μm is the width of the channel.

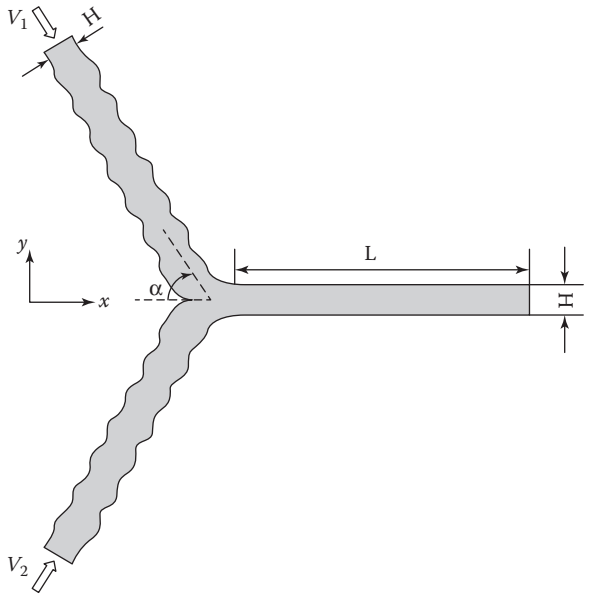


**FIGURE A3.1**
Schematic diagram of physical model.

The angle between the two inlet streams is varied ($\phi = 30°$, 45°, and 60°) to determine the angle that yields optimum mixing while maintaining the Y-configuration.

### A3.2.2 Assumptions

1. Laminar flow with constant fluid properties
2. Transient flow $\left(\dfrac{\partial}{\partial t} \neq 0\right)$
3. Incompressible flow ($\rho = C$)
4. Negligible end effects

### A3.2.3 Postulates

1. $\nabla p = \left[\dfrac{\partial p}{\partial x}; 0; 0\right]$
2. $\vec{v} = \left[v_x; v_y; 0\right]$

### A3.2.4 Governing Equations

To non-dimensionalize the system of N–S equations, the following non- dimensional variables are used:

$$v^* = \frac{\vec{v}}{V}, \nabla^* = \frac{\nabla}{1/L}, t^* = \frac{t}{1/f}, p^* = \frac{p}{\frac{1}{2}\rho V^2}, \text{ and } C^* = \frac{C}{C_o}$$

The continuity, momentum, and species-mass transfer equations are given below. For each case, the standard form of the equation is first presented, followed by the non-dimensional form.

#### *A3.2.4.1 Continuity Equation*

For incompressible flow, the mass conservation equation in divergence free form is given as

$$\nabla \cdot \vec{\upsilon} = 0 \tag{A3.3.4.1}$$

$$\nabla^* \cdot \upsilon^* = 0 \tag{A3.3.4.2}$$

#### *A3.2.4.2 Momentum Equation*

$$\frac{\partial \vec{\upsilon}}{\partial t} + \vec{\upsilon}.\nabla\vec{\upsilon} = -\frac{1}{\rho}\nabla p + v_{eff}\nabla^2\vec{\upsilon} \tag{A3.3.4.3}$$

$$St\frac{\partial \upsilon^*}{\partial t^*} + \upsilon^*.\nabla^* p^* + \frac{1}{\mathrm{Re}}\nabla^{*2}\upsilon^* + f_{body} \tag{A3.3.4.4}$$

#### *A3.2.4.3 Species-Mass Transfer Equation*

$$\frac{\partial C}{\partial t} + \vec{\upsilon}\cdot\nabla C = Deff\,\nabla^2 C \tag{A3.3.4.5}$$

$$St\frac{\partial C^*}{\partial t^*} + \upsilon^*.\nabla^* C^* + \frac{1}{Pe_D}\nabla^{*2}C^* \tag{A3.3.4.6}$$

### A3.3 Case-Study Setup

The CFD simulations presented in this report have been carried out using the open-source CFD software OpenFOAM® (see Appendix AI.7.4). The results are obtained after the simulation has reached a quasi-steady-state, when the solution no longer varies with time. This means that the simulations must run for a sufficiently long time, and appropriately sized time step sizes must be chosen.

#### *A3.3.1 Mesh*

Generating a good mesh is perhaps the most important and time-consuming part of setting up the simulation. If the mesh is not fine enough, the solution may not be accurate, and if the mesh is too fine, then it becomes computationally expensive, and it will take a long time for the solution to converge. The mesh can be generated in OpenFOAM itself by specifying the geometry and mesh parameters in the blockMeshDict file in the polyMesh folder. For this tutorial, the mesh has been generated in ANSYS ICEM. Care should be taken to ensure that the elements near the wall must be fine and must gradually increase in size as we move away from the wall. This helps to capture the large velocity gradients near the wall (Figure A3.2).

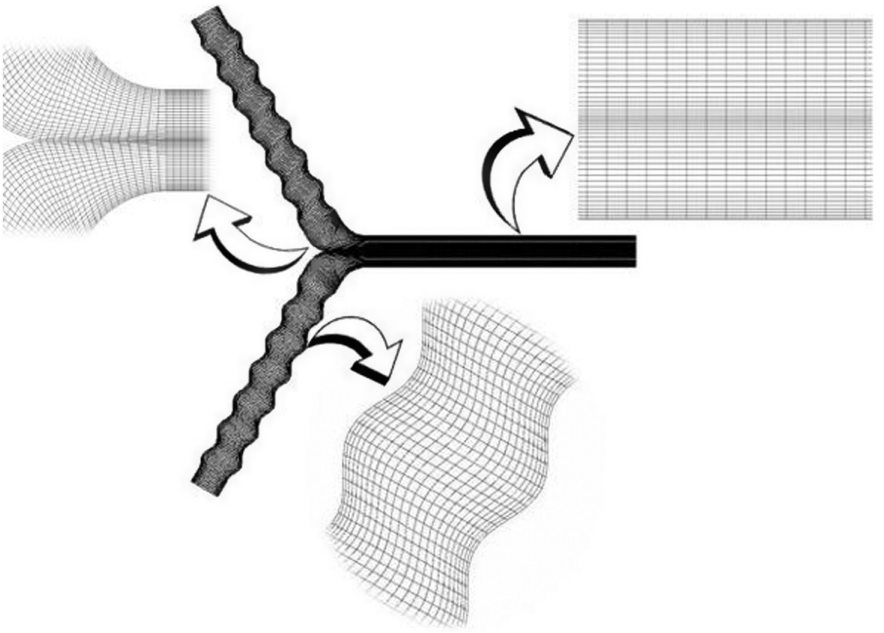

**FIGURE A3.2**
Grid layout for $\alpha = 60°$ and phase shift of 90°.

Since this mesh has been created in ANSYS ICEM, it needs to be converted into OpenFOAM format. This is done by using the command fluentMeshToFoam "name-of-mesh".msh. For example, if the mesh file is saved as Ychannel.msh, the command will be fluentMeshToFoam Ychannel.msh.

The impact of mesh size on the simulation results was also considered. To neglect end effects, the outlet channel length up to 160 μm has been considered in the results (Section A3.4).

Figure A3.3 shows the variation of the average degree of mixing along the outlet channel for different mesh sizes. It can be seen that a coarse grid overpredicts the degree of mixing, especially at the start of the outlet channel. The coarsest grid, which corresponds to $N = 1036$ elements, yields an error of 35.6% when compared with a refined grid comprising 20,711 hexahedral elements. A mesh-independence test has been performed to analyze the effect of mesh refinement on the accuracy of the solution. Representative results for three meshes are presented in Table A3.1 for an included angle of 30° between the two inlet streams and a phase shift of 90°. The solution is considered to have converged when the residuals resulting from solving the mass and momentum equations fall below $10^{-4}$.

From Table A3.1, it can be seen that as the number of hexahedral elements is increased from 6248 to 20,711, there is no appreciable change in the value of $\zeta$. So, to reduce the computational cost without compromising the accuracy of the result, Mesh 3 with 6248 hexahedral elements has been chosen for all computer simulations.

### *A3.3.2 Material Properties*

This report describes the mixing between two different nanofluids. A single-phase approach is considered. In this approach, the suspended nanometer-sized particles are in thermal equilibrium with the bulk liquid phase. The relative velocity between the two

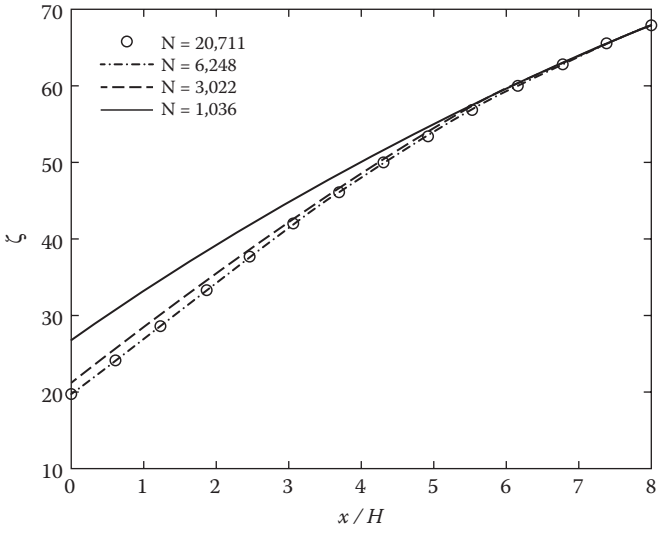


**FIGURE A3.3**
Impact on mesh size on the average degree of mixing.

phases is negligible. This is because the nanoparticles are so small that they closely follow the fluid streamlines, making the nanofluid behave like a homogeneous mixture.

The mixture properties in the case of nanofluids are a function of the particle volume fraction. If the particles are assumed to be spherical and mono-disperse and to form a homogeneous dilute suspension in the base fluid, the modified density and viscosity of the nanofluid can be expressed as follows:

$$\rho_{eff} = \phi\rho_p + (1-\phi)\rho bf \tag{A3.4.2.1}$$

and

$$\frac{\mu_{eff}}{\mu_{bf}} = (1-\phi)^{2.5} \tag{A3.4.2.2}$$

Equation A3.4.2.1 was developed by Brinkman (1952) to account for moderate particle concentrations up to 4%.

For these simulations, two different nanofluids were introduced through the two inlets. An $Al_2O_3$–water nanofluid with an $Al_2O_3$ volume fraction of 4% was introduced through the top inlet, and an $Al_2O_3$–water nanofluid with an $Al_2O_3$ volume fraction of 2% was injected through the bottom inlet. Table A3.2 gives the nanofluid properties in SI units.

**TABLE A3.1**
Meshes used in the Mesh Independence Study

| No. | Cell Size | ζ at |
|---|---|---|
| 1 | 1,036 | 42.8071 |
| 2 | 3,022 | 42.3142 |
| 3 | 6,248 | 42.0384 |
| 4 | 20,711 | 41.9370 |

**TABLE A3.2**

Material Properties of Nanofluids

| | Density ($\rho_{eff}$) | Viscosity ($\mu_{eff}$) |
|---|---|---|
| Inlet 1 | 1117.28 | $9.3\times10^{-4}$ |
| Inlet 2 | 1057.64 | $9.8\times10^{-4}$ |

### *A3.3.3 Boundary Conditions*

The boundary conditions are set in the "0" folder. The boundary conditions for pressure have been set in the p file in the "0" folder. Note that the pressure in OpenFOAM is the kinematic pressure $p/\rho$ and has the units of meters squared per seconds squared. The dimensions of a physical quantity in OpenFOAM are specified in square brackets. Each element inside the square brackets corresponds to the exponent of a fundamental unit: mass, length, time, temperature, quantity, current, and luminous intensity (Table A3.3).

The simulations are divided into two broad categories. In the first part, geometry optimization is the end goal. In these simulations, a uniform, constant velocity is assigned to each of the two inlets. A zero–pressure gradient boundary condition is applied at the exit of the outlet channel. A no-slip boundary condition is applied at the walls (Table A3.4).

The second part of the simulations involves inlet flow modifications. Instead of a uniform velocity, pulsating velocity profiles of the form $V+\delta V\sin(wt)$ $V+\delta V\sin(wt+\phi)$ are applied at the two velocity inlets. The $\phi$ denotes the phase shift between the two profiles. The exit is set as a pressure outlet (Table A3.5).

**TABLE A3.3**

Fundamental Units in OpenFOAM

| No. | Property | SI Unit |
|---|---|---|
| 1 | Mass | kilogram (kg) |
| 2 | Length | meter (m) |
| 3 | Time | second (s) |
| 4 | Temperature | Kelvin (K) |
| 5 | Quantity | kilogram-mole (kgmol) |
| 6 | Current | Ampere (A) |
| 7 | Luminous intensity | candela (cd) |

**TABLE A3.4**

Boundary Conditions for Geometry Modification

| Boundary | Boundary Condition |
|---|---|
| Inlet 1 | $\vec{\upsilon}\cdot\hat{n}=U_{in}$ |
| Inlet 2 | $\vec{\upsilon}\cdot\hat{n}=U_{in}$ |
| Wall | $\vec{\upsilon}=0$ |
| Outlet | $\dfrac{\partial p}{\partial x}=0$ |

**TABLE A3.5**

Boundary Conditions for Inlet Flow Modification

| Boundary | Boundary Condition |
|---|---|
| Inlet 1 | $V + \delta V \sin(wt)$ |
| Inlet 2 | $V + \delta V \sin(wt + \phi)$ |
| Wall | $\vec{v} = 0$ |
| Outlet | $\frac{\partial p}{\partial x} = 0$ |

### *A3.3.4 Numerical Schemes*

The N–S equations are converted from PDEs to algebraic form using the different discretization schemes. These should be chosen properly to suit the case that is being solved. For example, first-order schemes are too diffusive and underpredict the forces and gradients, but at the same time, the solution converges faster using a first-order scheme.

#### *A3.3.4.1 Time Schemes*

A number of temporal discretization schemes are available in OpenFOAM. When specifying time schemes, care must be taken to ensure that an appropriate discretization scheme is used. To specify time derivative terms, the keyword ddtSchemes is used. The commonly used discretization schemes are Euler, which is a first-order bounded implicit scheme, and crankNicholson (ψ), which is a second-order bounded implicit scheme. Other schemes are also available.

#### *A3.3.4.2 Laplacian Schemes*

Laplacian terms are computed using Gauss integration over the cell. To do this, the gradient values must be calculated first, which is done via interpolation schemes using cell and face center data. It requires a selection of both an interpolation scheme and a surface normal gradient scheme. The keyword laplacianSchemes is used to specify Laplacian schemes. Some of the commonly used interpolation schemes are linear, upwind, linearUpwind, and limitedLinear.

#### *A3.3.4.3 Gradient Schemes*

Gradient terms are calculated using the Gauss integration or least squares method. Other methods are also available although not commonly used. The Gauss integration method requires an interpolation scheme. Gradient limiters can be used to handle fluctuations in the solution flow field. The keyword gradSchemes is used to specify gradient schemes.

#### *A3.3.4.4 Divergence Schemes*

The easiest method for calculating divergence is the central difference method, which makes use of the Gauss Linear interpolation schemes. These are specified by using the keyword divSchemes.

### *A3.3.5 Solution and Algorithm Control*

The specifications of the linear solution solver, tolerances, and other algorithm controls are specified in the fvSolution file. The solvers in OpenFOAM can distinguish between

symmetric and asymmetric matrices. The symmetry depends on the structure of the equation being solved.

### *A3.3.6 Quasi-Stationary State*

The results presented in this report are all recorded when the simulation results no longer vary between subsequent cycles.

In Figure A3.4, the average degree of mixing, shown by the solid black line, is plotted along the length of the outlet channel. The dotted lines represent $\zeta + \sigma_\mu$ and $\zeta + \sigma_\zeta$, where $\sigma_\zeta$ is the standard deviation of the temporal fluctuations over a cycle at quasi-stationary state for each location. It can be seen that the average degree of mixing increases down the channel due to mass diffusion across the interface between the two inlet streams, while the temporal fluctuations decrease. This can be attributed to the fact that these fluctuations are damped due to viscous effects, which become more pronounced toward the channel outlet.

## A3.4 Results and Discussion

For low Re# flows through microchannels, the mixing length can be prohibitively long (1 cm). To reduce the mixing length, there must exist some transverse components that distort the volume of fluid over the channel cross section. The presence of secondary flow structures triggered by geometry modifications will help reduce the length over which diffusion must act to homogenize the unmixed regions in the outlet channel. These chaotic fluctuations in the flow serve to stretch and fold the fluid, thus reducing the overall mixing length.

### *A3.4.1 Comparison between Diffusion and Dispersion*

Figure A3.5 shows the variation of the average degree of mixing along the length of the outlet channel with and without geometry modifications. In this case, a wall phase shift of 0° is considered for the modified geometry. It can be seen that the peak average of mixing

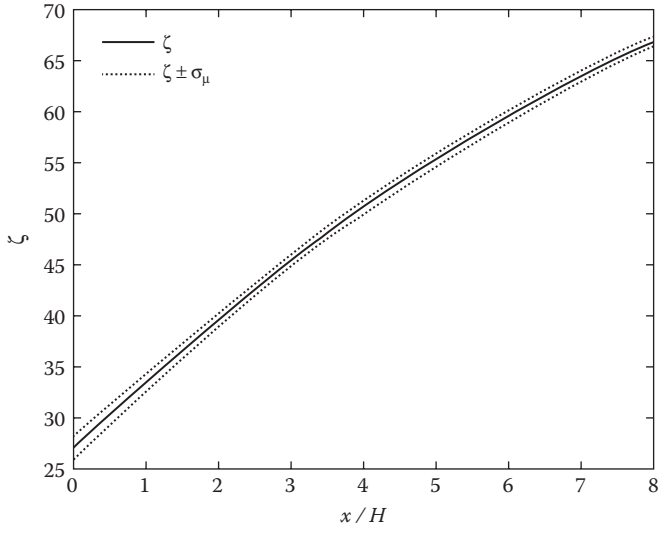


**FIGURE A3.4**
Variation of average degree of mixing and standard deviation along the length of the outlet channel.

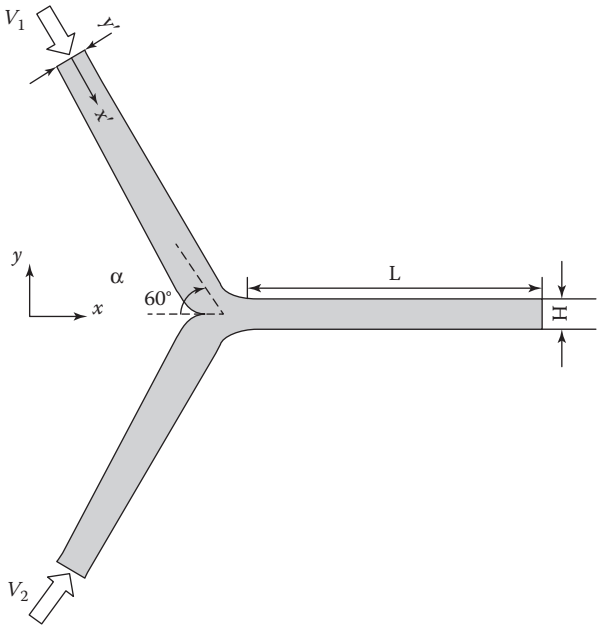


**FIGURE A3.5**
Schematic diagram of simple geometry.

in this case is smaller than for the modified geometry with wavy walls. This can be attributed to the additional flow structures generated in the flow by the wavy nature of the walls of the two inlet streams. The undulating walls present an anisotropic resistance to the flow. There is less resistance to flow in the direction parallel to the crests and troughs of the walls (along y′) than the orthogonal direction (along x′). Here, x′ and y′ represent the local coordinate axes as shown in Figure A3.6. This generates an axial pressure gradient along y′, which in turn, gives rise to transverse components in the flow, resulting in the formation of recirculation zones.

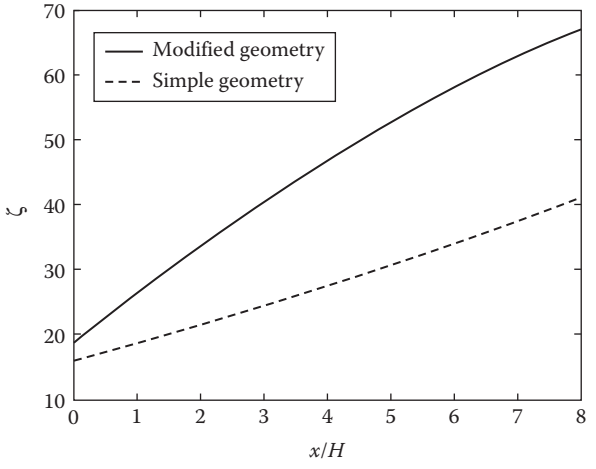


**FIGURE A3.6**
Comparison between simple and modified geometry.

### *A3.4.2 Modification of Geometry*

#### A3.4.2.1 Effect of Phase Shift

Numerical simulations for the transient mixing of two inlet streams were carried out for three different values of phase angles (0°, 90°, and 190°). Quasi-steady-state is reached when the same volume fraction of Nanofluid 1 appears for each of these phase angles.

Figure A3.6 shows the variation of the mixing index (see Equation A3.2.1) along the outlet channel for different phase shifts. It can be seen that for the phase shift $\phi = 90°$, the mixing index is the highest at every location along the outlet channel.

The vortical structures created due to wall-geometry modifications are shown in Figures A3.7 through A3.9 for different phase shifts. It can be seen that when $\phi = 180°$, the

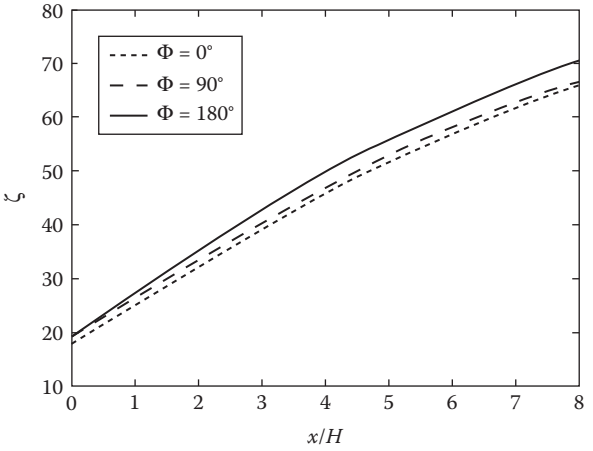


**FIGURE A3.7**
Variation of average degree of mixing for different phase shifts.

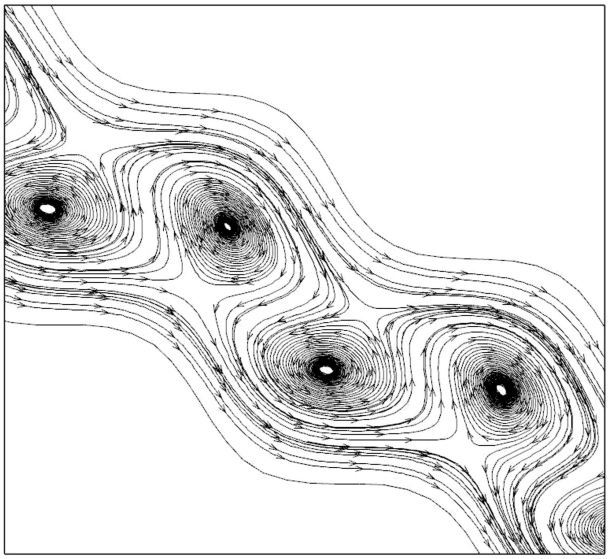

**FIGURE A3.8**
Streamline pattern for $\phi = 0°$.

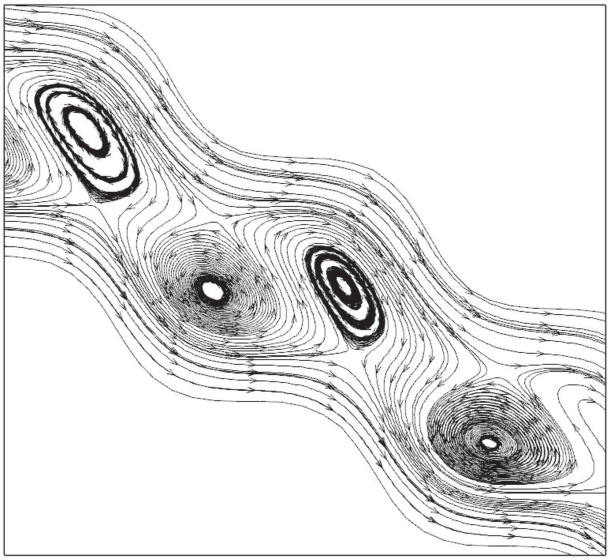

**FIGURE A3.9**
Streamline pattern for $\phi = 90°$.

vortices trapped in the troughs of the channel walls recirculate in the indentations without having much interaction with the core flow. For walls with $\phi = 0°$, the flow separates near the channel walls, and standing vortices are formed in the troughs created by the channel geometry. In this configuration, there is greater interaction between the mean flow and the vortices formed, which shows a higher, albeit marginal, increase in the degree of mixing compared with the case with $\phi = 180°$. With $\phi = 90°$, there is a perceptible increase in the degree of mixing, as shown in Figure A3.10. This enhanced mixing can be attributed to the impingement of the core flow into the space occupied by the vortices, resulting in greater interaction between the mean flow and the recirculation zones formed in the troughs. This increased interaction between the core flow and the vortices in the two inlet channels results in increased perturbations at the start of the outlet channel, which in turn, increases the average degree of mixing along the length of the outlet channel.

*A3.4.2.2 Effect of Included Angle*

The included angle $\alpha$ between the inlet channels has been varied to analyze the effect of the angle between the two inlet streams on the degree of mixing.

Figure A3.11 depicts the variation of the average degree of mixing along the outlet channel for different values, that is, $\alpha = 30°$, 45°, and 60°. With larger $\alpha$-values, the average degree of mixing increases. This can be attributed to the effect of gravity, which becomes more pronounced as the value of $\alpha$ increases. To counter the effect of gravity in the bottom channel, more pumping power would be required. However, because only the degree of mixing along the outlet channel was of interest, extraneous factors such as pumping power have been neglected in this study.

Extending this analysis for higher values of $\alpha$ suggests that the degree of mixing for a T-junction will be higher than for any of the cases considered. However, most of these microchannels are used in lab-on-a-chip and other miniaturized total analysis system ($\mu$-TAS) devices, where space constraints limit the modification of geometry of these devices.

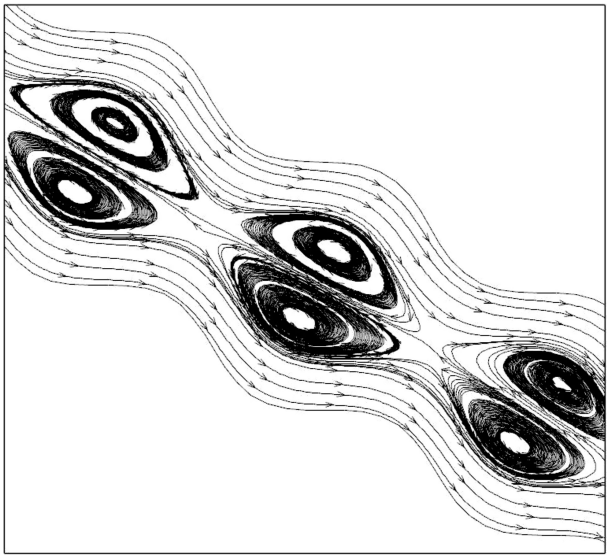

**FIGURE A3.10**
Streamline pattern for $\phi = 180°$.

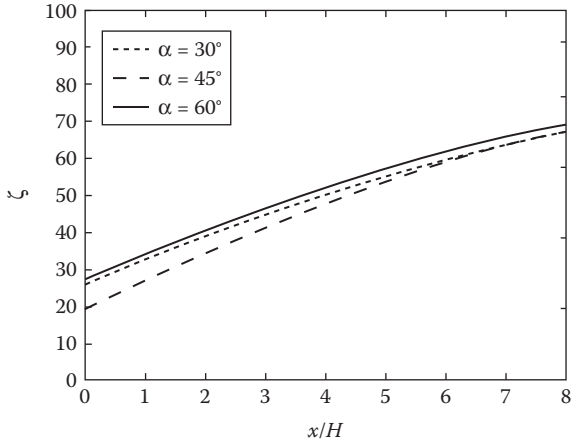


**FIGURE A3.11**
Variation of average degree of mixing along the outlet channel for different included angles.

### *A3.4.3 Modification of Inlet Flow Conditions*

#### *A3.4.3.1 Effect of Pulsation Amplitude*

Numerical simulations for the transient mixing of two pulsating streams were carried out for different values of pulsation amplitude, as shown in Table A3.6.

The simulations were run with $\phi = 90°$ and $St = 2$.

Figure A3.12 depicts the variation of the average degree of mixing for different values of $\delta V/V$ at three different locations down the outlet channel in the quasi-stationary state. From Figure A3.12, it can be seen that as the amplitude of the pulsating velocity profile increases, the mean degree of mixing also increases. It is also observed that as the length along the outlet channel increases, the average degree of mixing also increases. The slope

**TABLE A3.6**

Different Amplitude Values for $St = 2$

| $\delta V/V$ | $V$ | $\delta V$ |
|---|---|---|
| 0.5 | 0.05 | 0.025 |
| 2 | 0.05 | 0.1 |
| 3 | 0.05 | 0.15 |
| 4 | 0.05 | 0.2 |
| 5 | 0.05 | 0.25 |
| 6.5 | 0.05 | 0.325 |
| 7.5 | 0.05 | 0.375 |
| 10 | 0.05 | 0.5 |

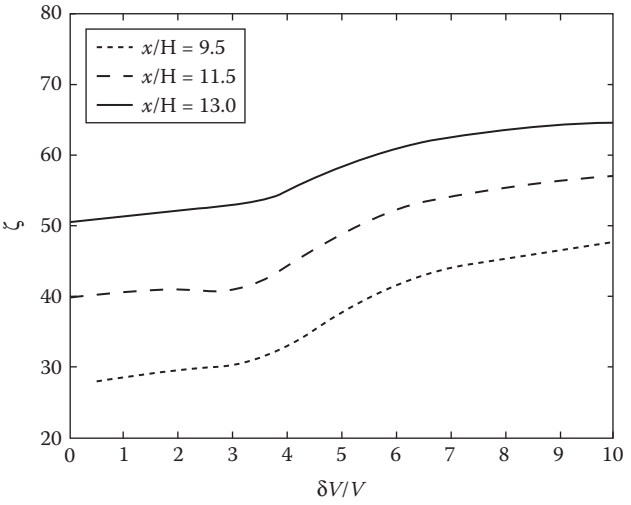


**FIGURE A3.12**
ζ versus $\delta V/V$ for $St = 2$ at $x/H = 9.5$, 11.5, and 13.0.

of the curve increases for all values of $\delta V/V$, which suggests that the average degree of mixing is not bounded by $\delta V/V$ values. However, it can be seen that for $3.5 \leq \delta V/V \leq 6.5$, the slope of the curve rises sharply, showing a marked improvement in mixing compared with other values of $\delta V/V$.

A close-up view of the outlet channel is shown in Figure A3.13 at different instants of time during one pulsation cycle for different $\delta V/V$.

Figure A3.13 shows the evolution of species mass fraction with the flow during one pulsation cycle at intervals of $T/6$ for $St = 1.0$ and $\delta V/V = 0.5$. Here, the mass fraction of only one species is shown. This is indicative of the average degree of mixing where $\zeta = 0.5$ denotes perfect mixing. The mass fraction variation of the species entering through the top channel along the length of the outlet channel is shown in Figure A3.13. Black indicates a mass fraction of 1. Grey indicates a mass fraction of 0. White represents a mass fraction of 0.5 indicating well-mixed regions. The interface region represented by the narrow white band, clearly separates the black and grey regions where the mass fractions are 0 and 1 respectively. The width of this interface region remains fairly constant as the flow develops. Figures A3.13 through A3.15 show the evolution of species mass fraction with the flow

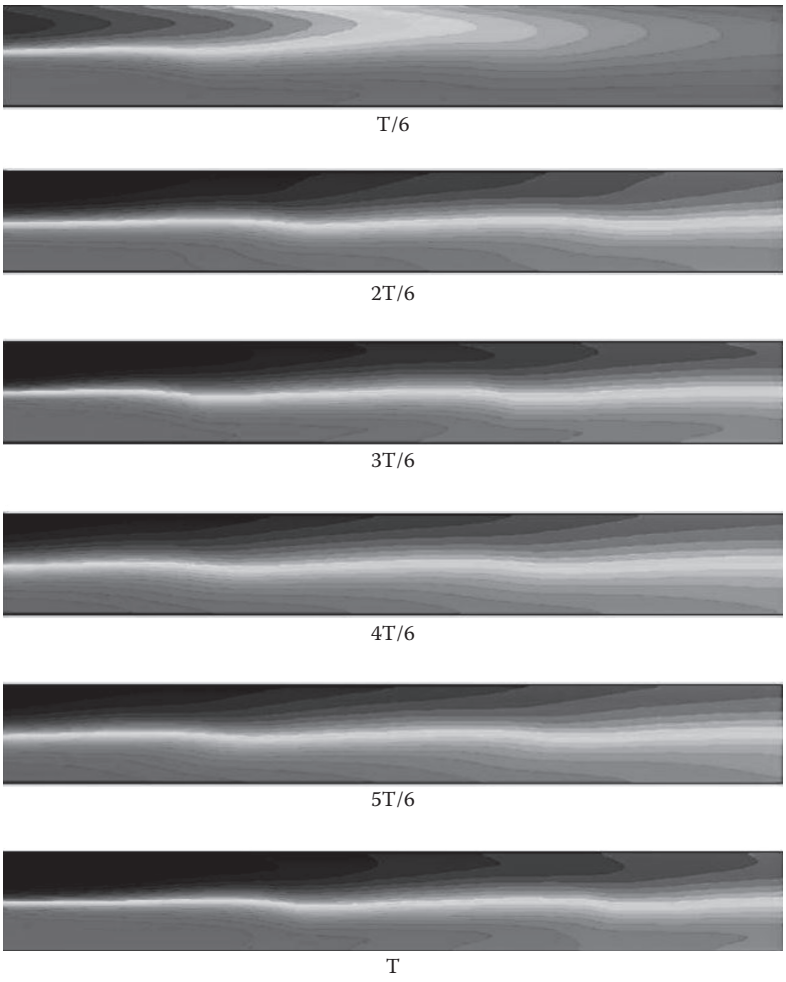


**FIGURE A3.13**
Average degree of mixing for $St = 1.0$ and $St = 0.5$.

during one pulsation cycle at intervals of $T/6$ for $St = 1.0$ and $\delta V/V = 2.0$ and 7.5 respectively. In both cases, the width of the interface region grows as the flow evolves and is greater than that at $\delta V/V = 0.5$. This results in better mixing. With $\delta V/V = 7.5$, the width of the interface region is almost double the interface width when $\delta V/V = 2.0$.

*A3.4.3.2 Effect of Pulsation Frequency*

Numerical simulations were carried out for different values of pulsation frequency to investigate the impact of frequency on the degree of mixing. Table A3.7 lists the different frequency values in terms of the non-dimensional Strouhal number for which the simulations were carried out.

The variation of the average degree of mixing along the outlet channel at different pulsation frequencies is plotted for three different values of pulsation amplitude: $\delta V/V = 0.5,3,5$.

From Figures A3.16 through A3.18, it can be seen that the average degree of mixing is small at high frequencies. At low frequencies as well, the average degree of mixing is

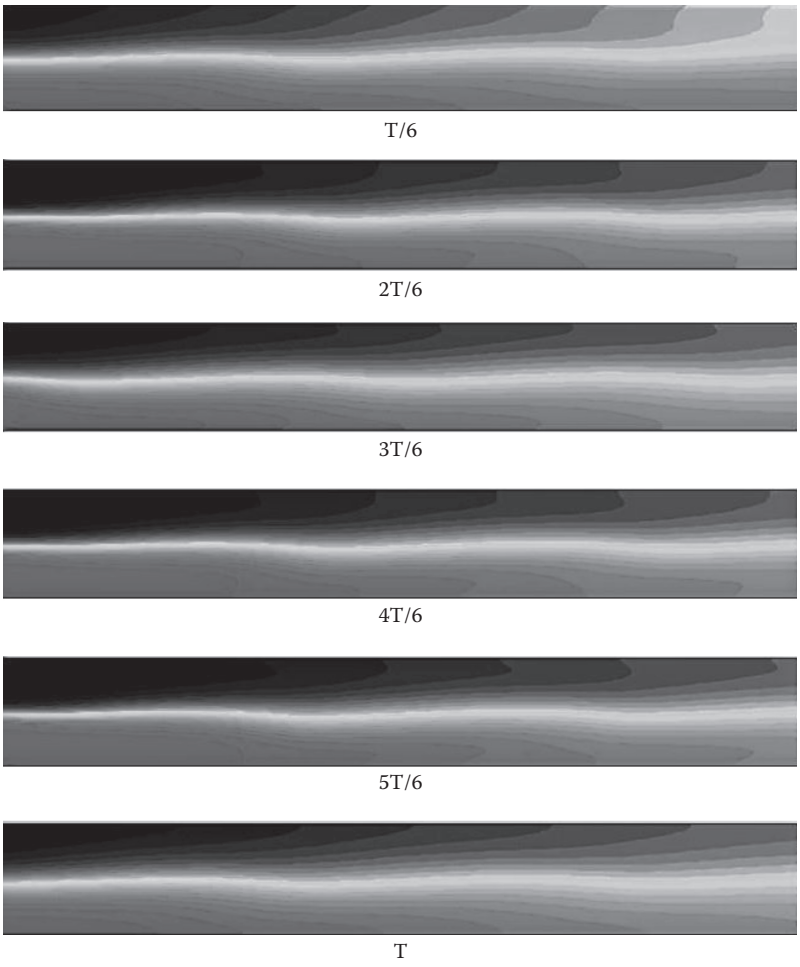


**FIGURE A3.14**
Average degree of mixing for $St = 1.0$ and $\delta V/V = 2.0$.

small. The highest degree of mixing occurs at a certain range of Strouhal numbers for each value of $\delta V/V$. The degree of mixing initially increases with increase in Strouhal number, reaches an optimum value and then decreases with further increase in Strouhal number. This can be attributed to the fact that pulsating flows increase the interface length between the two input streams across which mixing takes place. As the pulsation frequency increases, the interface length between the two streams increases which increases the degree of mixing. However, this property of pulsating flows is valid only up to certain frequencies beyond which the degree of mixing decreases with further increase in frequency. This is because at very large frequencies, the time period of pulsation is so small that the interface-overlap between the two streams is almost non-existent, resulting in a decrease in the overall degree of mixing. The Strouhal numbers which yield maximum degree of mixing decreases as the value of $\delta V/V$ increases. As the pulsation amplitude increases, the interface overlap at low frequencies increases. However, with further increase in frequency, the increase in the overlap length due to increase in amplitude is negated by the reduced time period of pulsations which reduces the overlap length.

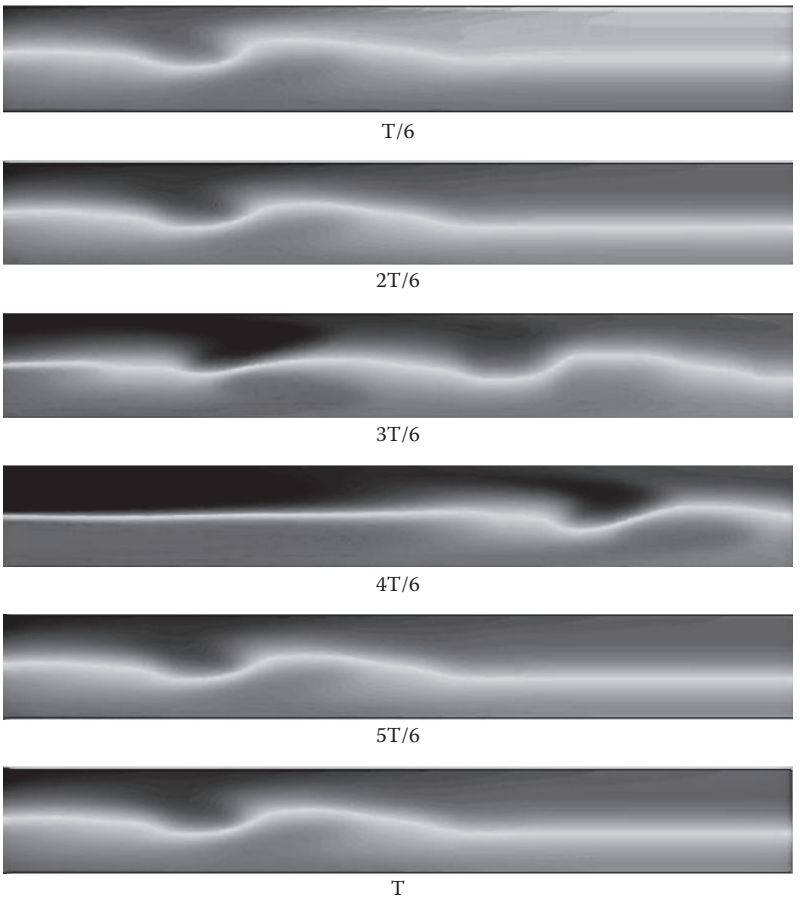


**FIGURE A3.15**
Average degree of mixing for $St = 1.0$ and $\delta V/V = 7.5$.

**TABLE A3.7**

Frequency Values at Different Strouhal Numbers for Different Pulsation Amplitudes

| *St* | *f* | $\delta V/V$ |
|---|---|---|
| 0.1 | 5 | 0.5, 3, 7.5 |
| 0.2 | 10 | 0.5, 3, 7.5 |
| 0.4 | 20 | 0.5, 3, 7.5 |
| 0.5 | 25 | 0.5, 3, 7.5 |
| 0.6 | 30 | 0.5, 3, 7.5 |
| 0.8 | 40 | 0.5, 3, 7.5 |
| 1.0 | 50 | 0.5, 3, 7.5 |
| 2.0 | 100 | 0.5, 3, 7.5 |
| 3.0 | 150 | 0.5, 3, 7.5 |
| 4.0 | 200 | 0.5, 3, 7.5 |

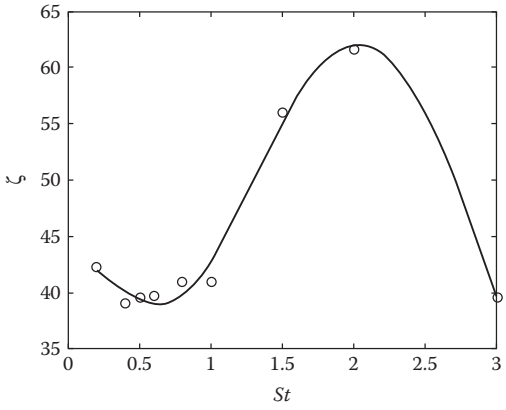


**FIGURE A3.16**
Average degree of mixing at different frequencies and $\delta V/V = 0.5$.

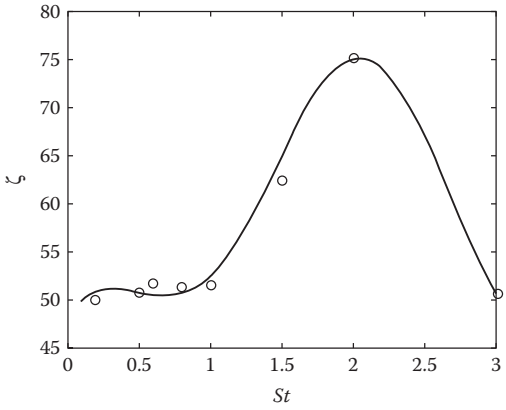


**FIGURE A3.17**
Average degree of mixing at different frequencies and $\delta V/V = 3.0$.

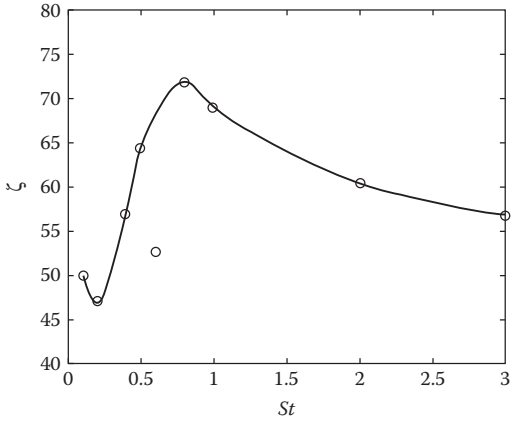


**FIGURE A3.18**
Average degree of mixing at different frequencies and $\delta V/V = 7.5$.

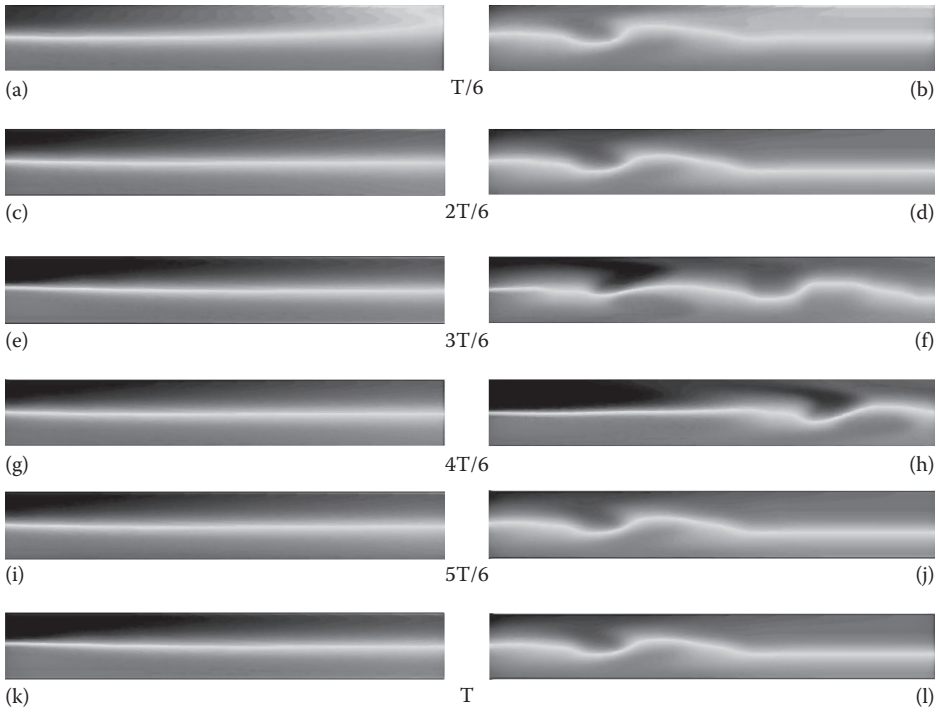


**FIGURE A3.19**
Average degree of mixing for $St = 1.0$ and 3.0 and $\delta V/V = 7.5$.

Figure A3.19 shows the evolution of flow at the outlet channel during one pulsation cycle for $\delta V/V = 7.5$ and $St = 3.0$ and 1.0. The figures shows the evolution of flow during one pulsation cycle for $St = 1.0$ and 3.0 and $\delta V/V = 7.5$. The figures on the left are for the case when $\delta V/V = 7.5$ and $St = 3.0$. The figures on the right indicate $\delta V/V = 7.5$ and $St = 1.0$. The color scheme has been selected in such a way that black indicates a volume fraction of 1 and grey indicates a volume fraction of 0. The change in the interface between the two fluids can be clearly seen at different stages of the flow cycle. Initially, the two fluids flow into the mixing channel. At the end of $T = T/6$, both streams reverse direction. That is, the stream represented by black flows into the bottom inlet channel, and the stream represented by grey flows into the top inlet channel. However, as the pulsation cycle progresses, this behavior diminishes, and a narrow, well-defined interface separating the two streams can be seen during the second half of the pulsation cycle. At large frequencies, the reduced time period of pulsations produces an interface whose width is much smaller than the characteristic length of the channel, $H$. Optimal mixing occurs at intermediate frequencies, where the interface width is of the same order of magnitude as $H$. At high frequencies, the Strouhal number is high. Hence, from Equation A3.3.4.6, it can be seen that the diffusive term, which is primarily responsible for mixing in laminar flows, is dominated by the transient term. On the other hand, at low frequencies, the transient term becomes negligible. This is because the transient term, which has the Strouhal number as its coefficient, is directly proportional to the frequency of pulsations. In this case, the balance is between the advective term and the diffusive term. From Figures A3.16 through A3.18, it can be seen that the

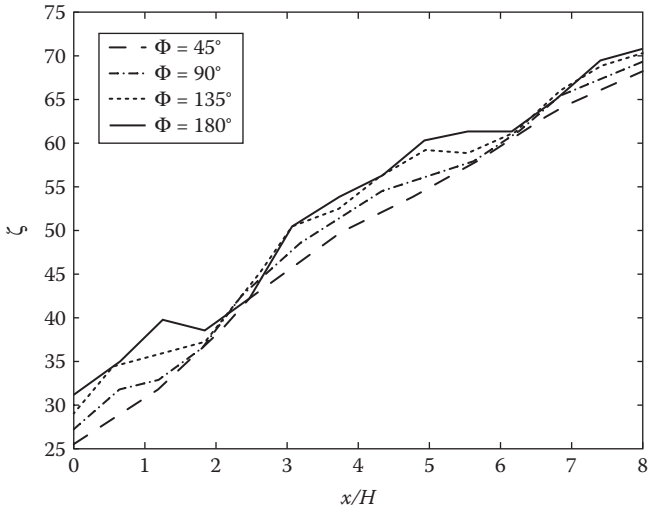


**FIGURE A3.20**
Average degree of mixing for different phase angles.

average degree of mixing is low at very low frequencies. This leads to the conclusion that at very low frequencies, the advective term is greater than and dominates the diffusive term. Thus, the mixing of the two inlet streams is bounded at both very high and very low frequencies.

*A3.4.3.3 Effect of Phase Difference*

In this section, the impact of phase difference between the two streams is discussed. The phase difference angles of 45°, 90°, 135°, and 180° are considered. The simulation is run with $\delta V/V = 0.5$.

Figure A3.20 shows the variation of the average degree of mixing along the outlet channel. It can be seen that the maximum degree of mixing is achieved for a phase difference of 180°.

## A3.5 Conclusions

This project focuses on the effects of both geometry optimization of a microscale Y-junction and variation in inlet flow conditions on the average mixing-level in the outlet channel. It is observed that a phase shift of 90° and a bifurcating angle of 60° yield the highest degree of mixing. The dependence of the average degree of mixing on nondimensional parameters such as $St$, $\delta V/V$, and $\phi$ is also presented. In the case of pulsating inlet flow, the average degree of mixing experiences both temporal and spatial fluctuations. For larger amplitudes ($\delta V/V > 5$), the peak degree of mixing occurs at lower frequencies. On the other hand, for smaller amplitudes ($\delta V/V < 5$), the peak shifts toward the higher-frequency side. Thus, to achieve optimal mixing, a trade-off must be made between frequency and amplitude. In most cases, a higher energy input is required to generate large pulsations (Cheaib et al., 2016). Hence, to minimize the energy cost, a low-amplitude, high-frequency pulsation is preferred to achieve optimal mixing. Also, the phase difference between the two streams has been varied, and its effect on the degree

of mixing has been analyzed. It is found that a phase shift of 180° between the two pulsations yields the highest degree of mixing.

*Critique:* Fundamentally, Project #11 provides new physical insight into microfluidics and species-mass transfer in wavy channels with pulsatile inflow conditions. Computer experiments with different geometric and flow parameters yielded significant improvements in terms of average mixing of two nanofluid streams in the outlet channel.

Of interest would be the development of a correlation for the mixing parameter as a function of the key dimensionless groups.

# References

## (Part A)


Bejan, A., 1995, *Convective Heat Transfer*, 2nd ed., Wiley, New York.

Bejan, A., 1996, *Entropy Generation Minimization: The Method of Thermodynamic Optimization of Finite-Size Systems and Finite-Time Processes*, CRC Press, Boca Raton, FL.

Bejan, A., 2002, *International Journal of Energy Research*, Vol. 26, pp. 545–565.

Bertin, J.J., 2002, *Aerodynamics for Engineers*, Prentice Hall, Upper Saddle River, NJ.

Bird, R.B., Stewart, W.E., Lightfoot, E.N., 2002, *Transport Phenomena*, 2nd ed., Wiley, New York, NY.

Blasius, H., 1908, *Zeitschrift für Mathematik und Physik*, Vol. 56, pp. 1–37.

Bogey, C., Bailly, C., 2010, Influence of nozzle-exit boundary-layer conditions on the flow and acoustic fields of initially laminar jets, *Journal of Fluid Mechanics*, Vol. 663, pp. 507–538.

Boussinesq, J., 1877, Essai sur la théorie des eaux courantes. *Mém. Acad. Sci. Inst. France*, Vol. 23, pp. 1–680.

Brinkman, H.C., 1947, *Physica*, Vol. 13(8), pp. 447–448.

Cimbala, J.M., Cengel, Y.A., 2008, *Essentials of Fluid Mechanics: Fundamentals and Applications*, McGraw-Hill, New York, NY.

Crowe, C.T., Schwarzkopf, J.D., Sommerfeld, M., Tsuji, Y., 2011, *Multiphase Flows with Droplets and Particles*, CRC Press, Boca Raton, FL.

Furuichi, N., Terao, Y., Wada, Y., and Tsuji, Y., 2015, Friction factor and mean velocity profile for pipe flow at high Reynolds numbers, *Physics of Fluids*, Vol. 27, pp. 095108.

Gnielinski, V., 1976, *International Journal of Chemical Engineering*, Vol. 16, pp. 359–368.

Incropera, F.P., DeWitt, D.P., Bergman, T.L., Lavine, A.S., 2007, *Introduction to Heat Transfer*, Wiley, New York, NY.

Kleinstreuer, C., 2006, *Biofluid Dynamics – Principles and Selected Applications*, Taylor & Francis Group, Boca Raton, FL.

Kleinstreuer, C., 1997, *Engineering Fluid Dynamics*, Cambridge University Press, New York, NY.

Kolmogorov, A.N., 1942, *Izvestiya Academy of Sciences USSR, Physics*., Vol. 6, pp. 56–58.

Libby, P.A., 1996, *An Introduction to Turbulence*, CRC Press, Boca Raton, FL.

Middleman, S., 1998, *An Introduction to Fluid Dynamics: Principles of Analysis and Design*, Wiley, New York, NY.

Nichols, W.W., O'Rourke, M.F., *et al.*, 1998, *McDonald's Blood Flow in Arteries: Theoretical, Experimental, and Clinical Principles*, Oxford University Press, New York, NY.

Panton, R.L., 2005, *Incompressible Flow*, Wiley, Hoboken, NJ.

Papanastasiou, T.C., 1994, *Applied Fluid Mechanics*, P T R Prentice Hall, Englewood Cliffs, NJ.

Petukhov, B.S., Zhilin, V.G., 1970, *Journal of Engineering Physics*, Vol. 19(3), pp. 1185–1194.

Polyanin, A.D., Zaitsev, V.F., 1995, *Handbook of Exact Solutions for Ordinary Differential Equations*, CRC Press, Boca Raton, FL.

Pope, S.B., 2011, *Turbulent Flows*, Cambridge University Press, Cambridge UK.

Schlichting, H., Gersten, K., Krause, E., Oertel, H., 2014, *Boundary-Layer Theory*, Springer, New York, NY.

von Kármán, T., 1921, *Zeitschrift für Angewandte Mathematik und Mechanik*, Vol. 1, pp. 233–252.

White, F.M., 2006, *Viscous Fluid Flow*, McGraw-Hill, New York, NY.

White, R.A., 1974, *The Calculation of Supersonic Axisymmetric Afterbody Flow with Jet-Interference and Possible Flow Separation*, Aeronautical Research Institute of Sweden, Aerodynamics Dept, Stockholm.

Wilcox, D.C., 2006, *Turbulence Modeling for CFD*, DCW Industries, La Canada, CA.

Womersley, J.R., 1955, *The Journal of Physiology*, Vol. 127, pp. 553–563.

## (Part B)

Armaly, B.F., Durst, F., Pereira, J.C.F., Schönung, B., 1983, Experimental and theoretical investigation of backward-facing step flow, *Journal of Fluid Mechanics*, Vol. 127, pp. 473–496.

Beattie, D., Whalley, P.B., 1982, A simple two-phase frictional pressure drop calculation method, *International Journal of Multiphase Flow*, Vol. 8, pp. 83–87.

Beavers, G.S., Joseph, D.S., 1967, *Journal of Fluid Mechanics*, Vol. 30(1), pp. 197–207.

Bejan, A., 2002, *International Journal of Energy Research*, Vol. 26, pp. 545–565.

Bertin, J.J., 2002, *Aerodynamics for Engineers*, Prentice Hall, Upper Saddle River, NJ.

Bhopte, S., Sammakia, B., B. Murray, 2007, Mixing enhancement in two component microchannel flow - geometric and pulsed flow effects, *ASME Internation Mechanical Engineering Congress and Exposition*, Vols. IMECE2007 - 43387, pp. 15–21.

Binu, K., Shenoy, B., Rao, D., and Pai, R., 2014, A variable viscosity approach for the evaluation of load carrying capacity of oil lubricated journal bearing with TiO2 nanoparticles as lubricant additives, *Procedia Materials Science*, Vol. 6, pp. 1051–1067.

Bird, G.A., 1994, *Molecular Gas Dynamics and Direct Simulation of Gas Flow*, Oxford University Press, Oxford, UK.

Bird, R.B., Armstrong, R.C., Hassager, O., 1987, *Dynamics of Polymeric Liquids*, 2nd ed., Wiley, New York, NY.

Bird, R.B., Stewart, W.E., Lightfoot, E.N., 2002, *Transport Phenomena*, John Wiley & Sons, New York, NY.

Biswas, G., Breuer, M., Durst, F., 2004, Backward facing step flows for various expansion ratios at low and moderate Reynolds numbers, *Journal of Fluids Engineering (ASME)*, Vol. 126, pp. 362–374.

Brinkman, H., 1952, The viscosity of concentrated suspensions and solutions, *Journal of Chemical Physics*, Vol. 20(4), pp. 571–571.

Brotherton, C.M., Sun, A.C., Davis, R.H., 2008, *Microfluid Nanofluid*, Vol. 5, pp. 43–53.

Brown, R., 1827, in King, P.P. (ed), *Narrative of a Survey of the Intertropical and Western Coasts of Australia, Performed Between Years 1818 and 1822*, John Murray, London, pp. 534–565.

Buchanan, J.R., Kleinstreuer, C., 1998, *ASME Journal of Biomechanical Engineering*, Vol. 120(3), pp. 446–454.

Buchanan, J.R., Kleinstreuer, C., Comer, J.K., 2000, Rheological effects on pulsatile hemodynamics in a stenosed tube, *Computers and Fluids*, Vol. 29(6), pp. 695–724.

Bushi, D., Grad, Y., Einav, S., Yodfat, O., Nishri, B., Tanne, D., 2005, Hemodynamic evaluation of embolic trajectory in an arterial bifurcation, *Stroke*, Vol. 36, pp. 2696–2700.

CFD Online. n.d. CFD online discussion forums. http://www.cfd-online.com/Forums/.

Carlsson, P., A dieselFoam tutorial. *A course at Chalmers University of Technology*.

Chandran, K.B., Rittgers, S.E., Yoganathan, A.P., 2007, *Biofluid Mechanics: The Human Circulation*, CRC Press, Boca Raton, FL.

Chang, C.-C., Yang, R.-J., 2007, *Microfluid Nanofluid*, Vol. 3, pp. 501–525.

Chang, H., Yeo, L.Y., 2010, *Electrokinetically Driven Microfluidics and Nanofluidics*, Cambridge University Press, New York, NY.

Cheaib F., Kekejian, G., Antoun, S., Cheikh, M., Lakkis, I., 2016, Microfluidic mixing using pulsating flows, *Miicrofluid Nanofluid*, Vol. 20:70 (1:19), no. doi:10.1007/s10404-016-1731-4.

Chein, R., Chuang, J., 2005, *Applied Thermal Engineering*, Vol. 25, pp. 3104–3114.

Choi, J.I., Kim, C.S., 2007, Mathematical analysis of particle deposition in human lungs: An improved single path transport model, *Inhalation Toxicology*, Vol. 19(11), pp. 925–939.

Choi, S.U.S., 1995, *Developments and Applications of Non-Newtonian Flows*, in Sininer, D.A., Wang, H.P. (eds), ASME, New York, NY, FEDVol. 231/MD-Vol. 66.

Chopkar, M., Kumar, S., Bhandari, D.R., Das, P.K., Manna, I., 2007, *Materials Science and Engineering B*, Vol. 139, pp. 141–148.

Chung, C.K., Shih, T.R., 2008, *Microfluid Nanofluid*, Vol. 4, pp. 419–425.

Cimbala, J.M., Cengel, Y.A., 2008, *Essentials of Fluid Mechanics: Fundamentals and Applications*, McGraw-Hill, New York, NY.
Clift, R., Grace, J.R., Weber, M.E., 1978, *Bubbles, Drops and Particles*, Academic, New York, NY.
Cooney, D.O., 1976, *Biomedical Engineering Principles*, Marcel Dekker, New York, NY.
Crowe, C.T. (ed), 2006, *Multiphase Flow Handbook*, CRC Press, Boca Raton, FL.
Crowe, C.T., Sommerfeld, M., Tsuji, Y., 1998, *Multiphase Flows with Droplets and Particles*, CRC Press, Boca Raton, FL.
Davidson, L., Qu, L., Norberg, C. et al., 2013, Quantitative numerical analysis of flow past a circular cylinder at Reynolds number between 50 and 200. *Journal of Fluids and Structures*, Vol. 39, pp. 347–370.
De Gruttola, S., Boomsma, K., Poulikakos, D., 2005, Computational simulation of a non-Newtonian model of the blood separation process, *Artificial Organs* , Vol. 29(12), pp. 949–959.
Dittus, F.W., Boelter, L.M.K., 1930, *Heat Transfer in Automobile Radiators of the Tubular Type*, University of California Publications in Engineering 2, Berkeley, CA, Vol. 13, pp. 443–461.
Durbin, P.A., Medic, G., 2007, *Fluid Dynamics with a Computational Perspective*, Cambridge University Press, New York, NY.
Dutta, P., Beskok, A., 2001, Analytical solution of time periodic electroosmotic flows: Analogies to Stokes' second problem, *Analytical Chemistry*, Vol. 73, pp. 5097–5102.
Ergun, S., 1952, *Analytical Chemistry*, Vol. 24(2), pp. 388–393.
Ewart, M.A., 2004, Mixing in microchannels. Masters dissertation, Imperial College, London.
Faghri, A., Zhang, Y., 2006, *Transport Phenomena in Multiphase Systems with Phase Change*, Elsevier, Burlington, MA.
Fang, Y., Liou, W.W., 2002, Computations of the flow and heat transfer in microdevices using DSMC with implicit boundary conditions, *Journal of Heat Transfer*, 124, 338–345.
Ferziger, J.H., Peric, M., 2002, *Computational Methods for Fluid Dynamics*, 3rd ed., Springer-Verlag, New York, NY.
Finlay, W.H., 2001, *The Mechanics of Inhaled Pharmaceutical Aerosols: An Introduction*, Academic, London, UK.
Finlayson, B., 1972, *The Method of Weighted Residuals and Variational Principles*, Vol. 87, Academic Press, New York, NY.
Floyd-Smith, T.M., Golden, J.P., Howell, P.B., Ligler, F.S., 2006, *Microfluid Nanofluid*, Vol. 2, pp. 180–183.
Forchheimer, P., 1901, *Zeitschrift des Vereines Deutscher Ingenieure*, Vol. 45, pp. 1782–1788.
Fung, Y., 1994, *A First Course in Continuum Mechanics: For Physical and Biological Engineers and Scientists*, Prentice Hall, Englewood Cliffs, NJ.
Glasgow I., Aubry, N., 2003, Enhancement of microfluidic mixing using time pulsing, *Lab Chip*, Vol. 3(2), pp. 114–120.
Goullet, A., Glasgow, I., Aubry, N., 2005, Dynamics of microfluidic mixing using time pulsing, *Discrete and Continuous Dynamical Systems Supplement*, 13 (2005), pp. 327–336.
Goullet A., Glasgow, I., Aubry, N., 2006, Effects of microchannel geometry on pulsed flow mixing, *Mechanics Research Communications*, Vol. 33, pp. 739–746.
Greenberg, M. D., 1998, *Advanced engineering mathematics*, Prentice Hall, Upper Saddle River, NJ.
Haaland, S.E., 1983, *Journal of Fluid Engineering*, Vol. 105(1), pp. 89–90.
Hardt, S., Drese, K.S., Hessel, V., Schonfeld, F., 2005, *Microfluid Nanofluid*, Vol. 1, pp. 108–118.
Harkins, W.D., Brown, F.E., 1919, The determination of surface tension (free surface energy), and the weight of falling drops: The surface tension of water and benzene by the capillary height method, *Journal of the American Chemical Society*, Vol. 41, pp. 499–524.
Heris, S.Z., Etemad, S.Gh., Esfahany, N.M., 2006, *International Communications in Heat and Mass Transfer*, Vol. 33, pp. 529–535.
Hochmuth, R.M., 1986, Properties of red blood cells, in Skalak, R., Chein, S. (eds), *Handbook of Bioengineering*, McGraw-Hill, New York, NY.
Hoffman, J.D., 2001, *Numerical Methods for Engineers and Scientists*, 2nd ed., CRC Press, Boca Raton, FL.
Hölzer, A., Sommerfeld, M., 2008, *Powder Technology*, Vol. 184, pp. 361– 365.

Hornyak, G.L., Tibbals, H.F., Dutta, J., Moore, J.J., 2009, *Introduction to Nanoscience and Nanotechnology*, CRC Press, Boca Raton, FL.

Horiuchi, K., Dutta, P., 2004, Joule heating effects in electroosmotically driven microchannel flows, *International Journal of Heat and Mass Transfer*, Vol. 47, pp. 3085–3095.

Hu, C., Bai, M., Lv, J., Wang, P., Li, X., 2014, Molecular dynamics simulation on the friction properties of nanofluids confined by idealized surfaces, *Tribology International*, Vol. 78, pp. 152–159.

Humphrey, J.D., Delange, S.L., 2004, *An Introduction to Biomechanics: Solids and Fluids, Analysis and Design*, Springer Verlag, Berlin.

Incropera, F.P., DeWitt, D.P., Bergman, T.L., Lavine, A.S., 2007, *Introduction to Heat Transfer*, Wiley, New York, NY.

Ingham, D.B., 1975, *Aerosol Science*, Vol. 6, pp. 125–132.

Ira, M. C. Kundu, P. K., 2010, *Fluid Mechanics*. Elsevier/Academic Press, Amsterdam.

Issa, L., 2016, Perturbation-based simplified models for unsteady incompressible microchannel flows, *AIP Advances*, Vol. 40, pp. 5301–5323. no. doi-org.prox.lib.ncsu.edu/10.1016/j.apm.2015.12.025.

Jang, S.P., Choi, S.U.S., 2006, *Applied Thermal Engineering*, Vol. 26, pp. 2457–2463.

Jordi Casacuberta Puig. Bidimensional laminar flow around a circular cylinder. *OpenFOAM Guide For Beginners.*

Kang, T.G., Singh, M.K., Kwon, T.H., Anderson, P.D., 2008, *Microfluid Nanofluid*, Vol. 4, pp. 589–599.

Khan, W.A., Culham, J.R., Yovanovich, M.M., 2007, *Journal of Thermophysics and Heat Transfer*, Vol. 21(2), pp. 372–378.

Kim, C.S., Fisher, D.M., 1999, Deposition characteristics of aerosol particles in sequentially bifurcating airway models, *Aerosol Science and Technology*, Vol. 31, pp. 198–220.

Kim, D.S., Lee, S.W., Kwon, T.H., Lee S.S., 2004, *Journal of Micromechanics and Microengineering*, Vol. 14, pp. 798–805.

Kirby, B.J., 2010, Micro-and Nanoscale Fluid Mechanics: Transport in Microfluidic Devices, Cambridge University Press, Cambridge, UK.

Kleinstreuer, C., 1997, *Engineering Fluid Dynamics*, Cambridge University Press, New York, NY.

Kleinstreuer, C., 2003, *Two-Phase Flow: Theory and Applications*, Taylor & Francis Group, New York, NY.

Kleinstreuer, C., 2006, *Biofluid Dynamics – Principles and Selected Applications*, Taylor & Francis Group, Boca Raton, FL.

Kleinstreuer, C., 2014, *Microfluidics and Nanofluidics: Theory and Selected Applications*, Wiley, Hoboken, NJ.

Kleinstreuer, C., Feng, Y., Childress, E., 2014, Drug-targeting methodologies with applications: A review, *World Journal of Clinical Cases*, Vol. 2, pp. 742.

Kleinstreuer, C., Li, J., 2008a, *Encyclopedia of Micro and Nanofluidics*, edited by Li, D., pp. 1314–1325, Springer-Verlag, Heidelberg, DE.

Kleinstreuer, C., Li, J., 2008b, *ASME Journal of Heat Transfer*, Vol. 130, pp. 025501-1-3.

Kleinstreuer, C., Li, J., Koo, J., 2008a, Microfluidics of nano-drug delivery, *International Journal of Heat and Mass Transfer*, Vol. 51, pp. 5590.

Kleinstreuer, C., Zhang, Z., Donohue, J.F., 2008b, Targeted drug-aerosol delivery in the human respiratory system. Annual Review in Biomedical Engineering *Annual Review of Biomedical Engineering*, Vol. 10, pp. 195–220.

Kleinstreuer C. and Xu, Z., 2016, Mathematical modeling and computer simulations of nanofluid flow with applications to cooling and lubrication, *Fluids*, Vol. 1, p. 16.

Kleinstreuer, C., Zhang, Z., 2003, Laminar-to-turbulent fluid-particle flows in a human airway model, *International Journal of Multiphase Flow*, Vol. 29, pp. 271–289.

Kleinstreuer, C., Zhang, Z., 2009, *Journal of Biomechanical Engineering*, Vol. 131(2), pp. 021007-1-10.

Kleinstreuer, C., Zhang, Z., Li, Z., 2008c, Modeling airflow and particle transport/deposition in pulmonary airways, *Respiratory Physiology and Neurobiology*, Vol. 163, p. 128.

Kleinstreuer, C., Zhang, Z., Kim, C.S., 2007, *Journal of Aerosol Science*, Vol. 38(10), pp. 1047–1061.

Ko, T.H., Wu, C.P., 2009, *International Communications in Heat and Mass Transfer*, Vol. 36(1), pp. 25–31.
Kolanjiyil, A.V., Kleinstreuer, C., 2016, Computationally efficient analysis of particle transport and deposition in a human whole-lung-airway model. Part I: Theory and model validation, *Computers in Biology and Medicine*, Vol. 79, p. 193.
Koo, J., Kleinstreuer, C., 2003, *Journal of Micromechanics and Microengineering*, Vol. 13, pp. 568–579.
Koo, J., Kleinstreuer, C., 2004a, *International Journal of Heat and Mass Transfer*, Vol. 47, pp. 3159–3169.
Koo, J., Kleinstreuer, C., 2004b, *Journal of Nanoparticle Research*, Vol. 6, pp. 577–588.
Labhasetwar, V., Leslie-Pelecky, D.L., 2007, *Biomedical Applications of Nanotechnology*, Wiley-Interscience, Hoboken, NJ. pp. 703–716.
Leal, L.G., 2007, *Laminar Flow and Convective Transport Processes*, 2nd ed., Butterworth-Heineman, Boston, MA.
Lee, C.-Y., Chang, C.-L., 2011, Microfluidic mixing – a review, *International Journal of Molecular Science*, Vol. 12(5), pp. 3263–3287, no. doi:10.3390/ijms12053263.
Lee, S.J., Sundararajan, N., 2010, *Microfabrication for Microfluidics*, Artech House, Boston, MA.
Lee, T., Mateescu, D., 1998, Experimental and numerical investigation of 2-D backward-facing step flow, *Journal of Fluids and Structures*, Vol. 12, pp. 703–716.
Li, J., Kleinstreuer, C., 2008, *International Journal of Heat and Fluid Flow*, Vol. 29(4), pp. 1221–1232.
Li, J., Kleinstreuer, C., 2009, *Microfluid Nanofluid*, Vol. 6 (5), pp. 661–668.
Li, J., Kleinstreuer, C., 2010, Entropy generation analysis for nanofluid flow in microchannels. *Journal of Heat Transfer*, 132(12), p.122401.
Li, J., Yan, L., Li, H., Li, J., Zha, F., Lei, Z., 2015, A facile one-step spray-coating process for the fabrication of a superhydrophobic attapulgite coated mesh for use in oil/water separation, *RSC Advances*, Vol. 5, p. 53802.
Lieber, B.B., Zhao, Y., 1998, Oscillatory flow in a symmetric bifurcation airway model, *Annals of Biomedical Engineering*, Vol. 26, p. 821.
Loth, E., Dorgan, A.J., 2009, An equation of motion for particles of finite Reynolds number and size, *Environmental Fluid Mechanics*, Vol. 9, p. 187.
Lv, J., Bai, M., Cui, W., Li, X., 2011, The molecular dynamic simulation on impact and friction characters of nanofluids with many nanoparticles system, *Nanoscale Research Letters*, Vol. 6, p. 200.
Mabotuwana, T.D.S., Cheng, L.K., Pullan, A.J., 2007, A model of blood flow in the mesenteric arterial system, *Biomedical engineering online*, 6(1), p.17.
Macosko, C.W., 1994, *Rheology: Principles, Measurements and Applications*, VHC Publishers, New York, NY.
Mahmud, S., Fraser, R.A., 2003, *International Journal of Thermal Sciences*, Vol. 42, pp. 177–186.
Majumdar, S., Rajani, B.N., Kandasamy, A., 2009, Numerical simulation of laminar flow past a circular cylinder, *Applied Mathematical Modelling*, Vol. 33, pp. 1228–1247.
Mansour, R.B., Galanis, N., Nguyen, C.T., 2006, *International Journal of Thermal Sciences*, Vol. 45, pp. 998–1007.
Marieb, E.N., 1998, *Human Anatomy and Physiology*, 4th ed., Benjamin Cummings Science Publishing, Menlo Park, CA.
Meng, X., Gomard, G., El Daif, O., Drouard, E., Orobtchouk, R., Kaminski, A., Fave, A., Lemiti, M., Abramov, A., i Cabarrocas, P.R., 2011, Absorbing photonic crystals for silicon thin-film solar cells: Design, fabrication and experimental investigation, *Solar Energy Materials and Solar Cells*, Vol. 95, p. S38.
Mengeaud, V., Josserand, J., Girault, H.H., 2002, Mixing processes in a zigzag microchannel : Finite Element simulations and optical study, *Analytical Chemistry*, Vol. 74(16), pp. 4279–4286.
Merrill, E.W., 1969, The rheology of blood, *Physiological Reviews*, Vol. 26, pp. 863–888.
Michaelides, E.E., 1997, *Journal of Fluids Engineering*, Vol. 119(2), pp. 233–247.
Middleman, S., 1972, *Transport Phenomena in the Cardiovascular System*, Wiley-Interscience, New York, NY.

Moridi, A., Hassani-Gangaraj, S.M., Guagliano, M., Dao, M., 2014, Cold spray coating: Review of material systems and future perspectives, *Surface Engineering*, Vol. 30, p. 369.
Munson, M.S., Yager, P., 2004, *Analytica Chimical Acta*, Vol. 507, pp. 63–71.
Naterer, G.F., 2002, *Heat Transfer in Single and Multiphase Systems*, CRC Press, Boca Raton, FL.
Naterer, G.F., Camberos, J.A., 2008, *Entropy-Based Design and Analysis of Fluids Engineering Systems*, CRC Press, Taylor & Francis Group, Boca Raton, FL.
Nguyen, N.-T., 2008, *Micromixers: Fundamentals, Design, and Fabrication*, William Andrew, Norwich, NY.
Nguyen, N.-T., Wereley, S.T., 2006, *Fundamentals and Applications of Microfluidics*, Arten House, Boston, MA.
Nguyen, N.-T., Wu, Z., 2005, *Journal of Micromechanics and Microengineering*, Vol. 15, pp. R1–R16.
Nichols, W., O'Rourke, M., Vlachopoulos, C., 2011, *McDonald's Blood Flow in Arteries: Theoretical, Experimental and Clinical Principles*, CRC Press, Boca Raton, FL.
Nichols, W.W., O'Rourke, M.F., 2005, *McDonalds Blood Flow in Arteries: Theoretical, Experimental, and Clinical Principles*, 5th ed., Hodder Arnold, Oxford University Press, New York, NY.
Nicoletti, R., 2014, The importance of the heat capacity of lubricants with nanoparticles in the static behavior of journal bearings, *Journal of Tribology*, Vol. 136, p. 044502.
Nield, D.A., Kuznetsov, A.V., 2013, An historical and topical note on convection in porous media, *Journal of Heat Transfer*, Vol. 135, p. 061201.
Niu, X. and Lee, Y.-K., 2003, Efficient spatial – temporal chaotic mixing in microchannels, *Journal of Micromechanics and Microengineering*, Vol. 13(3), p. 454. no. doi.org/10.1088/0960-1317/13/3/316.
Ochoa-Tapia, J.A., Whitaker, S., 1995, *International Journal of Heat and Mass Transfer*, Vol. 34(14), pp. 2635–2646.
Olinger, D.J., Sreenivasan, K.R., Strykowski, P.J., 1987, Hopf bifurcation, Landau equation and vortex shedding behind circular cylinders.
Ope, S.B., 2011, *Turbulent Flows*, Cambridge University Press, Cambridge, UK.
*OpenFOAM User Guide*, 2015.
Ou, J., Perot, B., Rothstein, J.R., 2004, *Physics of Fluids*, Vol. 16(12), pp. 4635–4643.
Ozisik, M. N., 1993, *Heat Conduction*, John Willey & Sons, Hoboken, New Jersey.
Païdoussis, M.P., 1998, *Fluid–Structure Interactions: Slender Structures and Axial Flow*, Vol. 1, Academic, London.
Palm, W.J., 2007, *Mechanical Vibration*, Wiley, Hoboken, NJ.
Papanastasiou, T.C., 1994, *Applied Fluid Mechanics*, Prentice-Hall, Englewood Cliffs, NJ.
Patankar, S., 1980, *Numerical Heat Transfer and Fluid Flow*, CRC Press, Boca Raton, FL.
Pawlowski, L., 2009, Suspension and solution thermal spray coatings, *Surface and Coatings Technology*, Vol. 203, p. 2807.
Pletcher, R.H., Tannehill, J.C., Anderson, D., 2011, *Computational Fluid Mechanics and Heat Transfer*, CRC Press, Boca Raton, FL.
Polyanin, A.D., Zaitsev, V.F., 1995, *Handbook of Exact Solutions for Ordinary Differential Equations*, CRC Press, Boca Raton, FL.
Pope, S.B., 2011, *Turbulent Flows*, Cambridge University Press, Cambridge, UK.
Prandtl, L., 1904. *Verhandlungen des III. Internationalen Mathematiker Kongress*, Heidelberg, Leipeizig, pp. 484–491.
Probstein, R.F., 1994, *Physicochemical Hydrodynamics: An Introduction*, Wiley, New York, NY.
Rahman, M.M., Karim, M.M., Alim, M.A., 2008, Numerical investigation of unsteady flow past a circular cylinder using 2-D finite volume method, *Journal of Naval Architecture and Marine Engineering*, Vol. 4(1), pp. 27–42.
Richards, A.L., Kleinstreuer, C., Kennedy, A.S., Childress, E., Buckner, G.D., 2012, Experimental microsphere targeting in a representative hepatic artery system, *IEEE Transactions on Biomedical Engineering*, Vol. 59, p. 198.
Roache, P. J., 1998, Verification of codes and calculations, *AIAA Journal*, Vol. 36, pp. 696–702.
Roark, R., Budynas, R., Young, W., 2001, *Roark's Formulas for Stress and Strain*, 7th ed., McGraw-Hill, New York, NY.

Sabersky, R.H., Acosta, A.J., Hauptmann, E.G., Gates, E.M., 1999, *Fluid Flow: A First Course in Fluid Dynamics*, Prentice-Hall, Englewood Cliffs, NJ.
Saeedi, M. Laminar vortex shedding. *Exploring OpenFOAM*.
Sahin, A.Z., 1998, *Heat Mass Transfer*, Vol. 33, pp. 425–430.
Sahin, A.Z., 2000, *International Journal of Heat Mass Transfer*, Vol. 43, pp. 1469–1478.
Saliterman, S.S., 2006, *Fundamentals of BioMEMS and Medical Microdevices*, Wiley-Interscience, SPIE Press, Bellingham, Washington.
Schlichting, H., Gersten, K., 2003, *Boundary-Layer Theory*, 2nd printing, McGraw-Hill, New York, NY.
Schmid-Schoenbein, G.W., 1986, Rheology of leukocytes, in Skalak, R., Chien, S. (eds), *Handbook of Bioengineering*, McGraw-Hill, New York, NY.
Shenoy, B.S., Binu, K.G., Pai, R., Rao, D.S., Pai, R.S., 2012, Effect of nanoparticles additives on the performance of an externally adjustable fluid film bearing, *Tribology International*, Vol. 45, pp. 38–42.
Silverthorn, D.U., 2004, *Human Physiology, an Integrated Approach*, Prentice Hall, Upper Saddle River, NJ.
Simiu, E., Scanlan, R.H., 1996, *Wind Effects on Structures: Fundamentals and Applications to Design*, 3rd ed., John Wiley, New York, NY.
Slattery, J.C., 1999, *Advanced Transport Phenomena*, Cambridge University Press, Cambridge, UK.
Soo, S.L., 1990, *Multiphase Fluid Dynamics*, Science Press/Gower Technical, Brookfield.
Spiegel, M. R., 1971, *Schaum's outline of theory and problems of advanced mathematics for engineers and scientists*, McGraw-Hill, Düsseldorf, Germany.
Steele, B.N., Olufsen, M.S., Taylor, C.A., 2007, *Computer Methods in Biomechanics and Biomedical Engineering*, Vol. 10(1), pp. 39–51.
Stone, H.A., Stroock, A.D., Ajdari, A., 2004, *Annual Review of Fluid Mechanics*, Vol. 36, pp. 381–411.
Stroock, A.D., Dertinger, S.K.W., Ajdari, A., Mezic, I., Stone, H.A., and Whitesides, G.M., 2002, *Science*, Vol. 295, pp. 647–651.
Szeri, A., 1980, *Tribology: Friction, Lubrication and Wear*, 1st ed., McGraw-Hill, New York, NY.
Tabeling, P., 2005, *Introduction to Microfluidics*, Oxford Unversity Press, Oxford, UK.
Tan, J.N. and Neild, A., 2012, Microfluidic mixing in a Y-junction open channel, *AIP Advances*, 2(3), p. 032160, no. doi:10.1063/1.4750483.
Tannehill, J.C., Anderson, D.A., Pletcher, R., 1997, *Computational Fluid Mechanics and Heat Transfer*, 2nd ed. (Series in Computional and Physical Processes in Mechanics and Thermal Sciences). Taylor & Francis, Washington, DC.
Tanner, R.I., Walters, K., 1998, *Rheology: An Historical Perspective*, Elsevier, Amsterdam.
Tavoularis, S., 2005, *Measurement in Fluid Mechanics*, Cambridge University Press, Cambridge, UK.
Thompson, A.G., Windsor, C.R., Cadby, G.W., 1999, Performance assessment of mesh for ground control applications, *Rock Support and Reinforcement Practice in Mining*, pp. 119–130.
Tong, L.S., Tang, Y.S., 1997, *Boiling Heat Transfer and Two-Phase Flow*, CRC Press, Boca Raton, FL.
Truskey, G.A., Yuan, F., Katz, D.F., 2004, *Transport Phenomena in Biological Systems*, Pearson/Prentice Hall, Upper Saddle River, NJ.
Tu, J., Yeoh, G.H., Liu, C., 2008, *Computational Fluid Dynamics: A Practical Approach*, Butterworth Heinemann, Burlington, MA.
Ugural, A.C., Fenster, S.K., 2003, *Advanced Strength and Applied Elasticity*, Prentice Hall PTR, Upper Saddle River, NJ.
Umbarkar, T.S., Kleinstreuer, C., 2015, Computationally efficient fluid-particle dynamics simulations of arterial systems, *Communications in Computational Physics*, Vol. 17, p. 401.
van Ertbruggen, C., Hirsch, C., Paiva, M., 2005, *Journal of Applied Physiology*, Vol. 98, pp. 970–980.
Versteeg, H.K., Malalasekera, W., 1996, *An Introduction to Computational Fluid Dynamics: The Finite Volume Method*, Prentice Hall, Upper Saddle River, NJ.
Wang, C. Hu, Y., 2010, Mixing of liquids using obstacles in Ytype microchannels, *Journal of Applied Science and Engineering*, Vol. 13(4), pp. 385–394.
White, F.M., 2006, *Viscous Fluid Flow*, McGraw-Hill, New York, NY.
White, F.M., 2016, *Fluid Mechanics*, McGraw-Hill, New York, NY.
Wilcox, D.C., 1998, *Turbulence Modeling for CFD*, 2nd ed., DCW Industries, La Canada, CA.

Wolf Dynamics, 2014, OpenFOAM tutorial – Flow around a cylinder. *Exploring OpenFOAM*.
Wu, H.Y., Cheng, P., 2003, *International Journal of Heat and Mass Transfer*, Vol. 46(14), pp. 2519–2525.
Xu, Z., Jernigan, S., Kleinstreuer, C., Buckner, G.D., 2016, Solid tumor embolotherapy in hepatic arteries with an anti-reflux catheter system, *Annals of Biomedical Engineering*, Vol. 44, pp. 1036–1046.
Zapryanov, Z., Tabakova, S., 1999, *Dynamics of Bubbles, Drops and Rigid Particles*, Kluwer Academic, Boston, MA.
Zhang, Z.M., 2007, *Nano/microscale Heat Transfer*, McGraw-Hill, New York, NY.
Zhang, Z., Kleinstreuer, C., 2003, Low-Reynolds number turbulent flows in locally constricted conduits: A comparison study, *AIAA Journal*, Vol. 41(5), pp. 831–840.
Zikanov, O., 2010, *Essential Computational Fluid Dynamics*, Wiley, Hoboken, NJ.

# *Appendix I: Review of Tensor Calculus, Differential Operations, Functions, Integral Transformations, ODE Solutions, Modeling Equations, and OpenFOAM Commands*

## AI.1 Tensor Calculus

Here, we restrict our review to tensor manipulations as needed in the text. Further information and solved examples can be found in the Appendix of Bird et al. (2002).

### AI.1.1 Definitions

*Recall:* Tensors of rank n have $3^n$ components. For example:

- A tensor of rank "zero" is a *scalar*, which has only one component, that is, its magnitude (e.g., pressure).
- A tensor of rank "one" is a *vector*, which has in general three components, that is, three magnitudes and three directions (e.g., velocity).
- A tensor of rank "two" is usually labeled a *tensor*, which has nine components (e.g., stress).

**Coordinate Systems**

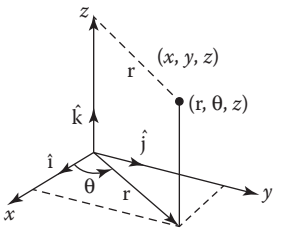


$$x = r\cos\theta$$

$$y = r\sin\theta$$

$$z = z$$

**Vector Products**

- Dot product

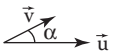


$$\vec{u}\cdot\vec{v} = \vec{v}\cdot\vec{u} = |\vec{u}||\vec{v}|\cos\alpha \rightarrow \text{scalar}$$

- Cross product

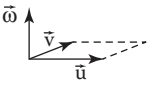


$$\vec{u}\times\vec{v} = -\vec{v}\times\vec{u} = \vec{\omega} \rightarrow \text{vector}$$

- Dyadic product

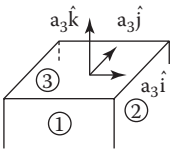


$$\vec{u}\vec{v} = \vec{\vec{a}} \longrightarrow \text{tensor}$$

Clearly, the type of vector product may result in a scalar (see dot product) or a tensor of rank two with nine components (see dyadic product). This is further illustrated when using the *del operator*, which has the characteristics of a vector (see Section AI.1.2).

### AI.1.2 Operations with $\nabla$

- By definition,
  a. In rectangular coordinates: $$\nabla \equiv \hat{i}\frac{\partial}{\partial x} + \hat{j}\frac{\partial}{\partial y} + \hat{k}\frac{\partial}{\partial z} \tag{AI.1.1a}$$
  b. In cylindrical coordinates: $$\nabla \equiv \hat{e}_r\frac{\partial}{\partial r} + \hat{e}_\theta\frac{1}{r}\frac{\partial}{\partial \theta} + \hat{e}_z\frac{\partial}{\partial z} \tag{AI.1.1b}$$
- When operating on a scalar, say, the pressure, $\nabla p$ generates a vector, that is, the *pressure gradient*:

$$\nabla p = \left(\hat{i}\frac{\partial}{\partial x} + \hat{j}\frac{\partial}{\partial y} + \hat{k}\frac{\partial}{\partial z}\right)p = \frac{\partial p}{\partial x}\hat{i} + \frac{\partial p}{\partial y}\hat{j} + \frac{\partial p}{\partial z}\hat{k} \tag{AI.1.2}$$

- When operating on a vector, it can produce:
  a. A scalar in the case of a dot product, for example, $\nabla \cdot \vec{\mathbf{v}}$
  b. A vector in the case of a cross product, for example, $\nabla \times \vec{\mathbf{v}}$
  c. A tensor in the case of a dyadic product, for example, $\nabla\vec{\mathbf{v}}$

*Note:* $\nabla \bullet \nabla = \nabla^2$ is the Laplacian operator (see Equation AI.1.8a and b). Specifically,

1. $\nabla \cdot \vec{\mathbf{v}} \equiv div\ \vec{\mathbf{v}}$ is the divergence of the velocity field:

$$\begin{aligned}\nabla \cdot \vec{\mathbf{v}} &= \left(\hat{i}\frac{\partial}{\partial x} + \hat{j}\frac{\partial}{\partial y} + \hat{k}\frac{\partial}{\partial z}\right)\cdot(u\hat{i} + \mathrm{v}\hat{j} + w\hat{k}) \\ &= (\hat{i}\cdot\hat{i})\frac{\partial u}{\partial x} + (\hat{i}\cdot\hat{j})\frac{\partial \mathrm{v}}{\partial x} + (\hat{i}\cdot\hat{k})\frac{\partial w}{\partial x} + \\ &\quad (\hat{j}\cdot\hat{i})\frac{\partial u}{\partial y} + (\hat{j}\cdot\hat{j})\frac{\partial \mathrm{v}}{\partial y} + (\hat{j}\cdot\hat{k})\frac{\partial w}{\partial y} + \\ &\quad (\hat{k}\cdot\hat{i})\frac{\partial u}{\partial z} + (\hat{k}\cdot\hat{j})\frac{\partial \mathrm{v}}{\partial z} + (\hat{k}\cdot\hat{k})\frac{\partial w}{\partial z} = \frac{\partial u}{\partial x} + \frac{\partial \mathrm{v}}{\partial y} + \frac{\partial w}{\partial z}\end{aligned} \tag{AI.1.3}$$

   because $\hat{i}\cdot\hat{i} = |i||i|\cos\alpha;\ \alpha = 0 \Rightarrow \hat{i}\cdot\hat{i} = 1$, while $\hat{i}\cdot\hat{j} = 0 <\alpha = 90^\circ>$

   In general, $\hat{\delta}_i \cdot \hat{\delta}_j = \delta_{ij} := \begin{cases} 1 & \textbf{if} \quad i = j \\ 0 & \textbf{if} \quad i \neq j \end{cases}$, known as the *Kronecker delta*

2. $\nabla \times \vec{\mathbf{v}} \equiv \mathrm{curl}\,\vec{\mathbf{v}}$ is the curl (or rotation) of the velocity field:

$$\nabla\times\vec{\mathbf{v}}=\left(\hat{i}\frac{\partial}{\partial x}+\hat{j}\frac{\partial}{\partial y}+\hat{k}\frac{\partial}{\partial z}\right)\times\left(u\hat{i}+\mathrm{v}\hat{j}+w\hat{k}\right)$$

$$=\left(\hat{i}\times\hat{i}\right)\frac{\partial u}{\partial x}+\left(\hat{i}\times\hat{j}\right)\frac{\partial \mathrm{v}}{\partial x}+\left(\hat{i}\times\hat{k}\right)\frac{\partial w}{\partial x}+ \tag{AI.1.4}$$

$$\left(\hat{j}\times\hat{i}\right)\frac{\partial u}{\partial y}\ldots\text{etc.}$$

Recalling the results for the cross products between unit (or base) vectors:

$$\begin{array}{lll}\hat{i}\times\hat{j}=\hat{k} & \hat{j}\times\hat{i}=-\hat{k} & \hat{i}\times\hat{i}=0\\ \hat{j}\times\hat{k}=\hat{i} & \hat{k}\times\hat{j}=-\hat{i} & \hat{j}\times\hat{j}=0\\ \hat{k}\times\hat{i}=\hat{j} & \hat{i}\times\hat{k}=-\hat{j} & \hat{k}\times\hat{k}=0\end{array}$$

we obtain

$$\nabla\times\vec{v}=\hat{i}\left(\frac{\partial w}{\partial y}-\frac{\partial v}{\partial z}\right)+\hat{j}\left(\frac{\partial u}{\partial z}-\frac{\partial w}{\partial x}\right)+\hat{k}\left(\frac{\partial v}{\partial x}-\frac{\partial u}{\partial y}\right)$$

or

$$\nabla\times\vec{v}=\text{curl }\vec{v}=\begin{vmatrix}\hat{i} & \hat{j} & \hat{k}\\ \dfrac{\partial}{\partial x} & \dfrac{\partial}{\partial y} & \dfrac{\partial}{\partial z}\\ u & v & w\end{vmatrix}\equiv\vec{\zeta}\left(\text{vorticity vector}\right) \tag{AI.1.5}$$

3. $\nabla\vec{v}\equiv\text{grad }\vec{v}$ is the dyadic product, or gradient, of the velocity field:

$$\nabla\vec{\mathbf{v}}=\left(\hat{i}\frac{\partial}{\partial x}+\hat{j}\frac{\partial}{\partial y}+\hat{k}\frac{\partial}{\partial z}\right)\left(u\hat{i}+\mathrm{v}\hat{j}+w\hat{k}\right)$$

$$=\left(\hat{i}\hat{i}\right)\frac{\partial u}{\partial x}+\left(\hat{i}\hat{j}\right)\frac{\partial \mathrm{v}}{\partial x}+\left(\hat{i}\hat{k}\right)\frac{\partial w}{\partial x}+ \tag{AI.1.6}$$

$$\left(\hat{j}\hat{i}\right)\frac{\partial u}{\partial y}+\ldots\text{etc.}$$

Now, the unit vector dyadic product $\hat{\boldsymbol{\delta}}_i\hat{\boldsymbol{\delta}}_j$ indicates the *location* (i.e., $\hat{\boldsymbol{\delta}}_i$ is the unit normal to the particular surface) and *direction* (i.e., $\hat{\boldsymbol{\delta}}_j$ gives the direction) of a tensor. Thus,

$$\nabla\vec{\mathbf{v}}=\text{grad }\vec{\mathbf{v}}=\begin{vmatrix}\dfrac{\partial u}{\partial x} & \dfrac{\partial v}{\partial x} & \dfrac{\partial w}{\partial x}\\ \dfrac{\partial u}{\partial y} & \dfrac{\partial v}{\partial y} & \dfrac{\partial w}{\partial y}\\ \dfrac{\partial u}{\partial z} & \dfrac{\partial v}{\partial z} & \dfrac{\partial w}{\partial z}\end{vmatrix}\sim\vec{\vec{\tau}}\quad\text{<stress tensor>} \tag{AI.1.7}$$

*Notes:*

- The use of $\nabla\cdot\vec{\mathbf{v}}$, $\nabla\times\vec{\mathbf{v}}$, and $\nabla\vec{\mathbf{v}}$, plus illustrations, was introduced in Chapter 1.
- The dot product *reduces* the rank of a tensor, for example, $\nabla\cdot\vec{\mathbf{v}}\rightarrow$ scalar and $\nabla\cdot\vec{\vec{\tau}}\rightarrow$ vector.
- The dyadic (or gradient) product increases the rank, for example, $\nabla p\longrightarrow$ vector and $\nabla\vec{\mathbf{v}}\longrightarrow$ tensor.
- The divergence of a scalar gradient is $\nabla\cdot\nabla s=\nabla^2 s=\Sigma\dfrac{\partial^2 s}{\partial x^2}$, where $\nabla^2$ *is the Laplacian operator* producing a scalar field:

$$\text{Rectangular coordinates:}\nabla^2\equiv\frac{\partial^2}{\partial x^2}+\frac{\partial^2}{\partial y^2}+\frac{\partial^2}{\partial z^2} \tag{AI.1.8a}$$

$$\text{Cylindrical coordinates:}\nabla^2\equiv\frac{1}{r}\frac{\partial}{\partial r}\left(r\frac{\partial}{\partial r}\right)+\frac{1}{r^2}\frac{\partial^2}{\partial\theta^2}+\frac{\partial^2}{\partial z^2} \tag{AI.1.8b}$$

- The transpose of a second-order tensor, $\vec{\vec{a}}$, with components $a_{ij}$ is denoted by $\vec{\vec{a}}^{tr}$ and is defined by

$$\left[a^{tr}\right]_{ij}=a_{ji} \tag{AI.1.9a}$$

For example,

$$\vec{\vec{a}}\equiv\vec{\mathbf{v}}\vec{\mathbf{w}}=\begin{pmatrix} v_1w_1 & v_1w_2 & v_1w_3\\ v_2w_1 & v_2w_2 & v_2w_3\\ v_3w_1 & v_3w_2 & v_3w_3\end{pmatrix} \tag{AI.1.9b}$$

whereas

$$\vec{\vec{a}}^{tr}\equiv(\vec{\mathbf{v}}\vec{\mathbf{w}})^{tr}=\begin{pmatrix} v_1w_1 & v_2w_1 & v_3w_1\\ v_1w_2 & v_2w_2 & v_3w_2\\ v_1w_3 & v_2w_3 & v_3w_3\end{pmatrix} \tag{AI.1.9c}$$

### *AI.1.2.1 Sample Problem Solutions*

To illustrate a few tensor manipulations, the following sample problems are solved. Given the components of a symmetric tensor $\vec{\vec{\tau}}$, that is, $\tau_{ij}=\tau_{ji}$:

$$\begin{aligned}&\tau_{xx}=3, && \tau_{xy}=2, && \tau_{xz}=-1,\\ &&& \tau_{yy}=2, && \tau_{yz}=1,\\ &&&&& \tau_{zz}=0\end{aligned}$$

and the components of a vector $\vec{\mathbf{v}}$, for example, $v_x=5$, $v_y=3$, $v_z=7$, evaluate

(a) $\vec{\vec{\tau}}\cdot\vec{\mathbf{v}}$; (b) $\vec{\mathbf{v}}\cdot\vec{\vec{\tau}}$; (c) $\vec{\mathbf{v}}\vec{\mathbf{v}}$; and (d) $\vec{\vec{\tau}}\cdot\vec{\vec{\delta}}$

where $\vec{\vec{\delta}}$ is the unit tensor, that is,

$$\delta_{ij} = \begin{pmatrix} 1 & & \varphi \\ & 1 & \\ \varphi & & 1 \end{pmatrix}$$

*Solution:* A good preliminary exercise is to write down the vectors and tensors in component form.

1. $$\vec{\vec{\tau}} \cdot \vec{v} = \sum_i \vec{\delta}_i \left\{ \sum_j \tau_{ij} v_j \right\} = \left( \vec{\delta}_1 \vec{\delta}_2 \vec{\delta}_3 \right) \begin{pmatrix} 3 & 2 & -1 \\ 2 & 2 & 1 \\ -1 & 1 & 0 \end{pmatrix} \begin{pmatrix} 5 \\ 3 \\ 7 \end{pmatrix}$$

$$= 14\vec{\delta}_1 + 23\vec{\delta}_2 - 2\vec{\delta}_3 < \text{a vector} >$$

where $\vec{\delta}_i \hat{=}$ unit vector in the $i$-direction, with $i = 1, 2, 3$.

2. $\vec{v} \cdot \vec{\vec{\tau}} = \vec{\vec{\tau}} \cdot \vec{v}$ because $\vec{\vec{\tau}}$ is symmetric

3. $$\vec{v}\vec{v} = \sum_i \sum_j \vec{\delta}_i \vec{\delta}_j v_i v_j = 25\vec{\delta}_1\vec{\delta}_1 + 15\vec{\delta}_1\vec{\delta}_2 + 35\vec{\delta}_1\vec{\delta}_3$$
$$+15\vec{\delta}_2\vec{\delta}_1 + 9\vec{\delta}_2\vec{\delta}_2 + 21\vec{\delta}_2\vec{\delta}_3$$
$$+35\vec{\delta}_3\vec{\delta}_1 + 21\vec{\delta}_3\vec{\delta}_2 + 49\vec{\delta}_3\vec{\delta}_3$$

4. $$\vec{\vec{\tau}} \cdot \vec{\vec{\delta}} = \sum_i \sum_l \vec{\delta}_i \vec{\delta}_l \left( \sum_j \tau_{ij} \delta_{jl} \right) = \vec{\vec{\tau}} = 3\vec{\delta}_1\vec{\delta}_1 + 2\vec{\delta}_1\vec{\delta}_2 - 1\vec{\delta}_1\vec{\delta}_3$$
$$+2\vec{\delta}_2\vec{\delta}_1 + 2\vec{\delta}_2\vec{\delta}_2 + 1\vec{\delta}_2\vec{\delta}_3$$
$$-1\vec{\delta}_3\vec{\delta}_1 + 1\vec{\delta}_3\vec{\delta}_2 + 0\vec{\delta}_3\vec{\delta}_3$$

### AI.1.3 Some Tensor Identities

$$\nabla rs = r\nabla s + s\nabla r \tag{AI.1.10}$$

$$(\nabla \cdot s\vec{v}) = (\nabla s \cdot \vec{v}) + s(\nabla \cdot \vec{v}) \tag{AI.1.11}$$

$$(\nabla \cdot [\vec{v} \times \vec{w}]) = (\vec{w} \cdot [\nabla \times \vec{v}]) - (\vec{v} \cdot [\nabla \times \vec{w}]) \tag{AI.1.12}$$

$$[\nabla \times s\vec{v}] = [\nabla s \times \vec{v}] + s[\nabla \times \vec{v}] \tag{AI.1.13}$$

$$[\nabla \cdot \nabla\vec{v}] = \nabla(\nabla \cdot \vec{v}) - [\nabla \times [\nabla \times \vec{v}]] \tag{AI.1.14}$$

$$[\vec{v} \cdot \nabla\vec{v}] = \tfrac{1}{2}\nabla(\vec{v} \cdot \vec{v}) - [\vec{v} \times [\nabla \times \vec{v}]] \tag{AI.1.15}$$

$$[\nabla \cdot \vec{v}\vec{w}] = [\vec{v} \cdot \nabla\vec{w}] + \vec{w}(\nabla \cdot \vec{v}) \tag{AI.1.16}$$

$$[\nabla \cdot s\vec{\vec{\delta}}] = \nabla s \tag{AI.1.17}$$

$$[\nabla \cdot s\vec{\vec{\tau}}] = [\nabla s \cdot \vec{\vec{\tau}}] + s[\nabla \cdot \vec{\vec{\tau}}] \tag{AI.1.18}$$

$$\nabla(\vec{\mathbf{v}} \cdot \vec{\mathbf{w}}) = [(\nabla \vec{\mathbf{v}}) \cdot \vec{\mathbf{w}}] + [(\nabla \vec{\mathbf{w}}) \cdot \vec{\mathbf{v}}] \tag{AI.1.19}$$

## AI.2 Differentiation

### AI.2.1 Differential Time Operators

To understand and solve fluid mechanics problems, the basic skills in linear algebra, differentiating and integrating functions, graphing and analyzing functions, as well as curve fitting are definitely *prerequisites*. If a review is necessary, the reader may want to consult M. Spiegel (1971), Schaum's Outline series, or M. D. Greenberg (1998), Prentice-Hall, among many other texts.

The different notations and the physical meanings of various *time* derivatives (i.e., differential operators) are presented as follows:

- Partial time derivative: $\partial \#/\partial t \triangleq$ Changes in variable "#" with time observed from a *fixed* position in space, that is, stationary observer.
- Substantial or material time derivate: $D\#/Dt \triangleq$ Changes of variable "#" with time *following* the fluid/material element in motion. The *Stokes (or material) derivative* is defined as

$$\frac{D\#}{Dt} \equiv \frac{\partial \#}{\partial t} + \left(\vec{\mathbf{v}} \cdot \nabla\right)\# \tag{AI.2.1}$$

$D/Dt$ of Equation AI.2.1 can operate on a vector or a scalar, where in any case, the Lagrangian time-rate-of-change is expressed in terms of Eulerian derivatives. For example, c being a species concentration[$M/L^3$], the material time derivative is

$$\frac{Dc}{Dt} \equiv \frac{\partial c}{\partial t} + \left(\vec{\mathbf{v}} \cdot \nabla\right)c \tag{AI.2.2a}$$

In rectangular coordinates,

$$\frac{Dc}{Dt} = \frac{\partial c}{\partial t} + u\frac{\partial c}{\partial x} + \mathrm{v}\frac{\partial c}{\partial y} + w\frac{\partial c}{\partial z} \tag{A2.2b}$$

while in tensor notation,

$$\frac{Dc}{Dt} = \frac{\partial c}{\partial t} + \mathrm{v}_k \frac{\partial c}{\partial x_k}; \qquad k = 1, 2, 3 \tag{AI.2.2c}$$

where:

$\frac{\partial c}{\partial t} \hat{=}$ local time derivative (i.e., accumulation of species $c$)

$v_k \frac{\partial c}{\partial x_k} \hat{=}$ convective derivatives (i.e., mass transfer by convection)

*Note:* Repeated indices imply summation of these terms; here, $k = 1, 2, 3$ <Einstein convention>.

- Total time derivative: $d\#/dt \hat{=}$ Changes of # with respect to time observed from a point *moving differently* from the flow field. For example,

$$\frac{dc}{dt} = \frac{\partial c}{\partial t} + \frac{dx}{dt}\frac{\partial c}{\partial x} + \frac{dy}{dt}\frac{\partial c}{\partial y} + \frac{dz}{dt}\frac{\partial c}{\partial z} \tag{AI.2.3}$$

where $dx/dt = u$, $dy/dt = v$, and $dz/dt = w$ are the velocity components of the moving observer.

### AI.2.2 The Total Differential

The derivation of the material derivative $D\#/Dt$ of Equation AI.2.1 starts with the definition of the total derivative. For example, the fluid velocity is a function of three spatial coordinates, say, $x$, $y$, and $z$, and time $t$ if the flow is unsteady; thus, $\vec{\mathbf{v}} = \vec{\mathbf{v}}(x, y, z, t)$. The total differential is defined as

$$d\vec{\mathbf{v}} = \frac{\partial \vec{\mathbf{v}}}{\partial x}dx + \frac{\partial \vec{\mathbf{v}}}{\partial y}dy + \frac{\partial \vec{\mathbf{v}}}{\partial z}dz + \frac{\partial \vec{\mathbf{v}}}{\partial t}dt \tag{AI.2.4}$$

If the spatial coordinates $x$, $y$, and $z$ are also functions of time, then the total (particle) time derivative is

$$\frac{d\vec{\mathbf{v}}}{dt} = \frac{\partial \vec{\mathbf{v}}}{\partial x}\frac{dx}{dt} + \frac{\partial \vec{\mathbf{v}}}{\partial y}\frac{dy}{dt} + \frac{\partial \vec{\mathbf{v}}}{\partial z}\frac{dz}{dt} + \frac{\partial \vec{\mathbf{v}}}{\partial t} \tag{AI.2.5}$$

Actually, Equation AI.2.5 represents the total acceleration of a *particle*. For *fluid-element* acceleration, $\frac{d\vec{\mathbf{v}}}{dt}$ is replaced by $\frac{D\vec{\mathbf{v}}}{Dt}$, with $dx/dt = u$, $dy/dt = v$, and $dz/dt = w$ being the three velocity components in Cartesian coordinates. Such differentiation can be extended to the calculation of fluid acceleration and mass transport, where the local quantities change with time. For a scalar, say, the steady-state pressure, we have

$$dp = \frac{\partial p}{\partial x}dx + \frac{\partial p}{\partial y}dy + \frac{\partial p}{\partial z}dz \tag{AI.2.6}$$

### AI.2.3 Truncated Taylor Series Expansions and Binomial Theorem

To approximate a function, say, $y(x)$, around some point $x = x_0$, we employ two or three terms of the Taylor series. For one independent variable,

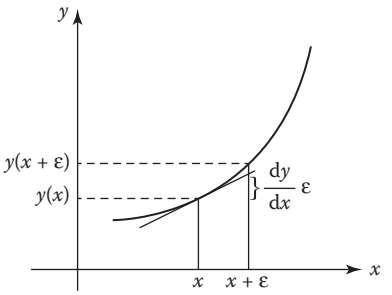


$$y(x) = y\Big|_{x=x_0} + \frac{dy}{dx}\Big|_{x=x_0}(x-x_0) + \frac{1}{2}\frac{d^2y}{dx^2}\Big|_{x=x_0}(x-x_0)^2 + \frac{1}{6}\frac{d^3y}{dx^3}\Big|_{x=x_0}(x-x_0)^3 + \ldots \tag{AI.2.7}$$

Clearly, the first two terms provide a straight-line fit and the first three a parabolic fit of $y(x)$ at $x = x_0$.

If we want to estimate the value of $y$ a very small distance away from the known $y(x)$, that is, what is $y(x+\varepsilon)$ where $\varepsilon \ll 1$, we can write with Equation AI.2.7:

$$y(x+\varepsilon) \approx y(x) + \frac{dy}{dx}\Big|_{x=\varepsilon}\varepsilon \tag{AI.2.8}$$

As the previous graph for y(x) indicates, the step size ε and local curvature of $y(x)$ determine the accuracy of Equation AI.2.8. Equation AI.2.8 is employed in Section 1.3 to derive equations in differential form.

For functions of two variables, for example, $f(x, y)$, we write:

$$f(x+\varepsilon, y+\delta) \approx f(x,y) + \frac{\partial f}{\partial x}\Big|_{x=\varepsilon}\varepsilon + \frac{\partial f}{\partial y}\Big|_{y=\delta}\delta \tag{AI.2.9}$$

When dealing with rational *fractional* functions, it is often advantageous to express them in terms of partial fractions and then expand them using the *binomial theorem*. For example, the expansion

$$(c+\varepsilon)^n = c^n + nc^{n-1}\varepsilon + \frac{n(n-1)}{2!}c^{n-2}\varepsilon^2 + \frac{n(n-1)(n-2)}{3!}c^{n-3}\varepsilon^3 + \cdots \tag{AI.2.10}$$

is valid for all values of $n$ if $|\varepsilon| < |c|$. If $|c| < |\varepsilon|$, the expansion is valid only if $n$ is a non-negative integer.

## AI.3 Functions

### AI.3.1 Hyperbolic Functions

Next to the circular trigonometric functions, the hyperbolic functions sinh($x$), cosh($x$), and tanh($x$) appear frequently in science and engineering and hence, in the present text.

| Graphs | Relations |
|---|---|
| 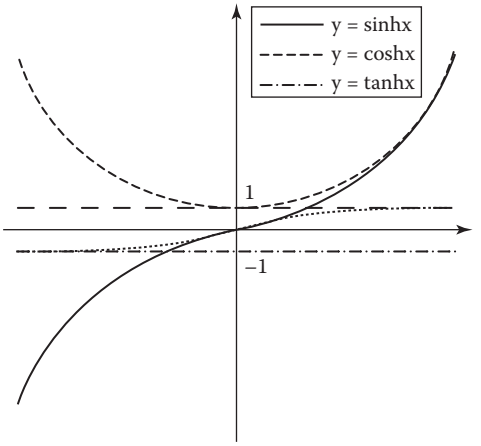  | $\sinh(x)=\frac{1}{2}(e^{x}-e^{-x})$<br>$\cosh(x)=\frac{1}{2}(e^{x}+e^{-x})$<br>$\cosh^{2}(x)-\sinh^{2}(x)=1$<br>$\sinh(x\pm y)=\sinh(x)\cosh(y)$<br>$\pm\cosh(x)\sinh(y)$<br>$\cosh(x\pm y)=\cosh(x)\cosh(y)$<br>$\pm\sinh(x)\sinh(y)$ |

### AI.3.2 Error Functions

Numerous natural phenomena follow exponential functions. For example,

$$erf(x)=\frac{2}{\sqrt{\pi}}\int_{0}^{x}e^{-\xi^{2}}d\xi \tag{AI.3.3a}$$

where

$$erf(0)=0 \quad \text{and} \quad erf(\infty)=1 \tag{AI.3.3b, c}$$

The integrand $\exp(-\xi^2)$ is a normal probability distribution. Thus, Equation AI.3.3 is a solution part of processes governed by Gaussian-type distributions. The "complementary error function" is defined as

$$1-erf(x)\equiv erfc(x) \tag{AI.3.4}$$

The error function, complementary error function, trigonometric functions, and exponential function have been plotted in Figure AI.1.

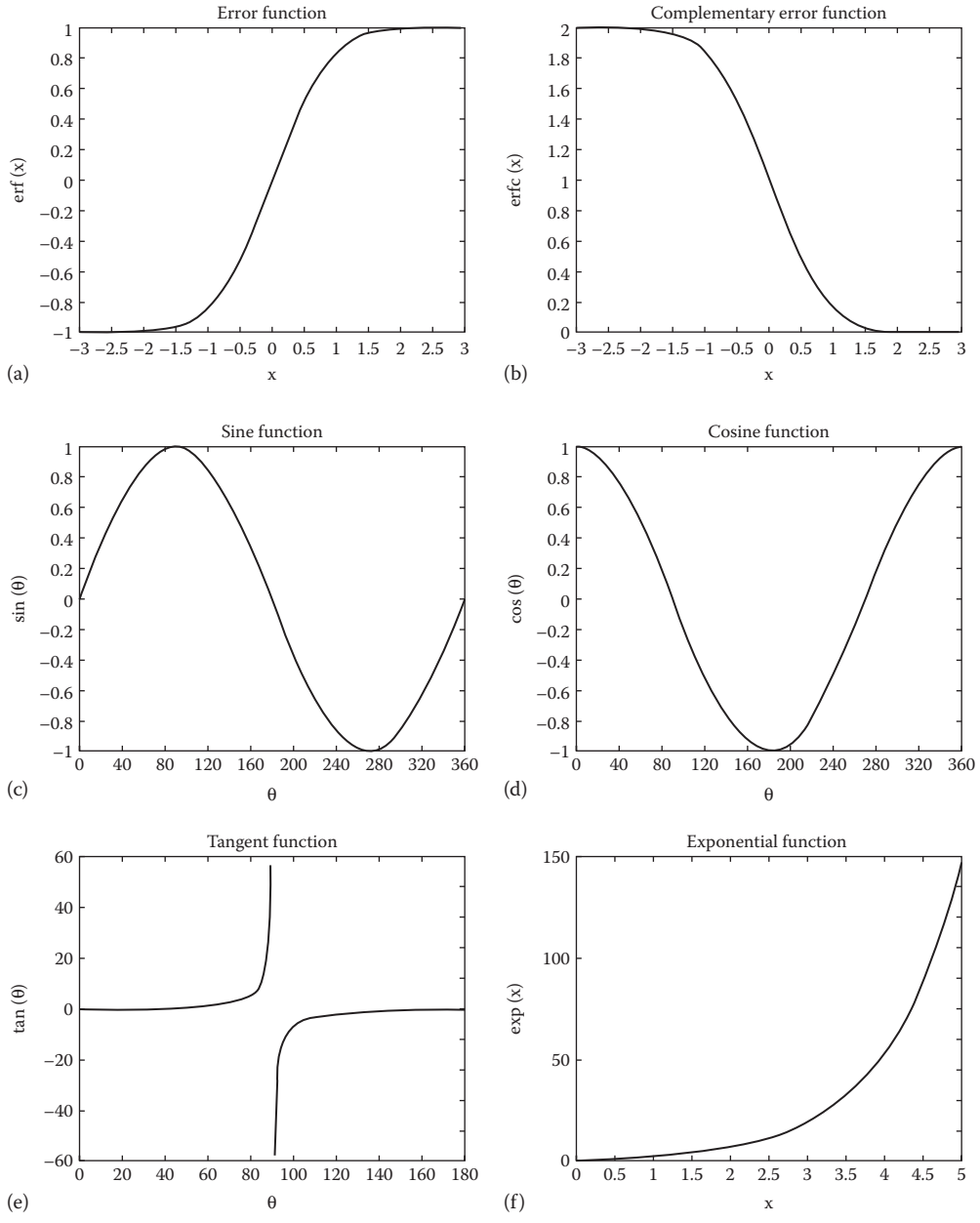


**FIGURE AI.1**
Graphs of useful functions. (a) Error function, (b) complementary error function, (c) sine, (d) cosine, (e) tangent, and (f) exponential.

## AI.4 Integral Transformations

### AI.4.1 The Divergence Theorem

As established by Gauss, the divergence theorem states that the integration over the dot product of a vector field, $\vec{\mathbf{v}}$, with a closed regular area element, $d\vec{\mathbf{A}}$, is equal to the integration of the divergence of $\vec{\mathbf{v}}$, that is, $\nabla \cdot \vec{\mathbf{v}}$, over the interior volume, $\forall$:

$$\iint_A \vec{\mathbf{v}} \cdot d\vec{\mathbf{A}} = \iiint_{\forall} \left(\nabla \cdot \vec{\mathbf{v}}\right) d\forall \tag{AI.3.1}$$

Equation AI.3.1 is used in Section 1.3 when all surface integrals in the Reynolds Transport Theorem are converted into volume integrals to express the conservation laws of mass, momentum, and energy in *differential form*.

*Sample Problem:* Given $\vec{\mathbf{v}} = 4xz\hat{i} - y^2\hat{j} + yz\hat{k}$, that is, $u = 4xz$, $v = -y^2$, and $w = yz$, in a unit cube, that is, $0 \le x \le 1$, $0 \le y \le 1$, and $0 \le z \le 1$, show that Equation AI.3.1 holds.

*Solution:*

1. Six-sided surface integral: $\iint_A \vec{\mathbf{v}} \cdot d\vec{\mathbf{A}} = \int_0^1 \int_0^1 \vec{\mathbf{v}} \cdot \vec{\mathbf{n}} dA$

   where:

   $\hat{n} = \hat{i}$ at x = 1 and $\hat{n} = -\hat{i}$ at x = 0 with $dA = dydz$

   $\hat{n} = \hat{j}$ at y = 1 and $\hat{n} = -\hat{j}$ at y = 0 with $dA = dxdz$

   $\hat{n} = \hat{k}$ at z = 1 and $\hat{n} = -\hat{k}$ at z = 0 with $dA = dxdy$

   Thus,

$$\int_0^1 \int_0^1 \vec{\mathbf{v}} \cdot \hat{i} dA = \int_0^1 \int_0^1 4xz\big|_{x=1} dydz = 4y\Big|_0^1 \left(\frac{1}{2} z^2 \Big|_0^1\right) = 2$$

   Similarly,

$$\int_0^1 \int_0^1 \vec{\mathbf{v}} \cdot \hat{j} dA = -1; \int_0^1 \int_0^1 \vec{\mathbf{v}} \cdot \hat{k} dA = \frac{1}{2}$$

   and the other three negative surface integrals are zero. Hence,

$$\iint_A \vec{\mathrm{v}} \cdot \hat{n} dA = 2 - 1 + \frac{1}{2} + 0 + 0 + 0 = \frac{3}{2}$$

2. Volume integral: $\iiint_{\forall} \nabla \cdot \vec{\mathbf{v}} d\forall = \int_0^1 \int_0^1 \int_0^1 \left(\frac{\partial u}{\partial x} + \frac{\partial \mathrm{v}}{\partial y} + \frac{\partial w}{\partial z}\right) dxdydz$

$$\int_0^1 \int_0^1 \int_0^1 (4z - 2y + y) dxdydz = \left|\frac{4z^2}{2} - \frac{z}{2}\right|_0^1 = \frac{3}{2}$$

*Comment*:

It is evident that such integral operations over *variable* vector fields result in scalars (i.e., numbers); this implies that the Reynolds Transport Theorem generates scalar quantities, that is, numerical values for flow rates, averaged velocities, forces, wall stresses, pressure drops, and so on.

### AI.4.2 Leibniz Rule

A switch in the order of operation is justified by Leibniz's Rule: if $F(t) = \int_a^b f(x,t)dx$ and $a$, $b$ are constants, then

$$\frac{dF}{dt} \equiv \frac{d}{dt}\left[\int_a^b f(x,t)dx\right] = \int_a^b \frac{\partial f}{\partial t}dx \tag{AI.3.2}$$

Equation AI.3.2 is occasionally applied when dealing with the transient term <volume integral> in the RTT. In general, the Leibniz rule reads:

$$\frac{d}{dt}\int_{a(t)}^{b(t)} f(x,t)dx = \int_a^b \frac{\partial f}{\partial t}dx + b'f[b(t),t] - a'f[a(t),t]$$

### AI.4.3 Integral Methods

Two solution techniques dealing with integral equations are briefly discussed. The first method starts with the integration of a given set of partial differential equations (PDEs) that describe a given flow system, known as the *integral method*. The second approach starts with balance equations in integral form, that is, the Reynolds Transport Theorem, which ensures the conservation laws for a control volume.

*Von Karman Integral Method:* In contrast to separation of variables and similarity theory, the integral method is an *approximation* method. The Von Karman integral method is the most famous member of the family of integral relations, which in turn, is a special case of the method of weighted residuals (MWR). Specifically, a transport equation in normal form can be written as (cf. Equation 1.7)

$$L(\varphi) \equiv \frac{\partial \varphi}{\partial t} + \nabla \cdot \left(\vec{\mathbf{v}}\varphi\right) - \nu\nabla^2\varphi - S = 0 \tag{AI.3.5}$$

where:

- $L$ is a (nonlinear) operator
- $\varphi$ is a dependent variable
- $S$ represents sink/source terms

Now, the unknown φ-function is replaced by an *approximate* expression, that is, a "profile" or functional $\tilde{\varphi}$ that satisfies the boundary conditions but contains a number of unknown coefficients or parameters. As can be expected,

$$L(\tilde{\varphi}) \neq 0, \text{i.e.}, L(\tilde{\varphi}) \equiv R \tag{AI.3.6a, b}$$

where $R$ is the residual. In requiring that

$$\int_{\Omega} WRd\Omega = 0 \tag{AI.3.6c}$$

we force the weighted residual over the computational domain $\Omega$ to be zero and thereby determine the unknown coefficients or parameters in the assumed $\tilde{\varphi}$ -function. The type of weighing function $W$ determines the special case of the MWR, for example, integral method, collocation method, Galerkin finite element method, control volume method, and so on (cf. Finlayson 1978).

The Von Karman method is best applicable to laminar/turbulent similar or non-similar *boundary layer–type* flows for which appropriate velocity, concentration, and temperature profiles are known; that is, thin and thick wall shear layers as well as plumes, jets, and wakes. Solutions of such problems yield global or integral system parameters, such as flow rates, fluxes, forces, boundary-layer thicknesses, shape factors, drag coefficients, and so on.

In general, a two-dimensional (2-D) partial differential equation is integrated in one direction, typically normal to the main flow, and thereby transformed into an ordinary differential equation (ODE), which is then solved analytically or numerically. Implementation of the integral method rests on two general characteristics of boundary layer–type problems: (1) the boundary conditions for a particular system simplify the integration process significantly, so that a simpler differential equation is obtained, and (2) all extra unknown functions, or parameters, remaining in the governing differential equation are approximated on physical grounds or by empirical relationships. Thus, closure is gained by using, for example, the entrainment concept for plumes, jets, and wakes or by expressing velocity and temperature profiles with power expansions for high–Reynolds number flows past submerged bodies.

*Sample Problem*: Integral method applied to the Blasius problem ($U_0 = u_\infty = ¢$, that is, $\partial p/\partial x = 0$)

| **Sketch** | **Assumptions** |
|---|---|
| 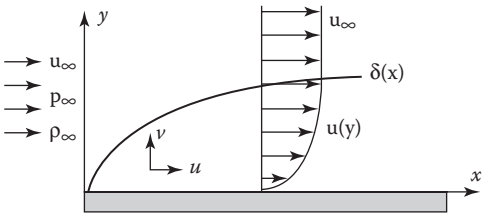 | • Steady laminar 2-D flow with constant fluid properties |



*Recall:* For the Blasius problem, the boundary-layer equations reduce to

$$\frac{\partial u}{\partial x} + \frac{\partial \mathrm{v}}{\partial y} = 0 \quad \text{and} \quad \frac{\partial u}{\partial t} + u\frac{\partial u}{\partial x} + \mathrm{v}\frac{\partial u}{\partial y} = \frac{1}{\rho}\frac{d\tau_{yx}}{dx}$$

- Solving for $v$ in the continuity equation yields

$$\mathrm{v} = -\int \frac{\partial u}{\partial y}\,dy + f(x) := -\int_0^y \frac{\partial u}{\partial x}\,dy$$

- Integration across the $x$-momentum equation yields

$$\int_{y=0}^{\delta(t)} \left( u\frac{\partial u}{\partial x} + \mathrm{v}\frac{\partial u}{\partial y} \right) dy = \frac{1}{\rho}\int_0^{\delta} \frac{d\tau_{yx}}{dx}\,dy := -\frac{\tau_w}{\rho}$$

- Inserting $v(x, y)$ and integrating the term $\int_0^{\delta} \mathrm{v}\frac{\partial u}{\partial y}\,dy$ by parts, that is, $\int u\,d\mathrm{v} = u\mathrm{v} - \int \mathrm{v}\,du$, yields

$$\int_0^{\delta} \frac{\partial}{\partial x}\left[ u(U-u) \right] dy = \frac{\tau_w}{\rho}$$

where $U = u_\infty$. Now, a suitable $u(x, y)$ profile has to be postulated, which matches the boundary conditions at $y = 0$ and $y = \delta(x)$.

*Solution*: For laminar flow over a flat plate,

$$\frac{u}{u_\infty} = 2\frac{y}{\delta} - \left(\frac{y}{\delta}\right)^2$$

is a suitable profile, where $\delta(x)$ is the key unknown.

With the previously derived *momentum integral relation*,

$$\tau_w(x) = \rho\frac{d}{dx}\int_0^{\delta} u(U-u)\,dy := 0.133\rho U^2\frac{d\delta}{dx}$$

We also know that

$$\tau_w(x) = \mu\left.\frac{\partial u}{\partial y}\right|_{y=0} := \mu U\frac{2}{\delta}$$

Combining both results leads to an ODE for $\delta(x)$:

$$\frac{\mu dx}{0.0665\rho U} = \delta d\delta \text{ subject to } \delta(x=0) = 0$$

Integration yields

$$\delta(x) = 5.48\sqrt{\frac{\mu x}{\rho U}}$$

and hence,

$$\tau_w(x) = 0.356\rho U^2 \sqrt{\frac{\mu}{\rho U x}}$$

*Graph*:

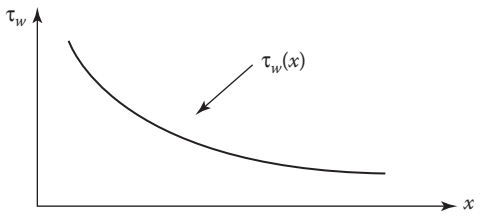


## AI.5 Ordinary Differential Equations

For most fluid mechanics applications, the key differential equations are the equation of continuity, that is, conservation of fluid mass, and the Navier–Stokes equations, that is, conservation of linear momentum for constant fluid properties, as well as the scalar transport equations for species-mass and heat transfer. They reflect the conservation laws in terms of differential balances for fluid mass, momentum, species concentration, and energy.

If the dependent variable, say, the velocity, is a function of more than one independent variable (e.g., $x$, $y$, $z$, $t$ or $r$, $\theta$, $z$, $t$), then the describing equation is a PDE; otherwise, it is an ODE. Clearly, solving PDEs requires usually elaborate transformations or numerical algorithms (see Ozisik 1993; Hoffman 2001). For that reason and to gain direct physical insight, *simplified base-case problems* are discussed (see Chapter 1), where the continuity equation is fully satisfied and the Navier–Stokes equations are reduced to ODEs. Exact solutions for ODEs are listed in Polyanin and Zaitsev (1995). Numerical ODE solutions may be obtained with commercial software such as MatLab and Mathcad, which for their underlying finite-difference approximations rely on selected terms of the Taylor Series (see Section AI.2.3).

After the development of a mathematical model describing approximately the fluid flow problem at hand, the resulting ODE (or system of coupled ODEs) has to be classified. One has to determine whether the ODE, say, for $y(x)$, is

- Linear or nonlinear (e.g., $y^2$, $yy'$, $\sqrt{y''}$, etc.)
- With constant coefficients or not
- Homogeneous or inhomogeneous
- Of first, second, or $n$-th order
- An initial value problem (IVP) or a boundary value problem (BVP)

The last two types of ODEs can be solved numerically with the Runge-Kutta method (IVPs) or a shooting method (BVPs) as available from www.netlib.org/odepack.

Fortunately, most introductory fluid flow problems are governed by ODEs of the form

$$\frac{d^n}{dy^n}\left[f(y)\right] = g(y) \tag{AI.4.1}$$

which can be solved by direct integration, subject to n boundary conditions (BCs).

Typically, $n = 2$ and $g(y) \equiv K$, a constant, so that Equation AI.4.1 can be rewritten as

$$\frac{d}{dy}\left[\frac{df}{dy}\right] = K \tag{AI.4.2a}$$

or

$$d\left[\frac{df}{dy}\right] = Kdy \tag{AI.4.2b}$$

Hence,

$$\frac{df}{dy} = Ky + C_1 \tag{AI.4.2c}$$

and integrating again yields

$$f(y) = \frac{K}{2}y^2 + C_1 y + C_2 \tag{AI.4.3}$$

where the integration constants are determined with two given boundary conditions for $f(y)$.

In cylindrical coordinates, we may encounter an ODE somewhat similar to Equation AI.4.1 of the form

$$\frac{1}{r}\frac{df(r)}{dr} + \frac{d^2 f(r)}{dr^2} = g(r) \tag{AI.4.4a}$$

which can be rewritten for direct integration as

$$\frac{1}{r}\frac{d}{dr}\left(r\frac{df(r)}{dr}\right) = g(r) \tag{AI.4.4b}$$

For example, with $g(r) \equiv K =$ constant and $f \equiv v$, say the fully developed axial velocity in a tube of radius $R$, we have

$$d\left(r\frac{dv(r)}{dr}\right) = Krdr \tag{AI.4.5a}$$

so that after integration

$$\frac{dv(r)}{dr} = \frac{K}{2}r + \frac{C_1}{r} \tag{AI.4.5b}$$

Integrating again yields

$$\mathrm{v}(r) = \frac{K}{4} r^2 + C_1 \ln r + C_2 \tag{AI.4.6}$$

The differences between the solutions of Equations AI.4.3 and AI.4.6 as well as the impact of different BCs on Equation AI.4.6 were discussed in Section 1.3.

Another interesting case where term contraction allows direct integration is as an ODE of the form

$$\frac{df(x)}{dx} + \frac{n}{x} f(x) \equiv \frac{1}{x^n} \frac{d}{dx}\left[ x^n f(x) \right] = g(x); \quad n = 1, 2 \tag{AI.4.7a}$$

which yields after the first integration

$$x^n f(x) = \int x^n g(x) dx + C_1 \tag{AI.4.7b}$$

The term $\int x^n g(x) dx$ could be solved via integration by parts, that is,

$$\int_a^b u dv = (uv)\Big|_a^b - \int_a^b v du \tag{AI.4.8}$$

Numerous natural processes can be described by a linear, inhomogeneous second-order ODE with constant coefficients, that is,

$$f'' + Af' + Bf = F(x) \tag{AI.4.9}$$

where $F(x)$ is a prescribed (forcing) function. Typically,

$$f(x) = f_{\text{homog.}} + f_{\text{inhomog.}} \tag{AI.4.10a}$$

In general, $f_{\text{homog.}}$ admits exponential solutions, for example,

$$f(x) \sim e^{\lambda x} \tag{AI.4.10b}$$

where $\lambda$ can be obtained from the quadratic equation

$$\lambda^2 + A\lambda + B = 0 \tag{AI.4.10c}$$

so that

$$f(x) = C_1 e^{\lambda_1 x} + C_2 e^{\lambda_2 x} \tag{AI.4.10d}$$

Table AI.1 summarizes typical ODEs describing transport phenomena, where $f$ and $g$ are functions of $x$ and the quantities $a$, $b$, and $c$ are real constants.

**TABLE AI.1**

Typical ODEs and Their General Solutions

| Equation | General Solution |
|---|---|
| $\frac{dy}{dx} = \frac{f(x)}{g(y)}$ | $\int g\,dy = \int f\,dx + C_1$ |
| $\frac{dy}{dx} + f(x)y = g(x)$ | $y = e^{-\int f dx}\left(\int e^{\int f dx} g\,dx + C_1\right)$ |
| $\frac{d^2y}{dx^2} + a^2 y = 0$ | $y = C_1 \cos ax + C_2 \sin ax$ |
| $\frac{d^2y}{dx^2} - a^2 y = 0$ | $y = C_1 \cos \mathrm{h}ax + C_2 \sin \mathrm{h}ax$ or $y = C_3 e^{+ax} + C_4 e^{-ax}$ |
| $\frac{1}{x}\frac{d}{dx}\left(x^2 \frac{dy}{dx}\right) + a^2 y = 0$ | $y = \frac{C_1}{x}\cos ax + \frac{C_2}{x}\sin ax$ |

## AI.6 Transport Equations (Continuity, Momentum Transfer, and Heat Transfer)

### AI.6.1 Continuity Equation

$$\frac{\partial \rho}{\partial t} + \nabla \cdot (\rho \vec{\mathbf{v}}) = 0$$

*Note:* For $\rho = \not{c} \quad \Rightarrow \quad \nabla \cdot \vec{\mathbf{v}} = 0$

- Rectangular coordinates: $\frac{\partial \rho}{\partial t} + \frac{\partial}{\partial x}(\rho u) + \frac{\partial}{\partial y}(\rho v) + \frac{\partial}{\partial z}(\rho w) = 0$
- Cylindrical coordinates: $\frac{\partial \rho}{\partial t} + \frac{1}{r}\frac{\partial}{\partial r}(\rho r v_r) + \frac{1}{r}\frac{\partial}{\partial \theta}(\rho v_\theta) + \frac{\partial}{\partial z}(\rho v_z) = 0$

### AI.6.2 Equation of Motion (or Linear Momentum Equation)

***Cauchy Equation***

$$\rho \frac{D\vec{\mathbf{v}}}{Dt} = -\nabla p + \nabla \cdot \vec{\vec{\tau}} + \rho \vec{\mathbf{g}}$$

where

$$\frac{D\#}{Dt} \equiv \frac{\partial \#}{\partial t} + (\vec{\mathbf{v}} \cdot \nabla)\#$$

- Rectangular coordinates

$$\rho\left(\frac{\partial u}{\partial t} + u\frac{\partial u}{\partial x} + v\frac{\partial u}{\partial y} + w\frac{\partial u}{\partial z}\right) = -\frac{\partial p}{\partial x} + \left[\frac{\partial}{\partial x}\tau_{xx} + \frac{\partial}{\partial y}\tau_{yx} + \frac{\partial}{\partial z}\tau_{zx}\right] + \rho g_x$$

$$\rho\left(\frac{\partial v}{\partial t}+u\frac{\partial v}{\partial x}+v\frac{\partial v}{\partial y}+w\frac{\partial v}{\partial z}\right)=-\frac{\partial p}{\partial y}+\left[\frac{\partial}{\partial x}\tau_{xy}+\frac{\partial}{\partial y}\tau_{yy}+\frac{\partial}{\partial z}\tau_{zy}\right]+\rho g_y$$

$$\rho\left(\frac{\partial w}{\partial t}+u\frac{\partial w}{\partial x}+v\frac{\partial w}{\partial y}+w\frac{\partial w}{\partial z}\right)=-\frac{\partial p}{\partial z}+\left[\frac{\partial}{\partial x}\tau_{xz}+\frac{\partial}{\partial y}\tau_{yz}+\frac{\partial}{\partial z}\tau_{zz}\right]+\rho g_z$$

- Cylindrical coordinates

$$\rho\left(\frac{\partial v_r}{\partial t}+v_r\frac{\partial v_r}{\partial r}+\frac{v_\theta}{r}\frac{\partial v_r}{\partial \theta}+v_z\frac{\partial v_r}{\partial z}-\frac{v_\theta^2}{r}\right)=-\frac{\partial p}{\partial r}$$
$$+\left[\frac{1}{r}\frac{\partial}{\partial r}\left(r\tau_{rr}\right)+\frac{1}{r}\frac{\partial}{\partial \theta}\tau_{\theta r}+\frac{\partial}{\partial z}\tau_{zr}-\frac{\tau_{\theta\theta}}{r}\right]+\rho g_r$$

$$\rho\left(\frac{\partial v_\theta}{\partial t}+v_r\frac{\partial v_\theta}{\partial r}+\frac{v_\theta}{r}\frac{\partial v_\theta}{\partial \theta}+v_z\frac{\partial v_\theta}{\partial z}+\frac{v_r v_\theta}{r}\right)=-\frac{1}{r}\frac{\partial p}{\partial \theta}$$
$$+\left[\frac{1}{r^2}\frac{\partial}{\partial r}\left(r^2\tau_{r\theta}\right)+\frac{1}{r}\frac{\partial}{\partial \theta}\tau_{\theta\theta}+\frac{\partial}{\partial z}\tau_{z\theta}+\frac{\tau_{\theta r}-\tau_{r\theta}}{r}\right]+\rho g_\theta$$

$$\rho\left(\frac{\partial v_z}{\partial t}+v_r\frac{\partial v_z}{\partial r}+\frac{v_\theta}{r}\frac{\partial v_z}{\partial \theta}+v_z\frac{\partial v_z}{\partial z}\right)=-\frac{\partial p}{\partial z}$$
$$+\left[\frac{1}{r}\frac{\partial}{\partial r}\left(r\tau_{rz}\right)+\frac{1}{r}\frac{\partial}{\partial \theta}\tau_{\theta z}+\frac{\partial}{\partial z}\tau_{zz}\right]+\rho g_z$$

### AI.6.3 Momentum Equation for Constant-Property Fluids

***Navier–Stokes Equation***

$$\rho\frac{D\vec{\mathbf{v}}}{Dt}=-\nabla p+\mu\nabla^2\vec{\mathbf{v}}+\rho\vec{\mathbf{g}}$$

- Rectangular coordinates

$$\rho\left(\frac{\partial u}{\partial t}+u\frac{\partial u}{\partial x}+v\frac{\partial u}{\partial y}+w\frac{\partial u}{\partial z}\right)=-\frac{\partial p}{\partial x}+\mu\left[\frac{\partial^2 u}{\partial x^2}+\frac{\partial^2 u}{\partial y^2}+\frac{\partial^2 u}{\partial z^2}\right]+\rho g_x$$

$$\rho\left(\frac{\partial v}{\partial t}+u\frac{\partial v}{\partial x}+v\frac{\partial v}{\partial y}+w\frac{\partial v}{\partial z}\right)=-\frac{\partial p}{\partial y}+\mu\left[\frac{\partial^2 v}{\partial x^2}+\frac{\partial^2 v}{\partial y^2}+\frac{\partial^2 v}{\partial z^2}\right]+\rho g_y$$

$$\rho\left(\frac{\partial w}{\partial t}+u\frac{\partial w}{\partial x}+v\frac{\partial w}{\partial y}+w\frac{\partial w}{\partial z}\right)=-\frac{\partial p}{\partial z}+\mu\left[\frac{\partial^2 w}{\partial x^2}+\frac{\partial^2 w}{\partial y^2}+\frac{\partial^2 w}{\partial z^2}\right]+\rho g_z$$

- Cylindrical coordinates

$$\rho\left(\frac{\partial v_r}{\partial t}+v_r\frac{\partial v_r}{\partial r}+\frac{v_\theta}{r}\frac{\partial v_r}{\partial \theta}+v_z\frac{\partial v_r}{\partial z}-\frac{v_\theta^2}{r}\right)=-\frac{\partial p}{\partial r}$$
$$+\mu\left[\frac{\partial}{\partial r}\left(\frac{1}{r}\frac{\partial}{\partial r}\left(rv_r\right)\right)+\frac{1}{r^2}\frac{\partial^2 v_r}{\partial \theta^2}+\frac{\partial^2 v_r}{\partial z^2}-\frac{2}{r^2}\frac{\partial v_\theta}{\partial \theta}\right]+\rho g_r$$

$$\rho\left(\frac{\partial v_\theta}{\partial t}+v_r\frac{\partial v_\theta}{\partial r}+\frac{v_\theta}{r}\frac{\partial v_\theta}{\partial \theta}+v_z\frac{\partial v_\theta}{\partial z}+\frac{v_r v_\theta}{r}\right)=-\frac{1}{r}\frac{\partial p}{\partial \theta}$$
$$+\mu\left[\frac{\partial}{\partial r}\left(\frac{1}{r}\frac{\partial}{\partial r}\left(rv_\theta\right)\right)+\frac{1}{r^2}\frac{\partial^2 v_\theta}{\partial \theta^2}+\frac{\partial^2 v_\theta}{\partial z^2}+\frac{2}{r^2}\frac{\partial v_r}{\partial \theta}\right]+\rho g_\theta$$

$$\rho\left(\frac{\partial v_z}{\partial t}+v_r\frac{\partial v_z}{\partial r}+\frac{v_\theta}{r}\frac{\partial v_z}{\partial \theta}+v_z\frac{\partial v_z}{\partial z}\right)=-\frac{\partial p}{\partial z}$$
$$+\mu\left[\frac{1}{r}\frac{\partial}{\partial r}\left(r\frac{\partial v_z}{\partial r}\right)+\frac{1}{r^2}\frac{\partial^2 v_z}{\partial \theta^2}+\frac{\partial^2 v_z}{\partial z^2}\right]+\rho g_z$$

### AI.6.4 Heat and Species-Mass Transfer Equation for Constant-Property Fluids

***Heat Transfer Equation***

$$\rho c_p\frac{DT}{Dt}=k\nabla^2 T+\mu\Phi;\quad \frac{\mathrm{k}}{\rho c_p}\equiv\alpha\ \text{(thermal diffusivity)}$$

- Rectangular coordinates (see Section AI.6.6 for viscous dissipation function Φ)

$$\frac{\partial T}{\partial t}+u\frac{\partial T}{\partial x}+v\frac{\partial T}{\partial y}+w\frac{\partial T}{\partial z}=\alpha\left[\frac{\partial^2 T}{\partial x^2}+\frac{\partial^2 T}{\partial y^2}+\frac{\partial^2 T}{\partial z^2}\right]+\frac{\mu}{\rho c_p}\Phi$$

- Cylindrical coordinates

$$\frac{\partial T}{\partial t}+v_r\frac{\partial T}{\partial r}+\frac{v_\theta}{r}\frac{\partial T}{\partial \theta}+v_z\frac{\partial T}{\partial z}=\alpha\left[\frac{1}{r}\frac{\partial}{\partial r}\left(r\frac{\partial T}{\partial r}\right)+\frac{1}{r^2}\frac{\partial^2 T}{\partial \theta^2}+\frac{\partial^2 T}{\partial z^2}\right]+\frac{\mu}{\rho c_p}\Phi$$

***Species-Mass Transport Equation***

- For species-mass transport of concentration $c$ (M/L$^3$):

$$\frac{Dc}{Dt}=\mathcal{D}_{AB}\nabla^2 c+S_c;\ \mathcal{D}_{AB}=\frac{\kappa_B T}{3\pi\mu d_p}\ \text{(Stokes–Einstein binary mass diffusivity)}$$

- Rectangular coordinates

$$\frac{\partial C}{\partial t}+u\frac{\partial C}{\partial x}+v\frac{\partial C}{\partial y}+w\frac{\partial C}{\partial z}=\mathcal{D}_{AB}\left[\frac{\partial^2 C}{\partial x^2}+\frac{\partial^2 C}{\partial y^2}+\frac{\partial^2 C}{\partial z^2}\right]\pm S_C$$

- Cylindrical coordinates

$$\frac{\partial C}{\partial t}+v_r\frac{\partial C}{\partial r}+\frac{v_\theta}{r}\frac{\partial C}{\partial \theta}+v_z\frac{\partial C}{\partial z}=\mathcal{D}_{AB}\left[\frac{1}{r}\frac{\partial}{\partial r}\left(r\frac{\partial C}{\partial r}\right)+\frac{1}{r^2}\frac{\partial^2 C}{\partial \theta^2}+\frac{\partial^2 C}{\partial z^2}\right]\pm S_C$$

*Note:* The equations of Section AI.6.3 in conjunction with Sections AI.6.1 plus AI.6.4 are nowadays summarized as the *System of Navier–Stokes Equations.*

### AI.6.5 Dissipation Function for Newtonian Fluids

- Rectangular coordinates

$$\Phi=2\left[\left(\frac{\partial u}{\partial x}\right)^2+\left(\frac{\partial v}{\partial y}\right)^2+\left(\frac{\partial w}{\partial z}\right)^2\right]+\left[\frac{\partial v}{\partial x}+\frac{\partial u}{\partial y}\right]^2+\left[\frac{\partial w}{\partial y}+\frac{\partial v}{\partial z}\right]^2+\left[\frac{\partial u}{\partial z}+\frac{\partial w}{\partial x}\right]^2$$

- Cylindrical coordinates

$$\Phi=2\left[\left(\frac{\partial v_r}{\partial r}\right)^2+\left(\frac{1}{r}\frac{\partial v_\theta}{\partial \theta}+\frac{v_r}{r}\right)^2+\left(\frac{\partial v_z}{\partial z}\right)^2\right]+\left[r\frac{\partial}{\partial r}\left(\frac{v_\theta}{r}\right)+\frac{1}{r}\frac{\partial v_r}{\partial \theta}\right]^2+\left[\frac{1}{r}\frac{\partial v_z}{\partial \theta}+\frac{\partial v_\theta}{\partial z}\right]^2+\left[\frac{\partial v_r}{\partial z}+\frac{\partial v_z}{\partial r}\right]^2$$

### AI.6.6 Stresses: $\vec{\vec{\tau}}=\mu\left[\nabla\vec{\mathbf{v}}+\left(\nabla\vec{\mathbf{v}}\right)^{tr}\right]$ (Stokes) and Fluxes: $\vec{\mathbf{q}}_{cond}=-k\nabla T$ (Fourier)

*Note:* For incompressible fluids:

- Rectangular coordinates

$$\tau_{xx}=2\mu\frac{\partial u}{\partial x};\quad \tau_{yy}=2\mu\frac{\partial v}{\partial y};\quad \tau_{zz}=2\mu\frac{\partial w}{\partial z}$$

$$\tau_{xy}=\tau_{yx}=\mu\left[\frac{\partial v}{\partial x}+\frac{\partial u}{\partial y}\right]$$

$$\tau_{yz}=\tau_{zy}=\mu\left[\frac{\partial w}{\partial y}+\frac{\partial v}{\partial z}\right]$$

$$\tau_{zx}=\tau_{xz}=\mu\left[\frac{\partial u}{\partial z}+\frac{\partial w}{\partial x}\right]$$

$$q_x=-k\frac{\partial T}{\partial x};\quad q_y=-k\frac{\partial T}{\partial y};\quad q_z=-k\frac{\partial T}{\partial z}$$

- Cylindrical coordinates

$$\tau_{rr} = 2\mu\frac{\partial v_r}{\partial r};\quad \tau_{\theta\theta} = 2\mu\left(\frac{1}{r}\frac{\partial v_\theta}{\partial \theta} + \frac{v_r}{r}\right);\quad \tau_{zz} = 2\mu\frac{\partial v_z}{\partial z}$$

$$\tau_{r\theta} = \tau_{\theta r} = \mu\left[r\frac{\partial}{\partial r}\left(\frac{v_\theta}{r}\right) + \frac{1}{r}\frac{\partial v_r}{\partial \theta}\right]$$

$$\tau_{\theta z} = \tau_{z\theta} = \mu\left[\frac{1}{r}\frac{\partial v_z}{\partial \theta} + \frac{\partial v_\theta}{\partial z}\right]$$

$$\tau_{zr} = \tau_{rz} = \mu\left[\frac{\partial v_r}{\partial z} + \frac{\partial v_z}{\partial r}\right]$$

$$q_r = -k\frac{\partial T}{\partial r};\quad q_\theta = -k\frac{1}{r}\frac{\partial T}{\partial \theta};\quad q_z = -k\frac{\partial T}{\partial z}$$

### AI.6.7 Fick's law

It relates the diffusive flux to the concentration gradient under steady-state conditions.

$$\vec{j} = -D\nabla C$$

where:
$\vec{j}$ = diffusive flux
$D$ = diffusion coefficient or diffusivity

The negative sign indicates that the flux is positive when there is movement from a higher to a lower concentration.

## AI.7 Supplementary Material

### AI.7.1 Prefixes and Length-Scale Information

For proper communication and relative-size appreciation, prefixes and a few length-scale examples are given here.

***Unit Prefixes:***

| | | |
|---|---|---|
| Femto | → | $10^{-15}$ |
| Pico | → | $10^{-12}$ |
| Nano | → | $10^{-9}$ |
| Micro | → | $10^{-6}$ |
| Milli | → | $10^{-3}$ |
| Kilo | → | $10^{3}$ |
| Mega | → | $10^{6}$ |
| Giga | → | $10^{9}$ |
| Tera | → | $10^{12}$ |
| Peta | → | $10^{15}$ |

***Length-Scale Examples:***

| Nature | Man-made |
|---|---|
| • Human hair ≈ 80 μm<br>• Air particle ≈ 6 μm | • Nanomaterial (1–$10^3$ nm)<br>• Microelectromechanical system (MEMS) (0.5–$10^3$ μm)<br>• Nanoelectromechanical system (NEMS) (10–500 nm)<br>• Pollutants (1 nm to millimeters) |

***Length Scales of Nano- and Microsystems:***

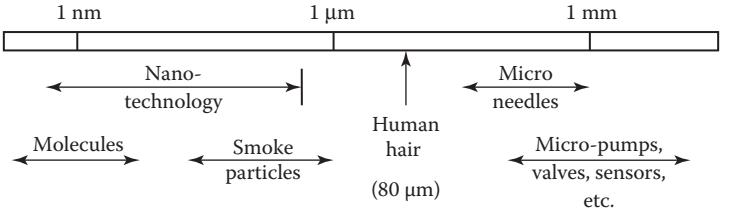


### AI.7.2 Prandtl's Boundary-Layer Equations

In his seminal work published in 1904, Prandtl observed that when a solid body was introduced into the flow, the effects of friction were felt over only a limited region in the vicinity of the submerged body. This distance is typically much smaller compared with the characteristic length-scale in the streamwise direction. Prandtl's theory of boundary-layer flow is shown in Figure AI.2.

The figure shows steady laminar flow over a horizontal wall. The viscous effects are felt over a short distance $\delta(x)$ from the plate. The flow beyond this short distance is free of friction effects, or, in other words, it is assumed to be inviscid. This region, where the viscous and the inertial forces are both influential, is known as the boundary layer, and it is contained within the coordinates $0 \le y \le \delta(x)$ and $0 \le x \le l$, where $l$ is the plate length. $\delta(x)$ denotes the thickness of the boundary layer, and its variation in the streamwise direction is given by the relation: $\delta(x) \sim \sqrt{x}$ . Moreover, the boundary-layer thickness is lower for lower viscosities.

This implies that as $\mathrm{Re} \to \infty$, the boundary-layer thickness $\delta(x) \to 0$. The system of Navier–Stokes equations for a 2-D steady laminar incompressible flow is as follows:

$$\text{(Continuity)} \qquad \frac{\partial u}{\partial x} + \frac{\partial v}{\partial y} = 0$$

$$\text{(x-momentum)} \qquad u\frac{\partial u}{\partial x} + v\frac{\partial u}{\partial y} = -\frac{1}{\rho}\frac{\partial p}{\partial x} + \nu\left(\frac{\partial^2 u}{\partial x^2} + \frac{\partial^2 u}{\partial y^2}\right) + g_x$$

$$\text{(y-momentum)} \qquad u\frac{\partial v}{\partial x} + v\frac{\partial v}{\partial y} = -\frac{1}{\rho}\frac{\partial p}{\partial y} + \nu\left(\frac{\partial^2 v}{\partial x^2} + \frac{\partial^2 v}{\partial y^2}\right) + g_y$$

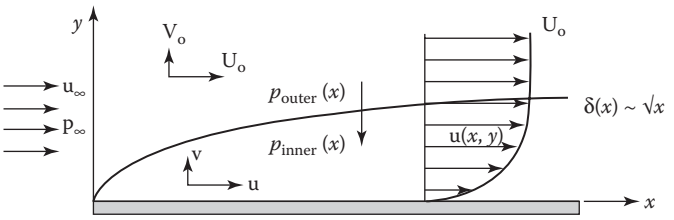


**FIGURE AI.2**
Steady laminar flat-plate boundary-layer flow.

Prandtl was able to use the aforementioned information to reduce this system of equations to a more tractable form. This reduced form of the equations came to be famously known as the *Boundary-Layer Equations*.

The first step in this direction would be to non-dimensionalize this system of equations using the free-stream velocity ($U_\infty$) as the characteristic velocity and the plate length ($l$) as the characteristic length. In the $x$-momentum equation, the pressure terms and the inertial terms must be of the same order for the equation to be satisfied.

$$u\frac{du}{dx} \sim -\frac{1}{\rho}\frac{\partial p}{\partial x}$$

$$U_\infty \frac{U_\infty}{l} \sim \frac{1}{\rho}\frac{p - p_\infty}{l}$$

$$U_\infty^2 \sim p - p_\infty$$

Therefore, we use the term ($\rho U_\infty^2$) to non-dimensionalize the pressure. Non-dimensionalizing allows us to recast the existing set of equations into a more compact and physically meaningful form. Thus, all the variables are non-dimensionalized as follows:

$$\hat{u} = \frac{u}{U_\infty} \qquad \hat{v} = \frac{v}{U_\infty} \qquad \hat{x} = \frac{x}{\ell} \qquad \hat{y} = \frac{y}{\ell}$$

$$\hat{p} = \frac{p}{\rho U_\infty^2}$$

By non-dimensionalizing the equations in this manner and neglecting the body force components, we can obtain a non-dimensional form of the governing equations as follows:

$$\frac{\partial \hat{u}}{\partial \hat{x}} + \frac{\partial \hat{v}}{\partial \hat{y}} = 0$$

$$\hat{u}\frac{\partial \hat{u}}{\partial \hat{x}} + \hat{v}\frac{\partial \hat{u}}{\partial \hat{y}} = -\frac{\partial \hat{p}}{\partial \hat{x}} + \frac{1}{\mathrm{Re}}\left(\frac{\partial^2 \hat{u}}{\partial \hat{x}^2} + \frac{\partial^2 \hat{u}}{\partial \hat{y}^2}\right)$$

$$\hat{u}\frac{\partial \hat{v}}{\partial \hat{x}} + \hat{v}\frac{\partial \hat{v}}{\partial \hat{y}} = -\frac{\partial \hat{p}}{\partial \hat{y}} + \frac{1}{\mathrm{Re}}\left(\frac{\partial^2 \hat{u}}{\partial \hat{x}^2} + \frac{\partial^2 \hat{u}}{\partial \hat{y}^2}\right)$$

It can be observed that for the boundary layer, the streamwise and the cross-stream expanse can be given by $0 \le y \le \delta(x)$ and $0 \le x \le l$. Also, it is assumed that for a flow with a reasonably high Re, the boundary-layer thickness is extremely small compared with the plate length ($\delta \ll l$). The ratio of the boundary-layer thickness to the plate length is denoted by the symbol ε. Therefore, we can express the orders of the spatial coordinates as follows:

$$\hat{x} = \frac{x}{\ell} \sim \frac{\ell}{\ell} \sim 1 \qquad \hat{y} = \frac{y}{\ell} \sim \frac{\delta}{\ell} \sim \varepsilon$$

According to the definition of the boundary layer, as $y \to \delta(x)$, the streamwise velocity approaches the free-stream velocity ($u \to U_\infty$). Within the boundary layer, the streamwise velocity varies from zero to the free-stream velocity ($0 \le u \le U_\infty$). It follows from this that the order of the non-dimensional streamwise velocity is 1.

If we now examine the continuity equation, we observe that the orders of $\hat{x}$ and $\hat{u}$ are 1, and therefore, the order of the first term in the continuity equation is 1. To satisfy the continuity equation, the order of the second term must also be 1. However, the order of $\hat{y}$ is ε, and therefore, the order of $\hat{v}$ must also be ε.

$$\hat{u} = \frac{u}{U_\infty} \sim \frac{U_\infty}{U_\infty} \sim 1 \qquad \hat{v} = \frac{v}{U_\infty} \sim \varepsilon$$

While the flow is largely inviscid outside the thin boundary-layer region, the inertial forces and the viscous forces are comparable within the boundary-layer region.

Inertial Forces ~ Viscous Forces

$$\rho u \frac{\partial u}{\partial x} \sim \mu \frac{\partial^2 u}{\partial y^2}$$

$$\rho U_\infty \frac{U_\infty}{\ell} \sim \mu \frac{U_\infty}{\delta^2}$$

$$\frac{\delta^2}{\ell^2} \sim \frac{\mu}{\rho U_\infty \ell}$$

$$\varepsilon \sim \sqrt{\frac{1}{\mathrm{Re}}}$$

Thus, it can be seen that for flows with a reasonably high Reynolds number, the ratio of the boundary-layer thickness to the plate length would be very small, and of an order much less than 1. If we investigate the inertia terms and the viscous terms in the *x*-momentum equation, it is seen that the inertial terms are of the order of 1.

$$\hat{u} \frac{\partial \hat{u}}{\partial \hat{x}} \sim 1 \frac{1}{1} \sim 1 \qquad \hat{v} \frac{\partial \hat{u}}{\partial \hat{y}} \sim \varepsilon \frac{1}{\varepsilon} \sim 1$$

$$\frac{1}{\mathrm{Re}} \left( \frac{\partial^2 \hat{u}}{\partial \hat{x}^2} + \frac{\partial^2 \hat{u}}{\partial \hat{y}^2} \right) \sim \frac{\varepsilon^2}{1} \left( \frac{1}{1} + \frac{1}{\varepsilon^2} \right) \sim \left( \frac{\varepsilon^2}{1} + \frac{1}{1} \right)$$

We can see that the first term among the viscous terms that physically represents the axial diffusion is of the order $\varepsilon^2$, which is extremely small compared with 1. As the Reynolds number increases, the effects of axial diffusion fizzle out. As a result, the axial diffusion term can be neglected in the x-momentum equation while considering flows with a reasonably high Re. It can be seen from AI.6.1.2 and from the definition of $\hat{x}$ that the order of the pressure term would also be 1.

$$\frac{\partial \hat{p}}{\partial \hat{x}} \sim \frac{1}{1} \sim 1$$

Thus, the entire x-momentum equation is of the order 1, except for the axial diffusion term, which is of the order of $\varepsilon^2 \ll 1$.

If we look at the y-momentum equation, it is seen that both the inertial terms and the viscous terms are of the order ε, except for the axial diffusion term, which is of the order of $\varepsilon^3 \ll \varepsilon$. It follows from this that the pressure term must also be of the order of ε for the equation to be satisfied.

$$\hat{u}\frac{\partial \hat{v}}{\partial \hat{x}} \sim 1\frac{\varepsilon}{1} \sim \varepsilon \qquad \hat{v}\frac{\partial \hat{v}}{\partial \hat{y}} \sim \varepsilon\frac{\varepsilon}{\varepsilon} \sim \varepsilon$$

$$\frac{1}{\mathrm{Re}}\left(\frac{\partial^2 \hat{v}}{\partial \hat{x}^2} + \frac{\partial^2 \hat{v}}{\partial \hat{y}^2}\right) \sim \frac{\varepsilon^2}{1}\left(\frac{\varepsilon}{1} + \frac{\varepsilon}{\varepsilon^2}\right) \sim \left(\frac{\varepsilon^3}{1} + \frac{\varepsilon}{1}\right)$$

$$\frac{\partial \hat{p}}{\partial \hat{y}} \sim \varepsilon$$

It can be seen that while the pressure variation in the *x*-direction is of the order 1, the variation in the *y*-direction is of the order ε. Thus, the variation of pressure in the *x*-direction is more pronounced than the variation along the y-direction. As $\mathrm{Re} \to \infty$, the pressure variation along the y-direction asymptotically goes to zero. Thus, the *y*-momentum equation essentially reduces to express the fact that the pressure variation along the y-direction across the boundary layer is negligible or zero.

$$\frac{\partial \hat{p}}{\partial \hat{y}} = 0 \qquad \therefore p = p(\hat{x})$$

It is reasonable to assume that for a high Reynolds number, the pressure is only a function of the *x*-coordinate. As the pressure does not vary significantly across the boundary layer, it is said that the pressure is "imposed" or "impressed" on the boundary layer by the external flow. This means that the pressure distribution can be estimated through the use of the inviscid Euler's equation at the boundary.

$$U\frac{\partial U}{\partial x} = -\frac{1}{\rho}\frac{\partial p}{\partial x}$$

On integrating the Euler's equation, we obtain the Bernoulli's equation, which establishes a relation between pressure, velocity, and the density of the fluid.

$$p + \frac{\rho U^2}{2} = \text{constant}$$

Thus, we can now state the non-dimensional form of the boundary-layer equations, as follows:

$$\frac{\partial \hat{u}}{\partial \hat{x}} + \frac{\partial \hat{v}}{\partial \hat{y}} = 0$$

$$\hat{u}\frac{\partial \hat{u}}{\partial \hat{x}} + \hat{v}\frac{\partial \hat{u}}{\partial \hat{y}} = -\frac{\partial \hat{p}}{\partial \hat{x}} + \frac{1}{\mathrm{Re}}\left(\frac{\partial^2 \hat{u}}{\partial \hat{y}^2}\right)$$

$$\frac{\partial \hat{p}}{\partial \hat{y}} = 0$$

Reverting to the original system of dimensional variables, we get

$$\frac{\partial u}{\partial x} + \frac{\partial v}{\partial y} = 0$$

$$u\frac{\partial u}{\partial x} + v\frac{\partial u}{\partial y} = -\frac{1}{\rho}\frac{\partial p}{\partial x} + \frac{\mu}{\rho}\left(\frac{\partial^2 u}{\partial y^2}\right)$$

$$\frac{\partial p}{\partial y} = 0$$

### AI.7.3 Turbulent Velocity Profiles in Pipes

#### *AI.7.3.1 Composite (Log-Law) Profile*

- Law of the wall: $u^+ = y^+,\ u^+ \equiv \dfrac{u}{u_\tau},\ y^+ \equiv \dfrac{yu_\tau}{\nu}$
  where:

  | | |
  |---|---|
  | $y = R - r$ | is the wall coordinate |
  | $u_\tau \equiv \sqrt{\tau_{wall}/\rho}$ | is the friction velocity |
  | $\nu = \mu/\rho$ | is the kinematic viscosity |

  *Note:* The linear profile $u^+ = y^+$ holds within the viscous sublayer $0 \le y^+ \le 5$, that is,

  $$y = \delta_{sublayer} = 5\nu/u_\tau$$

- Logarithmic law: $u^+ = 2.5\ln y^+ + 5.0;\ y^+ > 5.0$

  *Note:* The log law matches experimental data outside the viscous sublayer $0 \le y^+ \le 5$.

#### *AI.7.3.2 One-Seventh Power Law ($n \approx 7$):*

$$\frac{u}{u_{\max}} = \left(\frac{y}{R}\right)^{\frac{1}{n}} = \left(1 - \frac{r}{R}\right)^{\frac{1}{n}}$$

*Note:* The power law fails to (i) generate a zero slope at the pipe centerline and (ii) calculate the wall shear stress correctly. However, it is easy to use, and when $n = n(\mathrm{Re}_D)$ is selected, it provides reasonable profiles.

- Power-law exponent $n = n(\mathrm{Re}_D)$

| $\mathrm{Re}_D = \frac{u_{avg} D}{\nu}$ | $4 \times 10^3$ | $2.3 \times 10^4$ | $1.1 \times 10^5$ | $1.1 \times 10^6$ | $3.2 \times 10^5$ |
|---|---|---|---|---|---|
| $n$ | 6.0 | 6.6 | 7.0 | 8.8 | 10.0 |
| $\frac{u_{\text{average}}}{u_{\max}}$ | 0.791 | 0.807 | 0.817 | 0.850 | 0.865 |

### AI.7.4 OpenFOAM Commands

#### AI.7.4.1 About OpenFOAM

OpenFOAM (Open Field Operations and Manipulation) is a C++ library of efficient computational fluid dynamics (CFD) modules to solve complex transient 2-D and 3-D flow and fluid–structure interaction problems. OpenFOAM is publicly distributed with a vast number of executables called *applications*, which can be customized, or new library modules can be programmed. The applications fall into two categories: solvers, which are each designed to solve a specific problem in continuum mechanics, and utilities, which are designed to perform tasks that involve data manipulation. One can easily modify solvers and utilities to create custom applications with some prior knowledge of the underlying method, physics, and programming skills involved. The overall structure of OpenFOAM is shown in Figure AI.3.

#### *AI.7.4.2 Basic File Structure in OpenFOAM*

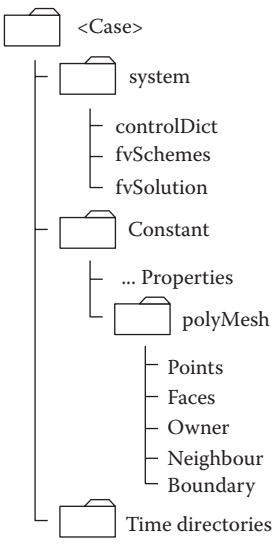


File Structure in OpenFOAM

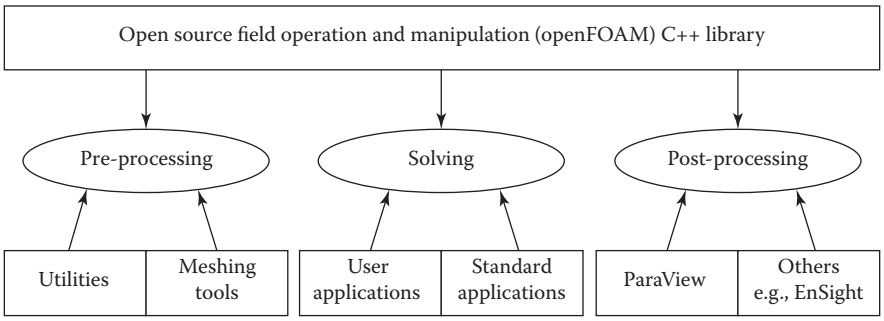


**FIGURE AI.3**
File structure in OpenFOAM.

*AI.7.4.2.1 System Directory*

The system directory consists of three sub-directories: controlDict, where run-time control parameters such as start time, end time, and write interval are included; fvSchemes, where the discretization schemes are selected; and fvSolution, where the solvers for the momentum and pressure equations, tolerances, and residual controls are set.

*AI.7.4.2.2 Constant Directory*

The constant directory has a folder called polyMesh, where details about the mesh are present. It also has a file called transportProperties, where physical properties of the fluid such as kinematic viscosity, density, thermal diffusivity, and so on are set.

*AI.7.4.2.3 Time Directories*

The boundary fields such as $U$ and $p$ for the patches defined in the mesh must always be initialized in a folder that corresponds to the startTime in the controlDict. Since usually, all simulations start at time $t = 0$, this folder is called the "0" folder. Data for subsequent time steps is written by the solver in folders below the "0" folder.

### *AI.7.4.3 OpenFOAM Solvers*

OpenFOAM does not have a generic solver applicable to all cases. Instead, users must choose a specific solver for a class of problems to solve. The solvers with the OpenFOAM distribution are in the *$FOAM_SOLVERS* directory. Some of the commonly used solvers have been listed in the table below. The description of the solvers is taken from the ESI OpenCFD website.

**'Basic' CFD codes**

| | |
|---|---|
| laplacianFoam | Laplace equation solver for a scalar |
| scalarTransportFoam | Passive scalar transport equation solver |

**Incompressible flow**

| | |
|---|---|
| icoFoam | Transient solver for incompressible, laminar flow of Newtonian fluids |
| nonNewtonianIcoFoam | Transient solver for incompressible, laminar flow of non-Newtonian fluids |
| simpleFoam | Steady-state solver for incompressible flows with turbulence modeling |
| pimpleFoam | Large time-step transient solver for incompressible, turbulent flow, using the PIMPLE (merged PISO-SIMPLE) algorithm |

**Compressible flow**

| | |
|---|---|
| rhoCentralFoam | Density-based compressible flow solver based on central-upwind schemes of Kurganov and Tadmor |
| rhoPimpleFoam | Transient solver for turbulent flow of compressible fluids for heating, ventilation, and air conditioning and similar applications |
| rhoSimpleFoam | Steady-state solver for turbulent flow of compressible fluids |
| sonicFoam | Transient solver for trans-sonic/supersonic, turbulent flow of a compressible gas |

**Multiphase flow**

| | |
|---|---|
| cavitatingFoam | Transient cavitation code based on the homogeneous equilibrium model from which the compressibility of the liquid/vapor "mixture" is obtained |
| compressibleInterFoam | Solver for two compressible, non-isothermal immiscible fluids using a VOF (volume of fluid) phase fraction–based interface capturing approach |
| interFoam | Solver for two incompressible, isothermal immiscible fluids using a VOF phase fraction–based interface capturing approach |
| multiphaseEulerFoam | Solver for a system of many compressible fluid phases including heat transfer |
| twoLiquidMixingFoam | Solver for mixing two incompressible fluids |
| twoPhaseEulerFoam | Solver for a system of two compressible fluid phases with one phase dispersed, for example, gas bubbles in a liquid including heat transfer |

**Heat transfer and buoyancy-driven flows**

| | |
|---|---|
| buoyantBoussinesqPimpleFoam | Transient solver for buoyant, turbulent flow of incompressible fluids |
| buoyantBoussinesqSimpleFoam | Steady-state solver for buoyant, turbulent flow of incompressible fluids |
| buoyantPimpleFoam | Transient solver for buoyant, turbulent flow of compressible fluids for ventilation and heat transfer |
| buoyantSimpleFoam | Steady-state solver for buoyant, turbulent flow of compressible fluids, including radiation, for ventilation and heat transfer |
| chtMultiRegionFoam | Transient solver for buoyant, turbulent fluid flow and solid heat conduction with conjugate heat transfer between solid and fluid regions |

**Particle-tracking flows**

| | |
|---|---|
| DPMFoam | Transient solver for the coupled transport of a single kinematic particle cloud including the effect of the volume fraction of particles on the continuous phase |
| icoUncoupledKinematicParcelFoam | Transient solver for the passive transport of a single kinematic particle cloud |
| reactingParcelFoam | Transient solver for compressible, turbulent flow with a reacting, multiphase particle cloud and optional sources/constraints |
| sprayFoam | Transient solver for compressible, turbulent flow with a spray particle cloud |
| uncoupledKinematicParcelFoam | Transient solver for the passive transport of a particle cloud |

### *AI.7.4.4 OpenFOAM Utilities*

Some of the commonly used OpenFOAM utilities/commands are:

#### *AI.7.4.4.1 Pre-Processing*

*applyBoundaryLayer*

Apply a simplified boundary-layer model to the velocity and turbulence fields based on the one-seventh power law.

*changeDictionary*

Utility to change dictionary entries; for example, can be used to change the patch type in the field and polyMesh/boundary files.

*engineSwirl*

Generates a swirling flow for engine calculations.

*foamUpgradeCyclics*

Tool to upgrade mesh and fields for split cyclics.

*mapFields*

Maps volume fields from one mesh to another, reading and interpolating all fields present in the time directory of both cases. Parallel and non-parallel cases are handled without the need to reconstruct them first.

*mapFieldsPar*

Maps volume fields from one mesh to another, reading and interpolating all fields present in the time directory of both cases.

*mdInitialise*

Initializes fields for a molecular dynamics (MD) simulation.

*setFields*

Sets values on a selected set of cells/patch faces through a dictionary.

*wallFunctionTable*

Generates a table suitable for use by tabulated wall functions.

*AI.7.4.4.2 Mesh Generation*

*blockMesh*

A multi-block mesh generator.

*extrudeMesh*

Extrude mesh from existing patch (by default outward facing normals; optional flips faces) or from patch read from file.

*extrudeToRegionMesh*

Extrude faceZones (internal or boundary faces) or faceSets (boundary faces only) into a separate mesh (as a different region).

*foamyHexMesh*

Conformal Voronoi automatic mesh generator.

*snappyHexMesh*

Automatic split hex mesher. Refines and snaps to surface.

3.6.3 Mesh conversion

*ansysToFoam*

Converts an ANSYS input mesh file, exported from I-DEAS, to OpenFOAM format.

*cfx4ToFoam*

Converts a CFX 4 mesh to OpenFOAM format.

*datToFoam*

Reads in a datToFoam mesh file and outputs a points file. Used in conjunction with blockMesh.

*fluent3DMeshToFoam*

Converts a Fluent mesh to OpenFOAM format.

*fluentMeshToFoam*

Converts a Fluent mesh to OpenFOAM format, including multiple region and region boundary handling.

*foamMeshToFluent*

Writes out the OpenFOAM mesh in Fluent mesh format.

*gambitToFoam*

Converts a GAMBIT mesh to OpenFOAM format.

*gmshToFoam*

Reads .msh file as written by Gmsh.

*star4ToFoam*

Converts a Star-CD (v4) pro-STAR mesh into OpenFOAM format.

*AI.7.4.4.3 Mesh Manipulation*

*attachMesh*

Attaches topologically detached mesh using prescribed mesh modifiers.

*autoPatch*

Divides external faces into patches based on (user-supplied) feature angle.

*checkMesh*

Checks validity of a mesh.

*createBaffles*

Makes internal faces into boundary faces. Does not duplicate points, unlike mergeOrSplitBaffles.

*createPatch*

Utility to create patches out of selected boundary faces. Faces come either from existing patches or from a faceSet.

*mergeMeshes*

Merges two meshes.

*mirrorMesh*

Mirrors a mesh around a given plane.

*moveDynamicMesh*

Mesh motion and topological mesh changes utility.

*moveMesh*

Solver for moving meshes.

*refineMesh*

Utility to refine cells in multiple directions.

*renumberMesh*

Renumbers the cell list to reduce the bandwidth, reading and renumbering all fields from all the time directories.

*rotateMesh*

Rotates the mesh and fields from direction n1 to direction n2.

*setsToZones*

Add pointZones/faceZones/cellZones to the mesh from similar named pointSets/faceSets/cellSets.

*splitMesh*

Splits mesh by making internal faces external. Uses attachDetach.

*stitchMesh*

"Stitches" a mesh.

*transformPoints*

Transforms the mesh points in the polyMesh directory according to the translate, rotate, and scale options.

*AI.7.4.4.4 Post-Processing*

*pdfPlot*

Generates a graph of a probability distribution function.

*temporalInterpolate*

Interpolates fields between time-steps, for example, for animation.

*particleTracks*

Generates a VTK file of particle tracks for cases that were computed using a tracked-parcel-type cloud.

*steadyParticleTracks*

Generates a VTK file of particle tracks for cases that were computed using a steady-state cloud. *Note:* case must be re-constructed (if running in parallel) before use.

*streamFunction*

Calculates and writes the stream function of velocity field U at each time.

*wallHeatFlux*

Calculates and writes the heat flux for all patches as the boundary field of a volScalarField and also prints the integrated flux for all wall patches.

*writeCellCentres*

Writes the three components of the cell centers as volScalarFields so that they can be used in post-processing in thresholding.

*AI.7.4.4.4.1 Post-processing data converters*

*foamDataToFluent*

Translates OpenFOAM data to Fluent format.

*foamToEnsight*

Translates OpenFOAM data to EnSight format.

*foamToGMV*

Translates foam output to GMV readable files.

*foamToTecplot360*

Tecplot binary file format writer.

*foamToVTK*

Legacy VTK file format writer.

*AI.7.4.4.5 Parallel Processing*

*decomposePar*

Automatically decomposes a mesh and fields of a case for parallel execution of OpenFOAM.

*reconstructPar*

Reconstructs fields of a case that is decomposed for parallel execution of OpenFOAM.

*reconstructParMesh*

Reconstructs a mesh using geometric information only.

*AI.7.4.4.6 Thermophysical-Related Utilities*

*chemkinToFoam*

Converts CHEMKINIII thermodynamics and reaction data files into OpenFOAM format.

*equilibriumCO*

Calculates the equilibrium level of carbon monoxide.

*equilibriumFlameT*

Calculates the equilibrium flame temperature for a given fuel and pressure for a range of unburned gas temperatures and equivalence ratios; the effects of dissociation on $O_2$, $H_2O$, and $CO_2$ are included.

*mixtureAdiabaticFlameT*

Calculates the adiabatic flame temperature for a given mixture at a given temperature.

*AI.7.4.4.7 Miscellaneous Utilities*

*foamDictionary*

Interrogates and manipulates dictionaries.

*foamFormatConvert*

Converts all IOobjects associated with a case into the format specified in the controlDict.

## AI.8 Greek Letters

| | |
|---|---|
| $\alpha$ | Thermal diffusivity ($m^2/s$) |
| $\beta$ | Coefficient of volume expansion |
| $\delta(x)$ | Boundary-layer thickness |
| $\Phi$ | Dissipation function |
| $\gamma$ | Specific weight ($N/m^3$) |
| $\eta$ | Non-Newtonian fluid viscosity |
| $\lambda_{mfp}$ | Mean-free-path |
| $\mu$ | Dynamic viscosity (kg.m/s) |
| $\nu$ | Kinematic viscosity ($m^2/s$) |
| $\rho$ | Density ($kg/m^3$) |
| $\tau_{ij}$ | Shear stress tensor |
| $\omega$ | Angular velocity (rad/s) |
| $\psi$ | Stream function |
| $\vec{\zeta}$ | Vorticity vector |

# *Appendix II*

## AII.1 Conversion Factors

| Dimension | Metric | Metric/English |
|---|---|---|
| Acceleration | 1 $m/s^2 = 100\ cm/s^2$ | 1 $m/s^2 = 3.2808\ ft/s^2$ |
| | | 1 $ft/s^2 = 0.3048^a\ m/s^2$ |
| Area | 1 $m^2 = 10^4\ cm^2 = 10^6\ mm^2 = 10^{-6}\ km^2$ | 1 $m^2 = 1550\ in.^2 = 10.764\ ft^2$ |
| | | 1 $ft^2 = 144\ in.^2 = 0.09290304^a\ m^2$ |
| Density | 1 $g/cm^3 = 1\ kg/L = 1000\ kg/m^3$ | 1 $g/cm^3 = 62.428\ lbm/ft^3 = 0.036127$ $lbm/in.^3$ |
| | | 1 $lbm/in.^3 = 1728\ lbm/ft^3$ |
| | | 1 $kg/m^3 = 0.062428\ lbm/ft^3$ |
| Energy, heat, work, internal energy, enthalpy | 1 $kJ = 1000\ J = 1000\ N\ m = 1\ kPa\ m^3$ | 1 kJ = 0.94782 Btu |
| | 1 $kJ/kg = 1000\ m^2/s^2$ | 1 Btu = 1.055056 kJ |
| | 1 kWh = 3600 kJ | $= 5.40395\ psia \cdot ft^3 = 778.169\ lbf \cdot ft$ |
| | 1 $cal^b = 4.184$ J | 1 $Btu/lbm = 25{,}037\ ft^2/s^2 = 2.326^a\ kJ/kg$ |
| | 1 IT $cal^b = 4.1868$ J | 1 kJ/kg = 0.430 Btu/lbm |
| | 1 $cal^b = 4.1868$ kJ | 1 kWh = 3412.14 Btu |
| | | 1 therm $= 10^5$ Btu $= 1.055 \times 10^5$ kJ (natural gas) |
| Force | 1 $N = 1\ kg \cdot m/s^2 = 10^5$ dyn | 1 N = 0.22481 lbf |
| | 1 kgf = 9.80665 N | 1 $lbf = 32.174\ lbm \cdot ft/s^2 = 4.44822$ N |
| Heat flux | 1 $W/cm^2 = 10^4\ W/m^2$ | 1 $W/m^2 = 0.3171\ Btu/h \cdot ft^2$ |
| Heat transfer coefficient | 1 $W/m^2 \cdot °C = 1\ W/m^2 \cdot K$ | 1 $W/m^2 \cdot °C = 0.17612\ Btu/h \cdot ft^2 \cdot °F$ |
| Length | 1 m = 100 cm = 1000 mm = $10^6$ μm | 1 m = 39.370 in. = 3.2808 ft = 1.0926 yd |
| | 1 km = 1000 m | 1 ft = 12 in. = $0.3048^a$ m |
| | | 1 mi. = 5280 ft = 1.6093 km |
| | | 1 in. = $2.54^a$ cm |
| Mass | 1 kg = 1000 g | 1 kg = 2.2046226 lbm |
| | 1 metric ton = 1000 kg | 1 lbm = $0.45359237^a$ kg |
| | | 1 oz = 28.3495 g |
| | | 1 slug = 32.174 lbm = 14.5939 kg |
| | | 1 short ton = 2000 lbm = 907.1847 kg |
| Power, heat transfer rate | 1 W = 1 J/s | 1 kW = 3412.14 Btu/h |
| | 1 kW = 1000 W = 1.341 hp | = 737.56 lbf · ft/s |
| | 1 $hp^c = 745.7$ W | 1 hp = 550 lbf · ft/s = 0.7068 Btu/s |
| | | = 42.41 Btu/min = 2544.5 Btu/h |
| | | = 0.74570 kW |
| | | 1 boiler hp = 33,475 Btu/h |
| | | 1 Btu/h = 1.055056 kJ/h |
| | | 1 ton of refrigeration = 200 Btu/min |

(*Continued*)

**(Continued)**

| Dimension | Metric | Metric/English |
|---|---|---|
| Pressure | 1 Pa = 1 N/m$^2$ | 1 Pa = 1.4504 × 10$^{-4}$ psia |
| | 1 kPa = 10$^3$ Pa = 10$^{-3}$ MPa | = 0.020886 lbf/ft$^2$ |
| | 1 atm = 101.325 kPa = 1.01325 bar | 1 psi = 144 lbf/ft$^2$ = 6.894757 kPa |
| | = 760 mm Hg at 0°C | 1 atm = 14.696 psia = 29.92 in. Hg at 30°F |
| | = 1.03323 kgf/cm$^2$ | 1 in. Hg = 3.387 kPa |
| | 1 mm Hg = 0.1333 kPa | |
| Specific heat | 1 kJ/kg · °C = 1 kJ/kg · K = 1 J/g · C | 1 Btu/lbm · °F = 4.1868 kJ/kg · °C |
| | | 1 Btu/lbmol · R = 4.1868 kJ/kmol · K |
| | | 1 kJ/kg · °C = 0.23885 Btu/lbm · °F |
| | | =0.23885 Btu/lbm · R |
| Specific volume | 1 m$^3$/kg = 1000 L/kg = 1000 cm$^3$/g | 1 m$^3$/kg = 16.02 ft$^3$/lbm |
| | | 1 ft$^3$/lbm = 0.062428 m$^3$/kg |
| Temperature | $T$(K) = $T$(°C) + 273.15 | $T$(R) = $T$(°F) + 459.67 = 1.8$T$(K) |
| | $\Delta T$(K) = $\Delta$ $T$(°C) | $T$(°F) = 1.8 $T$(°C) + 32 |
| | | $\Delta T$(°F) = $\Delta T$(R) = 1.8 $\Delta T$(K) |
| Thermal conductivity | 1 W/m · °C = 1 W/m · K | 1 W/m · °C = 0.57782 Btu/h · ft · °F |
| Velocity | 1 m/s = 3.60 km/h | 1 m/s = 3.2808 ft/s = 2.237 mi/h |
| | | 1 mi/h = 1.4667 ft/s |
| | | 1 mi/h = 1.6093 km/h |
| Volume | 1 m$^3$ = 1000 L = 10$^6$ cm$^3$ (cc) | 1 m$^3$ = 6.1024 × 10$^4$ in.$^3$ = 35.315 ft$^3$ |
| | | = 264.17 gal (U.S.) |
| | | 1 U.S. gal = 231 in.$^3$ = 3.7854 L |
| | | 1 fl oz = 29.5735 cm$^3$ = 0.0295735 L |
| | | 1 U.S. gal = 128 fl oz |
| Volume flow rate | 1 m$^3$/s = 60,000 L/min = 10$^6$ cm$^3$/s | 1 m$^3$/s = 15,850 gal/min (gpm) = 35.315 ft$^3$/s |
| | | = 2118.9 ft$^3$/min (cfm) |

[a] Exact conversion factor between metric and English units.

[b] Calorie is originally defined as the amount of heat needed to raise the temperature of 1 g of water by 1°C, but it varies with temperature. The international steam table (IT) calorie (generally preferred by engineers) is exactly 4.1868 J by definition and corresponds to the specific heat of water at 15°C. The thermochemical calorie (generally preferred by physicists) is exactly 4.184 J by definition and corresponds to the specific heat of water at room temperature. The difference between the two is about 0.06%, which is negligible. The capitalized calorie used by nutritionists is actually a kilocalorie (1000 IT cal).

[c] Mechanical horsepower. The electrical horsepower is taken to be exactly 746 W.

### AII.1.1 Some Physical Constants

| | |
|---|---|
| Universal gas constant | $R_u = 8.31447$ kJ/kmol · K |
| | = 8.31447 kPa · m³/kmol · K |
| | = 0.0831447 bar · m³/kmol · K |
| | = 82.05 L · atm/kmol · K |
| | = 1.9858 Btu/lbmol · R |
| | = 1545.37 ft · lbf/lbmol · R |
| | = 10.73 psia · ft³/lbmol · R |
| Standard acceleration of gravity | $g = 9.80665$ m/s² |
| | = 32.174 ft/s² |
| Standard atmospheric pressure | 1 atm = 101.325 kPa |
| | = 1.01325 bar |
| | = 14.696 psia |
| | = 760 mm Hg (0°C) |
| | = 29.9213 in Hg (32°F) |
| | = 10.3323 m $H_2O$ (4°C) |
| Stefan–Boltzmann constant | $\sigma = 5.6704 \times 10^{-8}$ W/m² · K⁴ |
| | $= 0.1714 \times 10^{-8}$ Btu/h · ft² · R⁴ |
| Boltzmann's constant | $k = 1.380650 \times 10^{-23}$ J/K |
| Speed of light in vacuum | $c = 6.71 \times 10^{8}$ mph |
| | $= 9.836 \times 10^{3}$ ft/s |
| Speed of sound in dry air at 0°C and 1 atm | $c = 331.36$ m/s |
| | = 1089 ft/s |
| Heat of fusion of water at 1 atm | $h_{if} = 333.7$ kJ/kg |
| | = 143.5 Btu/lbm |
| Enthalpy of vaporization of water at 1 atm | $h_{fg} = 2256.5$ kJ/kg |
| | = 970.12 Btu/lbm |

## AII.2 Properties

**Table AII.2.1** Molar Mass, Gas Constant, and Critical-Point Properties

| | | | | Critical-Point Properties | | |
|---|---|---|---|---|---|---|
| **Substance** | **Formula** | **Molar Mass (*M* kg/kmol)** | **Gas Constant (*R* kJ/kg · K[a])** | **Temperature (K)** | **Pressure (MPa)** | **Volume (m³/kmol)** |
| Air | — | 28.97 | 0.2870 | 132.5 | 3.77 | 0.0883 |
| Ammonia | $NH_3$ | 17.03 | 0.4882 | 405.5 | 11.28 | 0.0724 |
| Argon | Ar | 39.948 | 0.2081 | 151 | 4.86 | 0.0749 |
| Benzene | $C_6H_6$ | 78.115 | 0.1064 | 562 | 4.92 | 0.2603 |
| Bromine | $Br_2$ | 159.808 | 0.0520 | 584 | 10.34 | 0.1355 |
| *n*-Butane | $C_4H_{10}$ | 58.124 | 0.1430 | 425.2 | 3.80 | 0.2547 |
| Carbon dioxide | $CO_2$ | 44.01 | 0.1889 | 304.2 | 7.39 | 0.0943 |

(*Continued*)

**Table AII.2.1 (Continued)** Molar Mass, Gas Constant, and Critical-Point Properties

| Substance | Formula | Molar Mass ($M$ kg/kmol) | Gas Constant ($R$ kJ/kg · K[a]) | Critical-Point Properties | | |
|---|---|---|---|---|---|---|
| | | | | Temperature (K) | Pressure (MPa) | Volume ($m^3$/kmol) |
| Carbon monoxide | CO | 28.011 | 0.2968 | 133 | 3.50 | 0.0930 |
| Carbon tetrachloride | $CCl_4$ | 153.82 | 0.05405 | 556.4 | 4.56 | 0.2759 |
| Chlorine | $Cl_2$ | 70.906 | 0.1173 | 417 | 7.71 | 0.1242 |
| Chloroform | $CHCl_3$ | 119.38 | 0.06964 | 536.6 | 5.47 | 0.2403 |
| Dichlorodifluoromethane (R-12) | $CCl_2F_2$ | 120.91 | 0.06876 | 384.7 | 4.01 | 0.2179 |
| Dichlorofluoromethane (R-21) | $CHCl_2F$ | 102.92 | 0.08078 | 451.7 | 5.17 | 0.1973 |
| Ethane | $C_2H_6$ | 30.070 | 0.2765 | 305.5 | 4.48 | 0.1480 |
| Ethyl alcohol | $C_2H_5OH$ | 46.07 | 0.1805 | 516 | 6.38 | 0.1673 |
| Ethylene | $C_2H_4$ | 28.054 | 0.2964 | 282.4 | 5.12 | 0.1242 |
| Helium | He | 4.003 | 2.0769 | 5.3 | 0.23 | 0.0578 |
| *n*-Hexane | $C_6H_{14}$ | 86.179 | 0.09647 | 507.9 | 3.03 | 0.3677 |
| Hydrogen (normal) | $H_2$ | 2.016 | 4.1240 | 33.3 | 1.30 | 0.0649 |
| Krypton | Kr | 83.80 | 0.09921 | 209.4 | 5.50 | 0.0924 |
| Methane | $CH_4$ | 16.043 | 0.5182 | 191.1 | 4.64 | 0.0993 |
| Methyl alcohol | $CH_3OH$ | 32.042 | 0.2595 | 513.2 | 7.95 | 0.1180 |
| Methyl chloride | $CH_3Cl$ | 50.488 | 0.1647 | 416.3 | 6.68 | 0.1430 |
| Neon | Ne | 20.183 | 0.4119 | 44.5 | 2.73 | 0.0417 |
| Nitrogen | $N_2$ | 28.013 | 0.2968 | 126.2 | 3.39 | 0.0899 |
| Nitrous oxide | $N_2O$ | 44.013 | 0.1889 | 309.7 | 7.27 | 0.0961 |
| Oxygen | $O_2$ | 31.999 | 0.2598 | 154.8 | 5.08 | 0.0780 |
| Propane | $C_3H_8$ | 44.097 | 0.1885 | 370 | 4.26 | 0.1998 |
| Propylene | $C_3H_6$ | 42.081 | 0.1976 | 365 | 4.62 | 0.1810 |
| Sulfur dioxide | $SO_2$ | 64.063 | 0.1298 | 430.7 | 7.88 | 0.1217 |
| Tetrafluoroethane (R-134a) | $CF_3CH_2F$ | 102.03 | 0.08149 | 374.2 | 4.059 | 0.1993 |
| Trichlorofluoromethane (R-11) | $CCl_3F$ | 137.37 | 0.06052 | 471.2 | 4.38 | 0.2478 |
| Water | $H_2O$ | 18.015 | 0.4615 | 647.1 | 22.06 | 0.0560 |
| Xenon | Xe | 131.30 | 0.06332 | 289.8 | 5.88 | 0.1186 |

*Source:* Kobe, K.A. and Lynn, Jr., R.E. *Chem. Rev.*, 52, 117–236, 1953 and ASHRAE, *Handbook of Fundamentals*, American Society of Heating, Refrigerating and Air-Conditioning Engineers, Inc., Atlanta, GA, pp. 16.4 and 36.1., 1993.

[a] The unit kJ/kg · K is equivalent to kPa · $m^3$/kg · K. The gas constant is calculated from $R = R_u/M$, where $R_u = 8.31447$ kJ/kmol · K and $M$ is the molar mass.

## Table AII.2.2 Ideal-Gas Specific Heats of Various Common Gases

**(a) At 300 K**

| Gas | Formula | Gas Constant ($R$ kJ/kg · K) | $C_p$ (kJ/kg · K) | $C_v$ (kJ/kg · K) | $k$ |
|---|---|---|---|---|---|
| Air | — | 0.2870 | 1.005 | 0.718 | 1.400 |
| Argon | Ar | 0.2081 | 0.5203 | 0.3122 | 1.667 |
| Butane | $C_4H_{10}$ | 0.1433 | 1.7164 | 1.5734 | 1.091 |
| Carbon dioxide | $CO_2$ | 0.1889 | 0.846 | 0.657 | 1.289 |
| Carbon monoxide | CO | 0.2968 | 1.040 | 0.744 | 1.400 |
| Ethane | $C_2H_6$ | 0.2765 | 1.7662 | 1.4897 | 1.186 |
| Ethylene | $C_2H_4$ | 0.2964 | 1.5482 | 1.2518 | 1.237 |
| Helium | He | 2.0769 | 5.1926 | 3.1156 | 1.667 |
| Hydrogen | $H_2$ | 4.1240 | 14.307 | 10.183 | 1.405 |
| Methane | $CH_4$ | 0.5182 | 2.2537 | 1.7354 | 1.299 |
| Neon | Ne | 0.4119 | 1.0299 | 0.6179 | 1.667 |
| Nitrogen | $N_2$ | 0.2968 | 1.039 | 0.743 | 1.400 |
| Octane | $C_8H_{28}$ | 0.0729 | 1.7113 | 1.6385 | 1.044 |
| Oxygen | $O_2$ | 0.2598 | 0.918 | 0.658 | 1.395 |
| Propane | $C_3H_8$ | 0.1885 | 1.6794 | 1.4909 | 1.126 |
| Steam | $H_2O$ | 0.4615 | 1.8723 | 1.4108 | 1.327 |

*Source:* Kyte, B. G., *Chemical and Process Thermodynamics*, 3rd ed., Pearson Education, Inc., Upper Saddle River, NJ, 2000. Adapted with permission.

*Note:* The unit kJ/kg · K is equivalent to kJ/kg · °C.

**(b) At Various Temperatures**

| Temperature (K) | $C_p$ (kJ/kg K) | $C_v$ (kJ/kg K) | $k$ | $C_p$ (kJ/kg · K) | $C_v$ (kJ/kg K) | $k$ | $C_p$ (kJ/kg · K) | $C_v$ (kJ/kg K) | $k$ |
|---|---|---|---|---|---|---|---|---|---|
| | Air | | | Carbon dioxide, $CO_2$ | | | Carbon monoxide, CO | | |
| 250 | 1.003 | 0.716 | 1.401 | 0.791 | 0.602 | 1.314 | 1.039 | 0.743 | 1.400 |
| 300 | 1.005 | 0.718 | 1.400 | 0.846 | 0.657 | 1.288 | 1.040 | 0.744 | 1.399 |
| 350 | 1.008 | 0.721 | 1.398 | 0.895 | 0.706 | 1.268 | 1.043 | 0.746 | 1.398 |
| 400 | 1.013 | 0.726 | 1.395 | 0.939 | 0.750 | 1.252 | 1.047 | 0.751 | 1.395 |
| 450 | 1.020 | 0.733 | 1.391 | 0.978 | 0.790 | 1.239 | 1.054 | 0.757 | 1.392 |
| 500 | 1.029 | 0.742 | 1.387 | 1.014 | 0.825 | 1.229 | 1.063 | 0.767 | 1.387 |
| 550 | 1.040 | 0.753 | 1.381 | 1.046 | 0.857 | 1.220 | 1.075 | 0.778 | 1.382 |
| 600 | 1.051 | 0.764 | 1.376 | 1.075 | 0.886 | 1.213 | 1.087 | 0.790 | 1.376 |
| 650 | 1.063 | 0.776 | 1.370 | 1.102 | 0.913 | 1.207 | 1.100 | 0.803 | 1.370 |
| 700 | 1.075 | 0.788 | 1.364 | 1.126 | 0.937 | 1.202 | 1.113 | 0.816 | 1.364 |
| 750 | 1.087 | 0.800 | 1.359 | 1.148 | 0.959 | 1.197 | 1.126 | 0.829 | 1.358 |
| 800 | 1.099 | 0.812 | 1.354 | 1.169 | 0.980 | 1.193 | 1.139 | 0.842 | 1.353 |
| 900 | 1.121 | 0.834 | 1.344 | 1.204 | 1.015 | 1.186 | 1.163 | 0.866 | 1.343 |
| 1000 | 1.142 | 0.855 | 1.336 | 1.234 | 1.045 | 1.181 | 1.185 | 0.888 | 1.335 |

(*Continued*)

**Table AII.2.2 (Continued)** Ideal-Gas Specific Heats of Various Common Gases

| (b) At Various Temperatures | | | | | | | | | |
|---|---|---|---|---|---|---|---|---|---|
| Temperature (K) | $C_p$ ( kJ/ kg K) | $C_v$ ( kJ/ kg K) | $k$ | $C_p$ (kJ/ kg · K) | $C_v$ (kJ/ kg K) | $k$ | $C_p$ (kJ/ kg · K) | $C_v$ (kJ/ kg K) | $k$ |
| | Air | | | Carbon dioxide, $CO_2$ | | | Carbon monoxide, CO | | |
| | Hydrogen, $H_2$ | | | Nitrogen, $N_2$ | | | Oxygen, $O_2$ | | |
| 250 | 14.051 | 9.927 | 1.416 | 1.039 | 0.742 | 1.400 | 0.913 | 0.653 | 1.398 |
| 300 | 14.307 | 10.183 | 1.405 | 1.039 | 0.743 | 1.400 | 0.918 | 0.658 | 1.395 |
| 350 | 14.427 | 10.302 | 1.400 | 1.041 | 0.744 | 1.399 | 0.928 | 0.668 | 1.389 |
| 400 | 14.476 | 10.352 | 1.398 | 1.044 | 0.747 | 1.397 | 0.941 | 0.681 | 1.382 |
| 450 | 14.501 | 10.377 | 1.398 | 1.049 | 0.752 | 1.395 | 0.956 | 0.696 | 1.373 |
| 500 | 14.513 | 10.389 | 1.397 | 1.056 | 0.759 | 1.391 | 0.972 | 0.712 | 1.365 |
| 550 | 14.530 | 10.405 | 1.396 | 1.065 | 0.768 | 1.387 | 0.988 | 0.728 | 1.358 |
| 600 | 14.546 | 10.422 | 1.396 | 1.075 | 0.778 | 1.382 | 1.003 | 0.743 | 1.350 |
| 650 | 14.571 | 10.447 | 1.395 | 1.086 | 0.789 | 1.376 | 1.017 | 0.758 | 1.343 |
| 700 | 14.604 | 10.480 | 1.394 | 1.098 | 0.801 | 1.371 | 1.031 | 0.771 | 1.337 |
| 750 | 14.645 | 10.521 | 1.392 | 1.110 | 0.813 | 1.365 | 1.043 | 0.783 | 1.332 |
| 800 | 14.695 | 10.570 | 1.390 | 1.121 | 0.825 | 1.360 | 1.054 | 0.794 | 1.327 |
| 900 | 14.822 | 10.698 | 1.385 | 1.145 | 0.849 | 1.349 | 1.074 | 0.814 | 1.319 |
| 1000 | 14.983 | 10.859 | 1.380 | 1.167 | 0.870 | 1.341 | 1.090 | 0.830 | 1.313 |

*Source:* Wark, K., *Thermodynamics*, 4th ed., McGraw-Hill, New York, 1983, p. 783, Table A-4M. Originally published in *Tables of Thermal Properties of Gases*, NBS Circular 564, 1955.

**Table AII.2.3** Properties of Common Liquids, Solids, and Foods

| (a) Liquids | | | | | | | |
|---|---|---|---|---|---|---|---|
| | Boiling Data at 1 atm | | Freezing Data | | Liquid Properties | | |
| Substance | Normal Boiling Point (°C) | Latent Heat of Vaporization $h_{fg}$ (kJ/kg) | Freezing Point (°C) | Latent Heat of Fusion $h_{if}$ (kJ/kg) | Temperature (°C) | Density, P (kg/ m3) | Specific Heat$c_p$ (kJ/kg · K) |
| Ammonia | –33.3 | 1357 | –77.7 | 322.4 | –33.3 | 682 | 4.43 |
| | | | | | –20 | 665 | 4.52 |
| | | | | | 0 | 639 | 4.60 |
| | | | | | 25 | 602 | 4.80 |
| Argon | –185.9 | 161.6 | –189.3 | 28 | –185.6 | 1,394 | 1.14 |
| Benzene | 80.2 | 394 | 5.5 | 126 | 20 | 879 | 1.72 |
| Brine (20% sodium chloride by mass) | 103.9 | — | –17.4 | — | 20 | 1,150 | 3.11 |
| *n*-Butane | –0.5 | 385.2 | –138.5 | 80.3 | –0.5 | 601 | 2.31 |
| Carbon dioxide | –78.4[a] | 230.5 (at 0°C) | –56.6 | | 0 | 298 | 0.59 |
| Ethanol | 78.2 | 838.3 | –114.2 | 109 | 25 | 783 | 2.46 |
| Ethyl alcohol | 78.6 | 855 | –156 | 108 | 20 | 789 | 2.84 |

(*Continued*)

**Table AII.2.3 (Continued)** Properties of Common Liquids, Solids, and Foods

**(a) Liquids**

| | Boiling Data at 1 atm | | Freezing Data | | Liquid Properties | | |
|---|---|---|---|---|---|---|---|
| **Substance** | **Normal Boiling Point (°C)** | **Latent Heat of Vaporization $h_{fg}$ (kJ/kg)** | **Freezing Point (°C)** | **Latent Heat of Fusion $h_{if}$ (kJ/kg)** | **Temperature (°C)** | **Density, P (kg/m3)** | **Specific Heat (kJ/kg · K)** |
| Ethylene glycol | 198.1 | 800.1 | −10.8 | 181.1 | 20 | 1,109 | 2.84 |
| Glycerine | 179.9 | 974 | 18.9 | 200.6 | 20 | 1,261 | 2.32 |
| Helium | −268.9 | 22.8 | — | — | −268.9 | 146.2 | 22.8 |
| Hydrogen | −252.8 | 445.7 | −259.2 | 59.5 | −252.8 | 70.7 | 10.0 |
| Isobutane | −11.7 | 367.1 | −160 | 105.7 | 11.7 | 593.8 | 2.28 |
| Kerosene | 204–293 | 251 | −24.9 | — | 20 | 820 | 2.00 |
| Mercury | 356.7 | 294.7 | −38.9 | 11.4 | 25 | 13,560 | 0.139 |
| Methane | −161.5 | 510.4 | −182.2 | 58.4 | −161.5 | 423 | 3.49 |
| | | | | | −100 | 301 | 5.79 |
| Methanol | 64.5 | 1100 | −97.7 | 99.2 | 25 | 787 | 2.55 |
| Nitrogen | −195.8 | 198.6 | −210 | 25.3 | −195.8 | 809 | 2.06 |
| | | | | | −160 | 596 | 2.97 |
| Octane | 124.8 | 306.3 | −57.5 | 180.7 | 20 | 703 | 2.10 |
| Oil (light) | | | | | 25 | 910 | 1.80 |
| Oxygen | −183 | 212.7 | −218.8 | 13.7 | −183 | 1,141 | 1.71 |
| Petroleum | — | 230–384 | | | 20 | 640 | 2.0 |
| Propane | −42.1 | 427.8 | −187.7 | 80.0 | −42.1 | 581 | 2.25 |
| | | | | | 0 | 529 | 2.53 |
| | | | | | 50 | 449 | 3.13 |
| Refrigerant-134a | −26.1 | 217.0 | −96.6 | — | −50 | 1,443 | 1.23 |
| | | | | | −26.1 | 1,374 | 1.27 |
| | | | | | 0 | 1,295 | 1.34 |
| | | | | | 25 | 1,207 | 1.43 |
| Water | 100 | 2257 | 0.0 | 333.7 | 0 | 1,000 | 4.22 |
| | | | | | 25 | 997 | 4.18 |
| | | | | | 50 | 988 | 4.18 |
| | | | | | 75 | 975 | 4.19 |
| | | | | | 100 | 958 | 4.22 |

[a] Sublimation temperature. (At pressures below the triple-point pressure of 518 kPa, carbon dioxide exists as a solid or gas. Also, the freezing-point temperature of carbon dioxide is the triple-point temperature of −56.5°C.)

**Table AII.2.4** Properties of Common Liquids, Solids, and Foods (concluded)

**(b) Solids (Values Are for Room Temperature Unless Indicated Otherwise)**

| Substance | Density ($\rho$ kg/m³) | Specific heat, $c_p$ (kJ/kg · K) | Substance | Density ($\rho$ kg/m³) | Specific heat, $c_p$ (kJ/kg · K) |
|---|---|---|---|---|---|
| **Metals** | | | **Nonmetals** | | |
| Aluminum | | | Asphalt | 2,110 | 0.920 |
| 200 K | | 0.797 | Brick, common | 1,922 | 0.79 |
| 250 K | | 0.859 | Brick, fireclay (500°C) | 2,300 | 0.960 |
| 300 K | 2,700 | 0.902 | Concrete | 2,300 | 0.653 |
| 350 K | | 0.929 | Clay | 1,000 | 0.920 |
| 400 K | | 0.949 | Diamond | 2,420 | 0.616 |
| 450 K | | 0.973 | Glass, window | 2,700 | 0.800 |
| 500 K | | 0.997 | Glass, pyrex | 2,230 | 0.840 |
| Bronze (76% Cu, 2% Zn, 2% Al) | 8,280 | 0.400 | Graphite | 2,500 | 0.711 |
| | | | Granite | 2,700 | 1.017 |
| Brass, yellow (65% Cu, 35% Zn) | 8,310 | 0.400 | Gypsum or plaster board | 800 | 1.09 |
| | | | Ice | | |
| Copper | | | 200 K | | 1.56 |
| −173°C | | 0.254 | 220 K | | 1.71 |
| −100°C | | 0.342 | 240 K | | 1.86 |
| −50°C | | 0.367 | 260 K | | 2.01 |
| 0°C | | 0.381 | 273 K | 921 | 2.11 |
| 27°C | 8,900 | 0.386 | Limestone | 1,650 | 0.909 |
| 100°C | | 0.393 | Marble | 2,600 | 0.880 |
| 200°C | | 0.403 | Plywood (Douglas Fir) | 545 | 1.21 |
| Iron | 7,840 | 0.45 | Rubber (soft) | 1,100 | 1.840 |
| Lead | 11,310 | 0.128 | Rubber (hard) | 1,150 | 2.009 |
| Magnesium | 1,730 | 1.000 | Sand | 1,520 | 0.800 |
| Nickel | 8,890 | 0.440 | Stone | 1,500 | 0.800 |

(*Continued*)

**Table AII.2.4 (Continued)** Properties of Common Liquids, Solids, and Foods (concluded)

**(b) Solids (Values Are for Room Temperature Unless Indicated Otherwise)**

| Substance | Density ($\rho$ kg/m$^3$) | Specific heat, $c_p$ (kJ/kg · K) | Substance | Density ($\rho$ kg/m$^3$) | Specific heat, $c_p$ (kJ/kg · K) |
|---|---|---|---|---|---|
| **Metals** | | | **Nonmetals** | | |
| Silver | 10,470 | 0.235 | Woods, hard (maple, oak, etc.) | 721 | 1.26 |
| Steel, mild | 7,830 | 0.500 | Woods, soft (fir, pine, etc.) | 513 | 1.38 |
| Tungsten | 19,400 | 0.130 | | | |

**(c) Foods**

| Food | Water Content (%) (mass) | Freezing Point (°C) | Specific heat (kJ/kg K) Above Freezing | Specific heat (kJ/kg K) Below Freezing | Latent Heat of Fusion (kJ/kg) | Food | Water Content (%) (mass) | Freezing Point (°C) | Specific heat (kJ/kg K) Above Freezing | Specific heat (kJ/kg K) Below Freezing | Latent Heat of Fusion (kJ/kg) |
|---|---|---|---|---|---|---|---|---|---|---|---|
| Apples | 84 | −1.1 | 3.65 | 1.90 | 281 | Lettuce | 95 | −0.2 | 4.02 | 2.04 | 317 |
| Bananas | 75 | −0.8 | 3.35 | 1.78 | 251 | Milk, whole | 88 | −0.6 | 3.79 | 1.95 | 294 |
| Beet round | 67 | — | 3.08 | 1.68 | 224 | Oranges | 87 | −0.8 | 3.75 | 1.94 | 291 |
| Broccoli | 90 | −0.6 | 3.86 | 1.97 | 301 | Potatoes | 78 | −0.6 | 3.45 | 1.82 | 261 |
| Butter | 16 | — | — | 1.04 | 53 | Salmon fish | 64 | −2.2 | 2.98 | 1.65 | 214 |
| Cheese, Swiss | 39 | −10.0 | 2.15 | 1.33 | 130 | Shrimp | 83 | −2.2 | 3.62 | 1.89 | 277 |
| Cherries | 80 | −1.8 | 3.52 | 1.85 | 267 | Spinach | 93 | −0.3 | 3.96 | 2.01 | 311 |
| Chicken | 74 | −2.8 | 3.32 | 1.77 | 247 | Strawberries | 90 | −0.8 | 3.86 | 1.97 | 301 |
| Corn, sweet | 74 | −0.6 | 3.32 | 1.77 | 247 | Tomatoes, ripe | 94 | −0.5 | 3.99 | 2.02 | 314 |
| Eggs, whole | 74 | −0.6 | 3.32 | 1.77 | 247 | Turkey | 64 | — | 2.98 | 1.65 | 214 |
| Ice cream | 63 | −5.6 | 2.95 | 1.63 | 210 | Watermelon | 93 | −0.4 | 3.96 | 2.01 | 311 |

*Source:* Values are obtained from various handbooks and other sources or are calculated. Water content and freezing-point data of foods are from ASHRAE, Handbook of Fundamentals, SI version, American Society of Heating, Refrigerating and Air-Conditioning Engineers, Inc., Atlanta, GA, 1993, Chapter 30, Table 1. Freezing point is the temperature at which freezing starts for fruits and vegetables, and the average freezing temperature for other foods.

## AII.3 Drag Coefficient: (a) Smooth Sphere and (b) an Infinite Cylinder as a Function of Reynolds Number

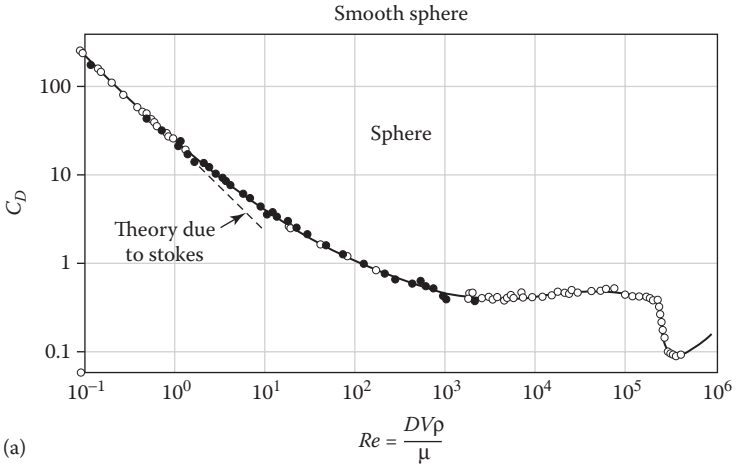


(a)

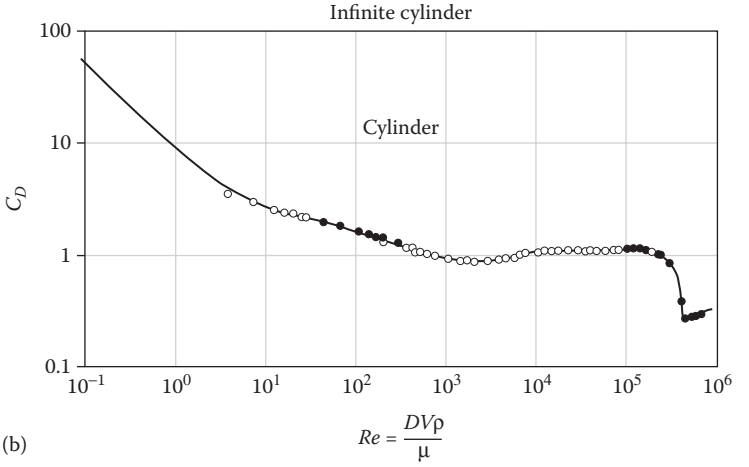


(b)

## AII.4 Moody Chart

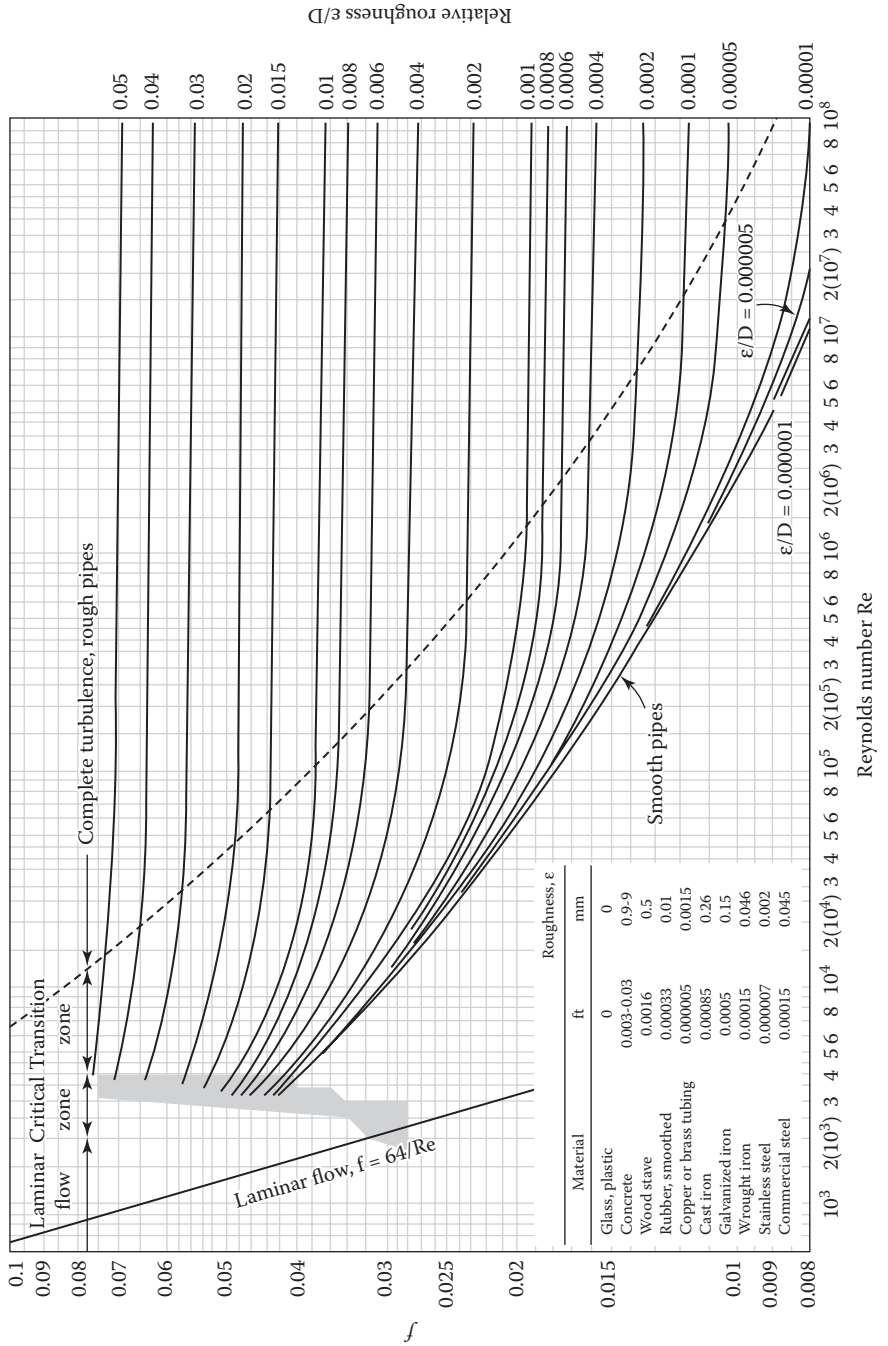

Taylor & Francis
Taylor & Francis Group
http://taylorandfrancis.com

# *Index*

Taylor & Francis
Taylor & Francis Group
http://taylorandfrancis.com